REMOTE-SENSING SOIL MOISTURE USING FOUR-DIMENSIONAL DATA ASSIMILATION

By
Paul Raymond Houser

Copyright © Paul Raymond Houser 1996

A Dissertation Submitted to the Faculty of the

DEPARTMENT OF HYDROLOGY AND WATER RESOURCES

In Partial Fulfillment of the Requirements
For the Degree of

DOCTOR OF PHILOSOPHY
WITH A MAJOR IN HYDROLOGY

In the Graduate College

THE UNIVERSITY OF ARIZONA

1996

THE UNIVERSITY OF ARIZONA ®
GRADUATE COLLEGE

As members of the Final Examination Committee, we certify that we have read the dissertation prepared by Paul Raymond Houser

entitled Remote Sensing Soil Moisture using Four Dimensional Data Assimilation

and recommend that it be accepted as fulfilling the dissertation requirement for the Degree of Doctor of Philosophy

W. James Shuttleworth — Date 11/20/96

Robert Dickinson — Date 11/1/96

Hoshin Gupta — Date 11/1/96

Charles Hutchinson — Date 11/1/96

Date

Final approval and acceptance of this dissertation is contingent upon the candidate's submission of the final copy of the dissertation to the Graduate College.

I hereby certify that I have read this dissertation prepared under my direction and recommend that it be accepted as fulfilling the dissertation requirement.

Dissertation Director — Date 11/20/96

STATEMENT BY AUTHOR

This dissertation has been submitted in partial fulfillment of requirements for an advanced degree at The University of Arizona and is deposited in the University Library to be made available to borrowers under rules of the Library.

Brief quotations from this dissertation are allowable without special permission, provided that accurate acknowledgment of source is made. Requests for permission for extended quotation from or reproduction of this manuscript in whole or in part may be granted by the copyright holder.

SIGNED: Paul R Hanna

ACKNOWLEDGMENTS

I would like to thank all those who have contributed time and effort to make this research effort a reality. This research builds on and uses a large collection of observations and simulation techniques that were collected and developed by many. Special thanks go to the personnel of the USDA-ARS for providing the data for this research.

My dissertation committee deserves special thanks for their guidance in my graduate endeavor. I must first thank my primary research advisor, Jim Shuttleworth. Jim always encouraged me to pursue my ideas, offered innumerable creative insights, and guided me with an unmatched wisdom. I thank my co-advisor, Soroosh Sorooshian, for his support and encouragement of excellence in all phases of my professional development. I thank Dave Goodrich for sharing his thoughtful insight and knowledge not only about Walnut Gulch, but hydrology in general. Robert Dickinson offered genuine support of my research and valuable insights on hydrologic data assimilation. Stuart Marsh's expertise and insights in remote-sensing were invaluable. I also thank Charles Hutchinson for participation in my final exam in the absence of Stuart Marsh. Finally, Hoshin Gupta offered valuable insights and discussion on hydrologic data assimilation and parameter calibration.

On a late-summer afternoon in Boulder, Jay Famiglietti unwittingly helped to spark this research. Since then, he has become an integral component of it through his valuable insights and advice, modeling expertise, and personal support. I also thank Judith Berglund for utilizing her GIS expertise to help develop the data sets used in this project and for her assistance in developing an excellent Walnut Gulch literature review.

I thank Cary White for his help with processing and checking Walnut Gulch data sets; our teamwork in dealing with frustrations and problems with compilation and simulation of this data enhanced both our research. Next thanks go to Cary, Jaime Garatuza, Altaf Mohammed, Russ Scott, Tim Keefer, and Chawn Harlow for their field assistance. Finally, I must thank the "lunch crew", Jean Morrill, Dave Quanrud, Jim Leehouts, Martha Whittaker, and Betsy Woodhouse for their patient ears.

I thank Jim Broermann and Dan Brathwaite for their patient and consistent computer assistance. I also thank Robert Dickinson, Soroosh Sorooshian, and Jay Famiglietti for the use of their computer systems in support of this research.

Special thanks go to Kamran Syed and the USDA-ARS for their assistance in spatial precipitation interpolation.

I thank NASA for their financial support of this research through grant #NAGW-4165 and through the award of a Global Change Fellowship.

I wish to thank my family for their unwavering support and encouragement. I thank my parents, Ron and Eileen, for instilling a sense of wonder and exploration in me. I thank my life-partner and best friend, Jennifer, who has been my primary support in this endeavor through her thoughtful advice, encouragement, and strength. Our future together is one of the primary motivating factors in my life. I also thank Jenny's parents, Dave, Shari, Paula, and Pat for years of unquestioning devotion to my pursuits of this degree.

Most importantly, I wish to thank my Savior and Creator, Jesus Christ. It is only through Him that my life has meaning and direction.

DEDICATION

This work is dedicated to:

My Family for their Love and Support

Jennifer

Alexandra

Ron and Eileen

Shari and Pat

Dave and Paula

TABLE OF CONTENTS

Page

LIST OF ILLUSTRATIONS 11

LIST OF TABLES 17

ABSTRACT 19

1. INTRODUCTION AND BACKGROUND 20
1.1 Overview and problem statement 20
1.2 Motivation and real world application 22
1.2.1 Definition of soil moisture 22
1.2.2 Soil moisture applications 24
1.2.2.1 Agriculture 25
1.2.2.2 Forest ecology and management 25
1.2.2.3 Civil engineering 26
1.2.2.4 Hydrologic management and modeling 26
1.2.2.5 Climate system modeling 29
1.2.2.6 Meteorology 30
1.2.2.7 Ecosystem modeling 31
1.2.2.8 Soil science and crop system modeling 31
1.2.3 Summary of remotely-sensed soil moisture applications and scales. 32
1.3 Objectives and scope 33
1.4 Approach 33
1.5 Structural overview 34
1.6 Background 34
1.6.1 Soil moisture measurement networks 35
1.6.2 Soil moisture remote-sensing 35
1.6.2.1 Dielectric constant 37
1.6.2.2 Various wavelengths 40
1.6.2.2.1 Visible and infrared wavelengths 40
1.6.2.2.2 Gamma wavelengths 42
1.6.2.2.3 Thermal wavelengths 42
1.6.2.2.4 Microwave wavelengths 44
1.6.2.2.5 Remote-sensing soil moisture summary 51
1.6.2.3 Measurements similar to soil moisture 51
1.6.2.3.1 Normalized difference vegetation index 51
1.6.2.3.2 Palmer drought severity index 52
1.6.2.3.3 Antecedent precipitation index 52
1.6.2.4 Remote-sensing platforms 52
1.6.2.4.1 PBMR 54
1.6.2.4.2 IROE multiband sensor package 55
1.6.2.4.3 AIRSAR 55
1.6.2.4.4 ESTAR 58
1.6.2.4.5 Landsat MSS/TM 58
1.6.2.4.6 SPOT 59
1.6.2.4.7 TIROS/NOAA 60
1.6.2.4.8 Explorer-A and Nimbus-7 60

TABLE OF CONTENTS - *Continued*

Page

1.6.2.4.9 Seasat 61
1.6.2.4.10 SIR-C 63
1.6.2.4.11 Japan's MOS-1 and ERS-1 63
1.6.2.4.12 ERS-1 63
1.6.2.4.13 Radarsat 64
1.6.2.4.14 SSM/I 64
1.6.2.4.15 NASA-EOS missions 64
1.6.2.4.16 GOES 66
1.6.2.4.17 Bhaskara-II 66
1.6.2.4.18 Priroda 67
1.6.2.4.19 Future smallsat soil moisture platforms 67
1.6.2.5 Remote-sensing soil moisture extrinsic effects 67
1.6.2.5.1 Vegetation/surface cover 68
1.6.2.5.2 Surface roughness 69
1.6.2.5.3 Atmospheric effects 70
1.6.2.5.4 Heterogeneity and mixed scenes 72
1.6.2.5.5 Field calibrations 73
1.6.2.6 Remote-sensing soil moisture examples 75
1.6.2.7 Soil moisture remote-sensing summary 77
1.6.3 Soil moisture modeling 83
1.6.4 Four-dimensional data assimilation 85
1.6.4.1 Methods 87
1.6.4.1.1 Direct insertion or updating 94
1.6.4.1.2 Newtonian nudging 94
1.6.4.1.3 Objective or statistical interpolation 98
1.6.4.1.4 Successive corrections 103
1.6.4.1.5 Variational methods 109
1.6.4.1.6 Adjoint methods 110
1.6.4.1.7 Kalman filtering 111
1.6.4.2 Operational data assimilation 113
1.6.4.3 Hydrologic data assimilation 113
1.7 Background summary 117

2. MODEL STRUCTURE AND DESCRIPTION 120
2.1 Introduction 120
2.2 The TOPLATS model 120
2.2.1 TOPMODEL 121
2.2.2 TOPLATS prognostic equations 127
2.2.2.1 Water-balance equations 127
2.2.2.2 Energy-balance, potential evapotranspiration, and surface temperature 132
2.2.2.3 Local water- and energy-balance fluxes 134
2.2.2.4 Aggregation to the catchment scale 134
2.2.2.4.1 Lateral subsurface flow and water table dynamics 135
2.2.2.4.2 Local water- and energy-balance 136
2.2.2.4.3 Saturated zone water-balance 137

TABLE OF CONTENTS - *Continued*

Page
2.2.2.4.4 Catchment water- and energy-balance fluxes 137
2.2.2.5 Aggregation to the macroscale 138
2.2.2.5.1 Saturated zone water-balance 139
2.2.2.5.2 Macroscale water- and energy-balance fluxes 140
2.2.3 Model sensitivities 140
2.3 TOPLATS modifications 140
2.3.1 Addition of remote-sensing sensitive surface layer 147
2.3.2 TOPLATS parameterization modification 150
2.3.3 Redefined input/output structure 155
2.3.4 Data assimilation modifications 156
2.4 Computational aspects 164
2.5 Conclusions 165

3. RESEARCH LOCATION AND EXPERIMENTAL DESIGN 166
3.1 Introduction 166
3.2 Walnut Gulch Experimental Watershed 167
3.2.1 Monsoon '90 169
3.2.2 Post-Monsoon '90 data base 172
3.3 Model domain 177
3.4 Area-average site characteristics 178
3.4.1 Soil parameters 178
3.4.2 Vegetation parameters 181
3.4.3 Saturated water surface 181
3.5 Spatially distributed site characteristics 185
3.5.1 Soil parameters 185
3.5.2 Vegetation parameters 189
3.5.3 Topography 192
3.6 Forcing data 195
3.6.1 Meteorology 195
3.6.2 Precipitation 197
3.6.2.1 Multiquadric-biharmonic interpolation 202
3.6.2.2 Rainfall data checking 202
3.7 Assimilation data 203
3.7.1 PBMR soil moisture 203
3.7.1.1 Soil moisture inversion 206
3.7.1.2 Correlation structure analysis 208
3.8 Validation data 213
3.8.1 Gravimetric soil moisture 213
3.8.2 Resistance soil moisture 213
3.8.3 TDR soil moisture 213
3.8.4 Surface energy fluxes 216
3.8.4.1 Comparison with regional fluxes 218
3.8.4.2 Monsoon '90 water-balance 223
3.8.4.3 Correction methodology 224
3.8.4.4 Lucky Hills 1996 eddy correlation observations 225
3.8.5 Infiltration and runoff 225
3.9 Conclusions 231

TABLE OF CONTENTS - *Continued*

Page

4. TOPMODEL AT WALNUT GULCH 233
4.1 Introduction and background 233
4.2 Model definition 233
4.3 Model performance measures 236
4.4 TOPLATS calibration results and verification 236
4.5 Conclusions 237

5. TOPLATS SENSITIVITY, CALIBRATION, AND VALIDATION 239
5.1 Introduction 239
5.2 Sensitivity to spatial parameters 241
5.3 Model calibration and verification 243
5.3.1 Calibration parameters 243
5.3.2 Objective functions 250
5.3.3 Model performance measures 251
5.3.4 Monte-Carlo calibration 251
5.3.4.1 Single-objective calibration 252
5.3.4.2 Elimination of nighttime data 252
5.3.4.3 Multi-objective Pareto set determination 253
5.3.4.4 Maximum error cut-off 254
5.3.4.5 Objective function reduction 255
5.3.4.6 Inclusion of soil characteristics in calibration 256
5.4 Acceptable model parameters 260
5.5 TOPLATS-Monsoon '90 control run 262
5.6 Aggregation study 268
5.7 Conclusions 268

6. SOIL MOISTURE DATA ASSIMILATION 272
6.1 Introduction 272
6.2 Calibrated control 273
6.3 Direct insertion 274
6.4 Statistical correction 282
6.5 Assimilation information sensitivity 283
6.6 Statistical correction with updating 287
6.7 Newtonian nudging 294
6.8 Statistical correction local nudging 298
6.9 Statistical interpolation 306
6.10 Comparison of assimilation methods 318
6.11 Conclusions 322

7. CONCLUSIONS AND FUTURE DIRECTIONS 323
7.1 Major conclusions and contributions 323
7.1.1 Precursory investigation 323
7.1.2 SVATS calibration 324
7.1.3 Data assimilation 325
7.1.3.1 Simple approaches 325
7.1.3.2 Newtonian nudging 326

TABLE OF CONTENTS - *Continued*

Page
7.1.3.3 Statistical interpolation 326
7.2. Concluding summary 327
7.3 Discussion 328
7.3.1 Walnut Gulch study area 328
7.3.2 Implications for hydrologic modeling 329
7.3.3 Practical aspects of hydrologic data assimilation 329
7.3.3.1 Tradeoff between data assimilation complexity and data representation 329
7.3.3.2 Resolution versus large area implementation 330
7.3.4 Operational implication for soil moisture remote sensing 330
7.3.4.1 Required soil moisture observation qualities 330
7.3.3.2 Required data 331
7.4 Recommended future research directions 331
7.4.1 Future SVATS enhancements 331
7.4.1.1 Runoff routing 332
7.4.1.2 Snow model 332
7.4.1.3 Programmatic enhancements 332
7.4.1.4 Additional suggested modifications 333
7.4.2 Additional assimilation techniques 333
7.4.3 Temperature assimilation 334
7.4.4 Extension to larger regional and global scales 334

APPENDIX A: ACRONYMS AND ABBREVIATIONS 335

APPENDIX B: REQUIRED TOPLATS DATA 337

APPENDIX C: WALNUT GULCH, MONSOON '90 METEOROLOGICAL DATA ... 338

APPENDIX D: USDA-ARS RAINFALL DATA FORMAT 340

APPENDIX E: USDA-ARS RAINFALL DATA SAMPLE 341

APPENDIX F: MONTE-CARLO CALIBRATION RESULTS 342

APPENDIX G: TOPLATS SPATIALLY DISTRIBUTED CALIBRATED CONTROL RUN DIAGNOSTICS 352

APPENDIX H: PERMISSIONS 363

REFERENCES 371

LIST OF ILLUSTRATIONS

Figure **Page**
Figure 1.1: Outline of four-dimensional data assimilation (4DDA). Observations are inserted into the data assimilation model (identical to the prediction model) as they become available (Bengtsson, 1985). 23
Figure 1.2: Increase in forecasting skill at ECMWF over a decade using data assimilation techniques (Lange, 1989). 23
Figure 1.3: Different soil moisture applications (Lawford, 1992). 27
Figure 1.4: Differences between clearcut and forested (Adams *et al*, 1991). 27
Figure 1.5: Atmospheric transmission and spectral wavelengths (Sabins, 1987). 38
Figure 1.6: Typical spectral reflectance curves (Lillesand and Keifer, 1987). 39
Figure 1.7: Soil texture triangle (Swain and Davis, 1978). 39
Figure 1.8: Organic matter versus reflectance (Swain and Davis, 1978). 39
Figure 1.9: Newtonia silt loan at various moisture contents (Swain and Davis, 1978). 39
Figure 1.10: Iron oxide versus soil reflectance (Swain and Davis., 1978). 41
Figure 1.11: Real and complex parts of the dielectric constant (Schmugge, 1985). 41
Figure 1.12: Electromagnetic spectrum on a log scale (Schmugge, 1985). 41
Figure 1.13: Spectral emitttance for different temperatures (Meier, 1981). 48
Figure 1.14: Microwave penetration depth with frequency (Engman, 1991a). 48
Figure 1.15: Sources of microwave radiation (Schmugge, 1985). 48
Figure 1.16: Schematic of radar intensity patterns (Schmugge, 1985). 49
Figure 1.17: Microwave emissivity versus soil moisture (Schmugge, 1985). 50
Figure 1.18: Monsoon '90 PBMR brightness temperatures. 56
Figure 1.19: PBMR brightness temperatures versus Metsite gravimetric soil moisture for Walnut Gulch (Schmugge *et al.*, 1994). Lines represent different model fits. 57
Figure 1.20: Components of a passive microwave signal (Lillesand and Keifer, 1987). . . . 71
Figure 1.21: Sources of radar backscatter (Schmugge, 1985). 71
Figure 1.22: Relationship between normalized brightness and soil moisture (Jackson, 1982) 71
Figure 1.23: Correlations for 2 different watersheds (Wang *et al.*, 1989). 78
Figure 1.24: Top 5cm soil moisture on 28 May 1987 (Wang *et al.*, 1989). 79
Figure 1.25: Top 5cm soil moisture on 4 June 1987 (Wang *et al.*, 1989). 79
Figure 1.26: False color PBMR brightness maps for a 4x4 km section of the FIFE study area (Schmugge *et al.*, 1992). 80
Figure 1.27: PBMR images of 20 cm brightness temperature during Monsoon '90. Metflux sites are marked with an X (Schmugge *et al.*, 1992). 80
Figure 1.28: ESMR brightness temperatures (Schmugge *et al.*, 1975). 81
Figure 1.29: The TOPLATS four-dimensional data assimilation process. 89
Figure 1.30: The direct insertion of 400 mb zonal wind with various levels of error (Charney *et al.*, 1969). 95
Figure 1.31: The horizontal weighting function can be determined by many techniques (Cressman, Barnes, optimal interpolation, etc.). 99
Figure 1.32: The Stauffer and Seaman, (1990) nudging vertical weighting function. 99
Figure 1.33: The Lyne *et al.* (1982) and Stauffer and Seaman (1990) nudging temporal weighting functions. 99
Figure 1.34: Observed-minus-background (climatology) correlation for the 500 mb height as a function of distance between station pairs (Schlatter, 1975). 105
Figure 1.35: United States station pair correlations: annual anomalies 1920-1980 (Gunst, 1995) 105

LIST OF ILLUSTRATIONS - *Continued*

Figure Page
Figure 1.36: Observed-minus-background correlation for the 500 mb geopotential as a function of distance between stations. Curve c is for a climatological background, and curve f is for a forecast background (Schlatter, 1975). 106
Figure 1.37: Horizontally correlated observation error for the 500 mb geopotential over western Europe (Baker *et al.*, 1987). 106
Figure 1.38: Vertical geopotential background error correlations (Lönnberg and Hollingsworth, 1986). 107
Figure 1.39: Vertical geopotential observation error correlations for radiosondes (Lönnberg and Hollingsworth, 1986). 108
Figure 1.40 Normalized error variance of x (Milly, 1986a). 119
Figure 1.41: Normalized increase in error variance of x (Milly, 1986a). 119
Figure 2.1: TOPLATS modeled processes. 122
Figure 2.2: Illustration of TOPMODEL water table dynamics. 128
Figure 2.3: Diagram of TOPMODEL storages. 128
Figure 2.4: Model representation of subgrid-scale land-surface heterogeneity in topography, soils, and soil moisture. a, b, and c represent a range of soil moisture states (Famiglietti, 1992). 141
Figure 2.5: Soil moisture characteristic relationships for matric head and hydraulic conductivity for several soil types (Famiglietti, 1992). 142
Figure 2.6: Potential evaporation for four different soil types, minimum stomatal resistance, and vegetation canopy height (Famiglietti, 1992). 143
Figure 2.7: Rate of capillary rise versus water table depth for different soil types (Famiglietti, 1992). 144
Figure 2.8: Actual evaporation versus time from a silt loam for four different values of initial soil moisture (Famiglietti, 1992). 144
Figure 2.9: Transpiration capacity versus soil moisture for four different soil types, root activity factor (F), and root resistances (R_u) (Famiglietti, 1992). 145
Figure 2.10: Drainage rates versus soil moisture for several soil types (Famiglietti, 1992) 146
Figure 2.11: Diagram of old versus new TOPLATS soil definition. 151
Figure 3.1: Schematic illustrating the location and boundaries of the USDA-ARS Walnut Gulch Experimental Watershed in Southeastern Arizona. Grass- or brush-dominated ecosystems are mapped, and the location of the Lucky Hills and Kendall sites are shown (Kustas and Goodrich, 1994). 170
Figure 3.2: The location of Walnut Gulch watershed boundaries, drainages, flume locations, and rain gauge locations. The grid represents the TOPLATS model domain. Each square on the figure represents 144 (12 x 12) model grids. 171
Figure 3.3: Location of Monsoon '90 remote-sensing flight lines in relation to Metflux sites. 174
Figure 3.4: Walnut Gulch Metflux site 1, otherwise known as Lucky Hills 175
Figure 3.5: Meteorological instrumentation at Walnut Gulch Metflux site 1. 175
Figure 3.6: Walnut Gulch Metflux site 2. 175
Figure 3.7: Walnut Gulch Metflux site 3. 175
Figure 3.8: Walnut Gulch Metflux site 4. 175
Figure 3.9: Flume measurement at Walnut Gulch Metflux site 5. 175
Figure 3.10: Meteorological instrumentation at Walnut Gulch Metflux site 5. 176
Figure 3.11: Soil profile at Walnut Gulch Metflux site 5. 176
Figure 3.12: Walnut Gulch Metflux site 6. 176

LIST OF ILLUSTRATIONS - *Continued*

Figure Page
Figure 3.13: Walnut Gulch Metflux site 7. 176
Figure 3.14: Walnut Gulch Metflux site 8. 176
Figure 3.15: Flume 1 at Walnut Gulch outlet. 176
Figure 3.16: (a) Lucky Hills, (b) Kendall-north, and (c) Kendall-south profile average soil temperatures for Monsoon '90 day 200 through 227. 182
Figure 3.17: (a) Lucky Hills, (b) Kendall-north, and (c) Kendall-south profile simulated soil temperatures for Monsoon '90 day 200 through 227. 183
Figure 3.18: Hydrogeologic map of the Walnut Gulch Experimental Watershed (Spangler, 1969). 186
Figure 3.19: GIS coverage of Walnut Gulch vegetation. 188
Figure 3.20: GIS coverage of Walnut Gulch soils. 188
Figure 3.21: TOPLATS spatially distributed soils parameters. 190
Figure 3.22: TOPLATS spatially distributed soils parameters. 191
Figure 3.23: TOPLATS spatially distributed vegetation parameters. 193
Figure 3.24: Walnut Gulch 40 m resolution orographic photo-derived DEM, filled sinks, and topographic index. 196
Figure 3.25: The 8 Metflux sites average (a) solar and net radiation, (b) interpolated precipitation, (c) air temperature, (d) specific humidity (Kendall and Lucky Hills sites), and (e) wind speed during the Monsoon '90 field campaign. 198
Figure 3.26: The Metflux average (a) solar and net radiation, (b) interpolated precipitation, (c) air temperature, (d) specific humidity (Kendall and Lucky Hills sites), and (e) wind speed for post-Monsoon '90 time periods. 199
Figure 3.27: Hourly multiquadric interpolated rainfall for a storm on day 213 of Monsoon '90 204
Figure 3.28: Hourly multiquadric interpolated rainfall for a storm on day 224 of Monsoon '90 205
Figure 3.29: PBMR-derived soil moisture for Monsoon '90. 210
Figure 3.30: Correlation distances for (a) PBMR soil moisture 6 point time series; (b) PBMR soil moisture 5- and 6-point time series; (c) PBMR brightness temperature 6-point time series; (d) PBMR brightness temperature 5- and 6-point time series. Data presented are a randomly selected 0.01% selection of the total. 211
Figure 3.31: Variograms for a random 1 percent selection of day (a) 212, (b) 214, (c) 216, (d) 217, (e) 221, PBMR brightness temperatures. 212
Figure 3.32: Monsoon '90 gravimetric time series for each Metflux site. 214
Figure 3.33: Monsoon '90 resistance soil moisture at each Metflux site. 215
Figure 3.34: Monsoon '90 TDR observations at Metflux sites 1 and 5. 217
Figure 3.35: Correlation distances for time series of temperature variance sensible and latent heat flux, soil heat flux, and resistance soil moisture. 220
Figure 3.36: Comparison of the observed sensible heat flux of four semi-arid locations for similar seasons (a) Monsoon '90, (b) Tucson Mt. Site, (c) an irrigated crop at Obregon, Mexico, and (d) a riparian site at Rio Rico, Arizona. 221
Figure 3.37: Monsoon '90 average Metsite temperature variance-derived latent heat flux versus eddy correlation-derived latent heat flux. 222
Figure 3.38: Latent and sensible water-balance corrected Monsoon '90 fluxes. 226
Figure 3.39: 20-minute sonic anemometer eddy correlation versus temperature variance latent heat flux. 228

LIST OF ILLUSTRATIONS - *Continued*

Figure Page
Figure 3.40: 20-minute sonic anemometer eddy correlation versus temperature variance sensible heat flux. 228
Figure 3.41: a) Downslope increase in soil moisture over several days in 1996, and b) position of transect in relation to Lucky Hills measurements. 229
Figure 3.42: Walnut Gulch watershed average precipitation and runoff (at Flume 1) during Monsoon '90. 232
Figure 4.1: TOPMODEL performance at Walnut Gulch, Monsoon '90. 238
Figure 5.1: Watershed average (a) latent heat flux, (b) sensible heat flux, (c) soil heat flux, and (d) soil moisture from the fully distributed TOPLATS control run with default parameters 240
Figure 5.2: TOPLATS spatial predictions of (a) surface soil moisture, (b) latent heat flux, and (c) sensible heat flux on day 219 using spatially variable soils and vegetation parameters 244
Figure 5.3: TOPLATS spatial predictions of (a) surface soil moisture, (b) latent heat flux, and (c) sensible heat flux on day 219 using spatially constant soils and vegetation parameters 245
Figure 5.4: TOPLATS control run of spatially variable surface soil moisture at 12:00 p.m. on days (a) 204, (b) 208, (c) 212, (d) 216, (e) 220, and (f) 224 using spatially variable soil and vegetation parameters. 246
Figure 5.5: TOPLATS control run of spatially variable surface soil moisture at 12:00 p.m. on days (a) 204, (b) 208, (c) 212, (d) 216, (e) 220, and (f) 224 using spatially constant soil and vegetation parameters. 247
Figure 5.6: TOPLATS spatially variable sensitivity runs. 248
Figure 5.7: TOPLATS spatially variable sensitivity runs. 249
Figure 5.8: Eight parameter Pareto set normalized day data objective function values. . . . 257
Figure 5.9: Day data objective function values versus the minimum stomatal resistance parameter for the original eight parameter Monte-Carlo calibration set. 258
Figure 5.10: Day data objective function values versus the percent sand parameter for the five soil parameter Monte-Carlo calibration set. 259
Figure 5.11: Pareto set size versus Monte-Carlo sample size for various parameter and objective function configurations. 263
Figure 5.12: Best five objective function values for the 13-parameter, 3-objective Pareto set. Normalized parameter and objective function values for day-corrected data are shown. Here, objective 1 = sensible heat flux, 2 = latent heat flux, 3= soil heat flux, and 4 = resistance soil moisture. Parameter 1 = RTACT, 2 = RTDENS, 3 = RTRES, 4 = SMPET, 5 = PSICRI, 6 = DHEAT, 7 = TDEEP, 8 = RSMIN, 9 = PSND, 10 = PCLY, 11 = KSAT, 12 = THETAS, and 13 = THETAR. 264
Figure 5.13: Pareto set normalized objective function and parameter values shown for the 13-parameter, 3-objective function Monte-Carlo calibration. Here, objective 1 = sensible heat flux, 2 = latent heat flux, 3= soil heat flux, and 4 = resistance soil moisture. Parameter 1 = RTACT, 2 = RTDENS, 3 = RTRES, 4 = SMPET, 5 = PSICRI, 6 = DHEAT, 7 = TDEEP, 8 = RSMIN, 9 = PSND, 10 = PCLY, 11 = KSAT, 12 = THETAS, and 13 = THETAR 265
Figure 5.14: Latent and sensible heat flux prediction range for the 13-parameter, 3-day corrected data objective function Pareto set. The 'best' parameter set TOPLATS prediction are indicated as well. 266

LIST OF ILLUSTRATIONS - *Continued*

Figure Page
Figure 5.15: Soil heat flux and soil moisture prediction range for the 13-parameter, 3-day corrected data objective function Pareto set. The 'best' parameter set TOPLATS prediction is indicated as well. 267
Figure 5.16: Comparison between the latent, sensible, and soil heat flux, and soil moisture as calculated by a single aggregate TOPLATS model and the distributed array of TOPLATS models for Monsoon '90. 269
Figure 5.17: Time series comparisons of latent, sensible, and soil heat flux, and soil moisture as calculated by a single aggregate TOPLATS model and the distributed array of TOPLATS models for Monsoon '90. 270
Figure 6.1: TOPLATS calibrated control simulation watershed average soil moisture. . . . 275
Figure 6.2: TOPLATS calibrated control simulation spatial surface soil moisture. 276
Figure 6.3: TOPLATS direct insertion assimilation simulation watershed average surface fluxes and temperature. 279
Figure 6.4: TOPLATS direct insertion assimilation simulation watershed average soil moisture 280
Figure 6.5: TOPLATS direct insertion assimilation simulation spatial soil moisture. 281
Figure 6.6: TOPLATS statistical corrections assimilation simulation watershed average surface fluxes and temperature. 284
Figure 6.7: TOPLATS statistical corrections assimilation simulation watershed average soil moisture. 285
Figure 6.8: TOPLATS statistical corrections assimilation simulation spatial soil moisture 286
Figure 6.9: Sensitivity of assimilation information on watershed average surface soil moisture prediction using statistical corrections. 288
Figure 6.10: Sensitivity of assimilation information on watershed average surface soil moisture prediction using statistical corrections. 289
Figure 6.11: Sensitivity of assimilation information on spatial surface soil moisture prediction using statistical corrections. 290
Figure 6.12: Sensitivity of assimilation information on spatial surface soil moisture prediction using statistical corrections. 291
Figure 6.13: TOPLATS statistical corrections updating assimilation simulation watershed average surface fluxes and temperature. 292
Figure 6.14: TOPLATS statistical corrections updating assimilation simulation watershed average soil moisture. 293
Figure 6.15: TOPLATS statistical corrections updating assimilation simulation spatial soil moisture 296
Figure 6.16: TOPLATS nudging(1) assimilation simulation spatial soil moisture. 299
Figure 6.17: TOPLATS nudging(2) assimilation simulation spatial soil moisture. 300
Figure 6.18: TOPLATS nudging(3) assimilation simulation spatial soil moisture. 301
Figure 6.19: TOPLATS nudging(4) assimilation simulation spatial soil moisture. 302
Figure 6.20: TOPLATS nudging(4) assimilation simulation watershed average surface fluxes and temperature. 303
Figure 6.21: TOPLATS nudging(4) assimilation simulation watershed average soil moisture 304
Figure 6.22: TOPLATS statistical corrections nudging assimilation simulation spatial soil moisture. 305

LIST OF ILLUSTRATIONS - *Continued*

Figure Page
Figure 6.23: (a) PBMR and (b) TOPLATS soil moisture error correlation versus distance, and PBMR soil moisture error versus distance for (c) the 100 random observation reanalysis and (d) the 100 super-observation reanalysis. 311
Figure 6.24: Surface soil moisture background error correlation versus distance for (a) 6-point time series, and (b) 5-point time series. Plots represent a 0.1% selection of total data 312
Figure 6.25: 6-point time series surface soil moisture background error correlation versus distance for (a) the 100 random observation reanalysis, and (b) the 100 super-observation reanalysis. Plots represent a 0.1% selection of total data. 313
Figure 6.26: TOPLATS 100 random observation statistical interpolation assimilation simulation spatial soil moisture. 314
Figure 6.27: TOPLATS 100 super-observation statistical interpolation assimilation simulation spatial soil moisture. 315
Figure 6.28: TOPLATS 100 super-observation statistical interpolation assimilation simulation watershed average surface fluxes and temperature. 316
Figure 6.29: TOPLATS 100 super-observation statistical interpolation assimilation simulation watershed average soil moisture. 317
Figure 6.30: Comparison of TOPLATS spatial surface soil moisture on day 219 from various assimilation simulations. 319
Figure 6.31: Comparison of TOPLATS spatial surface soil moisture on day 219 from various assimilation simulations. 320
Figure 6.32: a) Comparison of TOPLATS watershed average surface zone soil moisture time series from various assimilation simulations. b) Comparison of TOPLATS watershed average root zone soil moisture time series from various assimilation simulations. . . 321
Figure G.1: TOPLATS-calibrated control run watershed average surface meteorology. . . 353
Figure G.2: TOPLATS-calibrated control run watershed average radiation and hydrology 354
Figure G.3: TOPLATS-calibrated control run temperature, runoff, and precipitation watershed statistics. 355
Figure G.4: TOPLATS-calibrated control run watershed average energy-balance. 356
Figure G.5: TOPLATS-calibrated control run energy-balance watershed statistics. 357
Figure G.6: TOPLATS-calibrated control run watershed average soil moisture. 358
Figure G.7: TOPLATS-calibrated control run soil moisture watershed statistics. 359
Figure G.8: TOPLATS-calibrated control run Metflux sites 1-4 surface soil moisture. . . . 360
Figure G.9: TOPLATS-calibrated control run Metflux sites 5-8 surface soil moisture. . . . 361
Figure G.10: TOPLATS-calibrated control run Metflux sites 1 and 5 root zone soil moisture 362

LIST OF TABLES

Table **Page**
Table 1.1: Characteristics of soil moisture data needs (Engman, 1991a). 32
Table 1.2: Common microwave bands. 45
Table 1.3: Comparison of passive and active microwave systems (Engman, 1992b). 46
Table 1.4: Summary of remotely-sensed soil moisture approaches (Schmugge *et al.*, 1979, and Engman, 1991a). 51
Table 1.5: Landsat MSS multispectral scanner wavebands. 58
Table 1.6: Landsat Thematic Mapper wavebands (Mather, 1987). 59
Table 1.7: SPOT satellite and HRV sensor wavebands (Mather, 1987). 59
Table 1.8: NOAA/TIROS satellite details and AVHRR sensor (Mather, 1987). 60
Table 1.9: Explorer-A satellite and HCMM sensor (Mather, 1987). 61
Table 1.10: NIMBUS-7 satellite and CZCS sensor (Mather, 1987). 62
Table 1.11: Seasat satellite and SAR sensor (Mather, 1987). 62
Table 1.12: ASTER instrument satellite and wavebands (Enmark, 1993; and Ono *et al.*, 1991) 66
Table 3.1: Location of Metflux sites, the corresponding distributed model's pixel number and descriptions of vegetation cover and surface soil properties. 172
Table 3.2: Location, height, depth, and frequency of ground-based hydrometeorological and remote-sensing observations. 173
Table 3.3: Time intervals and types of data substituted from the climatological records of Hill 444 (31.70°N 110.23° W 4434' MSL), Ft. Huachuca, Arizona (White, 1996). 177
Table 3.4: Meteorological and energy-balance measurements and precision and maximum percent error (White, 1996). 177
Table 3.5 Distributed model domain definition. 177
Table 3.6: Water well information for the City of Tombstone (Gilbert, 1996). 184
Table 3.7: Spatially and temporally constant TOPLATS parameters for Walnut Gulch. . . 187
Table 3.8: Spatially and temporally constant TOPLATS parameters for Walnut Gulch. Some of these parameters were not specified as an eight Metsite average, but were rather determined in the model from other parameters in the model. In the case of residual soil moisture, the spatially-variable values were not reasonable, and were therefore not used 192
Table 3.9: Monsoon '90 water-balance based on hourly flux data (in units of mm depth) . 224
Table 4.1: TOPMODEL randomly restarting downslope simplex optimized parameters . 237
Table 5.1: Calibration parameters, ranges, and default values. 250
Table 5.2: Pareto set sizes for various error cut-off levels, Monte-Carlo set sizes, corrected or uncorrected data, and all data or day data. 255
Table 5.3: Acceptable calibrated TOPLATS parameters and default values. 261
Table 6.1: Water-balance information for the TOPLATS calibrated control simulation. . . 274
Table 6.2: Water-balance information for the TOPLATS direct insertion simulation. 278
Table 6.3: Water-balance information for the TOPLATS statistical correction simulation 283
Table 6.4: Newtonian nudging model parameters. 297
Table 6.5: Water-balance information for the TOPLATS Newtonian nudging simulation 298
Table 6.6: Optimized background horizontal error correlation function parameter values 308
Table 6.7: Vertical background error correlation. 308
Table 6.8: Water-balance information for the TOPLATS statistical interpolation simulation 310

LIST OF TABLES - *Continued*

Table Page
Table F.1: Results of Monte-Carlo calibration of TOPLATS and Monsoon '90 Metflux sites. Data were derived from the minimum objectives of 3,995,956 single-grid simulations 342
Table F.2: Results of Monte-Carlo calibration of TOPLATS and Monsoon '90 Metflux sites excluding night data. Data were derived from the minimum objectives of 2,120,922 single-grid simulations. 347
Table G.1: Water-balance information for the TOPLATS-calibrated control simulation . . 352

ABSTRACT

The feasibility of synthesizing distributed fields of remotely-sensed soil moisture by the novel application of four-dimensional data assimilation applied in a hydrological model was explored in this study. Six Push Broom Microwave Radiometer images gathered over Walnut Gulch, Arizona were assimilated into the TOPLATS hydrological model. Several alternative assimilation procedures were implemented, including a method that adjusted the statistics of the modeled field to match those in the remotely sensed image, and the more sophisticated, traditional methods of statistical interpolation and Newtonian nudging. The high observation density characteristic of remotely-sensed imagery poses a massive computational burden when used with statistical interpolation, necessitating observation reduction through subsampling or averaging. For Newtonian nudging, the high observation density compromises the conventional weighting assumptions, requiring modified weighting procedures.

Remotely-sensed soil moisture images were found to contain horizontal correlations that change with time and have length scales of several tens of kilometers, presumably because they are dependent on antecedent precipitation patterns. Such correlation therefore has a horizontal length scale beyond the remotely sensed region that approaches or exceeds the catchment scale. This suggests that remotely-sensed information can be advected beyond the image area and across the whole catchment.

The remotely-sensed data was available for a short period providing limited opportunity to investigate the effectiveness of surface-subsurface coupling provided by alternative assimilation procedures. Surface observations were advected into the subsurface using incomplete knowledge of the surface-subsurface correlation measured at only 2 sites. It is perceived that improved vertical correlation specification will be a need for optimal soil moisture assimilation.

Based on direct measurement comparisons and the plausibility of synthetic soil moisture patterns, Newtonian nudging assimilation procedures were preferred because they preserved the observed patterns within the sampled region, while also calculating plausible patterns in unmeasured regions. Statistical interpolation reduced to the trivial limit of direct data insertion in the sampled region and gave less plausible patterns outside this region. Matching the statistics of the modeled fields to those observed provided plausible patterns, but the observed patterns within sampled area were largely lost.

1. INTRODUCTION AND BACKGROUND

1.1 Overview and problem statement

Soil moisture is most often described as the moisture in the top several meters of soil that can interact with the atmosphere through evapotranspiration and precipitation and that is available to vegetation. Accurate assessments of the spatial and temporal variation of soil moisture are advantageous for numerous applications and for answering diverse research questions, because soil moisture is a basic link between the hydrologic cycle and the energy budget of land-surfaces through its regulation of latent heat fluxes. Thus, measurement of soil moisture is important for the study and understanding of all surface biogeophysical process. This includes: (a) agriculture, where knowledge of root zone soil moisture leads to efficient irrigation management, increased production, crop yield estimation, and pest detection and control; (b) forest ecology, where soil moisture information can lead to better harvesting management and yields; (c) civil engineering, where soil moisture can be an important structural consideration or can help to identify geologic hazards; (d) water resources, where water-balance studies, hydrologic process studies, flood forecasting, drought assessment, and precipitation pattern analysis depend on knowledge of soil moisture stores; (e) climate studies, where changes in long-term soil moisture stores have been identified as an indicator of climate change, and soil moisture information can calibrate and validate global climate models; (f) ecosystem modeling, where biogeochemical cycles are dependent on soil moisture states; and (g) soil science, where soil moisture plays a key role in erosion, mass movement, ecology, and land potential (Wetzel and Woodward, 1987). These consequences are all strongly determined by human-induced changes in soil moisture.

Given the crucial role that soil moisture plays in most land-surface processes, it is desirable that soil moisture be monitored with the same accuracy and frequency as other important environmental variables. Various investigations based on the above application needs have identified that the 'ideal' soil moisture measurement strategy would provide global soil moisture estimates at several levels in the root zone at least once a day and with a spatial resolution of no more than 100 meters.

Traditional, *in-situ* soil moisture measurement techniques (gravimetric, nuclear, electromagnetic, tensiometric, and hygrometric) provide point measurements that do not account for the spatial variability typical of soil moisture profiles. Because *in-situ* soil moisture measurements are generally expensive and often problematic, no large-scale 'soil moisture networks' exist to measure soil moisture at the 'ideal' high frequency, multiple depths, and fine spatial resolution that is needed. However, there is potential for remotely-sensed data to provide the necessary information. Remote-sensing of soil moisture might provide global fields of soil moisture data at high spatial and temporal resolutions that are impractical to achieve with *in-situ* methods. However, such measurements are limited by errors introduced by soil type, landscape roughness, and vegetation cover, and inadequate coverage in both space and time. Alternatively, many reliable hydrologic models are available for the calculation of soil moisture, but are subject to errors in structure and input. It has been suggested by many (i.e. Wei, 1995) that the best, operational soil moisture estimates might be obtained through a synthesis of remote-sensing and hydrologic modeling. Remote-sensing data, when combined with numerical simulation and other data, should provide estimates of soil moisture with higher spatial and temporal resolution and less error than remotely-sensed data alone.

There is clearly a need to develop an operational large-area remotely-sensed, soil moisture system. Several recommendations are relevant to the development of such a system. First, it is clear that a space-borne platform needs to be established with appropriate temporal and spatial resolution for soil moisture applications. This 'ideal' sensor may be quite expensive because of the large antenna needed to obtain fine temporal resolution in the microwave frequencies. Second, a large-area, *in-situ* soil moisture network must be developed for the calibration of remote-sensing systems. Third, automatic algorithms that classify various land types, then correct remote soil moisture measurements based on that classification, need to be developed. This is a very ambitious outline of suggested future research and may be unrealistic in the short term. Given current limits on scientific research funding and the state of current remote-sensing plans for the foreseeable future, the development of the 'ideal' soil moisture remote-sensing system is probably not possible within the next 20 years. Therefore, a more realistic plan might

be to use existing and planned sensors in a numerical modeling framework that assimilates all relevant data to produce synthetic soil moisture estimates.

A prototype system that uses four-dimensional data assimilation (4DDA) methods (Figures 1.1 and 1.2) within a macroscale land hydrology model to generate large-area soil moisture fields on a regular space and time interval was the focus of the research described in this dissertation. The 4DDA soil moisture fields so generated could be valuable for many of the topics addressed above, as well as (1) evaluating new systems for remote-sensing of soil moisture, (2) initiating and validating numerical weather prediction models, and (3) exploring the role of soil moisture in regulating the surface exchanges of water and energy at different spatial and temporal scales.

1.2 Motivation and real world application

The motivation for this research was multifaceted. Soil moisture measurements are expensive and tedious to collect, hence it is desirable to extend scarce measurements using a combination of model predictions and actual measurements. The four-dimensional data assimilation framework developed here provides accurate soil moisture estimates at regular temporal and spatial scales. The resulting model was a first step toward a new generation of meteorological models that have the capability assimilating both atmospheric and hydrologic observations for improved understanding of hydrology-weather interaction.

1.2.1 Definition of soil moisture

The clear definition of soil moisture is elusive because specialists from different disciplines perceive soil moisture differently (Figure 1.3). For example, for the atmospheric scientist, soil moisture is a condition which exists over a large area, that affects the transfer of moisture into the atmosphere, and may affect the production of precipitation (Lawford, 1992). For the hydrologist, soil moisture on the scale of the watershed preconditions the surface and influences the amount of runoff produced by a given amount of precipitation (Lawford, 1992). An agriculturalist views soil moisture as a valuable commodity that must be conserved at the farm level to ensure that next summer's crop will do well (Lawford, 1992). And, finally, the

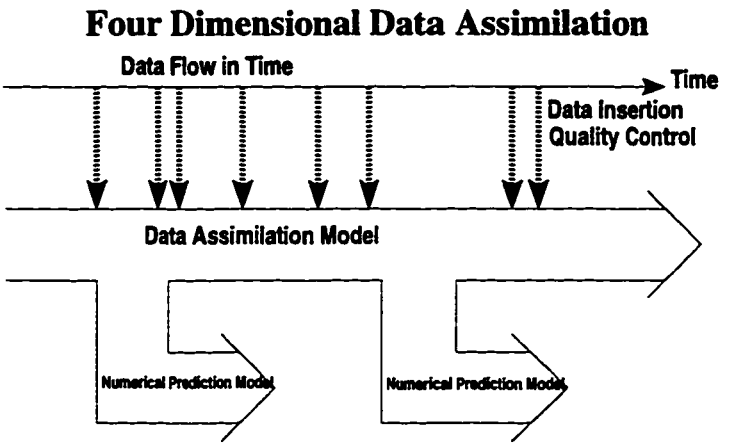

Figure 1.1: Outline of four-dimensional data assimilation (4DDA). Observations are inserted into the data assimilation model (identical to the prediction model) as they become available (Bengtsson, 1985).

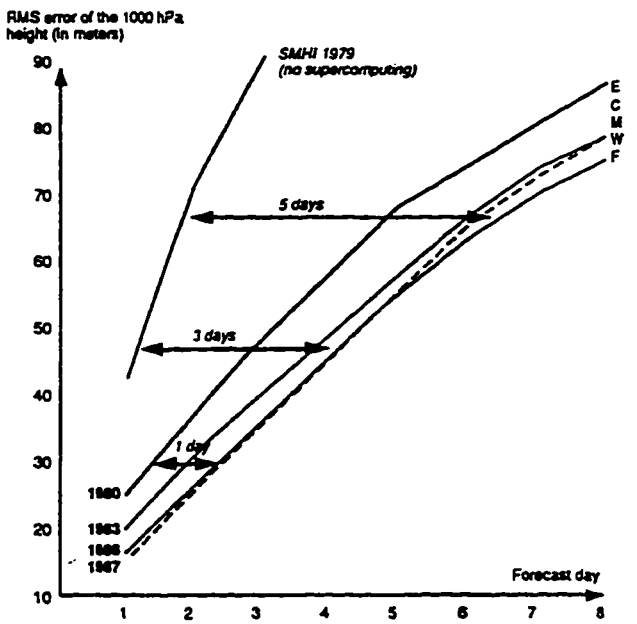

Figure 1.2: Increase in forecasting skill at ECMWF over a decade using data assimilation techniques (Lange, 1989).

hydrogeologist looks upon soil moisture as a potential water source for recharging local aquifers or wells and as a potential source of contaminants. Each of these specialties has distinct nomenclature and philosophies concerning soil moisture that serve specialized goals. However, there is overlap between each of these definitions that may lead to a common soil moisture definition.

For clarity, soil moisture is most often described as moisture in the surface layers of soil that can interact with the atmosphere through evapotranspiration and precipitation. This typically comprises the water contained in the top 1 to 2 meters of soil which accounts for about 0.005 percent of the total water on the Earth's surface (Schmugge *et al.*, 1979). A soil's volumetric soil water content expressed in percent is the most common measure of soil moisture used in remote-sensing.

1.2.2 Soil moisture applications

Accurate assessments of the spatial and temporal variation of soil moisture is important to numerous applications and for answering current research questions. Many of these questions relate to the water- and energy-balances of land-surfaces. The basic link between the hydrologic cycle and the energy budget of land-surfaces is the moisture content of the soil. Thus, measurement of soil moisture is important for the study and understanding of surface biogeophysical process. Additionally as the human race accelerates its modification of the land-surface, concern has increased about the feedbacks that these modifications have on weather, climate, water supplies, crop production, biochemical cycles, and ecological balances of the biosphere on various time scales (Wetzel and Woodward, 1987).

In this section, the potential benefits of remotely-sensed soil moisture data for various applications are reviewed. The use, as well as the required spatial and temporal resolutions, and required accuracies are noted for each application. Such understanding is vital so that the optimal combination of the remote-sensing system and the simulation algorithms can be chosen for each purpose.

1.2.2.1 Agriculture

Knowledge and management of moisture in the root zone of agricultural lands is important to crop production. Drought is most often defined as a deficiency of root zone soil moisture (rather than a lack of precipitation) that can lead to reduced crop yields. However, poor drainage leading to excessive soil moisture can also cause problems for crops. Thus, a moderate soil moisture level is desired and is often maintained in a controlled manner via irrigation. Soil moisture information over large areas would provide a means for scheduling irrigation and, in turn, predicting crop yields.

Despite the great value of remotely-sensed soil moisture in agriculture, this information has not been widely used. The primary reason for the lack of application of remote-sensing information in agriculture is the perceived need for real-time information, rather than the quality of that information. In order to make remote-sensing information a viable part of agricultural decision-making processes, a system must be devised in which the remote-sensing information can be effectively used and efficiently incorporated into the management decision process (Hatfield and Fuchs, 1990).

Insects and pests are generally dependent on some sustained level of soil moisture for breeding, hatching, and movement. Therefore, maps of soil moisture could provide a means for estimating potential pest or disease outbreaks and might be valuable in treating and controlling such outbreaks (Engman, 1992b).

1.2.2.2 Forest ecology and management

Trees generally have more conservative growth rates and demands compared to agricultural crops; thus, they are more tolerant of soil moisture deficit. However, soil moisture does affect the production of trees, as evidenced by their yearly variation in ring widths. Dendrochronology is based on the variability of tree ring widths in response to moisture stress and can be used to predict past seasonal soil moisture trends. Hence, forests are affected by long-term trends in soil moisture. As seen in the following example, these long-term trends can have important management implications: the common forest management practices of clearcut logging and slash burning can markedly alter soil moisture (Adams *et al.*, 1991). A few years after the burn,

invading vegetation may deplete soil moisture to levels comparable with those from forested areas. Patterns of initially higher soil moisture due to decreased evapotranspiration rates, followed by invasion of bushy vegetation (which dramatically increases evapotranspiration and lowers soil moisture), are common. The soil moisture remains low for an extended period thereafter due to rapidly increasing shrub cover (Figure 1.4). The management implication here is that lower soil moisture impairs seedling growth, so perhaps a brush control program should be enacted, or logging practices that have less effects on soil moisture should be utilized to ensure a rapid forest regeneration.

1.2.2.3 Civil engineering

The water content of soil can have significant effects on its structural properties. Water tends to make soil heavier, softer, more easily liquified, and less able to bear weight. Thus, for the construction of roads, airfields, earthdams, or other large soil structures, the state of soil moisture is an important consideration. Knowledge of soil moisture averages and trends can be important for design, and knowledge of current soil moisture conditions can be important to construction scheduling and planning.

Another important application of soil moisture information in civil engineering is for the prediction and prevention of geologic hazards. Mud slides, landslides, debris flows, and other mass movements are often triggered by high soil moisture. Pinpointing areas of high soil moisture in suspect terrain may help in predicting or preventing these hazards.

1.2.2.4 Hydrologic management and modeling

Conservation of mass, energy, and momentum are the most fundamental scientific principles on which scientific knowledge is built. The conservation of mass of water, is the fundamental building block on which hydrology is built. The mass conservation equation is:

$$D = P - E \pm \Delta s \tag{1.1}$$

where D is discharge, P is precipitation, E is evaporation, and Δs is soil moisture difference (Meier, 1981). Ideally, for water-balance studies, each component of this balance should be

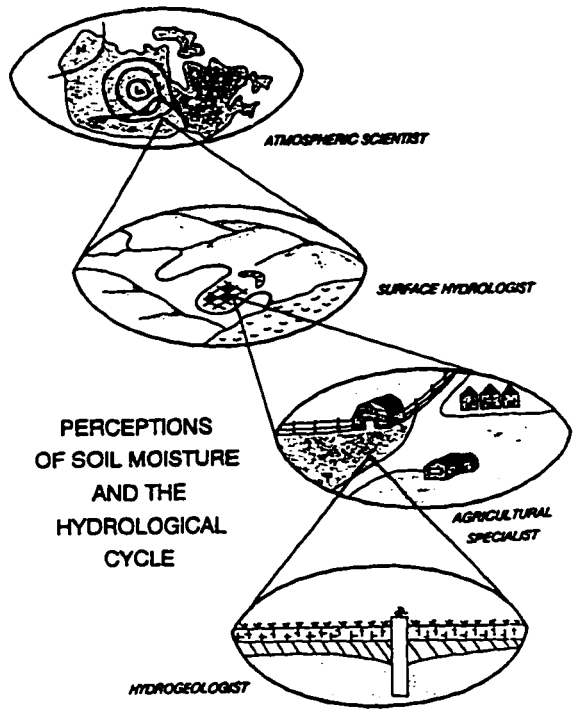

Figure 1.3: Different soil moisture applications (Lawford, 1992).

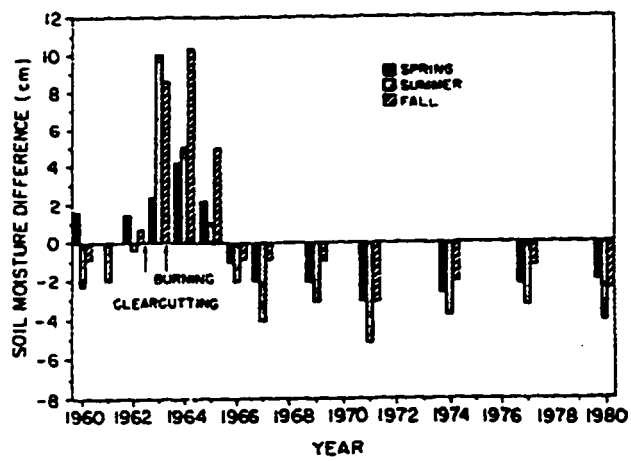

Figure 1.4: Differences between clearcut and forested (Adams *et al.*, 1991).

measured. Discharge and precipitation, have been successfully measured over large scales, but soil moisture and evapotranspiration (which is related to soil moisture) remain elusive.

Water-balance studies, hydrologic process studies, flood forecasting, and precipitation pattern analysis all depend on knowledge of soil moisture stores. Soil moisture patterns, both temporal and spatial, are a key to understanding the spatial variability and scale problems that are paramount in hydrology. Frequent soil moisture measurements would provide new information giving closure in water-balance studies and new information for the development of precipitation algorithms. Soil moisture information is of extreme importance in the prediction of floods by controlling the conversion of rainfall to runoff (Engman, 1992b). For example, our inability to predict the 1993 midwest United States flooding has been widely attributed to a underestimation of soil moisture stores (Betts *et al.*, 1994).

Drought assessment is just as important as flood forecasting. Ideally, droughts should be assessed based on the soil moisture deficit rather than on a simple rainfall index. Such an assessment would be more accurate and give an indication of when and where to take remedial action.

Soil moisture is an essential element of regional and global water-balance and climate-related studies. Traditionally, hydrology has been divided into two camps: (1) engineers who focus on floods or on securing municipal supplies, where soil moisture is a precondition for an extreme event and soil moisture is relegated to an initial condition and subsequent rate of infiltration, and (2) agricultural hydrologists who are concerned with average conditions of infiltration and evapotranspiration. This latter group emphasizes infiltration and downplays runoff as incidental (Dick, 1992).

Basinwide remotely-sensed averages of initial soil water content have been found to be sufficient for runoff simulations (Goodrich, 1993). This has implications on the potential use of satellite-based microwave systems to derive soil moisture estimates for event-based runoff simulations. In certain cases, the low spatial resolutions typical of such sensors may not seriously impact runoff simulation results (Goodrich *et al.*, 1994).

1.2.2.5 Climate system modeling

"From a climate perspective, soil moisture is the temporary storage of precipitation" (Engman, 1992b). That is, soil moisture is stored until it evaporates or transpires or moves downgradient to groundwater or streamflow. Soil moisture also integrates the occurrence and amount of precipitation and, thus, is an indicator of climate change (Engman, 1991a). Furthermore, soil moisture is a key element in the recycling of precipitation over land-surfaces. Hence, changes in the general patterns of soil moisture could indicate changes in precipitation distribution and therefore climatic changes.

Climate system modeling is instrumental in the prediction of near-term weather problems and future climate changes. Climate system modeling utilizes two similar modeling approaches: General Circulation Models (GCMs) and Numerical Weather Forecasting (NWF) models. GCMs and NWFs are based on very similar atmospheric dynamic theory and primarily differ in the time scales and resolutions for which they make predictions. Due to limitations in computer processing speeds, a tradeoff between resolution and prediction time is made. NWF models are designed to predict weather 1 to 10 days into the future, so they are initialized with real-time weather information and then model the Earth at a high spatial and temporal resolution. GCM models are initialized with average climatic conditions and are then run at low temporal and spatial resolutions for decades or centuries into the future.

Numerous investigations have demonstrated that simulations of surface climate by GCMs are very much dependent on the formulation of their land-surface schemes with regard to the treatment of soil moisture and snow cover (Verseghy, 1991). These land-surface processes are relatively well understood in principal, but schemes need to be developed which would be complete enough to account for the main processes, but would be simple enough to be incorporated realistically into GCMs. A common land-surface scheme is the 'bucket approach', where vegetation resistance is represented by some aridity factor and where the actual evapotranspiration (ET) rate is taken to be proportional to the amount of water available in the upper soil layer (Budyko, 1955). New representations of land-surface processes that include very detailed descriptions of physical phenomenon have been proposed (BATS; Dickinson *et al.*, 1986).

A model of soil moisture changes can integrate measured soil moisture (taken from a few points, a few times a year, or frequent remotely-sensed measurements during the snow-free season) with weather forecasts or climatology to estimate the current and forecast conditions. Further refinement of measurement integration is one of the most important goals of soil moisture modeling development (Eley, 1992). One such example is CLASS (Canadian Land-Surface Scheme) (Verseghy, 1991). The CLASS general climate model land-surface scheme incorporates three soil layers with physically based calculations of surface heat and moisture transfers. Snow cover is modeled as a discrete layer and is treated separately from snow-free areas. The energy-balance equation is solved iteratively for the surface temperature, and the surface infiltration rate is calculated using a simplified theoretical analysis allowing for surface ponding. Precipitation and ponding is assumed uniform over a grid (which can cause problems when precipitation is convective). Additional problems arise from the model's inability to simulate lateral water movement such as overland or subsurface flow. Generally, CLASS is a significant improvement over previous GCM soil moisture models.

Soil moisture measurements can also serve to validate GCM and NWF models. It is believed that access to soil moisture information would help to improve these models and make them more physically defensible. More specifically, knowledge of moisture that is available to the atmosphere could be used to improve the accuracy and duration of weather forecasts by providing information about where water and energy transfers may change the atmospheric makeup (Engman, 1992b).

1.2.2.6 Meteorology

The energy-balance of a soil or vegetated surface is governed by the energy conservation equation, which involves soil heat flux, net radiation, and the sensible and latent heat fluxes (Engman, 1992b). Soil moisture is seen as available water for evapotranspiration into the atmosphere effectively controls the partitioning of sensible and latent heat. That is, the sensible and latent heat fluxes from the surface are usually balanced with the available solar energy. Thus, when water stores are limited, latent heat fluxes decline, sensible heat fluxes predominate,

and when plenty of water is available, this process is reversed, with evaporation primarily dependent on the atmospheric demand for water.

The increased understanding of the complex partitioning of sensible and latent heat fluxes as controlled by the available water is important for understanding land-surface, atmospheric coupling, and thus meteorological processes. For example, it has been observed that understanding of the moisture potentially available to the atmosphere is an important component in forecasting severe storms that result in flash flooding and wind damage. It is believed that the severity of these storms is dependent on the available moisture upwind of the storm location and differential heating that generates the atmospheric circulation (Engman, 1992b).

1.2.2.7 Ecosystem modeling

Biogeochemical cycles are dependent on the availability of water within the land/plant complex. For example, photosynthesis involves the movement of soil moisture to the plant, and many of the nitrogen cycle reactions are soil moisture dependent. Additionally, transport of chemicals in the natural environment is dependent on soil moisture. For example, evapotranspiration and sediment transport by runoff are both generally controlled by soil moisture. Thus, the study of biogeochemical studies in the natural environment are enhanced by remotely measured soil moisture estimates (Lawford, 1992).

Understanding of the long-term spatial and temporal trends of soil moisture fluctuations is also valuable in studies of desertification. It is generally unclear if soil moisture deficits are the cause or result of desertification, but they certainly accompany it. Long-term analysis of soil moisture in key desert fringe areas may increase understanding of the desertification process and improve the management of those sensitive areas.

1.2.2.8 Soil science and crop system modeling

The thin layer of soil on the Earth's surface is essential for life, because soil is an essential ingredient for food production; therefore, understanding soil surface processes is essential. Knowledge of the processes that degrade the soil, such as erosion and mass movement, is necessary for the best management and preservation of this invaluable resource.

Computational simulation of the moisture regime of the soil is useful in studying land potential, ecology, and land degradation processes such as erosion. "Land degradation is a problem of major order that erodes the basis of civilization" (Blaikie and Brooksfield, 1987). Water is a fundamental factor for determining soil erosion, mass movement, and ecology, and thus is essential in determining land potential. Therefore, to understand and model land degradation, it is essential to model the soil moisture regime in a wide variety of landscapes, which requires soil moisture measurements over large areas which is not currently feasible (Van Den Berg, 1989).

1.2.3 Summary of remotely-sensed soil moisture applications and scales.

The 'best guess' estimates of the data needs for different soil moisture applications are summarized in Table 1.1. The fact that soil moisture data are not currently being used makes defining soil moisture needs difficult (Engman, 1991a).

Table 1.1: Characteristics of soil moisture data needs (Engman, 1991a).

Use	Spatial Res.	Swath Width (km)	Revisit Time (days)	Depth (cm)	Accuracy Levels
Climate Studies	100km	1000	10	0-10	4
Water Budget Studies	10m	50	1	0-10	10
Hydrology Process	10m	50	2-3	0-10	10
Climate Models	10km	500	1	0-10	4
Weather Forecasting	1km	500	1	0-5	5
Energy-balance	10km	50	1-3	0-10	10
Biogeochemical Cycles	100m	500	3-5	0-10	5
Satellite Precip. Estimates	1km	1000	1-3	0-10	4
Precip. Patterns	100m	500	1	0-5	4
Pest Management	100m	500	3-5	0-5	5
Crop Yield Model	1km	1000	5	0-10	4
Drought	1km	1000	5-10	0-10	4
Flood Forecasting	1km	1000	1	0-5	5

1.3 Objectives and scope

The principal objectives of this research were to develop and validate 4DDA methods within a hydrometeorological model and to calculate synthetic, regional-scale fields of the soil moisture profile from all available remote-sensing, meteorological and hydrological data.

Several other objectives were addressed in a qualified way by this study (limited to a small watershed and a few weeks): (1) the identification of the most valuable observations needed for large-area 4DDA soil moisture modeling; (2) assessment of the ability of 4DDA techniques to quantify and improve the error properties of the resultant soil moisture fields; and (3) definition of the temporal and spatial scales that the integrated observation and 4DDA modeling framework can accurately estimate unknown soil moisture values.

1.4 Approach

The research philosophy used here was to combine and develop those elements of past research that together allow soil moisture estimation through integrated observational modeling and to investigate the feasibility and optimal implementation of this technique in this initial study at the small watershed scale using existing data from the USDA-ARS Walnut Gulch Experimental watershed. On the basis of the understanding so produced, a future objective is to then extend the observational modeling principle to regional scales. The data needs of this research -- both from remote-sensing and other sources -- were great, because the goal was to use all available information to estimate large area fields of soil moisture at high temporal and spatial resolution. Accurate accounting of these data and access to the relative value of different types of data in determining the model-calculated soil moisture fields were crucial throughout.

The final goal of the research which this study initiates is to produce large-area, reasonably accurate four-dimensional fields of soil moisture utilizing all available sources of soil moisture information. Ultimately, it would be desirable to derive remote-sensing based sub-grid scale soil moisture estimates on grids of 10000 km^2 over entire continents. Due to the complexity of the observational modeling concept (and the data resources required to implement the model), the plan was to develop the model in a small, data-rich test areas, and then, as understanding of the

modeling issues and data needs improves, study areas and grid sizes will be progressively increased.

The research described here explored the development and application of data assimilation at the small watershed scale.

1.5 Structural overview

A wide variety of complex soil moisture modeling, remote-sensing, data processing, and data assimilation methodologies were used in this research. Therefore, Chapter 1 is devoted to an assessment of relevant and current understanding, theory, and applications. Information and theory on the actual modeling and data assimilation techniques used in this research is provided in Chapter 2. Then a review of the preparation of data sets required for application of the modeling system is described in Chapter 3. An exploration of parameter calibration and sensitivity issues of this modeling structure is shown in Chapters 4 and 5. The data assimilation results are shown in Chapter 6, and Chapter 7 is devoted to discussion, conclusions, and future research directions.

Tables are generally incorporated into the text while figures are grouped at the end of each section for reader convenience. Graphs and tables not central to the research discussion are given in appendices. The appendices also contain acronym definitions and author permissions.

1.6 Background

The review of background material is presented in seven major sections. The first summarizes the current availability of large-scale soil moisture measurement networks. The background theory, namely, soil moisture remote-sensing techniques, land-surface hydrologic modeling, and data assimilation techniques are explored in the second, third, and fourth sections. The current operational application of data assimilation in atmospheric sciences and hydrology are explored in the last two sections respectively.

1.6.1 Soil moisture measurement networks

There are many well-established methodologies for *in-situ*, point measurement of soil moisture, although these vary considerably in their accuracy, calibration, sensitivity, and cost. The methodologies include gravimetric, resistive, capacitive, heat flux, nuclear, tensiometric, and time domain reflectrometry techniques (Lawford, 1992).

The spatial and temporal variability of soil moisture is known to be significant even on small scales, making spatially representative, *in-situ* soil moisture measurement difficult. This, together with the difference in sampled depth, represents a serious source of error when *in-situ* soil moisture point measurements are used to calibrate remote-sensing systems or hydrologic models.

Because *in-situ* soil moisture measurements are generally expensive and often problematic, no large-scale 'soil moisture networks' exist to measure soil moisture at high frequency, multiple depths, and fine spatial resolution. Several large-scale soil moisture networks with low frequency sampling and coarse spatial resolution have been established, including the SCS Soil Moisture Study, the Nevada Cooperative Soil Climate Study, the Global Climate Change Pilot Project, the Wisconsin Individual Soil Climate Study, the Illinois Climate Network (Georgakakos and Baumer, 1994), and a soil moisture monitoring program in the USSR (now discontinued). Several small-area soil moisture measurement sites have also been established, such as those in the Walnut Gulch and Little Washita experimental watersheds. These sites have fine spatial coverage but are monitored infrequently (typically every few weeks).

1.6.2 Soil moisture remote-sensing

Almost everyone has observed the darkening, or decrease in reflectance, of soil when it becomes wet. As a raindrop falls on dry sand at the beach, on dry soil in a garden, or even on a sidewalk, that spot becomes darker (Swain and Davis, 1978). This distinct threshold between wet and dry surfaces (in the visible part of the spectrum) suggests the concept that remote-sensing of soil moisture is possible. Wavelengths where atmospheric transmission allows remote-sensing of surface characteristics are shown in Figure 1.5.

The soil reflectance curve in Figure 1.6 shows considerably less variation in comparison to the other reflectance curves. This demonstrates that the factors which influence soil reflectance act over less-specific spectral bands. Some of the complex and interrelated factors that affect soil reflectance are moisture content, soil texture (proportion of sand, clay, and silt), surface roughness, iron oxide content, and organic matter content. In general, soil moisture will decrease soil reflectance, with its greatest effects at the water absorption bands (1.4, 1.9, and 2.7 μm). However, soil moisture is strongly related to soil texture; coarse soils are usually well-drained, resulting in low moisture and high reflectance, whereas, poorly drained fine-textured soils will have lower reflectance. Without water, fine-textured soils have smoother surfaces that can reflect more radiation and therefore appear lighter than coarse-textured soils (Lillesand and Keifer, 1987). The relative amounts of clay, silt, and sand that make up different textured soils (Swain and Davis, 1978) is shown in Figure 1.7. Complicating this situation is the overlay of vegetation on soil which can completely mask the soil reflectance or introduce significant error due to the strong water absorption effects of vegetation reflectance.

Large amounts of organic matter (5%) in a soil will tend to make the soil dark, whereas smaller amounts will result in brown or grey tones (Figure 1.8). These relationships change with the degree of decomposition of the organic matter, the type of organic matter, and the climatic location (Swain and Davis, 1978).

Figure 1.9 is an outstanding example of the relationship between increasing soil moisture content and the decreasing level of reflectance (Swain and Davis, 1978). Notice that, even in the visible regions of the spectrum, increases in moisture content result in decreased reflectance.

The soil's iron oxide content can have a significant effect on the reflectance of the soil. The red color of many soils is attributed to unhydrated iron oxide, but this color can also be attributed to partially hydrated iron oxide and manganese dioxide. An increase in iron oxide can cause a significant decrease in reflectance (Figure 1.10) by as much as 40%. The effect of iron oxide on the reflectance of soils is not uniform over all wavelengths (Swain and Davis, 1978).

The applicability of different spectral bands to soil moisture remote-sensing are reviewed in the following section. Then the past, present and planned remote-sensing sensors are examined for their soil moisture sensing capabilities. Finally, the usefulness of different spectral

bands to soil moisture mapping and an assessment of the applicability of currently available remote sensing platforms to soil moisture mapping are summarized.

1.6.2.1 Dielectric constant

Water has many unique properties that set it apart from other substances. One such property that is of great importance in remote-sensing is water's high dielectric constant. Water has a dielectric constant of 80 at the lower microwave frequencies that results from the alignment of the permanent electric dipole moment of the water molecule (Schmugge, 1985). This is much higher than the dielectric constant of 3 to 5 for dry soils. These properties produce a large range of soil emissivities (from about 0.95 for dry soils to 0.6 or less for wet soils) with changes of corresponding magnitude in the soil's reflectivity (Schmugge, 1985).

Several laboratory studies have been conducted to investigate the effects of soil moisture, bulk density, and soil texture on the net dielectric behavior of soil mediums (Dobson and Ulaby, 1986). The results of these studies show: (1) the dielectric constant of dry soil is independent of microwave frequency and is primarily dependent on bulk density, (2) the initial addition of water to a soil medium that is 'bound' to the soil matrix increases the dielectric less than subsequent additions of 'bulk water'. 'Bound' water is not able to rotate in response to an electrical field as easily as unbound water (Schmugge, 1985), (3) the amount of 'bound water' is dependent on soil texture and mineralogy; thus, differences in soil type result in differences of dielectric constant, (4) soil type dependent dielectric constant differences are wavelength dependent, and are largest at low frequencies (3 GHz) where the effective salinity of soil fluids exerts significant influence, (5) the frequency dependence of soil dielectric properties is of the Debye type and is similar to that observed for water, (6) the preferred measure of soil moisture is volumetric, because the dielectric constant is proportional to the number of water dipoles per unit volume.

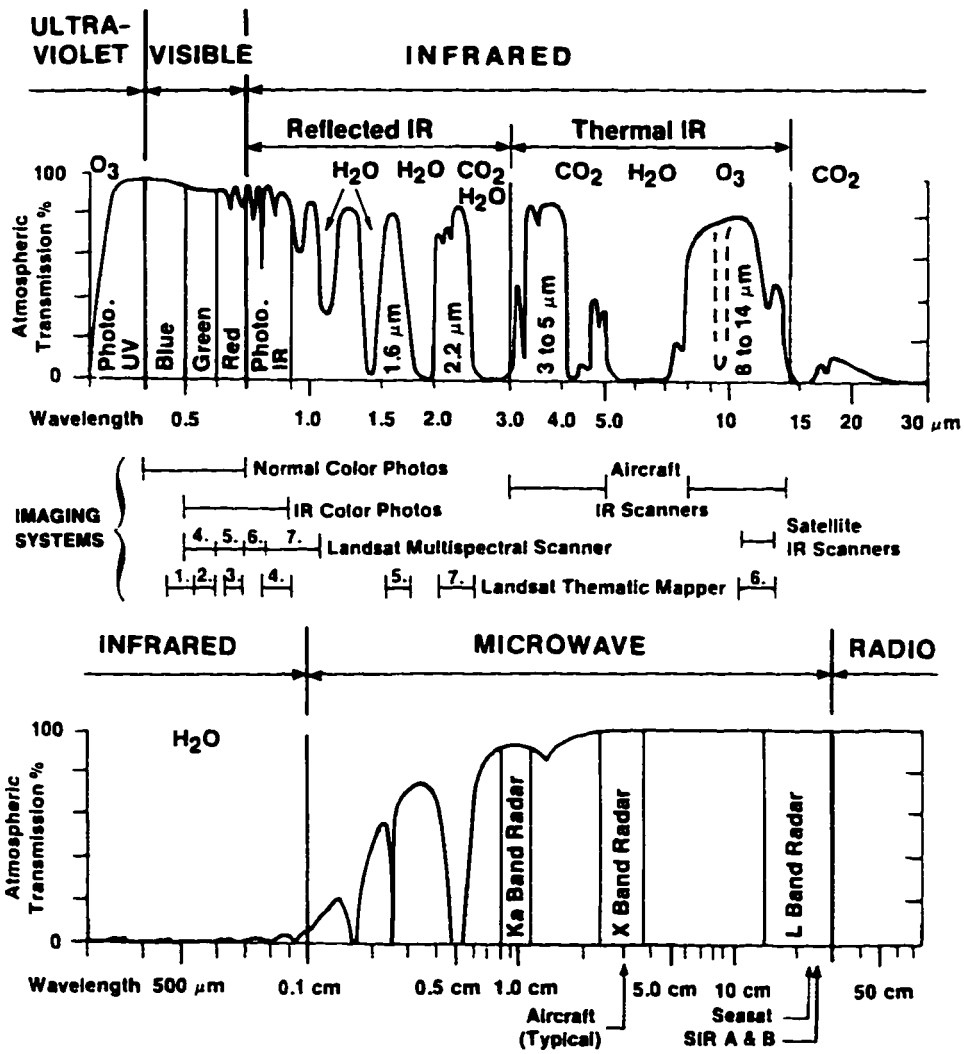

Figure 1.5: Atmospheric transmission and spectral wavelengths (Sabins, 1987).

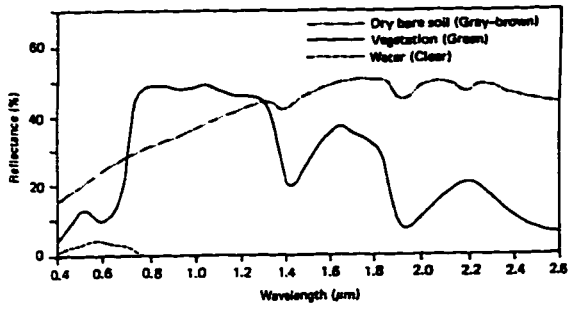

Figure 1.6: Typical spectral reflectance curves (Lillesand and Keifer, 1987).

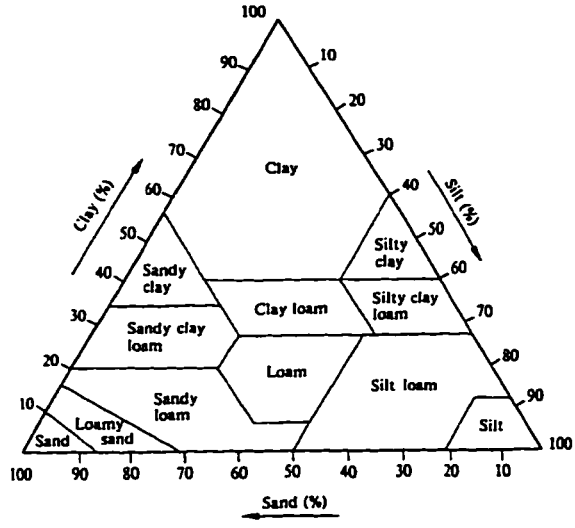

Figure 1.7: Soil texture triangle (Swain and Davis, 1978).

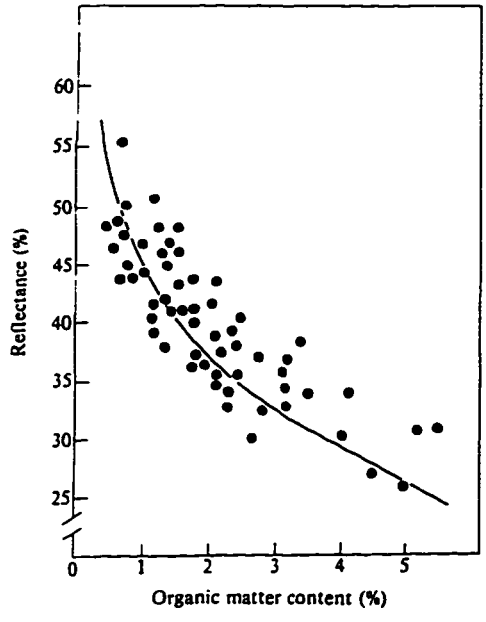

Figure 1.8: Organic matter versus reflectance (Swain and Davis. 1978).

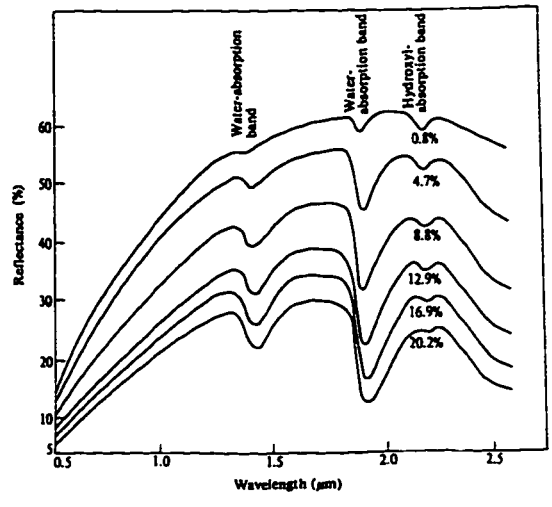

Figure 1.9: Newtonia silt loan at various moisture contents (Swain and Davis, 1978).

The dielectric constant can be described by the following relation:

$$k=k'+jk'' \tag{1.2}$$

Here, k is the dielectric constant, which is a measure of the response of the material to an applied electric field (an electromagnetic wave). The response is split into a factor that determines the propagation characteristics of the wave, and one that determines the energy losses as the wave travels through the material. These two factors are described by the real (k') and imaginary (k'') parts of the complex dielectric constant as illustrated in Figure 1.11 (Schmugge, 1985).

1.6.2.2 Various wavelengths

Remote-sensing of soil moisture is not limited to the spectral bands discussed above. Almost any frequency where there is little atmospheric absorption can be used (Figure 1.12) to sense soil moisture (Schmugge, 1985). In fact, the longer microwave wavelengths offer great potential to remotely sense soil moisture content with depth due to differential microwave absorption with varying dielectric constant.

1.6.2.2.1 Visible and infrared wavelengths

Generally, wet soil is darker than dry soil in the visible and infrared portions of the spectrum. By developing a relationship between the albedo of a soil and its moisture content, this technique may provide useful information for the first few centimeters of soil. There are numerous aspects that confuse the interpretation of the data. For instance, different soil types, roughness, texture, color, vegetation cover, angle of incidence, and variations in illumination can change the darkness of a soil without changing the soil moisture content. These 'noise' elements make visible and infrared techniques for measuring soil moisture impractical.

However, if imagery from two or more dates could be compared, a change from a light to a dark tone would suggest that the change was due to a temporary influence (soil moisture) rather than a more permanent soil characteristic such as roughness or organic content. If an area is dark on both images, one cannot be sure of the cause (Swain and Davis, 1978).

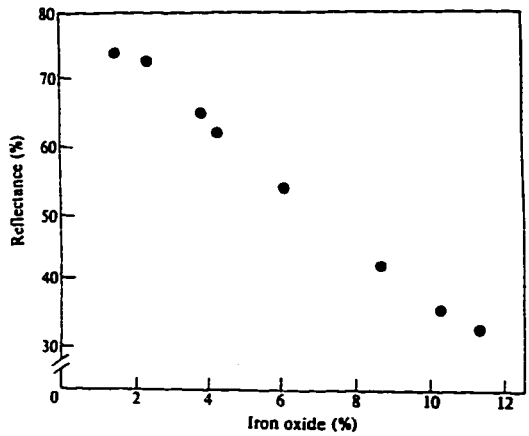

Figure 1.10: Iron oxide versus soil reflectance (Swain and Davis, 1978).

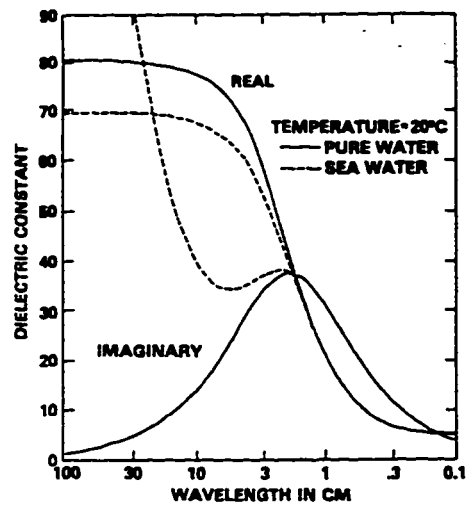

Figure 1.11: Real and complex parts of the dielectric constant (Schmugge, 1985).

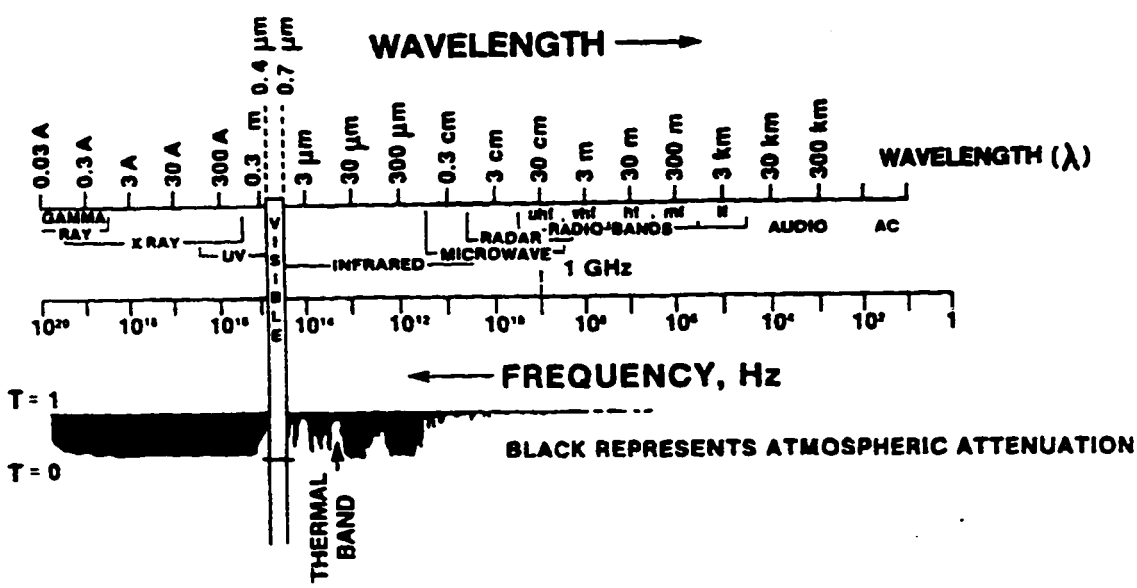

Figure 1.12: Electromagnetic spectrum on a log scale (Schmugge, 1985).

1.6.2.2.2 Gamma wavelengths

Remote-sensing of soil moisture content using gamma wavelength radiation (wavelengths of less than 0.03 nm) is based on the difference between the natural terrestrial gamma radiation emission for wet and dry soils. Water in the surface layers of soil increases the attenuation of gamma radiation emitted from below; hence the gamma radiation flux is less for wet soils than for dry soils. The relationship between soil moisture, *M*, and gamma radiation flux can be expressed as:

$$M = \frac{\frac{C}{C_\epsilon}(100 + 1.11 M_\epsilon) - 100}{1.11} \tag{1.3}$$

Where M_0 is the background soil moisture, C_0 is the background gamma count rate, and C is the measured gamma count rate (Engman, 1991a).

There are difficulties with using gamma radiation in soil moisture assessment. The most significant is that gamma radiation is readily absorbed by the atmosphere; thus any remotely-sensed data must be collected relatively close to the surface, using aircraft flying 100-200 meters above the surface (Engman, 1991a). For example, Carrol (1981) used an operational gamma radiation system that accurately estimates soil moisture in the upper 10 cm with an error of 2.5%. His system is mounted on a low-flying aircraft (150 m above the ground), with a resolution of about 300 m. This system also accounts for the attenuation of the air mass between the sensor and the ground.

1.6.2.2.3 Thermal wavelengths

Every particle of mass that has a temperature higher than 0 °K emits electromagnetic waves. According to Plank's formula, the spectral radiance emission depends on the temperature of the body. Thus, as seen in Figure 1.13, this temperature can be determined remotely by measuring the spectral emitttance of the body (Meier, 1981).

Soil surface temperature depends on interaction with the atmosphere and the thermal inertia of the soil. The thermal inertia of the soil depends on the thermal conductivity and heat capacity of that soil. Heat capacity increases with increasing water content water content can be linked

to thermal inertia, so making thermal techniques a potential method for determining soil moisture. By measuring the amplitude of the diurnal temperature change, the ability of a soil to resist temperature change can be estimated (Engman, 1991a). Then, a relationship between temperature change and soil moisture can be developed. These relationships change with differing soil types and may be altered by the presence of vegetation; therefore, a new calibration between diurnal temperature change and soil moisture content would need to be developed for every soil and vegetation scheme.

Thermal remote-sensing techniques have been successfully used to measure the first few centimeters of soil moisture, but the results obtained with one soil could not be successfully applied to other soils, except when moisture was expressed as pressure potential. Other studies have found little sensitivity to soil moisture in the thermal ranges when vegetation is present (Engman, 1991a).

Surface temperature is modulated by moisture in two ways. First, the thermal inertia of the soil increases when the water content of the soil increases, which decreases its response to an exposed heat flux. Second, evapotranspiration from the soil surface and vegetation further reduces temperature changes because the evaporating water absorbs the heat of the phase change. The importance of the thermal inertia decreases with increasing vegetation cover (Wetzel and Woodward, 1987).

Raw digital infrared images are converted to skin temperature change maps and then to soil moisture maps in several steps. First, visible channels can be used to eliminate cloud-covered areas. Then, subtraction of the appropriate images produces uncorrected temperature change maps. Next, these maps are corrected for the effects of atmospheric water vapor using surface and sounding meteorological data. A number of algorithms are available to convert surface temperature data to soil moisture data. The approach is to invert an air-earth interface energy budget model which is diagnostic of surface temperature. The soil heat storage and evaporation terms are directly or indirectly dependent on soil moisture (Wetzel and Woodward, 1987).

Numerous sources of noise(including vegetation, evapotranspiration, topography, and atmospheric absorption) and environmental variables (such as solar radiation, temperature, and wind) can complicate the soil moisture signal in thermal infrared data (Heilman and Moore,

1979). Anthropogenic land-surface modifications would also be expected to complicate this signal.

1.6.2.2.4 Microwave wavelengths

Remote-sensing in the microwave region offers most potential for truly quantitative soil moisture measurements from space (Newton, 1979). Two types of microwave remote-sensing (passive and active) have particular advantages, and are based on similar theory. All microwave techniques are based on the large changes in the soil dielectric constant with changing soil moisture (Ulaby *et al.*, 1979). "Because the dielectric constant for water is at least 10 times that for dry soil, the presence of water in the top few centimeters of bare (unvegetated) soil can be detected in radar imagery. Soil moisture and surface wetness condition become particularly apparent at longer wavelengths. Soil moisture normally limits the penetration of radar waves to depths of a few centimeters. However, signal penetrations of several meters have been observed under extremely dry soil conditions with L-band radar" (Lillesand and Keifer, 1987).

Similar principles govern the depth of the penetration of a microwave signal for both passive and active systems. Mo *et al.* (1980) determined that the sampling depth is between 0.06 and 0.1 times the wavelength, while Newton *et al.* (1979) determined that the penetration depth was 0.2 times the wavelength. The measurement depth is related to the moisture content of the soil and to instrument frequency, as shown in Figure 1.14 (Engman, 1991a).

Microwave techniques for measuring soil moisture have a strong theoretical basis and are not limited to cloud-free areas as many of the other techniques are. Often, the microwave energy is not affected by vegetation, which is a distinct advantage. One of the most important aspects of microwave techniques is that they are all-weather and day/night techniques, because they do not depend on solar radiation and can penetrate most clouds (Eley, 1992).

The major limits on the accuracy of the estimation of soil moisture include surface roughness, vegetative cover, soil heterogeneity, incidence angle dependence, surface cover heterogeneity, atmospheric effects, and mixed scene problems (Schmugge *et al.*, 1986).

The most important problem with microwave remote-sensing of soil moisture is the relationship of the whole rooting depth to the thin surface layer soil moisture that can be

measured with confidence. Presently, this is modeled from other information for agricultural applications and is largely ignored for hydrological applications where near-surface soil moisture is of primary concern (Eley, 1992).

Soil texture affects microwave detection of soil moisture by changing the dielectric constant. As the surface area of the particles that make up a soil increases, water molecules will have more places to bind to soil particles. Bound water molecules tend to increase the dielectric constant more slowly than unbound water molecules; thus, increased soil particle surface area will decrease the dielectric constant (Ulaby *et al.*, 1979).

One approach for using microwave data to detect soil moisture is through change detection. With this approach, it is assumed that the change occurring in microwave reflectance is only due to changes in soil moisture (i.e. soil texture, roughness, and vegetation remain constant). Therefore, any change in microwave measurements can be directly related to the change in soil moisture (Engman, 1991a).

Some common microwave wavelengths used for soil moisture remote-sensing are summarized in Table 1.2, and the limitations and advantages of active and passive microwave are summarized in Table 1.3 (Engman, 1992b):

Table 1.2: Common microwave bands.

Band	**Frequency (GHz)**	**Wavelength (cm)**
Ka	37.5 - 27.3	0.8 - 1.1
K	17.6 - 27.3	1.1 - 1.7
Ku	17.6 - 12.5	1.7 - 2.4
X	12.5 - 7.9	2.4 - 3.8
C	7.9 - 4.0	3.8 - 7.5
S	4.0 - 2.0	7.5 - 15.0
L	2.0 - 1.0	15.0 - 30.0
P	1.0 - 0.3	30.0 - 100.0

Table 1.3: Comparison of passive and active microwave systems (Engman, 1992b).

Characteristic	Passive Microwave	Active Microwave
Signal to Noise	good-very good	fair-good
Data Rate	low	very high
Spatial Resolution	10-100 km	10 m
Swath Width	wide	narrow-moderate
Vegetation effect	moderate-serious	moderate
Roughness Effect	slight	serious
Topographic Effect	slight	serious
Revisit Time	good	poor-moderate

In passive microwave remote-sensing, a radiometer measures the intensity of microwave emission from a soil surface. At shorter microwave wavelengths, where the atmosphere may attenuate the signal, emission can be expressed as follows (see also Figure 1.15):

$$T_o = t(H)[rT_{sky} + (1-r)T_{soil}] + T_{atm} \tag{1.4}$$

where T_B is the microwave brightness temperature, $t(H)$ is the atmospheric transmission, r is the surface reflectivity, and T_{sky}, T_{soil}, and T_{atm} are the temperatures of the sky, soil, and atmosphere, respectively (Engman, 1991a, and Schmugge, 1985). At longer wavelengths, the atmospheric attenuation decreases, yielding the following simplified relation:

$$T_o = (1-r)T_{soil} = eT_{soil} \tag{1.5}$$

where $e=1-r$ is the emissivity (Engman, 1991a).

"The strong sensitivity of microwave emissivity to soil moisture provides the basis for passive microwave remote-sensing of soil moisture" (McFarland, 1992). That is, because of the high dielectric constant of water, emissivity decreases from about 0.95 to about 0.60 as the soil increases in moisture content from dry to saturated (McFarland, 1992). Attenuation of this emitted radiation can be caused by vegetative cover, soil surface roughness, and snow.

Schmugge *et al.* (1986) stated that "a 21-cm wavelength [passive] radiometer was the best single sensor for soil moisture research". A 21-cm wavelength, L-band passive microwave sensor is considered to be the best soil moisture sensor because it has little contamination by vegetation and roughness, it has no man-made contamination sources, and it penetrates the soil to a depth of several centimeters. The drawbacks are that it requires a very large antenna to get reasonably small IFOVs, and the size of the antenna increases as a function of distance from the

surface being sensed. This makes space-borne passive microwave sensors extremely expensive or impractical to construct, though the use of inflatable antennas show promise (Shuttleworth, 1996).

An active microwave sensor or radar, transmits a pulse of microwave radiation and measures the return reflected back, as represented in Figure 1.16 (Schmugge, 1985). The backscattering coefficient describes the intensity of the reflected signal. The advantage of a radar is that the energy in the received pluses can be angularly separated into the return from different ground location; thus, it is possible to produce a radar backscatter image of the ground (Schmugge, 1985).

For active microwave remote-sensing, a simple model can be used to relate the various important quantities, thus:

$$S_{\theta}=S_{\Lambda}+\frac{S_{h}}{L} \tag{1.6}$$

where S_V is the backscatter from vegetation, L is the attenuation caused by the vegetation canopy, S_t is the measured radar backscatter, and S_S is the backscatter from soil, which can be related directly to soil moisture by $S_S=RcM_V$, where R is the surface roughness term, c is a soil moisture sensitivity term, and M_V is the volumetric soil moisture (Engman, 1991a).

The effects of roughness and vegetation can be more severe for radar systems as compared to passive systems, but appropriate angles of incidence, polarization, and frequency can minimize these effects. The size of the antenna, D, determines the angular resolution of the radiometer, which is approximately λ/D. Thus, a 1-m antenna at the 21-cm wavelength yields a resolution of 12°, whereas a 1.4 GHz radiometer with a 10-m antenna operating from a satellite in a 500-km orbit has a spatial resolution of 10 km (Schmugge, 1985).

There is an approximate linear decrease of emissivity with increasing soil moisture. This is illustrated by an aircraft platform microwave radiometer operated for nine flights over central South Dakota. Scatterplots of the 1.4 GHz emissivity measured at 300 m versus soil moisture ground observations is shown in Figure 1.17. The error bars indicate the standard deviations of the ground measurements (Schmugge, 1985).

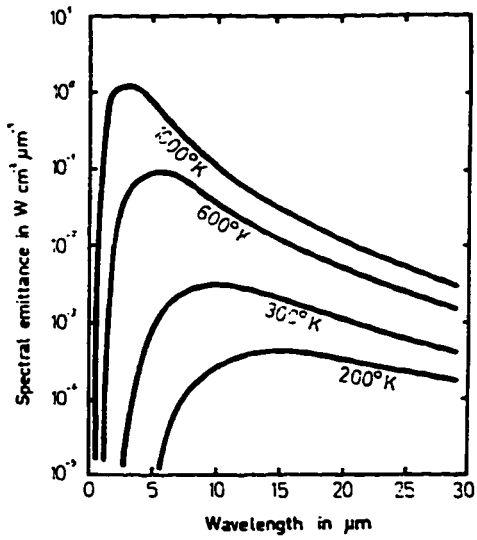

Figure 1.13: Spectral emitttance for different temperatures (Meier, 1981).

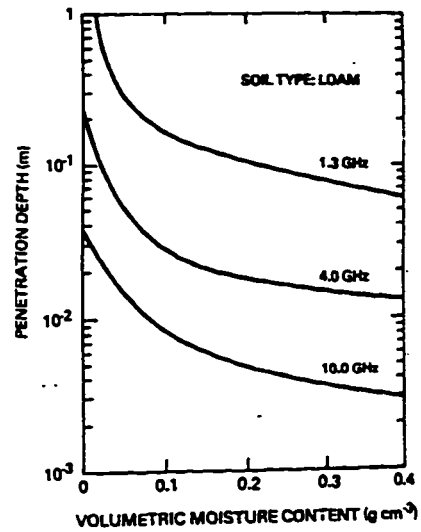

Figure 1.14: Microwave penetration depth with frequency (Engman, 1991a).

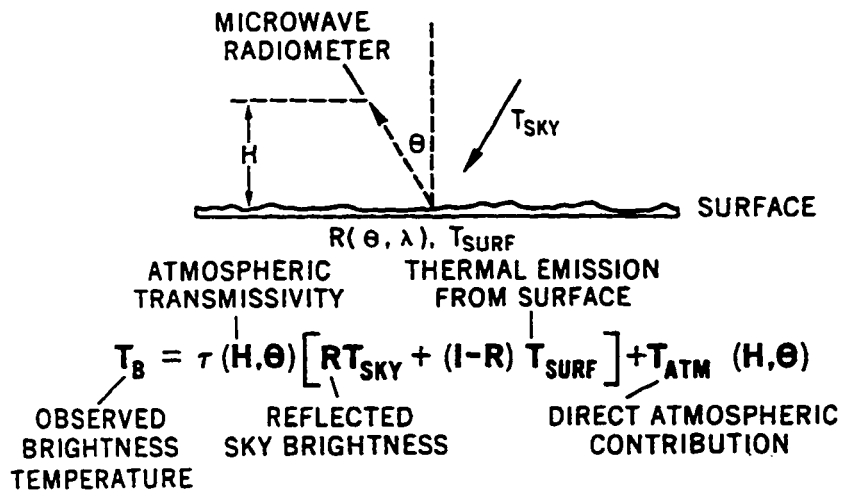

Figure 1.15: Sources of microwave radiation (Schmugge, 1985).

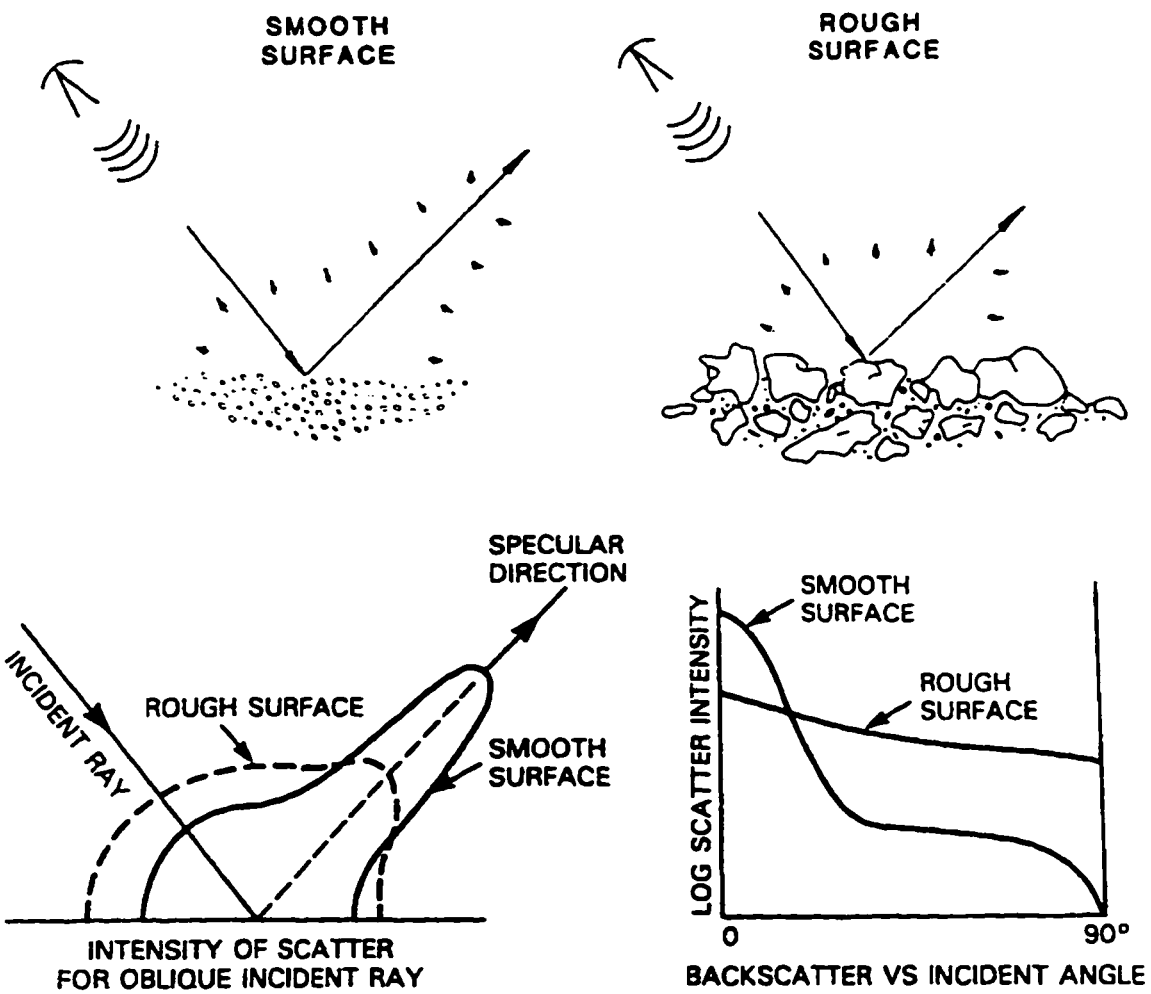

Figure 1.16: Schematic of radar intensity patterns (Schmugge, 1985).

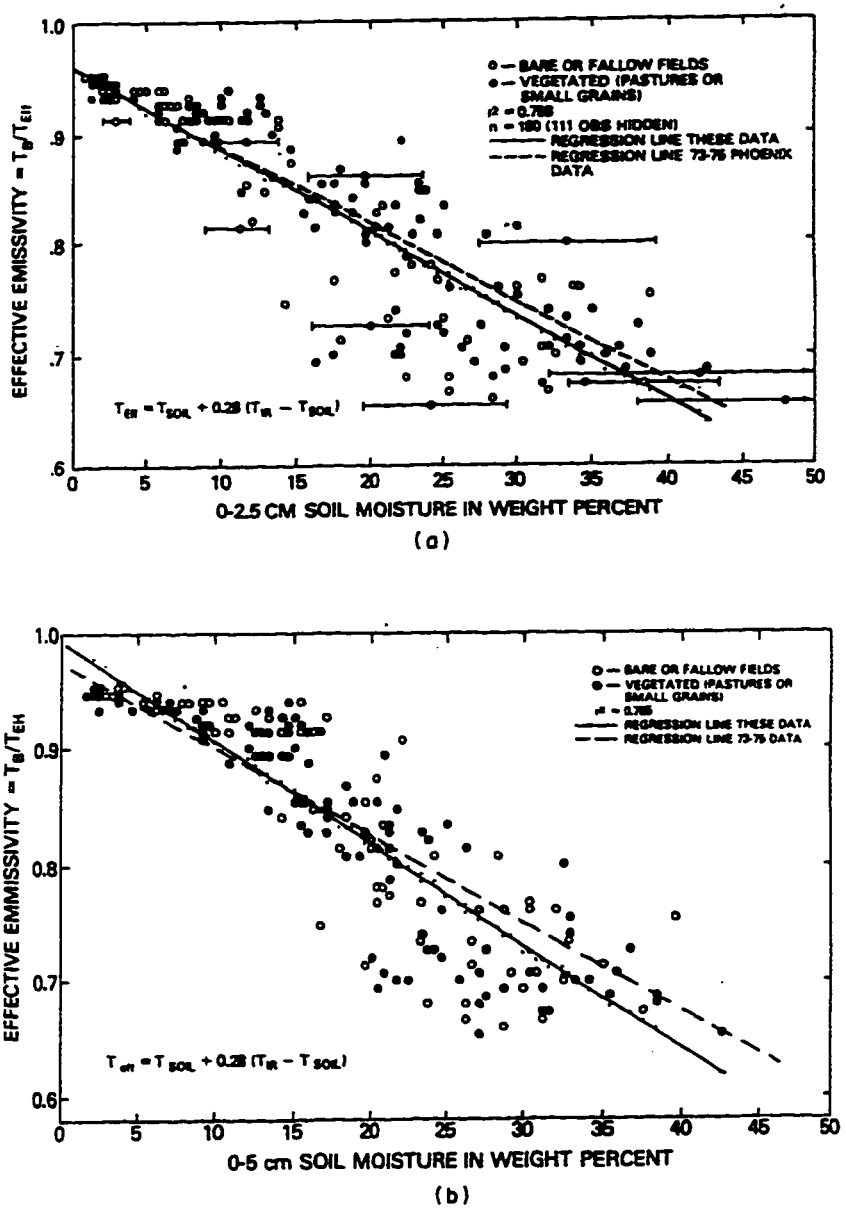

Figure 1.17: Microwave emissivity versus soil moisture (Schmugge, 1985).

1.6.2.2.5 Remote-sensing soil moisture summary

The soil moisture remote-sensing approaches described above are summarized in Table 1.4 (Schmugge *et al.*, 1979, and Engman, 1991a).

Table 1.4: Summary of remotely-sensed soil moisture approaches (Schmugge *et al.*, 1979, and Engman, 1991a).

Wavelength	Property Observed	Advantages	Limitations	Noise Sources
Gamma				
	Gamma flux attenuation	Known theory	Collected at low altitudes	Atmospheric absorption
Reflected solar				
	Soil albedo Index of refraction	Lots of data	Many noise sources	Numerous
Thermal infrared				
	Surface temperature	High res. Large swath Coverage frequency Physics well understood	Cloud cover limits coverage frequency	Met. conditions Topography Veg. cover
Active Microwave				
	Backscatter coefficient Dielectric properties	Low atmo. noise High resolution	Limited swath width Calibration of SAR	Roughness Surface slope Veg. cover
Passive Microwave				
	Microwave emission Dielectric properties Soil temperature	Low atmo. noise Moderate veg. penetration	Manmade radiation limits operating range	Roughness Veg. cover Temperature

1.6.2.3 Measurements similar to soil moisture

Measurements or indexes that contain soil moisture information do exist, but do not explicitly describe soil moisture. These measures and indexes are reviewed in this section.

1.6.2.3.1 Normalized difference vegetation index

The normalized difference vegetation index (NDVI) is a measure of vegetation health and, is therefore an indirect, integrated measure of root zone soil moisture. NDVI is computed as follows:

$$NDVI=(R_{\infty}-R_{\gamma})/(R_{\infty}+R_{\gamma}) \tag{1.7}$$

where R_3 is the radiance from the Landsat Thematic Mapper Channel 3, and R_4 is the radiance from the Landsat Thematic Mapper Channel 4 (Carlson *et al.*, 1990). NDVI is the normalized difference of the radiance differences between spectral intervals on either side of the near-infrared vegetation reflectance discontinuity.

1.6.2.3.2 Palmer drought severity index

Palmer (1965) developed a water-balance indexing approach to characterize drought. The analysis is based on a weekly or monthly water-balance, and output from the approach is an index that ranges from -4 to +4. Negative values indicate drought, and positive values indicate wet periods. The index is calculated as a function of the difference between the actual rainfall and the normal (climate-based) rainfall. Because it is essentially an assessment of the depletion of the soil moisture state, the index can be used as a surrogate for soil moisture.

1.6.2.3.3 Antecedent precipitation index

The antecedent precipitation index (API) indicates the effect of previous rainfall in wetting the soil and subsequent logarithmically decreasing natural evapotranspiration on soil moisture. The index can be calculated from:

$$I_t = I_0 k^t \tag{1.8}$$

where I_t is the API on day t, and I_0 is the API at the start of a given calculation period. k is a constant of about 0.9, controlling the rate of soil moisture reduction, and t is time since the last rainfall in days (Dunne and Leopold, 1978). API has been used for predicting storm runoff (Linsley and Kohler, 1951) and is a reasonable indication of soil moisture states.

1.6.2.4 Remote-sensing platforms

Most measurements of soil moisture using remote-sensing have been from air-borne platforms and a few space platforms. The L-band radiometer on Skylab provided low resolution data that were indirectly related to an antecedent precipitation index (Engman, 1991a). It has been demonstrated that the HCMM (Heat Capacity Mapping Mission) has the potential for mapping soil moisture albeit with numerous limitations (Heilman and Moore., 1979). The

SMMR (Scanning Multichannel Microwave Radiometer) was used with a vegetation index to model surface soil moisture using visible and infrared wavelengths (Engman, 1991a). A low-elevation aircraft mounted L-band push broom radiometer, air-borne gamma radiation flights, various air-borne passive and active microwave sensors, a C-band scatterometer, the shuttle imaging radar-B, and the Seasat SAR were all used with various levels of success to map soil moisture (Engman, 1991a). The applicability of each of these systems to soil moisture mapping are explored in the following sections.

Generally, most of the air-borne sensors described in the following section have been deployed as both truck-mounted and aircraft-mounted. This is often for calibration and development purposes. A truck-mounted sensor can be more easily aimed at a given single target and thus provide a calibration for the less easily aimed air-borne system. The ultimate goal in using ground and air-borne sensors is the development of reliable space-borne sensors. The typical progression of sensor mounting would be from ground-based, to air-borne, and finally to space-borne. This provides less-expensive opportunities for optimization and evaluation of many different systems.

Air-borne soil moisture sensors are usually mounted on medium-sized aircraft and used for small-scale, short-duration studies. Hence, they provide a small spatial and temporal window of soil moisture measurements that has been largely used to evaluate their performance and, to a lesser extent, has used to produce quantitative soil moisture maps.

Space-borne sensors are the most desirable for soil moisture collection because of their global coverage and relatively stable calibrations. Disadvantages of these sensors are their poor spatial and temporal coverage and increased atmospheric noise components.

In the process of exploring the various space-borne sensors for their applicability in soil moisture mapping, it would be desirable to define the optimum or ideal specifications of a soil moisture sensor. According to Burke and Burke (1979), the optimum satellite sensor system for monitoring soil moisture would include at least two microwave radiometers (X and L bands) and a thermal infrared sensor. The X-band sensor is necessary to delineate surface features and to observe surface moisture content, and the L-band sensor would further delineate subsurface

moisture conditions. The thermal infrared sensor is required to obtain emissivity values for the microwave data because actual surface temperature directly affects brightness temperature.

Using an extended Kalman filter framework for the integration of a simple linear model of soil moisture, (Milly, 1986a) explored the relations between measurement frequency and accuracy of estimates of soil moisture. Based on this work, he suggested that daily measurements of soil moisture would be optimum for reliable estimates of soil moisture.

The following is a 'best guess' at the desired specifications of the ideal space-borne soil moisture sensor, based on the above research and application needs.

Spectral Bands:	3 microwave bands: Passive is preferred, but active OK Longwave: L or P bands Mediumwave: C band Shortwave: X or K bands Thermal Infrared band(s) Visible (Red), and NIR - for vegetation identification
Temporal Resolution:	<24 hour revisit time
Spatial Resolution:	<100m

1.6.2.4.1 PBMR

The Push Broom Microwave Radiometer (PBMR) is usually flown on the NASA C-130 aircraft. The PBMR has 4 beams pointing at ±8° and ±24° from nadir. Each beam has a full width at half-maximum power of about 16°, so the total swath width is 1.2 times the aircraft altitude (Wang *et al.*, 1989). This is a real aperture instrument, rather than a synthetic aperture radar (SAR). Engman (1991a) described the 21-cm wavelength, passive microwave PBMR instrument as "a mature and reliable instrument with a good history of soil moisture measurements".

PBMR data are recorded directly from the instrument onto a floppy disk on board the aircraft. These data are then calibrated as a function of time using a second software package. The C-130 flights are typically plotted using video tapes of the flight on copies of high-altitude photos obtained by NASA. These flight lines are then digitized directly into UTM coordinates using easily identified landmarks. This produces maps of aircraft position in UTM coordinates as a function of time for each flight line. Before creating the final images with these data, the outer beams are corrected for incidence angle effects (limb darkening) by multiplying them by

the ratio of the average of the center beam to the outer beam on each side. This darkening is due to the decrease in emissivity with angle for horizontal polarizations.

For the Monsoon '90 experiment performed at Walnut Gulch, Arizona, the C-130 was flown at 600 meters above average ground level. This produced an instantaneous field of view (IFOV) of 180 meters and a swath of 720 meters. After processing, the data were smeared out over the appropriate number of 40 meter pixels. The PBMR flew on 6 flights over Walnut Gulch during a 10-day period in July and August of 1990. The period was very dry for the first flight (day 212), which was followed by 5 cm of rain on day 213 falling over most of the study area. This produced a significant increase in brightness temperature (50 °K to 60 °K) on day 214. The successive flights on days 216, 217, 220, and 221 showed the effects of some smaller rains and drydown of the area. On day 221, the brightness temperatures rose to their pre-rain values (Figure 1.18). The city of Tombstone is clearly identifiable as a small, persistently cool area in the southwest portion of the images. Irrigation leading to persistently high soil moisture accounts for this anomaly.

The relationship between brightness temperature and soil moisture for Walnut Gulch in 1990 is shown in Figure 1.19. This plot clearly shows that there is a strong relationship between passive microwave remote-sensing and soil moisture, but it also shows that there is significant scatter from this relationship, probably due to vegetation, roughness, and soil variations.

1.6.2.4.2 IROE multiband sensor package

The Multiband Sensor Package (MSP) is designed for land studies; it includes Dicke-type radiometers at 1.4 GHz, 9.6 GHz, and 36.6 GHz, a thermal infrared sensor, and a color TV antenna. It is generally aircraft-mounted but may also be used on a land platform (Paloscia, 1990).

1.6.2.4.3 AIRSAR

The Airborne Synthetic Aperture Radar (AIRSAR), operated by NASA, is mounted on the JPL DC-8 aircraft. It is a 3-frequency (C, L, and P band) polarimetric Synthetic Aperture Radar. It is capable of resolutions from 3 to 12 meters (Engman, 1992a).

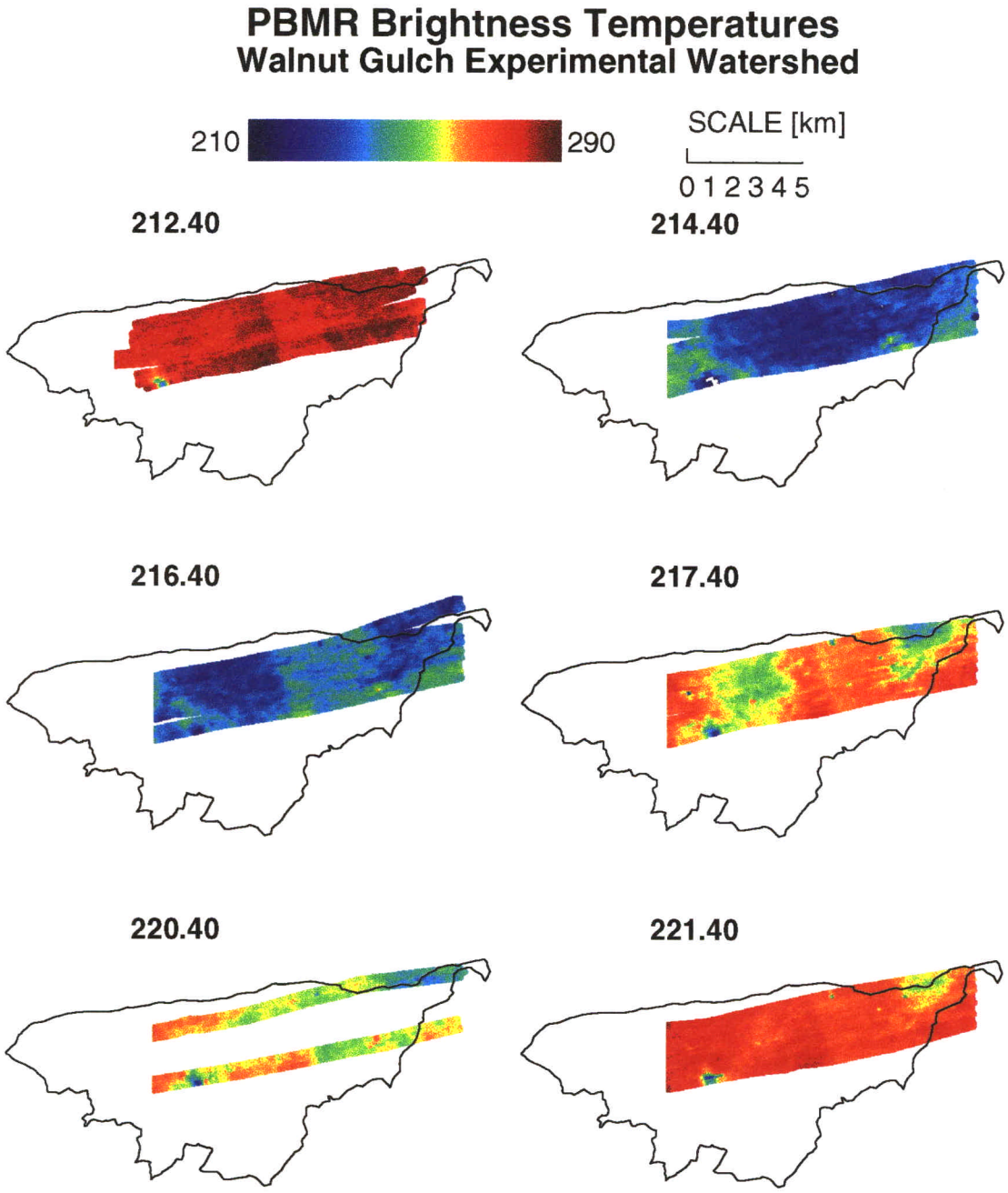

Figure 1.18: Monsoon '90 PBMR brightness temperatures.

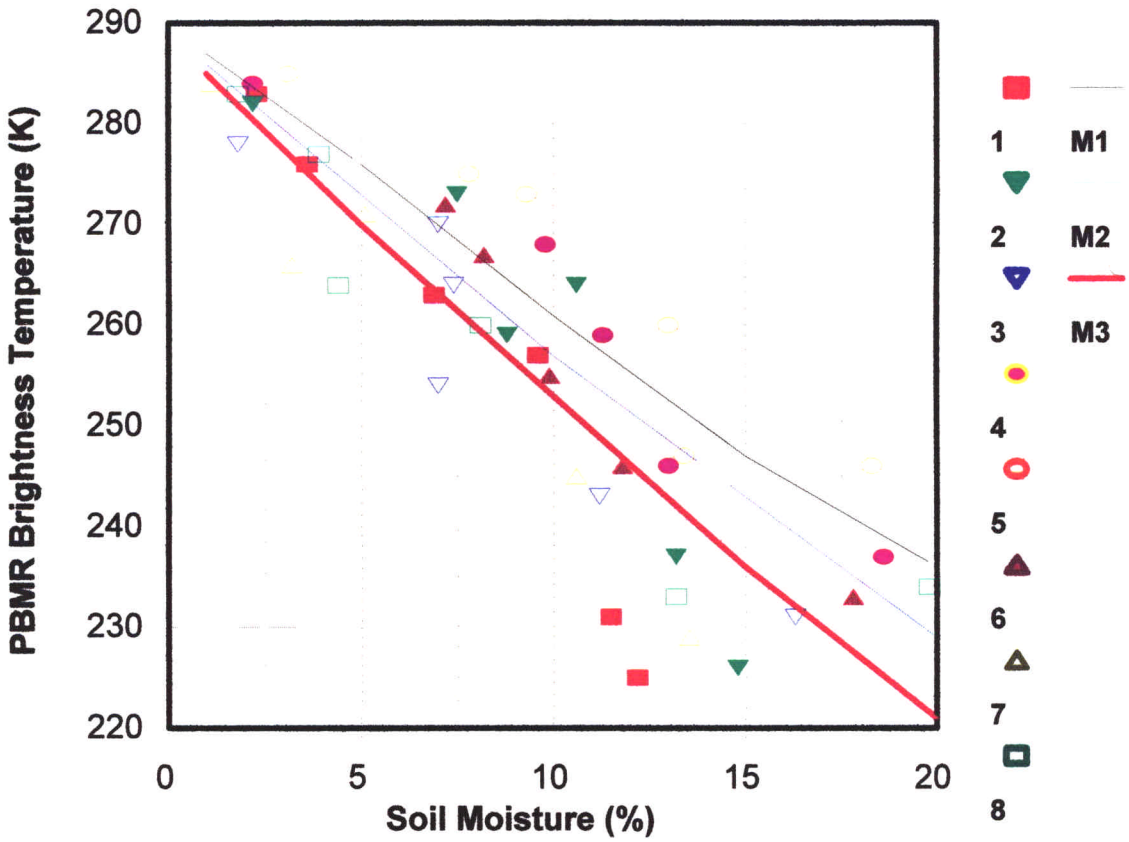

Figure 1.19: PBMR brightness temperatures versus Metsite gravimetric soil moisture for Walnut Gulch (Schmugge *et al.*, 1994). Lines represent different model fits.

1.6.2.4.4 ESTAR

The Electronically Steered Thinned Array L-band Radiometer (ESTAR) is a synthetic aperture microwave radiometer for measuring soil moisture. It was compared with the PBMR measurements made over Walnut Gulch, Arizona, and gave very comparable results. The advantage of this instrument over the PBMR is its much smaller antenna. This is a prototype space platform system (Le Vine *et al.*, 1992), and has the capacity of providing 7 beam positions within its ±45 degree field of view (twice that of the PBMR). The ESTAR is mounted on a C-130 aircraft. The Walnut Gulch experiments show that ESTAR is capable of providing soil moisture with the same accuracy as existing systems (Jackson *et al.*, 1992).

1.6.2.4.5 Landsat MSS/TM

The Landsat Multispectral Scanner (MSS) satellites provide visible and near-infrared images at an 80-meter resolution and an 18-day repeat cycle (Mather, 1987). These visible images are of limited use to soil moisture applications because of soil moisture interference problems outlined earlier. Additionally, the 18-day repeat cycle may be lengthened by cloudy days making data from this system unacceptably temporally scarce. It is possible that, through change detection using multitemporal images, some qualitative skin soil moisture information could be extracted for bare soil surfaces. Additionally, through the use of greenness or other vegetation indexes, qualitative descriptions of deeper root zone soil moisture might be extracted.

Table 1.5: Landsat MSS multispectral scanner wavebands.

Platform	Landsat MSS
Orbit	near-polar, sun sync
Altitude (km)	919 km
Inclination	99.09
Period (minutes)	103
Equatorial Crossing Time	0930
Swath Width (km)	185
Radiometric Resolution	6 bits
Repeat Cycle (days)	18

Band	**Waveband (μm)**	**Resolution (m)**
1	0.5-0.6	80
2	0.6-0.7	80
3	0.7-0.8	80
4	0.8-1.1	80

The Landsat Thematic Mapper (TM) sensors have increased radiometric sensitivity over the MSS. They have 7 spectral bands covering 0.45 to 12.5 μm, i.e. the blue/green visible through the thermal infrared (Mather, 1987). The visible images provided by this system are of limited use to soil moisture mapping as outlined above.

Table 1.6: Landsat Thematic Mapper wavebands (Mather, 1987).

		Band	Waveband (μm)	Resolution (m)
Platform	Landsat TM			
Orbit	near-polar, sun sync	1	0.45-0.52	30
Altitude (km)	705	2	0.52-0.60	30
Inclination	98.2	3	0.63-0.69	30
Period (minutes)	99	4	0.75-0.90	30
Equatorial Crossing Time	0945	5	1.55-1.85	30
Swath Width (km)	185	6	10.40-12.5	120
Radiometric Resolution	8 bits	7	2.08-2.35	30
Repeat Cycle (days)	16			

1.6.2.4.6 SPOT

The French National Space Centre (CNES) SPOT (Satellite Pour i'Observation de la Terre) sensor was first launched in 1986. It has improved spatial resolution over the Landsat systems, but compromises temporal frequency (26-day repeat cycle). SPOT has a pointable sensor that can be used to decrease this repeat cycle or to provide stereo imagery. SPOT, like Landsat MSS, provides only visible and near-infrared imagery and, therefore, is of limited use for soil moisture applications.

Table 1.7: SPOT satellite and HRV sensor wavebands (Mather, 1987).

		Band	Waveband (μm)	Resolution (m)
Platform	SPOT			
Orbit	near-polar, sun sync	1	0.5-0.59	20
Altitude (km)	832 km	2	0.61-0.68	20
Inclination	98.7	3	0.79-0.89	20
Period (minutes)	not available	Panchromatic		
Equatorial Crossing Time	1030	1	0.51-0.73	10
Swath Width (km)	117			
Radiometric Resolution	8 bits			
Repeat Cycle (days)	26			

The next SPOT satellite may have a SAR on board, which could have significant soil moisture sensing applications, depending on its wavelength and resolutions.

1.6.2.4.7 TIROS/NOAA

The Television Infrared Observation Satellite (TIROS) program began in 1960. This weather satellite is one of the most widely known satellite systems. This series of satellites are now called NOAA-n (National Oceanic and Atmospheric Administration). The repeat cycle on these satellites is very high (12 hours), which compromises spatial resolution (1.1 km). The AVHRR (Advanced Very High Resolution Radiometer) sensor is carried on these satellites; it has 5 spectral bands ranging from visible to thermal infrared wavelengths (Mather, 1987). The two thermal infrared bands are suited to soil moisture studies, except for the low temporal resolution.

Table 1.8: NOAA/TIROS satellite details and AVHRR sensor (Mather, 1987).

Platform	AVHRR
Orbit	near-polar, sun sync
Altitude (km)	833-870
Inclination	98.7
Period (minutes)	102
Equatorial Crossing Time	0730,1930,1400,0200
Swath Width (km)	3000
Radiometric Resolution	10 bits
Repeat Cycle (days)	12

Band	**Waveband (μm)**	**Resolution (m)**
1	0.58-0.68	1100
2	0.725-1.10	1100
3	3.55-3.93	1100
4	10.3-11.3	1100
5	11.5-12.5	1100

1.6.2.4.8 Explorer-A and Nimbus-7

The HCMM (Heat Capacity Mapping Mission) thermal infrared scanner carried by the Explorer-A and the Nimbus-7 spacecraft cross a given area twice in one day (1400 and 0200) with a 16-day repeat cycle. The aim is to register these day/night pairs with the intention of discriminating between rock types, monitoring soil moisture changes, mapping snow and ice fields, and to detect thermal effluent (Mather, 1987).

Heilman and Moore (1979) investigated the application of HCMM data to soil moisture mapping. Thermal data were found to be related to soil moisture through conductive heat

Table 1.9: Explorer-A satellite and HCMM sensor (Mather, 1987).

Platform	Explorer-A
Orbit	near-polar, sun sync
Altitude (km)	620 km
Inclination	97.6
Swath Width (km)	716
Repeat Cycle (days)	16

Band	**Waveband (μm)**	**Resolution (m)**
1	0.5-1.1	500
2	10.5-12.5	600

transfer (affected by thermal inertia) and evaporation, but complicated by vegetation, evapotranspiration, topography, atmospheric absorption, and other environmental variables such as solar radiation, temperature, wind, etc. These complications seem to limit the utility of these data to a qualitative assessment of soil moisture. For example, cooler surfaces tend to be wetter. Similar results were presented in a subsequent paper by Heilman and Moore (1981).

The Coastal Zone Colour Scanner (CZCS) carried aboard the Explorer-A and Nimbus-7 satellites was intended to measure the color and temperature of coastal water and open oceans using visible and thermal infrared wavelengths. If the imagery was also available over land, there might be some application of this system to soil moisture mapping. The application would be limited by the low spatial resolution of this scanner.

The Electrically Scanning Microwave Radiometer (ESMR) instrument on the Nimbus-5 satellite, operating at a 1.55-cm wavelength, has limited applicability for soil moisture sensing. The instrument has a 2500-km swath, and the satellite is in a sun synchronous orbit of 1100 km. The main limitations of this sensor are vegetation interference and its coarse resolutions of 10-25 kilometers (Burke and Burke, 1979; and Schmugge *et al.*, 1975).

The Nimbus-7 Scanning Multichannel Microwave Radiometer (SMMR) produced brightness temperatures at 0.81, 1.36, 2.80, and 4.54 cm wavelengths (McFarland, 1992).

1.6.2.4.9 Seasat

The Seasat satellite system was launched in 1978 and operated for only 106 days, but carried the first space-borne active microwave imaging sensor, a Synthetic Aperture Radar (SAR). This system creates its own microwave energy and detects the amount of energy returned to the system from the Earth's surface. This has the advantage of working at night, and

Table 1.10: NIMBUS-7 satellite and CZCS sensor (Mather, 1987).

		Band	Waveband (μm)	Resolution (m)
Platform	CZCS	1	0.433-0.453	825
Orbit	near-polar, sun sync	2	00.510-0.530	825
Altitude (km)	955 km	3	0.540-0.560	825
Inclination	99.3	4	0.660-0.680	825
Period (minutes)	104	5	0.700-0.800	825
Equatorial Crossing Time	1200	6	10.50-12.50	825
Swath Width (km)	1566			
Repeat Cycle (days)	6			

microwave radiation at these wavelengths can penetrate clouds and haze, thus providing surface images under any weather condition. A SAR uses a mathematical processing technique that accounts for forward momentum of the satellite and radar returns. With a normal radar system, a 25 meter-spatial resolution would require an antenna several kilometers in diameter. By using the SAR technique, the Seasat antenna was only 12 m in length. Thus, the images were generated mathematically from a simulated or synthetic antenna or aperture. The Seasat satellite system was originally intended to be used for measuring the roughness of the sea surface, but great utility was found for soil moisture studies because the microwave radiation is capable of penetrating vegetation cover and down into the soil where it can be reflected by the high dielectric properties of the soil moisture in that soil (Mather, 1987). Several similar SAR sensors have been flown aboard the NASA space shuttle in the 1980s with various success (Mather, 1987).

Table 1.11: Seasat satellite and SAR sensor (Mather, 1987).

		Band	Waveband (cm)	Resolution (m)
Platform	Seasat	1	23.5cm, 1274.8GHz	25
Orbit	circular, sun sync			
Altitude (km)	790 km			
Inclination	108			
Period (minutes)	101			
Equatorial Crossing Time	0930			
Swath Width (km)	100			
Repeat Cycle (days)	152			

1.6.2.4.10 SIR-C

The Shuttle Imaging Radar-C and X-Band Synthetic Aperture Radar (SIR-C/X-SAR) is a joint project between NASA, the German Space Agency, and the Italian Space Agency. SIR-C acquires images in both L-band, C-band, and with multiple polarizations, this being important for surface characterization. This sensor has been shown to be valuable in soil moisture measurement, but its use is limited by the short observation times available (NASA, 1994). In its current configuration, SIR-C is mounted in the payload bay of NASA's space shuttle, but future modifications may allow it to fly independently for long-term monitoring.

1.6.2.4.11 Japan's MOS-1 and ERS-1

The Japanese government launched the Marine Observation Satellite (MOS-1) in 1987. It carries the pushbroom Multispectral Electronic Self-Scanning Radiometer (MESSR), which has a 50-meter resolution and operates in 4 spectral bands centered at 0.55, 0.65, 0.76, and 0.95 μm. The swath width is 100 kilometers with a return period of 34 days. The MOS-1 satellite also carries a visible and thermal infrared radiometer with one visible (900 m resolution) and three thermal infrared (2.7 km resolution) channels (Mather, 1987). The JERS-1 carries a synthetic aperture radar and a visible/near infrared imaging sensor for land observation (Mather, 1987).

1.6.2.4.12 ERS-1

The European Space Agency launched the ERS-1 satellite on July 17, 1991, with a 100-km swath (ERS-1, 500 days in orbit). It carries an along-track scanning radiometer, an imaging sensor, and a C-Band synthetic aperture radar (SAR). A similar ERS-2 satellite is planned for launching in 1992-93 (Mather, 1987). The Active Microwave Instrument (AMI) is a SAR that operates only over specific regions due to power and data-handling limitations. It produces strips of high-resolution imagery, 100 km in width (ERS User Handbook, 1993). The ERS-1 appears to be one of the most successful SAR satellites to date.

Cognard *et al.* (1995) found a poor correlation between ERS 1 SAR signals and surface soil moisture at the field scale. They found this relation depends strongly on vegetation cover. At

the basin scale during periods of low vegetation density, they found a linear relationship between mean radar data and point measurements, which is encouraging.

1.6.2.4.13 Radarsat

The Canadian, United States, and United Kingdom governments launched the satellite Radarsat in 1995. It carries a C-band synthetic aperture radar, an upgraded AVHRR, and a 0.24-0.88 μm optical sensor with resolutions of about 30 meters (Mather, 1987). Currently, Radarsat's applicability to soil moisture estimation is uncertain, but it is thought to be encouraging.

1.6.2.4.14 SSM/I

The Special Sensor, Microwave Imager (SSM/I) is an operational passive microwave radiometer on the United States Department of Defense DMSP spacecraft. The satellite is in a circular, sun-synchronous, near-polar orbit at a 833-kilometer altitude. The SSM/I radiometer scans to the aft of the satellite at a 45-degree angle, and an incidence angle to the Earth of 36.9 degrees. The scan angle is 102 degrees which translates to a swath width of 1400 km. The radiometer receives horizontally and vertically polarized radiation at 19.3, 37.0, and 85.5 GHz (1.55, 0.81, and 0.36 cm) and vertically polarized radiation at 22.2 GHz (1.36 cm). Resolutions range from 12.5 km at small wavelengths to 50 km at large wavelengths (McFarland, 1992). This sensor is primarily sensitive to atmospheric water vapor, but it has been successfully used for soil moisture estimation (McFarland, 1992).

1.6.2.4.15 NASA-EOS missions

The United States National Aeronautic and Space Administration (NASA) Earth Observing System (EOS) intends to deploy a suite of Earth observation satellites in the late 1990s and beyond. A few of the proposed sensors that have relevance to soil moisture research are briefly described here.

The Atmospheric Infrared Sounder (AIRS) is a high-spectral resolution, multispectral infrared sounder that will provide skin surface temperature and day/night temperature

differences. It has been selected for flight on the EOS-PM series satellites. EOS-PM is planned for launch in December 2000, EOS-PM2 in December 2005, and EOS-PM3 in December 2010. They will be in a polar, sun-synchronous, 705 km orbit with an afternoon crossing time. Horizontal spatial resolution is 13.5 km, with a swath of 1650 km and an accuracy of 1 °K (Asrar and Dokken, 1993).

The Advanced Microwave Sounding Unit (AMSU) is a passive microwave radiometer that measures atmospheric temperature. It will provide skin surface temperature and day/night temperature differences. Horizontal spatial resolution is 13.5 km with a swath of 1650 km. It has been selected for flight on the EOS-PM Series (Asrar and Dokken, 1993).

The Advanced Spaceborne Thermal Emission and Reflection Radiometer (ASTER) will provide surface radiative (brightness) temperature, which is related to thermophysical properties (such as thermal inertia), vegetation health, soil moisture, temporal land classification (e.g., wet vs. dry, vegetated vs. bare soil), and evapotranspiration. Resolution is 15 m with a 60-km swath width and an accuracy of 1 to 3 °K. It has been selected for flight on EOS-AM1. EOS-AM1 is planned for launch in June 1998. It will be in a polar, sun-synchronous, 705-km orbit with a 10:30 a.m. crossing time (Asrar and Dokken, 1993). ASTER is a multinational instrument to be built in Japan and managed by a U.S.-Japanese team (Ono *et al.*, 1996). ASTER will have the capability of in-track stereo viewing (Enmark, 1993).

The Multifrequency Imaging Microwave Radiometer (MIMR) will provide active microwave observations of soil moisture with a horizontal, wavelength-dependent, resolution of 4.86 to 60.3 km and a swath width of 1400 km, allowing complete global coverage in 3 days. This sensor builds on the successful design of the Special Sensor Microwave/Imager (SSM/I). It has been selected for flight on the EOS-PM series (Asrar and Dokken, 1993).

The Moderate-Resolution Imaging Spectrometer (MODIS) will provide land-surface temperature with a 1 km horizontal resolution, day and night, with an accuracy of 1 °K. The swath width is 2300 km. It has been selected for flight on EOS-AM and EOS-PM series (Asrar and Dokken, 1993).

The primary remotely-sensed soil moisture tool which EOS provides is detailed surface temperature observations. Additionally, EOS will provide both active and passive microwave observations that may be extremely beneficial for soil moisture mapping.

Table 1.12: ASTER instrument satellite and wavebands (Enmark, 1993; and Ono *et al.*, 1991).

Platform	ASTER
Orbit	near-polar, sun sync
Altitude (km)	705 km
Inclination	not available
Period (minutes)	not available
Equatorial Crossing Time	1030
Swath Width (km)	60 km
Radiometric Resolution	8-12 bits
Repeat Cycle (days)	16 days

Band	**Waveband (μm)**	**Resolution (m)**
1	0.52-0.60	15
2	0.63-0.69	15
3N	0.76-0.86	15
3B	0.76-0.86	15
4	1.6-1.7	30
5	2.145-2.185	30
6	2.185-2.225	30
7	2.235-2.285	30
8	2.292365	30
9	2.360-2.430	30
10	8.125-8.475	90
11	8.475-8.825	90
12	8.925-9.275	90
13	10.25-10.95	90
14	10.95-11.65	90

1.6.2.4.16 GOES

The Geostationary Operational Environmental Satellite (GOES) is in a geostationary orbit above the Earth at an altitude of 36,000 km. It has a thermal infrared and a visible band that can view the entire hemisphere every half hour. This is useful for frequent large area analysis, but limits its resolution (Lillesand and Keifer, 1987). The applicability of this sensor to soil moisture mapping is very limited due to its low resolutions and unsuitable wavelengths.

1.6.2.4.17 Bhaskara-II

The Indian satellite, Bhaskara-II, has 3 microwave radiometers operating at 19.35, 22.235, and 31.4 GHz, and 4 look angles of +5.6, +2.8, -2.8, and -5.6 degrees along the ground trace. The spatial resolution is circular with a 125-km diameter (Rao *et al.*, 1986).

Rao *et al.* (1986) utilized the microwave radiometers on the Bhaskara-II satellite to create brightness temperature maps that "have good correlation with soil moisture".

1.6.2.4.18 Priroda

The Russian Space Agency has deployed a powerful remote sensing complex called Priroda (Russian for Nature) on the Russian space station MIR that is expected to be operational during 1996 and 1997. Priroda carries optical and infrared scanners, an imaging spectrometer, a LIDAR, scanning and pointing microwave radiometers, synthetic aperture radar, and high resolution stereo digital cameras. Its has 5 nadar-looking passive microwave radiometers that operate in the 0.3, 0.8, 1.35, 2.25, and 6.0 cm wavelengths with 60 km resolution and swath, a 4 channel passive microwave scanning radiometer at 0.8, 1.35, 2.25, and 4.0 cm with a 40° off-nadar scan angle and a 400 km swath with resolutions ranging from 8 to 50 km, and a three-channel panorama passive microwave radiometer at 2.25 and 6.0 cm with a 40° off-nadar scan angle and a 750 km swath and a resolution of 75 km. Priroda's SAR operates at 9.0 and 23.0 cm with a 50 km swath and 0.15 km resolution. With its wide variety of remote-sensing technology, it is envisioned that Priroda will have a capacity for soil moisture estimation using multi-sensor algorithms to correct for the large soil and vegetation noise components that will be present in its 6 cm passive microwave observations.

1.6.2.4.19 Future smallsat soil moisture platforms

Several future passive microwave L-band satellite-based platforms are in the planning stages. HydroSTAR, an L-band synthetic aperture passive radiometer modeled after the ESTAR sensor (LeVine *et al.*, 1994), is one such system (Cavalieri and St. Germain, 1995). An alternative system is the Inflatable Radiometric Imaging System (IRIS) that uses a large inflatable antenna to observe high resolution passive L-band microwave signals.

1.6.2.5 Remote-sensing soil moisture extrinsic effects

As was seen in the previous sections, there are numerous sources of noise that contaminate the soil moisture signal in most spectral bands. This noise is often due to vegetation, roughness, or atmospheric interference of the spectral signal. For example, a passive microwave sensor not only measures the energy emitted by the soil moisture, but also the energy emitted by the atmosphere, reflected from the surface, and emitted or transmitted from the subsurface (Figure

1.20). A review of the mechanisms that introduce noise into soil moisture remote-sensing is valuable in formulating correction algorithms and subsequent soil moisture mapping.

1.6.2.5.1 Vegetation/surface cover

Vegetation cover affects microwave remote-sensing of soil moisture by attenuating the microwave emission from the soil and by adding to the total radiative flux with its own emission (Figure 1.21). These effects depend on the mass of vegetation and the microwave wavelength, with less vegetation interference at longer wavelengths. Vegetation correction algorithms must include all the significant physical parameters, but must only require data that can be easily obtained (Jackson and Schmugge 1991). The effect of vegetation on the active microwave remote-sensing of soil moisture is complicated by instrument incidence angle, frequency, and polarization. The attenuation for horizontal polarization is relatively weak, but the vertically polarized data are attenuated to a high degree because of the vertical canopy structure. Penetration depth increases with a decrease in frequency or an increase in wavelength (Engman, 1991a).

A parametric approach based on a theoretical model has been developed by Jackson *et al.* (1982) and by Basharinov and Shutko (1975). In this model, vegetation is an absorbing layer that can be quantified in terms of the water content of the vegetation:

$$M_v = 78.9 - 78.4[1 + (e-1)\exp(0.22W)] \tag{1.9}$$

where M_v is the volumetric soil moisture, e is the measured emissivity, and W is the water content of the vegetation. The effect of vegetation on the relationship between microwave brightness temperature and soil moisture is shown in Figure 1.22.

Theis *et al.* (1984) demonstrated a total satellite remote-sensing approach to vegetation correction of soil moisture microwave imagery utilizing a perpendicular vegetation index (PVI) derived from visible and infrared data. For PVI values less than 4.3, the PVI was used to correct the L-band emissivity successfully.

The effect of vegetation on the active microwave remote-sensing of soil moisture is complicated by instrument incidence angle, frequency, and polarization. The attenuation for horizontal polarization is relatively weak, but the vertically polarized data are attenuated to a

high degree because of the vertical canopy structure. Penetration depth increases with a decrease in frequency or an increase in wavelength (Engman, 1991a).

Schmugge and Jackson (1991) developed a dielectric model of the vegetation effects on the microwave emission from soils. This model predicted the absorption loss and optical depth of plant canopies for frequencies between 1 and 40 GHz, based on a vegetation parameter and the vegetation water content value. For vegetation ranging from prairie grass to corn, the "data fit the curve for the refractive model quite well" (Schmugge and Jackson, 1991).

O'Neill and Chauhan (1992) developed a similar algorithm for estimating soil moisture from active and passive microwave correcting for vegetation and roughness effects. The data were collected during the MACHYDRO experiment in Pennsylvania in July 1990. NASA's AIRSAR and PBMR collected active and passive microwave data simultaneously with *in-situ* collection of soil moisture data. Various microwave parameters, such as active, passive, polarization, frequency, incidence angle, etc., were investigated in an attempt to determine which values best captured the soil moisture signal. Engman (1992a) summarized the synthetic aperture radar data collected in this campaign as showing "patterns that are similar to the ground data collected in a small watershed". A similar experiment (MAC 91) with encouraging preliminary results was carried out in 1991 over several sites in Europe, using similar instrumentation (Canuti *et al.*, 1992).

During the Monsoon '90 experiment performed at Walnut Gulch, near Tombstone, Arizona in 1990, AIRSAR imagery was obtained in March and August. By coincidence, the soil moisture conditions (*in-situ* measurements) during the two flights were identical. The C-band data showed significant differences between the two dates due to vegetation differences, while the L-band P-band imagery remained unchanged. This reaffirms the concept that less vegetation correction is needed at longer wavelengths (Dubois *et al.*, 1992).

1.6.2.5.2 Surface roughness

Microwave emission from the soil is dependent on roughness, which is dependent on the microwave frequency being sensed. Longer microwave frequencies tend to portray the surface as smoother than shorter microwave frequencies (Engman, 1991a). Choudhury *et al.* (1979) and

Wang and Schmugge (1980) showed that soil roughness affects soil reflectivity (R) in the following way:

$$R=R_0\exp(-h) \tag{1.10}$$

Here, R_0 is the smooth surface reflectivity, and h is a roughness parameter. This model can be combined with a radiative transfer model of the soil to obtain good agreement with the observed brightness temperatures (Choudhury, 1979).

More recent work has shown less than 3% error for L-band microwave-sensed agricultural rows in which the row height to row spacing is less than 2 (Promes *et al.*, 1988).

The possibility of using a multisensor approach to improve the estimates of soil moisture under field conditions was explored by Theis *et al.*, (1986). Scatterometer measurements were used to account for the effects of surface roughness. Inclusion of terms related to the emissivity measured by the radiometer and the scatterometer roughness improved the R^2 values from 0.22 to 0.65 for C-band and from 0.69 to 0.95 for L-band.

For active microwave, the surface roughness effect depends on both the wavelength and the incidence angle. This effect can be minimized with incidence angles of less than 15 or 20 degrees (Engman, 1991a).

Shi *et al.* (1991, 1992) developed an algorithm that retrieves soil moisture estimates from SAR at high incidence angles. It was found that the co-polarization ratio is sensitive to soil moisture change, but not surface roughness, making surface roughness measurements unnecessary. The study showed that incidence angles greater than 40° are optimal for this monitoring; this conflicts with the previous study's findings (Engman, 1991a).

1.6.2.5.3 Atmospheric effects

Microwave electromagnetic radiation interacts with the atmosphere in two ways: (1) absorption by clouds and rain, and (2) absorption and scattering by atmospheric gases. Water vapor and oxygen are the gases that primarily interact with microwaves. Water vapor absorption lines are at 22.2 GHz (1.35 cm) and 183 GHz (0.164 cm), and oxygen absorption is at 60 GHz (0.50 cm) and 118 GHz. By taking into account the densities of these gases, it is found that, for

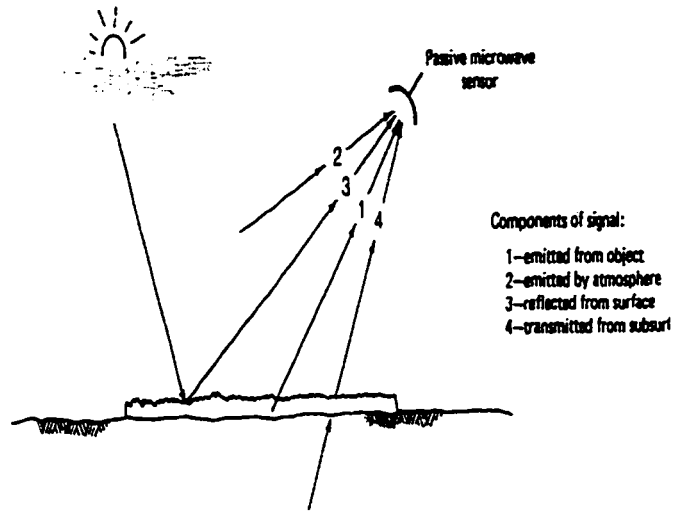

Figure 1.20: Components of a passive microwave signal (Lillesand and Keifer, 1987).

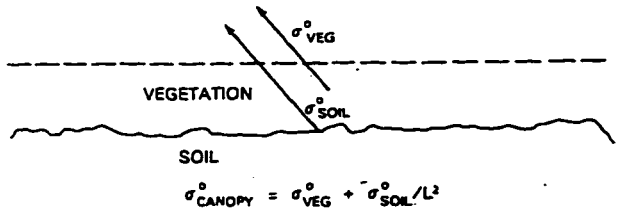

Figure 1.21: Sources of radar backscatter (Schmugge, 1985).

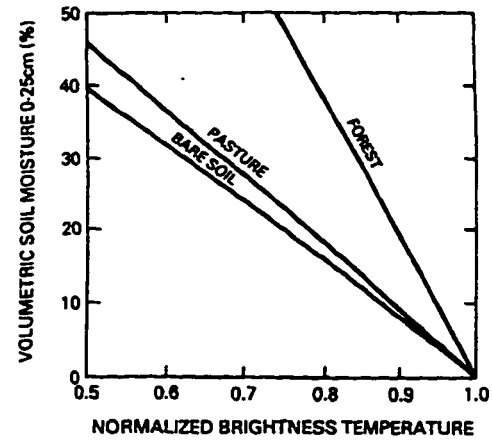

Figure 1.22: Relationship between normalized brightness and soil moisture (Jackson, 1982).

frequencies below 10 GHz and wavelengths above 3 cm, the transmission through the atmosphere is better than 99%.

The effect of clouds depends on the phase of the water in the clouds and the water droplet size. An electromagnetic wave will cause motion of the charges contained in the particle, which will absorb some of the energy, and radiate some, producing a scattered field. A few general statements can be made about this interaction: (1) Clouds of ice particles have little effect on microwave radiation because of small particle sizes and the small dielectric constant of ice. (2) Non-raining clouds of water particles have little effect on frequencies below 15 GHz. (3) The effect of raining clouds with large particles must be considered for frequencies above 3 GHz (Schmugge, 1985).

According to Schmugge *et al.* (1986), at the longer wavelengths best suited for soil moisture sensing (21 cm), atmospheric effects are minimal.

1.6.2.5.4 Heterogeneity and mixed scenes

By their very nature, remote sensors integrate the spectral signal they measure over a finite surface area (the IFOV, or pixel). This area is typically from 20 meters to several kilometers, depending on the sensor. Soil moisture and noise sources (vegetation, roughness, etc.) vary considerably on scales much smaller than this. Hence, this variability is averaged by the sensor and is lost. "This mixing is particularly troublesome in some applications, such as the mapping of soils or vegetation in sparsely vegetated arid areas" (Schowengerdt, 1983). Some examples of the difficulties which mixed scenes can cause are as follows: (1) Validation and comparison of remotely-sensed soil moisture with surface point measurements is problematic. These two measurements are not representative of the same area. For example, point measurement do not reflect the average of a larger area. (2) Vegetation and roughness may vary across the integrated area, making correction for such noise effects difficult. (3) Integration of soil and non-soil (water bodies, snow, rock, urban areas, etc.) areas could introduce significant error to the soil moisture signal. (4) Depending on the size of the IFOV, very dry areas and wet areas could be averaged to produce a moderate soil moisture estimate. This could be problematic when, for example, wet areas near rivers are averaged with dry mountain areas. A flood forecaster may use this

information and vastly underestimate the runoff. (5) The differential interaction between sensor view angle and plant canopy geometry with different view directions can also be difficult to resolve (Schowengerdt, 1983). According to Schowengerdt (1983), some research into techniques for eliminating class proportions has been done by Horwitz *et al.*, (1977), Salvato, (1973), and others. No research that analyzed these mixed scene problems in relation to operational soil moisture mapping has been found.

1.6.2.5.5 Field calibrations

Remote sensors are only capable of measuring the amount of radiance in their instantaneous field of view. As has been seen, this radiance is a mixture of different signals, one of which may be related to soil moisture. Therefore, *in-situ* ground measurements are necessary for establishing some relationship between soil moisture and observed radiance. These measurements are also essential for analyzing and isolating noise components and for evaluating the sensitivity of individual spectral bands to soil moisture.

There are many, well-established methodologies for *in-situ* point measurement of soil moisture. Some of these are gravimetric, resistive, capacitive, heat flux, nuclear, tensiometric, and time-domain reflectrometry techniques. These different methodologies vary tremendously in their accuracy, calibration, and sensitivity. A few are described below, but for a complete description, see Klute (1986).

Gravimetric observations: The oven-drying soil moisture measurement technique is the standard for calibration of all other methods (Schmugge *et al.*, 1980). The method involves obtaining a wet soil sample weight, W_w, drying the sample at 105 °C for 24 hours, then obtaining the dry sample weight, W_d. Then with a measurement of the bulk density, Y_d, and the density of water, Y_w, the volumetric water content can be found (Schmugge *et al.*, 1980):

$$\theta = \frac{W_w Y_d}{W_d Y_w} 100\% \tag{1.11}$$

Neutron thermalization: The neutron scattering method indirectly determines soil moisture by measuring the thermal or slow neutron density. High-energy neutrons are emitted by a radioactive source into the soil and are slowed down by elastic collisions with nuclei of atoms

and become thermalized. The energy loss is much greater with atoms of low atomic weight; thus, hydrogen can slow fast neutrons more effectively than any other soil element. Therefore, the density of the resultant cloud of slow neutrons is a function of the soil moisture. To measure the soil moisture, the number of slow neutrons returning to the detector are counted per unit time, and the volumetric soil moisture is determined with a previously established calibration curve (Schmugge *et al.*, 1980).

TDR: Time Domain Reflectometry (TDR) measures the apparent dielectric constant of the soil, ϵ, by measuring the transmit time, t, of a voltage pulse applied to a transmission line or soil probe of length, L, embedded in the soil:

$$\epsilon=(ct/2L)^2 \tag{1.12}$$

where c is the speed of light in a vacuum (Klute, 1986). Soil dielectric constant is directly dependent on volumetric soil moisture content, and well-established methods exist to convert between them.

Tensiometric techniques: This method measures the capillary or moisture potential through a liquid filled porous cup connected to a vacuum gage. Then to convert to soil moisture, a water characteristic curve must be found through knowledge of soil characteristics or by measurement in the lab.

Bulk density: Bulk density is an important variable for converting between gravimetric and volumetric soil moisture, for calculating porosity, and for unsaturated flow modeling. Bulk density is the ratio of the mass of dry solids to the bulk volume of soil (the volume of solids and pore space). Generally, the volume is determined in the field, and the mass is determined after drying (Klute, 1986).

It has been observed that the spatial and temporal variability of soil moisture is significant on small scales, making spatially representative, *in-situ* soil moisture measurements difficult. This situation is a serious source of error when *in-situ* soil moisture measurements are being used to calibrate remote-sensing systems. Another source of error would be obtaining *in-situ* soil moisture measurements that are characteristic of the depth of penetration of the remote-sensing spectral band. This is complicated by changing spectral penetration with soil moisture content and decreasing sensitivity of the radiance with depth.

In-situ soil moisture measurements are generally expensive and problematic. Therefore, at this writing, few 'soil moisture networks' exist for the calibration of remote-sensing systems. Most soil moisture remote-sensing research utilizes a small number of *in-situ* soil moisture measurements that fail to address any of the above complications.

1.6.2.6 Remote-sensing soil moisture examples

The ultimate goal of developing remotely-sensed data is to produce accurate soil moisture maps that have the appropriate temporal and spatial resolutions to be used in various applications. In this section, several examples of the successful production of soil moisture maps are presented.

The 21-cm wavelength, passive microwave PBMR instrument was used to map surface soil moisture patterns as part of the International Satellite Land-Surface Climatology Project's (ISLSCP) first field experiment (FIFE). Measurements were made for two small watersheds in the Konza Prairie a few kilometers south of Manhattan, Kansas. Gravimetric, ground-truth soil moisture measurements were made under the flight lines in the top 5 cm layer at 50-m intervals. The PBMR instrument is capable of producing two-dimensional brightness temperature maps which can be calibrated with ground-truth data to infer soil moisture patterns. A simple linear regression between normalized brightness temperature *(e)* and *in-situ*, volumetric soil moisture *(W)* revealed excellent correlations between *W* and *e* (Figure 1.23; Wang *et al.*, 1989). The correlation coefficients were better than 0.96 for two different studies. A decrease in sensitivity in the presence of vegetation was also noted. A soil moisture map that was produced in this manner is shown in Figure 1.24. This soil moisture pattern was observed shortly after a rainfall event. After six days of drying, another map was observed (Figure 1.25), in which the soil moisture patterns displayed distinct separation between the two small watersheds (Wang *et al.*, 1989). Additional PBMR images of the FIFE site are shown in Figure 1.26 (Schmugge *et al.*, 1992).

Ladson and Moore (1992) explored the same data presented above, with less successful results. They concluded that the PBMR was capable of measuring the overall drying trend of the surface soil, but that the utility of the data was limited by registration problems. They also

concluded that the spatial distribution of soil water was not well predicted by the microwave remote-sensing.

Jackson *et al.* (1987) used the PBMR sensor to produce a large-area soil moisture map over a 2700-km^2 area in the Texas High Plains Underground Water Conservation District. The microwave data were processed to provide emissivity data at a 0.32 km^2 resolution. It was combined with existing soil texture and land cover data bases to estimate surface soil moisture over the area (Jackson, 1988).

Schmugge and Jackson (1991) used the PBMR sensor, flown on 6 C-130 flights, to map soil moisture over Walnut Gulch, Arizona during the Monsoon '90 experiment. They found that the PBMR data were useful in mapping rainfall patterns and the subsequent spatial and temporal variations of the surface moisture during the drydown process. They were also able to make direct comparisons between soil moisture and brightness temperature as was accomplished by Wang *et al.* (1989) in FIFE. Schmugge and Jackson observed a variation in sensitivity from site to site, which they suspected may be a result of the large surface rock fraction. An example of these Walnut Gulch PBMR images is shown in Figure 1.27 (Schmugge *et al.*, 1992).

Kostov *et al.* (1991) developed a program to map soil moisture during the period 1987-1989 in Bulgaria using L-band passive microwave sensors. Forty-six agricultural fields with a total area of 1700 km^2 were overflown, and the data were processed to provide soil moisture maps of the top 1 meter. They encouraged additional research on the effects of vegetation on the microwave emission with depth.

Schmugge *et al.* (1975) used the Nimbus-5 satellite ESMR microwave instrument to produce some preliminary brightness temperature maps that are closely related to soil moisture. These maps were produced for the central Illinois-Indiana, the Mississippi Valley, and the Great Salt Lake areas. The main limitation in this mapping was the interference of vegetation and the coarse resolution of the sensor (10-25 km). An example of the Illinois-Indiana area map produced by this system is shown in Figure 1.28.

Carrol (1981) presented an operational gamma radiation system that accurately estimates soil moisture in the upper 20 cm with an error of 2.5%. This system is mounted on a low-flying aircraft (150 m above the ground), with a resolution of about 300 m. A network of 240 flight

lines of 6 km^2 each has been collected in the upper Midwest and used to calculate real-time, aerial soil moisture values. He established that the air-borne gamma radiation technique is capable of measuring real-time, mean, areal soil moisture values over large areas with adequate accuracy for hydrological and agricultural applications. He identified the problems that this technique assumes a uniform horizontal soil moisture distribution over the flight line and a uniform vertical distribution in the upper 20 cm of the soil. Both of these assumptions are not valid and, together with the low flight elevations required for gamma measurement, seriously limit this operational application of technique.

A number of conclusions can be made based on the examples presented above. First, it is clear that remote-sensing of soil moisture is not yet a fully operational technology. The above examples comprise a set of isolated trials at soil moisture mapping. They are mostly performed with aircraft based measurements, and leave many unanswered questions about noise sources. Second, it is clear that microwave remote-sensing of soil moisture is the most promising technology for remote soil moisture measurement. Clearly, it has been demonstrated through these examples that soil moisture mapping utilizing remote-sensing is possible, but significant progress to be made to make it an operational technology.

1.6.2.7 Soil moisture remote-sensing summary

Remote-sensing of soil moisture content is not a truly operational technology as yet, although the theory and methods to develop this important remote-sensing resource do exist. The following observations can be made regarding the current state of large-scale quantitative soil moisture mapping based on remote-sensing.

(a) Large-scale soil moisture mapping based on remote-sensing would be valuable in many different applications, both practical and theoretical.

(b) There is a strong theoretical basis for believing remote-sensing of soil moisture is possible using many different parts of the electromagnetic spectrum, but the contamination of these soil moisture signals by other surface properties is not fully understood, and thus correction algorithms are both scarce and difficult to transfer from one application to another.

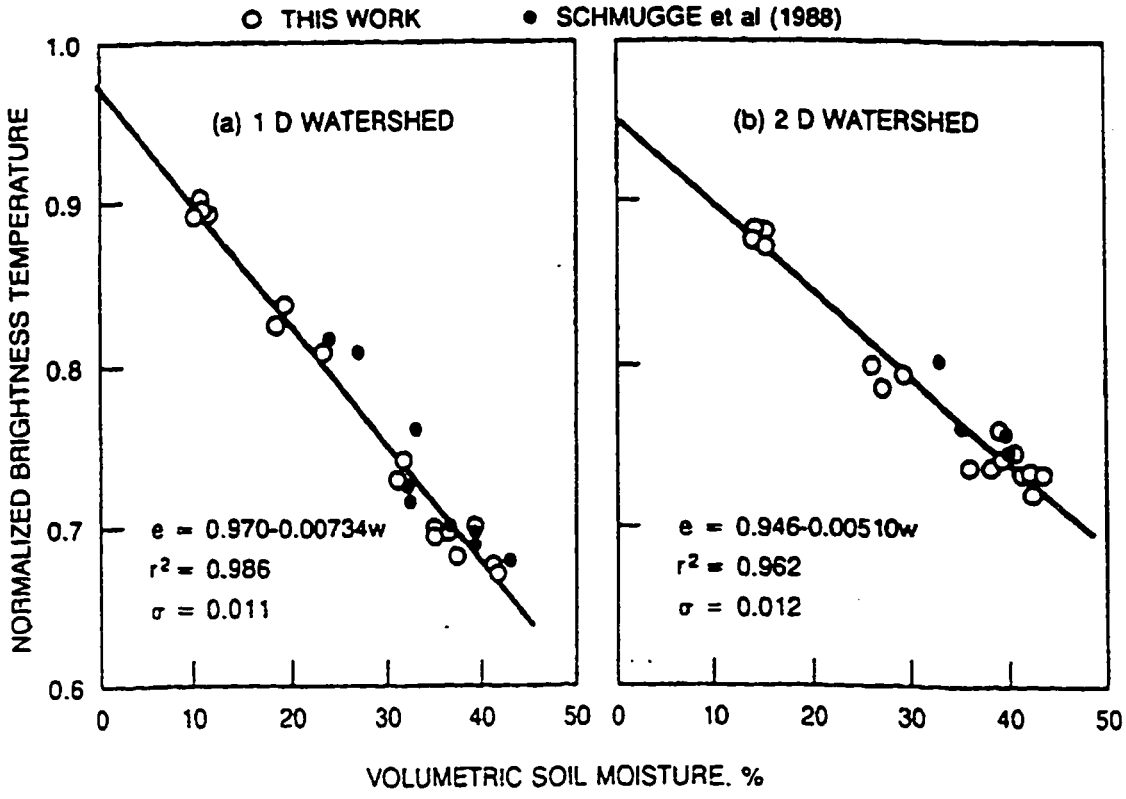

Figure 1.23: Correlations for 2 different watersheds (Wang *et al.*, 1989).

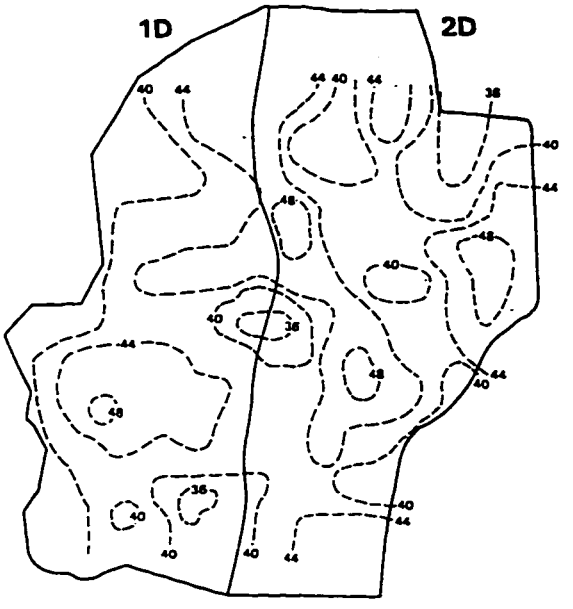

Figure 1.24: Top 5cm soil moisture on 28 May 1987 (Wang, *et al.*, 1989).

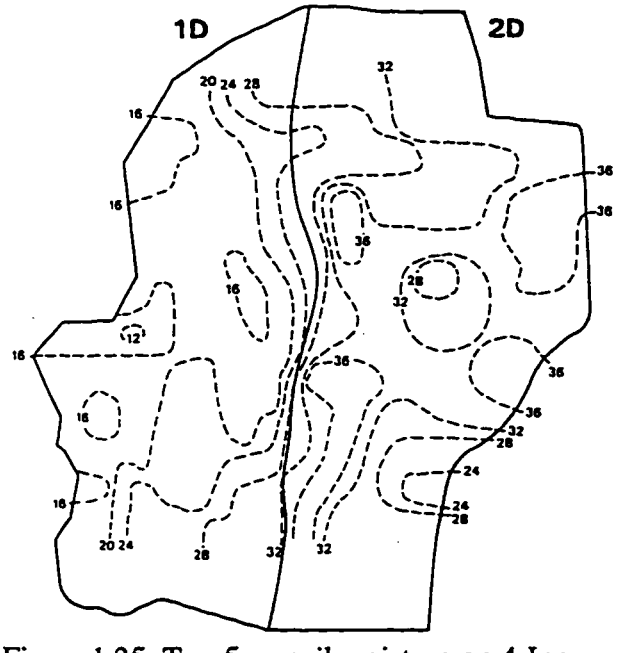

Figure 1.25: Top 5cm soil moisture on 4 June 1987 (Wang, *et al.*, 1989).

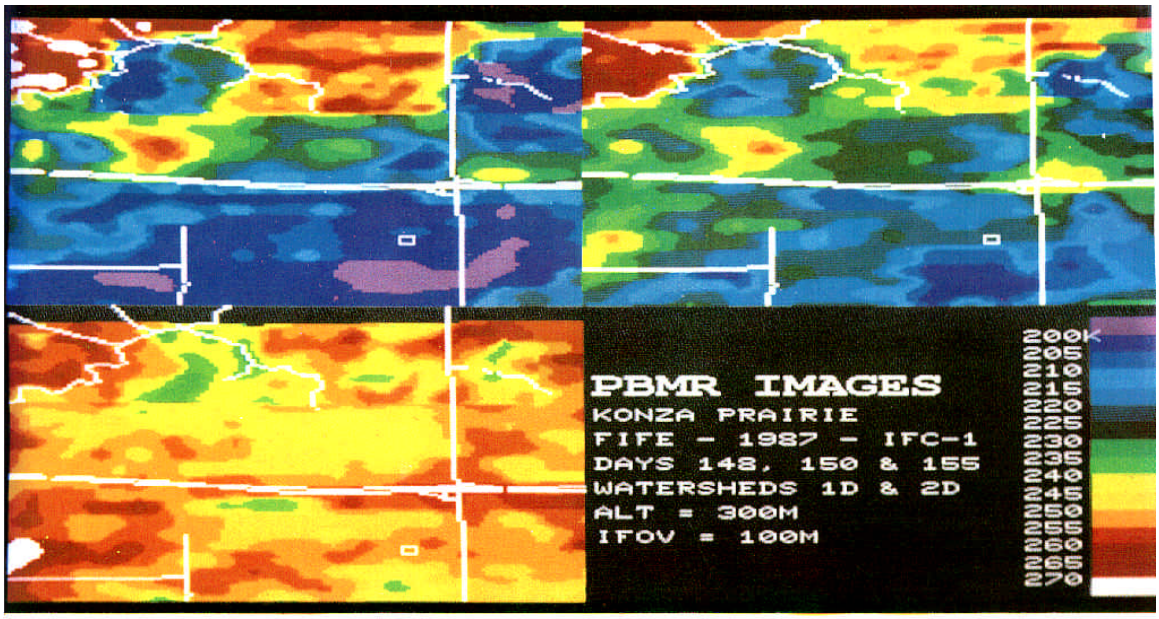

Figure 1.26: False color brightness maps for a 4x4 km section of the FIFE study area (Schmugge *et al.*, 1992).

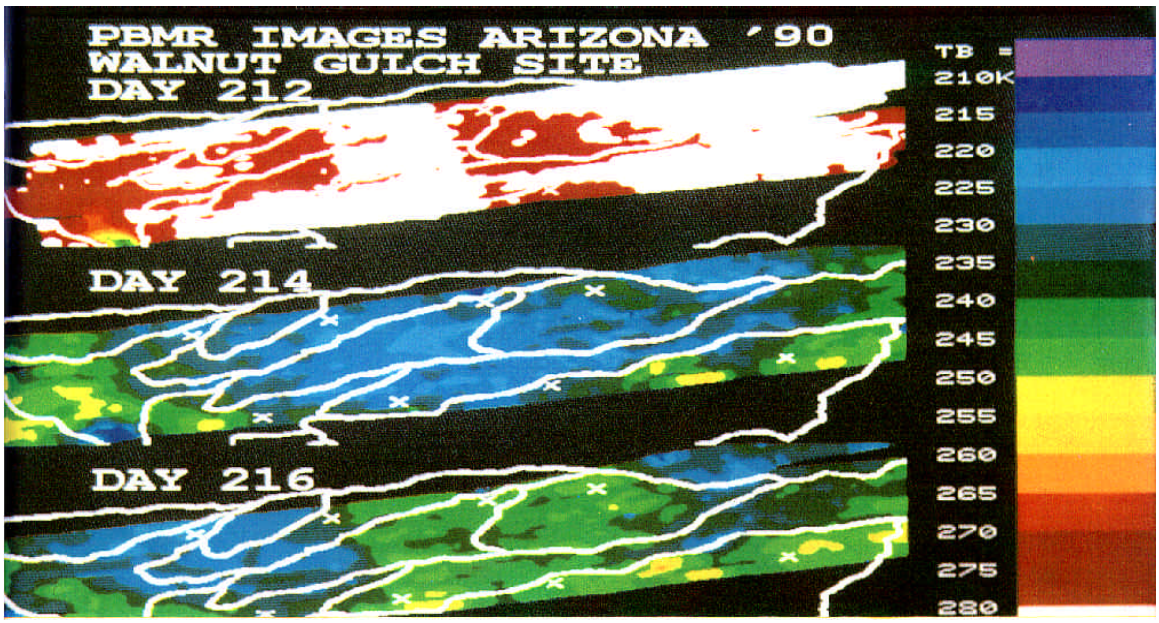

Figure 1.27: PBMR images of 21 cm brightness temperature over the Walnut Gulch watershed during Monsoon '90. Metflux sites are marked with an X. (Schmugge *et al*, 1992).

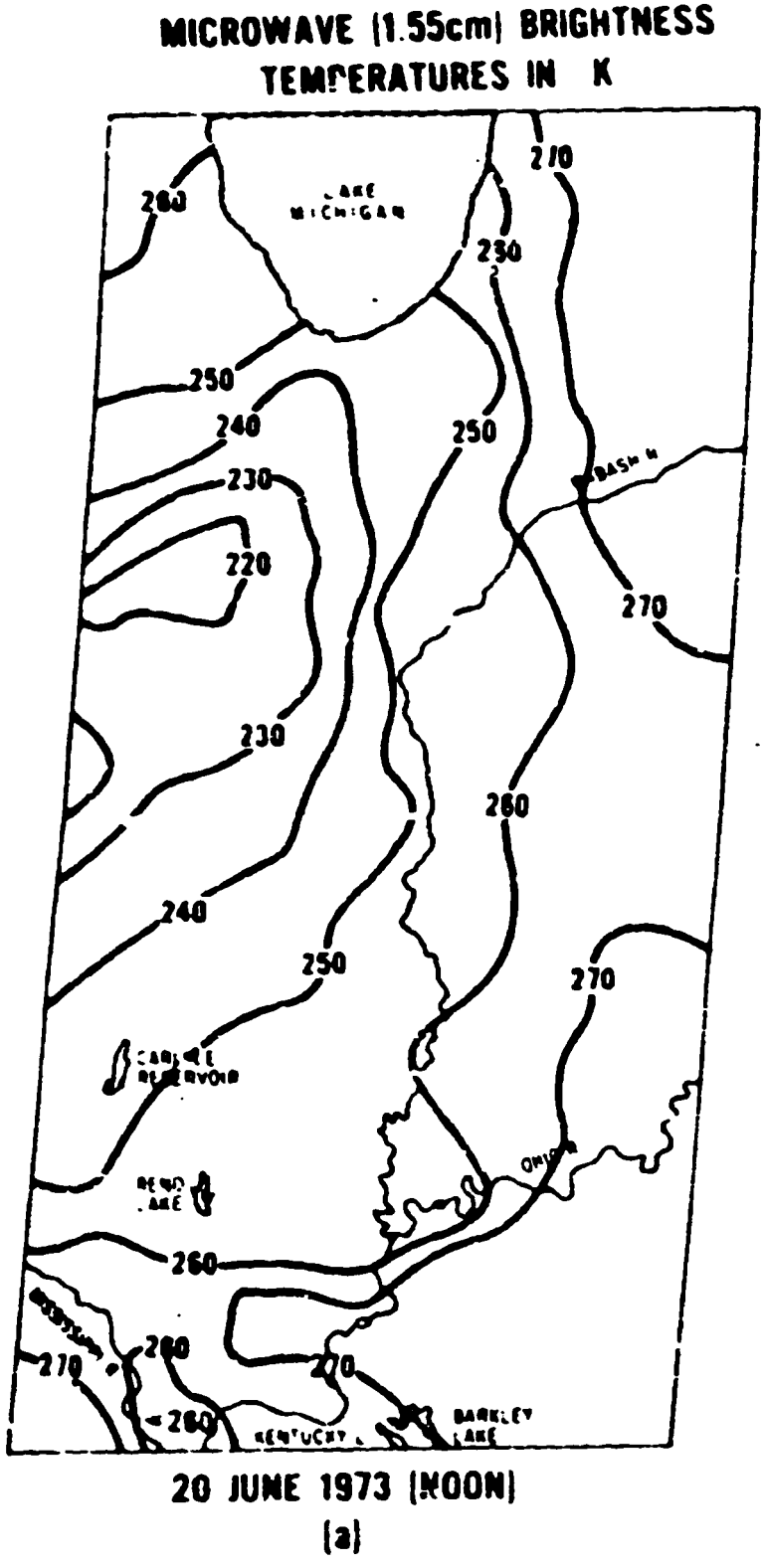

Figure 1.28: ESMR brightness temperatures (Schmugge *et al.*, 1975).

(c) Many existing or planned sensors on remote-sensing platforms, both air-borne and space-borne, have some capacity to sense soil moisture, but none of these sensors has been designed to be an 'ideal' soil moisture sensor. Typically, the sensor either lacks sufficient temporal or spatial resolution for soil moisture investigations or it operates in a part of the spectrum that is insensitive to soil moisture. Several sensors have the qualitative capability to determine whether a soil surface is wet or dry, but their quantitative measurement capabilities are limited.

(d) Most remote-sensing and image-processing research into soil moisture has focused on developing and testing conversion and correction algorithms, and a few have applied those algorithms to map soil moisture, albeit in a very small spatial and temporal window. However, the goal of developing an operational, large-area quantitative soil moisture mapping system has been impeded, primarily by the lack of suitable remotely-sensed data.

(e) Although long-wave passive microwave remote-sensing is preferable for soil moisture remote-sensing, it's 'ideal' global space-platform operation is limited by the large antenna size needed. Therefore, research at in the near future will primarily use synthetic aperture radar (SAR), and passive microwave with relatively low resolutions.

(f) Multitemporal and multiwavelength image-processing techniques have the most utility in maximizing the soil moisture signal, but a combination of numerical simulation methods and remotely-sensed data sources may be the best route for developing an operational soil moisture mapping system, given that data limitations are unlikely to change in the near future. It has been demonstrated that soil moisture mapping utilizing remote-sensing is possible, but there is a need for substantial progress to make it an operational technology.

(g) The spatial patterns of soil moisture observed by remotely sensing affords a major advantage over surface point measurements. Methods to incorporate the soil moisture pattern information provided by remote-sensing into model simulations are essential to fully use this valuable data source.

Traditionally, hydrologists have used lumped models based on point measurements. Because of the spatial nature of remotely-sensed soil moisture information, there is a need to modify these models or to develop new models that can use this new information source.

Further, there is a need for hydrologic models that can estimate soil moisture profiles from surface measurements or from a time series of near surface measurements (Goodrich *et al.*, 1994). To quote Engman (1991a), "There is a need to develop software ... that can truly integrate GIS, remote-sensing data from several sensors, and hydrologic models, so that all the calibration, scale, format ... problems become transparent to the hydrologist, and he can concentrate on the hydrologic analysis".

1.6.3 Soil moisture modeling

There has been extensive research to investigate the transport of water through the soil and to investigate soil moisture interactions with the atmosphere. Many numerical models are available to estimate soil moisture, although predictions are, of course, influenced by model structure and errors in input variables and model parameters. As described above, the theory of soil moisture remote-sensing is well developed, but, in application, remotely-sensed measurement of this critical parameter is inexact. Therefore, given the complementary strengths and weaknesses of remote-sensing and modeling, it has been suggested (Schmugge *et al.*, 1980) that a combination of these two approaches be used to derive estimates of soil moisture.

The goal in this research is to utilize the wealth of existing knowledge on soil moisture movement in an operational framework that incorporates both observations and modeling. The work of Milly (1986a) is a precursor for this research. Milly used a Kalman filter framework, integrated with a simple linear reservoir/soil moisture model to assimilate remotely-sensed soil moisture measurements. Although his research was designed to address questions related to sampling frequency and response time, it nonetheless demonstrated the potential usefulness of the integrated observational modeling concept.

A significant problem when estimating soil moisture using numerical models has been the largely non-physical nature of the soil moisture variables in the models themselves. For example, many models represent the soil moisture store as a bucket that fills or empties, depending on the precipitation and evaporation at the surface, and that has a finite size -- with excess precipitation converted to runoff. Thus, in the case of the bucket model, soil moisture is represented as a depth of water, which is not comparable with the volumetric measurements

provided by most soil moisture measurement systems. Recognizing these conceptual problems, this research gives special attention to the realism of the modeled soil moisture states.

A further major problem in the application of remotely-sensed soil moisture to operational problems (agriculture, climate studies, etc.) is that the depth of measurement is typically very small -- though multifrequency microwave measurements, which penetrate the soil to different depths can provide some measure of the soil moisture profile. Physical models can be used to estimate the root-zone profile of soil moisture by using remotely-sensed surface soil moisture in combination with soil parameters and previous conditions. Ragab (1992) reviewed the following approaches to model the profile of soil moisture from surface measurements.

(a) Analytical solution of Richard's equation: Camillo and Schmugge (1983) used this approach, along with a sink term for plant water uptake, and tested the hypothesis against laboratory and field soil moisture profile measurements with good agreement.

(b) Hydraulic equilibrium of the soil profile: This approach assumes that soil water flows in response to a potential difference until equilibrium is attained. Jackson (1980), Kondratyev *et al.* (1977), and Famiglietti and Wood (1991b) used this approach to estimate the available soil water in the top meter of soil based on passive microwave measurements, with satisfactory results.

(c) Statistical correlation between soil moisture at the surface and that in the profile: This regression technique was used by Jackson *et al.* (1987), Zotova and Geller (1985), Reutov and Shutko (1986), and Mkrtchjan *et al.* (1988) with reasonable success.

(d) The antecedent precipitation index (API) approach: This approach uses simple correlation between API and soil moisture at different depths to estimate profile soil moisture. It was explored by Saxton and Lenz (1967), Blanchard *et al.* (1981), and Wetzel and Woodward (1987).

(e) The boundary layer modeling approach: A boundary layer model, which included a single layer canopy and two soil layers to calculate the surface energy- and moisture-balance, was developed and is described by Deardroff, (1978), Soares *et al.* (1988), Noilhan and Planton (1989), and Jacquemin and Noilhan (1990). Several studies were carried out with this model in which it successfully estimated profile soil moisture (Ragab, 1992).

In this research, a detailed, multi-layer soil moisture model which uses an analytical solution of Richard's equation to predict moisture movement through several soil layers is used. This model belongs to a group of models known as Soil-Vegetation-Atmosphere Transfer Schemes (SVATS), whose aim is to simply and realistically represent water, energy, and often carbon fluxes to the atmosphere in General Circulation Models (GCMs) or Numerical Weather Prediction Models (NWPs).

The term parameterization usually refers to functional relationships that describe the modeled processes. The most commonly used land hydrology parameterization is Budyko's 'bucket' model (Manabe, 1969), which highly simplifies the infiltration and evaporation processes and uses constant parameter values over the globe. Recognizing the shortcomings of this type of SVATS, researchers have developed alternatives. Fully developed biosphere-atmosphere land-surface models that calculate the transfer of mass, energy, and momentum between a vegetated surface and the atmosphere have been developed. Two relevant examples are the Biosphere-Atmosphere Transfer Scheme (BATS) (Dickinson *et al.*, 1986) and the Simple Biosphere Model (SiB) (Sellers *et al.*, 1986).

The development of SVATS schemes was motivated by recent advances in plant physiology, micrometeorology, and hydrology that control biosphere-atmosphere interactions (Wood *et al.*, 1992). But many limitations of the SVATS approach remain. The development of realistic parameterizations that represent the relevant land-surface dynamics at the GCM grid scale (on the order of 10,000 km^2) remains a challenge. The global estimation of parameters also remains a problem. And finally, understanding how to represent the sub-GCM grid scale spatial variability in these models is critical (Wood *et al.*, 1992).

1.6.4 Four-dimensional data assimilation

There are insufficient observations at any one time to determine the state of the Earth's system; hence, if this is to be accomplished, additional information must be used (Lorenc, 1995a). For example, knowledge of the typical structure of water well drawdown allows an 'analysis' of the water table state, based on scattered observations. Advancement beyond this subjective approach requires the integration of water table behavior in a forecast model. This

enables the use of observations that are distributed in time and provides a means for representing Earth system processes. "Assimilation is the process of finding the model representation which is most consistent with the observations" (Lorenc, 1995a). Charney *et al.* (1969) first suggested combining current and past data in an explicit dynamical model, using the model's prognostic equations to provide time continuity and dynamic coupling among the fields. This concept has evolved into a family of techniques known as four-dimensional data assimilation (Stauffer and Seaman, 1990).

The use of four-dimensional data assimilation (4DDA) in hydrology is based on the likelihood that environmental observations are irregularly distributed in time and space and are obtained using a wide variety of instrumentation and methods, so they will continue to be inhomogeneous in accuracy (NRC, 1991). In essence, 4DDA incorporates a range of diverse data fields to update the state variables in a numerical model to provide that model with the best estimate of the current state of the natural environment so that it can then make more accurate predictions. The principle of 4DDA is illustrated in Figure 1.29.

The basis of geophysical model data assimilation is the four-dimensional representation of a unified, dynamically evolving geophysical system by a mathematical model. This model has the capacity to predict dynamic changes occurring in the system, accept the insertion of new observational data distributed heterogeneously in time and space, and blend earlier information and current information objectively under rigorous quality control. The use of data assimilation leads to an estimate of the state of the system that is more accurate and complete than that which can be achieved from a single set of observations taken at a particular time. The model is used to extrapolate information numerically in time -- from the recent past to the present. The predicted present model state constitutes the 'background' field against which a current set of observations are checked for quality control, interpreted, and synthesized with the extrapolations of all previous information. From this updated state, the model is then integrated into the future to provide a forecast and the background field for the next assimilation.

Four-dimensional data assimilation can be implemented through a statistical or optimal interpolation technique (using a Kalman filter, or the adjoint method), or in a continuous data insertion manner (Newtonian nudging technique) (NRC, 1991). Some techniques can run the

model backwards and forwards in time to optimize the resulting fields, and it is possible that 4DDA could be used to develop a 'self-optimizing model', which would update not only the states of the model, but also the model parameters.

Four-dimensional data assimilation was developed in meteorologic forecasting applications. It has been successfully used to improve numerical weather forecast models, many of which already have well-developed meteorological 4DDA systems in place (NRC, 1991). It has been successfully used in ocean sciences (Budgell, 1986) and in rainfall analysis (Bussires and Hogg, 1989). However, the technique is not yet been widely used in hydrologic modeling partly, because of its complexity and the irregularly shaped coordinate systems used in watershed modeling but also because of hydrology's focus on water-balance studies and the lack of a comprehensive hydrologic data exchange system (NRC, 1991).

The potential benefit of data assimilation in Earth system science is tremendous and can be summarized as follows (Rood *et al.*, 1994): (1) Data assimilation objectively places a diverse set of observations on a regular spatial and temporal grid. The raw observations are organized and given dynamical consistency, thereby enhancing their usefulness. (2) Data assimilation is a methodology for estimating unobservables. This allows the progress of research that would be impossible without assimilation. (3) Assimilation propagates information into regions of sparse observations. (4) Data assimilation provides a valuable data quality control function. Through comparison of observations with previous forecasts, data assimilation can identify and eliminate spurious data. (5) Data assimilation is the ultimate means of validating and improving Earth-system models. Continuous model confrontation with real data helps to identify model weaknesses.

1.6.4.1 Methods

The development of a viable four-dimensional data assimilation scheme to update modeled soil moisture states using all available soil moisture and soil moisture related measurements is a critical new component of this research. Data assimilation schemes typically include the following steps.

(1) *An error-checking procedure is established for each data type that is to be assimilated to correct or eliminate erroneous data* (Bengtsson, 1985). This is necessary because incorrect data can have a detrimental effect on the analysis and can significantly reduce the quality of the 4DDA predicted fields. Soil moisture observations can contain different types of error, including errors due to faulty instruments, improper processing, or unsatisfactory communication of the data. Experience in meteorological models suggests that two levels of data checking are required. The first will involve checking for gross errors before the data enter the data assimilation process. The second check is more subtle and involves comparison against modeled predictions and nearby observations and rejection of values deviating more than a prescribed tolerance.

In this study, soil moisture errors were minimized through the use of in-situ observations in the inversion algorithm (eliminates overall bias), and through the elimination of outliers by only allowing the assimilation of soil moisture observations within the model's predefined soil moisture range. This second check eliminates unrealistic observations (i.e. negative values).

(2) *Because observations seldom occur at the exact location of model grid points, a three-dimensional interpolation process is typically employed to project the observed data onto the grid of the model.* Well-established optimum interpolation methodology first proposed by Eliassen (1954) and Gandin (1963) has emerged as the preferred interpolation method for 4DDA methodologies (Bengtsson, 1985).

A 'semi-continuous' assimilation scheme is employed in this research; that is, whenever observational data are available, they are assimilated into the model at the nearest model time step. In doing this, it is assumed that soil moisture, for instance, does not undergo substantial change between consecutive (1 hours) time steps. This assumption is violated during storms, so assimilation during or 'across' storm events is not done.

(3) *The best initial state for the next predictive model step is obtained by merging the new observations with the information from past observations carried forward by the model.* The system was designed so that the values of initial states are an optimum function of the predicted model states and the new observations, this being dependent on the relative accuracy of the data and the model predictions (Bengtsson, 1985). Blending of observational and model data can be

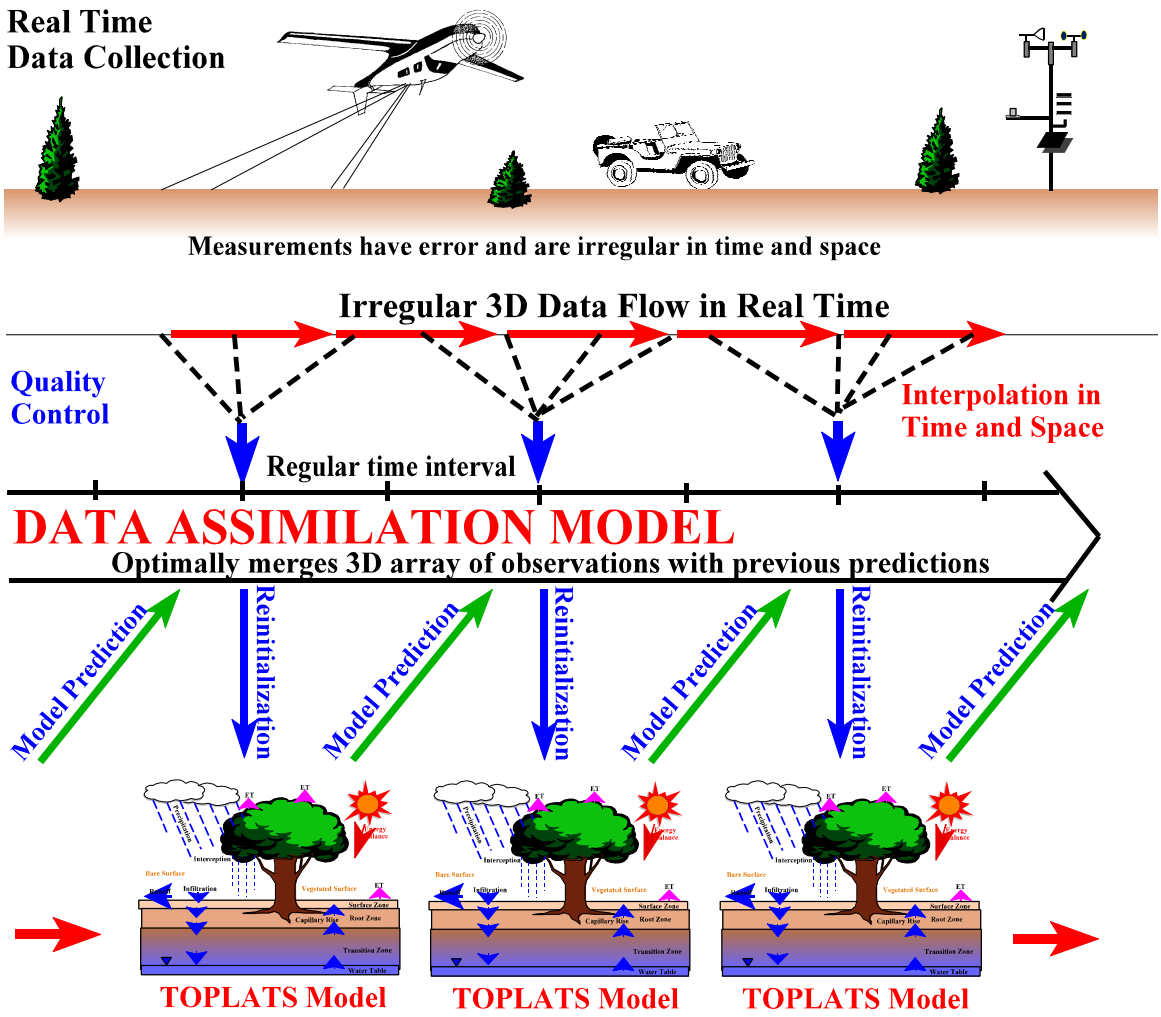

Figure 1.29: The TOPLATS four-dimensional data assimilation process.

done by assuming the model is reasonably accurate at all times, so corrections are only done where data are available (McPherson *et al.*, 1979) or, alternatively, by allowing a few sparse data points to correct the entire state field. Because soil moisture data are typically scarce, it is possible that whole-field correction might ultimately prove to be the preferred technique. One way this can be accomplished is by using an objective analysis optimum matching technique, as described by Gandin (1963). Four-dimensional assimilation can be alternatively defined as objective analysis with the added dimension of time.

(4) *The model is reinitialized with the analysis, or merged field, and integrated forward in time.* The assimilation cycle then restarts when observation data are once again available.

Data assimilation may be either continuous where, observations are continuously being inserted into a running model, or intermittent where observations are inserted at discrete separate times (Bengtsson, 1975).

Bayesian derivation of analysis equations: It can be shown that a logical progression starting with Bayes' theorem can lead to a variational equation for 'best' data assimilation analysis. Bayes' theorem shows that the posterior probability of event A occurring, given that event B occurred, is proportional to the prior probability of A multiplied by the probability of B occurring, given that A is known to have occurred:

$$P(A|B) \propto P(B|A)P(A) \tag{1.13}$$

Then, if A is the event $x=x_t$, and B is the event $y=y_0$:

$$P(x=x_t|y=y_0) \propto P(y=y_0|x=x_t)P(x=x_t) \tag{1.14}$$

where t indicates the true value, and o indicates the observed value. The previous equation defines an N_x-dimensional probability distribution function that specifies all that can be known about the analysis, which is defined as $P_a(x)$. The 'best' estimate x_a is either the mean or mode of $P_a(x)$:

$$x_a = \int x P_a(x) dx \tag{1.15}$$

or:

$$x_a = x \ \textit{that maximizes} \ P_a(x) \tag{1.16}$$

These are the minimum variance and maximum likelihood estimates of x_a respectively.

The prior probability $P(x=x_t)$ contains all pre-observation knowledge about x. Next, this is written in terms of deviations from a known background x_b:

$$P(x=x_t)=P_b(x-x_b) \tag{1.17}$$

Observations are subject to random errors, so if the true values of y are given by $y_1=y_t$ then these errors can be expressed by:

$$P(y=y_0|y_1=y_t)=P_0(y_0-y_t) \tag{1.18}$$

P_0 may be a function of x_t or x_b. Next, $P(y=y_0|x=x_t)$ needs to be found and can be written as $P_{of}(y_o-y_f)$, where $y_f=K_n(x_t)$. Then, if the generalized interpolation K_n is exact:

$$y_f=y_t \tag{1.19}$$

and:

$$P_{of}(y_o-y_f)=P_o(y_o-y_f) \tag{1.20}$$

In general, K_n is inexact, and its error is described by:

$$P(y_1=y_t|x=x_t)=P_f(y_1-y_f) \tag{1.21}$$

where P_f is the interpolation operator error function. $P(A)=\int P(A|B)P(B)db$, where B is the event that some parameter has a value between b and $b+db$:

$$P(y=y_0|x=x_t)=\int P(y=y_0|x=x_t;y_1=y_t)P(y_1=y_t|x=x_t)dy_1 \tag{1.22}$$

Substitution into (1.14) gives:

$$P_{of}(y_0-y_f)=\int P_0(y_1-y_0)P_f(y_1-y_f)dy_1 \tag{1.23}$$

$$P_a(x)\propto P_{of}(y_0-K_n(x))P_b(x-x_b) \tag{1.24}$$

$$P_a(x)\propto\left[\int P_0(y_1-y_0)P_f(y_1-K_n(x))dy_1\right]P_b(x-x_b) \tag{1.25}$$

The assumption is made here that background and observational errors are uncorrelated or that $P_b(x-x_b)$ and $P_{of}(y_0-K_n(x))$ are independent. To proceed further, the PDFs P_b, P_0, and P_f must be specified. For simplicity, the PDFs are commonly assumed to be multidimensional Gaussian:

$$P_b(x-x_b)\propto\exp\left[-\frac{(x-x_b)^T(x-x_b)}{2B}\right] \tag{1.26}$$

$$P_o(x-x_o)\propto\exp\left[-\frac{(x-x_o)^T(x-x_o)}{2B}\right] \tag{1.27}$$

$$P_f(x-x_f) \propto \exp\left[-\frac{(x-x_f)^T(x-x_f)}{2B}\right] \tag{1.28}$$

It can then be shown that B, O, and F are covariance matrices:

$$B=<(x_b-x_t)(x_b-x_t)^T> \tag{1.29}$$

$$O=<(y_o-y_t)(y_o-y_t)^T> \tag{1.30}$$

$$F=<(y_t-K_n(x_t))(y_t-K_n(x_t))^T> \tag{1.31}$$

and P_{of} is given by:

$$P_{of}(y_o-y_f) \propto \exp\left[-\frac{(y_o-y_f)^T(y_o-y_f)}{2(O+F)}\right] \tag{1.32}$$

Furthermore, the minimum variance and maximum likelihood estimates of x_a are identical. For the maximum likelihood estimate, maximize:

$$P_a(x)=P_{of}(y_o-K_n(x))P_b(x-x_b) \propto \exp\left[-\frac{(y_o-K_n(x))^T(y_o-K_n(x))}{2(O+F)}+\frac{(x-x_b)^T(x-x_b)}{2B}\right] \tag{1.33}$$

Minimizing P_a is equivalent to minimizing $-ln(P_a)$, i.e., to minimizing:

$$J=\frac{(y_o-K_n(x))^T(y_o-K_n(x))}{(O+F)}+\frac{(x-x_b)^T(x-x_b)}{B} \tag{1.34}$$

This formulation appears in many variational approaches. Then, K is written as the matrix of partial derivatives of K_n with respect to x:

$$K_n(x+dx)=K_n(x)+Kdx \tag{1.35}$$

and the value of x_a that minimizes J is:

$$0=K^T(O+F)^{-1}(y_o-K_n(x_a))+\frac{(x_b-x_a)}{B} \tag{1.36}$$

This is often solved using iterative methods.

Now, if the linearization of K_n is valid over the entire range of x in the region of x_b, then an explicit solution can be found by evaluating K at $x=x_b$:

$$K_n(x_a)=K_n(x_b)+K(x_a-x_b) \tag{1.37}$$

Substitution in (1.36) gives an explicit solution which can be manipulated into several forms:

$$x_a = x_b + \frac{BK^T(y_o - K_n(x_b))}{(O+F)\left[\frac{BK^TK}{(O+F)}\right]} \tag{1.38}$$

$$x_a = x_b + \frac{BK^T(y_o - K_n(x_b))}{(O+F)\left[\frac{KBK^T}{(O+F)} + I\right]} \tag{1.39}$$

$$x_a = x_b + \frac{BK^T(y_o - K_n(x_b))}{(KBK^T + O + F)} \tag{1.40}$$

For the linearized Gaussian case, the expected analysis error covariance is:

$$<(x_a - x_t)(x_a - x_t)^T)> = B - \frac{BK^TKB}{KBK^T + O + F} \tag{1.41}$$

The solution x_a also minimizes this.

Data assimilation techniques can generally be classified into three classes (Dimet and Talagrand, 1986): (1) simple algorithms of spatial interpolation, where spatial information is introduced as an influence function; (2) Optimal Interpolation (OI) algorithms that produce analyzes that are linear combinations of the observations which minimize the mean quadratic error for a large number of realizations of the analysis. OI provides a practical and internally consistent approach for treating large sets of inhomogeneous observations and is currently the approach that provides the best results for operational application in meteorology; and (3) the third class is variational. They produce an analysis that minimizes the distance between the simulation and the observations. Variational approaches provide exact consistency between the analysis and dynamics and, therefore, appear to be superior to other approaches. Their high mathematical and computational costs strongly limit their use.

A variety of data assimilation techniques are reviewed below. These are general approaches that tend to evolve within specific applications and with various data characteristics. In-depth reviews are provided for those methods that are used in this research, with sufficient overviews of other methods.

1.6.4.1.1 Direct insertion or updating

"The process of replacing model values by 'observed' ones is called direct insertion" (Daley, 1990b) or updating. This method assumes 'perfect' observations, or observations with no error. Thus, model predictions that are known to contain error are totally rejected and replaced with the perfect observation. Any spatial or temporal information advection is performed entirely through the model physics.

Direct insertion of updating generally leads to severe error growth at the time of insertion characterized by huge jumps in the field (Daley, 1990b). Charney *et al.* (1969) observed that, as more noise is added to the observations, the performance of direct insertion degrades (Figure 1.30). In direct insertion, error due to complexity of real observations, such as differential instrument types, gross errors due to human or electronic problems, and natural observation bias, is preserved in the model forecast. On the positive side, there is a reasonable reduction in error with updating. So updating does indeed tend to have the desired effect of bringing the model closer to reality, but in a sub-optimal way.

1.6.4.1.2 Newtonian nudging

Newtonian nudging, or 'nudging', was originally designed for dynamic initialization, where it is used in a model preforecast period to produce model-balanced initial conditions for a subsequent numerical prediction (Anthes, 1974; Stauffer and Seaman, 1990). It has been utilized in many studies ranging from hurricane prediction (Hoke and Anthes, 1976), latent heating based on observed rainfall (Wang and Warner, 1988), wind profiler data assimilation (Kou and Guo, 1989), to operational use in a global model at the United Kingdom Meteorological Office (Lyne *et al.*, 1982). "Nudging is basically a successive-correction technique which uses a numerical model to include the time dimension" (Stauffer and Seaman, 1990). Nudging has some distinct advantages (Seaman, 1990), including: (1) because the assimilating model is complete, irreversible processes (i.e., latent heating) are included easily; (2) any data type that can be represented as a tendency of a prognostic variable can be assimilated; (3) in analysis-nudging, analyzes only need to be performed once, making computation economical; (4) the method is simple, both numerically and computationally;

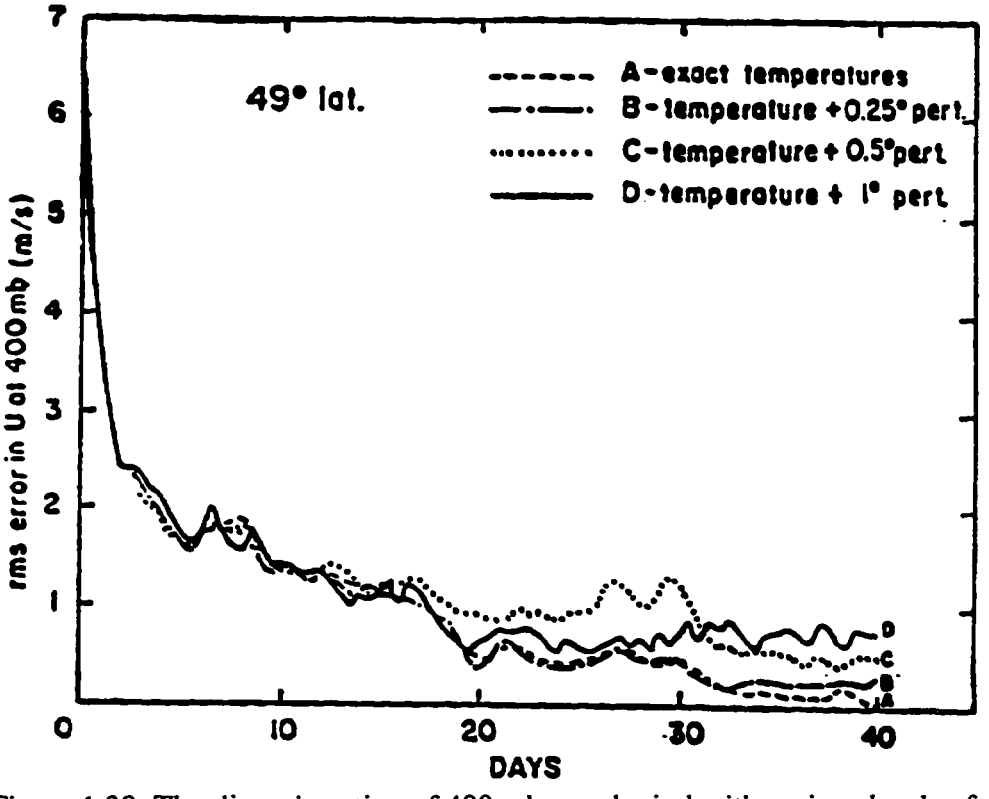

Figure 1.30: The direct insertion of 400 mb zonal wind with various levels of error (Charney, 1969).

(5) it allows for scale interactions in the calculation of the weighting function; and (6) it does not require a separate balance step when used for dynamic initialization. Nudging also has some distinct disadvantages: (1) The nudging constant is assigned in an application-dependent, semi-arbitrary manner; (2) The constitution of a 'best' or optimal analysis is not clear; (3) Observation nudging is based on continuous analysis and can become computationally expensive; (4) Use of real data in observation nudging may cause assimilation of local or unrepresentative components; (5) Observation nudging is well-behaved in regions of low data density (Benjamin and Seaman, 1985), but may degrade in quality and computational expense in areas of high data density.

Newtonian nudging continuously adds a forcing function to the model's prognostic equations to gradually 'nudge' the model state toward the observations. These small forcing terms, based on the difference between the simulated and observed state, gradually correct the model fields, which are assumed to remain in approximate balance at each time step (Stauffer and Seaman, 1990). Two separate nudging techniques have been developed for use with either gridded analyzes or individual observations.

Nudging to analyzes: In this first technique, the observations have been pre-interpolated to the model grid. The analysis-nudging term is proportional to the difference between the simulation and the observation calculated at every point. The general form of the predictive equation of variable $\alpha(x,t)$ in flux form is (Stauffer and Seaman, 1990):

$$\frac{\partial p^{*}\alpha}{\partial t} = F(\alpha,x,t) + G_{\alpha} W_{\alpha}(x,t) \epsilon_{\alpha}(x) p^{*}(\hat{\alpha}_{o} - \alpha) \tag{1.42}$$

The model's forcing terms are represented by F, where α are the model's dependent variables, x are the independent spatial variables, and t is time. G_{α} is the nudging factor that determines the relative magnitude of the term to all other model processes. The nudging factor is usually selected so that the time scale of the slowest physical adjustment process in the model and the nudging term are similar. If this value is too large, the model state is forced too strongly towards the observation. If it is too small, the observations will have a minimal effect on the evolution of the model state, allowing phase and amplitude errors to grow. The four--dimensional weighting function, W, determines its spatial and temporal variation. The analysis quality factor,

ϵ, varies between 0 and 1 and is based on the quality and distribution of the observations. The gridded observation is $\hat{\alpha}_o$,

Nudging to individual observations: This scheme does not require gridded observations and uses only those observations which fall within a predetermined time window. Here, the difference between the simulated and observed state is determined at the observation locations, and then is analyzed back onto the model grid. The tendency for $\alpha(x, t)$ is given as (Stauffer and Seaman, 1990):

$$\frac{\partial p^{*}\alpha}{\partial t} = F(\alpha,x,t) + G_{\alpha}p^{*}\frac{\left[\sum_{i=1}^{N} W_i^2(x,t)\gamma_i(\alpha_o - \hat{\alpha})_i\right]}{\sum_{i=1}^{N} W_i(x,t)} \tag{1.43}$$

the subscript i denotes the ith observation of a total of N that are within a preset radius, α_0 is the locally observed value of α, and $\hat{\alpha}$ is the model's prognostic variable interpolated to the observation location in three dimensions. The observational quality factor, γ, varies from 0 to 1 and accounts for characteristic errors in measurement systems and representativeness. The four-dimensional weighting function accounts for the separation distance, both spatially and temporally of the ith observation from a given grid point at a given time.

For the analysis-nudging technique, the four-dimensional weighting function is generally given by:

$$W(x,t) = 1 \tag{1.44}$$

For the observation-nudging technique, the weighting function for each observation I is written as:

$$W(x,t) \equiv w_{xy} w_z w_t \tag{1.45}$$

where w_{xy} is a Cressman-type horizontal weighting function defined by (Cressman, 1959):

$$w_{xy} = \frac{R^2 - D^2}{R^2 + D^2}, \qquad 0 \le D \le R \tag{1.46}$$

$$w_{xy} = 0, \qquad D > R \tag{1.47}$$

where R is the radius of influence, and D is the distance from the ith observation to the gridpoint. The vertical weighting function, w_z, is also a distance weighting function defined as:

$$w_z = 1 - \frac{|z_{obs} - z|}{R_z}, \qquad |z_{obs} - z| \le R_z \tag{1.48}$$

$$w_z = 0, \qquad |z_{obs} - z| > R_z \tag{1.49}$$

where R_z is the vertical radius of influence, and z_{obs} is the vertical position of the ith observation. The temporal weighting function is given by:

$$w_t = 1, \qquad |t - t_o| < \frac{\tau}{2} \tag{1.50}$$

$$w_t = \frac{(\tau - |t - t_0|)}{\tau/2}, \qquad \frac{\tau}{2} \le |t - t_0| \le \tau \tag{1.51}$$

$$w_t = 0, \qquad |t - t_o| > \tau \tag{1.52}$$

where t is the model-relative time, t_0 is the model-relative time of the ith observation, and τ is the half-period of a predetermined observation influencing time window.

These weighting functions can be modified or replaced appropriate to the application. A variety of techniques, such as successive scans or optimal interpolation can be utilized to determine these weighting functions (Seaman, 1990). Graphic examples of several weighting functions are shown in Figures 1.31, 1.32, and 1.33.

1.6.4.1.3 Objective or statistical interpolation

Statistical interpolation is a minimum variance method that is closely related to kriging (Bhargava and Danard, 1994). Currently, most numerical weather prediction centers use statistical interpolation data assimilation operationally (Daley, 1991). The technique can be traced back to Kolmogorov (1941) and Weiner, (1949), who applied it to various areas of science and engineering. In oceanography the method is called the *Gauss-Markov method*, and Weiner called the approach *optimal interpolation;* however, in practice, it is rarely optimal, so it is more appropriately termed *statistical interpolation* (Daley, 1991). Statistical interpolation has been utilized in atmospheric science since the 1950s. With the development of computer power, and through the inspiration of Gandin's famous publication, *Objective Analysis of Meteorological Fields* (Gandin, 1963), most major western meteorological services were using statistical interpolation operationally by the mid-1970s.

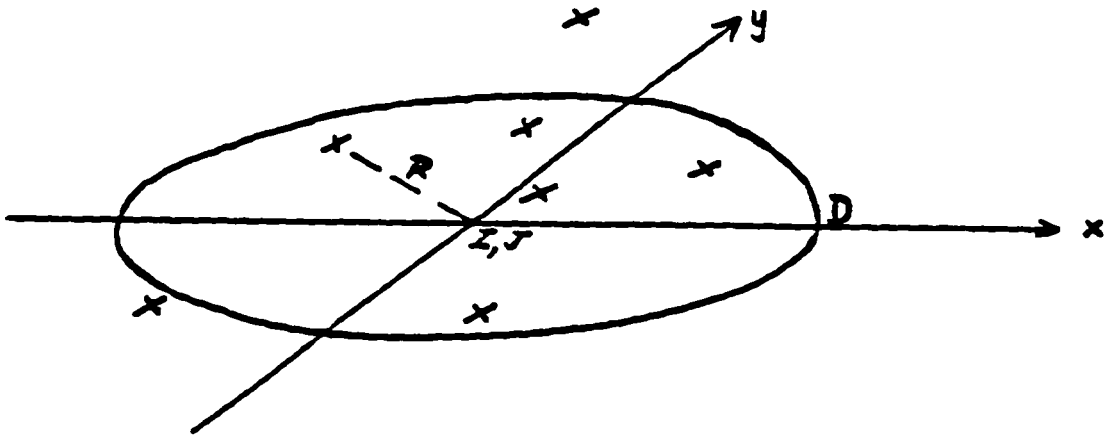

Figure 1.31: The horizontal weighting function can be determined by many techniques (Cressman, Barnes, optimal interpolation, etc.).

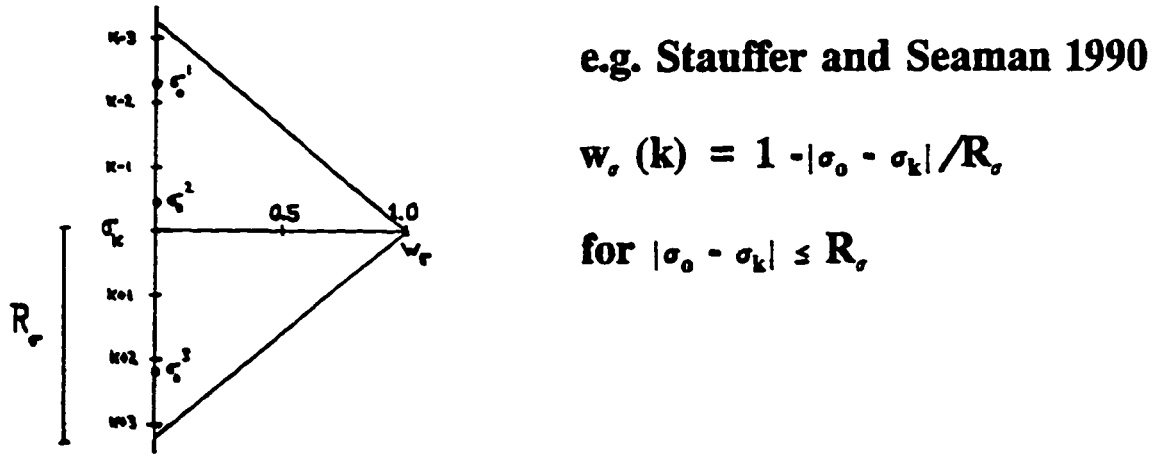

Figure 1.32: The Stauffer and Seaman (1990) nudging vertical weighting function.

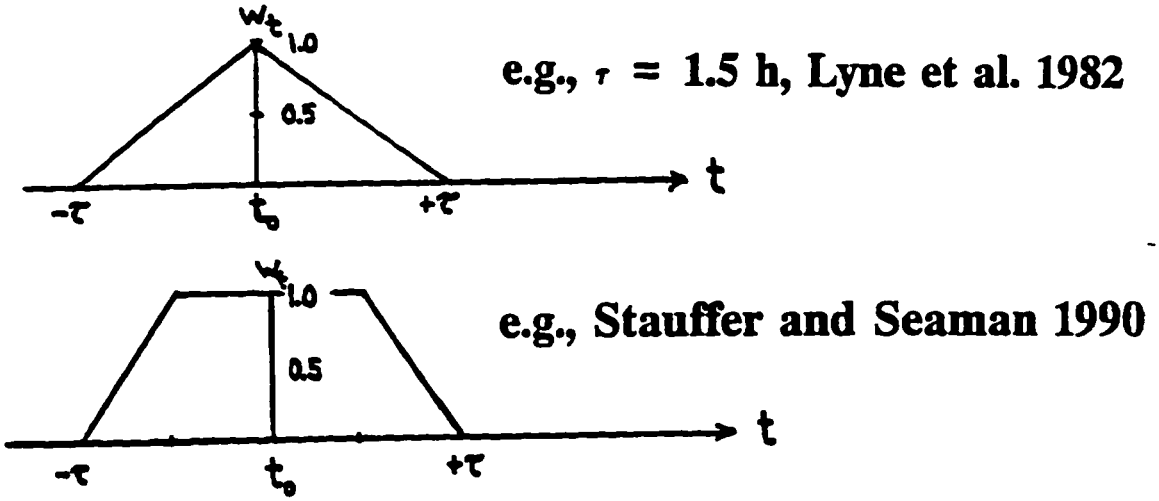

Figure 1.33: The Lyne *et al.* (1982) and Stauffer and Seaman (1990) nudging temporal weighting functions.

The statistical interpolation algorithm is derived as follows (Daley, 1991):

$$f_A(r_i)=f_B(r_i)+\sum_{k=1}^{K} W_{ik}[f_O(r_k)-f_B(r_k)] \tag{1.53}$$

where K is the number of observation points, W_{ik} is the weight function, $f(r)$ is the analysis variable (soil moisture), r is the three-dimensional spatial coordinates, $f_Z(r_i)$ is the analyzed value of f at the analysis gridpoint r_i, $f_B(r_i)$ is the background, or first guess value of f at r_i, and $f_O(r_k)$ and $f_B(r_K)$ are the observed and background values, respectively, and the observation station r_k.

It is convenient to introduce a simpler notation, defining $A_i=f_A(r_i)$, $O_k=F_o(R_k)$, $B_k=f_B(r_k)$,...,:

$$A_i=B_i+\sum_{k=1}^{K} W_{ik}[O_k-B_k] \tag{1.54}$$

Where (A_i-B_i) is the analysis increment or correction, and (O_k-B_k) is the observation increment or innovation. Because, both observation and background values contain error, the true values of the function at points I and k are defined to be $f_T(r_i)$ or T_i and $f_T(r_k)$ or T_k. Numerical forecasts are generally only available on a regular grid; therefore, to obtain $f_B(r_k)$, it is often necessary to interpolate $f_B(r_i)$ to the observation location using an established interpolation procedure.

Next, subtract the true values at the analysis gridpoint r_i from each side:

$$A_i-T_i=B_i-T_i+\sum_{k=1}^{K} W_{ik}[O_k-B_k] \tag{1.55}$$

The weights are determined by least squares minimization of the above, and with the assumptions that B_i, B_k, and O_k are unbiased, that there is no correlation between background and observation error, that the error correlation isotropic, and that the error correlation is time invariant.

The expectation value of any random variable s is defined as:

$$<s>=\int_{-\infty}^{\infty} sp(s)ds \tag{1.56}$$

Continue by squaring both sides of equation (1.55) and applying the expectation operator:

$$<(A_i-T_i)^2>=<(B_i-T_i)^2>+2\sum_{k=1}^{K} W_{ik}<O_k-B_k)(B_i-T_i)>+ \sum_{k=1}^{K}\sum_{l=1}^{K} W_{ik}W_{il}<(O_k-B_k)(O_l-B_l)> \tag{1.57}$$

here l is a dummy index running over the observation locations.

The goal is to find the weights W_{ik} that minimize equation (1.57). Thus, differentiating equation (1.57) with respect to each of the weights W_{ik}, $1 \le k \le K$, gives:

$$0=\frac{\partial E_A^2}{\partial W_{ik}}=2<(O_k-B_k)(B_i-T_i)>+2\sum_{l=1}^{K} W_{il}<(O_k-B_k)(O_l-B_l)> \tag{1.58}$$

or:

$$\sum_{l=1}^{K} W_{ik}<(O_k-B_k)(O_l-B_l)>=-<(O_k-B_k)(B_i-T_i)> \tag{1.59}$$

The right hand term can be defined:

$$<(O_k-B_k)(B_i-T_i)>=<(O_k-T_k)(B_i-T_i)>-<(B_k-T_k)(B_i-T_i)> \tag{1.60}$$

Terms of the form $<(O_m-T_m)(B_n-T_n)>$ are covariances between the background error and the observation error. Covariances of this type vanish if one assumes no correlation between background and observation error, which is reasonable for most observation systems (except those that do use background information to derive observations. With this assumption, it can be written:

$$\sum_{l=1}^{K} W_{il}[<(B_k-T_k)(B_l-T_l)>+<(O_k-T_k)(O_l-T_l)>]=<(B_k-T_k)(B_i-T_i)> \tag{1.61}$$

Here, $<(B_k-T_k)(B_i-T_i)>$ is the background error covariance between the observation station r_k the analysis gridpoint r_i $<(B_k-T_k)(B_l-T_l)>$ is the background error covariance matrix, and $<(O_k-T_k)(O_l-T_l)>$ is the observation error covariance matrix.

The background error covariances can be simplified if the horizontal and vertical structures are assumed to be separable:

$$C_B(r_k,r_l)=C_B(x_k,y_k,z_k,x_l,y_l,z_l)=C_B^H(x_k,y_k,x_l,y_l)C_B^V(z_k,z_l) \tag{1.62}$$

where $C_B(r_k,r_l) = <(B_k-T_k)(B_l-T_l)>$, C_B^V and C_B^H are the vertical and horizontal covariances respectively, and $r=(x,y,z)$, where x and y are horizontal coordinates, and z is the vertical component.

Then, under homogenous conditions, the background error covariance matrix is equal to a simple constant (the variance) times the background *correlation* matrix:

$$C_B(r_k,r_l)=\sigma_B\rho_B \tag{1.63}$$

where σ_B is the background error variance, and ρ_B is background error correlation matrix. In practice, the background error correlations are assumed to be isotropic and homogenous and are determined using prespecified correlation functions. With these assumptions, the weights can be determined from:

$$\sum_{l=1}^{K} W_{il}[\rho_B(r_l-r_k)+\epsilon_O^2\rho_O(r_l-r_k)]=\rho_B(r_i-r_k) \tag{1.64}$$

where ρ_O is the observation error correlation matrix, ρ_B is the background error correlation matrix, and $\epsilon^2=1/\rho(0)-1$. Thus, this results in a set of K linear equations with K unknowns, where K is the number of observations being assimilated (Reynolds and Smith, 1994). Often, data are combined into 'super-observations' to reduce the dimension of the problem (Lorenc, 1981).

Therefore, implementation of the methodology requires estimates of ρ_O and ρ_B. The most satisfactory way of estimating ρ_B is to use observations from a dense homogenous observation network in concert with model predictions of those observations. A good example of this is provided by Schlatter (1975) (Figure 1.34) or Gunst (1995) (Figure 1.35). The next step is to fit a curve through all the points using an appropriate fitting procedure to produce a single curve. Two examples of such curves are provided in Figure 1.36 (Schlatter, 1975). Calculation of background error correlations can be made much more efficiently if correlations are specified as analytic functions or *correlation models* (Buell, 1972; and Julian and Thiebaux, 1975). The spectral densities of these functions must be strictly positive. Two commonly used correlation models are as follows (Thiebaux, 1976):

$$\rho_B(r)=\left[\cos(cr)+\frac{\sin(cr)}{Lc}\right]e^{-\frac{r}{L}} \tag{1.65}$$

$$\rho_B(r)=\exp\left(\frac{-r^2}{2L^2}\right) \tag{1.66}$$

where c and L are specified constants used to fit the function to the data.

For newer satellite-borne instruments that may have correlated observation error, ρ_O is determined similarly to procedure above, except that another uncorrelated observation of the

variable is required. Here, the correlation model is fit to the correlation of the difference or error between the spatially correlated data and the assumed uncorrelated data. For example, Baker *et al.* (1987) determined the horizontally correlated observation error for the 500 mb geopotential using satellite and radiosonde observations (Figure 1.37).

The final subject in statistical interpolation theory is the vertical question. Generally, the treatment of vertical background error correlation in the literature is much less satisfactory than the horizontal. This is mainly due to the vertical structure of the atmosphere being much shorter than the horizontal (note: the correlation structure of soil moisture parallels the atmosphere), explicit or semi-explicit boundaries existing at the top and bottom of the atmosphere, and the practice of making single-level observations. One extreme approach that has been adopted is to draw for the observation at its own vertical level and allow the objective analysis to revert to the background field at all other levels, essentially assuming Kronecker δ functions for the vertical error correlation functions (Daley, 1991). At the other extreme, one can allow a single observation to affect all levels equally. Ideally, one should determine the error correlations for the observations and background fields using adequate data and following similar methodologies as utilized in determining the horizontal functions. An example of this is provided by Lönnberg and Hollingsworth (1986) (Figures 1.38 and 1.39).

An interesting problem with statistical interpolation is that if a observation of sufficient quality was located precisely at a model grid point location, its weight would become one, and it would be accepted in place of the background model prediction (McPherson *et al.*, 1979; and Daley, 1991). Hence, in this case the statistical interpolation algorithm reverts to direct insertion or updating.

1.6.4.1.4 Successive corrections

The successive corrections data assimilation method owes its creation to Bergthorsson and Doos (1955), who introduced the single correction method which is a simple ad hoc procedure which specifies the assimilation weights in advance to avoid expensive matrix operations. Cressman (1959) proposed more specific *a posteriori* weights to improve the method.

The successive corrections method provides a smoothed representation of the data at the analysis grid. Weighting functions are applied successively to derive the desired smoothing characteristics. Starting with simple ad hoc procedures, the method leads to the optimum interpolation technique (Daley, 1990c).

First, it is assumed that all observations are made with the same type of instrument, with spatially uncorrelated error. The first iteration is then:

$$f_A^1(r_i)=f_B(r_i)+w_i^T(f_o-f_B) \tag{1.67}$$

then, the elements of w_i^T are:

$$w_{ik}=\frac{w(r)}{\sum_{k=1}^{K_i} w(r)+\epsilon_0^2} \tag{1.68}$$

where f_O is the observation field, f_B is the background field, f_A is the analyzed field, f_B is the background field, and r_i and r_k represent the locations for analysis and observation points. For successive iterations, forward interpolate the analyzed values, $f_A^I(r_i)$, for all I to the observation location and repeat. Therefore, the general iteration is given as:

$$f_A^{j+1}(r_i)=f_A^j(r_i)+w_i^T(f_O-f_A^j) \tag{1.69}$$

where $f_A^O=f_B$.

For the weights, Cressman (1959) used:

$$w(r)=\frac{R^2-r^2}{R^2+r^2} \quad if\ r\le R \quad ; \quad 0\ if\ r>R \tag{1.70}$$

where R is a constant, and:

$$r^2=(x_i-x_k)^2+(y_i-y_k)^2 \tag{1.71}$$

Sasaki (1970) proposed the Gaussian weight function:

$$w_{ik}=\exp\left(\frac{-r^2}{2R^2}\right) \tag{1.72}$$

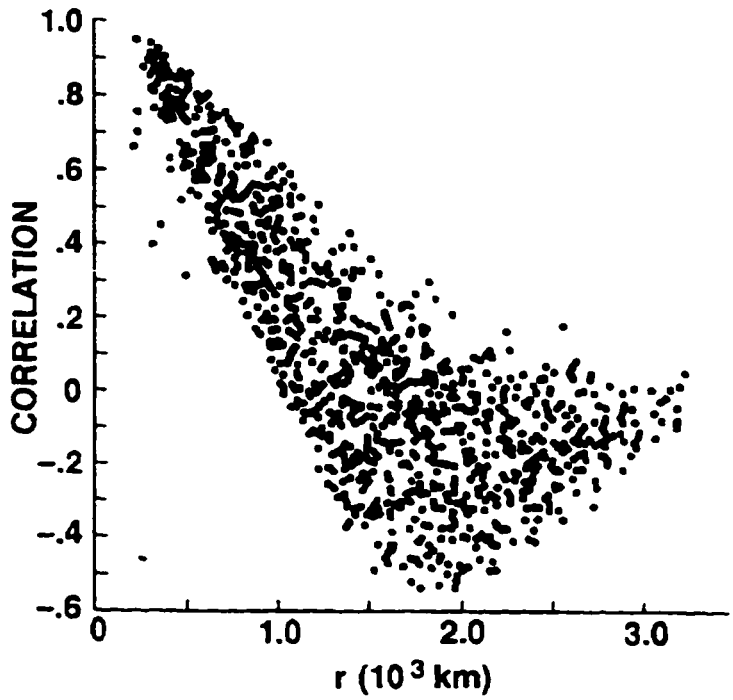

Figure 1.34: Observation-minus-background (climatology) correlation for the 500 mb height as a function of distance between station pairs (Schlatter, 1975).

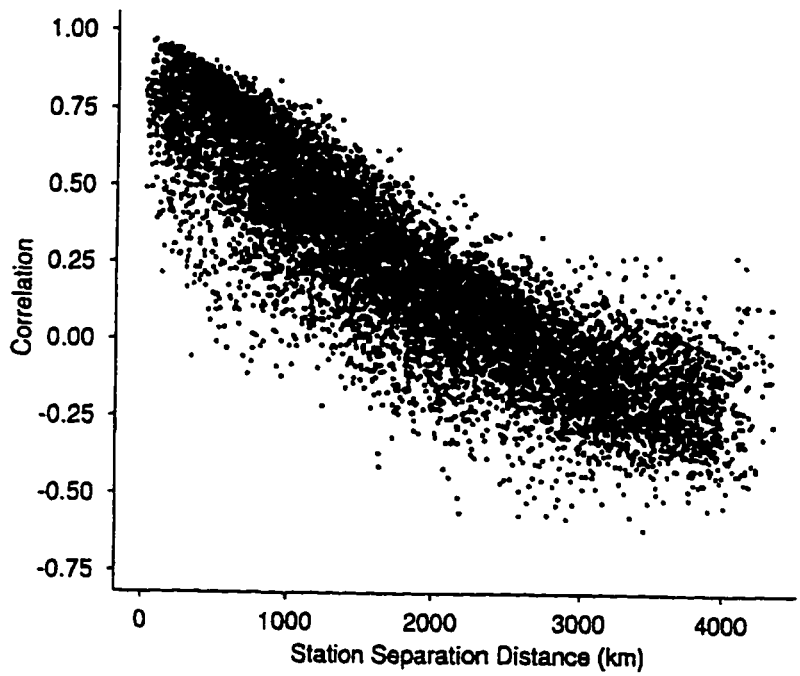

Figure 1.35: United States station pair correlations: annual anomalies 1920-1980 (Gunst, 1995).

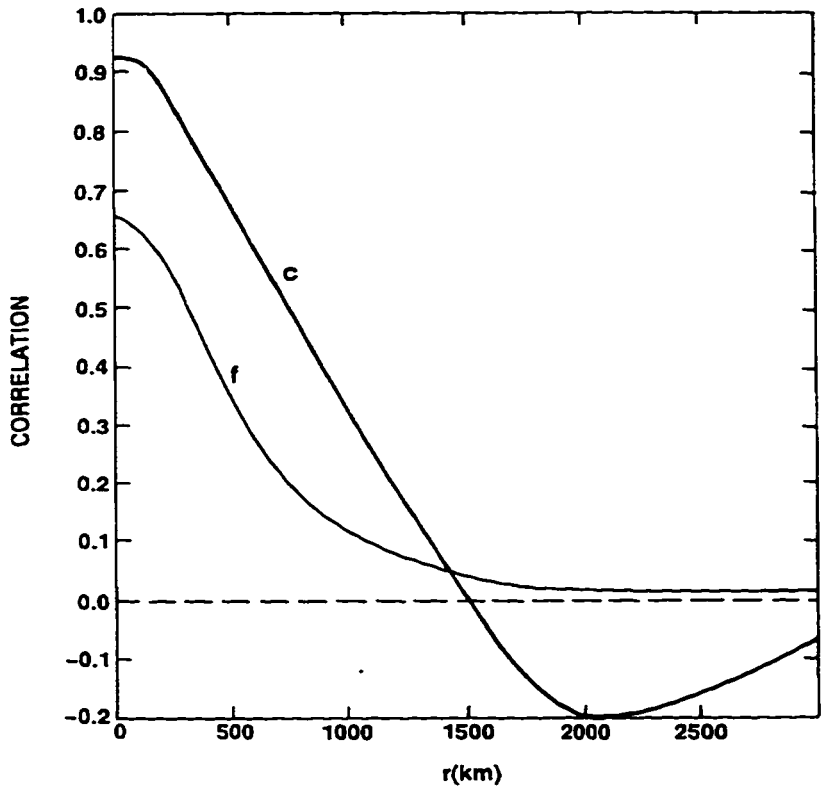

Figure 1.36: Observed-minus-background correlation for the 500 mb geopotential as a function of distance between stations. Curve c is for a climatological background, and curve f is for a forecast background (Schlatter, 1975).

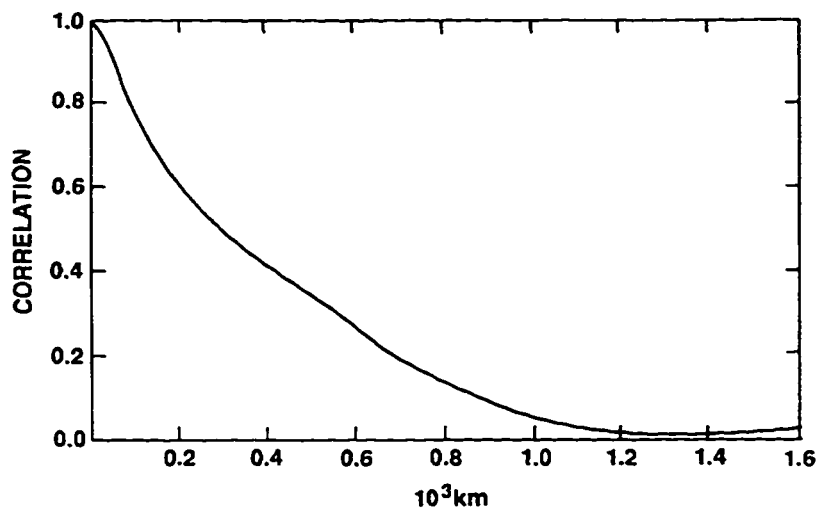

Figure 1.37: Horizontally correlated observation error for the 500 mb geopotential over western Europe (Baker *et al.*, 1987).

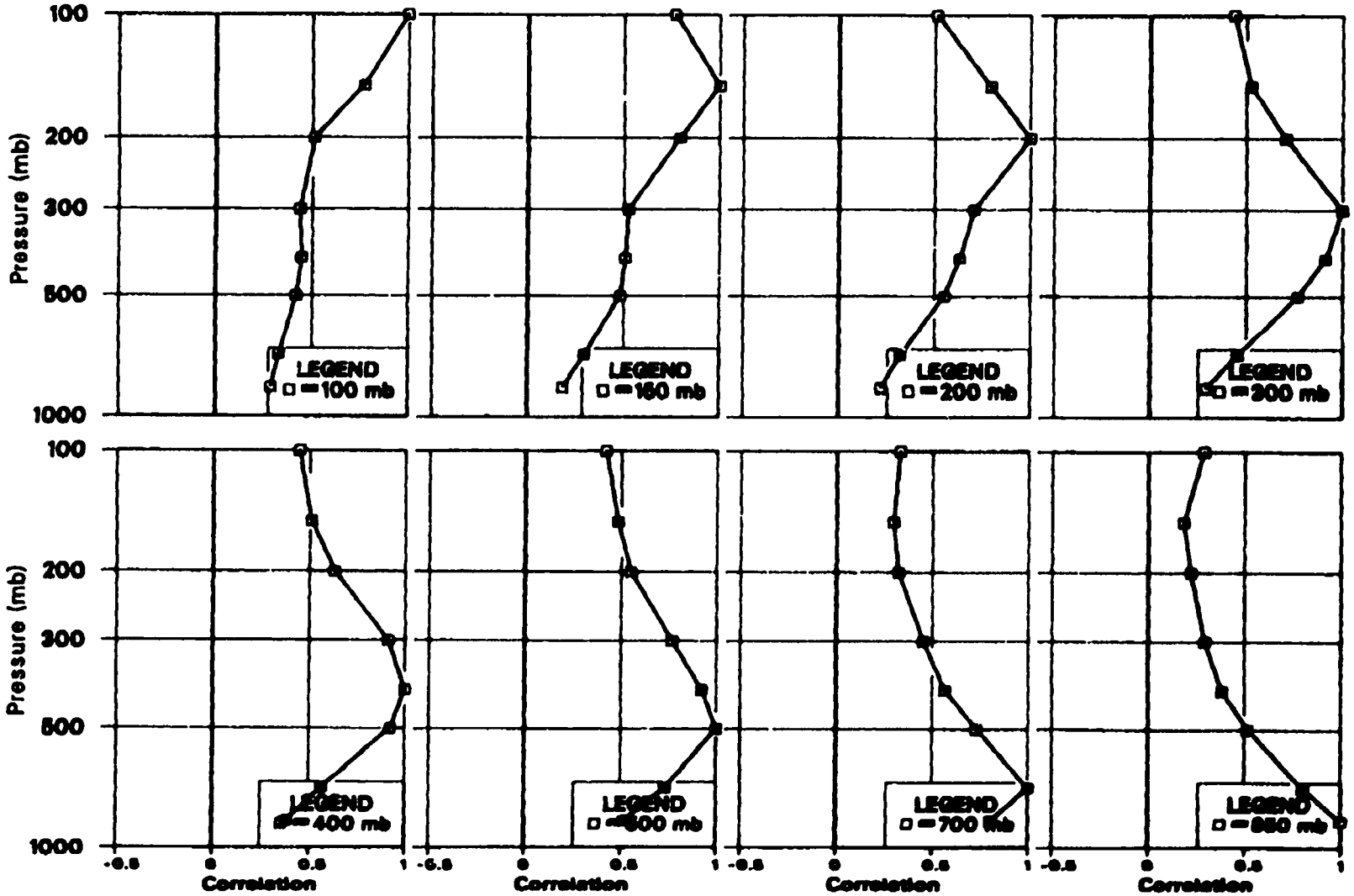

Figure 1.38: Vertical geopotential background error correlations (Lönnberg and Hollingsworth, 1986).

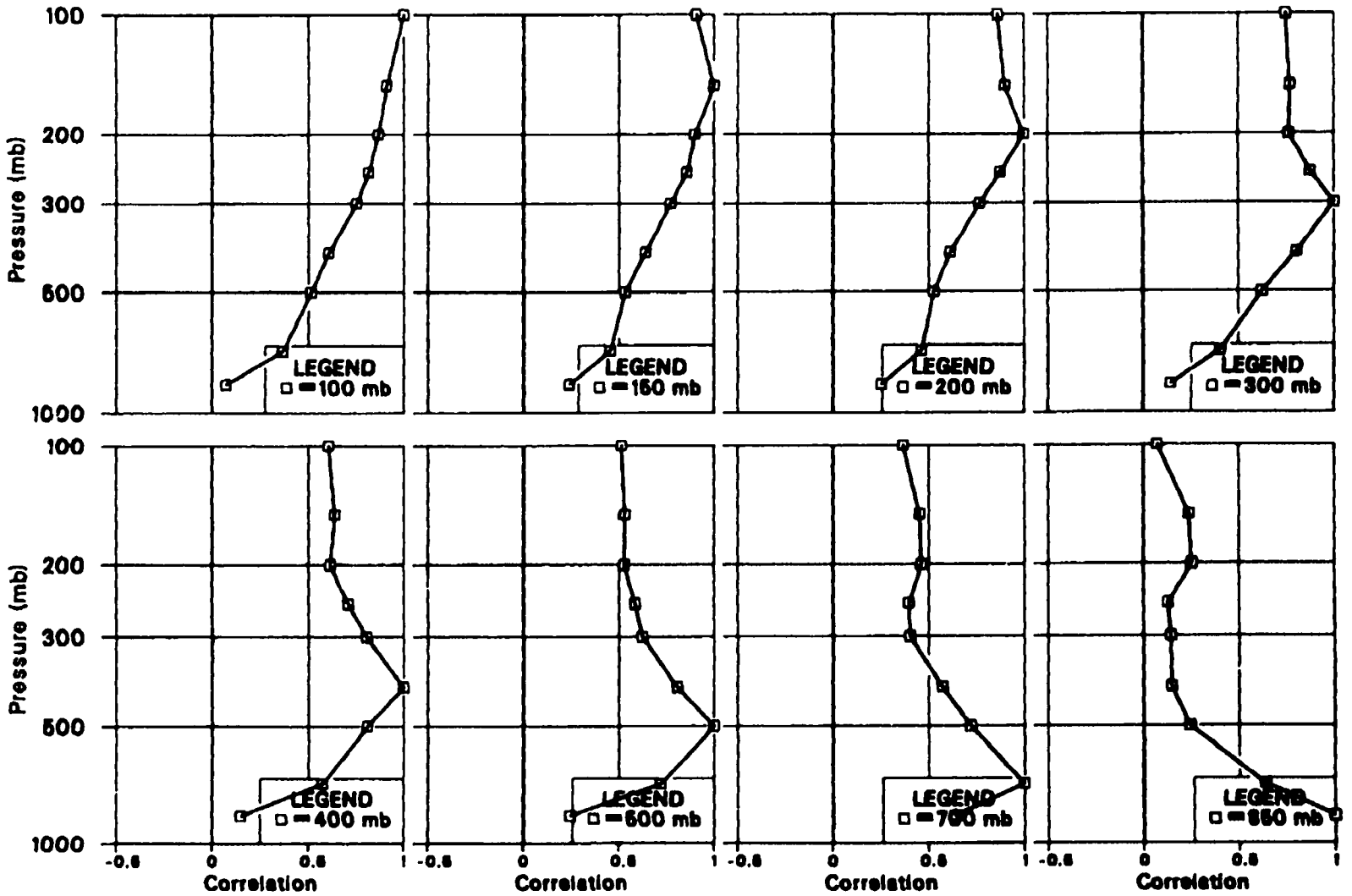

Figure 1.39: Vertical geopotential observation error correlations for radiosondes (Lönnberg and Hollingsworth, 1986).

The successive corrections method is a very successful, empirically based iterative analysis method (Lorenc, 1990). In practice, convergence can be slow when there are no detailed accurate initial estimates.

1.6.4.1.5 Variational methods

Variational methods were first introduced by Sasaki in 1958, and their use proved effective because they can incorporate many constraints easily (Ikawa, 1984). "The variational algorithm requires the computation of the gradient of the distance function to be minimized with respect to the model state at the beginning of the assimilation period" (Courtier and Talagrand, 1990). Thus, variational assimilation is principally very simple. One first defines a scalar function that describes the distance between the observations and the model prediction. Then, one simply seeks the model solution that minimizes this function (Courtier and Talagrand, 1990). The complexity comes from the generally large size of the minimization problem.

Variational assimilation has the advantage over other assimilation methods of being able to directly take into account the model-driven dynamics and physics when performing the analysis. It provides a conceptually simple and consistent procedure for assimilating large numbers of observations that are spatially and temporally inhomogeneous and of varied accuracy (Talagrand and Courtier, 1987a,b).

The most common method for minimizing the difference between the model prediction and observations is the adjoint method (described below), but other methods have also been developed. Wahba and Wendelberger (1980) used splines to avoid the problem of solving partial differential equations directly, but found that other challenging numerical problems arose. In addition, Dimet and Talagrand (1986) used a generalization of the classical Lagrange multiplier technique.

Currently, the United Kingdom Meteorological Office is in the development stage of an operational variational assimilation scheme using the adjoint method. It is expected to be fully operational in 1997 and will have the capacity of extracting useful information from satellite radiances (Lorenc, 1995b).

1.6.4.1.6 Adjoint methods

Adjoint methods are tools that are used to find derivatives of model output with respect to model input. Data assimilation using adjoint methods usually follows the following sequence at each point in the initial condition space (Lewis, 1990): (1) An assumed 'perfect' model is forward integrated; (2) A basic set of key variables (those that can be used to reconstruct all others) is saved; (3) An adjoint of the basic model or a 'backward model' is integrated backward in time to provide the gradient of J, where J is a goodness-of-fit scalar defined as:

$$J=\int_0^T \langle X(t)-Y(t),X(t)-Y(t)\rangle dt \tag{1.73}$$

where $t=0$ is the initial time, $t=T$ is the period the model is run and observations are collected, and $\langle .,. \rangle$ is the vector dot product for the spectral amplitude vector $Y(t)$ and the observation amplitude vector $X(t)$. The adjoint is the inner product in linear space. For example, a linear operator L^* is the adjoint of L if for all x and y in linear space S:

$$\langle y,Lx\rangle = \langle L^*y,x\rangle \tag{1.74}$$

Therefore, the adjoint tells us how to find the derivatives or the gradient; (4) The goal in data assimilation is to "minimize the cost functional which describes the discrepancy between model output and observation" (Lewis, 1990). Hence, a minimization technique is used at this step in the procedure to determine the next set of states to use that will project the model closer to the desired minimum; and (5) Another forward integration of the basic model using an improved estimate of the states is performed to find the 'stepsize', or the distance to move along the current estimate of the J gradient to move toward a minimum. Thus, for each iteration, 3 model integrations and storages are needed. The minimum is found in a series of iterations.

Generally, the adjoint method is considered to be a tool that is used to solve the classical variational adjustment problem, and not a separate data assimilation procedure. Li and Leweis (1990) considered its use to be very computationally demanding and not suitable for large problems or operational use. But recently, Lorenc (1995b), Dirkenheuer (1996), and Deblonde *et al.* (1995) have demonstrated that operational variational assimilation is feasible.

The use of the adjoint approach is limited to models that are continuously differentiable with respect to the initial conditions (Lewis and Derber, 1985). Unfortunately, most

hydrological models contain threshold processes that can induce discontinuities in the function to be minimized (Talagrand, 1990). These threshold processes, and the chaotic character of the Earth system, can also have the effect of resulting in multiple minima (Talagrand, 1990). There also remains a need to introduce the imperfection of the assimilating model into this theory. Finally, the costs of this method are increased by the required development of a separate adjoint model (Courtier and Talagrand, 1987).

The adjoint method has only been applied to relatively simple models which show that the method is capable of finding the model solution that fits best a given set of observations (Talagrand, 1990).

1.6.4.1.7 Kalman filtering

The Kalman filter has been extensively utilized in data assimilation research (Ghil *et al.*, 1981; and Cohn, 1982). The Kalman filtering approach for implementation in data assimilation can be derived as follows (Daley, 1990a). First, define a time-independent regular analysis r_j, $1 \leq j \leq J$, and s_n to be the column vector of true values of all states on the grid at time t_n. Then, define s_n^f and s_n^a to be the simulated and analyzed vectors of s on the grid. Next, define M_n to be matrix representing a linear model:

$$s_{n+1}^f = M_n S_n^a \tag{1.75}$$

Here, M_n is a $J \times J$ matrix. Assuming the model is not perfect, define the model error growth between t_n and t_{n+1} as ϵ_n^q. Then:

$$s_{n+1} = M_n s_n + \epsilon_n^a \tag{1.76}$$

Subtract the previous two equations:

$$\epsilon_{n+1}^f = M_n \epsilon_n^a - \epsilon_n^q \tag{1.77}$$

where $\epsilon_n^f = s_n^f - s_n$ and $\epsilon_n^a = s_n^a - s_n$ are the forecast and analysis errors. Next, assume model error is unbiased and spatially correlated. Then, taking the outer product and applying the expectation operator gives:

$$P_{n+1}^f = M_n P_n^a M_n^T + Q_n \tag{1.78}$$

where $Q_n = <\epsilon_n^q(\epsilon_n^q)^T>$, $P_n^f = <\epsilon_n^f(\epsilon_n^f)^T>$, $P_n^a = <\epsilon_n^a(\epsilon_n^a)^T>$ are the model, forecast and analysis error covariance matrices. T is a transposed matrix.

Next, consider a time-dependent observation network and a column vector of length I_n of observations d_n on this network at time t_n A linear expression for the analysis s_n^a from observations d_n is:

$$s_n^a - s_n^f = \hat{K}_n[d_n - H_n s_n^f] \tag{1.79}$$

where H_n is an $I_n \times J$ forward interpolation matrix from the analysis to observation. $\hat{K}_n$ is a $J \times I_n$ *gain* matrix of weights to be determined. $D_n - H_n s_n^f$ is the innovation vector or observation increment, and $s_n^a - s_n^f$ is the correction vector or analysis increment.

Add s_n^f and subtract the true value of s_n:

$$\epsilon_n^a = [I - \hat{K}_n H_n]\epsilon_n^f + \hat{K}_n \epsilon_n^o \tag{1.80}$$

where $\epsilon_n^o = d_n - H_n s_n$ is the observation error vector that accounts for instrument and prediction error. I is the identity matrix. Take the outer product and apply the expectation operator:

$$P_n^a = [I - \hat{K}_n H_n]P_n^f[I - \hat{K}_n H_n]^T + \hat{K}_n R_n \hat{K}_n^T \tag{1.81}$$

where $R_n = <\epsilon_n^o(\epsilon_n^o)^T>$ is the $I_n \times I_n$ observation error covariance matrix.

Minimizing the analysis error variance at the analysis gridpoints yields the optimal Kalman gain matrix K_n:

$$K_n = \frac{P_n^f H_n^T}{H_n P_n^f H_n^T + R_n} \tag{1.82}$$

Substitution provides:

$$P_n^a = [I - K_n H_n]P_n^f \tag{1.83}$$

Kalman filter theory can be extended to non-linear cases using the extended Kalman filter, and the Kalman smoother can make use of future observations. The need to know and process large matrices in Kalman filtering is a big practical disadvantage (Lorenc, 1990 a,b).

1.6.4.2 Operational data assimilation

Data assimilation techniques are used in (1) one-time research applications to demonstrate new techniques or application, (2) operational applications where it is used for routine applications to benefit society, such as weather forecasting; and (3) reanalysis applications for use in further optimizing techniques or providing improved products for other applications.

Some of the major weather forecasting centers that are using data assimilation techniques to improve their forecasts are the U.S. National Meteorological Center (Mitchell *et al.*, 1994), the United Kingdom Meteorological Office (Jones, 1996; Golding, 1990), the French Direction de la Météorologie Nationale (DMN) (Gleyn, 1990), and the joint Nordic Dutch HIRLAM project (Gustafsson, 1990). Additionally, the U.S. NASA Goddard Space Flight Center is developing the GEOS model and Data Assimilation System (DAS) for use in Earth Observation System (EOS) applications (Bloom *et al.*, 1995; Molod *et al.*, 1996; Schubert *et al.*, 1995). Future DAO plans include the development of a land-surface model based on a combination of the Mosaic land-surface model (Koster and Suarez, 1992) and the SiB land-surface model (Sellers *et al.*, 1986). Then, the DAO plans the assimilation of surface temperatures, snow water equivalent, and soil moisture (Joiner *et al.*, 1996) into this scheme.

1.6.4.3 Hydrologic data assimilation

As mentioned before, data assimilation was developed and is most often used in atmospheric forecasting (Daley, 1991). More recently, significant development of data assimilation has also occurred in oceanography (Ghil and Malanotte-Rizzoli, 1991). Data assimilation has found very limited use in hydrology, mostly due to the limited and widely scattered sources of traditional hydrologic data such as rain gauges, stream gauges, and wells (McLaughlin, 1995). Some important hydrologic questions such as characterization of spatial and temporal hydrologic variability can be well posed in a data assimilation setting. Data assimilation is likely to play a key role in hydrology as new technologies such as remote-sensing allow us to construct more continuous hydrologic data fields.

Data assimilation has been used in hydrology in three general areas: (1) Precipitation modeling, or improvement of precipitation processes in the atmosphere. (2) Surface hydrology

including land-atmosphere interaction and soil moisture modeling; and (3) Subsurface groundwater modeling including aquifer property mapping and transport modeling.

Precipitation in meteorological and hydrological models is scale-dependent. Generally, meteorological models are of a resolution too coarse to resolve precipitation events, but some models such as MM4 (Hostetler and Giorgi, 1993) are capable of simulating frontal precipitation events. These types of models have been used in assimilation studies using precipitation measurements or precipitation surrogates, such as radar reflectivity. Precipitation data assimilation has also been successful using hydrologic models of convective or cloud-scale processes. McLaughlin *et al.* (1990), and Jinno *et al.* (1993) used statistical or empirical distributed parameter Kalman filter of cokriging algorithms to estimate ground surface precipitation from scattered rain gauge measurements. Similarly, French *et al.* (1994) used a physically based model to estimate precipitation from radar and satellite data.

Data assimilation techniques have been applied to subsurface hydrology, but are rarely identified as such. A classic example is the mapping of aquifer geologic and hydraulic properties (McLaughlin, 1995). Methods such as cokriging (Hoeksema and Kitanidis, 1984) have been used in this manner, and a spatially discretized Kalman filter based on the MODFLOW model has been used to estimate water table elevations from scattered well measurements (Van Geer *et al.*, 1991; and Yangxaio *et al.*, 1991). Variational data assimilation techniques have also been applied to many groundwater flow and transport problems (Samper *et al.*, 1990; Medina *et al.*, 1990; and Lee *et al.*, 1993). Subsurface data assimilation has matured to the point that the U.S. Geological Survey has incorporated it into some of its standard subsurface hydrology modeling packages (McLaughlin, 1995; and Hill, 1992).

Many distributed parameter SVATS that describe interactions between precipitation, evapotranspiration, infiltration, and runoff (Beven *et al.*, 1987, Famiglietti, 1992; and Goodrich *et al.*, 1991) could be used to assimilate satellite and ground measurements with great impact on estimation of recharge, contributing areas, and land-atmosphere fluxes. None have yet to be applied in this way (McLaughlin, 1995). Some previous work has made progress towards this goal and is detailed below.

Milly (1986a) introduced a soil moisture estimation system that optimally integrates the information provided by a soil moisture model and remotely-sensed observations. This system is presented in the context of estimating the optimal sampling frequency and response time of a soil moisture remote-sensing instrument, because none currently exist. A Kalman filter based four-dimensional data assimilation technique is used to periodically update the model soil moisture state with an optimal combination of the model prediction and a remotely-sensed soil moisture observation. This optimal combination is largely based on the error characteristics of the model and the data being assimilated. The availability of the state error covariances in the Kalman filter allows the evaluation of various measurement schemes without actual measurements.

The simple linear soil moisture model used in this study is described by the following:

$$\frac{dx}{dt}=\alpha x+b(\hat{p}+\omega) \tag{1.84}$$

This linear model is assumed to be perfect, and the flow parameter, α, is assumed to be perfectly known. The true values of the uncertain input are represented by p, and the estimate is denoted by $\hat{p}$. The errors in the estimation of p are denoted using ω, which is a zero mean white noise process. Similarly to input uncertainty, $\hat{x}$ is the estimate of state, $\bar{x}$ is the true state. The error covariance of $\hat{x}$ is then:

$$P=E[(\hat{x}-x)(\hat{x}-x)^T] \tag{1.85}$$

which grows in the absence of state measurements.

The Kalman filter merges a measurement with a previous prediction to arrive at an optimal state estimate. The state update is given as:

$$\hat{x}(t_k+)=\hat{x}(t_k-)+K_k[z_k-H\hat{x}(t_k-)] \tag{1.86}$$

where K_k is the Kalman gain, t_k is the time that a remote-sensing soil moisture measurement z_k is available, and $H=[0\ 1]$, depending on the availability of a measurement. The equations can be solved to provide the growth or reduction of error covariance with the availability of measurements.

Because this was a study to determine the optimum temporal characteristics of a soil moisture sensor, synthetic data are produced and utilized, because such data are currently non-

existent. Assuming that storm durations are small compared to interstorm periods, that storms are separated by a constant duration, and that the infiltration depth for every storm is the same, infiltration rate is treated as a series of equally spaced Dirac delta functions. No information is provided for the assumptions of the nature of the remotely-sensed observations.

Dimensionless forms of the previous equations were used to advance the error covariance through time until steady state was achieved. The results are shown in Figures 1.40 and 1.41, where αT is a measure of the response time (a large response time implies that the soil moisture store decays quickly), and the number printed next to each curve describes the uncertainty of the measurement of the state to the uncertainty in infiltration. The effect of the number of measurements between storms (N) on the average variance of the soil moisture state is shown in Figure 1.40. This figure also shows that the variance of estimates is more effectively reduced in systems with a slow response (small αT); thus, less information is gained in fast response measurement systems compared to slow response systems. The effect of the number of measurements between storms (N) on the net increase per storm of the variance of the soil moisture state is shown in Figure 1.41. The predicted soil moisture state is generally unobservable, and thus grows without constraint, but its rate of growth can be significantly reduced with measurements. Reductions in the error variance due to measurement assimilation may translate into better estimates of soil moisture and show the utility of updating soil moisture models with new information gained from remote-sensing. It is also shown that it is critical to obtain measurements of soil moisture soon after a storm (before redistribution). Hence, doubling N can have the same effect on the model prediction as a 10-fold increase in measurement accuracy.

This research is a precursor for a potentially valuable family of techniques for combining land-surface data with model predictions in a 4DDA framework that results in regularly distributed estimates of soil moisture or other land-surface states which have been previously unavailable due to poor quality measurements and predictions or inadequate spatial and temporal resolutions.

Bouttier *et al.* (1993a) utilized a meso-scale, three-dimensional soil moisture model to assimilate HAPEX-MOBILHY (Andre *et al.*, 1986) data. They used an optimal interpolation

algorithm that assimilated screen-level temperatures and relative humidities that were used to infer realistic soil moisture contents. They found that, after 48 hours, soil moisture converged near-reference values regardless of the initialization (Bouttier *et al.*, 1993b).

Entekhabi *et al.* (1994) developed an algorithm to solve the inverse problem for the retrieval of soil moisture and temperature profiles based on multispectral remotely-sensed observation Kalman filtering, a model of coherent wave radiative transfer, and a model of coupled heat and moisture diffusion in porous media. This enables estimation of the soil moisture and temperature in the soil profile. The system is tested synthetically, and it is shown capable of predicting the profile information beyond the depth of observation, even with poor initialization. This research illustrates how data assimilation might extend remote-sensing surface observations to lower depths.

Ragab (1995) developed a two-layer model designed to extrapolate surface remotely-sensed soil moisture to deeper zones using an empirical drying and wetting relationship or a solution of Richard's equation with specific boundary conditions. In static mode, the model can predict root zone soil moisture given surface zone soil moisture, but, in dynamic mode, the system can be dynamically initialized with surface soil moisture to obtain root zone soil moisture at later times and between satellite overpasses. This research, while not using true data assimilation, shows that combining information from satellite and simulations may be valuable for improving predictions.

1.7 Background summary

Soil moisture is generally defined as the water in the near-surface soil zone that is available to the atmosphere through evaporation or through vegetation transpiration. Knowledge of its spatial and temporal variability is valuable for application in agricultural management, forest management, civil engineering, hydrologic forecasting, climate change estimation, and meteorologic prediction. Additionally, knowledge of soil moisture distributions will result in improved understanding of water and energy interactions between the land surface and the atmosphere, the role of vegetation in the climate system, and soil-water dynamics. Currently, accurate measurements of soil moisture at the spatial and temporal scales needed in applications

and research are unavailable due to observation limitations. Therefore, a prototype methodology to provide these soil moisture estimates through the assimilation of remotely-sensed soil moisture into a land-surface water and energy balance model was developed. This system results in soil moisture estimates that have the best qualities of modeling (spatial and temporal regularity) and observations (physical realism).

Daily, global, 100 m resolution, profile soil moisture measurements with accuracies of a few percent would be optimum for use in applications and research. To achieve global coverage, a space-based sensor is needed. Soil moisture can be remotely-sensed in most parts of the electromagnetic spectrum, but it is best observed in long passive microwave wavelengths. Several longwave passive microwave sensors are available on aircraft platforms and some near-ideal (active microwave) sensors are currently available on space platforms. A longwave passive microwave space platform soil moisture sensor may be available within the next 10 years. But, measurements from all these sensors are obscured by vegetation and roughness, can only sense soil moisture in the top few centimeters of soil, and will not meet the desired resolution requirements. Therefore, data assimilation studies will be beneficial well into the future.

Models of soil-vegetation-atmosphere interactions are relatively advanced, but must be compatible with remotely-sensed soil moisture measurements to be useful in data assimilation studies. They must have: (1) physically-realistic soil moisture predictions (i.e. in volumetric percent rather than some non-physical equivalent water depth), (2) remote-sensing compatible soil moisture prediction depths, and (3) the ability to feedback surface zone soil moisture corrections into other model components through appropriate physics.

There are several established techniques for the assimilation of observations into simulation models, including direct insertion, Newtonian nudging, statistical interpolation, successive corrections, variational approaches, and Kalman filtering. These techniques were developed in meteorology where scattered observations such as radiosondes measurements are used. Therefore, adaptations for much higher data densities and single-level vertical observation must be made for their application in soil moisture data assimilation. Data assimilation has been applied in precipitation modeling, and ground water simulation, but it has never been applied in a STATS setting for the optimal estimation of soil moisture.

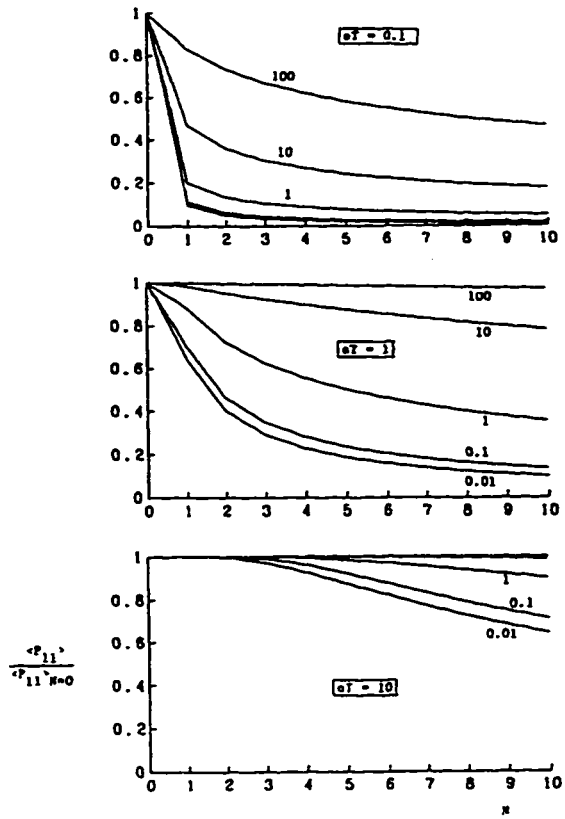

Figure 1.40: Normalized error variance of x (Milly, 1986a).

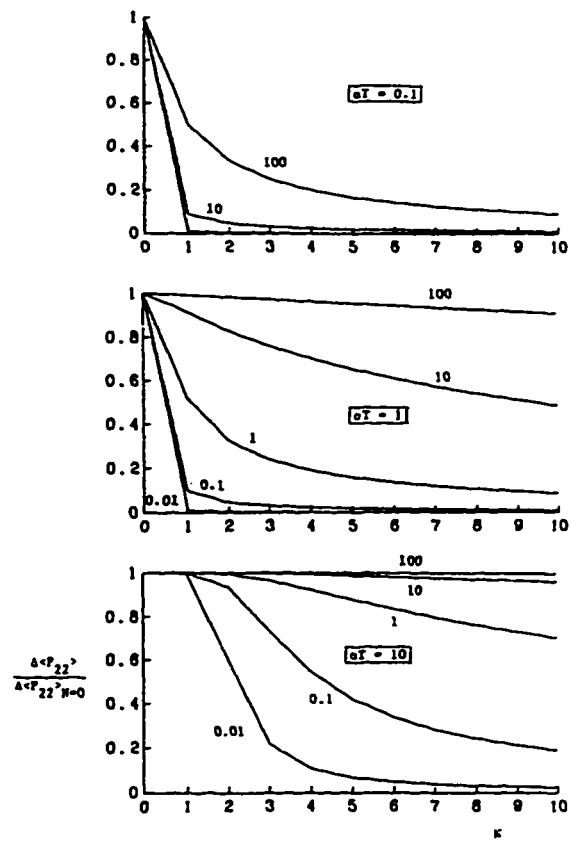

Figure 1.41: Normalized increase in error variance of x (Milly, 1986a).

2. MODEL STRUCTURE AND DESCRIPTION

2.1 Introduction

The TOPLATS model and specific modifications for its use at Walnut Gulch and in data assimilation studies are described below. First, the established model equations are reviewed, then their modification to include a remote-sensing thin surface layer are detailed. Next, specific modifications to the model structure to assure compatibility with the Walnut Gulch data sets are described. Finally, the data assimilation methodologies and algorithms used in this study are presented.

2.2 The TOPLATS model

The TOPLATS (TOPMODEL (Beven and Kirby, 1979)-based Land Atmosphere Transfer Scheme) (Famiglietti and Wood, 1994a), which parameterizes subgrid-scale variability in runoff, energy fluxes, and soil moisture, was used and enhanced in this study. The purpose of the model is to predict diurnal dynamics of the water and energy fluxes at the land-surface and to predict the local vertical recharge to the water table. It intentionally uses simpler algorithms than are used in operational SVATS so that it can be applied repeatedly in space and time. For example, the vertical soil moisture fluxes are represented using approximate analytical solutions to the governing equations for unsaturated zone soil water flow (Richards, 1931) in the manner of Eagleson (1978). The resulting model is simple, yet arguably detailed enough to represent the essential physics at the land-atmosphere interface.

The SVATS incorporates simple representations of atmospheric forcing, vertical soil moisture transport, plant-controlled transpiration, interception, evaporation, infiltration, surface runoff, and sensible and ground heat fluxes, as shown in Figure 2.1. The land-surface is partitioned into bare soil and vegetated components which are assumed uniformly distributed. An interception store is maintained in the canopy, so that wet and dry canopy conditions are recognized. Latent, sensible, and ground heat fluxes, infiltration, and surface runoff are computed for each of these land-surface components separately. The vertical soil moisture fluxes are represented using an approximate analytical solution to Richards equation (Eagleson, 1978). Runoff generation occurs by both infiltration excess and saturation excess mechanisms.

The subsurface soil column is currently partitioned into two layers; a root zone that extends from the surface to the rooting depth, and a transmission zone that extends from the bottom of the root zone to the top of the capillary fringe. Infiltration, evapotranspiration, drainage, and capillary rise are modeled in the root zone, while only drainage and capillary rise are modeled in the transmission zone.

The model incorporates a diurnal cycle and is driven with standard meteorological data with a time step of 1-2 hours, this being considered sufficient to resolve the dynamics of the land-atmosphere interaction. The driving variables and soil and vegetation parameters required by the TOPLATS are given in Appendix B. Modeled states include the depth of water in the canopy store, ω_c, surface temperature, T_s, moisture content in the root zone, θ_{rz}, moisture content in the root zone, θ_{tz}, and the local water table depth, z (positive down).

The TOPLATS model can also use a statistical-dynamical method to describe subgrid scale variability in runoff, energy fluxes, and soil moisture. The actual spatially distributed representation of variables which show significant variability are replaced by a simpler, statistical representation. The formulation incorporates subgrid scale spatial variability in topography and soils to model downslope redistribution of soil water; and this feeds back through the model structure to yield the description of subgrid spatial variability in water table depth, soil water storage, root zone moisture content, and thus runoff and energy fluxes (Famiglietti and Wood, 1994a).

2.2.1 TOPMODEL

TOPMODEL is a simple, physical hydrological model that represents the effects of catchment heterogeneity and topography on the dynamics of hydrological response (Quinn and Beven, 1993). Originally conceived by Beven and Kirby (1979), TOPMODEL is considered to be a set of conceptual tools that can be used to reproduce the behavior of a catchment in a distributed or semi-distributed manner, particularly the dynamics of the surface and subsurface contributing areas. It is based on three basic assumptions: (1) The dynamics of the saturated zone can be approximated by successive steady-state representations; (2) The saturated zone hydraulic gradient can be approximated by the local surface topographic slope, $\tan(\beta)$; (3) the

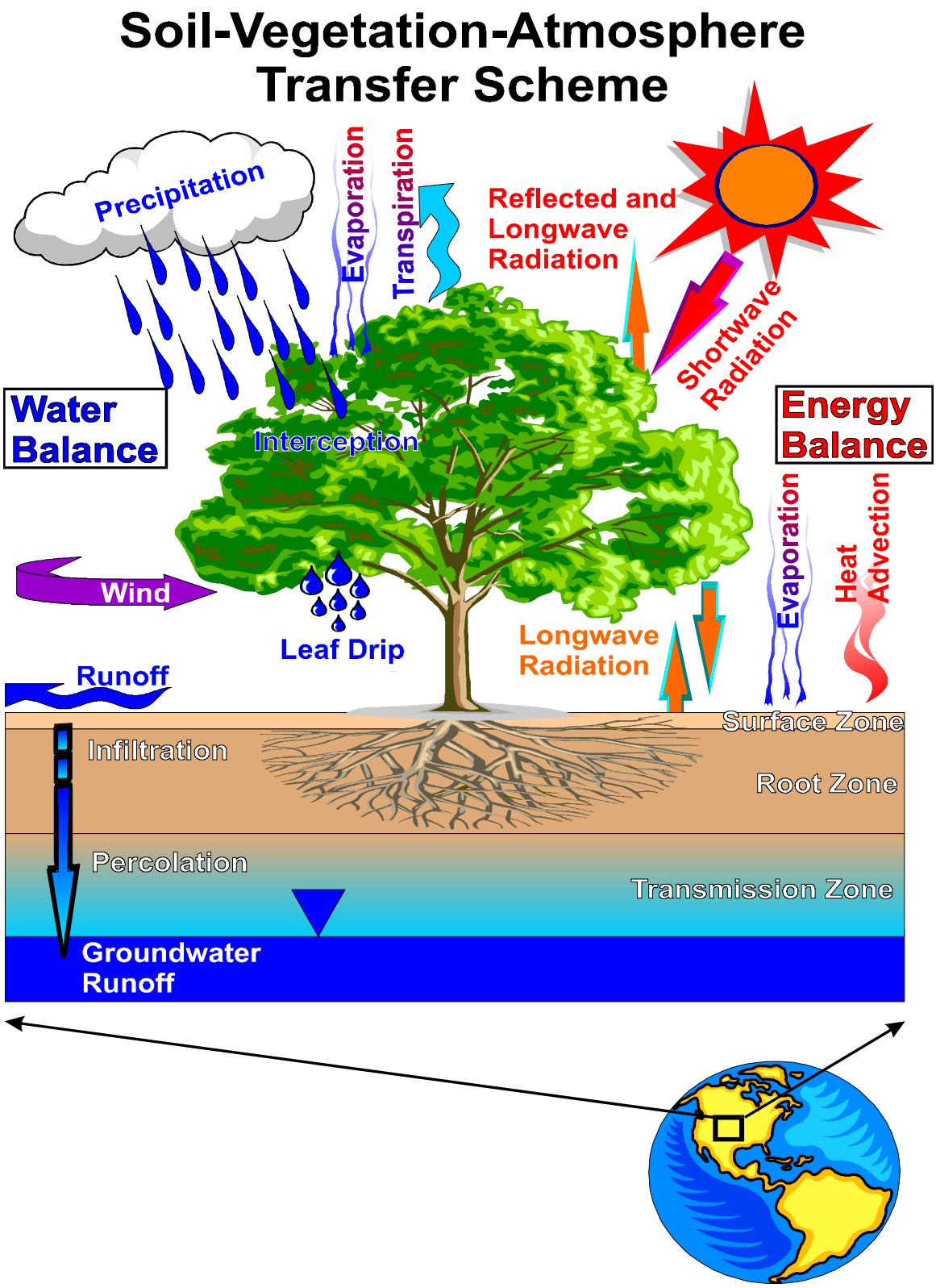

Figure 2.1: TOPLATS modeled processes.

distribution of the downslope transmissivity with depth is an exponential function of storage deficit or depth to the water table. This last assumption can be written as:

$$T=T_0 e^{\frac{-S}{m}} \tag{2.1}$$

where T_0 is the saturated lateral transmissivity, S is the local storage deficit or depth, and m is a parameter. In terms of water table depth, z, this can be written as:

$$T=T_0 e^{-fz} \tag{2.2}$$

where f is a scaling parameter. The f and m parameters are related by:

$$f=\frac{\Delta\theta_1}{m} \tag{2.3}$$

where $\Delta\theta_1$ is the effective water content change per unit depth in the unsaturated zone due to rapid gravity drainage. m is generally interpreted to control the effective depth of the catchment soil profile.

The assumption that saturated flow occurs parallel to the surface slope $\tan(\beta)$, enables specification of the downslope subsurface flow rate q_i at any point I on a hillslope:

$$q_i=T_0\tan(\beta)e^{-fz_i} \tag{2.4}$$

Then, using the first assumption and assuming a spatially homogeneous recharge rate r the subsurface downslope flow per unit contour length q_i can also be given by:

$$q_i=ra \tag{2.5}$$

where a is the area of the hillslope per unit contour length that drains through point I. Then, through combining the previous two equations, an equation is derived relating local water table depth to the topographic index $ln(a/\tan(\beta))$ at any point can be written as:

$$z_i=-\frac{1}{f}\ln\frac{ra}{T_0\tan(\beta)} \tag{2.6}$$

Then, the mean water table depth, $\bar{z}$, can be derived by integrating over the catchment area A:

$$\bar{z}=\frac{1}{A}\sum_i -\frac{1}{f}\ln\frac{ra}{T_0\tan(\beta)} \tag{2.7}$$

By using the previous two equations and assuming r is spatially constant, $ln(r)$ may be eliminated to find a relationship between mean water table depth, local water table depth, topographic variables, and saturated transmissivity:

$$\bar{z}=z_i-\frac{1}{f}\left[\gamma-\ln\frac{a}{T_0\tan\beta}\right] \tag{2.8}$$

where $ln(a/T_0\tan(\beta))$ is the soil-topographic index of Beven (1986), and:

$$\gamma=\frac{1}{A}\sum_i \ln\frac{a}{T_0\tan(\beta)} \tag{2.9}$$

An average value of transmissivity can also be defined:

$$lnT_e=\frac{1}{A}\sum_i \ln T_0 \tag{2.10}$$

Equation (2.8) can be rearranged to give:

$$f(\bar{z}-z_i)=\left[\ln\frac{a}{\tan(\beta)}-\lambda\right]-[\ln T_0-\ln T_e] \tag{2.11}$$

or in terms of storage deficit:

$$\frac{\bar{S}-S_i}{m}=\left[\ln\frac{a}{\tan(\beta)}-\lambda\right]-[\ln T_0-\ln T_e] \tag{2.12}$$

where:

$$\lambda=\frac{1}{A}\sum_i \ln\frac{a}{\tan(\beta)} \tag{2.13}$$

is a topographic constant for the catchment.

These equations express the deviation between that average water table depth and the local water table depth at any point in terms of the local topographic index from its areal mean, and the deviation of the logarithm of local transmissivity from its areal integral value. The parameters m and f scale the relationship. Hence, given a value of $\bar{z}$ and the spatial distribution of the soil-topographic index, the pattern of water table depths over a catchment can be predicted. The previous relationships also imply that every point having the same soil-topographic index behaves functionally identically. This allows specification and discretization

of the soil-topographic index distribution function. Thus, for a small range of soil-topographic index values, only one model integration needs to be made, bringing an obvious computational advantage.

When the local water table is predicted to lie above the land-surface, saturated overland flow is predicted to occur, and any rainfall falling on these areas is assumed to be runoff. An illustration of TOPMODEL water table dynamics is shown in Figure 2.2.

A formulation of stores in TOPMODEL is shown in Figure 2.3 (Quinn *et al.*, 1991). Conversion between a storage deficit due to drainage and water table depth assumes that rapid gravity drainage affects only large pores, down to the field capacity, and that the difference in storage between saturation and field capacity is independent of depth:

$$S_i=(\theta_S-\theta_{fc})(z_i-\psi_0)=\Delta\theta_1(z_i-\psi_0) \tag{2.14}$$

where S_i is the local gravity storage deficit, q_v is local recharge to the saturated zone, θ_s is the saturation moisture content, θ_{fc} is the field capacity moisture content, $\Delta\theta_l$ is an effective drained porosity, and ψ_0 is the effective depth of the capillary fringe.

Beven and Wood (1983) suggested a functional form for vertical unsaturated flux, q_v at any point I:

$$q_v=\frac{S_u z}{S_t t_d} \tag{2.15}$$

where $S_u z$ is unsaturated zone storage, S_t is the local saturated zone deficit due to gravity drainage and dependent on depth to the local water table. t_d is a time-constant parameter.

An alternative approach is based on Darcian flux at the base of the unsaturated zone (Beven, 1986):

$$q_v=\alpha K_0 e^{-fz_i} \tag{2.16}$$

where α is the effective vertical hydraulic gradient parameter, K_0 is the surface hydraulic conductivity, and z_i is the local water table depth.

Beven (1991) calculated TOPMODEL evaporation at the full potential rate, E_p for free unsaturated drainage and for areas of surface saturation. When the gravity drainage zone is depleted, evapotranspiration may continue to deplete the root zone at the rate E_a:

$$E_a = E_p\left(1 - \frac{S_{rz}}{S_{r_{max}}}\right) \tag{2.17}$$

where S_{rz} is the root zone storage deficit, z_{rz} is the root zone depth, and S_{rmax} is the maximum allowable storage deficit, which is calculated:

$$z_{rz}(\theta_{fc} - \theta_{wp}) = z_{rz}(\Delta\theta_2) \tag{2.18}$$

where θ_{wp} is the wilting point moisture content.

If the flux of water entering the water table locally is q_v, then the total recharge Q_v is:

$$Q_v = \sum_{i=1}^{n} q_{v,I} A_i \tag{2.19}$$

where A_i is the fractional area associated with topographic index I as a fraction of the total catchment area.

Output from the saturated zone, or baseflow, Q_b can be calculated in a distributed sense by the summation of subsurface flows along each of m stream channel reaches of length l. Recalling Equation (2.4):

$$Q_b = \sum_{j=1}^{m} l_j (T_0 \tan(\beta)) e^{-fz_j} \tag{2.20}$$

Substituting for z_j using equation (2.7) and rearranging:

$$Q_b = \sum_{j=1}^{m} l_j a_j e^{-\gamma} e^{-f\bar{z}} \tag{2.21}$$

Because a_j is the contributing area per unit contour length:

$$\sum_{j=1}^{m} l_j a_j = A \tag{2.22}$$

Therefore:

$$Q_b = A e^{-\gamma} e^{-f\bar{z}} \tag{2.23}$$

where A is the total catchment area. Now, it is possible to calculate baseflow in terms of average catchment water table depth $\bar{z}$:

$$Q_b = Q_0 e^{-f\bar{z}} \tag{2.24}$$

where:

$$Q_0 = Ae^{-\gamma} \tag{2.25}$$

is the discharge when $\bar{z}$ or $\bar{S}$ equals zero. Solution of (2.24) for a pure recession with zero input shows that discharge has an inverse hyperbolic relationship to time:

$$\frac{1}{Q_b} = \frac{1}{Q_0} + \frac{t}{m} \tag{2.26}$$

Thus, a plot of $1/Q_b$ versus time should plot as a straight line with slope $1/m$. Therefore, given some recession curves, it should be possible to set the value of m with minimal calibration.

The catchment average storage deficit before each time step is updated by subtracting the unsaturated zone recharge and adding the baseflow from the previous step:

$$\bar{z}_t = \bar{z}_{t-1} + \Delta\theta_1 [Q_{b_{t-1}} + Q_{c_{t-1}}] \tag{2.27}$$

2.2.2 TOPLATS prognostic equations

The TOPMODEL-based Land-Atmosphere Transfer Scheme (TOPLATS) utilizes the elegance of the TOPMODEL scheme for groundwater influences on surface hydrologic processes and adds a simple, yet comprehensive soil-vegetation-atmosphere transfer scheme for inclusion of both energy- and water-balance. The complete description of modeled processes in the TOPLATS model is given below (Famiglietti and Wood, 1994a).

2.2.2.1 Water-balance equations

The canopy water-balance is given by:

$$\frac{d\omega}{dt} = p - w_{\omega c} - p_{net} \qquad 0 \le \omega_c \ge \omega_{sc} \tag{2.28}$$

where p is the precipitation rate, $e_{\omega c}$ is the wet canopy evaporation rate, p_{net} is the net precipitation which occurs when the canopy water storage capacity ω_{sc} has been exceeded, e_{wet} is the rate of evaporation from the entire wet canopy, and ω_{wc} is the areal fraction of wet canopy, which is determined from Deardorff (1978) as:

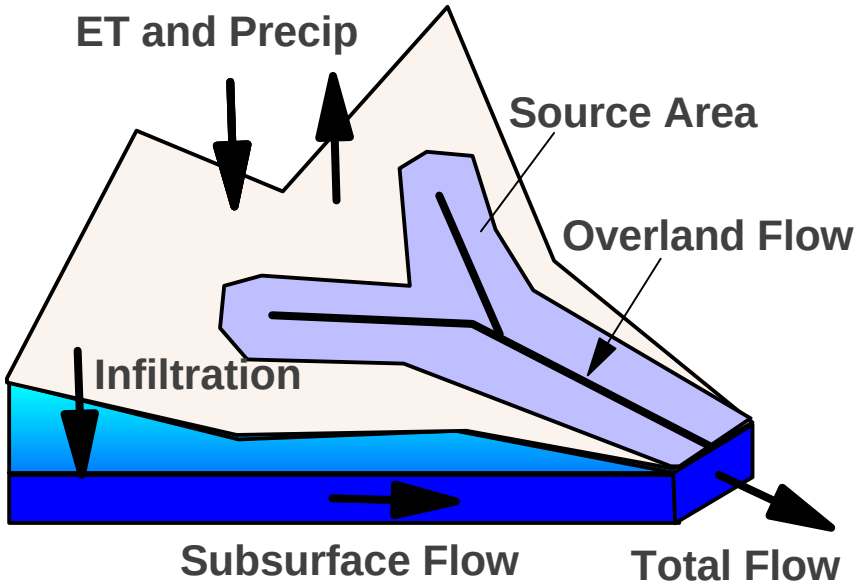

Figure 2.2: Illustration of TOPMODEL water table dynamics.

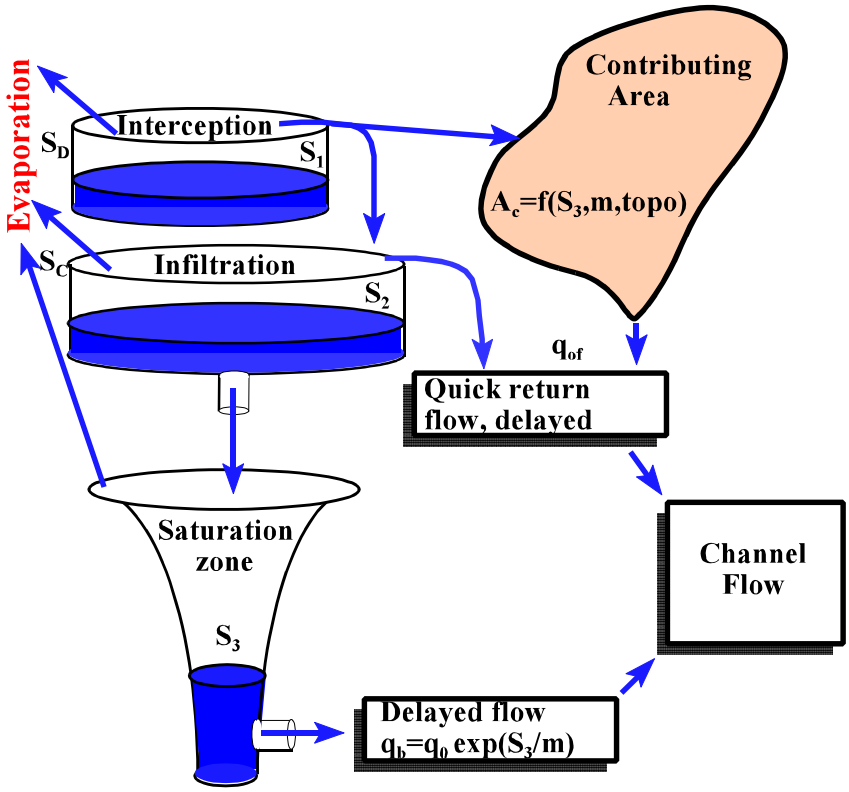

Figure 2.3: Diagram of TOPMODEL storages.

$$\omega_{wc}=\left(\frac{\omega_c}{\omega_{sc}}\right)^{\left(\frac{2}{3}\right)} \qquad when \qquad e_{wet}>0 \tag{2.29}$$

$$\omega_{\omega c}=1 \qquad when \qquad e_{wet}\leq 0 \tag{2.30}$$

The canopy water storage capacity is calculated as a function of leaf area index, *LAI* (Dickinson, 1984):

$$\omega_{sc}=0.0002\ LAI \tag{2.31}$$

Soil type, texture, and properties are described using the Brooks and Corey (1964) model, whose parameters include the saturated hydraulic conductivity, K_s, the saturation moisture content, θ_s, the residual moisture content, θ_r, the pore size distribution index, B, and, ψ_c, the air-entry suction head. Soil moisture and hydraulic conductivity in unsaturated soils can be described in terms of the matric head ψ as:

$$\theta(\psi)=\theta_r+(\theta_s-\theta_r)\left(\frac{\psi_c}{\psi}\right)^B \qquad \psi>\psi_c \tag{2.32}$$

$$K(\psi)=K_s\left(\frac{\psi_c}{\psi}\right)^{2+3B} \qquad \psi>\psi_c \tag{2.33}$$

$$K(\psi)=K_s \qquad \theta(\psi)=\theta_s \qquad \psi\leq\psi_c \tag{2.34}$$

Two cases (reflecting different water table depths) are considered for the root and transmission zone water-balance equations. In Case 1, the top of the capillary fringe lies beneath the bottom of the root zone as a depth z - ψ_c. The unsaturated zone is partitioned into a root zone of depth z_{rz} and an underlying transmission zone extending between the top of the capillary fringe and the base of the root zone, z_{tz}. In Case 2, the top of the capillary fringe lies within the root zone; therefore, there is no transmission zone.

The root zone water-balance equation for Case 1 is:

$$z_{rz}\frac{d\theta_{rz}}{dt}+f_{bs}i_{bs}+f_v i_v+\omega-f_{bs}e_{bs}-f_v e_{dc}-g_{rz}, \tag{2.35}$$

$$for \qquad z-\psi_c\geq z_{rz} \qquad \theta_r\leq\theta_{rz}\leq\theta_s$$

where f_{bs} is the fraction of bare soil land-surface, i_{bs} is the bare soil infiltration, f_v is the fraction of vegetated land-surface, i_v is the infiltration rate into vegetated soils, ω is the rate of capillary rise from the water table, e_{bs} is the bare soil evaporation rate, e_{dc} is the dry canopy transpiration rate, and g_{rz} is the downward soil water flux from the base of the root zone.

The transmission zone water-balance equation is:

$$z_{tz}\frac{d\theta_{tz}}{dt}=g_{rz}-g_{tz} \qquad z_{tz}>0 \tag{2.36}$$

$$for \quad z_{rz}^{*}=z-\psi_c \qquad z_{rz}>z-\psi_c\geq 0 \qquad \theta_r\leq\theta_{rz}\leq\theta_s$$

where θ_{rz} is the uniform soil moisture in the zone extending from the top of the capillary fringe to the soil surface.

The actual infiltration rate for bare soil is taken as the minimum of the infiltration capacity, $I^{*}(I)$, or the precipitation rate:

$$i_{bs}=\min[i^{*}(I),p] \tag{2.37}$$

Actual infiltration into vegetated soil is the minimum of the infiltration capacity or the net precipitation rate:

$$i_v=\min[i^{*}(I),p_{net}] \tag{2.38}$$

The infiltration capacity for bare and vegetated soils is given by Milly (1986b):

$$i^{*}(I)=cK_s\left(1+\left(\left(1+\frac{4cK_sI}{S^2}\right)^{\left(\frac{1}{2}\right)}-1\right)^{-1}\right) \tag{2.39}$$

where S is the sorptivity, and c is a dimensionless constant.

The rate of capillary rise is based on the result of Gardner (1958) for steady upward flow from the water table:

$$\omega=\frac{Ca}{(z-\psi_c)^b} \tag{2.40}$$

where the parameters C, a, and b are functions of soil type and are given by Eagleson (1978) in terms of the Brooks and Corey (1964) soil parameters:

$$C=1+\left(\frac{1.5}{1+3B}\right) \tag{2.41}$$

$$a = K_s \psi_c^{2+3B} \tag{2.42}$$

$$b = 2 + 3B \tag{2.43}$$

The actual rate of bare-soil evaporation is taken as the minimum of the soil-controlled exfiltration capacity, $e^*(E_c)$, or the atmospherically-controlled potential evaporation rate, e_{pe}:

$$e_{bs} = \min[e^*(E_c), e_{pe}] \tag{2.44}$$

The bare-soil exfiltration capacity is given by Milly (1986b):

$$e^*(E_c) = \frac{S_e^2}{2E_c} \tag{2.45}$$

where S_e is the desorptivity, and E_c is the cumulative exfiltration. Hence, exfiltration capacity only depends on cumulative exfiltration and the initial conditions at the start of the interstorm period.

The actual rate of transpiration from the dry canopy is obtained from the minimum of the vegetation-controlled transpiration capacity, τ^*, or the atmospherically controlled unstressed transpiration rate, t_{unst}:

$$e_{dc} = \omega_{dc} \min[\tau^*, t_{unst}] \tag{2.46}$$

where ω_{dc} is a canopy water-balance variable which expresses the current areal fraction of dry canopy. Thus, the term 'vegetation control' refers to a state of increased stomatal resistance beyond unstressed levels. The transpiration capacity, τ^* is based on the soil water extraction model of Feyen *et al.* (1979) and is a function of the matric potential of the soil, ψ_s, the critical leaf water potential, ψ_{crit}, the hydraulic resistance of the soil, R_s, and the hydraulic resistance of the plant, R_p:

$$\tau^* = \frac{z_{rz}(\psi_s - \psi_{crit})}{R_s + R_p} \tag{2.47}$$

where:

$$R_s = \frac{1}{FK(\theta_{rz})L} \tag{2.48}$$

$$R_p = \frac{R_u}{L} \tag{2.49}$$

Here, $K(\theta_{rz})$ is the hydraulic conductivity of the root zone, L is the root density (root length per unit soil volume), F is an empirical constant taken as an effective root activity factor, and R_u is the root resistivity per unit length.

Drainage from the base of the root zone, θ_{rz}, and transmission zone, θ_{tz}, is assumed to proceed at gravity-driven rates:

$$g_{rz}=K_s\left(\frac{\theta_{rz}-\theta_r}{\theta_s-\theta_r}\right)^{\eta} \tag{2.50}$$

where:

$$\eta=\frac{2+3B}{B} \tag{2.51}$$

and g_{tz} is given by replacing θ_{rz} with θ_{tz} above.

Both saturation excess runoff and infiltration excess runoff are computed within the model. The bare soil and vegetated runoff are:

$$q_{bs}=p; \qquad \theta_{rz}=\theta_s \tag{2.52}$$

$$q_{bs}=p-i^*(I); \qquad \theta_{rz}<\theta_s \qquad p>i^*(I) \tag{2.53}$$

$$q_v=p_{net}; \qquad \theta_{rz}=\theta_s \tag{2.54}$$

$$q_v=p_{net}-i^*(I); \qquad \theta_{rz}<\theta_s \qquad p_{net}>i^*(I) \tag{2.55}$$

The lower boundary condition of the SVATS is the top of the capillary fringe, which is controlled by the local water table depth. The space-time dynamics of the local water table depth are modeled using a spatially aggregated procedure described later.

2.2.2.2 Energy-balance, potential evapotranspiration, and surface temperature

The actual evapotranspiration rate depends on the evaporation rate from the wet canopy, e_{wc}, the unstressed transpiration rate, e_{dc}, and the bare soil potential evaporation rate, e_{bs}. These potential rates are determined from energy-balances for the wet canopy, dry canopy, and bare soils, respectively.

The energy-balance equation is:

$$R_n = \rho_\omega LE + H + G \tag{2.56}$$

where R_n is the net radiation, ρ_ω is the density of liquid water, and $\rho_\omega LE$ is the latent heat flux into the atmosphere, H is the sensible heat flux into the atmosphere, and G is the soil heat flux or the heat flux into the ground. Net radiation is computed as follows:

$$R_n = R_{sd}(1-\alpha) + \epsilon R_{ld} - \epsilon\sigma T_l^4 \tag{2.57}$$

where R_{sd} is the downward shortwave radiation, α is the albedo, ϵ is the emissivity, R_{ld} is the downward longwave radiation, σ is the Stefan-Boltzmann constant, and T_l is the temperature of the wet canopy, dry canopy, or bare-soil surface. Latent heat flux is given by Milly (1991) as:

$$\rho_\omega LE = \frac{\rho c_p}{\gamma(r_c + r_{av})}(e^*(T_l) - e_a) \tag{2.58}$$

where ρ is the density of air, c_p is the specific heat of air at constant pressure, γ is the psychrometric constant, r_c is the canopy resistance, r_{av} is the aerodynamic resistance, $e^*(T_l)$ is the saturation vapor pressure at the surface temperature T_l, and e_a is the vapor pressure at some level above the canopy or soil surface, z_a. The sensible heat flux is given as:

$$H = \frac{\rho c_p}{r_{ah}}(T_l - T_a) \tag{2.59}$$

where r_{ah} is the aerodynamic resistance to heat flow, and T_a is the air temperature at z_a. Ignoring the effects of heat storage in the surface soil layer, heat flux into the surface, G, is assumed to be a linear function of the subsurface temperature gradient:

$$G = \frac{\kappa}{D}(T_l - T_2) \tag{2.60}$$

where κ is the thermal conductivity, D is the damping depth of the diurnal temperature oscillations, and T_2 is the temperature at depth D. The thermal conductivity is dependent on the matric head as given by McCumber and Pielke (1981). The temperature T_2 is presently prescribed. The aerodynamic resistances are given by:

$$r_{ah} = r_{av} = \frac{1}{k^2 u(z_a)}\left(\ln\left(\frac{(z_a - d)}{z_0}\right)\right)^2 \tag{2.61}$$

where k is von Karman's constant, $u(z_a)$ is the wind speed at level z_a d is the zero plane displacement, and z_0 is the roughness length of the canopy or soil surface.

Wet canopy evaporation, e_{wc}, is determined by solving the previous equations for the temperature of the wet vegetation. Setting α, z_0, and d to values representative of the vegetation type when wet, G and r_c equal to zero, and letting T_l represent the temperature of the wet vegetated surface yields the partitioning of R_n into $\rho_a LE$ and H. The unstressed transpiration, t_{unst}, is calculated in the same manner as e_{wc}, but with r_c representing canopy resistance as $r_c=r_{stmin}/LAI$, where r_{stmin} is a minimum value of stomatal resistance. The potential evaporation e_{pc} for bare soil is calculated using the above equations (2.56-2.61) with r_c equal to zero, α, z_0, and d consistent with the particular type of wet soil, and T_l as the temperature of the wet-bare soil surface.

These temperatures and fluxes determined are for potential or unstressed conditions. When stomatal resistance increases above its minimum level and the actual transpiration rate is less than the unstressed rate, e_{dc} is substituted for E in Equation (2.58), and Equation (2.56) is solved to find the correct vegetation temperatures and fluxes. When bare-soil evaporation proceeds at soil-controlled rates, e_{bs} is substituted for Equation (2.58), and Equation (2.56) is solved to find the correct bare-soil temperatures and fluxes.

2.2.2.3 Local water- and energy-balance fluxes

The local rates of evapotranspiration, E, and runoff, Q, are determined by summing the weighted areal fraction of the bare-soil and vegetated components:

$$E=f_{bs}e_{bs}+f_v(e_{dc}+e_{wc}); \tag{2.62}$$

$$Q=f_{bs}q_{bs}+f_v q_c \tag{2.63}$$

The remaining energy fluxes and surface temperatures are determined similarly.

2.2.2.4 Aggregation to the catchment scale

A spatially distributed model structure was developed for the catchment scale because of the significant effect which explicit patterns of spatially variable model inputs and parameters have on hydrologic responses at these scales. This methodology is not theoretically limited to

the catchment scale, but may be operationally limited by computational constraints, lack of available high-resolution data, and the cumbersome nature of spatially distributed input and output data. It may also be unnecessary to model explicit patterns of water- and energy-balance at large scales, because statistical representations may suffice (Wood *et al.*, 1988).

The spatially distributed model is discretized into elements based on the digital elevation model (DEM), and the SVATS is applied to each grid. Spatially distributed inputs and parameters are coregistered with the DEM, so that spatial variabilities in model outputs are represented explicitly. Then, the catchment-average response is simply an average of the local grid responses.

The topographic-soil index of Beven (1986) is used to parameterize spatial variability in topographic and soil properties, and thus couples the SVATS grids through its lower boundary, the water table depth.

2.2.2.4.1 Lateral subsurface flow and water table dynamics

All unsaturated water transport is assumed vertical and non-interactive between grids, but a simple topographic framework is used to simulate subsurface saturated flow between grids and patterns of water table elevations. The local water table depth affects local soil moisture storage and thus hydrologic fluxes. When the water table intersects the surface, the land-surface becomes saturated, and evaporation and transpiration proceed at potential rates. Additionally, rainfall on these areas is transformed into saturation excess runoff.

It is assumed that saturated subsurface flow between model grids is controlled by variability in topographic and soil properties, which is parameterized using the topographic-soil index:

$$\ln\left(\frac{aT_e}{T^i \tan\beta}\right) \tag{2.64}$$

where a is the area drained through the local unit contour, I is the local grid element index, T_e is the catchment average value of the saturated transmissivity coefficient, T^i is the local value of the transmissivity coefficient, and β is the local slope angle. The topographic-soil index is a local drainage index derived for quasi-steady-state conditions.

Sivapalan *et al.* (1987) derived a simple expression for the local water table depth, z^i, in terms of the local topographic-soil index:

$$z^i = \bar{z} - \frac{1}{f}\left(\ln\left(\frac{aT_e}{T^i \tan\beta} \right) - \lambda \right) \tag{2.65}$$

where $\bar{z}$ is the catchment average water table depth, and λ is the catchment average value of the topographic variable:

$$\ln\left(\frac{a}{\tan\beta} \right) \tag{2.66}$$

The spatial distribution of the topographic-soil index can be computed using a DEM and regional soil survey information. High values of the topographic-soil index imply a tendency toward surface saturation and are usually associated with topographic convergence. Conversely, low index values imply a deeper water table. Modeling the temporal dynamics in the catchment average water depth allows the spatial distribution to be updated in time, which is analogous to a simplified model of lateral subsurface water flow in the saturated zone. A number of algorithms have been developed to calculate this index, and some have even been incorporated into Geographical Information System (GIS) packages.

2.2.2.4.2 Local water- and energy-balance

Three specific regions within the catchment are recognized to properly apply the soil water-balance equations. Region 1 are those grids where the top of the capillary fringe lies beneath the root zone. In region 2, the top of the capillary fringe lies within the root zone, and therefore there is no transmission zone. Region 3 consists of grids where saturation has occurred. In this region, the root zone remains saturated so that:

$$z_{rz}\frac{d\theta_{rz}^i}{dt} = 0 \qquad z^i - \psi_c^i < 0 \qquad \theta_{rz}^i = \theta_s^i \tag{2.67}$$

and, as in region 2, there is no transmission zone.

2.2.2.4.3 Saturated zone water-balance

Equation (2.65) shows that dz^i/dt, the rate of change of the local water table depth, is equal to $d\bar{z}/dt$, the rate of change of the areal average water table depth. This was derived by global mass balance considerations for the discretized catchment as $\Delta z/\Delta t$, which is used to approximate the differential $d\bar{z}/dt$ as:

$$\frac{d\bar{z}}{dt} \approx \frac{\Delta z}{\Delta t} = \frac{\left(\sum_{i \in R_1, R_2} \omega^i + \sum_{i \in R_3} E^i + \frac{Q_b}{\Delta x \Delta y} - \sum_{i \in R_1} g_{tz}^i - \sum_{i \in R_2} g_{rz}^i \right)}{\left(\sum_{i \in R_1} (\theta_s^i - \theta_{tz}^i) + \sum_{i \in R_2} (\theta_s^i - \theta_{rz}^i) \right)} \tag{2.68}$$

where regions 1, 2, and 3 are represented by R_1, R_2, and R_3 respectively, Q_b is baseflow, and $\Delta x \Delta y$ is the area of the grid element.

Saturated zone storage depletions result from the sum of the capillary flux from regions 1 and 2, $\sum_{i \in R1R2} \omega^i$, evapotranspiration from region 3, $\sum_{i \in R3} E^i$, and baseflow, Q_b. Recharge to the water table results from the sum of the transmission zone drainage flux over region 1, $\sum_{i \in R1} g^i_{tz}$, and the sum of the root zone drainage flux over region 2, $\sum_{i \in R2} g^i_{rz}$. The terms of the denominator of Equation (2.68) represent the catchment storage deficit in the transmission and root zones, respectively.

2.2.2.4.4 Catchment water- and energy-balance fluxes

The catchment scale water- and energy-balance fluxes are the average of the grid element fluxes. The catchment scale evapotranspiration rate, $\bar{E}$, is:

$$\bar{E} = \frac{1}{N} \sum_{i \in C} E^i = \frac{1}{N} \sum_{i \in C} \left(f_{bs}^i e_{bs}^i + f_v^i (e_{dc}^i + e_{wc}^i) \right) \tag{2.69}$$

where C is the set of all catchment grid elements. The other catchment scale energy fluxes are determined similarly. The catchment scale runoff rate, $\bar{Q}$, is the average of the bare soil and vegetated runoff. TOPLATS currently does not route runoff to the catchment outlet, which might make explicit comparisons with observed runoff impractical, and prohibit TOPLATS from accounting for water redistributions via runoff routing processes. The lateral subsurface flow, Q_b, is also included in the catchment scale flux. The catchment scale runoff rate is:

$$\bar{Q}=\frac{1}{N}\sum_{i\in C} Q^{i}+\frac{Q_b}{A}=\frac{1}{N}\sum_{i\in C}\left(f_{bs}^{i}q_{bs}^{i}+f_{v}^{i}q_{v}^{i}\right)+\frac{Q_b}{A} \tag{2.70}$$

where A is the local catchment surface area. Baseflow is determined for the catchment by integrating the local saturated subsurface fluxes along the channel network (Sivapalan *et al.*, 1987), yielding:

$$Q_b=Q_0\exp(-f\bar{z}) \tag{2.71}$$

where:

$$Q_0=AT_e\exp(-\lambda) \tag{2.72}$$

The parameters Q_0 and f, as well as the spatial distribution of the topographic-soil index, are required here. Q_0 and f are most often estimated by optimizing modeled streamflow to observed.

Catchment scale water-balance is maintained by ensuring that canopy and soil water storage changes equal the sum of precipitation less evapotranspiration and runoff. Catchment scale energy-balance is guaranteed by enforcing:

$$R_n^{i}-G^{i}-\rho^{\omega}LE^{i}-H^{i}=0 \tag{2.73}$$

at each catchment grid element.

2.2.2.5 Aggregation to the macroscale

Explicit aggregation using a high-resolution spatially distributed model is not feasible at the macroscale. Subgrid-scale spatial variability in certain land-surface parameters and forcing do have significant impacts on energy and water fluxes, and therefore must be represented within macroscale models. The approach here is to identify the most important land-surface heterogeneity and to simplify its representation in a macroscale model using a statistical rather than spatially distributed approach. It is assumed that subgrid-scale spatial variability in soil moisture is the dominant control on the grid-scale water- and energy-balance. The spatial distribution of soil moisture determines the location, type, and magnitude of runoff and determines which land-surface regions evaporate at potential rates versus lower soil and vegetation-controlled rates. Second, it is assumed that a threshold modeling scale (or the representative elementary area (REA) Wood *et al.*, 1988) has been exceeded, so that the exact pattern of topographic and soil heterogeneites need not be explicitly represented, but rather, a

statistical representation will suffice. Therefore, a statistical distribution of the topographic-soil index is employed.

The distribution of the index is discretized into a number of intervals, and the local SVATS is applied to each interval. The intervals are coupled through the process of saturated subsurface lateral flow. The macroscale fluxes are interval-weighted averages of the local fluxes. This process is illustrated in Figure 2.4.

2.2.2.5.1 Saturated zone water-balance

As with the catchment-scale model, an areal average water table depth is required to update the spatial distribution of water table depths. The macroscale updating procedure involves balancing recharge and depletions to the saturated soil reservoir. x^{sat} is the topographic-soils index value at which the land-surface is just saturated and is given by:

$$x^{sat} = \lambda - f(\psi_c - \bar{z}) \tag{2.74}$$

Locations where $ln\{(aT_e)/(T_x \tan\beta)\}$ is greater than x^{sat} are saturated. x_{rz} refers to the maximum value of $ln\{(aT_e)/(T_x \tan\beta)\}$ in region 1. When $ln\{(aT_e)/(T_x \tan\beta)\}$ is greater then x_{rz} the top of the capillary fringe either lies within the root zone or at the soil surface. x_{rz} is given as:

$$x^{rz} = \lambda - f(\psi_c + z_{rz} - \bar{z}) \tag{2.75}$$

The rate of change of the areal average water table depth is:

$$\frac{d\bar{z}}{dt} = \frac{\left(\int_{x=-\infty}^{x=x^{sat}} \omega(x_{f_x}(x)dx + \int_{x=x^{sat}}^{x=\infty} E(x)f_x(x)dx + \frac{Q_b}{A} - \int_{x=-\infty}^{x=x^{rz}} g_{tz}(x)f_x(x)dx - \int_{x=x^{rz}}^{x=x^{sat}} g_{rz}f_x(x)dx \right)}{\left(\int_{x=-\infty}^{x=x^{rz}} (\theta_s - \theta_{tz}(x))f_x(x)dx + \int_{x=x^{rz}}^{x=x^{sat}} (\theta_s - \theta^*_{rz}(x))f_x(x)dx \right)} \tag{2.76}$$

Saturated zone storage is depleted by the aggregated flux of capillary rise from regions 1 and 2 *(first numerator term)*, evapotranspiration from saturated regions *(second numerator term)*, and baseflow Q_b. The water table is recharged by the downward flux from the transmission zone aggregated over region 1 *(fourth numerator term)*, and the downward flux from the root zone aggregated over region 2 *(fifth numerator term)*. The terms in the denominator represent the areal average storage deficit from the transmission and root zone, respectively.

2.2.2.5.2 Macroscale water- and energy-balance fluxes

The grid-scale water- and energy-balance fluxes are aggregated by weighting the fluxes by the probability of occurrence of the interval. Using this procedure, $\mathscr{E}[E]$, the expected macroscale evapotranspiration rate can be expressed as:

$$\mathscr{E}[E] = \int_{x=-\infty}^{x=\infty} E(x) f_x(x) dx = \int_{x=-\infty}^{x=\infty} \left(f_{bs} e_{bs}(x) + f_v (e_{dc}(x) + e_{\omega c})\right) f_x(x) dx \tag{2.77}$$

where $E(x)$ is the local evapotranspiration rate for a particular interval of the distribution. The expected value of the surface temperature and the remaining energy-balance fluxes are expressed similarly. The expected macroscale runoff rate $\mathscr{E}[Q]$, is given as:

$$\mathscr{E}[Q] = \int_{x=-\infty}^{x=\infty} Q(x) f_x(x) dx + Q_b = \int_{x=-\infty}^{x=\infty} \left(f_{bs} q_{bs}(x) + f_v q_v(x)\right) f_x(x) dx + Q_b \tag{2.78}$$

where $Q(x)$ is the local surface runoff rate for a particular interval of the distribution.

2.2.3 Model sensitivities

Famiglietti (1992) examined many of the sensitivities of TOPLATS predictions of evapotranspiration, runoff, and soil moisture to soil and vegetation parameters. Diurnal cycles of potential evaporation, unstressed transpiration, and wet canopy evaporation for some FIFE forcing data, and various soil and vegetation parameters are shown in Figure 2.5. The variation in the rate of capillary rise with water table depth are given in Figure 2.7. The effect of soil moisture on the diurnal pattern of actual evaporation are shown in Figure 2.8. The variation of transpiration capacity with soil moisture for several different soil types, root activity factors, and root resistances are shown in Figure 2.9. Finally, drainage rates versus soil moisture for several different soil types are shown in Figure 2.10.

2.3 TOPLATS modifications

The spatially distributed version of the TOPLATS model (Famiglietti and Wood, 1994a) was modified with a view to facilitating data assimilation of near-surface soil moisture derived from passive microwave radiometers which are only sensitive to moisture in the top 5-10

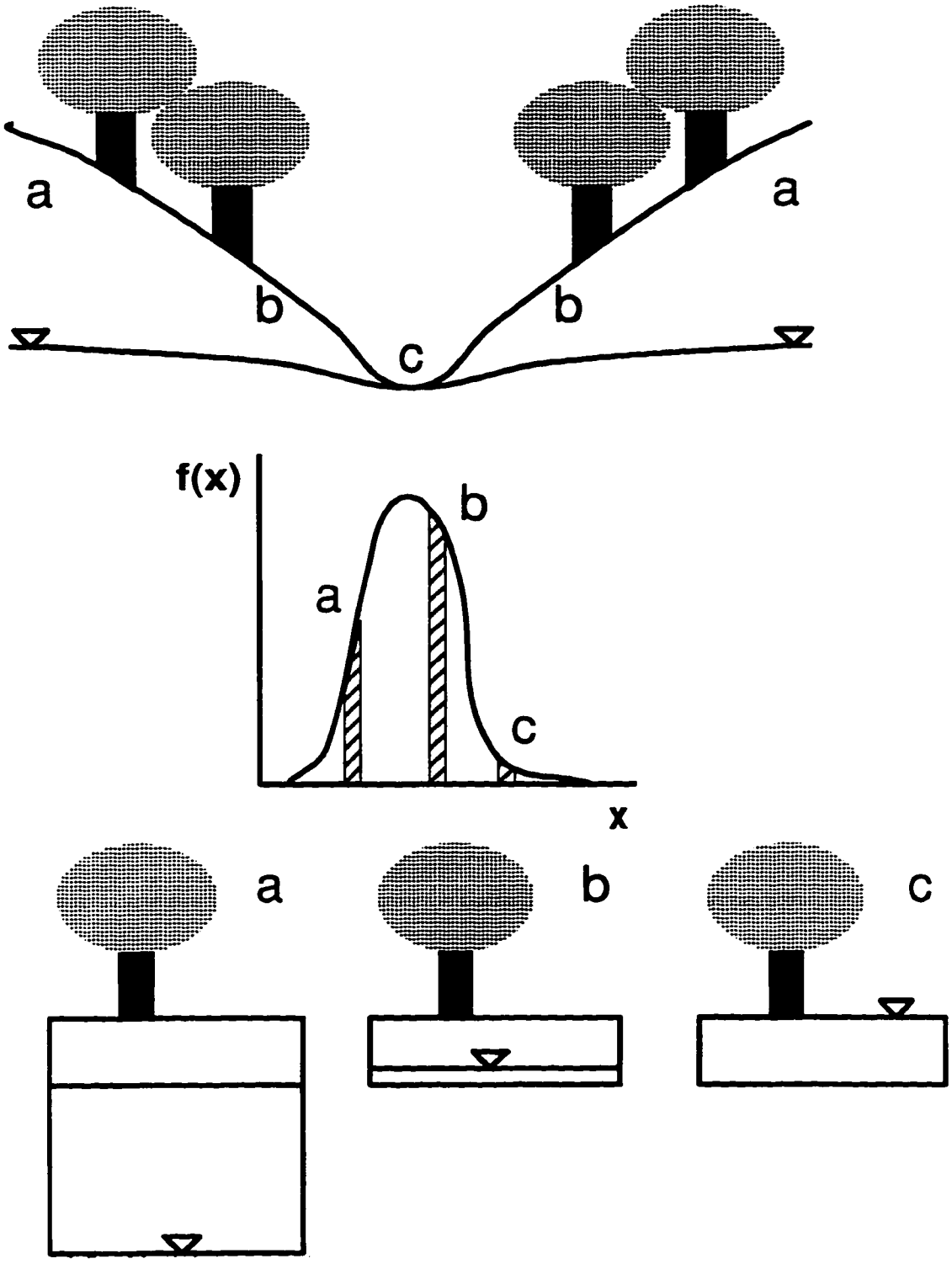

Figure 2.4: Model representation of subgrid-scale land-surface heterogeneity in topography, soils, and soil moisture. a, b, and c represent a range of soil moisture states (Famiglietti, 1992).

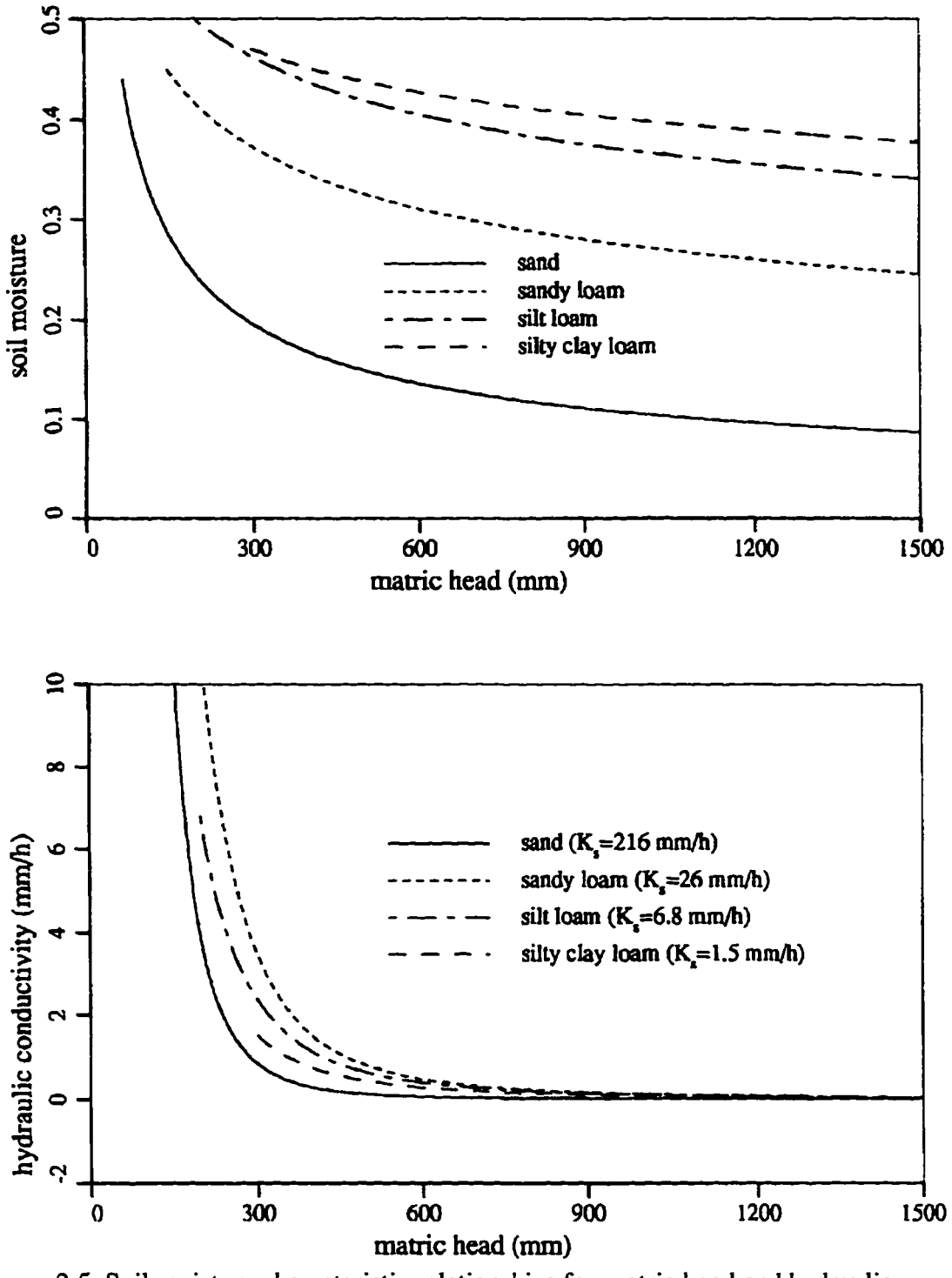

Figure 2.5: Soil moisture characteristic relationships for matric head and hydraulic conductivity for several soil types (Famiglietti, 1992).

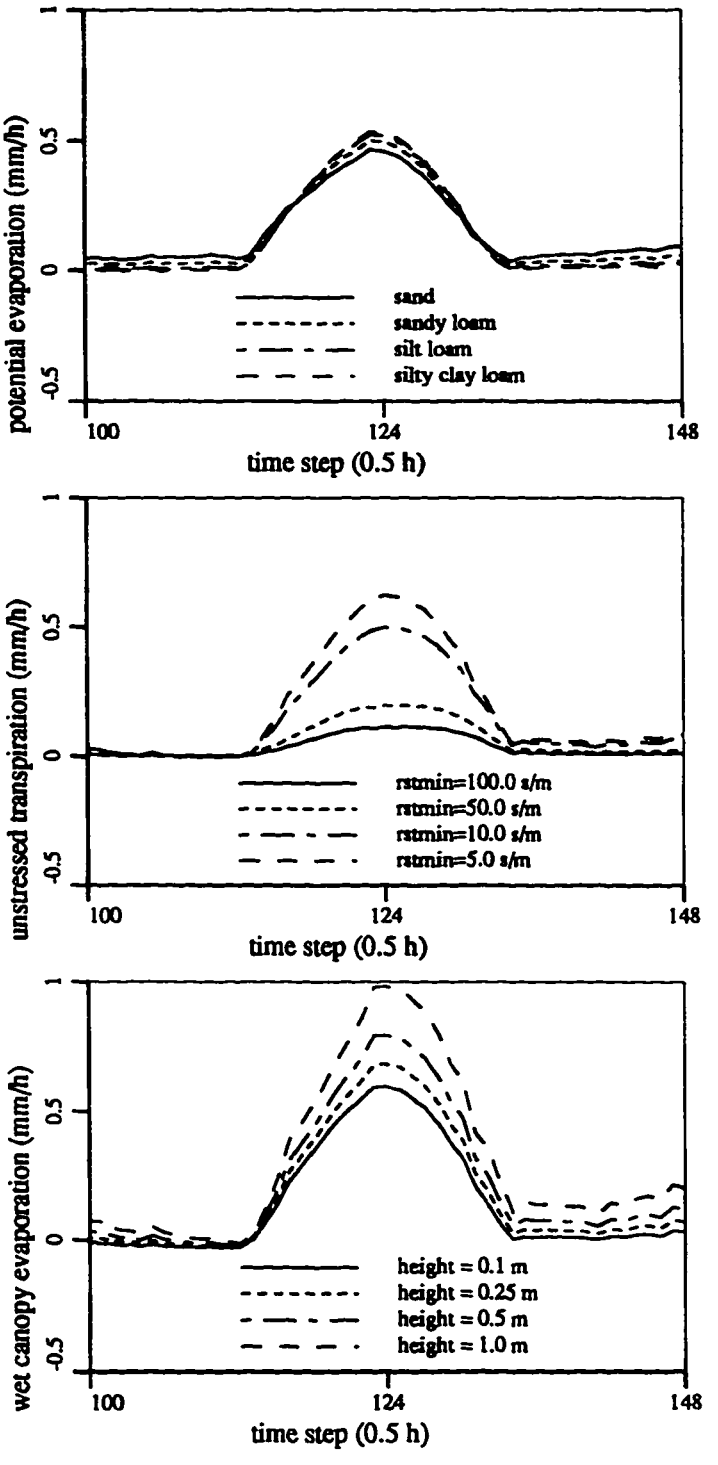

Figure 2.6: Potential evaporation for four different soil types, minimum stomatal resistance, and vegetation canopy height (Famiglietti, 1992)

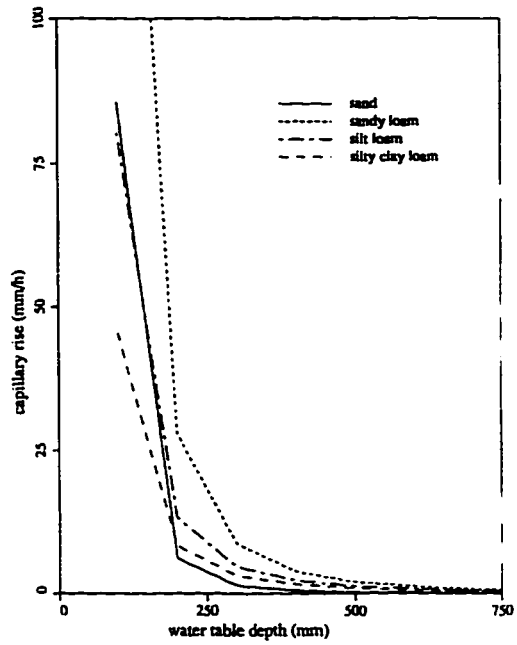

Figure 2.7: Rate of capillary rise versus water table depth for different soil types (Famiglietti, 1992).

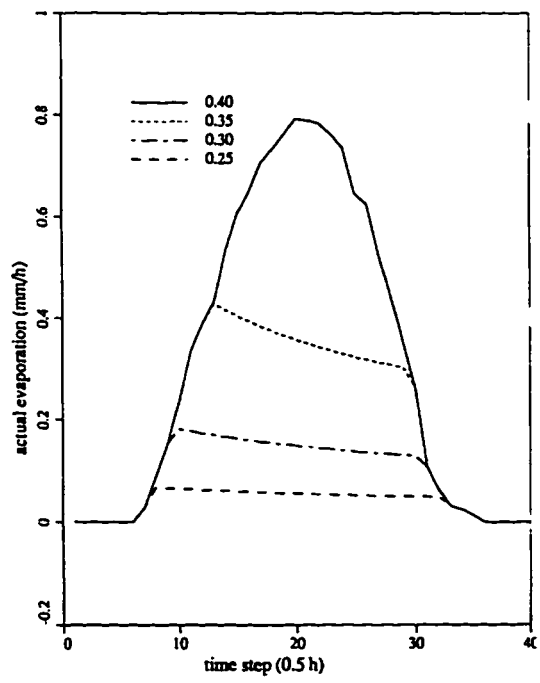

Figure 2.8: Actual evaporation versus soil moisture for four different values of initial soil moisture (Famiglietti, 1992).

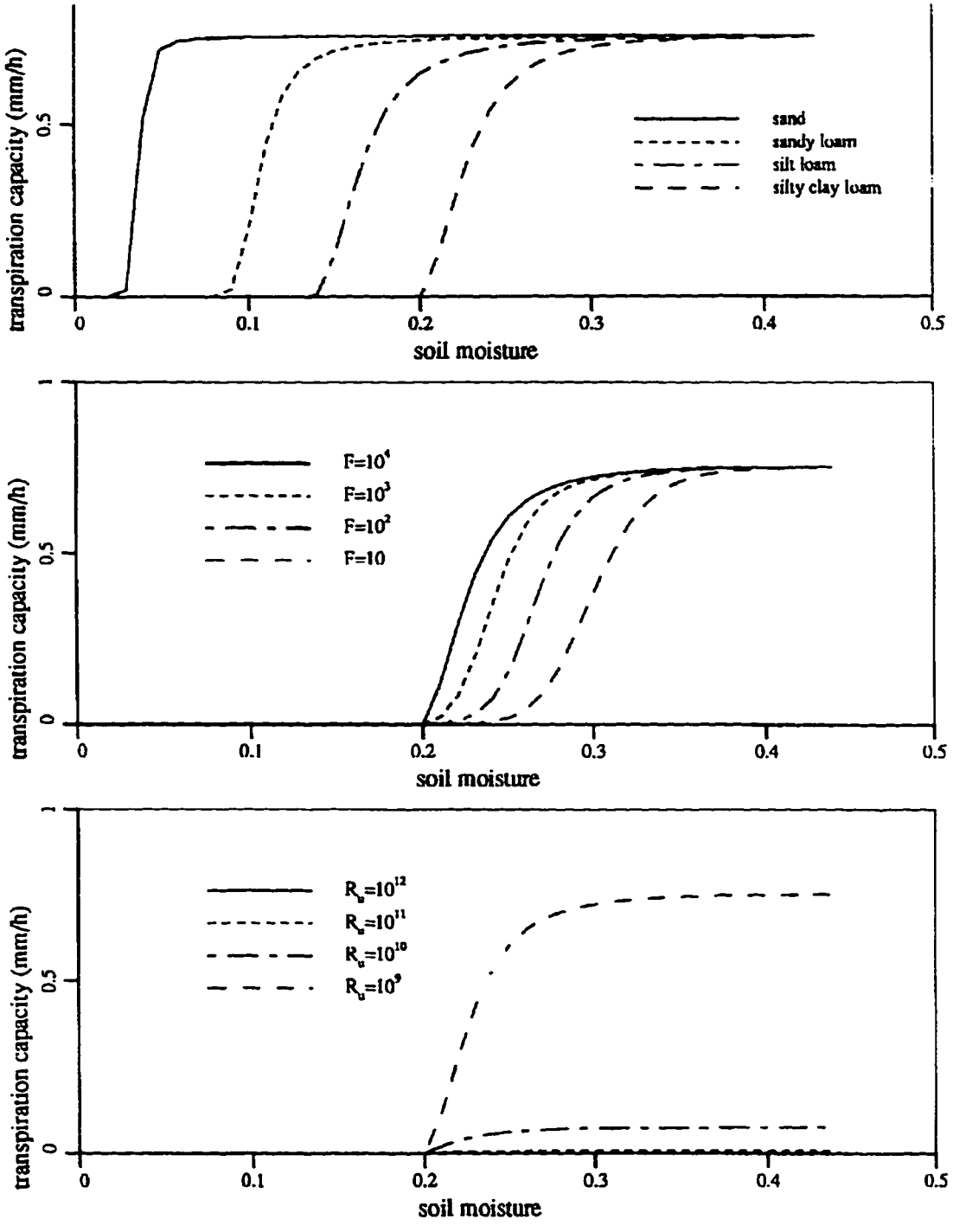

Figure 2.9: Transpiration capacity versus soil moisture for four different soil types, root activity factor (F), and root resistances (R_u) (Famiglietti, 1992).

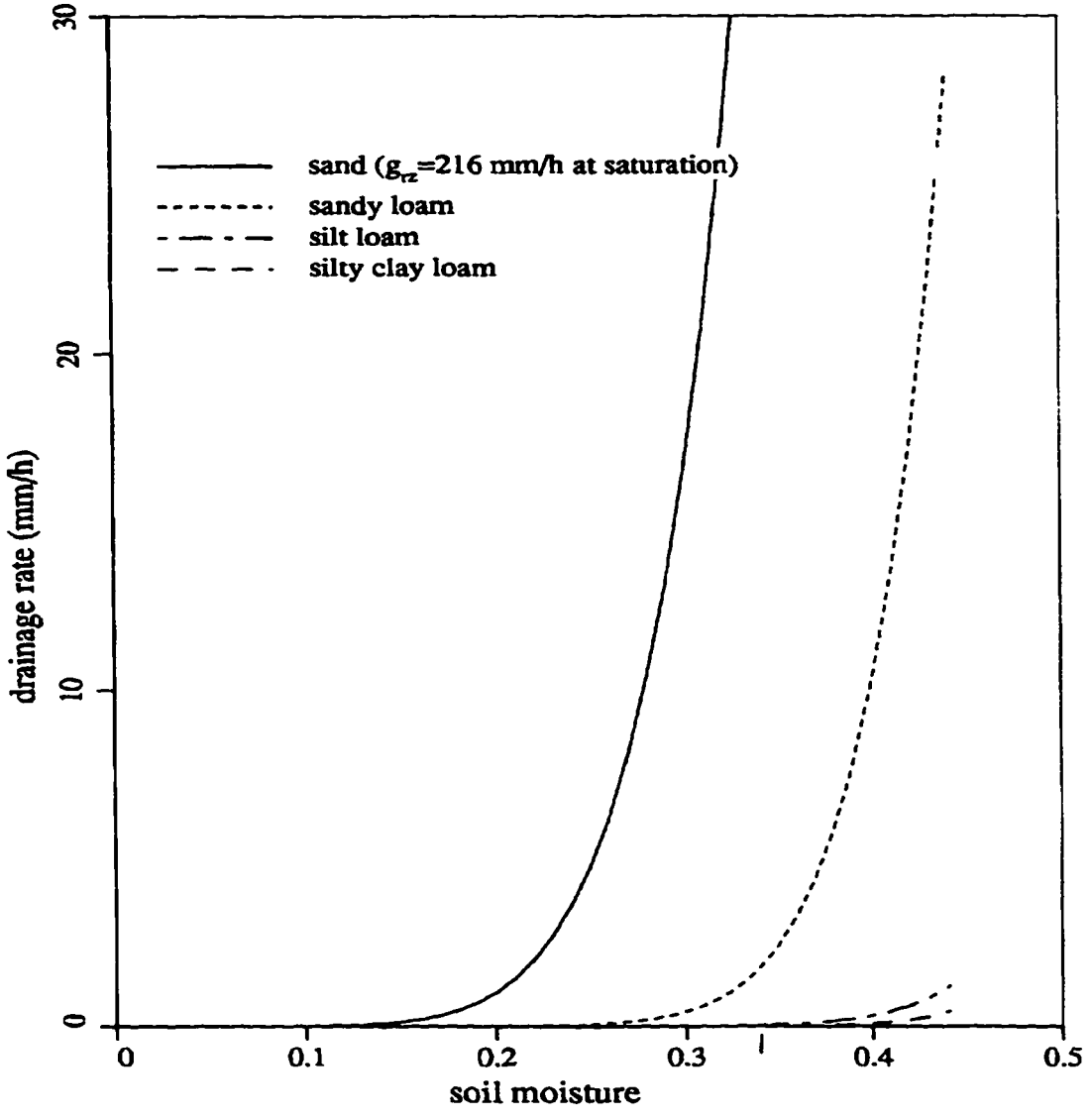

Figure 2.10: Drainage rates versus soil moisture for several soil types (Famiglietti, 1992).

centimeters of soil. The new soil-vegetation-atmosphere transfer (SVAT) component of the model is depicted in Figure 2.1.

The performance of this new, 3-layer version of the model was initially evaluated using FIFE and Walnut Gulch data. Results at the FIFE site showed that the model performed up to expectations in that grassland environment. Soil water dynamics in the shallow, near-surface layer were consistent with ground-based and remote observations of rapid wetting and drying on the Konza Prairie. Initial results from the Walnut Gulch data are given later in this report along with their implications for future research tasks.

A data assimilation module was developed and implemented to update the soil moisture states using observations. This data assimilation module was developed to have the capacity to assimilate data other than soil moisture, such as surface temperature, and with the capacity to assimilate point, grid, or multilevel observations. (Note: Eventually, this framework may be used to directly assimilate remotely-sensed radiances using an 'inverse' remote-sensing algorithm. 'Inverse' modeling predicts the radiance that would be observed by a remote sensor for a given soil moisture and other controlling factors (Vasiliev, 1991). Inverse modeling is likely to find more ready application in the context of 4DDA, because the objective is then only to make a differential correction to a 'first guess' field, which is already close to reality).

Finally, several components of the TOPLATS model were adjusted and its overall structure was refined for use at Walnut Gulch.

2.3.1 Addition of remote-sensing sensitive surface layer

TOPLATS and its TOPMODEL (Beven and Kirby, 1979) predecessors have been applied in a number of remote-sensing studies, including FIFE '87 (Famiglietti and Wood, 1991b; Famiglietti and Wood, 1994a,b), MACHYDRO '90 (Lin *et al.*, 1994), and Washita '92 (Pauwels *et al.*, 1996). While this research was generally successful, it highlighted a fundamental inconsistency in the current SVATS structure that significantly limits its utility with respect to remotely-sensed soil moisture observations. Because microwave remote-sensing only penetrates the upper 5-10 cm of the soil surface, hydrological models that make use of these data require a similarly thin surface layer for compatibility with the remote-sensing observations and to

effectively model the rapid dynamics of soil water in this active zone. In its current form, the TOPLATS SVATS has two soil layers, including a relatively deep root zone which is inconsistent with the required remote-sensing sensitive active surface zone. Therefore, a shallow, third soil layer was added above the root zone in the previously described 2-layer SVATS structure.

In the new 3-layer SVATS structure, the processes active in the shallow surface soil layer include bare-soil evaporation, infiltration, drainage to the root zone, and capillary rise from the water table. The underlying root zone then extends from the bottom of this surface zone to the top of the transmission zone. The root zone receives drainage from the surface zone, delivers its own drainage flux to the transmission zone, and provides soil water to vegetation for transpiration. Differences between the previous and current SVATS are shown in Figure 2.11.

To derive the new soil water-balance equations for the soil zones, four specific cases are considered with respect to the local water table depth (Famiglietti *et al.*, 1996). Case 1 applies to watershed grid elements in which the top of the capillary fringe lies beneath the bottom of the root zone at depth z-ψ_c, where z is the local water table depth and ψ_c is the air entry suction head. In Cases 2 and 3, the top of the capillary fringe lies within the root zone and surface zones, respectively. Case 4 applies to saturated grid elements. There is no transmission zone in Cases 2-4.

Case 1: The surface zone water-balance for Case 1 is:

$$z_{sz}\frac{d\theta_{sz}}{dt}=f_{bs}i_{bs}+f_v i_v+w-f_{bs}e_{bs}-g_{gz} \tag{2.79}$$

for:

$$z-\psi_c \geq z_{sz}+z_{rz}; \qquad \theta_r \leq \theta_{rz} \leq \theta_s \tag{2.80}$$

where z_{sz} is the depth of the surface zone layer, θ_{sz} is the surface zone moisture content, f_{bs} is the areal fraction of bare soil in the catchment grid element (equal to 1-f_{bs}), i_v is the rate of infiltration into vegetated soil, w is the rate of capillary rise from the water table, e_{bs} is evaporation from bare soils, g_{sz} is the drainage flux which exits from the bottom of the surface zone, z_{rz} is the root zone depth, θ_r is the residual soil moisture content, and θ_s is the saturation moisture content.

The root zone water-balance equation for Case 1 grid elements is:

$$z_{rz}\frac{d\theta_{rz}}{dt}=f_v e_{dc}+g_{sz}-g_{rz} \tag{2.81}$$

for:

$$z-\psi_c \geq z_{rz}; \qquad \theta_r \leq \theta_{rz} \leq \theta_s \tag{2.82}$$

where θ_{rz} is the root zone moisture content, e_{dc} is the transpiration rate, and g_{rz} is the drainage flux which percolates from the bottom of the root zone.

The water-balance equation for the transmission zone is:

$$z_{tz}\frac{d\theta_{tz}}{dt}=g_{rz}-g_{tz} \tag{2.83}$$

for:

$$z_{tz}=z-\psi_c-z_{rz}-z_{sz}; \qquad \theta_r \leq \theta_{tz} \leq \theta_s \tag{2.84}$$

where z_{tz} is the thickness of the transmission zone, θ_{tz} is the transmission zone moisture content, and g_{tz} is the downward soil water flux from the base of the transmission zone.

Case 2. The Case 2 surface zone water-balance equation is identical to Case 1. The root zone water-balance equation for Case 2 is:

$$z_{rz}^{*}\frac{d\theta_{rz}}{dt}=f_v e_{dc}+g_{sz}-g_{rz} \tag{2.85}$$

for:

$$z_{rz}^{*}=z-\psi_c-z_{sz} \qquad z_{rz}+z_{sz} \leq z-\psi_c \leq z_{sz} \qquad \theta_r \leq \theta_{rz} \leq \theta_s \tag{2.86}$$

There is no transmission zone in Cases 2 through 4.

Case 3: The surface zone water-balance equation for Case 3 is:

$$z_{sz}^{*}\frac{d\theta_{sz}}{dt}=f_{bs}i_{bs}+f_v i_v+w-f_{bs}e_{bs}-g_{sz} \tag{2.87}$$

for:

$$z_{sz}^{*}=z-\psi_c \qquad z_{sz} \leq z-\psi_c \leq 0; \qquad \theta_r \leq \theta_{sz} \leq \theta_s \tag{2.88}$$

The root zone water-balance equation for Case 3 is:

$$z_{rz}\frac{d\theta_{rz}}{dt}=0 \qquad \theta_{rz}=\theta_s \tag{2.89}$$

Case 4: The surface and root zone water-balance equations under Case 4 are:

$$z_{sz}\frac{d\theta_{sz}}{dt}=0 \qquad \theta_{sz}=\theta_s \tag{2.90}$$

and:

$$z_{rz}\frac{d\theta_{rz}}{dt}=0 \qquad \theta_{rz}=\theta_s \tag{2.91}$$

for:

$$z-\psi_c<0 \tag{2.92}$$

All remaining components of the SVATS are unchanged from the previous version.

Saturated zone water-balance equation: The rate of change of the areal-average water table depth, $d\bar{z}/dt$, is now given by:

$$\frac{d\bar{z}}{dt}=\frac{\left[\sum_{i\in C_{1,2,3}} w^i+\sum_{i\in C_4}(e_{dc}^i+e_{bs}^i)+\frac{Q_b}{\Delta x\Delta y}-\sum_{i\in C_1} g_{tz}^i-\sum_{i\in C_2} g_{rz}^i-\sum_{i\in C_3} g_{sz}^i\right]}{\left[\sum_{i\in C_1}(\theta_s-\theta_{tz})+\sum_{i\in C_2}(\theta_s-\theta_{rz})+\sum_{i\in C_3}(\theta_s-\theta_{sz})\right]} \tag{2.93}$$

where the superscript i refers to an individual grid element, C_1 through C_4 represent the collection of grid elements where SVATS equations for Cases 1 through 4 apply, Q_b is baseflow, and $\Delta x\Delta y$ is the area of the grid element.

2.3.2 TOPLATS parameterization modification

Several additional modifications were made to the TOPLATS model to adapt it for use with the Walnut Gulch Monsoon '90 data set. These modifications are described below.

The definition of the watershed boundaries varies for various spatial vegetation and soils data sets and DEMs (Digital Elevation Models). This variation is dependent on the quality and type of DEMs that were utilized in constructing the data set boundaries; in several cases, these boundaries were defined by a digitized, hand-drawn watershed delineation. Therefore, it was necessary to either (1) eliminate any watershed point in the model domain that was not contained in *every* spatial parameter set, or (2) define a watershed boundary and 'expand' or 'contract' the various spatial data sets to match that definition. With the first option, simulations that utilize

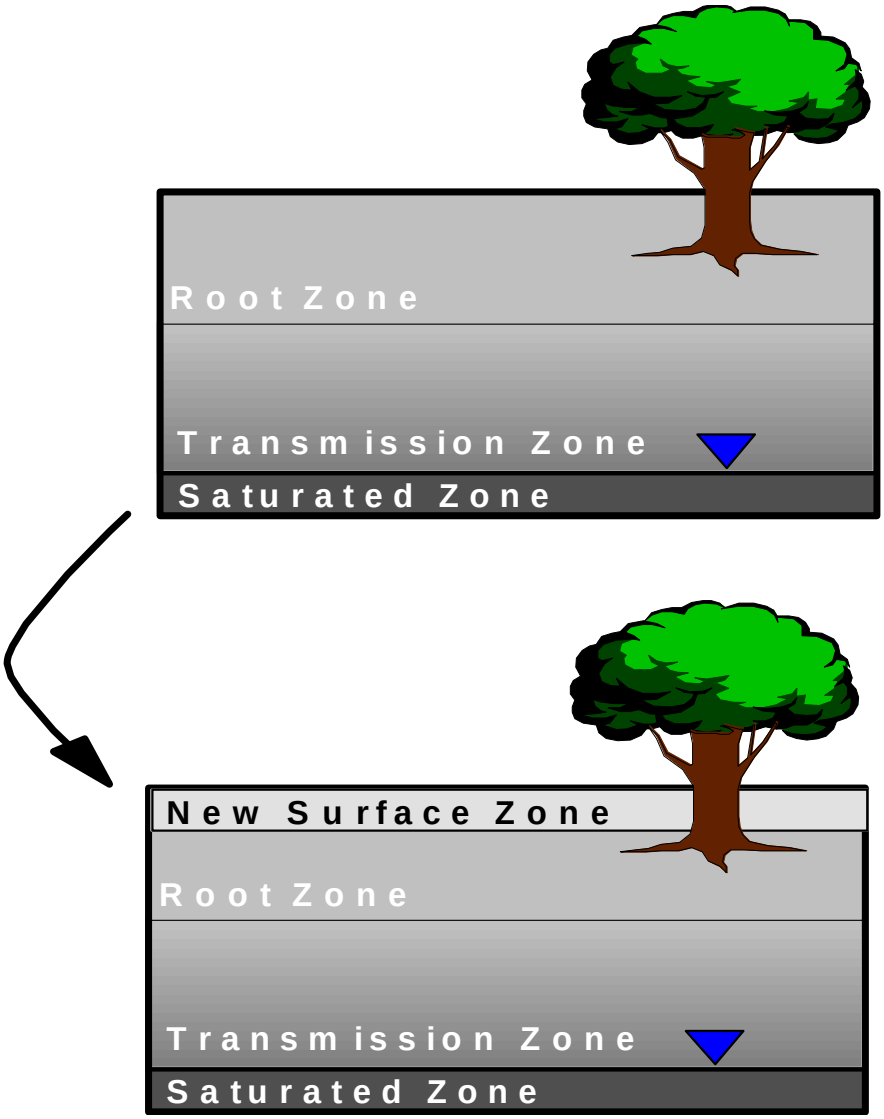

Figure 2.11: Diagram of old versus new TOPLATS soil definition.

different combinations of spatial data sets would result in different watershed delineations, which is undesirable. Therefore, the second option was adopted for ease of comparison between simulations. The 'standard' watershed delineation was chosen to be that based on the DEM (described in Chapter 3). Therefore, regions outside this delineation definition are simply ignored. If a region is defined to be inside the watershed as defined by the DEM, but is not defined in the spatial data set, then the nearest-defined value in that data set is adopted for the undefined point. In this way, the spatial data set can be expanded into undefined areas.

The saturated hydraulic conductivity of Walnut Gulch soils (as this is a difficult parameter to measure) was not well-known spatially, and it was found that published values of this variable in some cases caused excessive drainage in the surface zone (see Figure 2.10). This problem was attributed to a large coarse fraction in these soils that was not considered in the soil analysis, but did reduce the saturated hydraulic conductivity. Therefore, a saturated hydraulic conductivity coarse fraction correction was added to the model (Rawls *et al.*, 1993):

$$K_{sc}=K_s(1-\frac{F_c}{100}) \tag{2.94}$$

where K_s is the uncorrected saturated hydraulic conductivity, K_{sc} is the corrected hydraulic conductivity, and F_c is the fraction of coarse fragments in percent.

With the addition of the new remote-sensing sensitive surface layer in TOPLATS, the definition of the root zone thickness was redefined as:

$$z_{rz}=z_r-z_{sz} \tag{2.95}$$

where z_{rz} is the SVATS root zone depth, z_{sz} is the SVATS surface zone depth, and z_r is the depth of rooting. This enabled the SVATS surface layer to remain at a constant depth for remote-sensing purposes and also allowed the rooting depth to vary according to the vegetation type.

No direct measurements of zero plane displacement height, d, and roughness length, z_0, were available for Monsoon '90; thus, a second-order closure model relating these to the effective value of the mean drag coefficient, c_d, the leaf area index, L, and the vegetation height, h, was adopted (Shaw and Pereira, 1982; and Shuttleworth and Gurney, 1992):

$$d=1.1h\ \ln(1+X^{\frac{1}{4}}) \tag{2.96}$$

and:

$$z_0 = z_0' + 0.3h\ X^{\frac{1}{2}} \qquad 0<X<0.2 \tag{2.97}$$

$$z_0 = 0.3h(1-\frac{d}{h}) \qquad 0.2<X<1.5 \tag{2.98}$$

where z'_0 is the roughness length of the substrate, and:

$$X = c_d L \tag{2.99}$$

The next TOPLATS modification allowed Monsoon '90 measured soil characteristics such as percent sand, S, and percent clay, C, to be used to define the Brooks-Corey (Brooks and Corey, 1964) water retention function parameters through an empirically derived relationship (Rawls *et al.*, 1993):

$$\begin{aligned}\lambda = \exp(&-0.7842831 + 0.0177544S - 1.062498\phi - 0.00005304S^2 - 0.00273493C^2 + \\ &1.11134946\phi^2 - 0.003088295S\phi + 0.00026587S^2\phi^2 - 0.00610522C^2\phi^2 - \\ &0.00000235S^2C + 0.00798746C^2\phi - 0.00674491\phi^2C\end{aligned} \tag{2.100}$$

$$\begin{aligned}h_b = \exp(&5.3396738 + 0.1845038C - 2.48394546\phi - 0.00213853C^2 - 0.04356349PS\phi - \\ &0.61745089C\phi + 0.00143598S^2\phi^2 - 0.00855375C^2\phi^2 - 0.00001282S^2C + \\ &0.00895359C^2 * \phi - 0.00072472S^2\phi + 0.0000054C^2S + 0.5002806\phi^2C)\end{aligned} \tag{2.101}$$

$$\begin{aligned}\theta_r = &-0.0182482 + 0.00087269S + 0.00513488C + 0.02939286\phi - \\ &0.00015395C^2 - 0.0010827S\phi - 0.00018233C^2\phi^2 \\ &0.00030703C^2\phi - 0.0023584\phi^2C\end{aligned} \tag{2.102}$$

where ϕ is the porosity, h_b is the Brooks-Corey bubbling pressure, λ is the Brooks-Corey pore-size distribution index, and θ_r is the Brooks-Corey residual water content (volume fraction). This formulation for the residual water content provided values that were generally larger than was observed in the watershed; hence, θ_r was later reassigned to a constant low value across the watershed.

No atmospheric pressure measurements were available for Walnut Gulch during 1990, so the following formulation was implemented to the model to derive it hydrostatically (Smith, 1993):

$$p=p_s-g\rho z \tag{2.103}$$

where p is the pressure at elevation, z, p_s is the standard sea level pressure, and ρ is the density of air.

Rainfall was provided to the model as spatial fields with a file describing the precipitation across the array at each time step. To save disk space, only the files with non-zero precipitation were saved. The previous (spatially constant) precipitation input code was replaced with a more complex code that checked to see if a precipitation file existed for a given time step. If the file existed, it was read and used; if not, the whole precipitation array was set to zero.

TOPLATS requires a wet bulb temperature for calculation of vapor pressure, e. During Monsoon '90, humidity measurements were made with relative humidity, RH sensors, so this portion of the code was changed appropriately (Smith, 1993), thus:

$$e=611\frac{RH}{100}\exp\left(\frac{17.27T}{237.3+T}\right) \tag{2.104}$$

where T is air temperature in degrees Celsius.

During Monsoon '90, wind observations were not at the standard height, so an adjustment was made to account for this height difference (Shuttleworth, 1993):

$$\frac{U_2'}{U_2}=\frac{34.9648}{\ln\left(\frac{z_e-0.08}{0.001476}\right)\ln\left(\frac{z_u-0.08}{0.01476}\right)} \tag{2.105}$$

where U_2 is the wind speed at 2 m, U_2' is the wind speed at alternate height z_u, and, z_e, is the height of the humidity measurement.

Finally, TOPLATS requires downward longwave radiation, R_{ld}, which was not observed during Monsoon '90. Therefore, it was computed from net radiation, R_n, and downward shortwave radiation, R_{sd} (Famiglietti, 1992):

$$R_{ld}=R_n-R_{sd}(1-(\alpha_{bs}F_{bs}+\alpha_{wv}F_vf_w+\alpha_{dv}(F_v-F_vf_w))+0.0000000567(T+273.15)^4 \tag{2.106}$$

where α_{bs}, α_{dv}, and α_{wv} are the albedo of the bare soil, dry vegetation, and wet vegetation, respectively. F_{bs} is the fraction of total ground area that is bare soil, F_v is the fraction vegetation ($1-F_{bs}$), f_w is the fraction of the vegetation canopy that is currently wet, and T is temperature.

Additional modifications to the basic TOPLATS model are suggested by Peters-Lidard *et al.* (1996a,b) and are described in Chapter 7.

2.3.3 Redefined input/output structure

There were many changes made to the TOPLATS code to make it more user-friendly, efficient, and compatible with various operating environments.

The original TOPLATS model utilized seven input files with no documentation on parameter definitions for model parameter input. For ease of use, these files were merged into one input file with parameter definitions next to each parameter value to reduce confusion and mistakes.

A 'control file' was introduced that put all model options in a labeled ASCII file. By editing this file, the user could specify names and locations of input and output files, which model fields were to be specified as spatially constant or variable, a variety of different output options, and the required mode for data assimilation. Additional, more specific control files were also necessary in the case of optimum interpolation and Newtonian nudging assimilation, the need for these being noted in the TOPLATS control file.

A parameter output file was also added which provides a summary of all the selected modeling modes (i.e. the type of data assimilation, format and the placement of output, etc.), parameter values, and statistics on input spatial fields. This output proved particularly valuable for model diagnosis and for the identification of unintended input difficulties.

In spatially distributed mode, the TOPLATS model used a great deal of Random Access Memory (RAM), which made it impossible to use on conventional workstations. Therefore, an attempt was made to reduce the size of any unnecessary arrays. However, this was only partially successful, and only reduced the model's RAM usage by 10%.

The code was generally cleaned up, with a great reduction in length through the addition of a separate common file that stored all common block information for all subroutines outside the main program. This change also allowed much more efficient modification of the code.

An average statistics calculation algorithm was added to provide information on spatial variability for most of the model's spatially variable inputs and analyzes. This routine proved extremely valuable in assessing the temporal changes in the predicted spatial fields.

Code modifications were also made and tested to ensure that the program operated on Sun, IBM, Cray, Convex, and Silicon Graphics workstations.

Several modifications were made to facilitate data assimilation in the model structure as are detailed below.

2.3.4 Data assimilation modifications

The TOPLATS model was modified to allow the assimilation of soil moisture and other state variables. For ease of explanation, the following description assumes assimilation of observed surface soil moisture, θ_o. With minor modifications specific to the assimilated variable, the following description can be easily adjusted to be appropriate to other state variables, such as surface temperature.

Observation file acquisition and error checking: Between every time step, the TOPLATS data assimilation routines seek a file containing observations for the previous time step or, in the case of nudging, the routine looks for observations within a predefined temporal window of the current time step. If observations are found, the appropriate file is read. In the case of nudging, the routine also checks to see if precipitation occurred between the current time step and the time of observation. If precipitation did occur, temporal data assimilation through the precipitation event is not desirable because of the very different surface conditions (i.e., the precipitation may contain more soil moisture relevant information than the soil moisture state observations being assimilated). Hence, the nudging assimilation window is truncated at the time of the precipitation event.

Finally, the routine checks the observations to be certain they lie within reasonable bounds. It was found that, if values outside the models' defined maximum and minimum soil moisture values (θ_s, θ_r) were assimilated, errors occur in the models' prognostic equations. It was recognized that these values still contain information regarding the soil moisture of very dry or wet soil moisture states, so they were simply reassigned as follows:

$$\theta_o=\theta_r+0.1\% \qquad \theta_o\leq\theta_r \tag{2.107}$$

$$\theta_o=\theta_s-0.1\% \qquad \theta_o\geq\theta_s \tag{2.108}$$

where θ_o is the soil moisture observation. The observation is set to be just inside the models' soil moisture range to prevent rounding errors. Typically, less than 5% of the observations need to be corrected in this way. If a large number of observations fall outside the models' allowed range, it is most probably an indication that the models' allowed soil moisture range needs to be adjusted.

Updating or direct insertion assimilation: This was the most simple of data assimilation methods used in this study. The model prediction was simply replaced with an observation whenever an observation was available, i.e.:

$$\theta_{sz}=\theta_o \qquad \textit{if } \theta_o \textit{ observed} \tag{2.109}$$

In effect, this method assumes the observation was perfect, and no assimilation was performed outside the region where observations were available. Any advection of information was accomplished through subsequent model integrations.

Statistical corrections assimilation: This technique adjusts the spatial average and standard deviation of the surface soil moisture model state to match the PBMR-observed soil moisture average and standard deviation. It had the effect of correcting for any general model bias, while preserving the model-simulated pattern of soil moisture, and was implemented as follows: (1) The mean, $\bar{\theta}_o$, and standard deviation, σ^o_θ, of the observations were determined:

$$\bar{\theta}_o=\frac{\sum_{i=1}^{N}\theta_{o_i}}{N} \tag{2.110}$$

$$\sigma^o_\theta=\sqrt{\frac{\sum_{i=1}^{N}(\theta_{o_i}-\bar{\theta}_o)}{N}} \tag{2.111}$$

where N was the total number of observations; (2) The mean and standard deviation of the model state were similarly determined; (3) The model's standard deviation, σ_θ, was adjusted to the observation standard deviation as follows, thus:

$$\theta_i = \frac{\sigma^o_\theta}{\sigma_\theta}\theta_i \qquad \textit{for all } i \tag{2.112}$$

(4) The mean of the model-adjusted field of soil moisture states was redetermined following the adjustment of the standard deviation; (5) Finally, the mean of the model field was adjusted to match the observation field mean, thus:

$$\theta_i = \theta_i - (\bar{\theta} - \bar{\theta}_o) \qquad \textit{for all } i \tag{2.113}$$

This procedure was unable to assimilate observation patterns, so provisions were made for a subsequent direct insertion assimilation or a local nudging to observations to include observation patterns if preservation of such patterns was desirable.

Nudging: Newtonian nudging relaxes the model state towards the observed state by adding an artificial tendency term to the prognostic equations based on the difference between the two states. In this way the model could be nudged toward gridded analyzes (such as PBMR observations) or towards individual observations during the period of time around that observation.

Nudging towards a gridded analysis: The approach taken in this study was to ensure that the model and observation data were available at the same spatial resolution and that they were geolocated. This had the practical advantage that no interpolation was needed to colocate model predictions with observations. Therefore, the continuous gridded observations in the remote-sensing area were equivalent to an interpolated analysis that could be used in the nudging to the analysis method described in Chapter 1. Nudging towards analyzes in TOPLATS was implemented as follows:

$$\frac{\partial p^* \alpha}{\partial t} = F(\alpha, x, t) + G_\alpha W_\alpha(x,t) \epsilon_\alpha(x) p^*(\hat{\alpha}_o - \alpha) \tag{2.114}$$

The model's forcing terms were represented by F, where α were the model's dependent variables, x were the independent spatial variables, and t was time. G_α was the nudging factor which determined the magnitude of the nudging term relative to all other model processes, while the four-dimensional weighting function, W_α, specified its spatial and temporal variation. The analysis quality factor, ϵ, varied between 0 and 1 and was based on the quality and distribution

of the observations. The observation at the model grid was $\hat{\alpha}_o$, This equation was implemented for all three model soil layers, with the weighting decreasing with depth and time using the four-dimensional weighting function described later. The horizontal weighting function was always unity, because the only observation considered was that lying directly on the model grid that was being nudged.

Nudging to individual observations: The above scheme was well-suited for nudging within areas for which remotely-sensed data was available, but it was desirable to 'spread' this information content from within this area horizontally outwards into areas without observations. This was accomplished through the use of nudging to individual observations, where the difference between the simulated and observed state was determined at the observation locations and then was analyzed back to the model grid. The model's predictive equation was therefore:

$$\frac{\partial p^{*}\alpha}{\partial t}=F(\alpha,x,t)+G_{\alpha}p^{*}\frac{\left[\sum_{i=1}^{N}W_i^2(x,t)\gamma_i(\alpha_o-\hat{\alpha})_i\right]}{\sum_{i=1}^{N}W_i(x,t)} \tag{2.115}$$

the subscript i denotes the ith observation of a total of N that were within a preset radius, α_0 was the locally observed value of α, and $\hat{\alpha}$ was the model's prognostic variable interpolated to the observation location in three dimensions. The observational quality factor, γ, varied from 0 to 1 and accounted for characteristic errors in measurement systems and representativeness. The four-dimensional weighting function accounted for the separation distance, both spatially and temporally, of the ith observation from a given grid point at a given time. Again, this nudging technique was applied vertically to all model soil layers.

This scheme was also used within the remote-sensing area to nudge towards a 'region' of observations and had the effect of providing a more spatially continuous assimilation.

Temporal and spatial weighting functions: For the analysis-nudging technique, the four-dimensional weighting function was given by:

$$W(x,t)=1 \tag{2.116}$$

The gridded analysis (i.e. the remotely-sensed observations) were not available for all time steps and depths; hence, this weighting function was modified to allow nudging to gridded analyzes vertically and temporally:

$$W(x,t) \equiv w_z w_t \tag{2.117}$$

For the observation-nudging technique, the weighting function for each observation I was implemented in the traditional form:

$$W(x,t) \equiv w_{xy} w_z w_t \tag{2.118}$$

where w_{xy} was a Cressman-type horizontal weighting function defined by (Cressman, 1959):

$$w_{xy} = \frac{R^2 - D^2}{R^2 + D^2}, \qquad 0 \le D \le R \tag{2.119}$$

$$w_{xy} = 0, \qquad D > R \tag{2.120}$$

where R was the radius of influence, and D was the distance from the ith observation to the gridpoint. The vertical weighting function, w_z, was also a distance weighting function defined as:

$$w_z = 1 - \frac{|z_{obs} - z|}{R_z}, \qquad |z_{obs} - z| \le R_z \tag{2.121}$$

$$w_z = 0, \qquad |z_{obs} - z| > R_z \tag{2.122}$$

where R_z was the vertical radius of influence, and z_{obs} was the vertical position of the ith observation. The temporal weighting function was switchable between the Lyne *et al.* (1982) and the Stauffer and Seaman (1990) algorithm. The Lyne *at al.* algorithm was defined as:

$$w_t = 1, \qquad |t - t_o| < \frac{\tau}{2} \tag{2.123}$$

$$w_t = 0, \qquad |t - t_o| > \tau \tag{2.124}$$

$$w_t = \frac{(\tau - |t - t_0|)}{\tau/2}, \qquad \frac{\tau}{2} \le |t - t_0| \le \tau \tag{2.125}$$

The Stauffer and Seaman (1990) algorithm allowed for an 'enhanced observation period':

$$w_t = 1, \qquad |t - t_o| < \frac{\tau}{4} \tag{2.126}$$

$$w_t = \frac{(\tau - |t - t_0|)}{w_{\tau/4}}, \qquad \frac{\tau}{4} \le |t - t_0| \le \tau \tag{2.127}$$

$$|t - t_0| > \tau \tag{2.128}$$

where t was the model-relative time, t_0 was the model-relative time of the ith observation, and τ was the half-period of a predetermined observation influencing time window.

These weighting functions were well-behaved in areas of low observation density, but when applied in regions of high observation density (typical of remote-sensing observations), the weighting functions were found to degrade. Consider this simple example using only the established horizontal nudging weighting function given above (i.e. assume w_r, w_z, γ, G are unity) and the nudging to observations algorithm. Then, first determine the total weight given in the prediction equation, given only one observation at a distance of D=1 and a radius of influence of R=100:

$$total\ weight = \frac{\sum_{i=1}^{1} W_i^2(x)}{\sum_{i=1}^{1} W_i(x)} = \frac{\sum_{i=1}^{1} w_{xy}^2(x)}{\sum_{i=1}^{1} w_{xy}(x)} = \frac{\sum_{i=1}^{1}\left(\frac{R^2-D^2}{R^2+D^2}\right)^2}{\sum_{i=1}^{1}\left(\frac{R^2-D^2}{R^2+D^2}\right)} = \frac{\sum_{i=1}^{1}\left(\frac{100^2-1^2}{100^2+1^2}\right)^2}{\sum_{i=1}^{1}\left(\frac{100^2-1^2}{100^2+1^2}\right)} = 0.9998 \tag{2.129}$$

which is of course scaled by the summed difference between the observation and prediction. Now, consider adding 100 observations at a distance of D=99, for a total of 101 observations:

$$total\ weight = \frac{\sum_{i=1}^{100}\left(\frac{100^2-99^2}{100^2+99^2}\right)^2 + \sum_{i=1}^{1}\left(\frac{100^2-1^2}{100^2+1^2}\right)^2}{\sum_{i=1}^{100}\left(\frac{100^2-99^2}{100^2+99^2}\right) + \sum_{i=1}^{1}\left(\frac{100^2-1^2}{100^2+1^2}\right)} = 0.5037 \tag{2.130}$$

Therefore, by adding more information in the form of observations at a distance, this technique actually *decreases* the total magnitude of nudging performed. This is clearly undesirable, because the information provided by that one close observation has not really been changed by the addition of the other observations. This effect is a product of the normalization procedure used in the main nudging equation.

Having recognized this problem, it seemed sensible to seek an alternative procedure which increased the total weight as the number of observations increased. It was hard to define a suitable weighting function that did not exceed 1, but which maintained or increased the weight with additional observations. Therefore, the weighting of the closest observation in time and space was substituted for the summation of the total weight. Information from more distant

observations was still used (based on its individual weight), but the total weight was determined only by the closest observation. The modified predictive equation is:

$$\frac{\partial p^{*}\alpha}{\partial t}=F(\alpha,x,t)+G_{\alpha}p^{*}W_{\max}\frac{\left[\sum_{i=1}^{N}W_i(x,t)\gamma_i(\alpha_o-\hat{\alpha})_i\right]}{\sum_{i=1}^{N}W_i(x,t)} \tag{2.131}$$

where W_{max} was the maximum weight calculated for any single observation in the observation set.

The option to carry out a nudging-weighted statistical corrections assimilation was also implemented in this routine. Instead of nudging to actual observed values, nudging was towards the mean and standard deviation of observed data, which had the effect of correcting the mean and standard deviation of the model state as a function of its temporal and spatial distance from an observation.

Unlike the previously described assimilation methods, nudging requires the specification of 18 different parameters or options. These included the option to either nudge towards a point or towards a region in the observation area (i.e. a choice between observation and gridded analysis nudging); an option of temporal weighting function (Lyne *et al.* or Stauffer and Seaman); an option for nudging toward actual observations or the statistics of the observations, an option to limit nudging 'across' precipitation events; and the optimal values for the depth of observation, the temporal radius of influence, the horizontal radius of influence, the vertical radius of influence, the surface zone nudging constant, the root zone nudging constant, the transmission zone nudging constant, the surface zone analysis and observation quality control factors, the root zone analysis and observation quality control factors, and the transmission zone analysis and observation quality control factor.

Statistical interpolation: Optimal/statistical interpolation was implemented in all three soil layers in TOPLATS as follows:

$$f_A(r_i)=f_B(r_i)+\sum_{k=1}^{K}W_{ik}[f_O(r_k)-f_B(r_k)] \tag{2.132}$$

where K was the number of observation points, W_{ik} was the weight function, $f(r)$ was the analysis variable (soil moisture), r was the three-dimensional spatial coordinates, $f_Z(r_i)$ was the analyzed value of f at the analysis gridpoint r, $f_B(r_i)$ was the background or first-guess value of f at r_i, and $f_O(r_k)$ and $f_B(r_K)$ were the observed and background values, respectively, at the observation station r_k. Again, due to the correspondence between the model and observation grid, no interpolation was required to obtain the above fields.

The weights in the above equation were found by solving K equations for K unknowns, thus:

$$\sum_{l=1}^{K} W_{il}[\rho_{Bxy}(r_l-r_k)+\epsilon_O^2\rho_O(r_l-r_k)]=\rho_{Bxy}(r_i-r_k)\rho_{Bz}(z_i-z_k) \tag{2.133}$$

where ρ_O was the observation error correlation matrix, ρ_{Bxy} was the background horizontal error correlation matrix, and ρ_{Bz} was the vertical error correlation matrix. The functions chosen to represent the error correlation matrices ensure that they were symmetric and positive definite. Therefore, this system of linear equations was solved in TOPLATS using a simple and efficient Cholesky Decomposition method (Press *et al.*, 1986).

For the most part, the implementation of statistical interpolation in TOPLATS as presented above was very simple: it required just a few equations and little code. Unfortunately, each PBMR image contained over 35,000 observations, which meant solving 35,000 equations for 35,000 unknowns, a task which would require at least 1.5 gigabytes of random access memory and months of computer time. Since, these resources were not available, a method for simplifying this problem was required.

The logical simplification of this problem was to reduce the number of observations in a sensible way. Two attractive methods for doing this were included in TOPLATS. The first randomly selected a subset of $(N\text{-}1)$ observations, where N was the size of the reduced set (determined by available memory and CPU resources). So as to include the observation with most information and thus approximate the analysis that would have been made with all available observations, the Nth observation was assigned to be the closest observation to the gridpoint for which the assimilation is being made. Using this philosophy, an individual observation could be included in the reduced set more than once, in which case the observation was eliminated because it created a system of equations that was not solvable by Cholesky

Decomposition. The second method of reducing the observation set size was by the development of 'super-observations' these being regional averages of the regular observations. This was implemented by dividing the model domain into (N-1) grids (not corresponding to the model grid) and averaging all observations found in these grids to establish super-observations. Again, the nearest observation was established as a super-observation, and super-observation locations were not duplicated in the reduced set.

The effect of not including the nearest observation in the reduced observation set was generally undesirable, because it had the most consequence near the selected observations, giving the resulting field a blotchy pattern and making the locations of the eliminated observation obvious. On the other hand, inclusion of the nearest observation had the effect of including the observation with the most information along with subset of other observations that gave background information on the remainder of the field. Including the nearest observation was also noteworthy in that statistical interpolation reverted to direct insertion when the observation fell on the model grid. Thus, if the nearest observations were not selected, some observation locations underwent direct insertion while others did not. By selecting the nearest observation, every observation point was directly inserted in a consistent manner.

2.4 Computational aspects

In fully distributed mode, the model occupied about 180 megabytes of RAM and used a minimum of about 300 megabytes of disk space for a 25-day simulation. Most of the input file space was consumed by spatially distributed precipitation files. The RAM usage increased with some modes of assimilation. For example, depending on its configuration, statistical interpolation required as much as 1.5 gigabytes of RAM.

In its Monsoon '90 spatially distributed mode (defined in Chapter 3), the 'control' simulation with no assimilation took about 10 hours of computer time. Simulation time increased with the complexity of the assimilation. In the case of nudging, a model run took several weeks because assimilations at successive time steps increased the number of times that the required assimilation calculations were made.

2.5 Conclusions

For the implementation of TOPLATS in a data assimilation framework, a remote-sensing sensitive surface layer was added. Then for its implementation at Walnut Gulch, several of its basic parameterizations were modified, including the addition of a spatial data set contraction and expansion algorithm, a coarse fraction correction of saturated hydraulic conductivity, a second order closure model for zero plane displacement and roughness length, empirical algorithms to derive the soil-water characteristic relationships from basic soil properties, a height adjustment for wind speed, redefinition of the radiation and humidity parameterizations, and a consolidation of input structures. Finally, the direct insertion, statistical corrections, Newtonian nudging, and statistical interpolation algorithms were included in TOPLATS and modified for use in soil moisture data assimilation studies. It was found that for the specific case of assimilating remotely-sensed soil moisture, the established statistical interpolation and Newtonian nudging techniques required modification for use with large data sets. But even with these proposed simplifications, and implementation in a relatively small watershed, significant computational burdens arose which highlight the need for the development of more efficient information-based assimilation techniques. Such techniques may be based on a Fourier transform or statistical methodology.

3. RESEARCH LOCATION AND EXPERIMENTAL DESIGN

The location and design requirements of implementing spatially distributed hydrologic data assimilation at the Walnut Gulch watershed is the focus of this chapter. Experiment design and modeling needs are detailed, then data procurement, processing, and utilization issues are explored.

This study would not have been possible without the data provided by the USDA-Southwest Watershed Research Center and without their assistance in interpreting these data from the Walnut Gulch Experimental Watershed. The USDA-Southwest Watershed Research Center considers much of the data presented below to be preliminary and has not completed all checking and verification processes on them (Goodrich, 1996).

3.1 Introduction

Three types of data were required in this research: specifically (a) forcing data, (b) assimilation data, and (c) model parameters. These data were acquired at (or interpolated into) the model's four-dimensional, spatial and temporal grid. The required forcing data are spatially distributed time series of near-surface weather variables which are (or which influence) the fluxes of water and energy at the model's surface boundary and are required at every model time step. Assimilated data are information about the 'true' state of the natural system, which the model can use to adjust its own internal representation of those states. Assimilated data are not required at every time step, but are used to 'tune' the model whenever and when such data are available. The model parameters are spatial fields of information about the topography, vegetation and soil characteristics of the modeled area; some parameter fields, such as those related to vegetation vigor, may have a four-dimensional nature. A complete list of the data required by the TOPLATS model is given in Appendix B.

This research used several data sources that can be summarized as follows: (1) Walnut Gulch LERTS/UA-EOS and USDA-ARS maps of distributed basin characteristics. Characteristics include digital elevation data, soil physical and chemical properties, hydrologic properties, vegetation characterization, litter estimation, time series of soil moisture profiles, standard meteorological data, runoff data, and surface energy and water fluxes as available. The

meteorological data available as time series are described in Appendix C. (2) Walnut Gulch Monsoon '90 data set. During the Monsoon '90 experiment, several specialized soil moisture data sets were developed. These include high-resolution profile TDR soil moisture measurements, PBMR (Push Broom Microwave Radiometer), ESTAR (1991) (Electronically Steered Thinned Array (L-Band) Radiometer), and LANDSAT remote-sensing imagery.

3.2 Walnut Gulch Experimental Watershed

The Walnut Gulch Experimental Watershed (31° 43' N, 110° 41' W), which was designed, instrumented, and which is operated by the Southwest Watershed Research Center (SWRC), Agriculture Research Service (ARS), U. S. Department of Agriculture (USDA), is located about 120 km southeast of Tucson in Cochise County, and surrounds Tombstone, Arizona, in rangelands typical of the semi-arid southwestern United States. A map of Arizona with an enlarged view of Walnut Gulch is illustrated in Figure 3.1.

This rangeland region receives 250-500 mm of precipitation annually, typically ⅔ of it as convective precipitation during a summer monsoon season that encompasses the months of July through mid-September. The balance of precipitation primarily falls during winter frontal storms of Pacific origin. The monsoonal precipitation form is usually high-intensity convective thunderstorms of limited areal extent. The runoff in the ephemeral streams is of short duration and carries a large sediment load. The channels are also steep, resulting in flows being near critical depth (Renard *et al.*, 1993).

Walnut Gulch rises in the foothills of the Dragoon Mountains and drains ephemerally westward to join the San Pedro River at Fairbank, Arizona. The experimental watershed is defined by a flow-measuring flume on the main channel of Walnut Gulch approximately 2.5 miles (4 km) from its junction with the San Pedro River. It is further divided into a number of subbasins by supercritical-measuring flumes located at the outlet of each subwatershed on the channel network (Goitom and Woodward, 1988; Osborn and Lane, 1984; Diskin and Lane, 1972; Nichols *et al.*, 1994, Smith *et al.*, 1995). The catchment is an instrumented area comprising the upper 148 km^2 of the Walnut Gulch drainage basin. The soil types range from clays and silts to well-cemented boulder conglomerates (Kustas *et al.*, 1992), with the surface

soil textures (0-5 cm) being gravelly and sandy loams containing an average of 30% rock and little organic matter (Renard *et al.*, 1993; Kustas and Goodrich, 1994). The topography can be described as gently rolling hills incised by rather steep drainage channels, which are more pronounced at the eastern end of the watershed near the Dragoon Mountains. The mixed grass-brush rangeland vegetation, typical of southeastern Arizona and southwestern New Mexico, ranges from 20 to 60% in coverage. Grasses primarily cover the eastern half of the watershed, whereas the western half is brush-dominated.

Walnut Gulch is located primarily in a high, very deep (up to 400 m) alluvial fan portion of the San Pedro watershed. Depth to ground water varies from 45 m at the lower end, to 145 m in the central part of the watershed. The topography consists of low undulating hills dissected by stream channels whose routes are controlled by geologic structures. Hill slopes vary from 2 to 65%, with stream slopes ranging from 1 to 3%. Intrusive igneous dikes influence groundwater movement and surface drainage in the Tombstone hills, and the Schieffelin granodiorite alters the main stem of Walnut Gulch, acts as a ground water barrier, and has caused many perched water tables along its parameter.

Hydrologic research on the watershed began in 1954 (Kustas and Goodrich, 1994). Eighty-five recording rain gauges (24-hour time scale) are currently maintained in and around the watershed (Haider, 1994). This densely distributed rain gauge network (an average of one rain gauge per 1.76 km^2), 11 primary watershed runoff-measuring flumes and 2 sets of weather and energy flux stations make the Walnut Gulch Experimental Watershed a unique source of rainfall, runoff, meteorological, and energy flux data. The location of rain gauges, flumes, the Lucky Hills and Kendall micrometeorological stations, and the gridded area described by the distributed TOPLATS model are shown in Figure 3.2.

Currently, Walnut Gulch commands intensive hydrologic observation and modeling attention under the NASA Earth Observing System (EOS) project, *Hydrologic Cycle and Climatic Processes in Arid and Semi-Arid Lands* (LERTS/UA). This is a joint endeavor between NASA, LERTS, the USDA-ARS, and the University of Arizona. Its goal is to identify the dominant processes that control hydrologic fluxes at various spatial and temporal scales by separating the complicated composite spectral response of remotely-sensed data into physically

meaningful watershed characteristics, using spatially distributed modeling and a variety of hydrologic measurements (Sorooshian *et al.*, 1988). Maps of distributed basin characteristics, including soil physical and chemical properties, hydrologic properties, vegetation characterization, litter estimation, and soil moisture profiles, are being produced as a function of time as part of the LERTS/UA EOS project.

The USDA-ARS Walnut Gulch Experimental Watershed near Tombstone, Arizona, is an ideal location for the development and testing of the hydrologic data-assimilation model. No other semi-arid watershed in the world has instrumentation with comparable resolution in time and space. Moran *et al.* (1994c) and Goodrich *et al.* (1994) suggested that the unique ongoing research at the Walnut Gulch Experimental Watershed is ideal for studies that integrate remote-sensing and hydrologic modeling to aid the research community in large-scale modeling of mass and energy exchanges across the plant-soil-atmosphere interface. Close cooperation was established between the research described here and that under the LERTS/UA EOS project was established and has proved mutually beneficial.

3.2.1 Monsoon '90

The Monsoon '90 multi-disciplinary field campaign was a three-phased field experiment conducted over the summer of 1990 at the Walnut Gulch Experimental Watershed. The first campaign was held for two days in June to obtain baseline conditions during the dry season. The second campaign, which was conducted during the summer monsoon season from July 23 through August 10, 1990, collected data when the spatial and temporal variation in rainfall was historically largest and when the vegetation was most active. The last campaign, conducted on September 9, 1990, collected usable satellite data from SPOT and Landsat which were not available during the second campaign (Kustas and Goodrich, 1994).

During Monsoon '90, eight micrometeorological-energy flux (Metflux) sites instrumented to provide continuous measurement of local meteorological conditions and for estimating the surface energy-balance were deployed. Measurements at these sites included near-surface soil moisture, soil temperature, surface temperature, incoming solar radiation, net radiation, soil heat flux, and sensible heat flux via eddy correlation and/or temperature variance methods. The

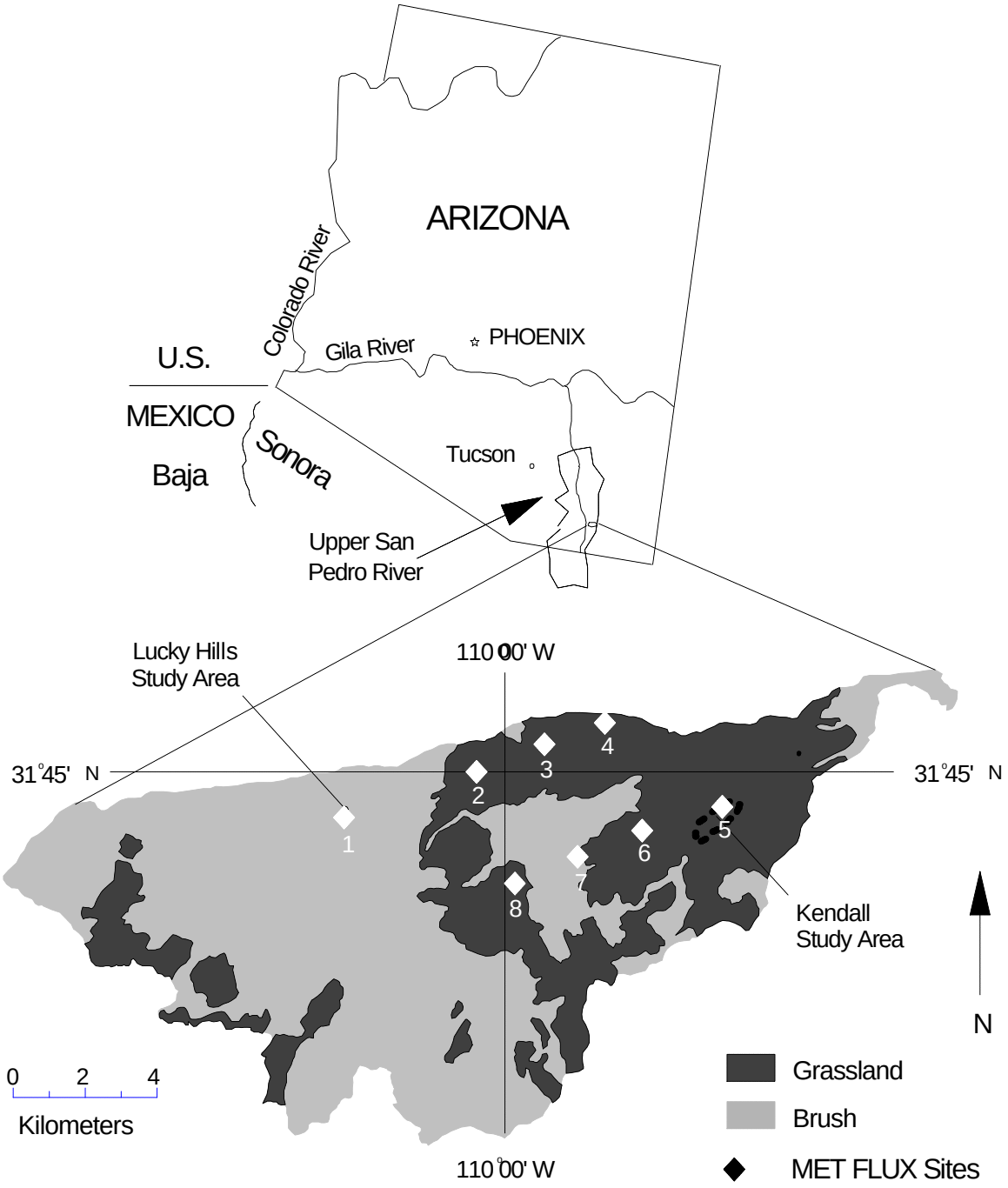

Figure 3.1: Schematic illustrating the location and boundaries of the USDA-ARS Walnut Gulch Experimental Watershed in Arizona. Grass- or brush-dominated ecosystems are mapped and the location of the Lucky Hills and Kendall sites are shown (Kustas and Goodrich, 1994).

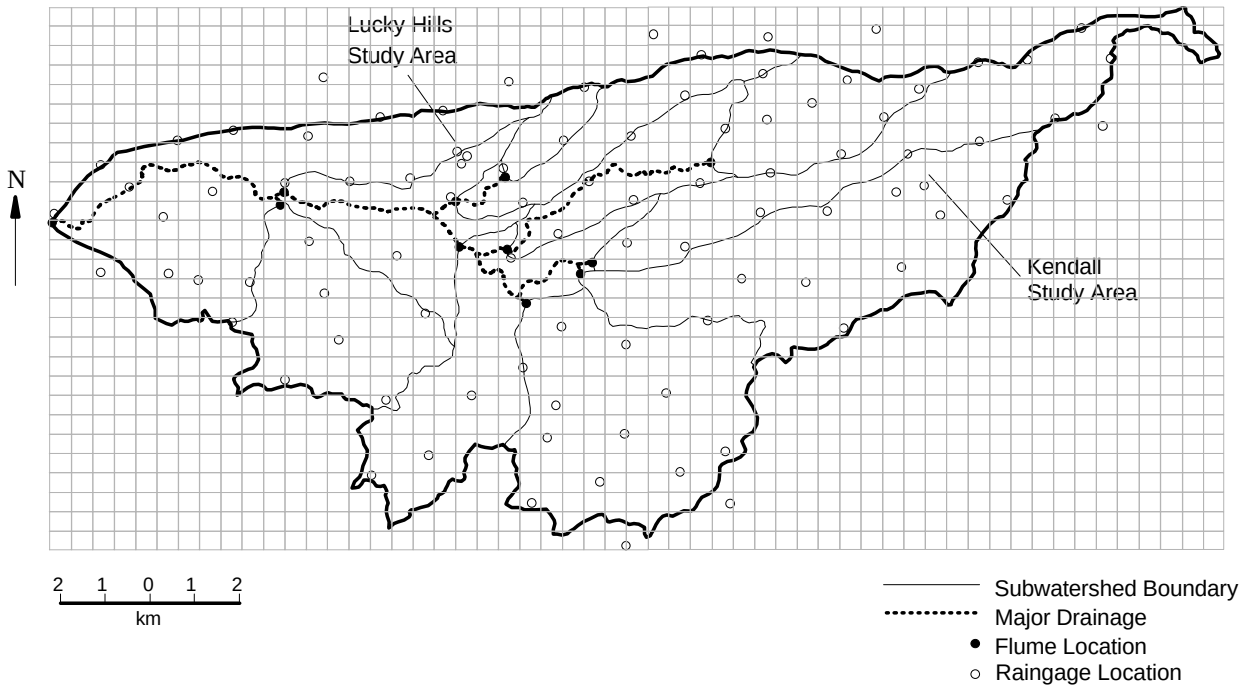

Figure 3.2: The location of Walnut Gulch watershed boundaries, drainages, flume locations, and raingage locations. The grid represents the TOPLATS model domain. Each square on the figure represent 144 (12 x 12) model grids.

Metflux stations were situated along transects parallel to remote-sensing flight lines and included the two dominant vegetation types (brush and grass) (Kustas *et al.*,1992; Kustas and Goodrich, 1994). The Metflux site locations and the subwatershed boundaries that define the main study area is illustrated in Figure 3.3. The Metflux sites were located along ridge tops so as to provide measurements of spatially averaged turbulent energy flux values indicative of the surrounding terrain. Pictures of the location of the Walnut Gulch Metflux sites and the prevalent vegetation are provided in Figures 3.4-3.15. The location, characteristics, corresponding rain gauge numbers, and TOPLATS grid numbers of the Metflux sites are documented in Table 3.1. A summary of the characteristics of Monsoon '90 measurements is presented in Table 3.2.

Table 3.1: Location of Metflux sites, the corresponding distributed model's pixel number and descriptions of vegetation cover and surface soil properties.

Metflux Sites Site	Pixel col,row		UTM East (m)*	UTM North (m)*	Elevation above MSL (m)	Canopy Cover, % Grass	Shrub	Forb	Soil Compostion (0-5cm), % Sand	Silt	Clay	Surface Rock Cover %	Rock Content (0-5cm) %
1	98,244	*Lucky Hills*	589843	3512240	1371	–	–	26	66	24	10	46	28
2	84,304		592251	3512767	1400	14	10	28	69	20	11	48	36
3	70,371		594945	3513344	1452	5	3	38	71	20	9	45	28
4	60,419		596862	3513748	1492	42	6	13	73	22	5	59	45
5	116,505	*Kendall*	600288	3511499	1526	35	1	4	69	20	11	54	38
6	138,400		596104	3510611	1460	5	4	28	67	25	8	52	31
7	153,333		593439	3510040	1393	14	6	12	80	14	6	10	10
8	165,275		591091	3509527	1375	–	1	38	72	20	8	58	21

* Zone 12, NAD 1927.

3.2.2 Post-Monsoon '90 data base

The ARS continued monitoring meteorological and energy flux data using various combinations of sensors at Metflux sites 1 (Lucky Hills) and 5 (Kendall) after Monsoon '90 to the present time. However, over the period, August 11, 1990 through December 31, 1991, this data set contained numerous periods of missing data that continuity of the meteorological time series. Of the two, records at the Kendall site were more complete, so this site was used as the foundation of the post-Monsoon '90 data set. Discontinuities in the Kendall data time series were filled through, interpolation of short gaps, substitution of Lucky Hills data, or substitution

Table 3.2: Location, height, depth, and frequency of ground-based hydrometeorological and remote-sensing observations.

Ground-Based Hydrometeorological and Remote-Sensing Observations

Measurement Type	*Sites*	*Nominal Height (Depth), m*	*Frequency of Observations*
Air temperature	1-8	4	20 minute
Air temperature	1, 5-8	9	20 minute
Temperature and relative humidity	1,5	2	20 minute
Wind speed and direction	1-8	4.5	20 minute
Solar radiation	1-8	3.5	20 minute
Net radiation and surface temperature	1-8	3	20 minute
Photosynthetically active radiation	1,5	3.5	20 minute
soil heat flux	1-8	(0.05)	20 minute
Soil temperature	1-8	(0.025), (0.05), (0.15)	20 minute
Soil moisture (resistance sensors)	1-8	(0.025), (0.05)	20 minute
Soil moisture (TDR)	1,5	(0.05)-(0.50)	daily
Soil moisture (gravimetric)	1-8	(0.0)-(0.05)	daily
Rainfall	85	1	continuous
Runoff	23	—	continuous
Remote-sensing	1,5	1	satellite and aircraft

of data from Hill 444 (31.70° N 110.23° W and at 4434 feet (1351 m) M.S.L.) on nearby Ft. Huachuca (White, 1996). Model comparisons made using data from Ft. Huachuca and Walnut Gulch during periods when both existed, showed little difference using the two alternate data sources (White, 1996). The time intervals and nature of substituted Ft. Huachuca data are listed in Table 3.3. The resulting meteorological data record extends from July 16, 1990 through December 31, 1991, with an energy flux record from July 23, 1990 through December 31, 1991. The precision of the meteorological and energy-balance measurements and the corresponding maximum % error of the measurements are listed in Table 3.4.

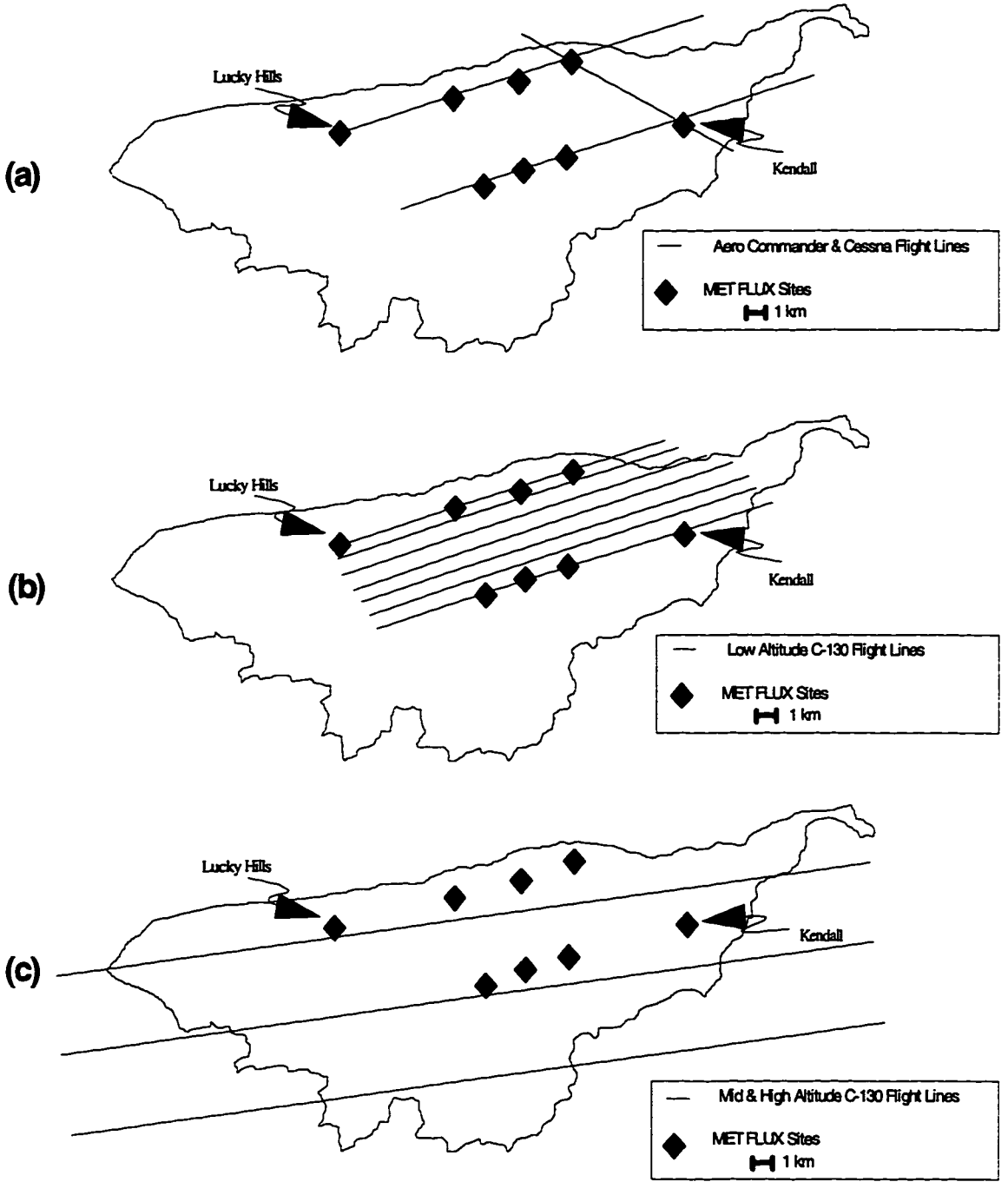

Figure 3.3: Location of Monsoon '90 remote sensing flight lines in relation to Metflux sites (Kustas and Goodrich, 1994).

Figure 3.4: Walnut Gulch Metflux site 1, otherwise known as Lucky Hills.

Figure 3.5: Meteorological instrumentation at Walnut Gulch Metflux site 1.

Figure 3.6: Walnut Gulch Metflux site 2.

Figure 3.7: Walnut Gulch Metflux site 3.

Figure 3.8: Walnut Gulch Metflux site 4.

Figure 3.9: Flume measurement at Walnut Gulch Metflux site 5.

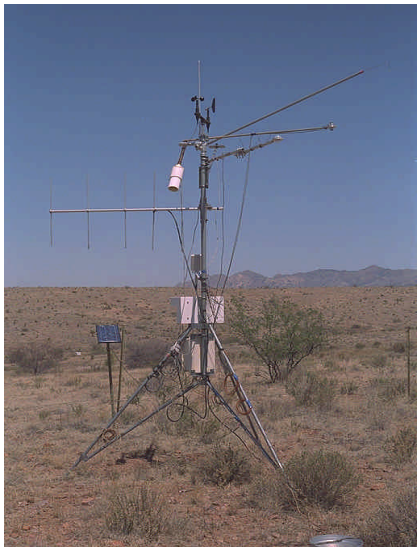

Figure 3.10: Meteorological instrumentation at Walnut Gulch Metflux site 5.

Figure 3.11: Soil profile at Walnut Gulch Metflux site 5.

Figure 3.12: Walnut Gulch Metflux site 6.

Figure 3.13: Walnut Gulch Metflux site 7.

Figure 3.14: Walnut Gulch Metflux site 8.

Figure 3.15: Flume 1 at Walnut Gulch outlet.

Table 3.3: Time intervals and types of data substituted from the climatological records of Hill 444 (31.70°N 110.23° W 4434' MSL), Ft. Huachuca, Arizona (White, 1996).*

Meteorological Forcing Data Substituted from Hill 444, Ft. Huachuca, Arizona

Time Interval of Hourly Data Substituted (Decimal DOY 1991)	Solar Radiation	Net Radiation	Air Temperature	Relative Humidity	Wind Speed
143.52 through 150.27	X	X	-	-	-
218.43 through 225.52	X	X	X	X	X
232.60 through 240.48	X	X	-	X	-

* Data Furnished by Atmospheric Science Laboratories' (ASL) Meteorological Team located at Ft. Huachuca, Arizona

Table 3.4: Meteorological and energy-balance measurements and precision and maximum percent error (White, 1996).

Rainfall	Solar Radiation	Net Radiation	Air Temperature	Relative Humidity	Sensible Heat Flux	Ground Heat Flux	Wind Speed
0.01"++	13 W m^{-2} +	12 Wm^{-2} +	0.2°C	5.0%	26 W m^{-2} +	16 W m^{-2} +	0.2 m s^{-1} *
1 %	< 2 %	3-14 %+	< 1 %	5 %	26 %**	~13%	< 5 %

++ Haider, 1994. * Kustas *et al.*, 1994c. **Blanford and Gay, 1992. +Stannard *et al.*, 1994.

3.3 Model domain

The TOPLATS distributed model domain for Walnut Gulch was defined minimized to conserve both memory and disk usage (Table 3.5). The model which has a resolution of 40 m is co-registered with the DEM and PBMR remote-sensing images for ease of use and to avoid unnecessary interpolations. This results in 93,622 modeled grid squares which cover the entire Walnut Gulch Experimental Watershed.

Table 3.5 Distributed model domain definition.

Defined Corners of the Rectangle Circumscribing the Walnut Gulch Watershed in Universal Transverse Mercator (UTM) Coordinates

Location	UTM* East (m)	UTM* North (m)
Upper Left (Northwest) Corner	3516160	580080
Upper Right (Northeast) Corner	3502840	580080
Lower Left (Southwest) Corner	3516160	606480
Lower Right (Southeast) Corner	3502840	606480

* Zone 12, NAD 1927.

3.4 Area-average site characteristics

The TOPLATS model requires the site-specific definition of many soils, vegetation, and topographic time-invariant parameters (Appendix B) properly to simulate the water- and energy-balance of a particular area. Parameterization of the SVATS was based largely upon the literature from the Monsoon '90 Field Campaign (Kustas *et al.*,1992, 1994a,b,c,d; Stannard *et al.*, 1994; Moran *et al.*, 1994a,b; Humes *et al.*, 1994a,b; Weltz *et al.*, 1994; Menenti and Ritchie, 1994; Hipps *et al.*, 1994) together with a BATS modeling study of a Sonoran Desert site near Tucson (Unland *et al.*, 1996). Most of the required parameters had been measured or estimated at many sites in Walnut Gulch for the Monsoon '90 field campaign. The vegetation parameters included the vegetation cover percentage, roughness length, zero-plane displacement height, albedo, and the maximum and minimum leaf area indices. Similarly, the list of known soil-related parameters included porosity, minimum soil suction, saturated hydraulic conductivity, and wet and dry soil albedos.

3.4.1 Soil parameters

Most of the soils in Walnut Gulch are of a sandy loam soil texture (White, 1996) with a gravelly and rocky nature (Kustas and Goodrich, 1994) that may impact infiltration rates. Most soil-related model parameters were determined through literature searches, and their specification is briefly described here. It should be noted that many of these parameters were only measured at the eight Monsoon '90 sites and their averages were used in this study. In addition, several parameters were not observed, and they were therefore either left the same as in the original TOPLATS model development (i.e. as 'default values', Famiglietti, 1992), or they were estimated. Spatially variable estimates of many of these parameters are also specified in GIS coverages; hence, the spatial average in many cases subsequently replaced the initial values given in this section. Finally, many of the unobservable or unknown parameters identified in this section are the subject of a parameter calibration study outlined later.

Because of the deep water table at Walnut Gulch (Section 3.4.3), SVATS processes show little sensitivity to TOPMODEL parameters. The watershed area and mean soil-topographic index values were determined from the spatially variable topographic index. The TOPMODEL

parameter, the parameter describing the decay of saturated hydraulic conductivity with depth and the parameter describing the maximum rate of capillary rise, were unknown, and thought to have an insignificant impact on model simulations; thus they were left at default values. A. subsequent and unsuccessful attempt to calibrate these parameters based on a TOPMODEL calibration study is described in Chapter 4.

Albedo of dry soil was specified on the basis of suggested parameters for the BATS model for the Walnut Gulch soil types (Dickinson *et al.*, 1993). Analyzes of soil profile temperature from three trenches at the Lucky Hills and Kendall sites were analyzed and modeled to determine the diurnal damping depth for temperature and the temperature of the deep soil layer. The time average diurnal cycle for the Monsoon '90 period was determined (Figure 3.16), and a simple model was then fit to these cycles and used to estimate the temperature damping depth:

$$T_i = \bar{T} + \left(\frac{T_{\max} - T_{\min}}{2} \exp\left(\frac{-d/100}{C_s} \right) \sin\left(\frac{2\pi}{24} \right) \left(i - i_{delay} \right) - \frac{d/100}{C_s} \right) \tag{3.1}$$

where T_i is the temperature at time i and depth d, C_s is the specific heat of soil, T_{min} is the minimum diurnal soil temperature, T_{max} is the maximum diurnal soil temperature, and i_{delay} is a time-delay parameter. This equation was fit to measurements (Figure 3.17), then used at depths deeper than the available measurements to determine the temperature damping depth. This turned out to be close to 0.5 m for both sites. Then, average temperatures at this depth were determined to be 295.86 °K for Lucky Hills and 298.13 °K for Kendall. It is interesting that the only difference between the north- and south-facing temperature profiles at the Kendall site is in the amplitude of the temperature cycle.

Percent clay, percent sand, bulk density, and soil rock fraction used in this study are the averages of values measured at the Metflux sites (Kustas and Goodrich, 1994). The saturation soil moisture was assumed to be close to the porosity ϕ, which was calculated using bulk density, BD, measurements (Rawls *et al.*, 1993) from:

$$\phi = 1 - \frac{BD}{PD} \tag{3.2}$$

where PD is the particle density which is normally taken as 2.65 g/cm^3. The calculation for residual soil moisture is included in the TOPLATS program and is based on hydraulic

conductivity, percent clay, and percent sand. The values calculated in this way were found to be unrealistically high, and they were later replaced with GIS-derived spatial values (which were individually too high, according to the PBMR-derived soil moisture values). As is described in Chapter 4, all the measured soil characteristic parameters were found to be biased due to the removal of the coarse fraction (i.e. rocks and gravel) prior to analysis. The surface saturated hydraulic conductivity was based on the porosity using the Kozeny-Carmen equation (Rawls *et al.*, 1993):

$$K_s = B\phi_e^n \tag{3.3}$$

where normally B=1058, and n=4. A coarse fraction correction is also performed.

Bare soil roughness length and bare soil zero plane displacement were estimated on the basis of on-site observations. Maximum surface zone depth was specified to the maximum reported L-band microwave penetration depth so as to ensure compatibility with remote-sensing. Assuming a shallower depth than this for the surface layer would have required a shorter model time step because the atmospheric interaction with the first few centimeters is rapid and is undesirable for computational reasons. Maximum root zone depth was initially set to 1.5 meters in accordance with the standard SVATS soil depths for this land cover (Schmugge and André, 1991).

Estimates of the initial root zone soil moisture, the initial surface zone soil moisture, and the initial transmission zone soil moisture were all based on surface gravimetric observations (Schmugge *et al.*, 1994). Profile TDR soil moisture observations at the Kendall and Lucky Hills sites were used to initialize the root and transmission zone soil moisture.

An 8-month fully distributed TOPLATS simulation was performed prior to Monsoon '90 using actual precipitation forcing, and 1991 the meteorological forcing data (meteorological observations) were non-existent prior to Monsoon '90. This simulation predicted soil moisture states that were much lower than observed; hence, this initialization simulation information was not used for spatially variable soil moisture initialization.

3.4.2 Vegetation parameters

Vegetation height and fraction were taken as the Monsoon '90 Metflux site average values reported in the literature (Kustas and Goodrich, 1994; Humes *et al.*, 1994a). The leaf area index values were also from measurements made during Monsoon '90 (Daughtry *et al.*, 1991).

Minimum stomatal resistance for this area is 250 s/m according to Chow *et al.* (1988), but Unland *et al.* (1996) suggested that this parameter be set to a very low value for semi-arid vegetation. It is the author's judgement that because desert vegetation generally has very good stomatal control, the higher value seems more reasonable. To be consistent with other studies in the area, the value suggested by Unland *et al.* (1996) was adopted. The root activity factor, root density, root resistivity, and critical leaf water potential were not measured, and indeed, many of these parameters are not observable quantities. Default values were therefore used. Subsequently, these parameters were calibrated using automatic techniques (described in Chapter 4).

The vegetation stress soil moisture parameter value was assumed to be halfway between the saturated and residual soil moisture values. While the wilting point was assumed to be equal to the value of residual soil moisture, because the author has never witnessed desert vegetation wilt. Soil moisture for calculation of potential evapotranspiration was assumed to be 10% below the saturation soil moisture, this being approximately the ratio used as a default parameterization in SiB (Sellers *et al.*, 1986).

The effective mean drag coefficient was set to 0.07 as suggested by Shuttleworth (1995).

Values for albedo of dry vegetation for semi-arid areas were obtained from Dickinson *et al.* (1993), and the albedo of wet vegetation was assumed to be 5% lower than for dry vegetation.

3.4.3 Saturated water surface

In the course of a geophysical study of the hydrogeology of the Walnut Gulch Experimental Watershed, Spangler (1969) developed a groundwater contour map (Figure 3.18) for the alluvial unconfined Walnut Gulch aquifer. He found that groundwater flow is west to northwest; i.e. towards the San Pedro River from the Dragoon Mountains in the east. Water table gradients vary from 2.5-3.0% in the upper end of the watershed to 0.5% in the lower portion of the

a)

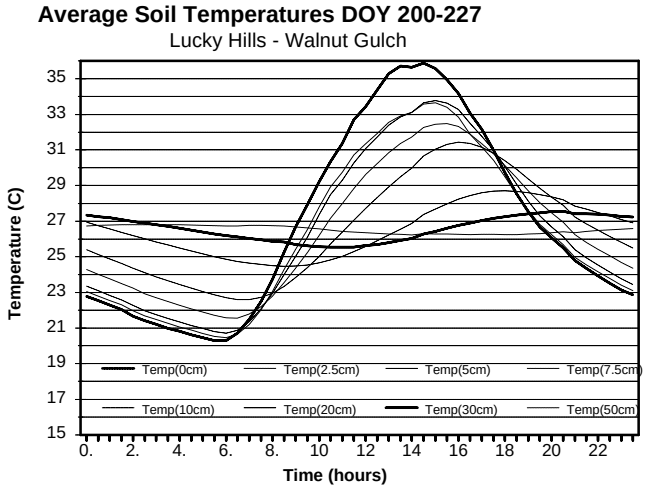

b)

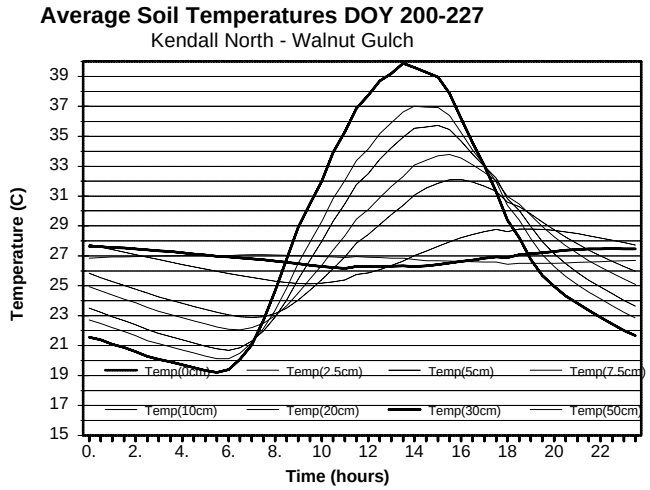

c)

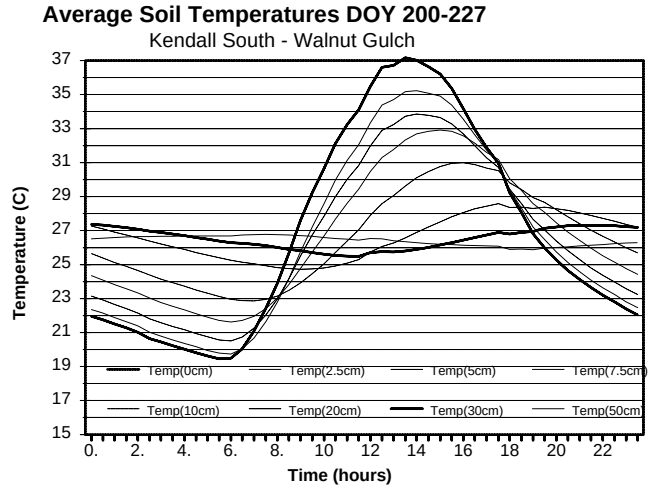

Figure 3.16: a) Lucky Hills, b) Kendall-north, and c) Kendall-south profile average soil temperatures for Monsoon ‘90 day 200 through 227.

a)

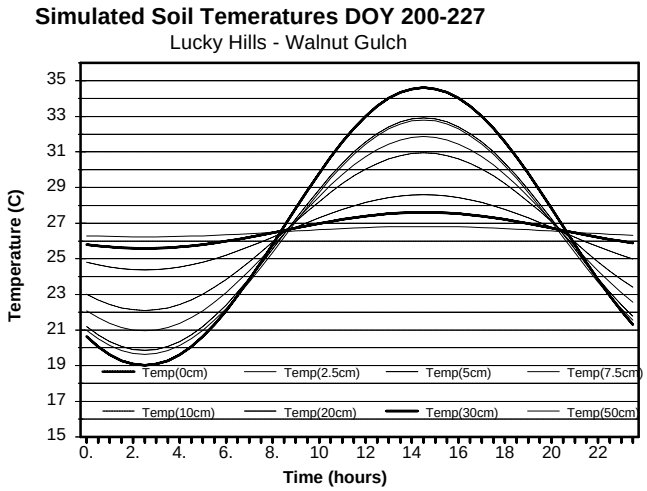

b)

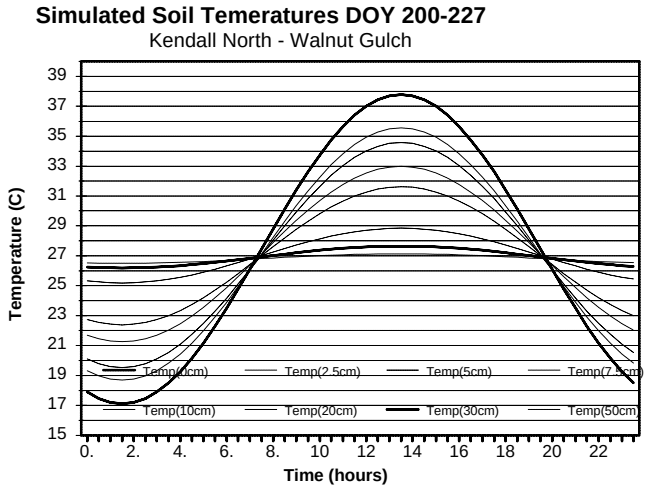

c)

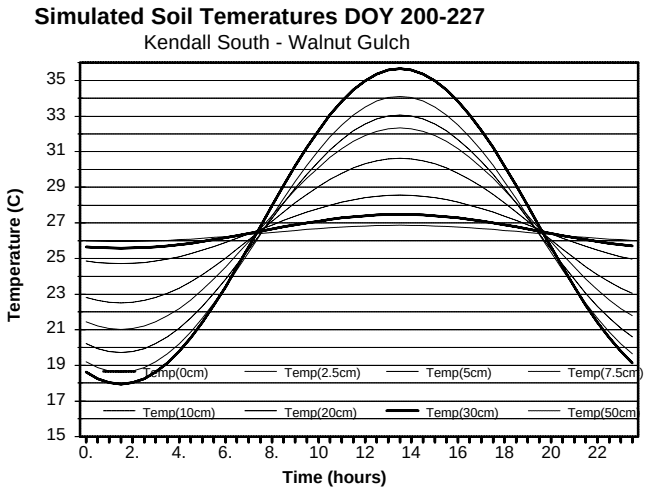

Figure 3.17: a) Lucky Hills, b) Kendall-north, and c) Kendall-south profile simulated soil temperatures for Monsoon ‘90 day 200 through 227.

watershed, while the depths from the surface to the regional water table varies from 35 feet (10.7 m) near the San Pedro River to 432 feet (131.7 m) in a well 6 miles (9.7 km) northeast of Tombstone. Spangler estimated that recharge in the watershed is negligible, and that most runoff therefore enters the groundwater system at the base of the Dragoon Mountains.

The City of Tombstone (Gilbert, 1996) maintains 3 wells in the Walnut Gulch watershed that give an indication of the elevation of the water table with respect to the land-surface (Table 3.6). The water table elevation has declined slightly over the period of record and is on the order of several hundred feet (100 m) below the ground surface. For simplicity, the saturated water surface depth in TOPLATS was set to 100 m below the surface.

Table 3.6: Water well information for the City of Tombstone (Gilbert, 1996).

Well #1: Located at Allen St. East of 6th street (Sec 11 T20S R22E)
Drilled: 1941
Discharge Elevation: 4556 feet (1389 m)
Depth: 612 feet (187 m)

Water Levels:	Date	Level (feet below ground)
	1969	430 (131 m)
	1990	407 (124 m)
	1992	406 (124 m)
	1993	404 (123 m)
	1994	406 (124 m)
	1995	406 (124 m)

Well #2: Located at Camino San Rafael (Sec 1 T20S R22E)
Drilled: 1967
Discharge Elevation: 4425 feet (1348 m)
Depth: 600 feet (183 m)

Water Levels:	Date	Level (feet below ground)
	1967	276 (84 m)

Well #3: Located at North Drive (Sec 1 T20S R22E)
Drilled: 1976
Discharge Elevation: 4520 feet (1378 m)
Depth: 890 feet (271 m)

Water Levels:	Date	Level (feet below ground)
	1976	333 (101 m)

3.5 Spatially distributed site characteristics

It is thought that optimal implementation of a distributed hydrological model requires the model to have knowledge of the spatial distributions of soil and vegetation parameters across the watershed. Therefore, GIS coverages or digital maps of vegetation and soils were obtained from the USDA-ARS (Renard *et al.*, 1993) (Figures 3.19 and 3.20), and the required parameters were either extracted from the coverages or GIS tools were used to estimate them as follows.

3.5.1 Soil parameters

Distributed estimates of effective porosity, saturated soil moisture, residual soil moisture, saturated hydraulic conductivity, percent clay, and percent sand parameters were derived from the soil GIS coverage obtained from the ARS. The Walnut Gulch soil survey was also extensively used (Breckenfeld, 1993). Most of the GIS analysis and spatial parameter estimation described below although supervised by the author was actually performed by Berglund (1995). However, this work is not reported elsewhere, and is presented here.

The Walnut Gulch soil survey (Breckenfeld, 1993) gives potential rooting depth information for each soil type. This was integrated into the GIS coverage and then gridded for model use (Berglund, 1995). Values of the effective porosity, ϕ_e, and residual soil moisture, θ_r, for each series in the soil survey were determined by Mayeux, (1995) using values suggested by Rawls *et al.*, (1993) for each soil type in the GIS coverage. Berglund (1995) calculated saturated soil moisture, θ_s for each soil class as follows:

$$\theta_s = \phi_e + \theta_r \tag{3.4}$$

Percent sand and clay were calculated by Berglund (1995) from values of percent material passing through certain sieves (Breckenfeld, 1993 -Tables H and J) in the soil survey. The data included a range of percentages passing sieves # 4, 10, 40, and 200, as well as percent fragments 3-10 inches (7.6 -25.4 cm) and >10 inches (25.4 cm) for each sample depth interval within each series name and within each of the 30 map units. Sieve #4 separates gravel from sand, hence 100 minus the average percent passing through sieve #4 gives the percent gravel. Similarly, sieve #10 separates coarse sand from medium sand. Sieve #40 separates medium sand from fine sand, and sieve #200 separates sand from silt (which includes clay). Once these percentages had

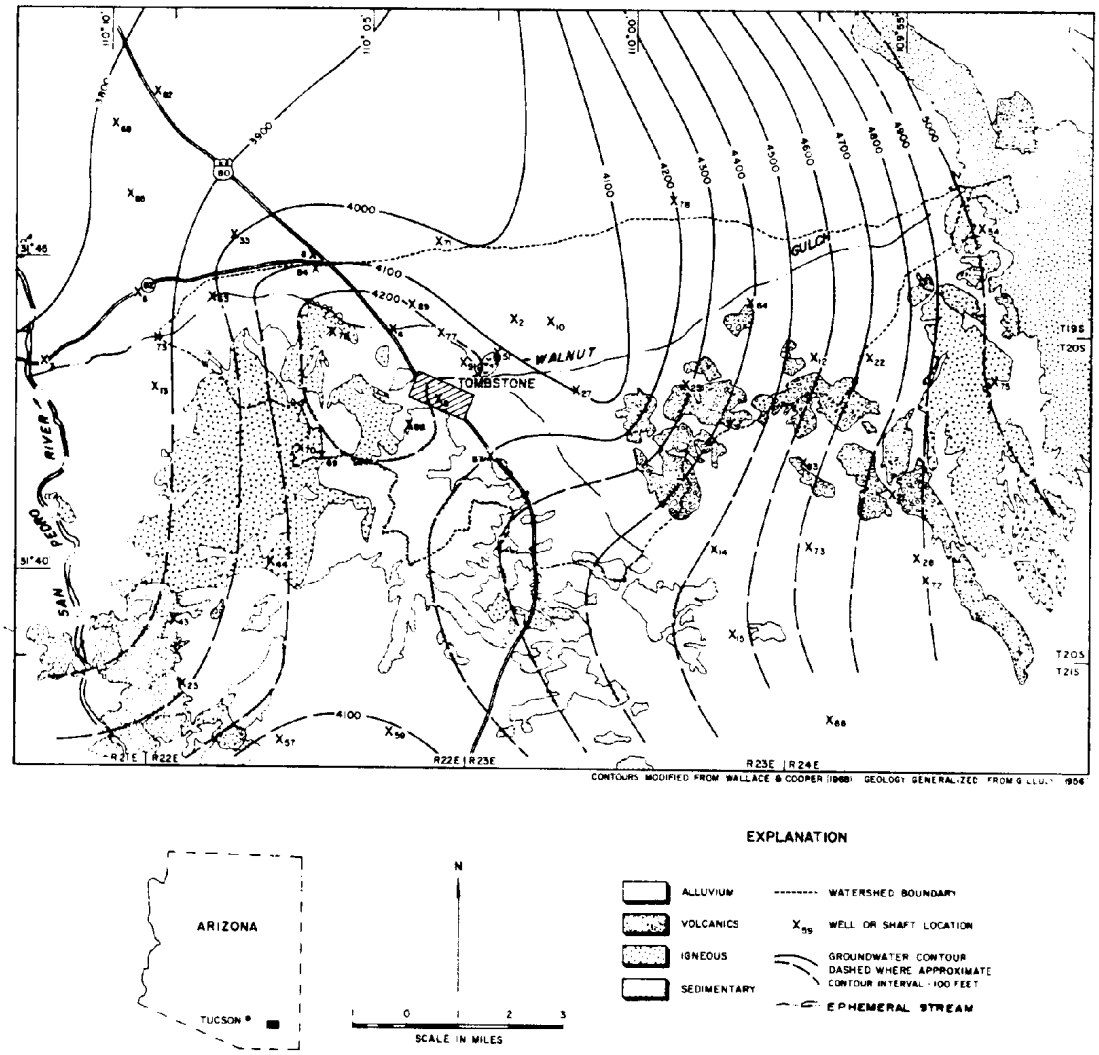

Figure 3.18: Hydrogeologic Map of the Walnut Gulch Experimental Watershed (Spangler, 1969).

Table 3.7: Spatially and temporally constant TOPLATS parameters for Walnut Gulch.

Parameter	Source	Value
Vegetation Parameters		
Veg. Height	Humes *et al.* (1994a)	0.22 m
Ref. height above veg.	Kustas *et al.* (1994a)	2.0 m
Leaf area index	Daughtry *et al.* (1991)	1.275
Min. stomatal resistance	Chow *et al.* (1988)	250 s/m
Initial water storage in canopy	Assumed dry at start of simulation	0 m
Desc. of wet canopy option	Allows wet canopy evaporation and transpiration	0
Unstressed Transp. SM	Assumed half way between θ_s and θ_r	.2
Wilting point SM	Assumed close to residual (cactus do not wilt)	0.05
Veg. Fraction	Kustas *et al.* (1994a)	0.42
Albedo, wet veg.	Dickinson *et al.* (1993) assumed 5% less than dry	.2
Albedo, dry veg.	Dickinson *et al.* (1993)	.25
Albedo, bare soil	Dickinson *et al.* (1993)	.33
Transpiration calc. Option	Assumed minimum of supply and demand	1
Root activity factor	Default (Famiglietti, 1992)	10000
Root density	Default (Famiglietti, 1992)	1m/m^3
Root resistivity	Default (Famiglietti, 1992)	1e9 s/m
Crit leaf water potential	Default (Famiglietti, 1992)	-210
Soil Parameters		
Surface zone depth	Based on PBMR sensitivity depth	0.1 m
Initial surface soil moisture	Schmugge *et al.* (1994)	0.098
Surface water- bal. tolerance	Famiglietti (1992)	-1e-15
Root zone depth	Schmugge *et al.* (1994)	1.5 m
Initial root zone soil moisture	Schmugge *et al.* (1994)	0.096
Sorptivity numerical correction	Default (Famiglietti, 1992)	1e-09
Root zone water- bal. tolerance	Default (Famiglietti, 1992)	-1e-15
THETAS numerical correction	Default (Famiglietti, 1992)	0.001
Max. rate of capillary rise	Default (Famiglietti, 1992)	0.1 m/s
Initial transmission zone SM	Schmugge *et al.* 1994	0.05
Percent sand	Kustas and Goodrich (1994)	70.88
Percent clay	Kustas and Goodrich (1994)	8.5
Bulk density	Kustas and Goodrich (1994)	1.64
Bare soil ref. height	Assumption	2.0 m
Bare soil roughness length	Assumption	0.001
Bare soil zero plane displacement	Assumption	0.0
TOPMODEL Parameters		
λ	Calculation from $A(\tan(B))$ image	8.314
Vert. K option	Assumed K declines exponentially with depth	0
FI	Famiglietti (1992)	7.0
ZBAR0	Gilbert (1996)	100.0
Energy-balance Parameters		
Energy-balance calc. option	Solution to energy-balance equations	0
SM for calc of PET	10% below saturation (Sellers *et al.* 1986)	0.28
Max Newton-Ralphson iterations	Default (Famiglietti 1992)	100
Energy- bal. calc. tolerance	Default (Famiglietti 1992)	0.001 °K
Diurnal heat penetration	Calculation from soil temperature measurements	0.5 m
Temp. of deep soil layer	Calculation from soil temperature measurements	297 °K

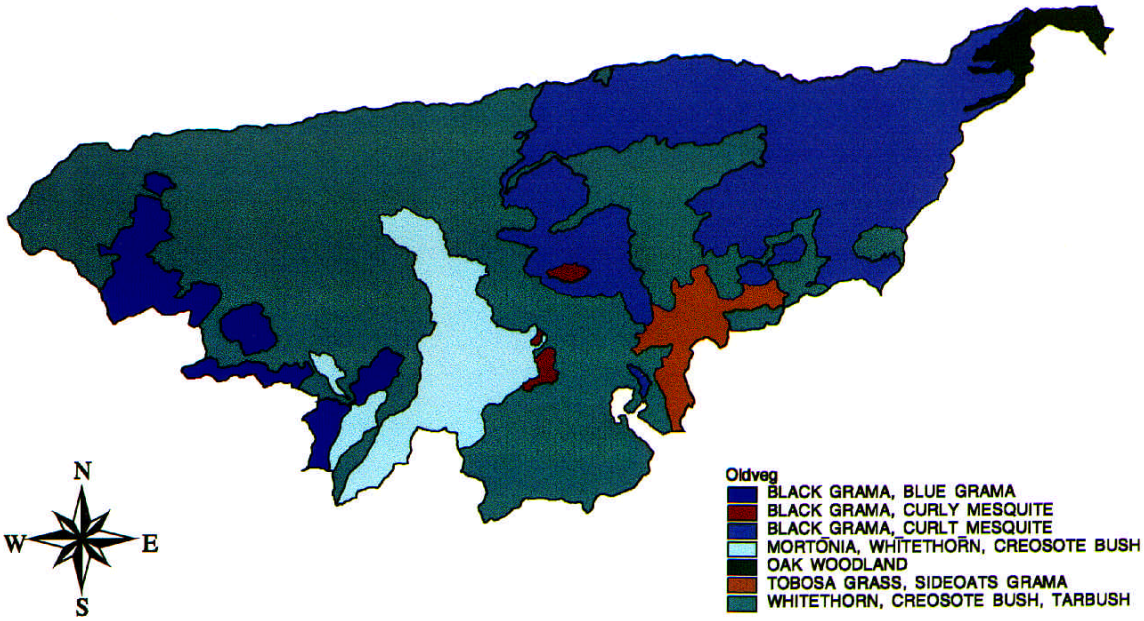

Figure 3.19: GIS coverage of Walnut Gulch vegetation.

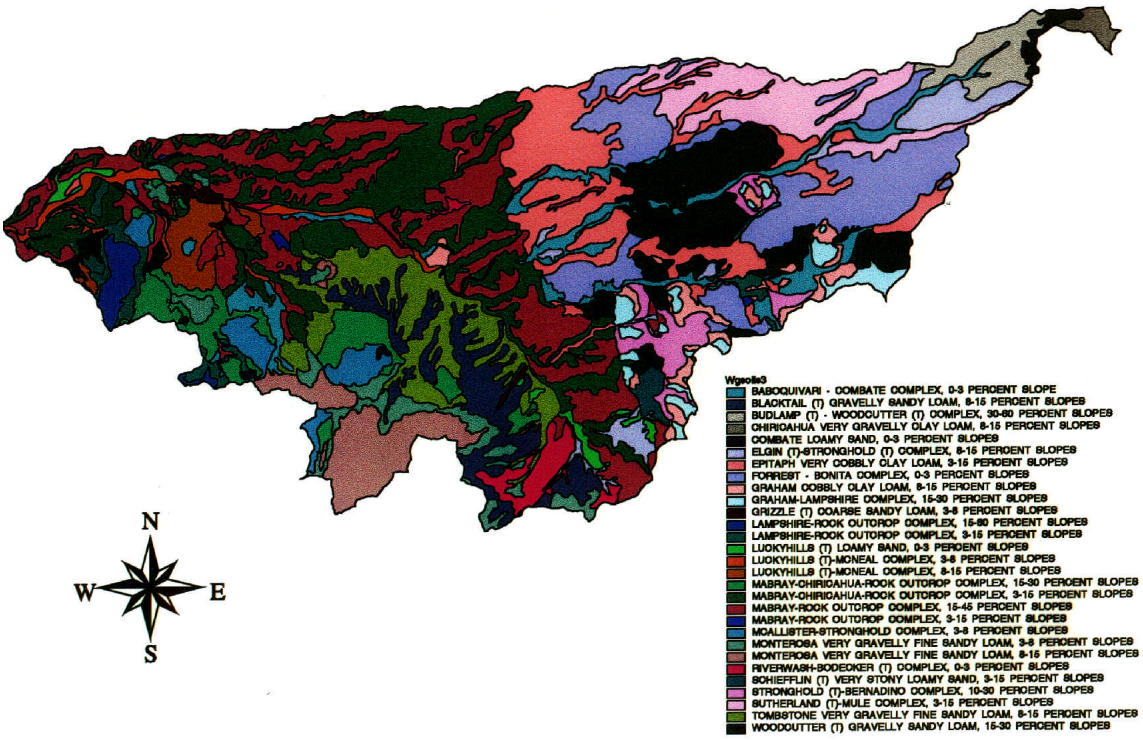

Figure 3.20: GIS coverage of Walnut Gulch soils.

been calculated, the percent gravel, percent coarse sand, percent medium sand, percent fine sand, and percent silt/clay were summed, and re-normalized by this total. Then coarse-, medium-, and fine-sand percents were summed to give the total percentage of sand. The percentage clay (obtained from Table J or 8 in the soil survey for each depth interval) was subtracted from the percentage of silt/clay to yield the percentage of silt.

These calculations were made for the depth interval of each series within each map unit, and the percent sand for each depth interval then was multiplied by the fractional depth which of the interval. These were summed to yield a weighted percentage of sand. This process was repeated to calculate the percentage of clay, silt, and gravel for each series name, and these weighted percentages were then multiplied by the fraction of the map unit made up of that series. They were then summed for each map unit.

Values of bulk density were collected at the Monsoon '90 Metflux sites. Spatial bulk density were estimated using an empirical formula (Rawls *et al.*, 1993):

$$BD = 1.51 + 0.0025(S) - 0.0013(S)(OM) - 0.0006(C)(OM) - 0.0048(C)(CEC) \qquad (3.5)$$

where S is percent sand, C is percent clay, OM is percent organic matter, and CEC is the cation-exchange capacity of clay normalized by percent clay.

All the resulting spatially distributer soil data sets are illustrated in Figures 3.21 and 3.22.

3.5.2 Vegetation parameters

For vegetation, the dominant species, common name, fractional cover, and current vegetation (shrub/grass/etc) was measured at the Metflux sites (Weltz *et al.*, 1994). The GIS vegetation coverage gives seven general subsets of up to three of the following species: black grama, blue grama, curly mesquite, mortonia, whitethorn, creosote bush, oak woodland, tobosa grass, sideoats grama, tobosa grass (swale), and tar bush. Unfortunately the vegetation at the eight Metflux sites all correspond to just three of the seven vegetation subsets, so they are of limited use for spatial estimation. Recognizing the general lack of vegetation measurements of at Walnut Gulch, the values given by Jones (1983) were used to make spatial estimates minimum stomatal resistance.

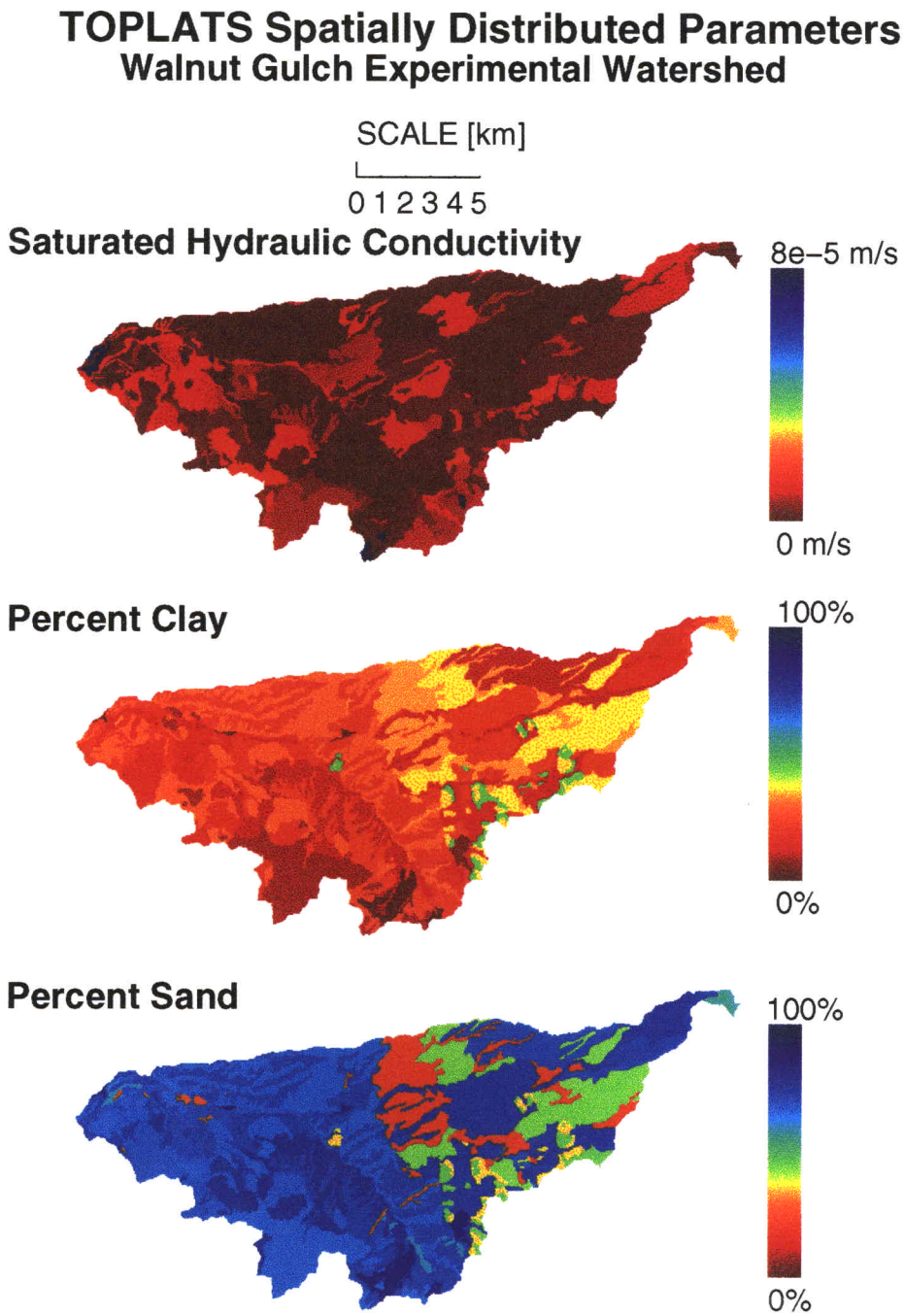

Figure 3.21: TOPLATS spatially distributed soils parameters.

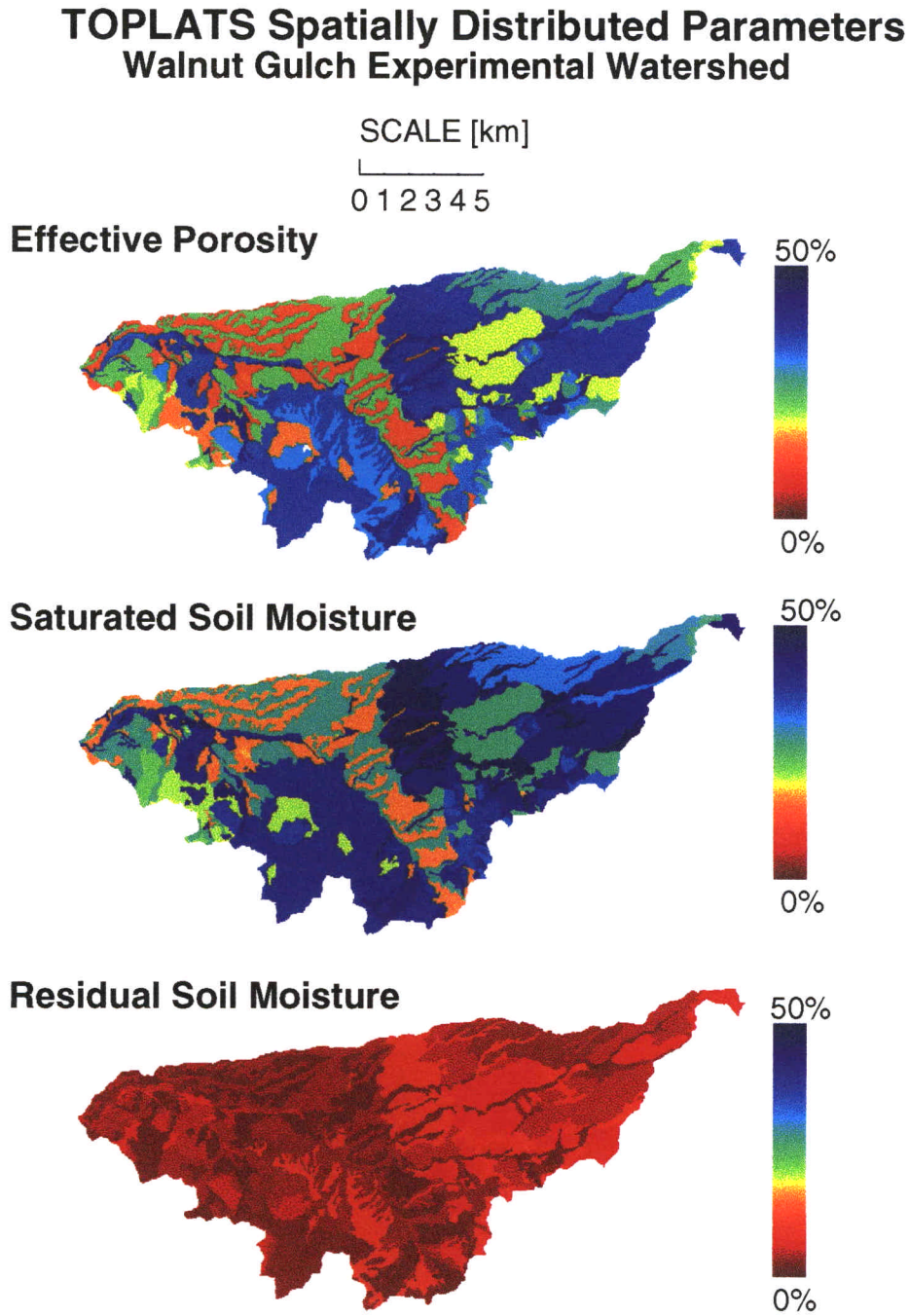

Figure 3.22: TOPLATS spatially distributed soils parameters.

The leaf area index (LAI) measurements at the eight Monsoon '90 Metflux sites (Daughtry *et al.*, 1991) and LAI ranges given by Jones (1983) were used in conjunction with the vegetation GIS coverage to estimate the spatial distribution of LAI.

All of the spatial vegetation data sets are illustrated in Figure 3.23. Additionally, the previously derived (Table 3.7) spatially constant variables derived were adjusted to the means of the new spatially distributed data sets in an attempt to derive more representative parameter values (Table 3.8).

Table 3.8: Spatially and temporally constant TOPLATS parameters for Walnut Gulch. Some of these parameters were not specified as an eight Metsite average, but were rather determined in the model from other parameters in the model. In the case of residual soil moisture, the spatially-variable values were not reasonable, and were therefore not used.

Parameter	8 Metsite Average Value	Aerially Average Value
Vegetation Parameters		
Root depth	1.5 m	0.795 m
Leaf area index	1.275	1.309
Min stomatal resistance	40 s/m	250 s/m
Soil Parameters		
Hydraulic conductivity	-	4.71E-6 m/s
Saturation soil moisture	-	0.33
Residual soil moisture	0.005	(0.001)
Percent sand	70.88	63.03
Percent clay	8.50	22.10

3.5.3 Topography

The TOPLATS model requires a topographic index map to make predictions. Two separate approaches were taken to derive this index map for Walnut Gulch. They differed mainly in the base DEM used and in some of the processing steps used to derive them.

In the first approach, a 40-meter resolution DEM was created from the 1° by 1° Douglas-West and the Nogales-East 1:250000 scale mapping sheets and imported into a GIS. Next, the two DEMs were merged and projected onto UTM coordinates. Because the default resolution was 93 meters, the DEM was resampled using a nearest neighbor algorithm onto a 40 meter grid. Finally, this DEM coverage was clipped at the Walnut Gulch watershed boundary (Berglund, 1995).

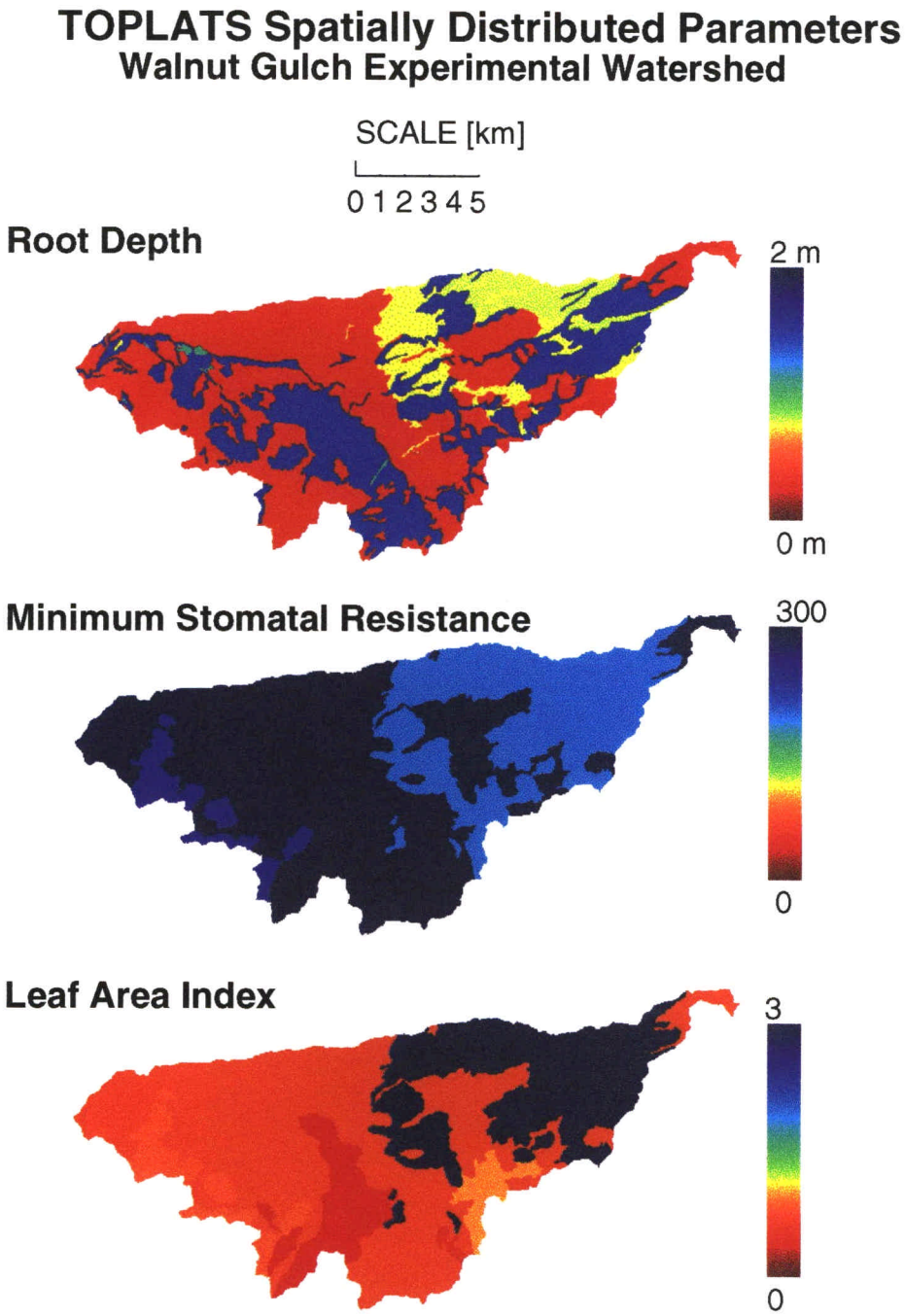

Figure 3.23: TOPLATS spatially distributed vegetation parameters.

The topographic index *(ln(a/tan(β))* was derived from this GIS DEM coverage by first filling the sinks of depressions in the DEM in such a way as to ensure that every grid had a clear flow direction for proper computation of the topographic index. Next, a flow direction grid and a flow accumulation grid were created in the GIS. Fortran programs were then used to compute the topographic index, *ln(a/tanβ)*.

The above procedure produced a DEM and topographic index maps with several problems. It was found that the GIS averaged the DEM to the nearest meter, which created 'shelves' in areas of gentle slope where clear flow directions were not defined. Moreover, the clipping technique used to delineate the watershed boundaries did not use the characteristics of the DEM and because of errors in the DEM and watershed boundary, areas that did not drain to the watershed outflow were included in the clipped DEM and *vice-versa*. These weaknesses made attempts to derive topographic indexes and river-routing algorithms impossible.

To circumvent the above problems a second approach was taken. It involved the use of DEMs derived from analytic photogrammetric methods employing low level areal photography. These DEMs were derived from 23 1:5000 stereo areal photos taken in 1988 via a stereo plotting method followed by computerized relief distortion correction. Using areal triangulation and ground surveys a vertical accuracy of about 0.3 m was estimated for these DEMs. (Washburne, 1994; Matthews, 1992).

Using these unique DEMs introduced a whole new set of challenges. Typical DEMs are interpolated from elevation contour data, and produces a relatively well-behaved DEM surface because of the well-defined nature of contours and smoothing effects of interpolation algorithms. However, each elevation in a orthophoto-derived DEM is independently measured, and therefore has an independent noise or error component. Additionally, with 23 overlapping sections, mosaiced together to create this DEM, the error component means that overlapping areas are necessarily identical and in fact, some overlapping areas differ by as much as 20 m.

To create a DEM with the required high vertical accuracy and clear drainage directions, a series of unconventional steps were taken, as follows: First, all overlapping areas were averaged, to reduce the random sampling error, and eliminate discontinuities between the mosaiced pieces of the DEM. Second, a 25 x 25 running average was passed through the image to provide an

interpolation and to give some spatial correlation within the image. Third, a 'sink-filling' routine was then run on the image to fill any remaining holes it might have. This routine searched the DEM for low elevations with no clear flow direction and added 0.001 m to that elevation. It then repeated the process until all areas had clear flow directions. In this case, the deepest 'hole' was 32.186 m deep and overall, 0.0038 m was added to the elevation of the entire image. Next, a unique watershed delineation algorithm that was used, which was specifically developed specifically for this study. Given a point on the DEM, this routine identified all the other DEM points that drained to this point. Finally, the topographic index was derived from this sink-free, delineated, and high vertical resolution (reported to 0.001 m) DEM using the standard methodology detailed by Beven (1995).

The original raw orthophoto DEM, the filled sinks, and the final delineated topographic index are shown in Figure 3.24.

3.6 Forcing data

This is the first study which has sought to apply a temporally continuous, spatially distributed land-surface hydrology model to Walnut Gulch, and the preparation of model input data and parameter sets proved to be a laborious and slow process. Because precipitation is considered the most important spatial forcing in semi-arid regions (due to its highly variable convective nature), much effort was devoted to deriving spatially distributed precipitation data sets for the Monsoon '90 experiment (Haider, 1994). All other meteorological forcing were assumed spatially constant and derived from averaging observations at the 8 'Metflux' stations in place during the experiment (Kustas and Goodrich, 1994; Kustas *et al.*, 1994a; Humes *et al.*, 1994a; Weltz *et al.*, 1994; Schmugge *et al.*, 1994; Stannard *et al.*, 1994; Moran *et al.*, 1994b).

3.6.1 Meteorology

The modified TOPLATS model requires atmospheric forcing through solar and net radiation, precipitation, air temperature, relative humidity, and wind speed. Most of these variables were measured at all 8 sites throughout the Monsoon '90 period on a 20-minute time

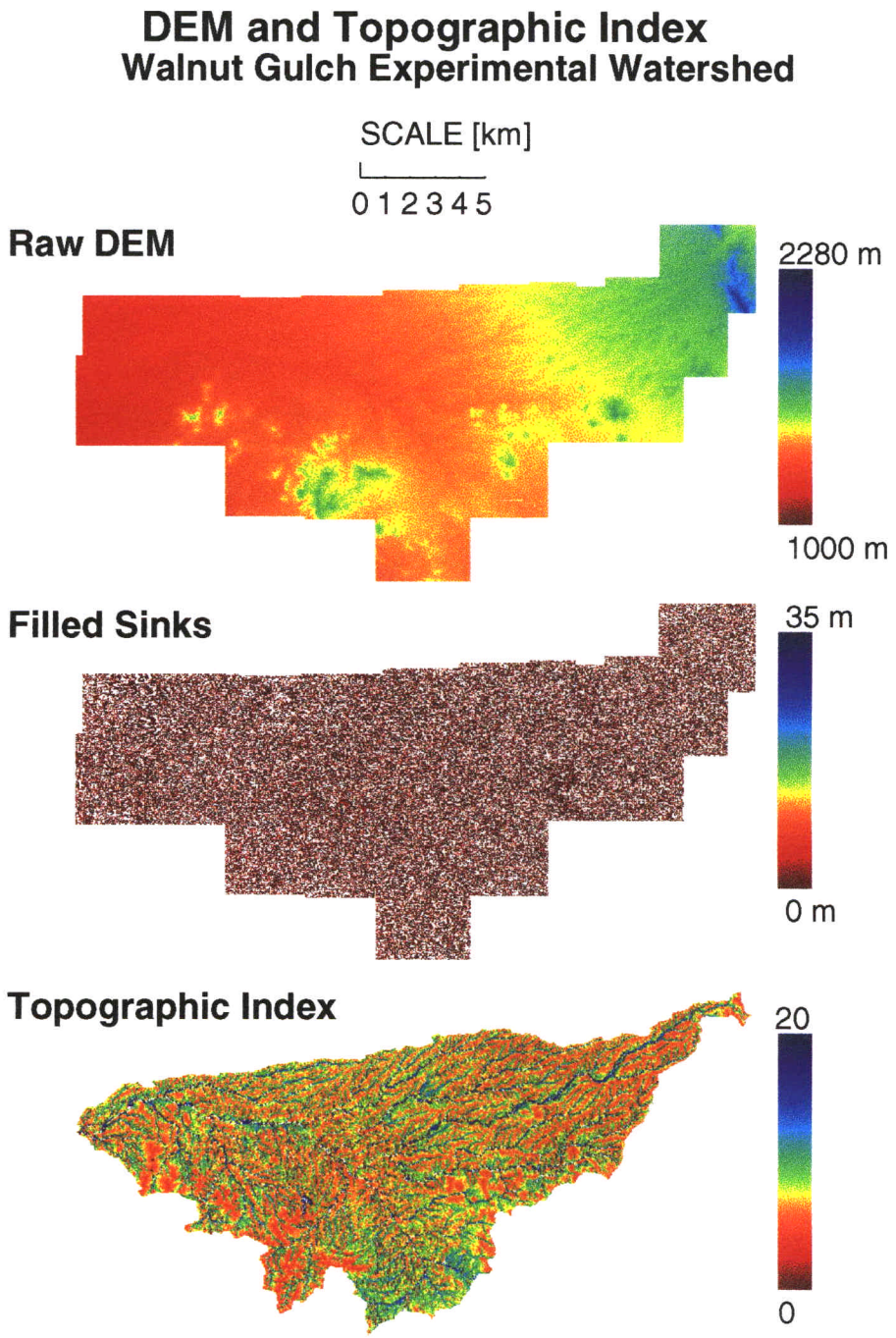

Figure 3.24: Walnut Gulch 40 m resolution orographic photo-derived DEM, filled sinks, and topographic index.

period. These data were spatially averaged from the 8 sites as available and averaged temporally to 1-hour resolution. This resulting forcing data are shown in Figure 3.25.

As described in Section 3.2.2, White (1996) developed a post-Monsoon '90 meteorological data set. Because no meteorological data are available for pre-Monsoon '90 for model initialization studies, the January-August 1991 portion of White's post-Monsoon '90 data set was used for model spin-up and initialization in this study (Figure 3.26).

3.6.2 Precipitation

In semi-arid areas precipitation is the meteorological variable which has the single-largest impact on spatial patterns of soil moisture. Therefore, in this study a great deal of effort is made to understand and derive the spatial patterns of precipitation and to include this information accurately in the model simulations.

Beginning in 1954, a recording rain gauge network was installed at Walnut Gulch to quantify and characterize precipitation at Walnut Gulch. Historically, as many as 95 rain gauges have been in operation; however, the number of gauges operating within any given time period has varied (Nichols *et al.*, 1993; Diskin and Lane, 1972). Currently, 85 well-distributed recording rain gauges (24-hour time scale) are operating in and around the watershed to provide continuous precipitation data.

Walnut Gulch is a region in the southwest United States where almost all of the thunderstorms result purely from surface heating (Fennessey *et al.*, 1986). These airmass thunderstorms produce intense afternoon and evening rains, which are characterized by extreme spatial variability, limited areal extent, and short durations (lasting from a few minutes to rarely more than two hours). These storms determine the rainfall-runoff relationship during the summer in southern Arizona as a whole, and in Walnut Gulch in particular (Osborn and Lane, 1969; Osborn and Hickok, 1968). There is much debate as to whether the moisture source of the summertime thunderstorms is from the Pacific Ocean or from the Gulf of Mexico (Fennessey *et al.*, 1986; Osborn and Lane, 1984). Winter precipitation results from frontal storms characterized by long duration, low intensity, and large area coverage (Nichols *et al.*, 1993; Osborn and Lane, 1984; Osborn *et al.*, 1979; Peebles *et al.*, 1981). Osborn and Laursen (1973)

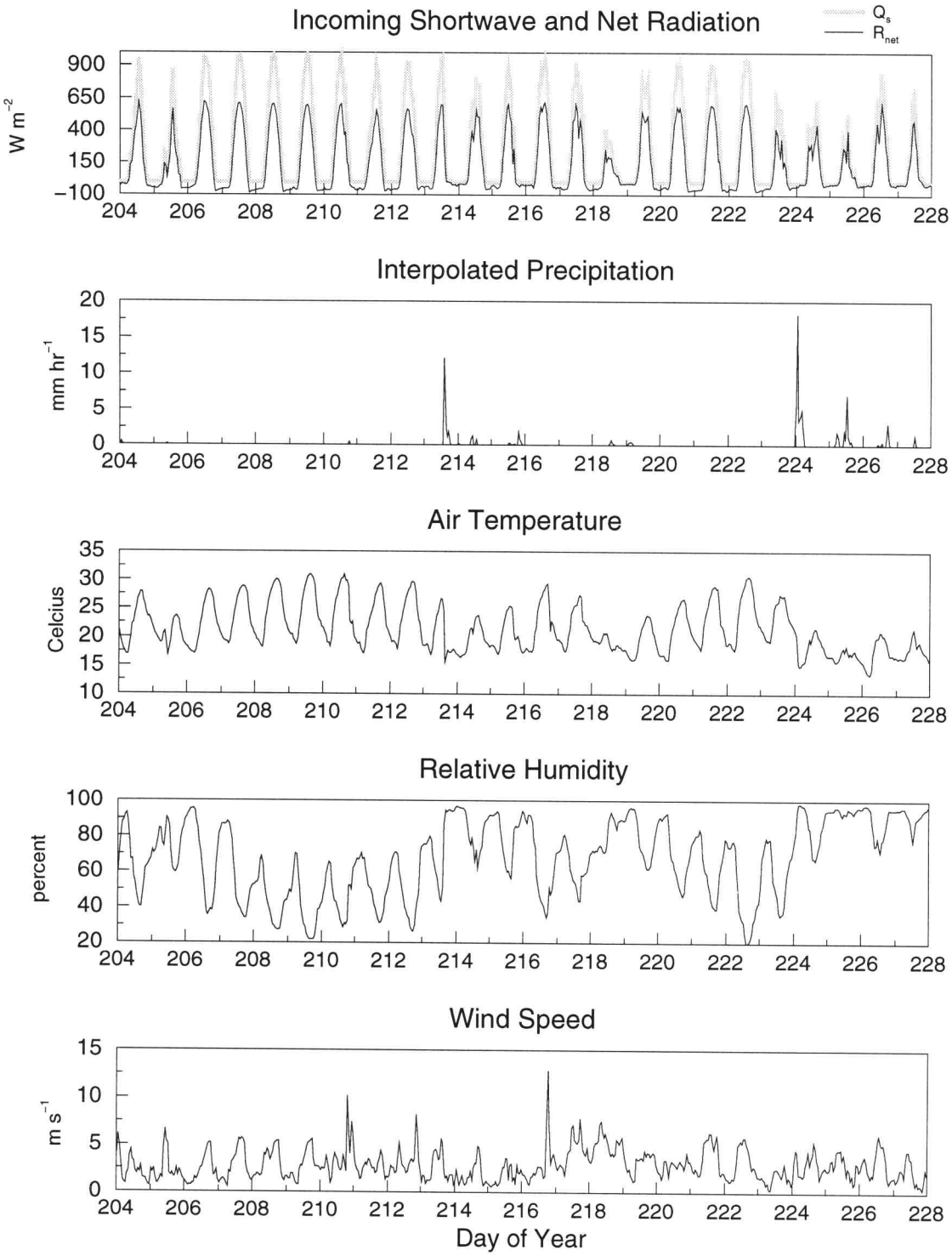

Figure 3.25: The 8 Metflux sites average (a) solar and net radiation, (b) interpolated precipitation, (c) air temperature, (d) specific humidity (Kendall and Lucky Hills sites), and (e) wind speed during the Monsoon '90 field campaign.

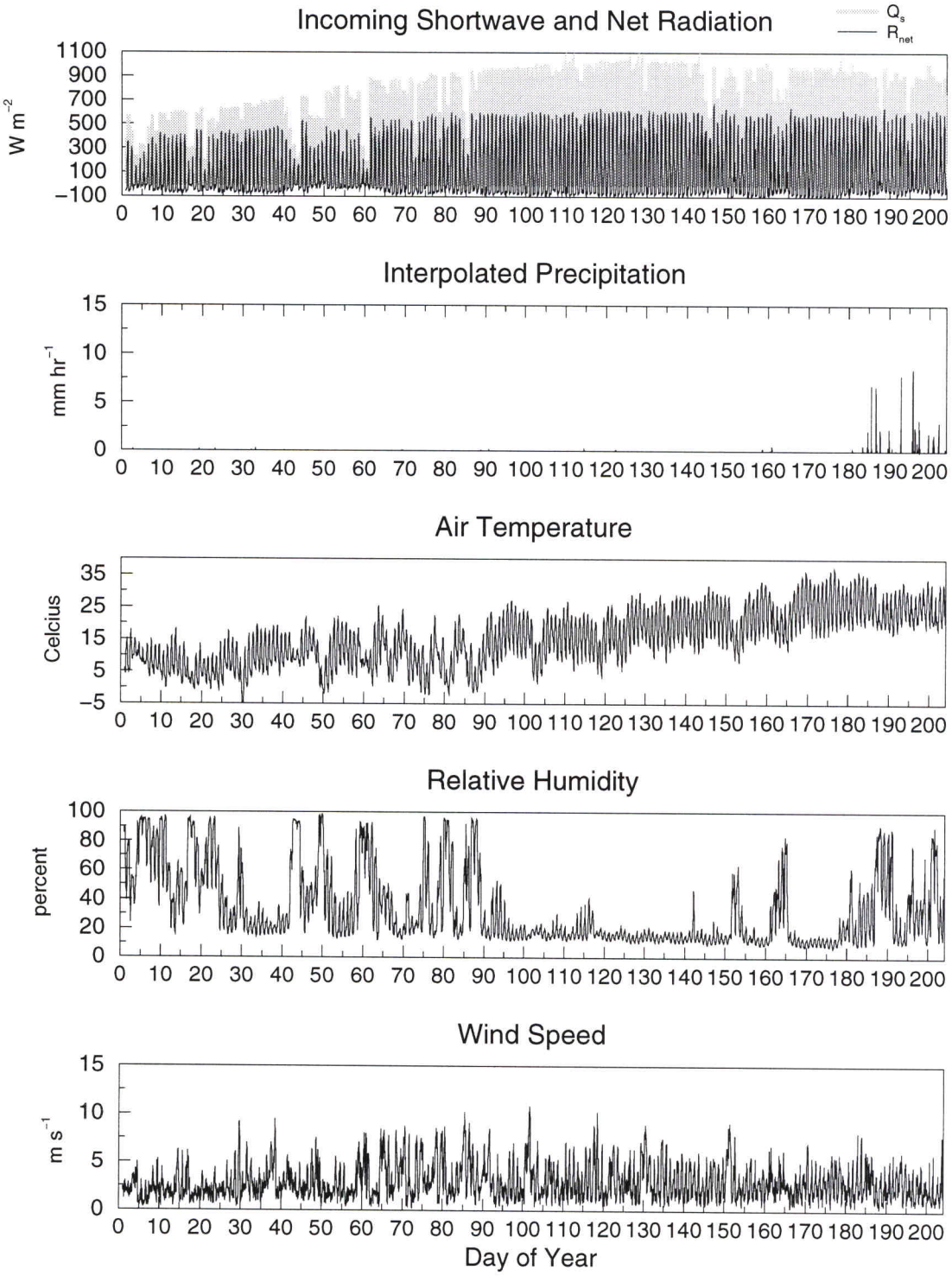

Figure 3.26: The Metflux average (a) solar and net radiation, (b) interpolated precipitation, (c) air temperature, (d) specific humidity (Kendall and Lucky Hills sites), and (e) wind speed for post-Monsoon '90 time periods.

report that such frontal convective thunderstorms are essentially non-existent in Walnut Gulch during the summer months (Fennessey *et al.*, 1986).

The extreme variability of thunderstorm rainfall and the variability of rainfall in the southwest has been discussed qualitatively by Osborn and Hickok (1968). Seventy percent of the annual precipitation of 285.0 mm (11.22 in) occurs in the summer months of June through September (Osborn and Hickok, 1968; Diskin and Lane, 1972; Osborn and Lane, 1984). Even annual average precipitation is highly variable, with the lowest annual point precipitation being about 50-60% of the highest point precipitation (Osborn and Hickok, 1968).

Historical precipitation data from Walnut Gulch are used to evaluate the spatial and temporal properties of precipitation and to quantify watershed-scale properties of the precipitation field (Nichols *et al.*, 1994; Osborn and Lane, 1984). Time-series analyzes have been used to describe temporal properties of the precipitation measured at individual rain gauges while interstation correlation analyzes are used to evaluate the spatial dependence structure of the precipitation data (Nichols *et al.*, 1993; Diskin and Lane, 1972; Osborn and Lane, 1984; Osborn *et al.*, 1979). Daily, seasonal, and annual correlations decrease with distance, although they never fall below the 99% significance level for distances up to 20 km. This is in contrast to individual storm rainfall correlation-distance relations for Walnut Gulch which show insignificant correlation beyond approximately 5 km (Nichols *et al.*, 1993; Osborn *et al.*, 1979; Fennessey *et al.*, 1986).

Historical precipitation data have also been used in climate change studies. Extreme variability between summer rainfall seasons in the 1880s was followed by a summer drought in the 1890s and early 1900s in southeastern Arizona. A small, but possibly meaningful, decline in summer rainfall has been observed in southeast Arizona over the past 100 years, accompanied by a more stable winter precipitation (Osborn and Lane, 1984). Higher than normal temperature may have played a role during specific periods of stress on the rangelands (Osborn and Lane, 1984).

Topography may also influence the variability of precipitation. Osborn and Hickok (1968) found that significantly more summer rainfall was recorded at the highest (~5000 feet; ~1525 m) elevations than on the lowest elevations. However, the largest summer rainfall (between

1955-1965) was recorded near the center of the watershed (~4500 feet; ~1370 m), which indicates influences other than watershed elevation. Generally, the record indicates a random distribution of precipitation with some possible dependance on elevation (Osborn and Hickok, 1968).

The weighting recording rain gauges used in Walnut Gulch have a 20-cm diameter orifice and record cumulative depth of precipitation on a continuous time base (Renard *et al.*, 1993). A 24-hour drum clock with an attached chart which is replaced each week (Haider, 1994). Two other types of recorders with 6-hourly and weekly charts are used on other gauges as an aid to interpretation of the start time of the events recorded on the 24-hourly charts (Haider, 1994). In a 24-hour chart one hour is divided into six partitions, while the depth scale across the chart is divided into 20 segments, corresponding to a time resolution of 10 minutes and a depth resolution of 0.05 inches (1.27 mm). Finer resolution is provided by ARS technicians via interpolation during the digitizing process through which the pen trace on the charts are converted to a time and accumulated data pairs (roughly ±5 min; ±0.01 in).

In Walnut Gulch, a rainfall event is defined to begin when rainfall is detected in just one gauge after at least one hour of rainfall inactivity over the whole watershed and continues until an hour of rainfall inactivity follows the last rainfall detected by any rain gauge. When it is not raining the line trace on the chart is horizontal. When it rains, the line changes slope and this slope change is called a 'breakpoint'.

During digitization, each breakpoint record comprises the accumulated precipitation and rainfall intensity for each interval (Haider, 1994). The breakpoint record is preceded by a header line and a maximum depth table. The choice to enter a rainfall depth as opposed to intensity arises when there is evidence that there was rain on the gage but this was not recorded due to a clock or pen malfunction. See Appendix D for the column descriptors and Appendix E for samples of an ARS rainfall record. The breakpoint times entered in the data base do not correspond to a common time base, and there is no fixed time interval between breakpoints. Breakpoints occur only when the rainfall intensity changes.

3.6.2.1 Multiquadric-biharmonic interpolation

An interpolation algorithm was used to produce spatially distributed precipitation values for the entire model domain from the available rain gauge data. Interpolation is the process by which estimates of a function are produced at unsampled locations. A variety of precipitation interpolation schemes, such as the classical Thiessen polygon method, inverse distance weighting, trend surface, kriging, and multiquadric-biharmonic interpolation have been developed. The multiquadric-biharmonic interpolation method was selected for this study because it had already been successfully used for rainfall interpolation at Walnut Gulch, in a comparison of rainfall interpolation methods (Haider, 1994) which showed that the performance of multiquadric-biharmonic interpolation was comparable to that given by kriging. Furthermore, multiquadric-biharmonic interpolation is preferable because it requires less effort and computer time than kriging.

3.6.2.2 Rainfall data checking

Eighty-five 24-hourly rain gauges were in place on the watershed over the study period, but only 82 rain gauges have complete records and were used in the interpolation. This ensured that erroneous 'zero' values were not used in the interpolation programs to bias the interpolation towards lower values of rainfall. The multiquadric-biharmonic interpolated rainfall (described in Section 3.6.2.2) pattern for the major Monsoon '90 rainfall events occurring on days 213 and 224 are shown in Figures 3.27 and 3.28. Randomly selected rain gauge totals were compared to interpolated rainfall totals made with that gage missing from the interpolation for the same grid point location as a means of checking the validity of the interpolation product; in all cases, total rainfall values differed by less than 1% (White, 1996). These differences occur when a rain gauge is not centered in a grid square, because multiquadric-biharmonic interpolation is an exact interpolation.

The interpolation of precipitation intensities to hourly time steps has the consequence of decreasing maximum instantaneous precipitation intensities which may require a respecification of the model's saturated hydraulic conductivity parameter value to ensure proper partitioning between runoff and infiltration. The use of a long (hourly) model time steps in an area with the

high-intensity, low duration storms such as the Sonoran desert coupled with a very thin upper soil zone can also be troublesome. Without soil drainage between time steps, this zone can become saturated quickly, leading to an excessive runoff prediction. These problems may be countered using a variable-length time step that shortens as precipitation intensities increase.

3.7 Assimilation data

Assimilation data are observations of model states that can be used in a data assimilation framework to correct the model's trajectory and to give improved model predictions.

3.7.1 PBMR soil moisture

NASA's Push Broom Microwave Radiometer (PBMR) collected six days (on Julian days 212, 214, 216, 217, 220, and 221) of microwave brightness temperature (*TB*) data over an 8 x 20 km area in the northeastern portion of the watershed during the Monsoon '90 field campaign (Schmugge *et al.*, 1994). The PBMR is an L-band passive microwave remote-sensing system that measures thermal emission from the surface. Emissivity at longer microwave wavelengths (>10 cm) is a function of moisture content because of the large dielectric contrast between water and dry soil. The emissivity decreases as the soil moisture increases. This decrease in emissivity is an approximately linear function of soil moisture content which is affected by factors such as soil texture, surface roughness, and vegetation cover. Texture affects the slope of the relation between emissivity and soil moisture but not the range of variation. While both roughness and vegetation reduce the range of variation, vegetation is more significant because it can totally obscure the soil surface if it is present in sufficiently large amounts. Fortunately, Walnut Gulch has minimal vegetation; hence this remote-sensing technique works well.

The spatial variations of soil moisture after rainfall were observed and mapped with PBMR during Monsoon '90 (Schmugge *et al.*, 1994). The decreases in *TB* were well-correlated with the rainfall amounts with a correlation coefficient R^2 of 0.9, and the comparison of *TB* with directly measured soil moisture was also good with R^2 value of 0.8. For the soil moisture, there was some dependence on the location at which the comparison was made, which may be due to soil or vegetation variations between sites. There is considerable variation in the

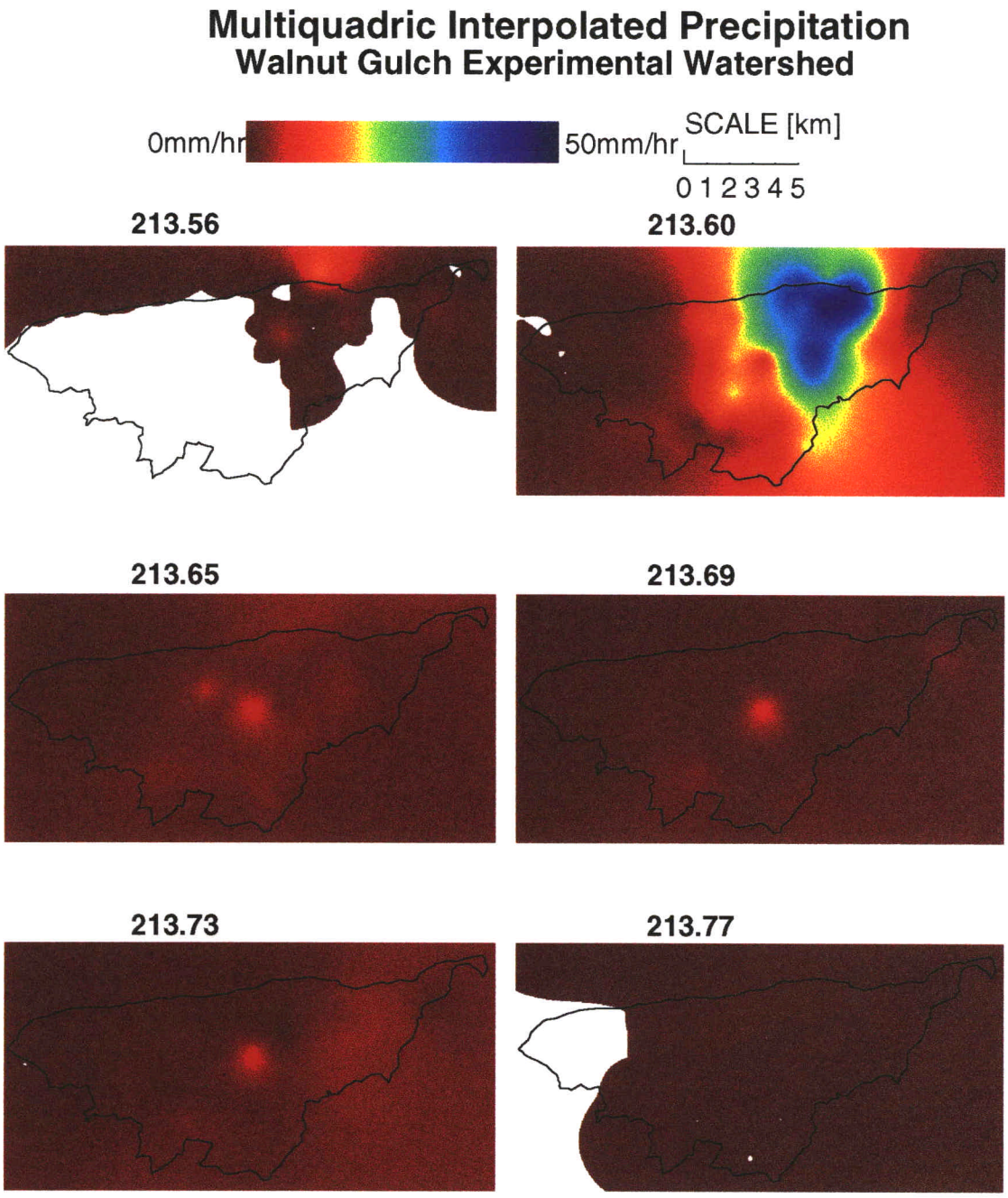

Figure 3.27: Hourly multiquadric interpolated rainfall for a storm on day 213 of Monsoon '90.

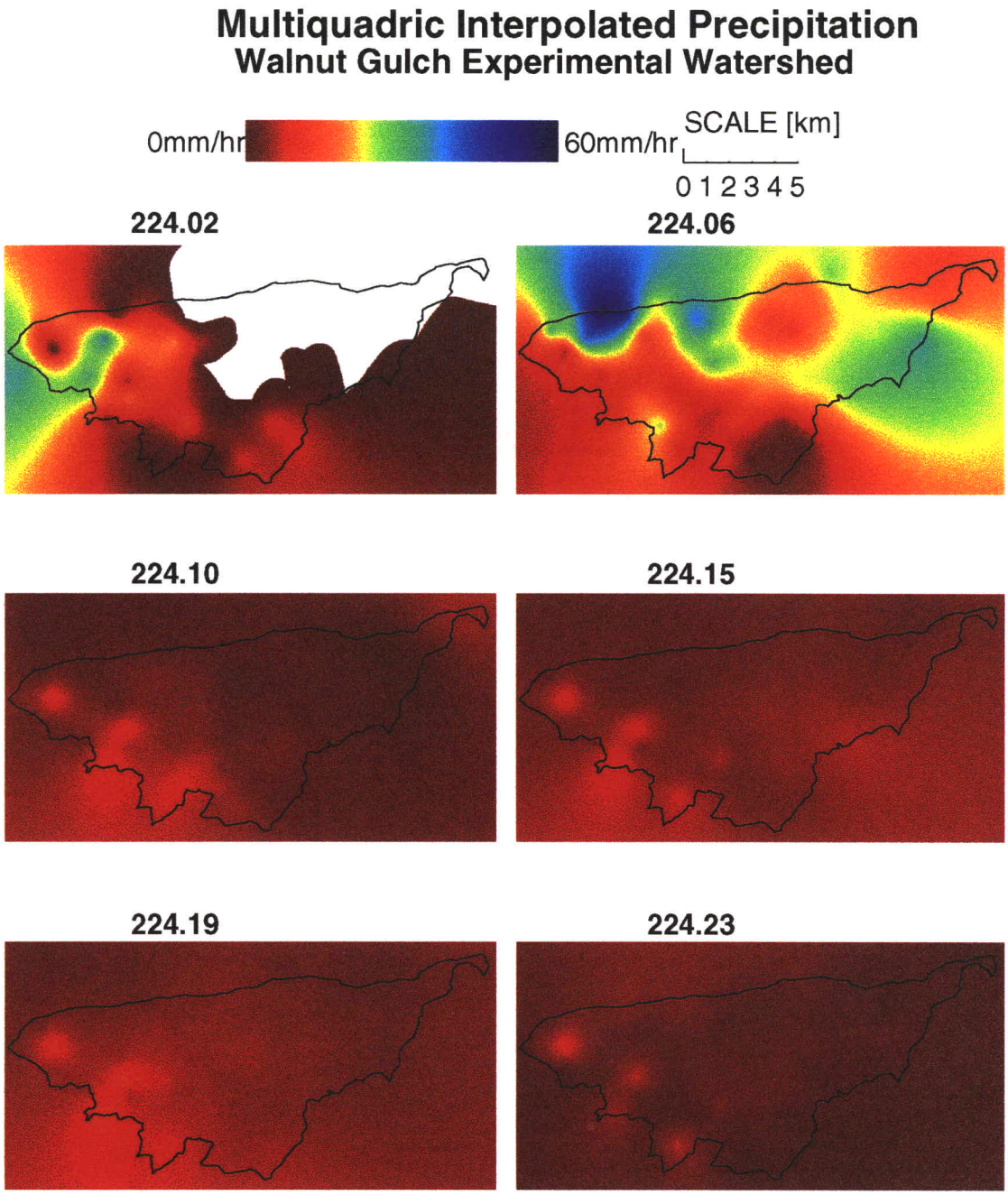

Figure 3.28: Hourly multiquadric interpolated rainfall for a storm on day 224 of Monsoon '90.

interrelationship of brightness temperature and gravimetric soil moisture, with Metflux sites on the western end of Walnut Gulch (sites 1 and 8) showing greater sensitivity to soil moisture than those on the eastern end of Walnut Gulch (sites 4 and 5) (Figure 1.19). In general, there is little correlation with the soil or vegetation at the calibration sites.

Variations in sensitivity of *TB* to soil moisture from site to site remain to be explained and are currently under study. One of the factors to consider is that of rock fraction. The rock volume varies from 10% to almost 50% between sites, and can have a significant effect on the microwave response (Jackson *et al.*, 1992). The authors also plan to analyze the day-to-day differences in soil moisture as a means of estimating the direct soil evaporation. For example, the moisture differences around Metflux site 5 from day 216 to 217 indicate soil evaporation of 3-4.4 mm, which is in reasonable agreement with the values determined from the surface flux data (Schmugge *et al.*, 1994).

3.7.1.1 Soil moisture inversion

Small sections of the PBMR images have been inverted to soil moisture (Goodrich *et al.*, 1994), but soil moisture maps had not made from the entire Monsoon '90 PBMR images prior to this study (Schmugge, 1995).

Linear relationships were established between microwave brightness temperature and gravimetric soil moisture collected during the aircraft overpasses at each of the Metflux sites (Figure 1.19). An inverse distance weighting scheme was used to invert each of the microwave brightness temperature images (Figure 1.18) to soil moisture (Figure 3.29). This results in a spatially distributed conversion algorithm that may account for some of the variation in vegetation cover and soil roughness. However, an inversion algorithm based on spatially distributed vegetation and roughness may be preferable and was pursued as an alternative.

An attempt was made to develop a PBMR brightness temperature to soil moisture inversion algorithm that included vegetation and roughness corrections. The central complication with developing such an algorithm is that although the calculation of brightness temperature from soil moisture is relatively straight forward, the non-linear nature of the algorithm means it is impossible to uniquely solve for soil moisture from brightness temperature. Consequently, a

parameter search procedure was employed, which calculates the error between the observed brightness temperature and that calculated based on a guessed soil moisture value. Then, using an automatic numerical method, this error is minimized by selecting successively better soil moisture values in the forward calculation. When the error has reached its most likely minimum, the final soil moisture value is taken as the inverted quantity.

The soil moisture to brightness temperature algorithm is formulated as follows (Schmugge, 1985; Schmugge *et al.*, 1992). First, using a simple dielectric mixing model, determine the dielectric constant of the soil given the soil moisture, thus:

$$k = W_c k_x + (P - W_c) k_a + (1 - P) k_t \qquad W_c \le W_t \tag{3.6}$$

with:

$$k_x = k_i + (k_w - k_i) \frac{W_c}{W_t} \gamma \tag{3.7}$$

and:

$$k = W_t k_x + (W_c - W_t) k_w + (P - W_c) k_a + (1 - P) k_t \qquad W_c > W_t \tag{3.8}$$

with:

$$k_x = k_i + (k_w - k_i) \gamma \tag{3.9}$$

where P is porosity, k_a, k_w, k_r, and k_i are the dielectric constants of air, water, rock, and ice , respectively, k_x is the dielectric constant of the initially adsorbed water, and γ is an empirical parameter:

$$\gamma = 0.48 - 0.57 WP \tag{3.10}$$

where WP is the wilting point.

Next, the reflectivity, R, is calculated using the Fresnel equations:

$$R_v = \left| \frac{\cos\theta - \sqrt{(k - \sin^2\theta)}}{\cos\theta + \sqrt{(k - \sin^2\theta)}} \right|^2 \tag{3.11}$$

$$R_h = \left| \frac{k\cos\theta - \sqrt{(k - \sin^2\theta)}}{k\cos\theta + \sqrt{(k - \sin^2\theta)}} \right|^2 \tag{3.12}$$

where the subscripts v and h refer to the vertical and horizontal polarizations of the wave and, θ is the nadar angle.

Then, the emissivity, e, is calculated from:

$$e = 1 - R \tag{3.13}$$

This emissivity is then corrected for vegetation and roughness:

$$e = 1 + (e_0 - 1)\exp(-h - 2\tau) \tag{3.14}$$

where e_0 is the smooth soil emissivity, h is an empirical roughness parameter, and τ is the optical vegetation depth, i.e.:

$$\tau = b\ w \tag{3.15}$$

where b is a plant-dependent constant, and w is the vegetation water content.

Finally, the brightness temperature, TB, is calculated from:

$$TB = \tau_{atm}(RT_{sky} + (1 - R)T_{soil}) + T_{atm} \tag{3.16}$$

Generally, this is a viable approach to inverting brightness temperature as soil moisture, and indeed many of the parameters in the inversion model can be specified as equivalent to TOPLATS parameters or predictions. Thus, the inversion algorithm could, in principle be incorporated into TOPLATS for radiance assimilation. However, there are enough empirical constants in the inversion model that direct calibration via comparison with surface gravimetric observations is still required, and for the purposes of this study first regression-based inversion technique was selected.

3.7.1.2 Correlation structure analysis

The ability of data assimilation methodologies to advect information from data-rich regions to data-poor regions is dependent on the assumption that there is some natural spatial structure (or correlation) in the data. A study of the spatial correlation in soil moisture is therefore warranted.

Loague (1992) found "tremendous variations [in soil moisture] in space and time for a relatively small catchment." northeast of Chickasha, Oklahoma, It was assessed that these variations would be "difficult, at best, to predict in either space or time." Munoz-Pardo *et al.* (1990) found that, for two rain-fed crops, the coefficient of variation ranged from 11% to 100% at a range smaller than the sampling interval to 80 m. Bell *et al.* (1980) found that the variation

of surface soil moisture at large field sites cannot be described by a single value of standard deviation or coefficient of variation.

In fact, studies of the spatial variability of soil moisture conducted at the Lucky Hills site in the Walnut Gulch watershed in 1990 and 1991 indicate negligible correlation beyond one meter (Whitaker *et al.*, 1991; Amer *et al.*, 1994). Some structure in soil moisture has been observed in this catchment: soil moisture measurements at lower elevation sites are generally wetter, and moisture penetration deeper because of preferential abstractions from overland flow during storms (Kincaid *et al.*, 1966).

All of the above is bad news from the perspective of assimilating soil moisture data, which relies on spatial correlation for observation information advection. However, the studies described above were looking for spatial structure in the small-scale variability in *point* soil moisture observations. It is the author's hypothesis that above some threshold scale of aggregation, soil moisture regains spatial structure as the micro-variations of soil and vegetation properties are averaged out. It would be very difficult and probably impossible to gather enough single point soil moisture samples to evaluate this hypothesis, but remote-sensing automatically provides the required averaging.

To test the hypothesis, the correlation structure of the PBMR data was analyzed. It was found that PBMR time series had a highly correlated spatial structure (Figure 3.30). In fact, it seems that the correlation structure extends well past the 15-km-long measurement area. The correlation could be projected to extend to ~60 km, assuming a linear correlation structures. It is also seen that including more points in the time series improve the definition of the spatial structure, and that the conversion from brightness temperature to soil moisture did not change this spatial relationship.

A geostatistical analysis carried out under the supervision of the author (Hartman, 1995) showed that the PBMR-derived soil moisture may have a correlation structure that varies with time. The first PBMR observations during a dry day shows a disorganized variogram spatial pattern, then after a large precipitation event the variogram becomes very organized that degrades with drydown (Figure 3.31).

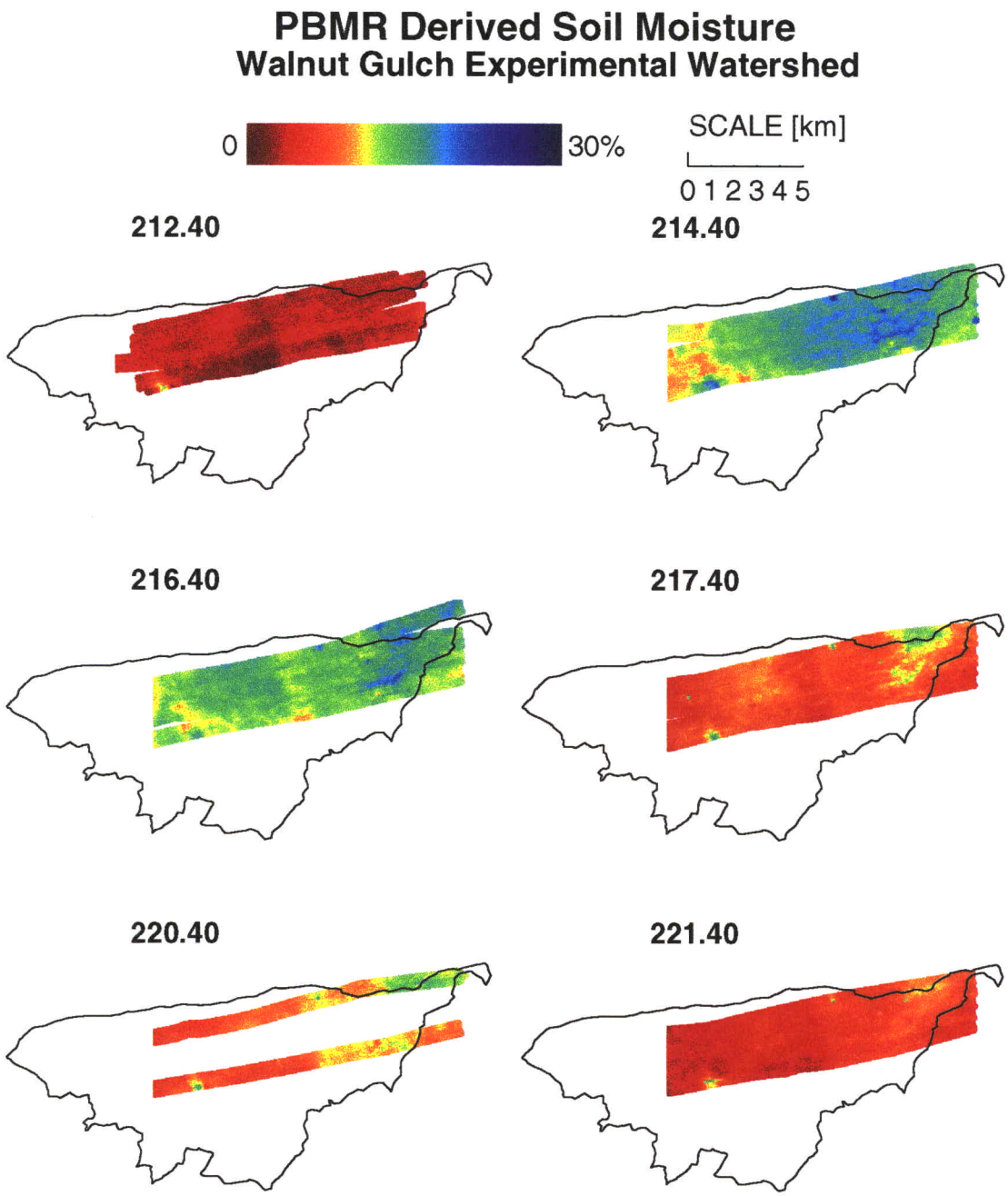

Figure 3.29: PBMR-derived soil moisture for Monsoon '90.

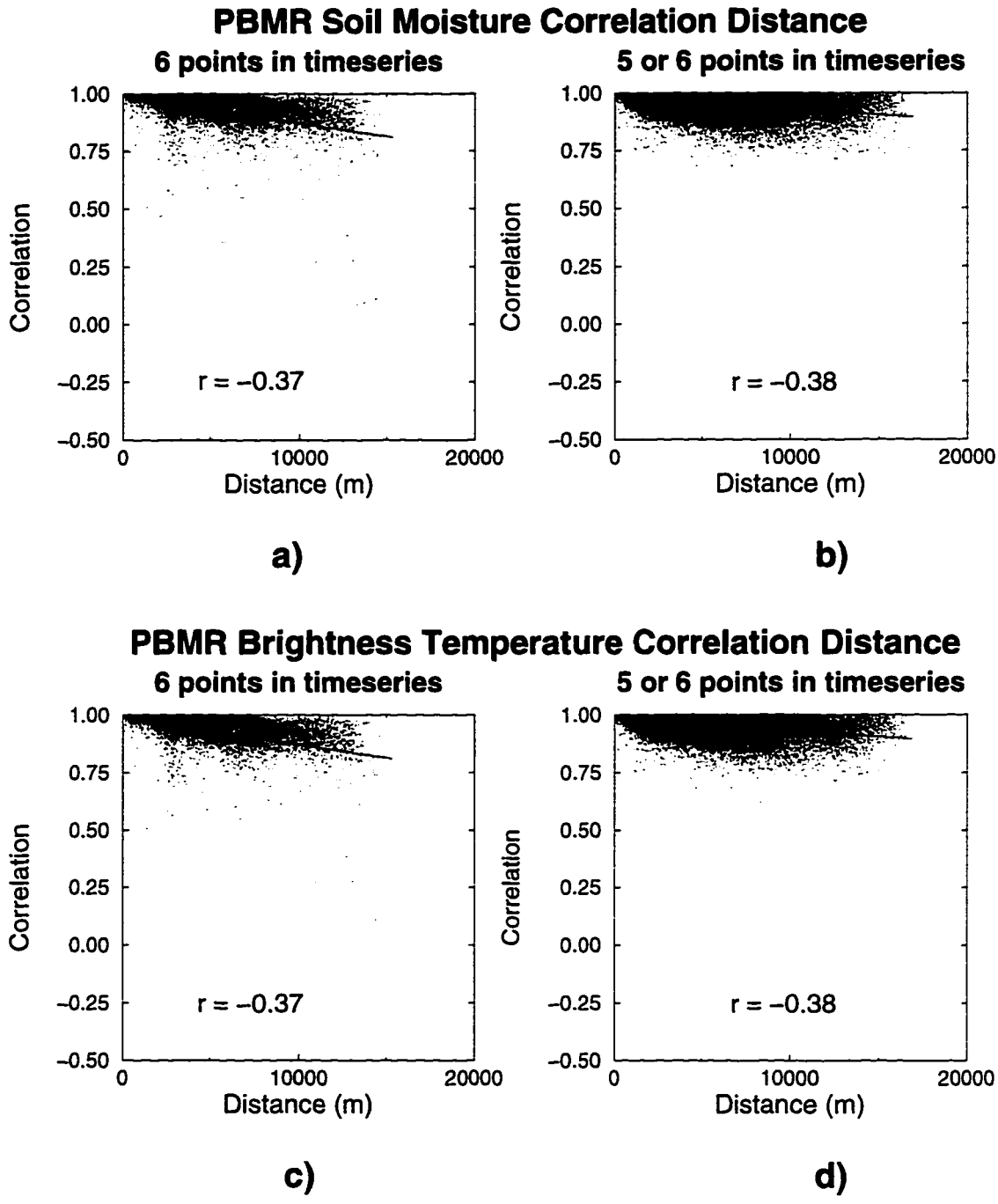

Figure 3.30: Correlation distances for (a) PBMR soil moisture 6 point time series; (b) PBMR soil moisture 5- and 6-point time series; (c) PBMR brightness temperature 6-point time series; (d) PBMR brightness temperature 5- and 6-point time series. Data presented are a randomly selected 0.01% selection of the total.

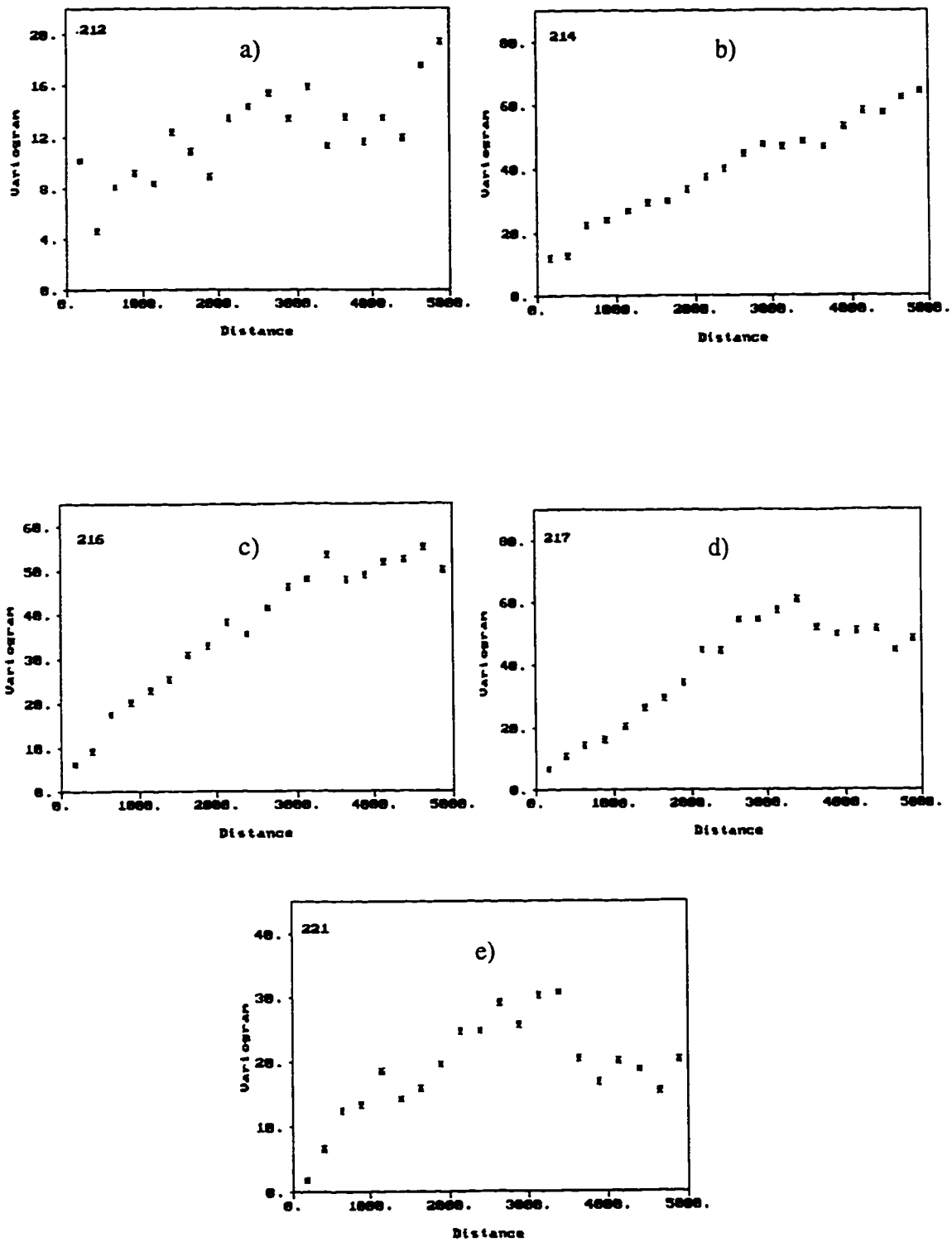

Figure 3.31: Variograms for a 1 percent selection of day a)212, b)214, c)216, d)217, and e)221, PBMR brightness temperatures.

This geostatistical analysis also showed little correlation between spatially variable soil and vegetation parameters, except that it is suggested that clay and sand content have an inverse relationship. In addition, the correlation between PBMR images improves for images on day 217 and 221, suggesting that most of the drydown occurred by day 217.

3.8 Validation data

The final category of data required in this study was validation data. These observations which are independent of model predictions help verify model results or help calibrate model parameters.

3.8.1 Gravimetric soil moisture

During Monsoon '90, 3 replicate gravimetric surface soil moisture samples were collected daily at the eight Metflux sites (Schmugge *et al.*, 1994). These were converted to volumetric soil moisture using bulk density measurements made at each site. The surface gravimetric time series for all 8 Metflux sites are shown in Figure 3.32.

3.8.2 Resistance soil moisture

The only continuous soil moisture measurements made during Monsoon '90 were those made with resistance sensors (Kustas and Goodrich, 1994). They were placed at 2.5 cm and 5 cm below the surface at all 8 Metflux sites. These sensors are generally difficult to calibrate and tend to drift. Therefore, following the recommendation of Stannard *et al.* (1994), the resistance data were calibrated against the gravimetric samples and then used to interpolate gravimetric data to each model time step. The Monsoon '90 resistance data are shown in Figure 3.33.

3.8.3 TDR soil moisture

TDR soil moisture observations are of critical importance to this study because they are the only soil moisture profile observations made during Monsoon '90. TDR measurements were made at daily intervals and at multiple depths down to 0.5 m at 2 of the Metflux sites (Kustas and Goodrich, 1994). For this study, all measurements in the surface of root zones defined in

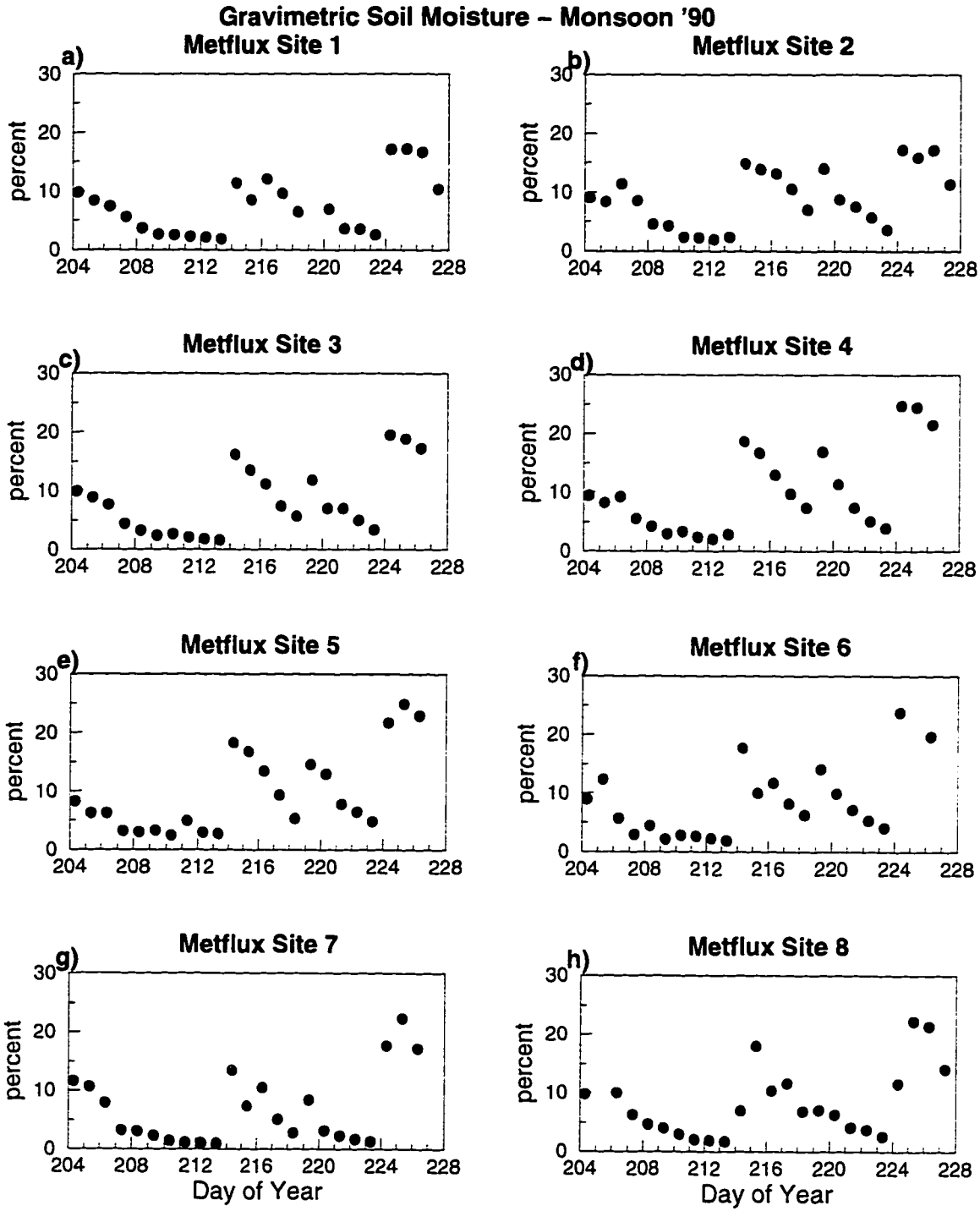

Figure 3.32: Monsoon '90 gravimetric time series for each Metflux site.

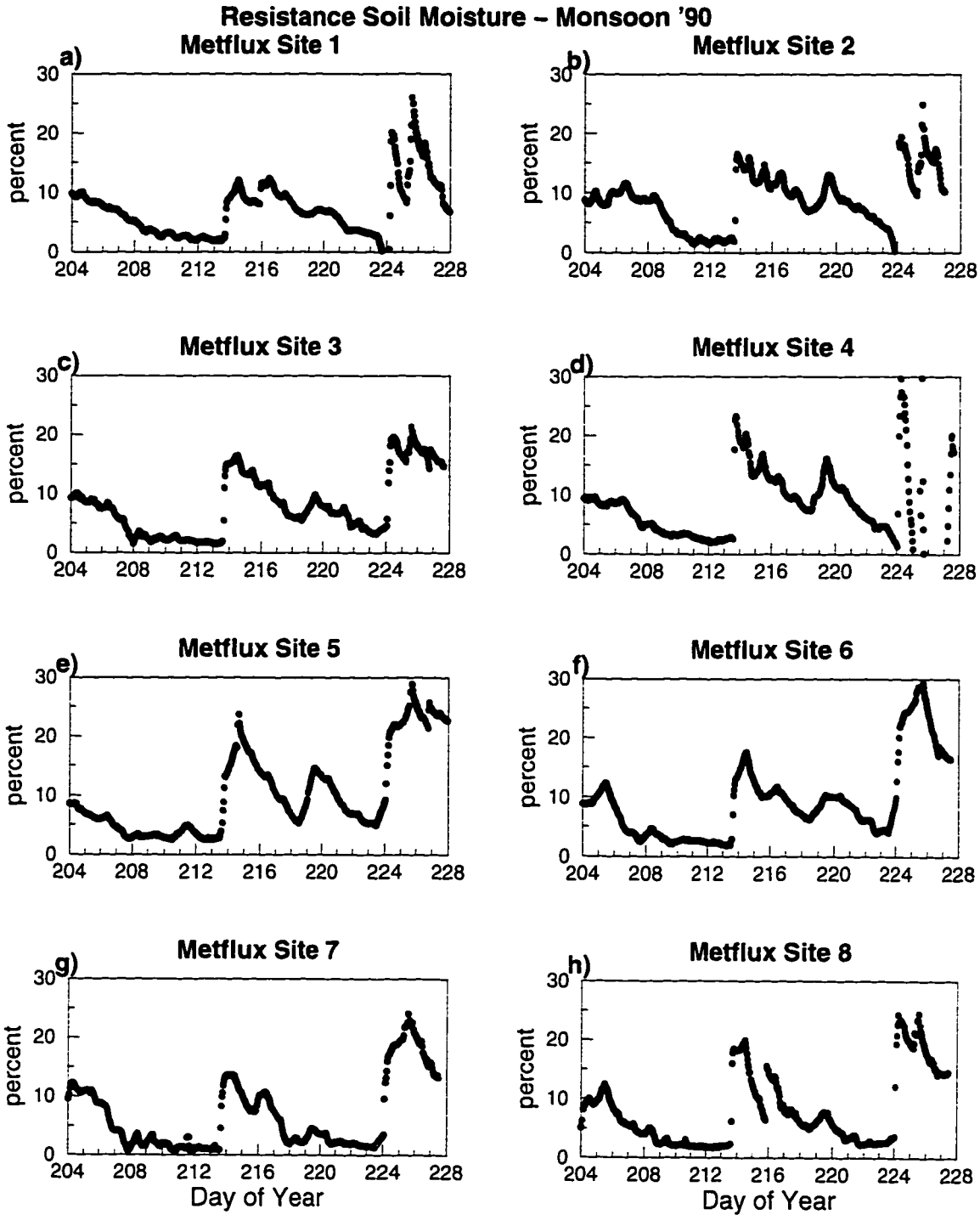

Figure 3.33: Monsoon '90 resistance soil moisture at each Metflux site.

TOPLATS were averaged for easy comparison with model results. The TDR data are plotted in Figure 3.34.

3.8.4 Surface energy fluxes

Estimating the sensible and latent heat fluxes requires (sometimes difficult) difficult micrometeorological measurements and the determination of moisture and plant parameters. As Chehbouni *et al.* (1994) state, accurate partitioning of available energy at the surface into sensible and latent heat fluxes is crucial to understanding the interaction between the hydrological cycle and climate processes at regional and global scales.

The energy-balance for Monsoon '90 and post-Monsoon '90 was determined from measurements of net radiation, R_n, soil heat flux, G, and estimates of sensible heat flux H by either eddy covariance (EC) or temperature variance (σT) methods. Consequently, if one assumes energy-balance closure, the latent heat flux L_e is solved as a residual (Brutsaert, 1982), thus:

$$L_e=(R_n-G-H) \tag{3.17}$$

Here, fluxes away from the surface are negative, while fluxes towards the surface are positive.

Kustas *et al.* (1994a) found that, when using the residual approach over nonhomogeneous surfaces, one can expect errors in LE estimates to be at least 20%, regardless of the technique used for providing H. Kustas *et al.* (1994a) reported that in unstable conditions, estimates of H and LE obtained by the variance method were within 20% of EC measurements which they considered to be satisfactory.

In the study by Stannard (1994), comparison of sensible and latent heat fluxes measured by the gradient-measuring and eddy correlation flux systems indicated that lower values of the Bowen ratio (H/LE) were obtained with a 9 m tower than with a 2 m tower on which eddy correlation measurements and a gradient-measuring system were installed. This dependence of measured fluxes on sensor height was supported by the results of a one-dimensional diffusion-area model, which indicated that measurements from the 2 m tower with eddy correlation and gradient-measuring systems were more heavily weighted toward the drier and less-vegetated ridge top conditions, whereas the eddy correlation measurements at the 9 m tower were sampling

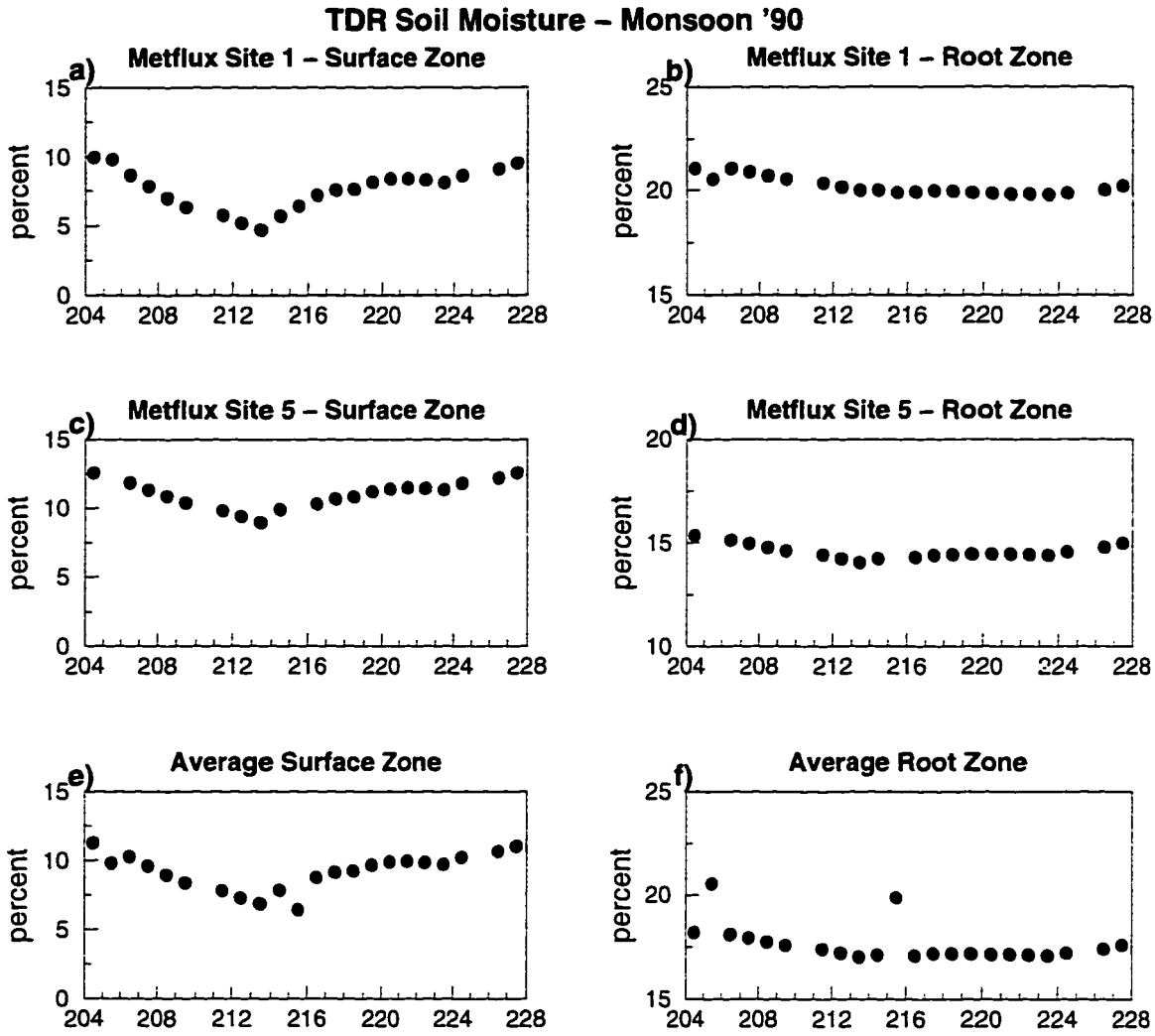

Figure 3.34: Monsoon '90 TDR observations at Metflux sites 1 and 5.

both the more vegetated ephemeral channels as well as the ridges (Stannard *et al.*, 1994; Kustas and Goodrich, 1994).

The greater leaf area in valleys partitioned more available energy into *LE* and less into *H* than the smaller leaf area on ridge tops and hillsides. Similar vegetation controlled partitioning of available energy in response to topography occurs at two of the Metsites (5 and 6). Regression analysis supports the above suggestion, but lack of energy-balance closure reduces confidence in the data. There is energy-balance closure at site 7, which has more uniform vegetation density and which produced more uniform flux distributions than at other sites. Hence, a logical conclusion is that *ET* from valleys is greater than from ridge tops and hillsides, and that the contrast between the two probably increases during monsoons. Bowen ratios are greater on sparsely vegetated ridge tops and hillsides than in densely vegetated valleys (Stannard *et al.*, 1994).

The spatial correlation structure of the sensible heat flux measured by the temperature variance method, the equivalent latent heat flux, soil heat flux, and soil moisture measured by resistance blocks are shown in Figure 3.35. This analysis shows that there is significant spatial correlation in these measurements within the watershed, but that the correlation degrades similarly with distance in each case. This result supports the validity of averaging meteorological forcing data and flux observations across the watershed.

3.8.4.1 Comparison with regional fluxes

Monsoon '90 sensible heat flux values were found to be considerably lower than those measured in two other nearby semi-arid settings at similar times of year. Comparisons of the observed sensible heat flux for Monsoon '90 with an agricultural site near Obregon, Sonora, Mexico, a riparian site at Rio Rico, Arizona and a desert site west of Tucson, Arizona (Unland *et al.*, 1996) are illustrated in Figure 3.36. There are several plausible reasons for this discrepancy between the Monsoon '90 data and that measured in other areas.

One possible reason might be the location of the Metflux sites themselves. As described above, Stannard *et al.* (1994) questioned the reliability of using the surface energy-balance

equation to evaluate the accuracy of flux measurements in hilly terrain due to source area mismatch and the possibility that horizontal flux divergence may occur.

It is equally likely that the instruments themselves are the source of these differences. The eddy correlation systems employed through Monsoon '90 and post-Monsoon '90 used vertically mounted 'Gill' propeller anemometers to measure the vertical wind velocity. In comparison studies between sensible heat flux estimated via eddy correlation systems equipped with both sonic- and Gill-type anemometers, Blanford and Gay (1992) reported that the Gill-type anemometer was less responsive to changes in vertical wind speed than was the sonic anemometer. This was particularly true during stable conditions, where the propeller had to overcome inertial forces if it stalled, as compared to the instantaneous response of the sonic anemometer. They determined that, during stable conditions, the Gill-type eddy correlation system estimated 74% of the sensible heat flux estimated by the sonic eddy correlation system. Similarly, during unstable conditions, the Gill-type eddy correlation system estimated 91% of sensible heat flux estimated by the sonic eddy correlation system. Because the Gill-type eddy correlation systems have been continuously used to estimate sensible heat flux at the Walnut Gulch Experimental Watershed over the study period, the sensible heat flux is believed to be underestimated.

Kustas *et al.* (1994c) showed that, during unstable conditions, the sigma-T estimates of sensible and latent heat flux were within 20% of the traditional Gill-type eddy correlation estimates. The sigma-T method of determining the sensible heat flux is generally regarded as being valid only during unstable conditions; therefore, a continuous energy-balance based upon the sigma-T method should be considered suspect. The good agreement between the Monsoon '90 sigma-T and eddy correlation estimated sensible heat flux as plotted in Figure 3.37, however, is in and of itself disconcerting because if the sigma-T method is 'suspect', it follows that the eddy correlation must similarly be 'suspect'. Closer scrutinizing of the procedures used showed that the estimates of sensible heat flux made with the sigma-T and eddy correlation methods were actually calibrated against the sonic anemometer based eddy correlation method, which explains their close agreement (Kustas *et al*, 1994a).

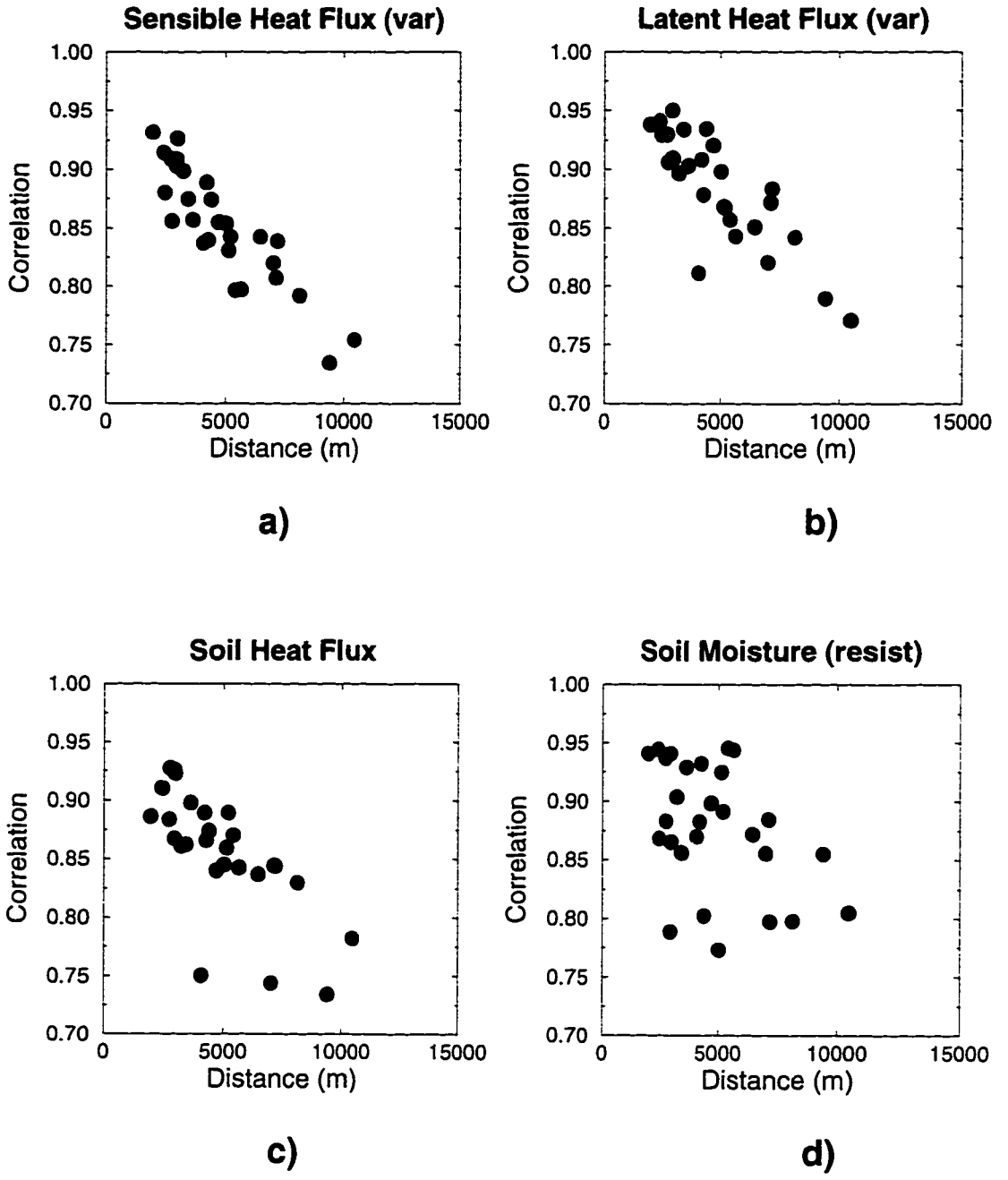

Figure 3.35: Correlation distances for time series of temperature variance sensible and latent heat flux, soil heat flux, and resistance soil moisture.

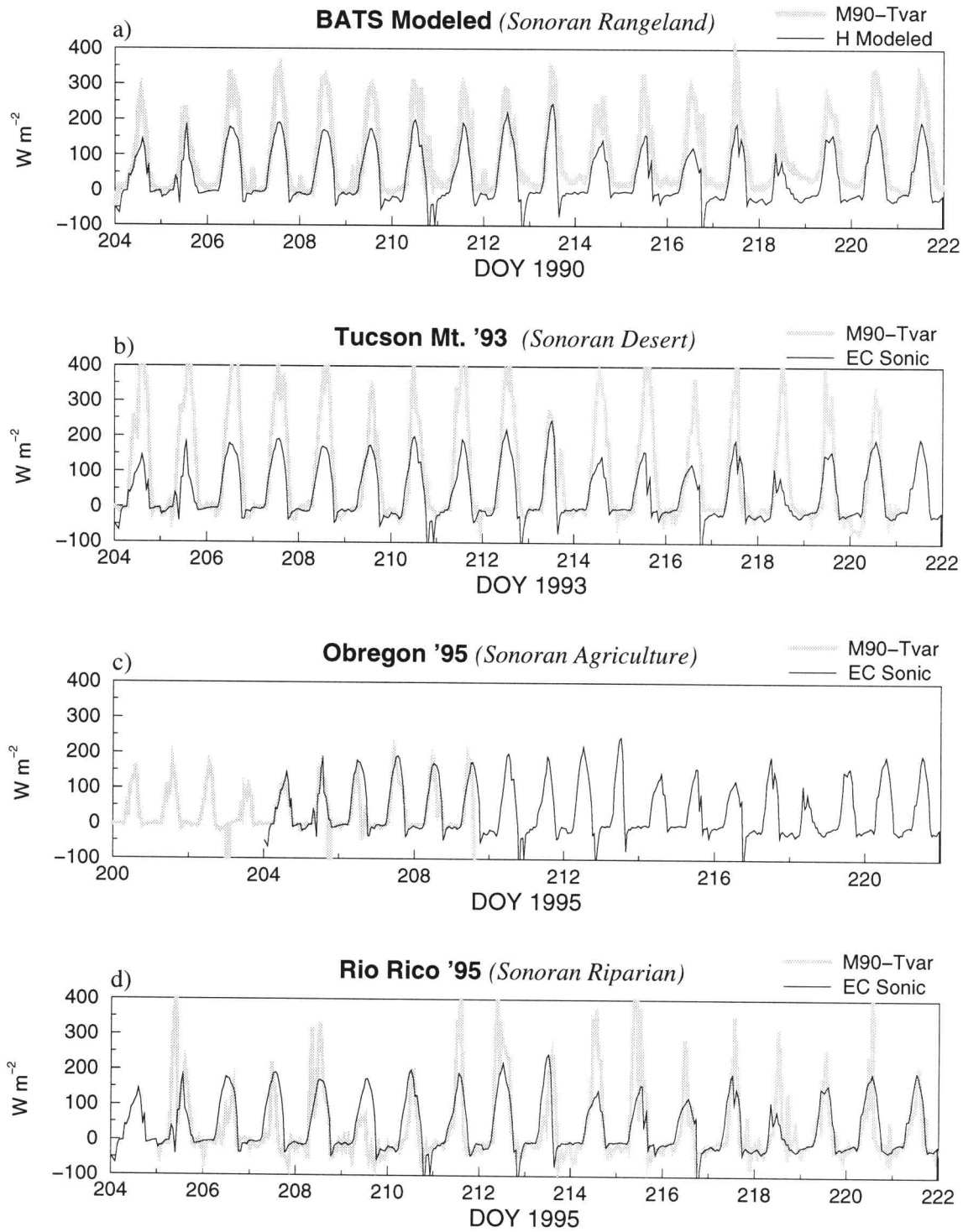

Figure 3.36: Comparison of the observed sensible heat flux of four semi-arid locations for similar seasons (a) Monsoon '90, (b) Tucson Mt. Site, (c) an irrigated crop at Obregon, Mexico, and (d) a riparian site at Rio Rico, Arizona.

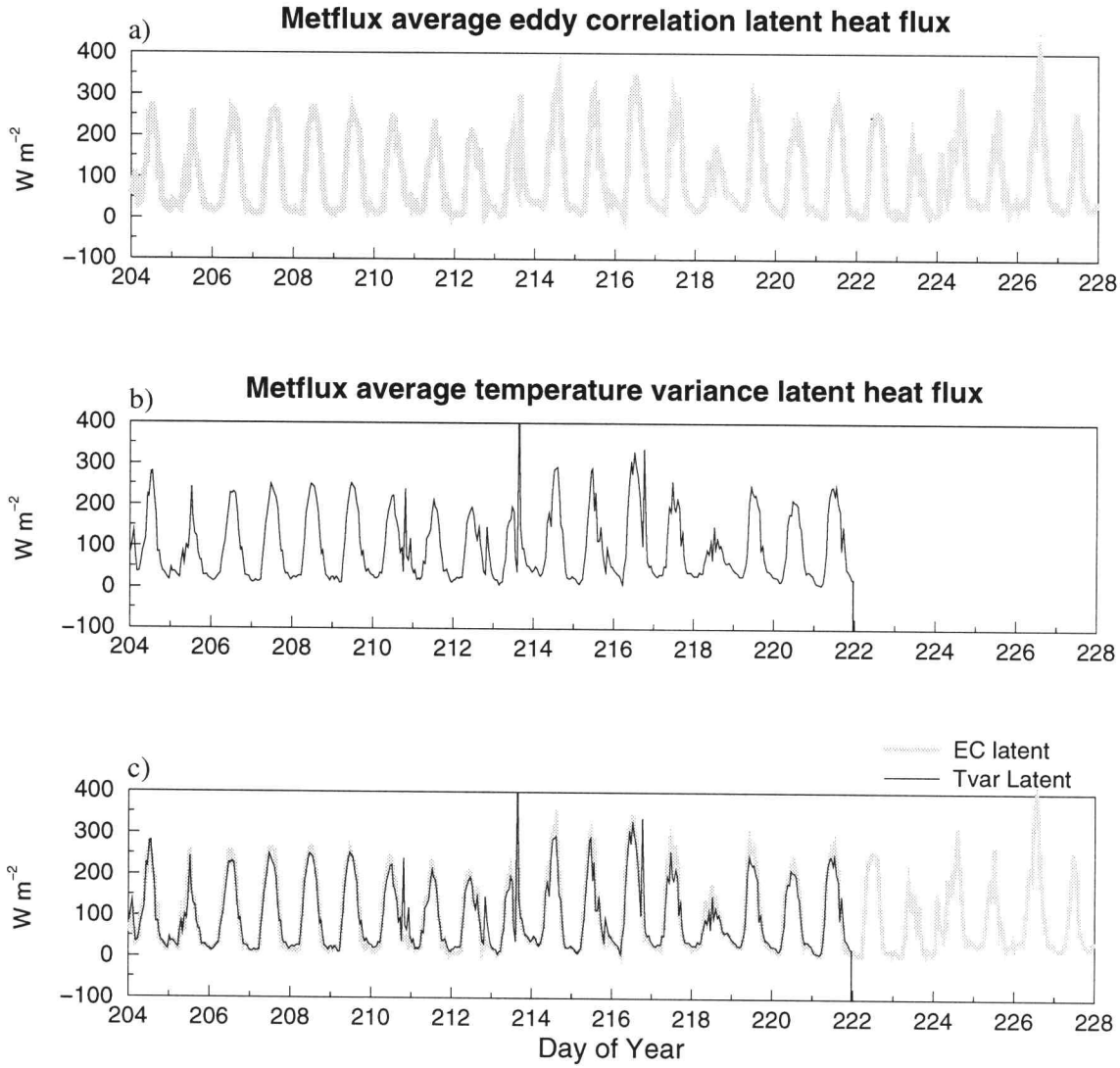

Figure 3.37: Monsoon '90 average Metsite temperature variance-derived latent heat flux versus eddy correlation-derived latent heat flux.

3.8.4.2 Monsoon '90 water-balance

Making the assumption that the Lucky Hills and Kendall 1992 energy-balances were valid only during unstable conditions (daytime), Williams (1996) determined that the estimated sensible heat flux was approximately 70% of what was required for water-balance closure.

A more detailed Monsoon '90 water-balance study showed even more severe water-balance problems consistent with underestimation of sensible heat flux. If P is precipitation, ET is evapotranspiration, RO is runoff, R is recharge, and ΔS is storage change, the water-balance requires that following relationship holds:

$$P - ET - RO - R - \Delta S = 0 \tag{3.18}$$

Water-balances are presented in Table 3.9 for hourly sensible and latent heat fluxes from both EC and σT measurement systems, for two different time periods, and for both interpolated and non-recording precipitation, assuming that recharge is zero. The water-balance over the period between day 204 and 221 starts and ends with approximately the same dry soil moisture regime and there is one large storm over this period. In contrast, the period between day 204 and 226 ends just after a very large rain event. The two periods give inconsistent results, probably because of the inability of the ridge top soil moisture measurements to adequately quantify the full change of storage of the area. It is likely that downslope areas were wetter after this event, and also possible that water was being stored in above-ground puddles and retention areas. The day 204 to 221 water-balance data are therefore considered to be more reliable. It is interesting to note that the water-balance is basically a balance between precipitation and evaporation.

A similar water balance was performed for the whole Walnut Gulch watershed as opposed to the micrometeorological site water balance described above. This water balance also suggested that the measured sensible heat flux was underestimated by a factor of 2.5.

Based on the above described water-balance study, it appears that the sensible heat flux in underestimated by about 100% leading to a 40% overestimate of latent heat flux. Williams, (1996) found similar results for a daily average Walnut Gulch water-balance that excluded nighttime data, when the sensible heat fluxes needed to be adjusted upwards by 54%.

Shuttleworth, (1996) suggested separate correction factors may be appropriate in stable (night) and unstable (day) conditions with a large correction in stable conditions and a smaller

correction in unstable conditions. This correction methodology is sound because Monsoon '90 observations show a slightly negative sensible heat flux at night (resulting in a unrealistic dew fall at night). However, to impose a correction that is largest at night and that meanwhile increase the overall sensible heat flux, the night-time sensible heat flux would need to be significantly increased. To support this large night-time sensible heat flux and to get the water-balance correct, a larger dew fall would need to occur at night; this is not observed. A constant correction methodology was used that instead assumes a very small or zero night-time evaporation flux.

3.8.4.3 Correction methodology

In an attempt to identify 'correction' factors for the Monsoon '90 fluxes, a summary of the Monsoon '90 water-balance at Metflux sites 1 and 5 was made:

$$P - R - ET - \Delta S - Q = 0 \tag{3.19}$$

$$36 - 0.00003 - 60 - 0.007 - 0 = -24$$

Table 3.9: Monsoon '90 water-balance based on hourly flux data (in units of mm depth).

Lucky Hills	Interp. PPT	RO	ET	Calc. Storage Change	Storage Change	Too much + in - out Error	New ET	% Corr on ET	Req. ET Corr	Prev H	New H	100 = no change %corr H
Var,GRAV 204-226	-	-	-	-	-	-	-	-	-	-	-	-
Var,GRAV 204-221	36.07	0.00	60.16	-24.10	10.83	-34.92	25.24	41.95	-34.92	24.61	59.53	241.93
EC,GRAV 204-226	92.89	0.05	77.72	15.12	-3.27	18.39	96.11	123.66	18.39	26.51	8.12	30.63
EC,GRAV 204-221	36.07	0.00	63.04	-26.98	10.83	-37.80	25.24	40.03	-37.80	21.80	59.60	273.42
Kendall												
Var,TDR 204-226	-	-	-	-	-	-	-	-	-	-	-	-
Var,TDR 204-221	36.07	0.00	60.16	-24.10	-0.72	-23.38	36.78	**61.14**	-23.38	24.61	47.99	**195.02**
EC,TDR 204-226	92.89	0.05	77.72	15.12	-1.21	16.33	94.05	121.01	16.33	26.51	10.18	38.41
EC,TDR 204-221	36.07	0.00	63.04	-26.98	-0.72	-26.26	36.78	**58.35**	-26.26	21.80	48.06	**220.46**
Lucky Hills	nonrec PPT											
Var,GRAV 204-226	-	-	-	-	-	-	-	-	-	-	-	-
Var,GRAV 204-221	37.66	0.00	60.16	-22.51	10.83	-33.33	26.83	44.59	-33.33	24.61	57.94	235.47
EC,GRAV 204-226	97.09	0.05	77.72	19.32	-3.27	22.59	100.31	129.07	22.59	26.51	3.92	14.78
EC,GRAV 204-221	37.66	0.00	63.04	-25.39	10.83	-36.21	26.83	42.56	-36.21	21.80	58.01	266.13
Kendall												
Var,TDR 204-226	-	-	-	-	-	-	-	-	-	-	-	-
Var,TDR 204-221	37.66	0.00	60.16	-22.51	-0.72	-21.79	38.37	**63.78**	-21.79	24.61	46.40	**188.55**
EC,TDR 204-226	97.09	0.05	77.72	19.32	-1.21	20.53	98.25	126.41	20.53	26.51	5.98	22.57
EC,TDR 204-221	37.66	0.00	63.04	-25.39	-0.72	-24.67	38.37	**60.87**	-24.67	21.80	46.47	**213.16**

Where P is gauge-measured precipitation, R is flume-measured runoff, ET is temperature variance evapotranspiration, ΔS is TDR-measured change in storage, and Q is groundwater recharge (assumed to be zero). This water-balance shows that evapotranspiration exceeds precipitation by 40%, which is not physically realistic. Therefore, for TOPLATS model validation purposes, ET was scaled down by 40%, and H was increased by 100% to be consistent with this water-balance.

This scaling correction on ET was performed in two ways. The first, termed 'time step correction', recalculated the ET as a function of the energy-balance. The second, termed 'period correction', simply scales each previous ET value by the correction factor. The time-step correction procedure tends to produce very noisy diurnal fluctuations due to large errors in the H value being scaled up and then lumped into ET, while the period correction method did not scale up errors, producing much more realistic time series variations (Figure 3.38).

3.8.4.4 Lucky Hills 1996 eddy correlation observations

A month-long field experiment was performed during the 1996 summer monsoon season to confirm the above water-balance findings. An alternative and arguably more accurate sonic anemometer-based eddy correlation system was deployed at the Lucky Hills micrometeorological site, close to the instruments that made the measurements which were in question. These independently derived correction factors are comparable to those derived with the water-balance method (Figures 3.39 and 3.40).

The results of a soil moisture transect study are shown in Figure 3.41. There was clear evidence in these observations of a downslope increase in soil moisture and a soil moisture variation of about 5% across the fetch of the hydrometeorological instruments.

3.8.5 Infiltration and runoff

The dominant factor in runoff quantity and variability on small watersheds is the variability of rainfall (Osborn and Lane, 1969, Goodrich *et al.*, 1995, Faurés *et al.*, 1995). But in general, runoff from Walnut Gulch is more variable than the incident precipitation (Osborn and Hickok, 1968) due to highly variable pre-storm soil moisture. Osborn and Hickok (1968) determined that

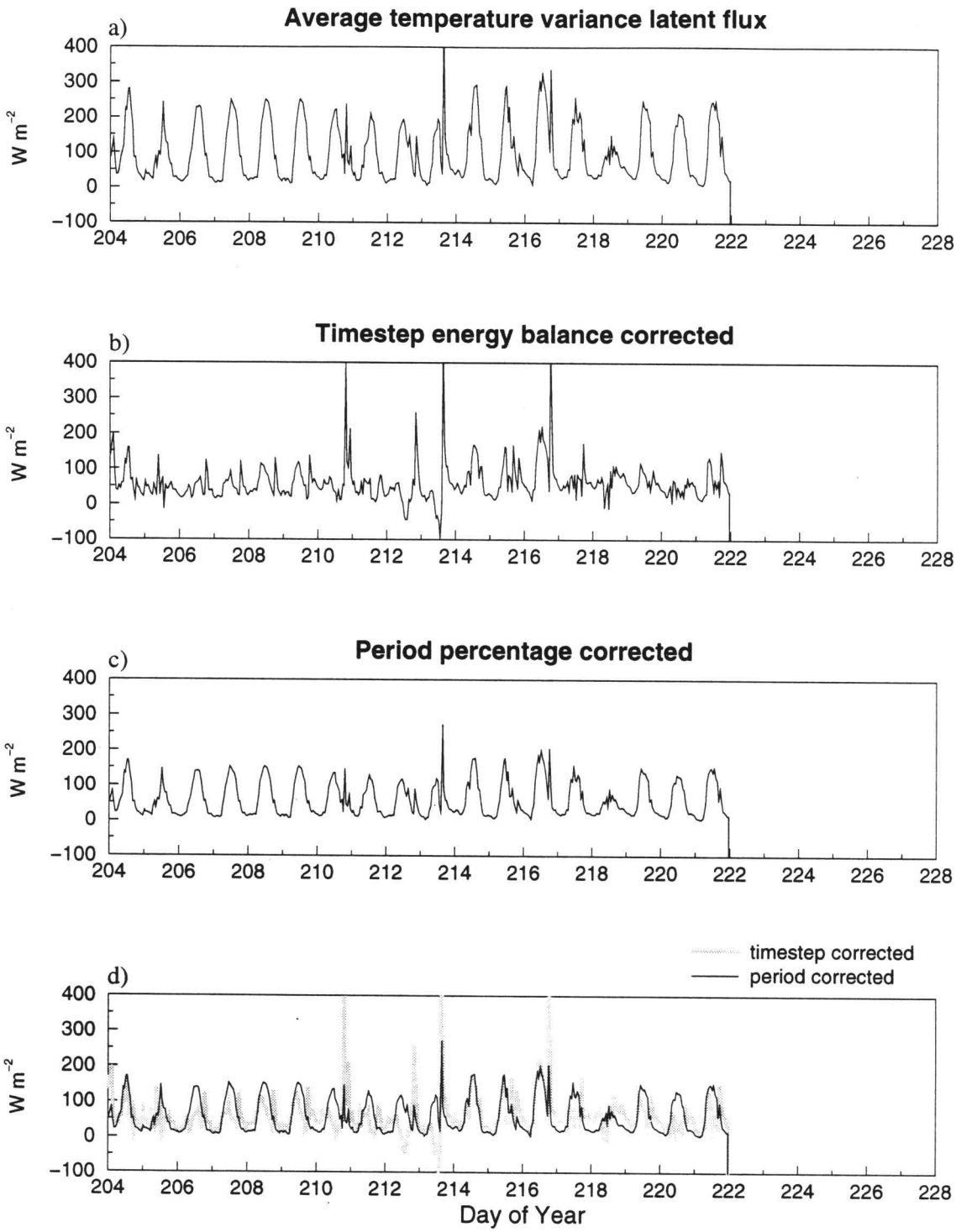

Figure 3.38: Latent and sensible water-balance corrected Monsoon '90 fluxes.

90% of the runoff and all major flood peaks for small (260 km^2 or less) rangeland watersheds in southeast Arizona resulted from thunderstorms (Osborn and Lane, 1984; Osborn and Lane, 1969; Osborn *et al.*, 1979; Fennessey *et al.*, 1986). The annual volume of runoff from the basins studied is small in comparison with the annual rainfall. Values of mean annual runoff for the various subbasins range from 0.07 to 0.75 inches (1.8-19.1 cm) (Diskin and Lane, 1972)., while the mean annual runoff at Flume 1, at the watershed outlet, is about 1000 acre-feet (1,200,000 m^3), corresponding to about 0.3 inches (7.6 mm) of runoff for the whole watershed area. This is less than 3% of the mean annual rainfall and is about 4% of the summer rainfall. There has been a suggestion to increase annual peak flows during the 100-year study conducted in southeast Arizona (Osborn and Lane, 1984). Significant winter runoff was not recorded on any subbasins larger than 20 acres during 11 years (1955-1965) of record (Osborn and Hickok, 1968; Diskin and Lane, 1972; Osborn and Lane, 1984, Goodrich *et al.*, 1996).

There is no groundwater contribution to surface flows in Walnut Gulch and ephemeral channel recession is truncated by infiltration losses to the permeable stream channel (Peebles *et al.*, 1981). Absorption of flood runoff in these alluvial streambeds (generally referred to as transmission losses) increases, and peak discharge and flow volume decrease as the bed width increases (Goitom and Woodward, 1988; Nichols *et al.*, 1994; Osborn and Hickok, 1968). Therefore, rainfall variability has a greater effect on runoff from smaller as opposed to larger watersheds (Osborn and Hickok, 1968). Subsequent evaporation of the water absorbed by transmission loss from the coarse alluvium and by transpiration from riparian vegetation greatly limits groundwater recharge (Renard, 1969).

The stream channels at Walnut Gulch are primarily coarse-grained alluvial material (Peebles *et al.*, 1981), with an estimated effective hydraulic conductivity of 25 mm/hr (Nichols *et al.*, 1994). The channels are dry 99% of the time, with runoff only occurring for short periods of time following intense rainfalls totaling a few hours per year (Diskin and Lane, 1972). Depending on watershed size, flows may last from minutes to hours (rather than days) and almost never continues past sunrise of the following day (Osborn and Hickok, 1968).

Local runoff (i.e. the runoff generated where the precipitation falls) may average about 2 inches (51 mm) per year at Walnut Gulch, but the net surface outflow from the entire basin is

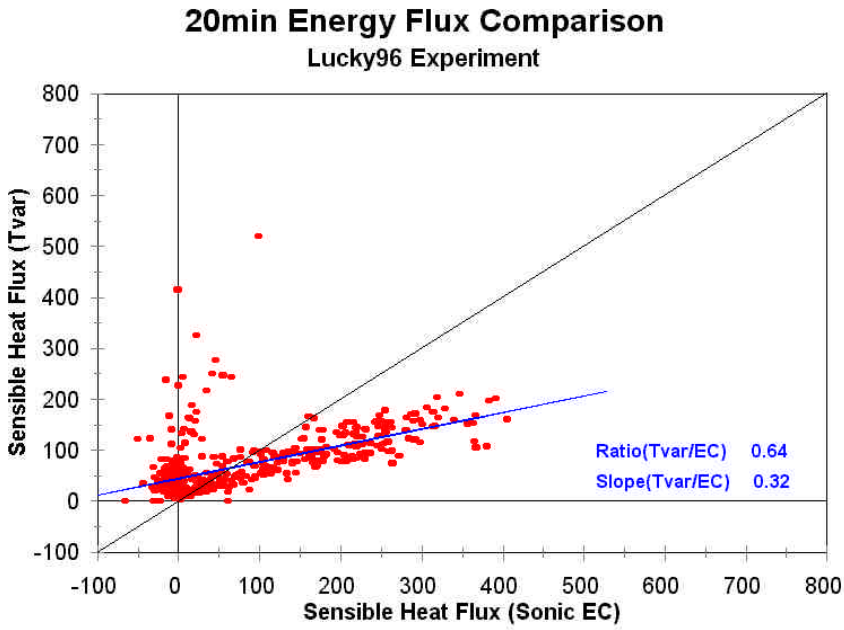

Figure 3.39: 20 minute sonic anemometer eddy correlation versus temperature variance latent heat flux.

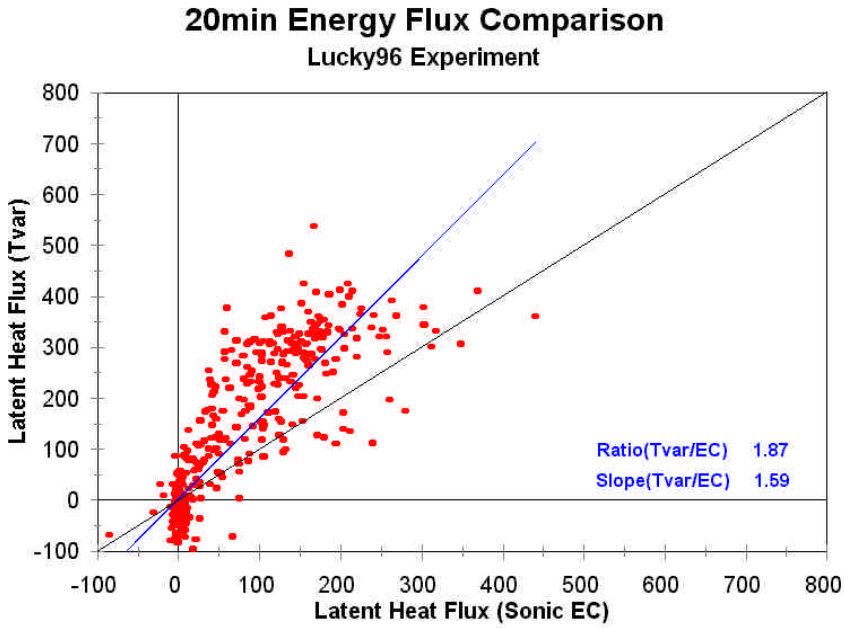

Figure 3.40: 20 minute sonic anemometer eddy correlation versus temperature variance sensible heat flux.

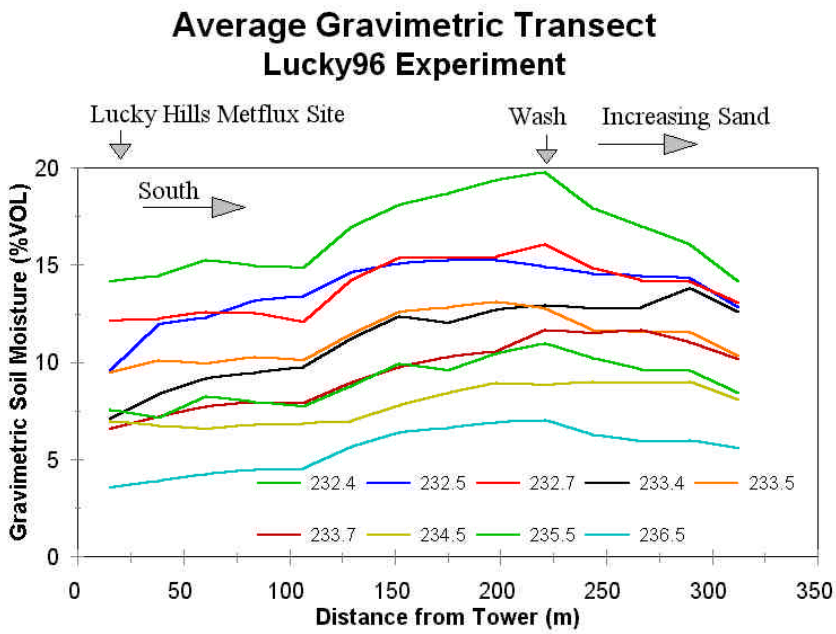

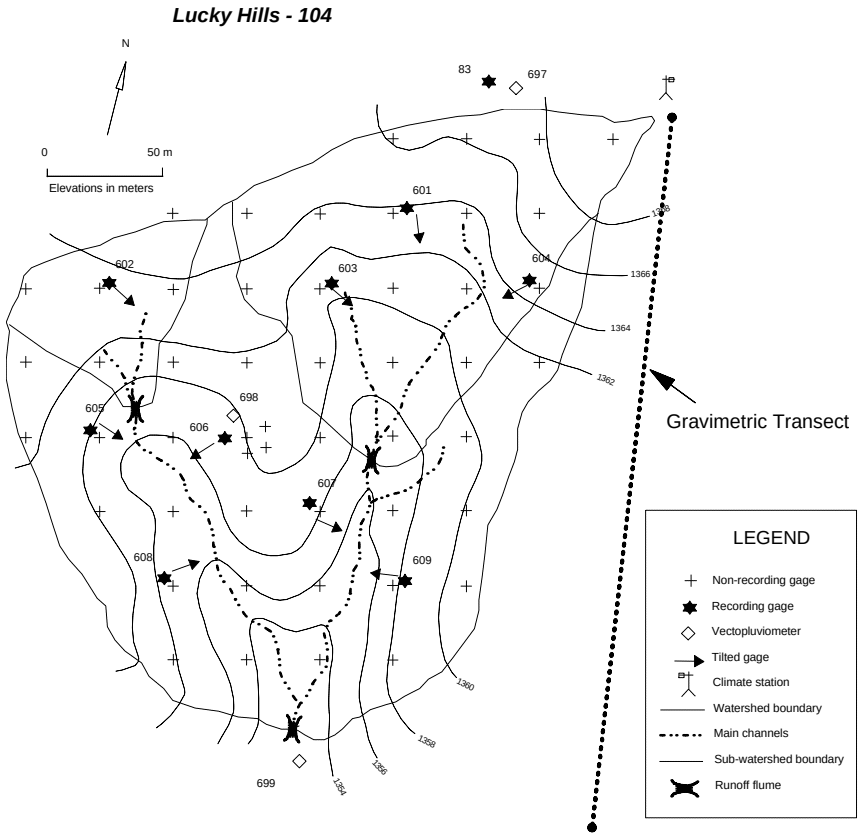

Figure 3.41: a) Downslope increase in soil moisture over several days in 1996, and b) position of transect in relation to Lucky Hills measurements.

only about 0.25 in/yr (6.4 mm/yr). The difference (1.75 in/yr or 44.5 mm/yr) is the transmission loss for the whole area. Thus, in Walnut Gulch the efficiency of the channels in conveying water to a downstream location is only 10-15% on average (Renard, 1969).

Infiltration rates vary greatly over short distances, and this spatial variability can have a profound effect on runoff (Abrahams and Parsons, 1991). Many factors influence infiltration temporally and spatially (Brakensiek and Rawls, 1994). The suction or capillary component dominates infiltration in short storms, affecting ponding time and transient loss rates. On a watershed basis, this influence is aggravated by rock content and the known spatial variability of soil physical properties and vegetation (Hawkins *et al.*, 1987).

Rock fragments affect infiltration by their presence in the soil matrix and on the soil surface. It appears that rock fragments in the soil reduce infiltration, while rock fragments on the soil surface may either decrease or increase infiltration (Brakensiek and Rawls, 1994). At Walnut Gulch, Tromble *et al.* (1974), Wilcox *et al.* (1988), and Abrahams and Parsons (1991) conducted a study on shrub and intershrub areas on semi-arid hillslopes and found a negative correlation between infiltration and stone cover and a positive correlation between infiltration and plant and litter covers. Conversely, Grant and Struchtemeyer (1959), Jung (1960), Dadkhah and Gifford (1980), and Simanton *et al.* (1984) found a positive correlation between infiltration and rock cover. Wilcox *et al.* (1988) and Tromble *et al.* (1974) suggested that infiltration rates are higher under shrubs than between them because decomposing organic matter aids the development of a permeable soil surface, and plant material intercepts rainfall. Abrahams and Parsons (1991) concluded that vegetation is the major control of soil infiltrability, and that rock cover is negatively correlated with infiltrability only because low vegetal covers are associated with high rock covers. Poesen *et al.* (1990) showed that the sign of the correlation for such surfaces also depends on whether the stones rest on the surface [then positive because stones inhibit surface sealing and enhance infiltration (Dadkhah and Gifford, 1980) or are embedded within the soil (then negative because stones reduce the proportion of surface where water can infiltrate) (Abrahams and Parsons, 1991).

Surface rock sizes have been shown to be directly related to the infiltration, i.e. smaller surface rocks decrease and large surface rocks increase infiltration (Wilcox *et al.*, 1988).

Because this study focuses on watershed-scale processes, the main runoff of interest is that for the entire watershed runoff measured at Flume 1 (Figure 3.42). For the water-balance studies described above, and certain other studies undertaken in this research, subbasin scale runoff was also of interest.

3.9 Conclusions

Three classes of data were required in this research, specifically (a) forcing data (b) assimilation data, and (c) model parameters. These data was in general acquired at (or interpolated into) the model's four-dimensional spatial and temporal grid. The forcing data are required at every model time step and, in the case of precipitation, is required as a spatially distributed time series available across the basin. Assimilated data gives information about the 'true' state of the natural system, which the model can use to adjust its own internal representation of those states, are not required at every time step, but are rather used to 'tune' the model whenever and when such data are available. The model parameters are spatial information fields which specify topography, vegetation and soil characteristics of the modeled area. Some parameter fields, such as those related to vegetation vigor, may have a four-dimensional nature.

Several important contributions to the study are described in this chapter, including: (1) the development and refinement of a set of forcing data required for implementation of long-term energy-balance modeling at Walnut Gulch; (2) specification and derivation of SVATS-specific areal average parameters; (3) derivation of spatially distributed precipitation forcing data; (4) derivation of a superior DEM and associated topographic index for Walnut Gulch; (5) derivation of crucial spatially distributed vegetation and soils data sets; (6) inversion of PBMR brightness temperature to soil moisture; (7) through comparison with regional surface energy fluxes, and through a comprehensive Monsoon '90 water-balance, the development of a correction algorithm for observed surface flux data; (8) verification of this correction algorithm with intense observations at the Lucky Hills Metflux site during the 1996 Monsoon season; and (9) a novel and extremely important analysis of the spatial structure of PBMR soil moisture.

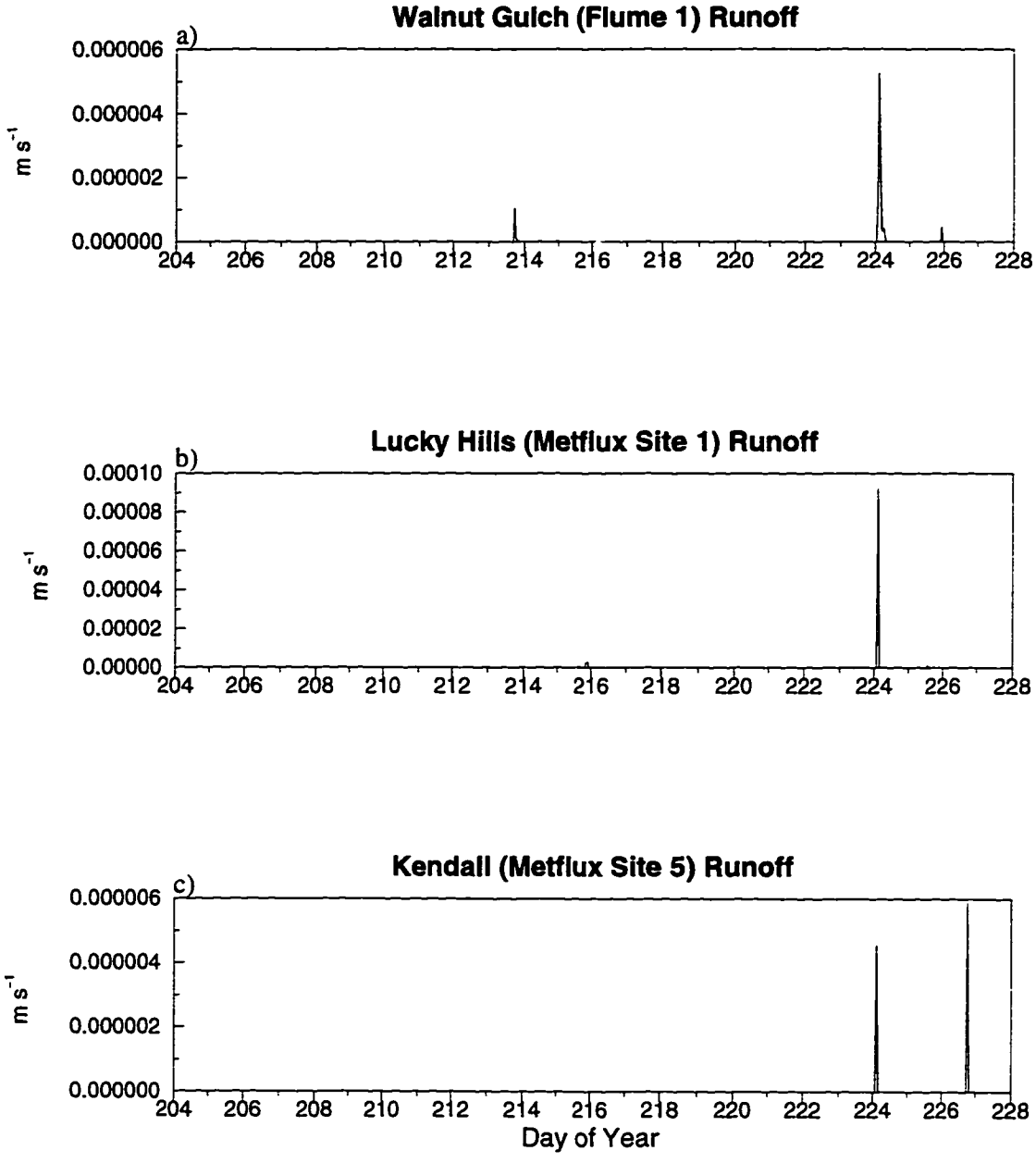

Figure 3.42: Walnut Gulch watershed average precipitation and runoff (at Flume 1) during Monsoon '90.

4. TOPMODEL AT WALNUT GULCH

4.1 Introduction and background

The TOPLATS model is based in part on concepts developed in the original TOPMODEL (Beven, 1995) and it therefore has some similar parameters and data structure. TOPMODEL assumes that the hydraulic gradient of the saturated zone can be approximated using local topographic characteristics and essentially predicts higher soil water availability in areas of hydrologic conversion and lower elevation. At Walnut Gulch, the water table is not a significant factor in surface soil moisture levels, because it is known to be about 100 m below the surface. Downslope gradients in vegetation (Stannard *et al.*, 1994; Kustas and Goodrich, 1994) and soil moisture have been observed (Figure 3.48). This effect is most likely due to reinfiltration of runoff downslope, but it might be possible to simulate this effect using TOPMODEL concepts.

To explore this possibility, a simple catchment TOPMODEL simulation was performed. The intention was to: assess the performance and shortfalls of the TOPMODEL portion of TOPLATS at Walnut Gulch; and to help derive TOPMODEL parameters for use in TOPLATS runs. TOPMODEL version 95.01 (Beven, 1995) was used. It is forced by average rainfall and potential evapotranspiration over the whole catchment. A linear routing scheme with constant main channel velocity is used. The program requires an $ln(a/\tan(\beta))$ distribution and uses exponential conductivity Green-Ampt model infiltration excess calculations.

This version of TOPMODEL was modified for automatic parameter calibration using a randomly restarting downslope simplex in multidimensions minimization technique. In this approach, $N+1$ sets of parameter values are randomly selected within a specified range (where N is the number of parameters being calibrated), and the simplex then finds the closest minimum point on the prediction error surface. Next, the simplex is restarted with the best parameter set from the previous simplex and N randomly selected parameter sets.

4.2 Model definition

The version of TOPMODEL used in this subsidiary study is identical to that described in Section 2.2.1, with the addition of the exponential conductivity Green-Ampt infiltration excess calculation (Beven, 1986) and the channel routing calculations.

The infiltration excess calculation uses the link between the spatially variable values of K_i and the saturated conductivity function. The time to ponding t_p is given by solving for the volume of infiltration at ponding $I_p=(\int_{t_p} r(t)dt)$:

$$r(t)=\frac{K_0 f}{\Delta\theta}\frac{(I_p+C)}{\left(e^{\frac{f I_p}{\theta}}-1\right)} \tag{4.1}$$

where $r(t)$ is the rainfall intensity at time t, $\Delta\theta=(\theta_s-\theta_i)$, θ_i is the initial moisture content, θ_s is the saturated moisture content, and C is the storage suction factor.

After ponding, total infiltrated flux is implicitly given by:

$$t-t_p=\frac{\Delta\theta}{K_0 f}\left[\ln(I+C)-\frac{1}{e^{\frac{-fC}{\Delta\theta}}}\left(\ln(I+C)+\sum_{n=1}^{\infty}\frac{\left(\frac{-f(I+C)}{\Delta\theta}\right)^n}{n!n}\right)-k\right] \tag{4.2}$$

where k is a constant, and I is the total infiltration at time t:

$$I=\ln(I_p+C)-\frac{1}{e^{\frac{-fC}{\Delta\theta}}}\left(\ln(I_p+C)+\sum_{n=1}^{\infty}\frac{\left(\frac{-f(I+C)}{\Delta\theta}\right)^n}{n!n}\right) \tag{4.3}$$

Overland flow is routed using a distance-related delay. The time taken to reach the basin outlet from any point is given as :

$$\sum_{i=1}^{N}\frac{x_i}{v\tan\beta_i} \tag{4.4}$$

where x_i is the length, and $\tan(\beta)$ is the slope of the ith segment of a flow path comprising N segments. The velocity parameter v is assumed constant. Hence, given v, this equation allows a unique time delay histogram to be derived on the basis of basin topography.

The precipitation forcing was the catchment average of the 40 m resolution interpolated precipitation array. Potential evaporation was calculated from Metflux data using the potential evaporation equation given by Shuttleworth (1993):

$$E_p = \frac{\Delta}{\Delta+\gamma}(R_n + A_h) + \frac{\gamma}{\Delta+\gamma}\frac{6.43(1+0.536U_2)D}{\lambda} \tag{4.5}$$

where R_n is the net radiation (mm/day), A_h is the energy advected to the water body (neglected in this study), U_2 is the wind speed measured at 2 m (m/s), and D is the vapor pressure deficit e_s-e (kPa). λ is the latent heat of vaporization of water given by:

$$\lambda = 2.501 - 0.002361T_s \tag{4.6}$$

where T_s is the water surface temperature. Δ is the gradient of the saturated water vapor content function given by:

$$\Delta = \frac{4098e_s}{(237.3+T)^2} \tag{4.7}$$

where e_s is the saturated vapor pressure, T is the air temperature, and γ is the psychrometric constant and is defined as:

$$\gamma = 0.0016286\frac{P}{\lambda} \tag{4.8}$$

where P is the atmospheric pressure. e_s is given as:

$$e_s = 0.6108\exp\left(\frac{17.27T}{237.3+T}\right) \tag{4.9}$$

e can be found through the product of e_s and relative humidity.

The topographic index was derived from the orthophoto DEM described in Chapter 3 and was binned into 49 equal intervals for use in TOPMODEL.

The automatic calibration technique (based on a randomly restarting downslope simplex minimization) was incorporated into the simple version of TOPMODEL. The downslope simplex minimization method uses a geometrical figure consisting of $N+1$ points and their interconnecting line segments (N is the number of dimensions). This figure takes a series of reflecting, expansion, or contraction steps to simulate a 'mathematical fluid blob' that moves downslope until it contracts to a point where it can no longer move farther downslope. Error in input data and model structure can cause local minimums and valleys of constant value in the error surface which make it probable that this method alone will not find the global minimum.

Thus, the simplex is restarted many times with N randomly selected parameter sets in an attempt to better locate the global minimum.

4.3 Model performance measures

The least squares objective function was chosen as:

$$e=\sum_{i=1}^{I}(\alpha_o(i)-\alpha(i))^2 \tag{4.10}$$

where i is the time step, I is the total number of time steps, e is the objective function value, α is the model prediction, and α_o is the observed value of the catchment average runoff measured at Walnut Gulch flume 1 as the objective function. With variable model parameter values, one can create an error or objective function surface which, when minimized, will provide the best parameter set.

4.4 TOPLATS calibration results and verification

The calibration was implemented with 100 random restarts that resulted in the set of optimized parameters shown in Table 4.1. Many of these parameters are not realistic for Walnut Gulch, especially the routing parameters. This most likely reflects the fact that these parameters are insensitive to Walnut Gulch hydrologic processes or that the model is either using or lacking some essential physics for simulating Walnut Gulch observations. For example, many rainfall events never produce runoff because of large channel losses. But since TOPMODEL does not have channel loss physics, this observation is re-cast in the calibrated TOPMODEL parameters as long delay times (and slow routing velocities). Interestingly, the calibrated TOPMODEL saturated hydraulic conductivity value is very similar to the value identified in Chapter 3. The root zone characteristics reflect a soil with much less water capacity than observed due to the limited effect of the water table on surface water availability. To simulate a deep water table, the storage deficit was set to a constant 0.87 m during Monsoon '90, while the calibrated wetted moisture content of the root zone was 2.91%. Through the relation $z=S/\Delta\theta$, where z is the water table depth, S is the storage deficit, and $\Delta\theta$ is the volumetric moisture deficit, it is found that the water table was calibrated to be about 30 m deep. This depth is too great to have effects on

surface moisture states; thus the predicted TOPMODEL root zone deficits do not vary spatially in response to topographic index.

Despite the generally poor comparison between the measured and calibrated TOPMODEL parameters, the performance of the model in predicting runoff is fair and evaporation is quite good. TOPMODEL overestimates evaporation by just 30% and it is able to predict the timing of the largest runoff event (Figure 4.1). Overall, these results clearly show that TOPMODEL in its original form is not appropriate for practical use in Walnut Gulch. The runoff calibration time series contains very little information, with only 3 very short runoff events. Perhaps better results might be found with a data set that contains more information for a range of catchment conditions.

Table 4.1: TOPMODEL randomly restarting downslope simplex optimized parameters.

TOPMODEL Parameter	***Calibrated***	***'Measured'***	***Units***
mainstream routing velocity	4.40	-	m/h
exponential storage parameter 'm'	0.0307	-	m
mean subcatchment value of $ln(T_0)$	2.726	-	$\ln(m^2/h)$
routing time delay per unit deficit	31.0277	-	h
available water capacity of the root zone	0.0927	0.2623	m
surface vertical hydraulic conductivity	0.02407	0.01696	m/h
wetting front suction	0.03466	-	m
wetted moisture content	2.91	32	%
subcatchment routing velocity	1.685	-	m/h
initial root zone deficit	0.0338	0.1272	m

4.5 Conclusions

The implementation and calibration of a simple version of TOPMODEL at Walnut Gulch yielded some important findings the most important being that the TOPMODEL physics are not relevant to this semi-arid watershed. Therefore, in this study TOPMODEL parameters in TOPLATS need not to be specified in a optimal manner. A deep water table effectively turns off the TOPMODEL physics. Second, the simple routing and evaporation algorithms in TOPMODEL performed fairly well, which might have implications for longer-term modeling of semi-arid catchments. Last, the downslope increases in vegetation and soil moisture observed at Walnut Gulch are not able to be predicted with the physics in this model.

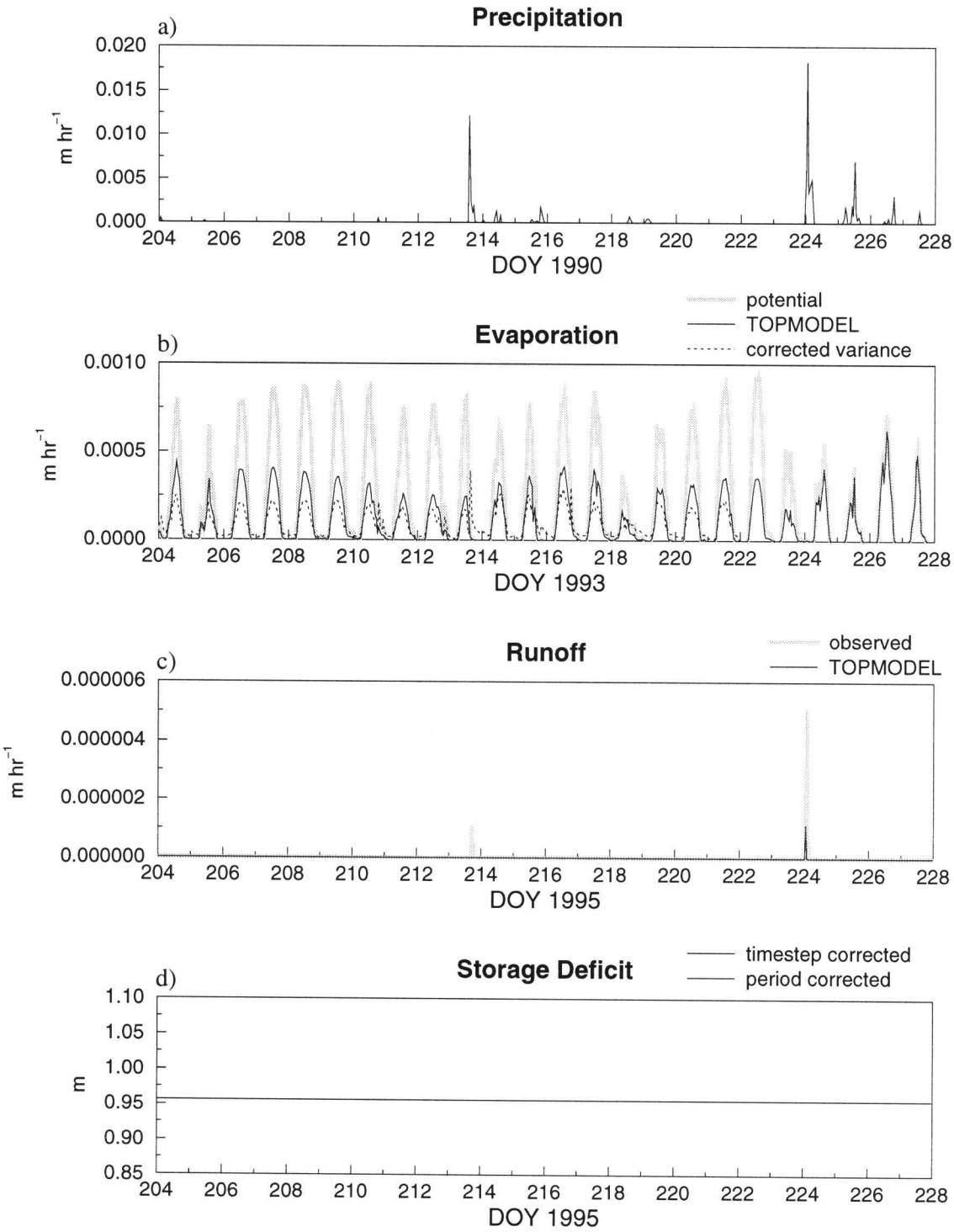

Figure 4.1: TOPMODEL performance at Walnut Gulch, Monsoon '90.

5. TOPLATS SENSITIVITY, CALIBRATION, AND VALIDATION

The calibration, sensitivity, and validation of the TOPLATS model at Walnut Gulch is the focus of this chapter. This was considered to be an important aspect of this study, because data assimilation is ultimately limited by the ability of the model to integrate forward in time successfully. The motivation for the work described here was the initially unsatisfactory performance of the model (Figure 5.1). The calibration process proved to be an evolutionary learning experience that resulted in many new insights into the application of automatic multi-objective calibration for spatially distributed SVATS. The most important steps in this learning processes are summarized, with most emphasis being placed on the final methodology used.

It should be noted that any improvement in model performance will decrease the magnitude of corrections made by data assimilation, tending to give the impression that data assimilation is less important, but that it will enable the information gained through data assimilation to be projected further into the future with less risk of model error.

5.1 Introduction

The TOPLATS model has a large number of fixed vegetation and soil parameters that must be specified correctly for a given site to give accurate water- and energy-balance simulations. Many of these parameters are physically realistic and observable; that is, they are dimensions or capacities that can be measured reliably. For these parameters observed values can be used as available. Other parameters are not observable or are not physically realistic. Such parameters may well be conceptual representations of abstract watershed characteristics or empirical constants that can be used to 'tune' the simulation results on a trial-and-error basis to match the simulations to observations.

A primary difficulty with calibration of the TOPLATS model with traditional calibration techniques is that it contains a large number of parameters. To make the problem more tractable, those parameters that were considered physically realistic and observable were excluded from the calibration process, leaving only the unobservable or unmeasured parameters for calibration.

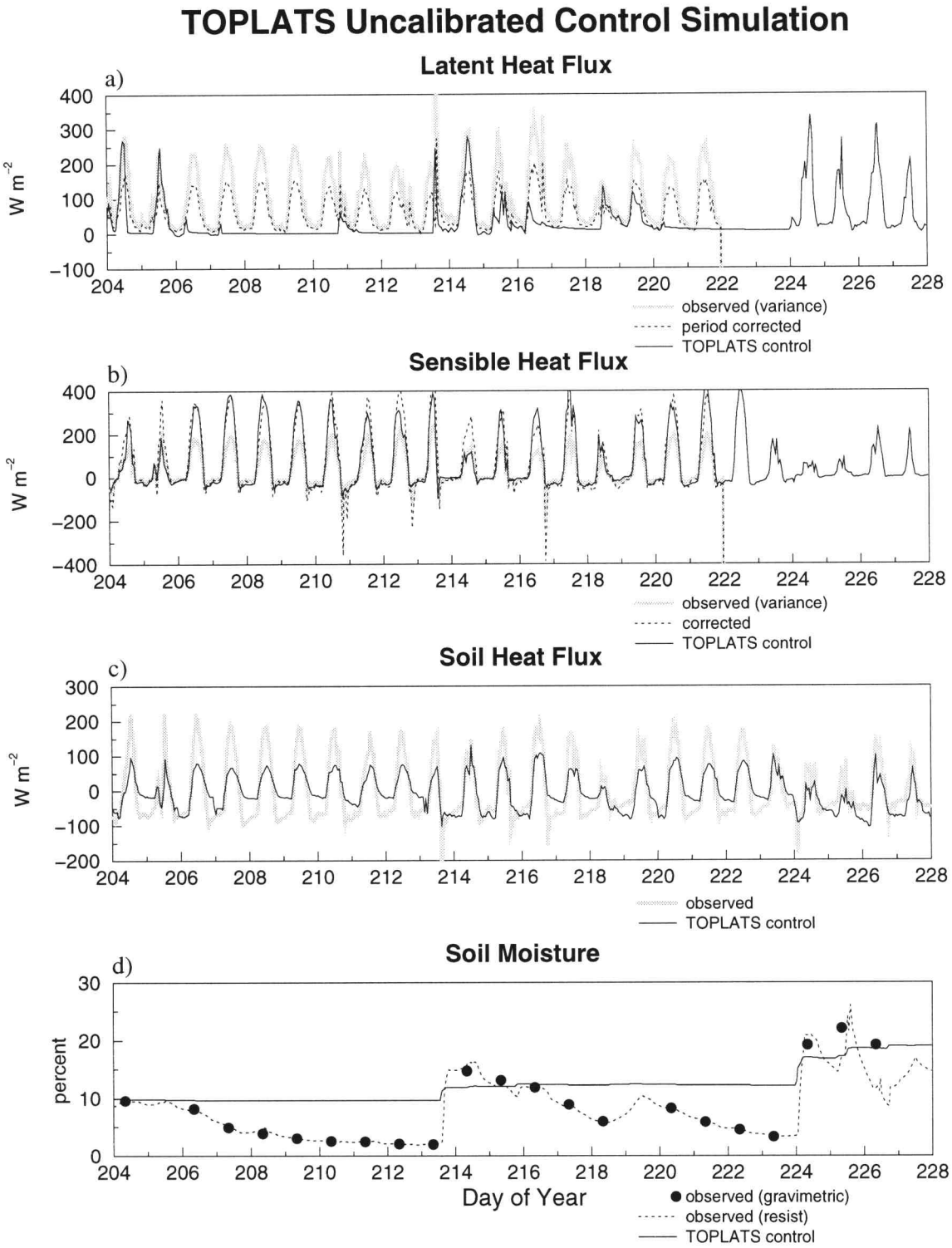

Figure 5.1: Watershed average (a) latent heat flux, (b) sensible heat flux, (c) soil heat flux, and (d) soil moisture from the fully distributed TOPLATS control run with default parameters.

Two aspects add complexity to the calibration problem in this study. First, because the model is implemented over spatially variable surface conditions, it was expected that its optimum parameters will also vary spatially. This suggested that calibration of the model at each point in the model's spatial domain may have been desirable. Second, it was desired that the model perform well in predicting soil moisture states in addition to the latent, sensible, and soil heat fluxes. This introduced a multi-objective dimension to the calibration process, since parameters must be chosen to minimize the error in many different aspects of model prediction.

The solution to the problem of calibrating TOPLATS in Walnut Gulch developed in evolutionary steps: (1) First, a sensitivity analysis was performed to assess the GIS-derived, spatially variable soil and vegetation parameters; (2) Next, a series of single-objective calibrations were performed, in which the parameter sets that minimized each of the objectives were chosen in hope that a common optimum set would be apparent; (3) Given the failure of the last approach, night data were excluded because it was thought these measurements were erroneous; (4) Next, a multi-objective minimization approach was adopted to find the Pareto parameter sets; (5) The number of Pareto parameter sets proved to be unreasonably large, and it was decreased by applying a maximum error cut off; and (6) Finally, to narrow the Pareto set farther, the number of objectives was decreased by eliminating those with high correlation.

5.2 Sensitivity to spatial parameters

The spatially distributed soil and vegetation data sets developed in Chapter 3 were used in the TOPLATS model to make spatial predictions. Under the assumption that better local specification of these parameters would enhance the model's local predictive ability. The nine specified parameters were: (1) minimum stomatal resistance, (2) root depth, (3) leaf area index, (4) residual soil moisture, (5) saturated soil moisture, (6) saturated hydraulic conductivity, (7) percent clay, (8) percent sand, and (9) effective porosity. In all Walnut Gulch TOPLATS model simulations used in this study, topographic index and precipitation are spatially variable, while other meteorological forcing variables, and all other parameters are spatially constant.

The modeled spatial patterns of surface soil moisture, latent heat flux, and sensible heat flux for a dry day (day 219) during Monsoon '90 given with spatially variable parameters are shown

in Figure 5.2. For comparison, the same variables at the same time for a run with soil and vegetation parameters set to be constant as the average of the spatial data sets is shown in Figure 5.3. The progression of simulated surface soil moisture over the Monsoon '90 period is shown in Figure 5.4, while this progression with constant parameters is shown in Figure 5.5. As the simulation progresses, the polygon patterns of soils and vegetation become increasingly pronounced. These soil and vegetation polygons have much too large an impact on the model predictions of soil moisture and land-surface water and energy fluxes when compared with the observed PBMR surface soil moisture where no such patterns are apparent (compare Figures 5.2, 5.3, and 3.29).

A series of sensitivity simulations was performed to determine which subset of spatial parameters caused these patterns. The surface soil moisture on day 219 for a series of simulations where only one spatially variable parameter set was used at a time is shown in Figures 5.6 and 5.7. In each case, the topographic index and the precipitation field were also spatially variable. Also shown are the control run with spatially constant soil and vegetation parameters, the control run with all soil and vegetation parameters spatially variable, a run with spatially constant precipitation (but variable topographic index), and a run with spatially constant topographic index (but variable precipitation). The simulations with spatially variable vegetation parameters look very similar to the control run, indicating that spatial variation in these parameters has little effect on model predictions. All of the simulations using spatially variable soil parameters show distinct polygon patterns. The parameter specifying saturated soil moisture has the most influence on simulated spatial patterns, while these which specify the percentages of sand and clay, the saturated hydraulic conductivity, and the residual soil moisture have a more moderate influence. Clearly soil characteristics are extremely important and vegetation characteristics are less important in regulating soil moisture variability and other surface water and energy components in this watershed.

It is also shown in these figures that the spatially variable topographic index, or the TOPMODEL portion of the TOPLATS, model has very little influence on the simulations (i.e., the one-dimensional topographic index and the control run are identical). This confirms the results obtained with TOPMODEL described in Chapter 4.

The artifact of enhanced spatial soil and vegetation polygon apparent in the simulations is probably not a simple mis-specification of parameter values, rather it is an artifact of discretely assigning a single set of parameters to large areas of soil. A more appropriate specification of spatial parameters might be more continuous (as obtained with remote sensing), and it might be possible to develop a smoothing algorithm that would use the soil polygon information to approximate continuously varying, spatially distributed parameters. Because this is not a central issue for this study, and because the simulations using spatially constant vegetation and soil parameters compare well to the PBMR patterns, soil and vegetation parameters were assumed spatially constant across the catchment in subsequent data assimilation studies, leaving only topographic index and precipitation as spatially varying entities.

5.3 Model calibration and verification

The calibration procedures used to determine the best set of parameters for spatial surface hydrology predictions during Monsoon '90 by the TOPLATS model is the focus of this section.

5.3.1 Calibration parameters

Eight unmeasured, or unphysical, parameters were identified for calibration. These are given in Table 5.1, along with the typical values of their range. These ranges were specified larger than might normally be expected to allow the calibration leeway in accounting for model and data error. Moreover, because some of the parameters are unphysical, specifying their ranges is somewhat arbitrary. The soil heat flux parameters (temperature of the deep soil layer and penetration of diurnal heating) were included in this list even though they were measured with confidence. Soil heat flux (Figure 5.1) was poorly simulated because the soil heat flux sub-model in TOPLATS is very simple and it may in itself be unphysical, and so may require unphysical parameters to perform adequately. The soil calibration parameters shown in Table 5.1 are used later in this chapter.

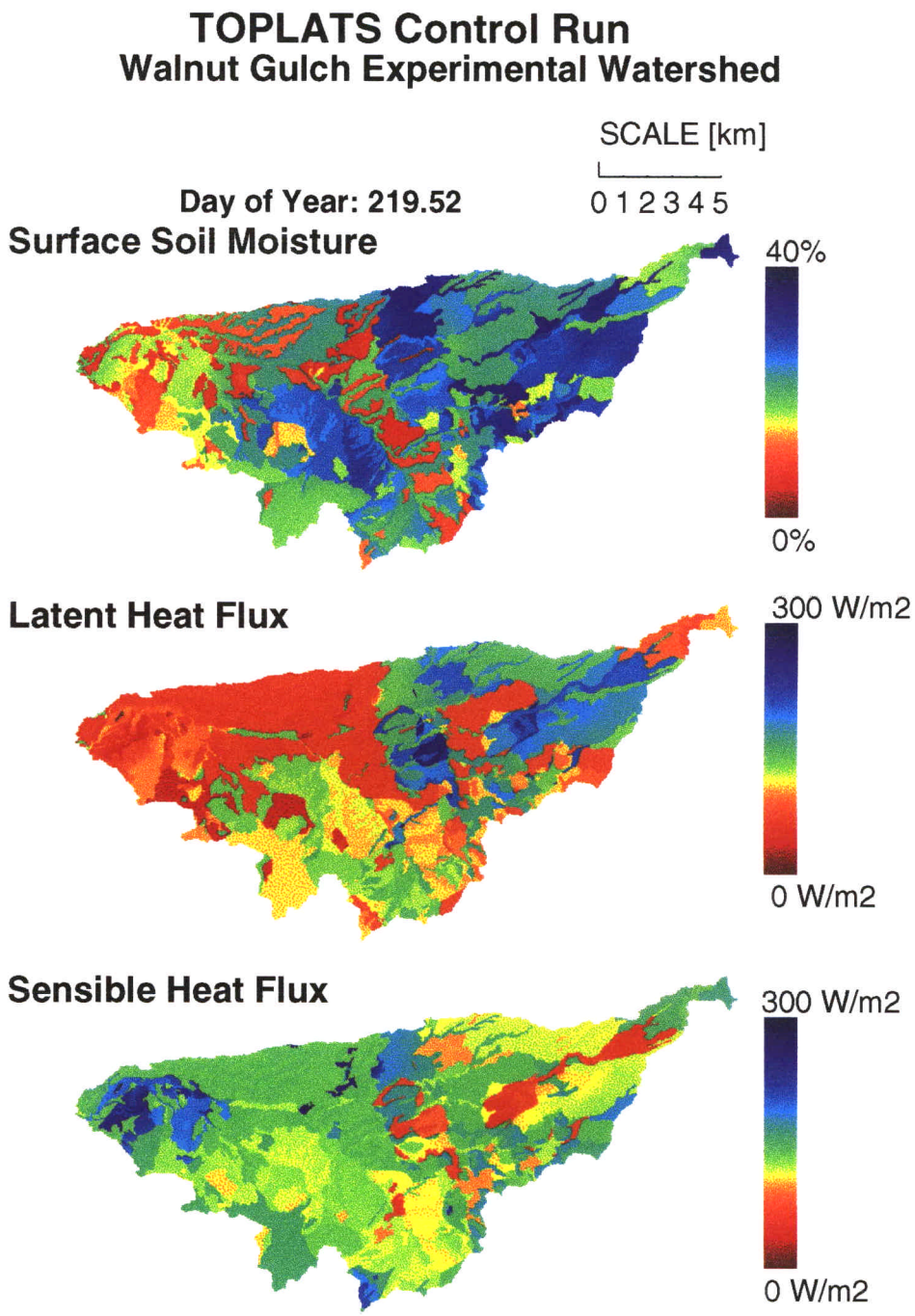

Figure 5.2: TOPLATS spatial predictions of (a) surface soil moisture, (b) latent heat flux, and (c) sensible heat flux on day 219 using spatially variable soils and vegetation parameters.

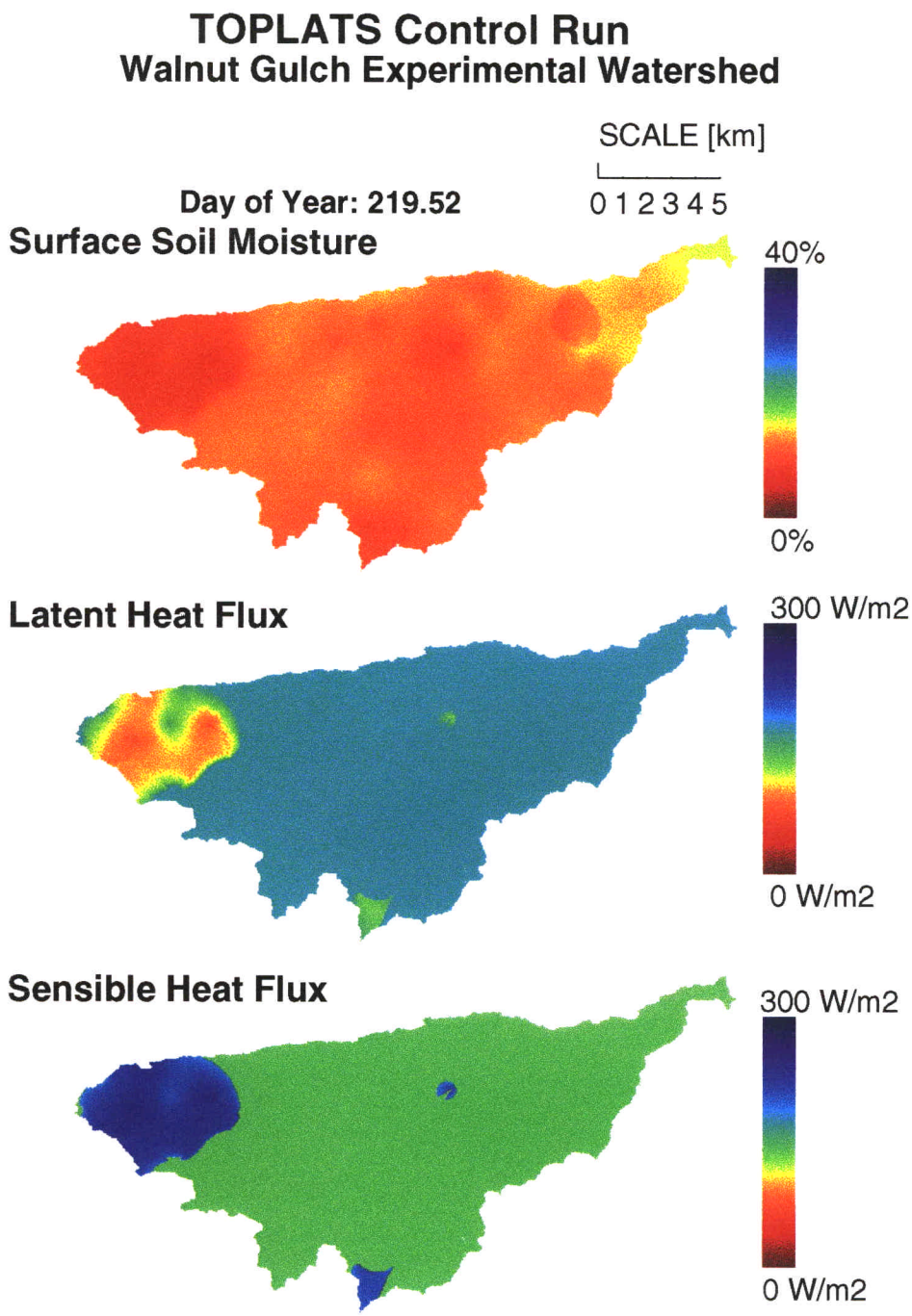

Figure 5.3: TOPLATS spatial predictions of (a) surface soil moisture, (b) latent heat flux, and (c) sensible heat flux on day 219 using spatially constant soils and vegetation parameters.

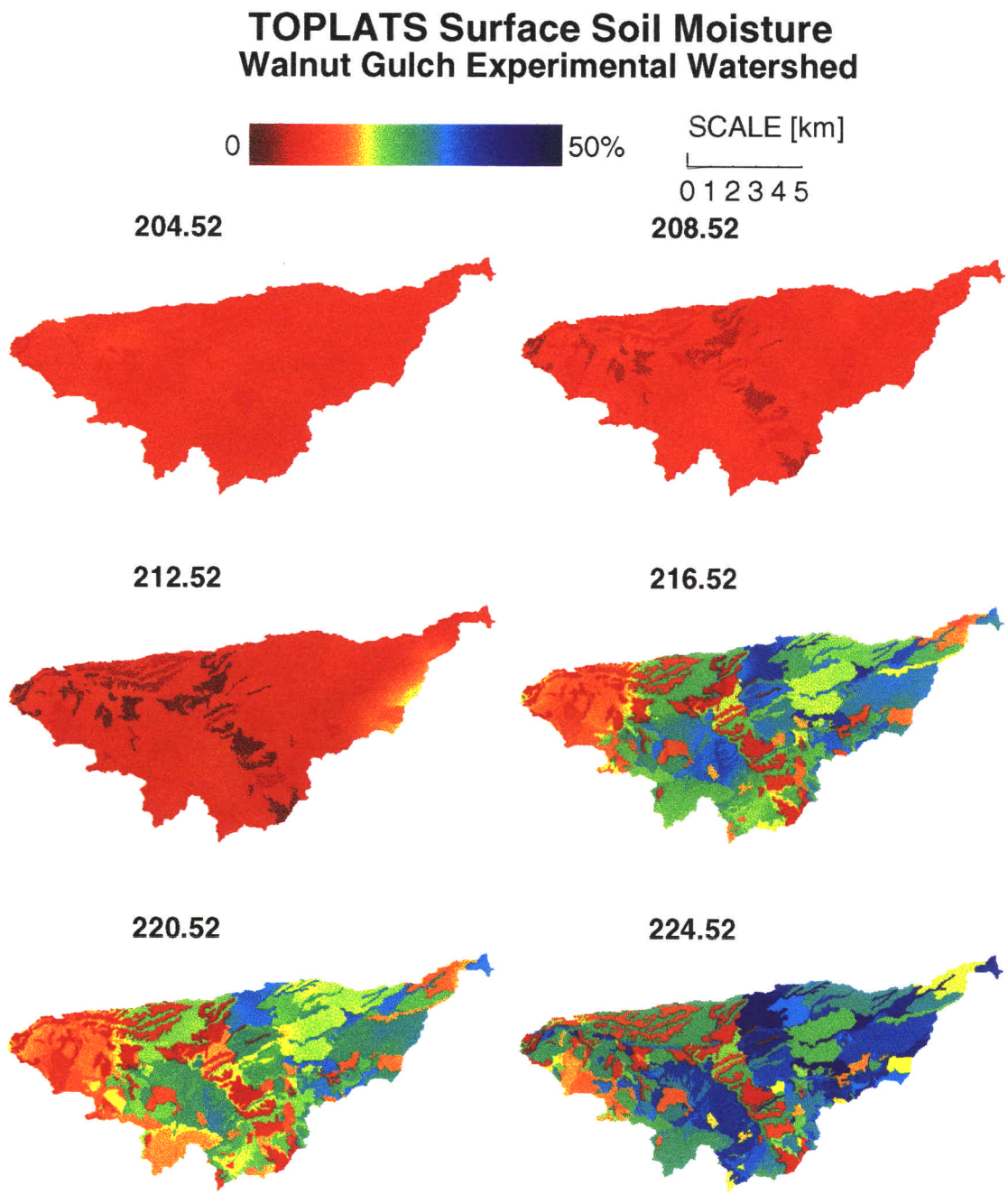

Figure 5.4: TOPLATS control run of spatially variable surface soil moisture at 12:00 p.m. on days (a) 204, (b) 208, (c) 212, (d) 216, (e) 220, and (f) 224 using spatially variable soil and vegetation parameters.

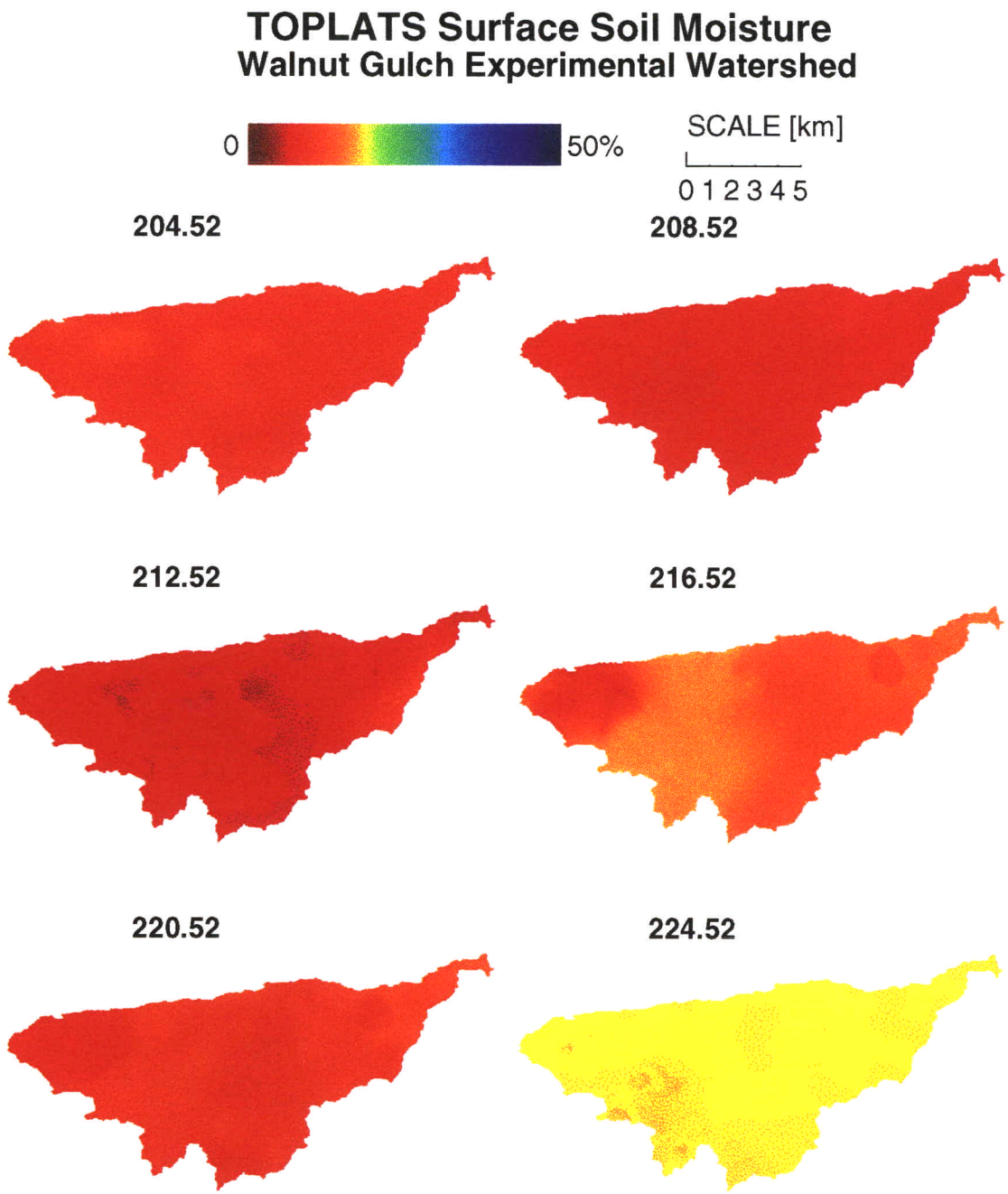

Figure 5.5: TOPLATS control run of spatially variable surface soil moisture at 12:00 p.m. on days (a) 204, (b) 208, (c) 212, (d) 216, (e) 220, and (f) 224 using spatially constant soil and vegetation parameters.

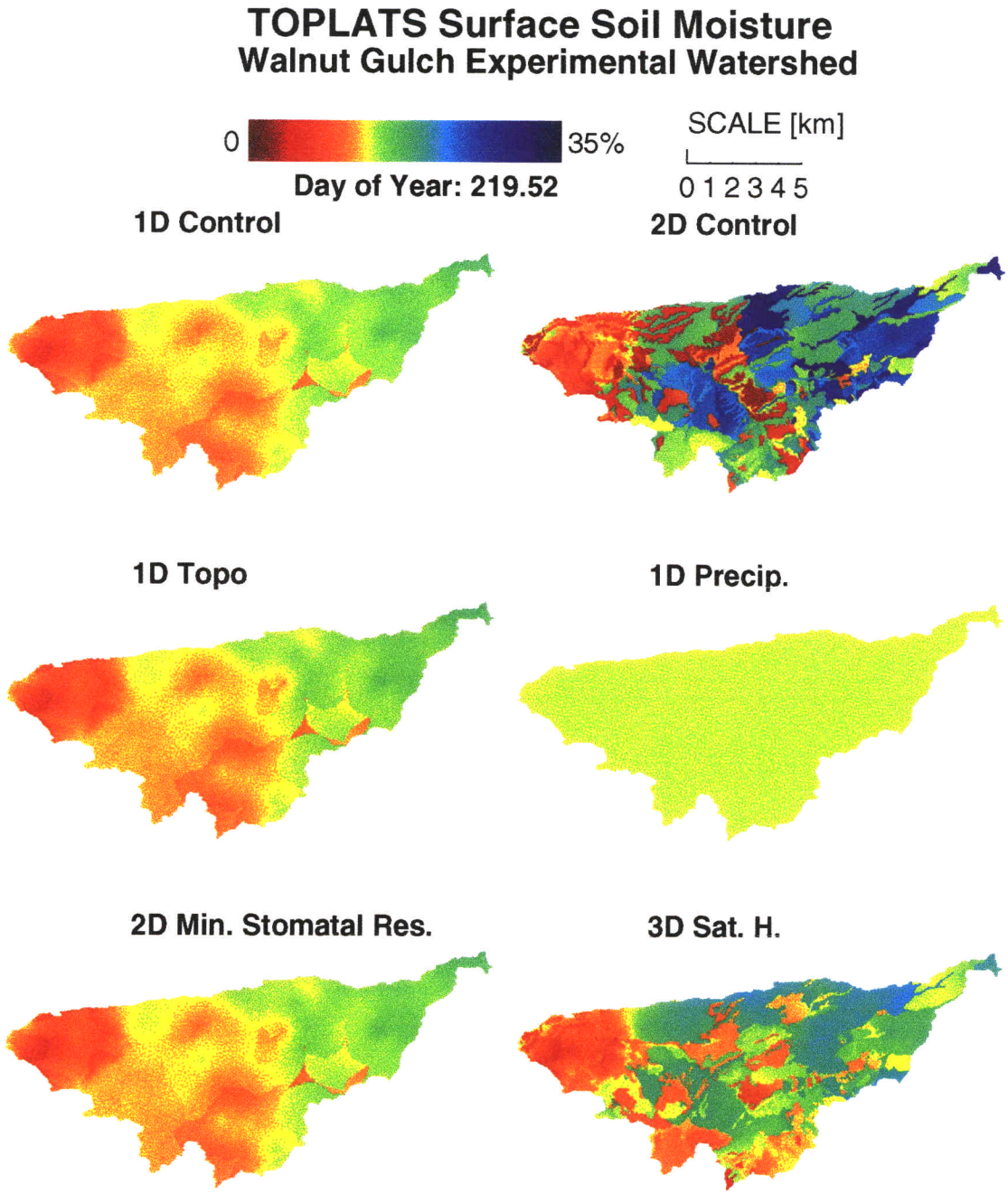

Figure 5.6: TOPLATS spatially variable sensitivity runs.

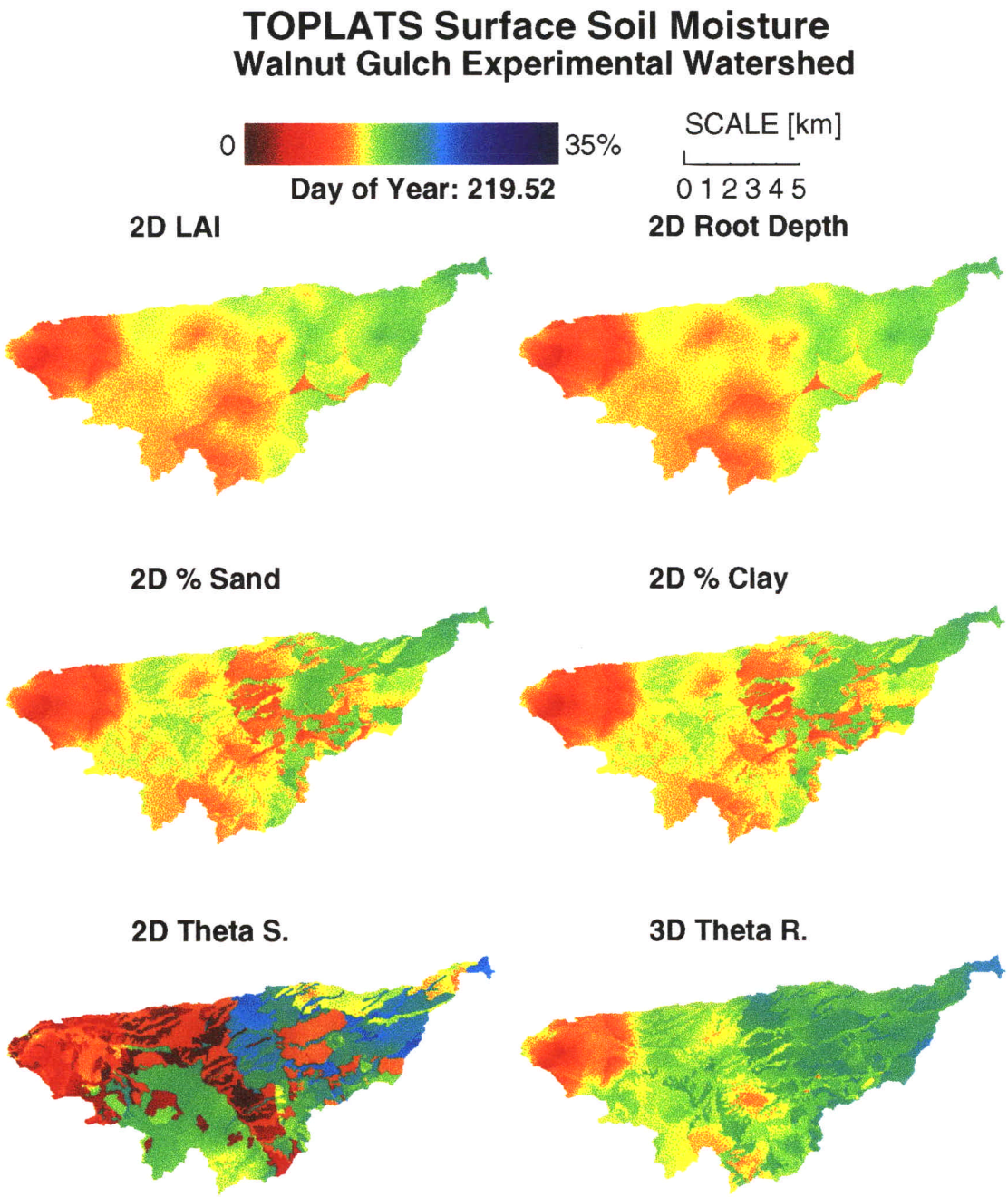

Figure 5.7: TOPLATS spatially variable sensitivity runs.

Table 5.1: Calibration parameters, ranges, and default values.

Calibration Parameter	**Possible Range**	**Default Value**
Initial Calibration Parameter Set		
Root activity factor (RTACT)	1 *to* 1e6	1e4
Root density (m/m^3) (RTDENS)	1 *to* 100	1
Root resistivity (s/m) (RTRES)	1e6 *to* 1e12	1e9
Critical leaf water potential (m) (PSICRI)	-1 *to* -1000	-300
Potential evaporation soil moisture (%) (SMPET)	10 *to* 50	0.28
Penetration of diurnal heating (m) (DHEAT)	0.1 *to* 0.7	0.5
Temperature of deep soil layer (K) (TDEEP)	285 *to* 310	297
Minimum stomatal resistance (s/m) (RSMIN)	0 *to* 700	250
Soil Calibration Parameter Set		
Percent clay(%) (PCLY)	1 *to* 100	22.1
Percent sand(%) (PSND)	1 *to* 100	63.0
Residual soil moisture(%) (THETAR)	1 *to* 20	0.5
Saturated soil moisture(%) (THETAS)	20 *to* 50	33.6
Surface saturated hydraulic conductivity (m/s) (KSAT)	5e-5 *to* 5e-7	4.7e-6

5.3.2 Objective functions

The main purpose of model calibration was to minimize an objective function (or measure model error) through the selection of model parameters. In this study, the desire was to select model parameters that minimized the error in predicted soil moisture and sensible, latent, and ground heat flux. This is a multi-objective calibration problem. A further desire was to assess the spatial variability of calibrated parameter values; hence, objective functions were calculated at each Metflux site where observations were available. At many sites multiple observations of surface fluxes and soil moisture made with different instruments also necessitates require multiple objective optimizations. Objective functions were also calculated for both corrected and uncorrected fluxes at each site and for hourly, daily, and Monsoon '90 soil moisture changes. Hence, 15 different objective functions were calculated for each of the eight Monsoon '90 Metflux sites, plus an average of the eight sites, giving a total of 135 objective functions.

5.3.3 Model performance measures

In this study objective functions, OF, were computed using the normalized sum of the squared difference between the observation, O_i, and the prediction, P_i, whenever the observation was available, thus:

$$OF=\frac{1}{n}\sum_{i=1}^{n}(O_i-P_i)^2 \tag{5.1}$$

where i is the time step.

5.3.4 Monte-Carlo calibration

Automatic parameter calibration can be performed in many ways, the most common being the gradient descent methods used to minimize the objective function as in the calibration of the TOPMODEL parameters described in Chapter 4. However, the calibration for the TOPLATS parameters a Monte-Carlo approach was chosen in which parameter sets are randomly selected from a given range, and the parameter set with the lowest error was selected model runs. This technique requires a very large number of model simulations. Here, the minimum number of model simulation used to provide a single calibration was around 1 million, and often as many as 10 million simulations were used. The Monte-Carlo approach was attempted for several reasons. First, the large data requirements of the TOPLATS model operation in spatially distributed configuration made at Walnut Gulch made coding it as a function for use in a gradient algorithm troublesome and computationally inefficient. Second, a Monte-Carlo approach cannot be trapped in local minima, which are likely to be plentiful because of the large observation errors and model thresholds. Finally, the Monte-Carlo approach allows exploration and analysis of the objective functions over the entire parameter set range. So giving insight into parameter sensitivity and model error.

Fortran, the computer language in which TOPLATS is coded, does not have an internal random number generator. A random number generator with a very long period ($> 2 \times 10^{18}$) that uses Bays-Durham shuffling and other safeguards was used (Press *et al.*, 1986).

5.3.4.1 Single-objective calibration

In the first calibration attempt, the set of parameters that minimize *each* objective independent of the other objectives was found. The hope was that, because all land-surface states and fluxes are closely linked, a set of common or very similar parameter sets would be found for the various objectives at a single site. Further, it was thought that the spatial variability of parameter sets from different sites could be assessed, and that a watershed average parameter set could be defined using the watershed average objective functions.

Some parameter set agreement was found between different objective functions and locations (Table F.1). Because of the generally large variation in minimum objective value parameter sets, selecting a 'best' parameter set became entirely subjective. A parameter averaging process was developed to help reduce this subjectivity by identifying the most commonly occurring parameter values, but it was found that these average parameter values produced poor model simulations because of parameter interaction. This averaging approach was therefore abandoned in favor of selecting a single-set of parameters from a single objective function minimization to reduce error increases due to parameter interaction. However, this also proved to be an unacceptable approach because it requires the subjective selection of one objective function minimization rather than the minimization of several. The parameter variations between sites was not assessable, because within-site parameter sets could not be identified.

Although ultimately futile, some valuable insights were gained from this exercise. First, the simulation error tended to decrease when the sensible and latent heat fluxes were corrected by the water balance. Second, some minimum objective parameters were similar when optimized for a single objective function at all sites, tending to suggest that the use of watershed-average parameters may be justified.

5.3.4.2 Elimination of nighttime data

It was thought that some of the confusion in identifying parameters above may have been due to erroneous observations of sensible and latent heat fluxes at night. These values were

eliminated and the parameters were recalibrated on only the daytime flux data using the Monte-Carlo method (Table F.2).

The elimination of night data did not help to identify better parameters. In fact, the main effect of eliminating nighttime data was to increase the values of the objective functions. This is attributable to the normalization that is used in computing these values. The nighttime data are generally of a small magnitude, as is the error associated with them, and the contribution of nighttime data error to the total error is small. The main effect of eliminating it to reduce the number of observations used to normalize the objective functions.

5.3.4.3 Multi-objective Pareto set determination

The next logical evolutionary step was to find a way to link the minimization of the various different objective functions to give a parameter set that minimizes the entire set of objectives simultaneously. This is the process of finding the 'Pareto set' of parameter values, i.e. these are the parameter sets that produce values of objective functions that are at least equal, and preferably better than all other parameter sets. Parameter sets that produce values of objective functions which are all worse than the other parameter sets are eliminated from further consideration. Every member of this Pareto set will match one set of observations better than every other member of the Pareto set, but in so doing they will compromise the match with some other observation set.

When finding the Pareto set, the number of objective functions was decreased to include only the most important objectives. This aids the computation Pareto set, eliminates data considered to be redundant or erroneous, and reduces the confusion and complexity of dealing with large numbers of objective functions. The corrected temperature variance sensible and latent heat fluxes, the soil heat flux, and resistance soil moisture objectives were retained for all Metflux sites so reducing the total number of objectives from 135 to 36.

Notwithstanding this reduction, the size of the Pareto set determined by this analysis remained excessive (see Table 5.2), and no useful parameter sets could be extracted from it. The set that produced the minimum 36 objective functions was found, but in practice this only

produced reasonable simulations of the sensible heat flux, because the value of this objective function dominated.

5.3.4.4 Maximum error cut-off

To minimize the size of the Pareto set, parameter sets were eliminated that contained objectives which exceeded a certain percentage of the total range of objective function error. This effectively eliminates parameter sets that produce objective functions with unacceptably large error. The size of the Pareto set with various levels of error cut-off, Monte-Carlo set sizes, corrected or uncorrected data, and all data or nighttime data excluded is summarized in Table 5.2. The model appeared to predict latent heat fluxes similar to the corrected values, but also tended to predict the uncorrected sensible heat flux. This hypothesis was also tested by comparing a fully corrected calibration with a calibration with uncorrected sensible heat flux and corrected latent heat flux objective functions.

The analysis showed that: (1) the Pareto set contains many parameters with a large objective function errors; (2) the effect on Pareto set size and objective function error of eliminating night fluxes is small; (3) the Pareto set contains no parameter sets that produce objectives which are all low (in some cases the objective function is above the 40% cut-off for every Pareto parameter set); (4) the model is able to achieve *much* lower error levels when uncorrected sensible heat flux is used. This implied that there may not be an error in the measured sensible heat flux, but in some other part of the energy-balance; (5) the fraction of the Monte-Carlo set that are Pareto sets generally decreased as the Monte-Carlo set size increases.

The goal here was to find a parameter set that minimizes all the objectives well. The fact that the Pareto set contains no such sets of parameters is a concern. Moreover, the parameter set with the least total error when used in a model simulation again was found to give poor results. These difficulties suggested that it was necessary to further decrease in the number of objective functions to make the best parameter set more identifiable.

Table 5.2: Pareto set sizes for various error cut-off levels, Monte-Carlo set sizes, corrected or uncorrected data, and all data or day data.

		Monte-Carlo Set Size:	
Simulation	**Error Cut-Off**	**100,000**	**200,000**
Corrected Sensible and Latent Flux, all data.	None	83354	161959
	50%	2871	5827
	40%	16	0
	30%	0	0
Corrected Sensible and Latent Flux, day data.	None	-	-
	50%	516	970
	40%	0	0
Uncorrected Sensible and Corrected Latent Flux, all data.	None	19098	35136
	50%	12560	23588
	40%	9190	-
	30%	3233	6348
	20%	83	181
	10%	0	0
Uncorrected Sensible and Corrected Latent Flux, day data.	None	20507	37804
	50%	13130	24812
	40%	9713	18451
	30%	3628	6990
	20%	212	512
	10%	0	0

5.3.4.5 Objective function reduction

The number of objective functions was once again reduced in an attempt to make the identification of the best parameter set tractable. Multiple-site objective functions were eliminated, leaving only four objective functions (area-average sensible, latent, and soil heat flux and soil moisture).

The Pareto set for these four daytime corrected objective functions was determined using 200,000 Monte-Carlo realizations, resulting in a Pareto set size of about 400 (see Figure 5.11), without the use of an error cut-off. Hence, reduction of the number of objective functions, reduces the Pareto set to a reasonable size.

Plots of normalized Pareto set objective function values versus other objective function values (Figure 5.8) reveal that the objective functions are all uncorrelated with each other, except for objective functions associated with latent and sensible heat fluxes. This suggests a

further reduction in the objective function set. The sensible heat flux objective function was eliminated because the TOPLATS model generally simulates sensible heat flux fairly well, and the latent heat flux is more critical to soil moisture states.

5.3.4.6 Inclusion of soil characteristics in calibration

The parameter set that produced the minimum sum of the four objective functions described in the previous section was found. This parameter set was evaluated in an 8-grid version of TOPLATS with each grid representing one of the Monsoon '90 Metflux sites and receiving appropriate forcing. This set of parameters performed well when simulating latent, sensible, and soil heat flux, but was unable to predict soil moisture variations well. Because accurate soil moisture prediction is critical in this research, further refinement of the calibration was necessary.

The objective function values were plotted against parameter values, see Figure 5.9 for example. It is obvious from this figure that there is some threshold in the model or error in the data which prevents the model from reducing soil moisture error below a threshold.

Soil moisture dynamics are highly dependent on soil properties and less dependent on surface fluxes. Up to this point the calibration processes had not included soil water characteristics but in an attempt to further minimize soil moisture prediction error, the five Brooks-Corey soil parameters (see Table 5.1) were added to those to be calibrated.

To determine if adding these parameters would further reduce the error in the soil moisture prediction, the original calibration parameters were set to the values that had provided the minimum sum of objective functions in the previous calibration. The soil parameters were then investigated in another Monte-Carlo simulation. An example of these results are shown in Figure 5.10. Here, the maximum magnitude of soil moisture objective function increases, but the model is none-the-less able to predict values of soil moisture that are closer to those observed. It is also interesting to note that soil moisture and sensible heat flux errors are both reduced with this change. This analysis supported the inclusion of the TOPLATS soil characteristic parameters in the calibration process.

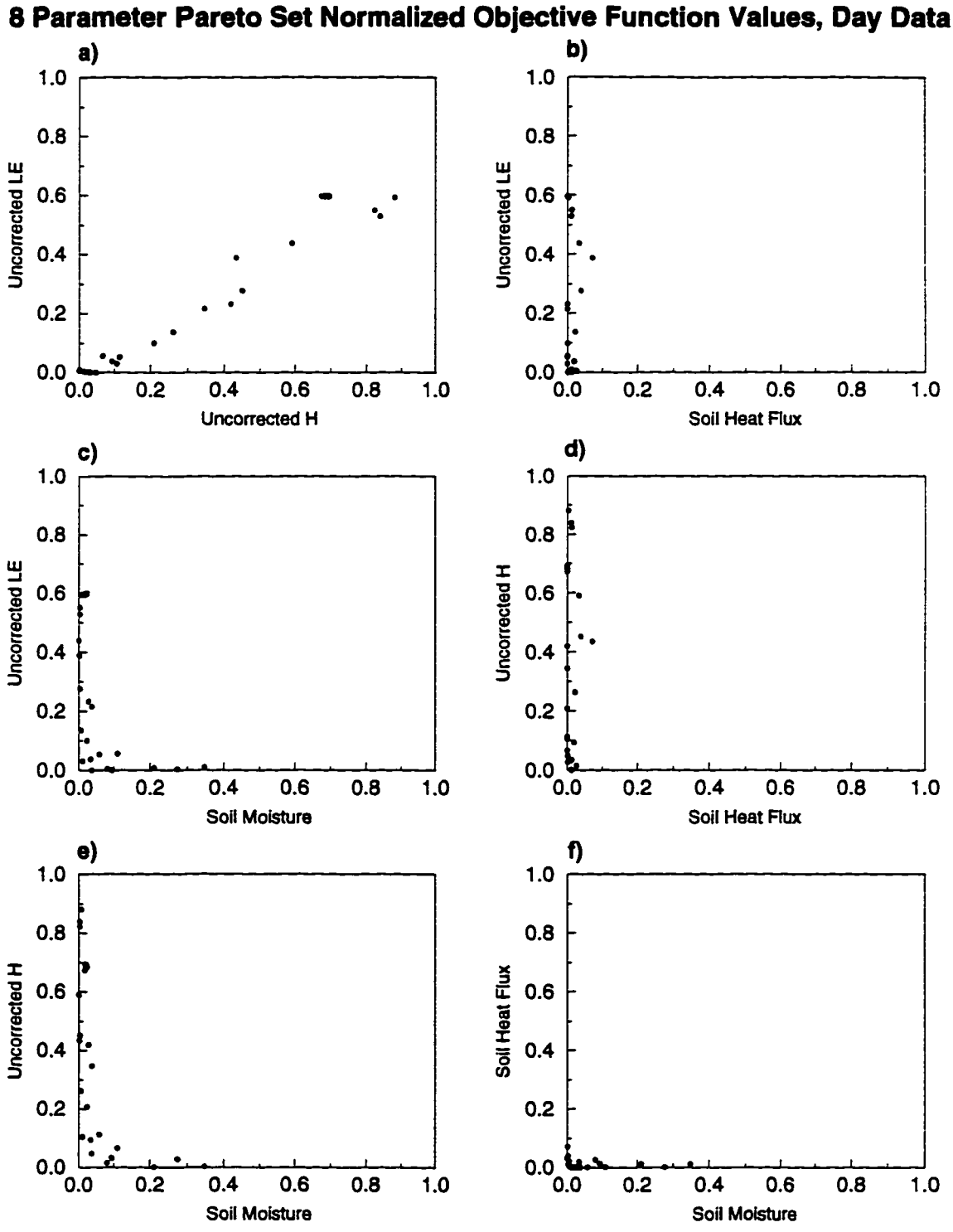

Figure 5.8: Eight parameter pareto set normalized day data objective function values.

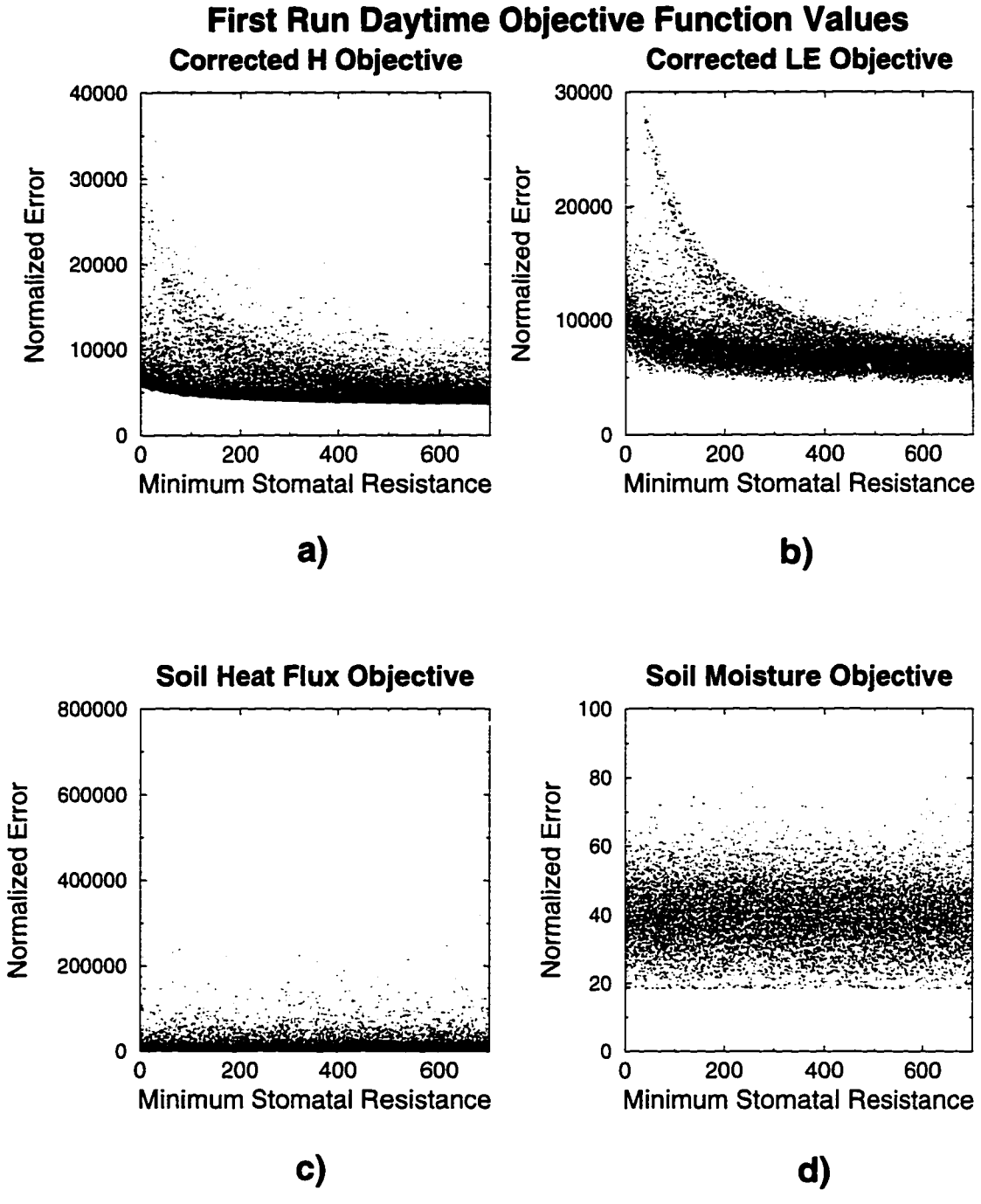

Figure 5.9: Day data objective function values versus the minimum stomatal resistance parameter for the original eight parameter Monte-Carlo calibration set.

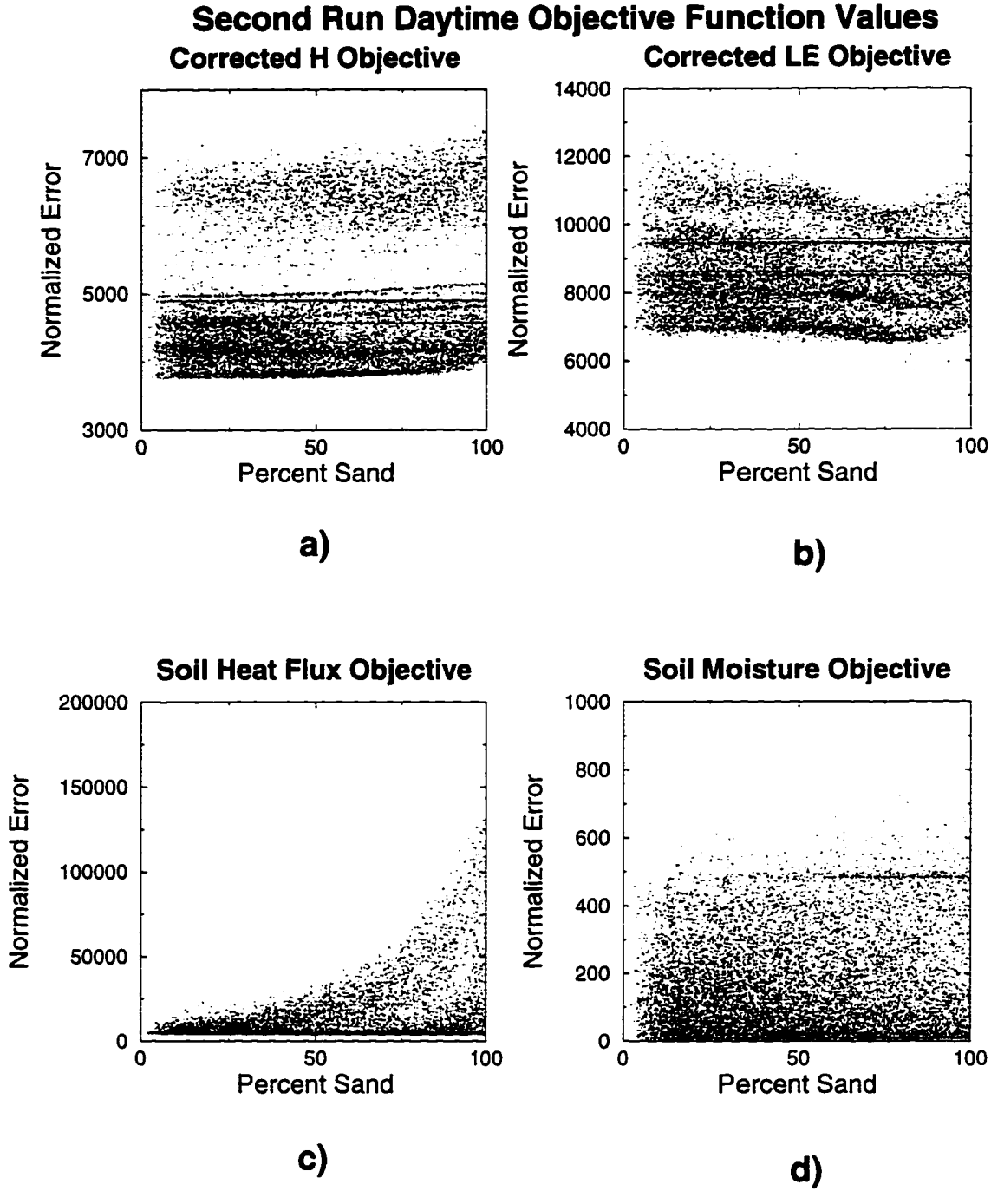

Figure 5.10: Day data objective function values versus the percent sand parameter for the five soil parameter Monte-Carlo calibration set.

5.4 Acceptable model parameters

A reasonable set of model parameters was finally determined from a 13-parameter, 3-objective function (areal average daytime-corrected temperature variance latent heat flux, soil heat flux, and resistance soil moisture), Pareto set, and a 200,000 sample Monte-Carlo calibration. The resulting Pareto set contained 125 parameter sets from which one had to be selected (see Figure 5.11 for the Pareto set size for various calibration configurations).

To make a more informed selection of the parameter set, the Pareto set parameter values were displayed in a form adopted by Sorooshian *et al.* (1993) (see Figure 5.12). Here, the best five parameter sets for each objective are normalized lie within the range zero-to-one, with zero corresponding to the minimum value of the parameter and one to the maximum value. In a similar way, the error or objective function values were also scaled from zero to one (note that zero does not mean zero error, but rather minimum error) and similarly plotted. Such plotting made it very easy to see which parameters are being well-identified and how these parameter values affect model errors. The sensible heat flux objective function was included amongst the plots for diagnostic purposes, but it was not used in the determination of the Pareto set.

It is important to note that many of the best five parameter sets were derived from similar parameter values, suggesting that the parameters are well identified and that any of these parameter sets would be a good choice. For reference, the entire Pareto set is displayed in Figure 5.13. The entire Pareto set shows low errors in most of the objectives, with most spread in soil moisture. The Pareto set parameter values are also generally confined to subranges of the parameter space, with some 'trade off' between parameters (i.e. the same objective function value can be obtained with a high value of parameter A and a low value of parameter B, or vice versa).

Despite the relatively low objective function values produced by the Pareto parameter sets, the total range of TOPLATS flux prediction for these Pareto set parameters remains high. The eight Metflux site average range of prediction obtained from the Pareto parameter sets using an eight-grid TOPLATS simulation are shown in Figures 5.14 and 5.15. Clearly, there is still a large amount of prediction variability even within the Pareto set, hence, the final parameter set must be chosen carefully.

The selection of a single best parameter set is a subjective exercise. Clearly, all the parameter sets left in consideration are good, but with different compromises as to which objective is minimized. It was decided that the soil moisture objective was most important for the purposes of this study; so, the parameter set that produced the lowest soil moisture objective was chosen (bolded line in Figure 5.12). The selected parameter values are shown in Table 5.3.

Table 5.3: Acceptable calibrated TOPLATS parameters and default values.

Calibration Parameter	**Default**	**Calibrated**
Initial Calibration Parameter Set		
Root activity factor (RTACT)	1e4	348025.41
Root density (m/m^3) (RTDENS)	1	86.55
Root resistivity (s/m) (RTRES)	1e9	4.787e11
Critical leaf water potential (m) (PSICRI)	-300	-500
Potential evaporation soil moisture (%) (SMPET)	0.28	0.46
Penetration of diurnal heating (m) (DHEAT)	0.5	0.33
Temperature of deep soil layer (K) (TDEEP)	297	287.6
Minimum stomatal resistance (s/m) (RSMIN)	250	574.32
Soil Calibration Parameter Set		
Percent clay(%) (PCLY)	22.1	8.13
Percent sand(%) (PSND)	63.0	14.41
Residual soil moisture(%) (THETAR)	0.5	2.20
Saturated soil moisture(%) (THETAS)	33.6	29.97
Surface saturated hydraulic conductivity (m/s) (KSAT)	4.7e-6	8.7e-6

It is interesting and necessary to note that many of these parameters are reasonably close to the default values, with the exception of the root parameters. And indeed that many of the calibrated parameters are more realistic than the default parameters. A root density of 86 m/m^3 is much more realistic than 1 m/m^3, for instance, and the low percentage of sand and clay reflects the large coarse fraction soil component which is not included in the soil analysis (the soil is usually sifted), while the high minimum stomatal resistance is realistic for water-conserving semi-arid plants. The large difference in soil heat flux parameters are probably an artifact of the model having an inadequate soil heat flux sub-model. Finally, the high values of critical leaf

water potential and soil moisture for the calculation of PET reflect the fact that the of plants do not wilt and that the an environment rarely experiences potential evaporation, respectively.

The generally increasing Pareto set sizes shown in Figure 5.11 are a result of randomly finding more parameter sets inside the Pareto set area. Occasionally, the Pareto set will decrease with increasing Monte-Carlo sample size because a superior parameter set is discovered that is able to eliminate others from consideration. This suggests that the parameter sets here called Pareto sets are not truly Pareto sets, but they are close. It is interesting to note that, even with very large Monte-Carlo sample sizes, the Pareto set continues to increase.

Many of the multi-objective Pareto set concepts used in this study were developed by Gupta *et al.* (1996). But the application of these concepts to the calibration of a SVATS model in this study is original.

5.5 TOPLATS-Monsoon '90 control run

A complete set of diagnostics for the fully distributed TOPLATS simulation during Monsoon '90 with the calibrated parameters defined as above without data assimilation is given in Appendix G. This simulation is here after referred to as the 'control run' and is used as the basis of comparison for other data assimilation runs.

There is a clear compromise in the calibration between latent heat flux prediction and soil moisture prediction (Figures 5.14 and 5.15). The range of prediction shows that latent heat flux can be calculated well by the model, but at the expense of soil moisture (see Figure 5.12). By choosing to predict soil moisture most accurately rather than latent heat flux, produces 'flat tops' or 'hats' in the latent heat flux time series. According to Schmugge and André (1991), "there is considerable observational evidence of [such] behavior in the field". This model predicted of latent heat flux may not be totally be in error, but it is certainly not supported by the Monsoon '90 observations. It should also be recalled, however, that the accuracy of these observations have been heavily questioned.

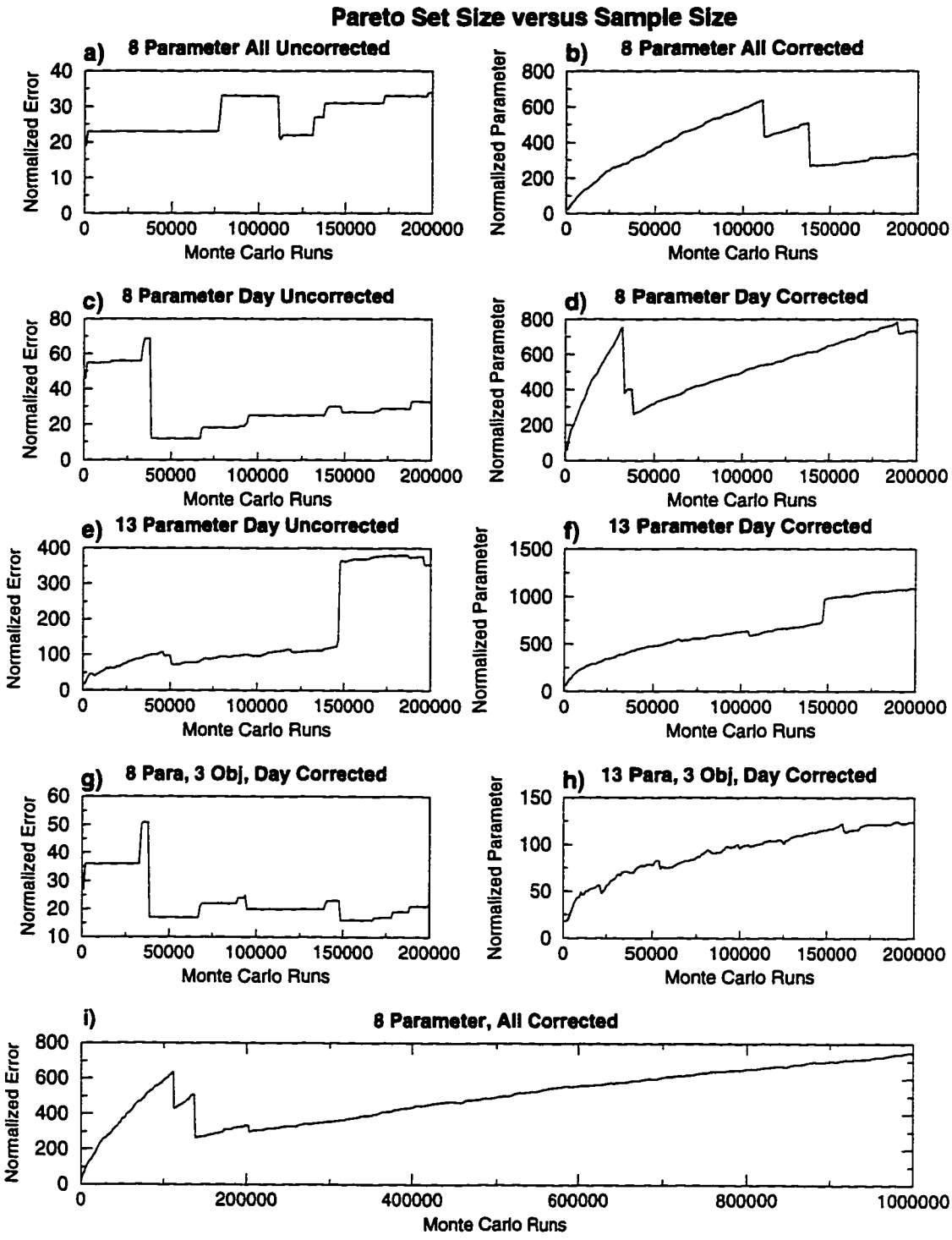

Figure 5.11: Pareto set size versus Monte Carlo sample size for various parameter and objective function configurations.

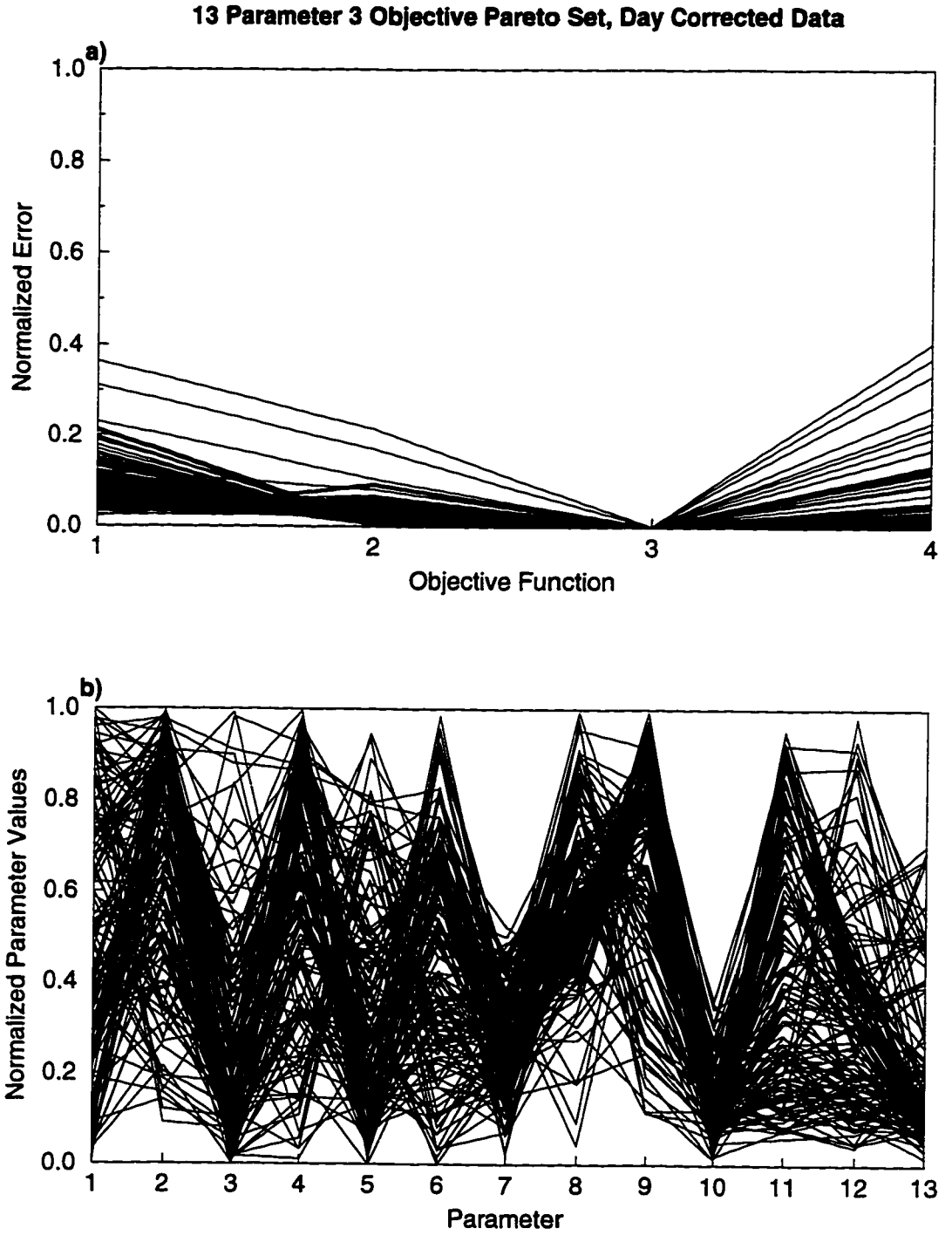

Figure 5.13: Pareto set normalized objective function and parameter values shown for the 13 parameter, 3 objective function Monte-Carlo calibration. Here, objective 1 = sensible heat flux, 2 = latent heat flux, 3= soil heat flux, and 4 = resistance soil moisture. Parameter 1 = RTACT, 2 = RTDENS, 3 = RTRES, 4 = SMPET, 5 = PSICRI, 6 = DHEAT, 7 = TDEEP, 8 = RSMIN, 9 = PSND, 10 = PCLY, 11 = KSAT, 12 = THETAS, and 13 = THETAR.

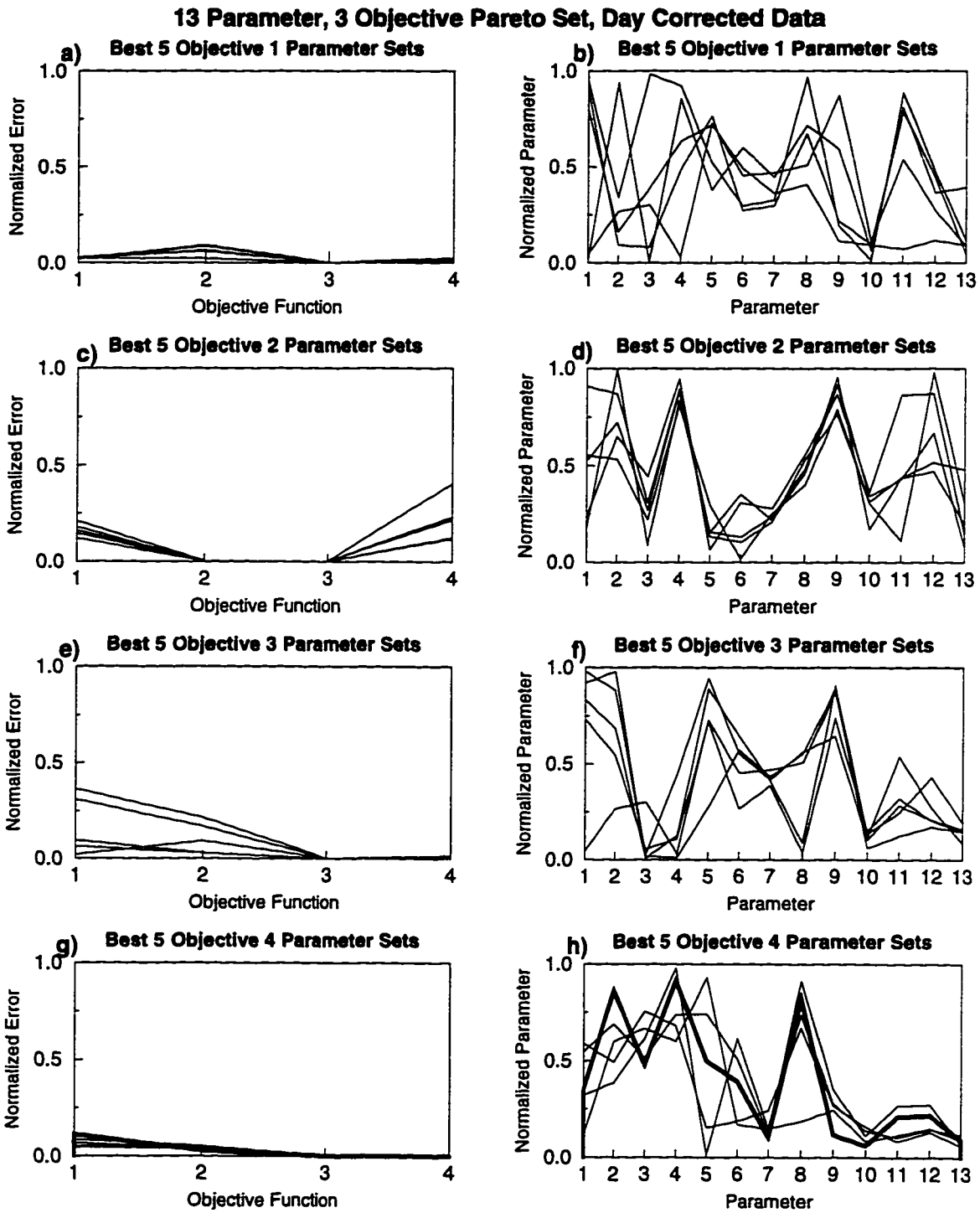

Figure 5.13: Pareto set normalized objective function and parameter values shown for the 13-parameter, 3-objective function Monte-Carlo calibration. Here, objective 1 = sensible heat flux, 2 = latent heat flux, 3= soil heat flux, and 4 = resistance soil moisture. Parameter 1 = RTACT, 2 = RTDENS, 3 = RTRES, 4 = SMPET, 5 = PSICRI, 6 = DHEAT, 7 = TDEEP, 8 = RSMIN, 9 = PSND, 10 = PCLY, 11 = KSAT, 12 = THETAS, and 13 = THETAR.

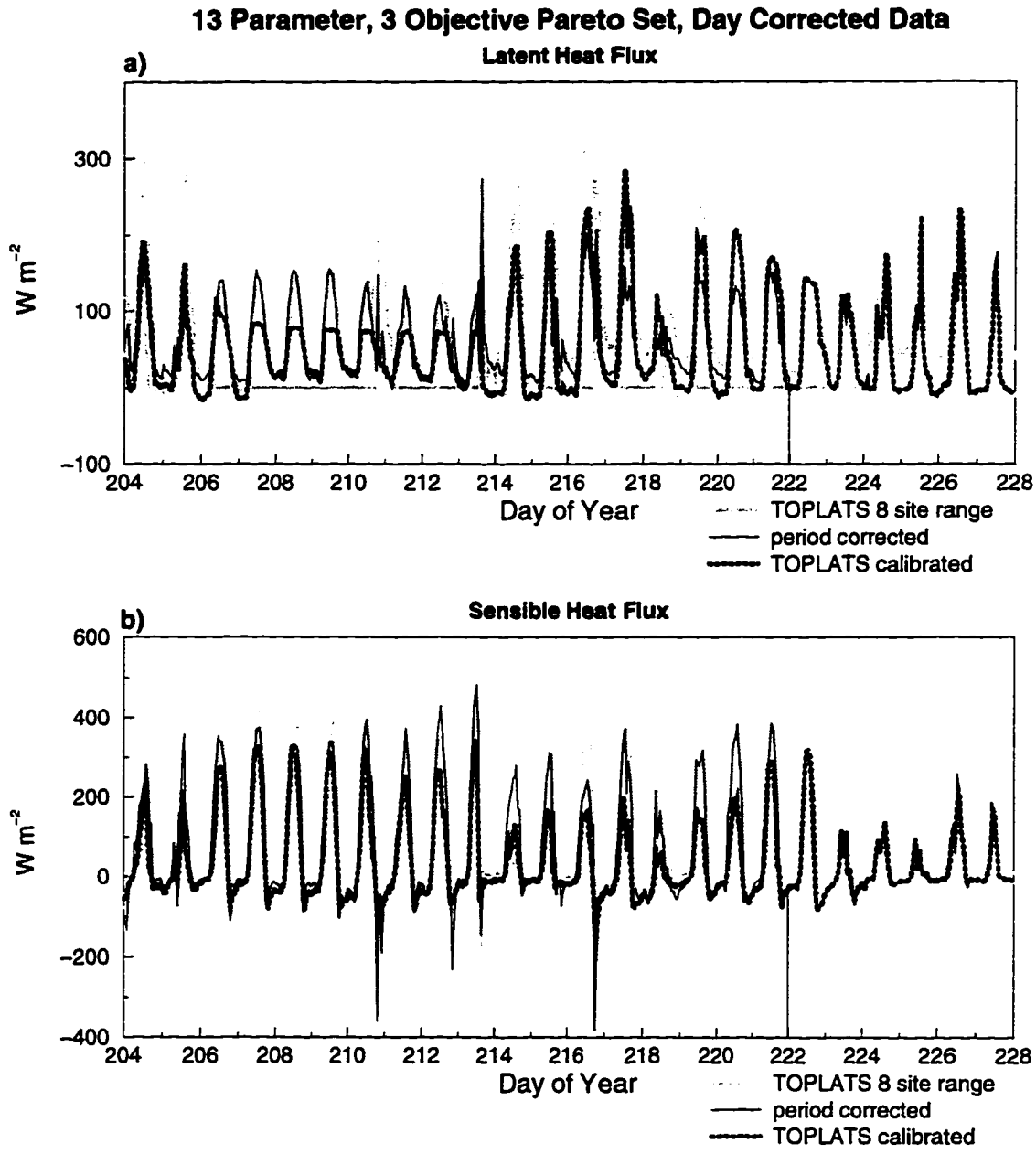

Figure 5.14: Latent and sensible heat flux prediction range for the 13-parameter, 3-day corrected data objective function Pareto set. The 'best' parameter set TOPLATS prediction are indicated as well.

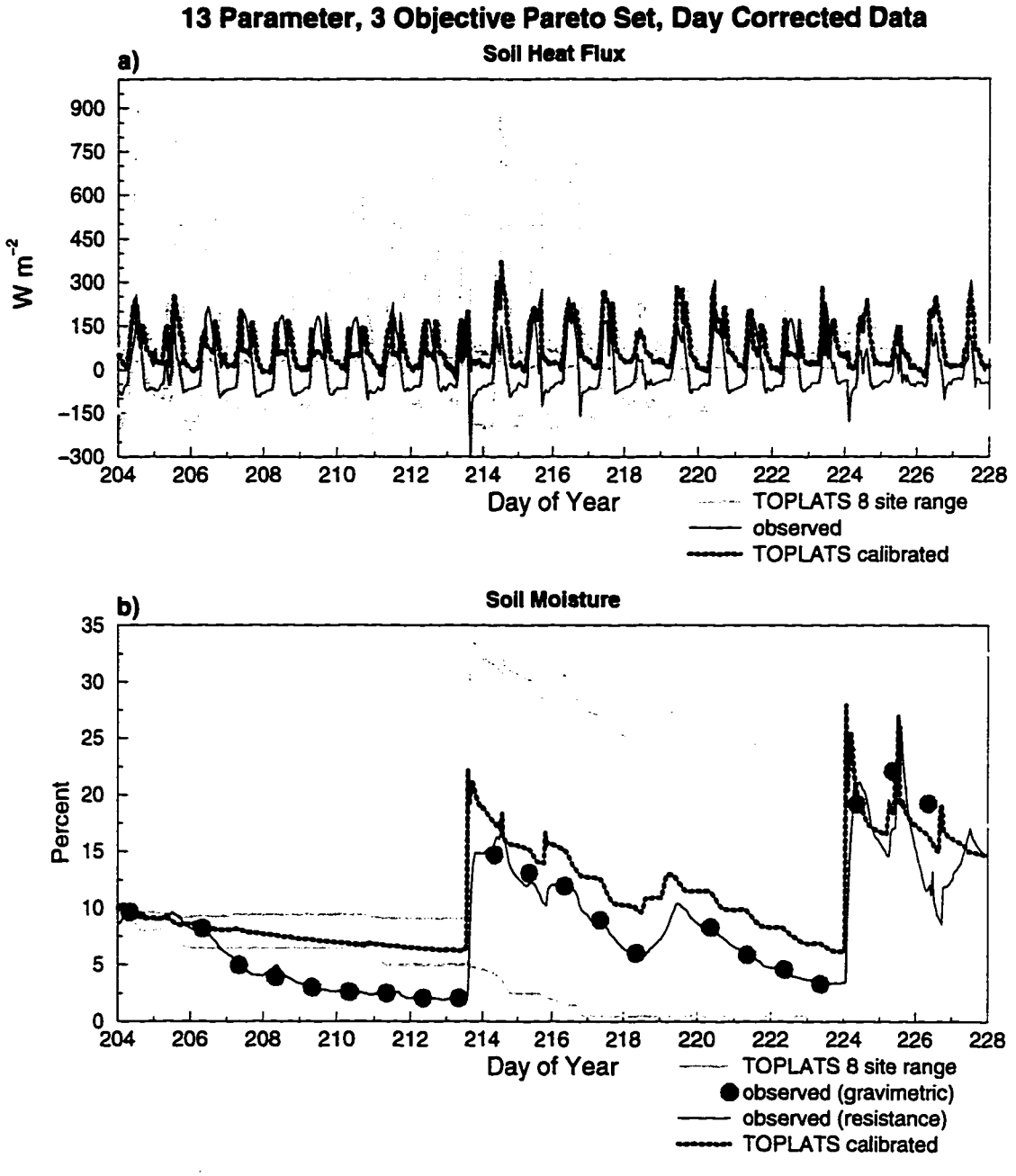

Figure 5.15: Soil heat flux and soil moisture prediction range for the 13-parameter, 3-day corrected data objective function Pareto set. The 'best' parameter set TOPLATS prediction is indicated as well.

5.6 Aggregation study

White *et al.* (1996) compared the area-averaged behavior of an array of distributed BATS models forced with spatially distributed precipitation with the behavior of a single aggregate BATS simulation with area-average precipitation forcing. The question asked was; "In the extreme case of the semi-arid environment subject to convective rainfall, are the ensuing real patterns of soil moisture such that they have significant impact on the area-average description of vegetation in meteorological models?" The answer was that the difference between the calculated surface energy fluxes given by a single aggregate BATS model and that given by a distributed array of BATS models is very small.

This conclusion was tested using the higher resolution (40 m versus 480 m resolution) distributed TOPLATS results with spatially variable precipitation forcing and an aggregate TOPLATS simulation with watershed average forcing. These results are shown in Figures 5.16 and 5.17. There is more variability in this comparison than White *et al.*, (1996) reported this is most probably being due to the higher resolution of the distributed model used here, but their overall conclusions cannot be disputed.

The relevance of this finding to the present study is that it supports the use of area-average parameters and that it suggests that a spatially distributed model with the resolution used in this study is probably not needed if catchment average surface fluxes are required. The spatially distributed model is required to allow prediction of spatial patterns of soil moisture at the resolution of the available observations.

5.7 Conclusions

The most important contribution of the work described in this chapter is the development of a multi-objective SVATS calibration technique that calibrates conceptual and unmeasured model parameters by finding the Pareto parameter sets from the larger Monte-Carlo set, then finding the 'best' parameter set in a semi-subjective way. Model calibration is beneficial to data assimilation studies because it improves model prediction performance, allowing it to better advect observation information into data-sparse temporal and spatial regions. It should be noted that any improvement in model performance will make subsequent data assimilation changes

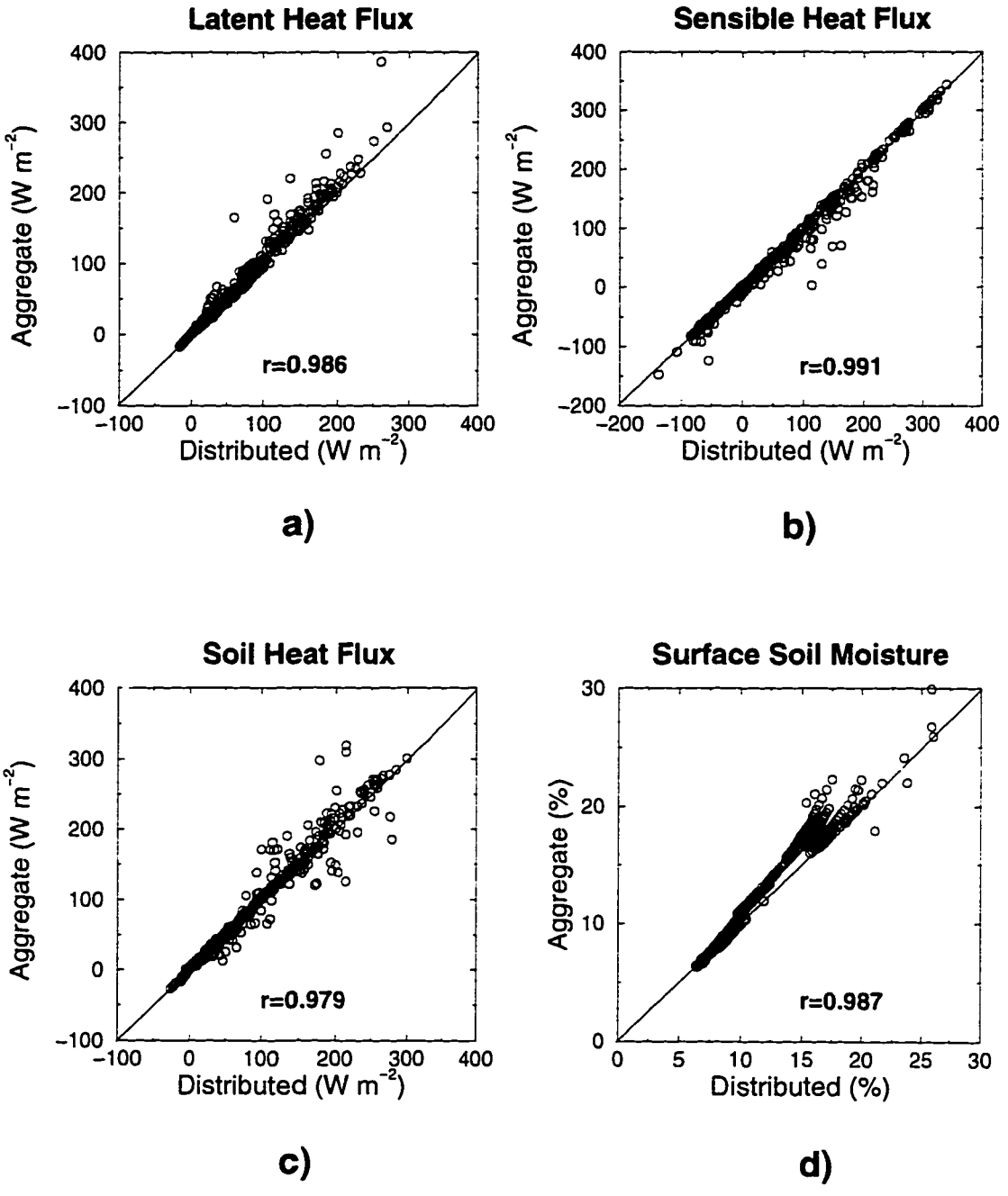

Figure 5.16: Comparison between the latent, sensible, and soil heat flux, and soil moisture as calculated by a single aggregate TOPLATS model and the distributed array of TOPLATS models for Monsoon '90.

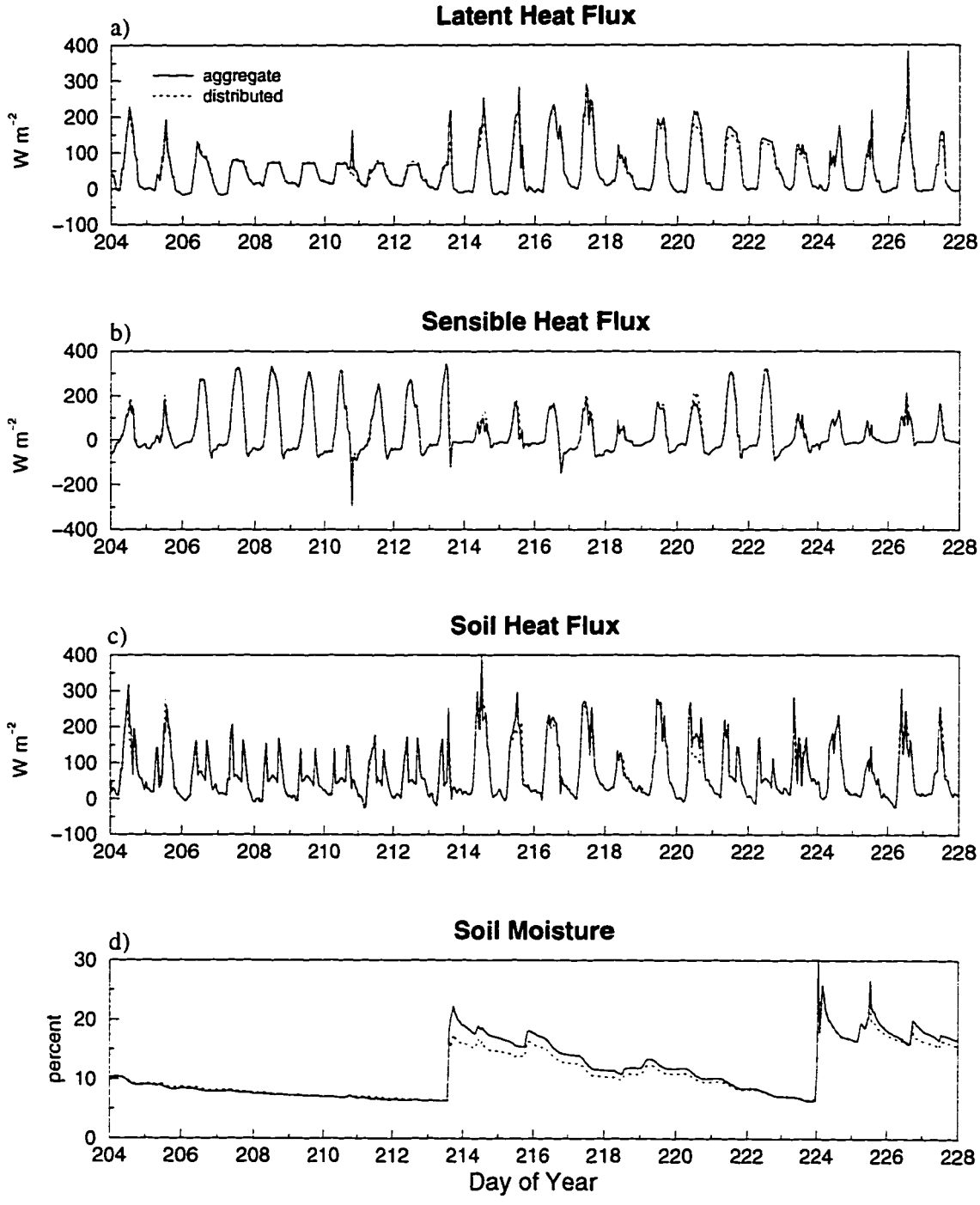

Figure 5.17: Time series comparisons of latent, sensible, and soil heat flux, and soil moisture as calculated by a single aggregate TOPLATS model and the distributed array of TOPLATS models for Monsoon '90.

less influential. However, the overall predictive capacity of the model is improved, and this is the primary goal of data assimilation techniques.

Other significant results are: (1) The polygon structure of the spatially variable vegetation and soil parameters can cause undesirable and unrealistic polygon edges in model predictions. This problem may be mitigated by using smoothed parameter fields. Meanwhile, these parameters have been left spatially constant in this study; (2) Some parameters tend to have similar values for minimum objectives from several sites, indicating that watershed average parameters may be acceptable; (3) The elimination of erroneous night data has little effect on the calibration; (4) Pareto parameter sets often produce objective functions with large error; (5) The proportion of the Monte-Carlo set that is Pareto decreases with Monte-Carlo set size; (6) Because sensible and latent heat fluxes contain similar information, only one of these should be used as an objective function during calibration; and (7) The inclusion of soil parameters in the calibration results in significantly better model performance.

6. SOIL MOISTURE DATA ASSIMILATION

Soil moisture data assimilation studies are the subject of this chapter. These results provide an example of the potential benefit of incorporating hydrologic observations in an intelligent manner. Assimilation of other hydrologic state variables such as temperature or water table depths might also have benefits, but assimilation of soil moisture is expected to have most influence because of its central role in regulating runoff, partitioning latent and sensible heat, and through determinating groundwater recharge. These data assimilation methodologies are expected to improve and have greater benefit when performed in the context of a coupled land-surface-atmosphere model. This study provides the groundwork for hydrologic data assimilation at regional, continental, and global scales.

6.1 Introduction

Four different data assimilation techniques were explored, namely: (1) direct insertion or updating, (2) 'statistical corrections', (3) Newtonian nudging, and (4) optimum or statistical interpolation. In the context of each of these several techniques were explored to find the those that were most feasible and beneficial.

All the TOPLATS simulations presented here use the calibrated parameters derived in Chapter 5 unless otherwise indicated. The modeled domain covers all of Walnut Gulch at a 40 m resolution spatially, and involve 93,622 model predictions per time step. Predictions are made at hourly intervals between days 204 and 228 of 1990. Model input and parameters are assumed to be spatially constant except for precipitation and topography. The assimilation data are PBMR-derived soil moisture estimates. Validation data is watershed-average latent and sensible heat flux (after correction) and gravimetric, TDR, and resistance *in-situ* soil moisture observations.

The parameter definitions and options for each of the assimilation methods are described briefly, and in each case a characteristic set of core results is shown. Finally the benefits and drawbacks of each method are assessed, and an intercomparison of techniques is shown.

Because the true spatial patterns of soil moisture are unknown, it is necessary to evaluate the relative performance of each data assimilation technique subjectively based on its ability to

produce reasonable spatial soil moisture patterns, on its ability to advect information, and on the improvement it gives to the time wise trajectory of the model.

6.2 Calibrated control

The calibrated TOPLATS control simulation described in the previous section is a useful benchmark for comparing the various data assimilation techniques. The control simulation can be considered an extreme case of data assimilation, in which it was assumed that the observations contain no information. The most critical spatial and temporal patterns that are used for comparison are shown in Figures 6.1 and 6.2. The spatial patterns of transmission zone soil moisture are not shown because they vary by only a small fraction of a percent over the model (temporal and spatial) domain, primarily because of the large depth and inertia of the transmission zone store.

The control simulation shows that surface soil moisture varies smoothly and follows the precipitation forcing. Variations in the root zone are much more subtle, and result from the variations in the input from the surface zone and in transpiration. Even with calibrated parameters, surface zone soil moisture is over-predicted, while the root zone is under-predicted because at initialization the model assumes spatially uniform soil moisture. The goal of the data assimilation studies is to merge observations with model predictions so as to provide realistic predictions of soil moisture variability from the model, despite its initialization, and to correct the positive bias of the model.

It should also be noted that precipitation has a profound effect on the variability of surface soil moisture. The storm on day 213 caused a large increase in the spatial variability, while the storm on day 224 caused an overall decrease in spatial variability. This difference is attributable to the variability of the precipitation in the storm itself. The decrease in surface soil moisture variability due to the storm on day 224 is not reflected in the root zone.

Data assimilation has the somewhat troublesome consequence that mass and energy is not conserved. That is, if the model has too much or too little water, the data assimilation process either creates or destroys water in the simulation in such a way as to make these states more realistic. This is a necessary consequence of the fact that the model did not properly simulate

the water fluxes. Water-balance information is therefore useful for comparing the differences between assimilation techniques. The simulated water-balances given by the control run for the eight monsoon '90 Metflux sites, and the watershed as a whole, are shown in Table 6.1. In this table *capillary rise* refers to the upward flux of water from the saturated surface, *ET* is evapotranspiration, *recharge* is the drainage to the saturated zone, *surface ΔS* is the sum of the changes in storage in the surface zone, *leaf ΔS* is the sum of the changes in storage in the interception store, *in-out* is the total input less the total output, *total ΔS* is the total change in storage, and *error* is *in-out* less *total ΔS*. From this table it is seen that the model conserves water without data assimilation.

Table 6.1: Water-balance information for the TOPLATS calibrated control simulation.

	Metflux Site:								Watershed
Variable (mm)	*1*	*2*	*3*	*4*	*5*	*6*	*7*	*8*	**Average**
Precip	99.33	82.66	118.87	114.32	107.12	116.49	92.25	90.56	93.44
Capillary Rise	0.00	0.00	0.00	0.00	0.00	0.00	0.00	0.00	0.00
ET	43.41	42.14	41.65	42.13	44.99	42.13	40.06	44.37	41.86
Runoff	14.70	0.00	13.92	19.38	5.15	15.84	0.00	1.92	6.21
Recharge	0.00	0.00	0.00	0.00	0.00	0.00	0.00	0.00	0.00
Surface ΔS	4.41	2.95	5.67	6.38	3.86	5.87	3.74	4.49	5.69
Root ΔS	30.96	31.41	48.19	38.70	44.19	43.13	38.75	33.59	33.51
Trans ΔS	5.85	6.15	9.43	7.72	8.87	9.51	9.62	6.18	6.14
Leaf ΔS	0.01	0.01	0.01	0.01	0.06	0.01	0.08	0.01	0.03
in-out	41.23	40.52	63.30	52.81	56.98	58.52	52.19	44.26	45.37
Total ΔS	41.23	40.52	63.30	52.81	56.98	58.52	52.19	44.26	45.37
Error	0.00	0.00	0.00	0.00	0.00	0.00	0.00	0.00	0.00

6.3 Direct insertion

Direct insertion or updating, the simplest form of data assimilation, was used as the first step in the development of a soil moisture data assimilation system. Model state variables are simply replaced with observed data at the time of the observation in an updating scheme, and no spatial propagation of the observations are made. Hence, this approach is the extreme case of data assimilation in which it is assumed that observations are perfect and that model

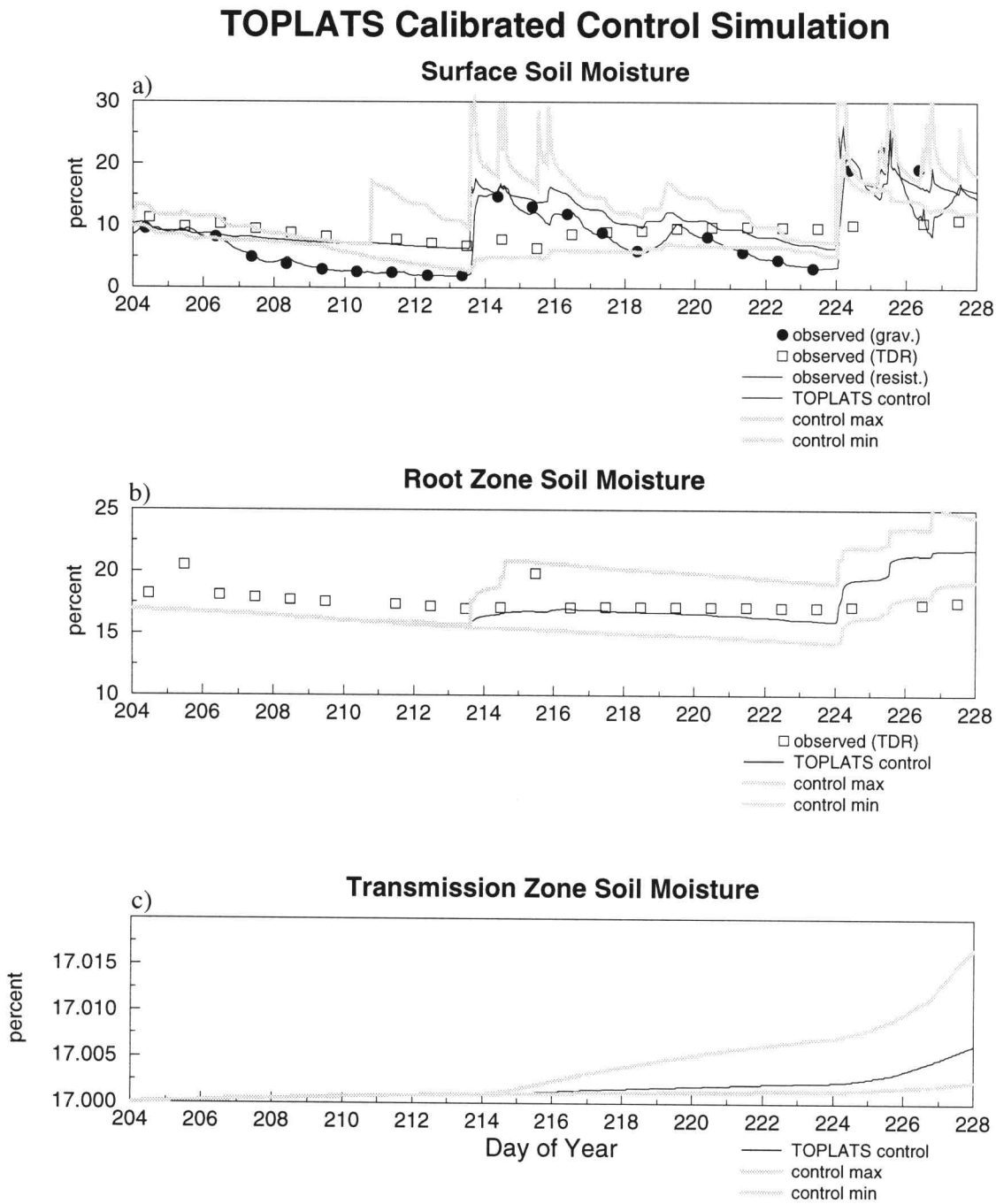

Figure 6.1: TOPLATS calibrated control simulation watershed average soil moisture.

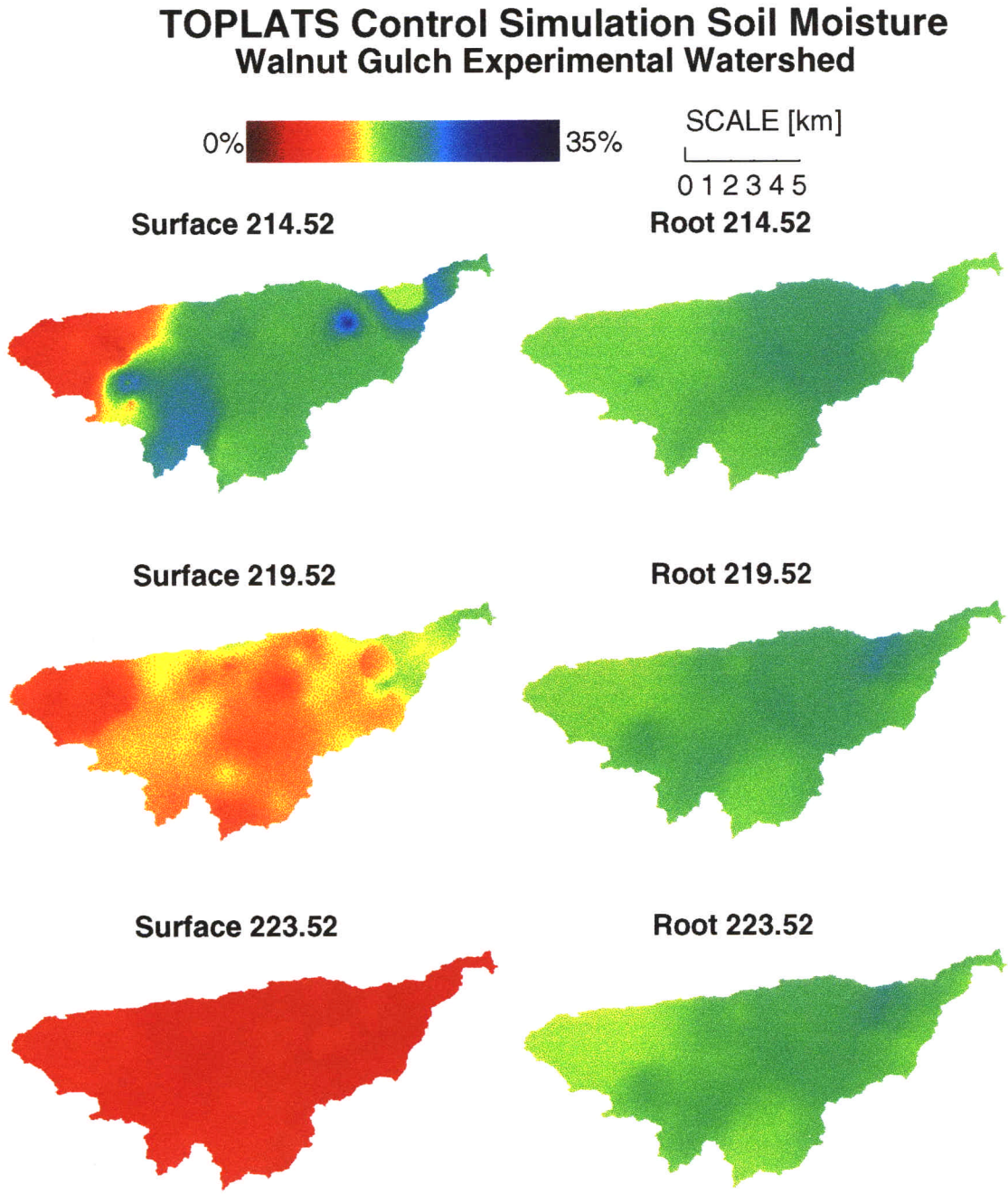

Figure 6.2: TOPLATS calibrated control simulation spatial surface soil moisture.

calculations contain no residual information of value. The opposite extreme is a model run without assimilation, assuming the model is perfect, i.e. the control run described above.

Time series plots of watershed average, model-predicted surface fluxes, temperature, soil moisture, and assimilation corrections are given in Figures 6.3 and 6.4 using the direct insertion assimilation technique. The direct insertion technique improves the time wise trajectory of the model catchment average soil moisture, but is unable to adjust it to the observed levels because the available data, and hence the correction is limited to only about one third of the watershed area. This correction does, however, feed back through the model to give lower latent heat fluxes and slight changes in other fluxes, but the root and transmission zone soil moisture status are also only slightly affected.

After the day 224 precipitation event there is little difference in surface soil moisture between the updating and control runs. This is a result common to all the data assimilation methods used in this study and is a model-related result. The storm on day 224 saturates the model's thin surface soil layer across the entire watershed, and all past assimilation information is forgotten. The surface soil moisture is replaced by the value of saturated soil moisture. This process does not occur in the model's root zone where memory of past assimilation is preserved. This sequence of events is not thought to be unrealistic, rather it suggests the time interval at which soil moisture observations are needed for data assimilation. This interval being less than or equal to the time interval between storm events.

The predicted spatial patterns of surface and root zone soil moisture at noon on a wet day (day 214) and on two dry days (days 219 and 223) are shown in Figure 6.5. Dry day prediction is emphasized because of the model's general predisposition to over-predict soil moisture in dry-periods. The direct insertion technique results in surface soil moisture predictions with very abrupt discontinuities at the boundary of the region for which observations are made and unpredictable spatial patterns within the observation area. These are undesirable qualities. There is a very slight reflection of these abrupt surface patterns in the root zone, and a data assimilation technique that can better advect information vertically would be preferable.

The water-balance information for the direct insertion simulation is given in Table 6.2. Clearly, as was expected the updating assimilation simulation does not conserve water. The

direct effect of the assimilation of surface soil moisture is an increase in the integrated root zone soil moisture change. This indirectly decreases evapotranspiration, runoff, and the change in the transmission zone. It is interesting that the surface zone soil moisture change does not change, because the day 224 precipitation event resets the surface soil moisture. In this case, about 4 mm of water was removed from the total area-average catchment water-balance.

Table 6.2: Water-balance information for the TOPLATS direct insertion simulation.

	Metflux Site:								Watershed
Variable (mm)	*1*	*2*	*3*	*4*	*5*	*6*	*7*	*8*	**Average**
Precip	99.33	82.66	118.87	114.32	107.12	116.49	92.25	90.56	93.44
Capillary Rise	0.00	0.00	0.00	0.00	0.00	0.00	0.00	0.00	0.00
ET	36.50	37.22	36.20	44.68	42.67	37.27	34.69	37.34	39.97
Runoff	12.15	0.00	11.00	16.90	5.58	12.64	0.00	0.00	5.68
Recharge	0.00	0.00	0.00	0.00	0.00	0.00	0.00	0.00	0.00
Surface ΔS	4.41	2.96	5.67	6.38	3.86	5.87	3.73	4.49	5.69
Root ΔS	23.67	28.20	46.04	37.73	42.42	42.66	33.67	25.66	32.31
Trans ΔS	3.76	5.13	8.56	7.45	7.81	9.50	7.20	3.86	5.75
Leaf ΔS	0.01	0.01	0.01	0.01	0.06	0.01	0.08	0.01	0.03
in-out	50.68	45.44	71.68	52.74	58.87	66.58	57.56	53.22	47.79
Total ΔS	31.85	36.29	60.28	51.57	54.15	58.04	44.68	34.02	43.78
Error	18.83	9.14	11.40	1.16	4.72	8.54	12.88	19.21	4.01

The direct insertion technique corrected the model's trajectory to give some improvement in soil moisture prediction. But the technique also preserves errors in the data and does not advect observation information.

This early attempt highlighted two key issues that need to be looked for as a baseline in subsequent assimilation methodologies. First, it is valuable if the technique that can spread or advect observation information both vertically and horizontally; second, it is important that the resulting patterns are continuous. This probably means that the resulting soil moisture patterns need to be similar in character to those predicted by the model without assimilation.

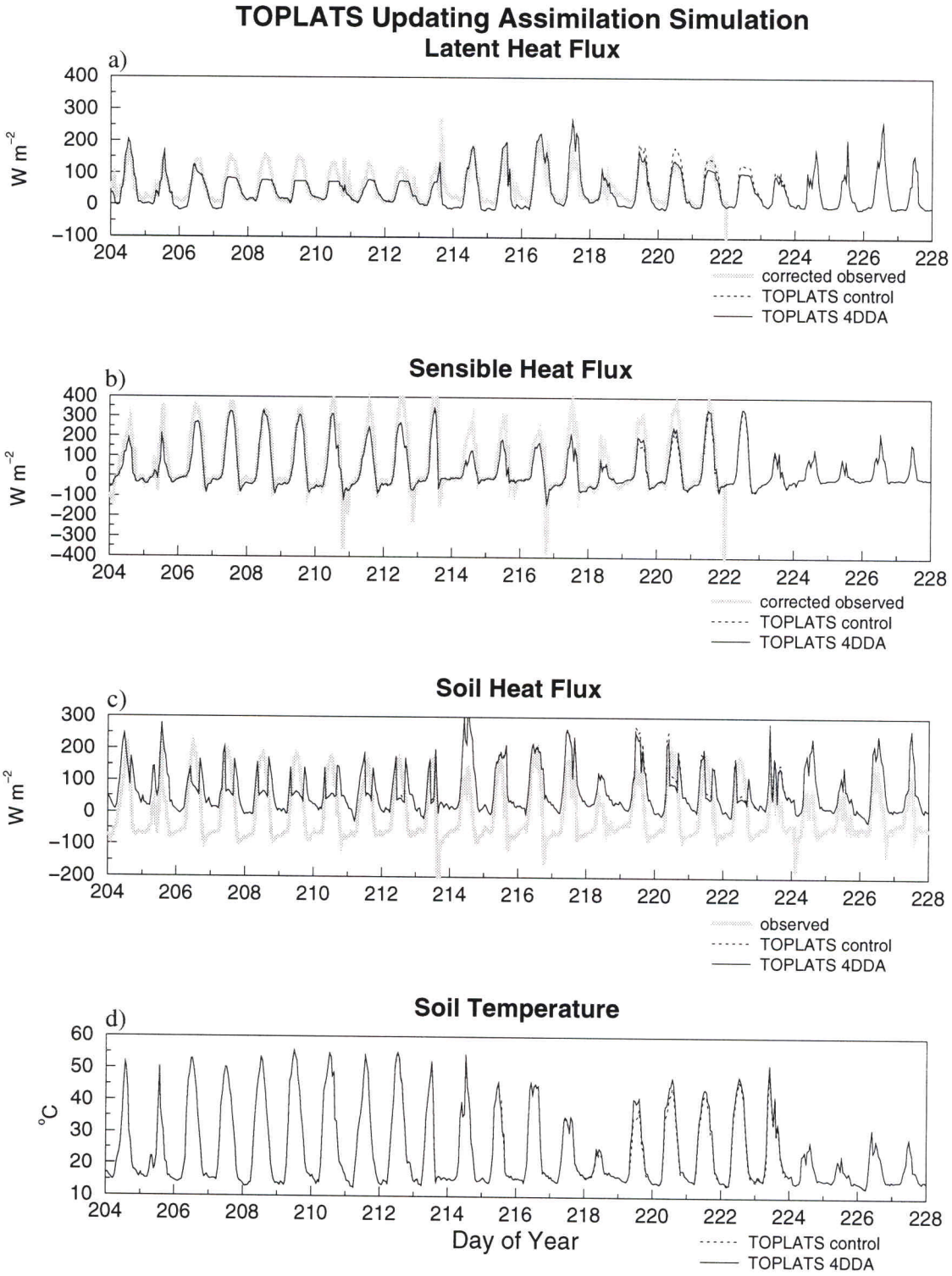

Figure 6.3: TOPLATS direct insertion assimilation simulation watershed average surface fluxes and temperature.

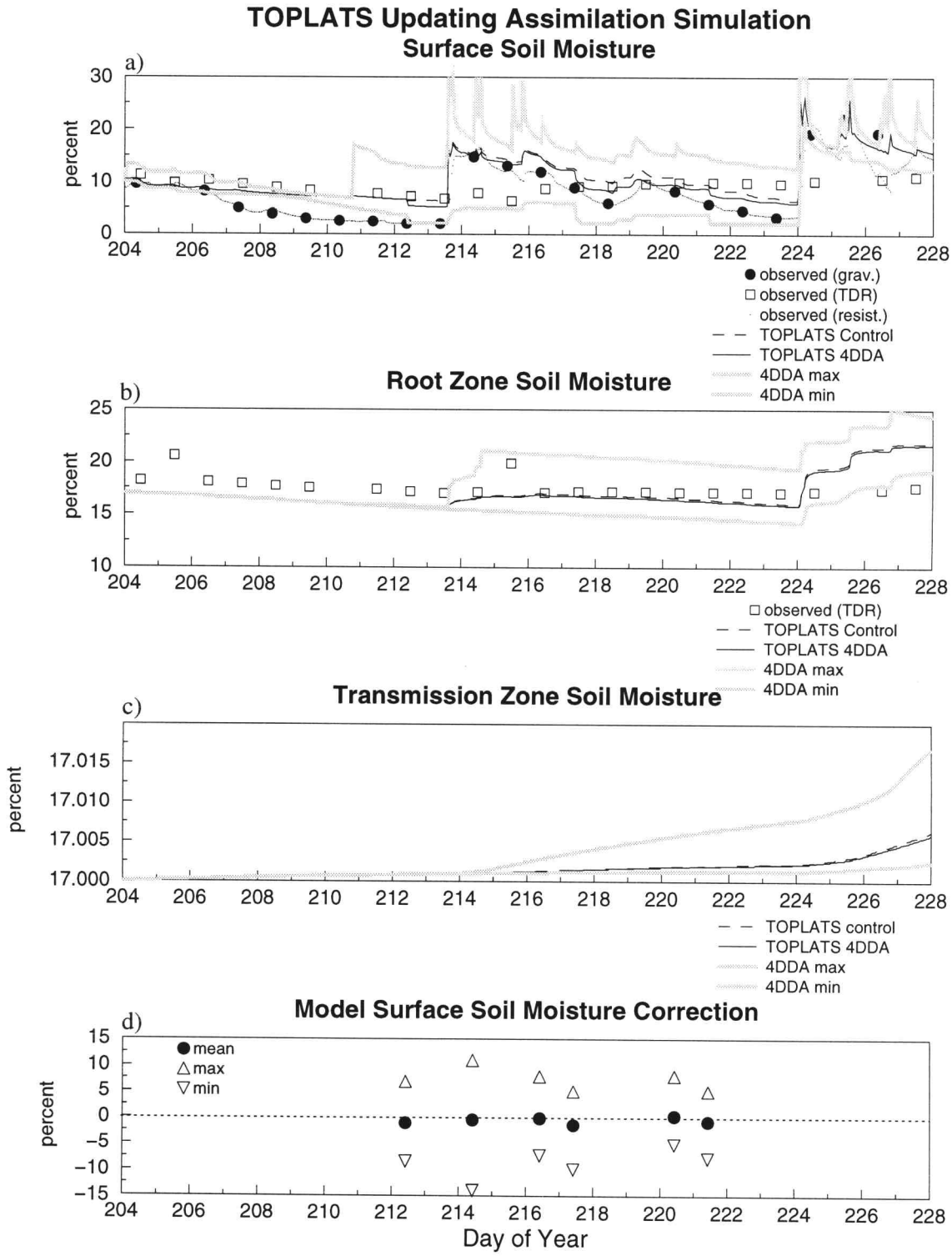

Figure 6.4: TOPLATS direct insertion assimilation simulation watershed average soil moisture.

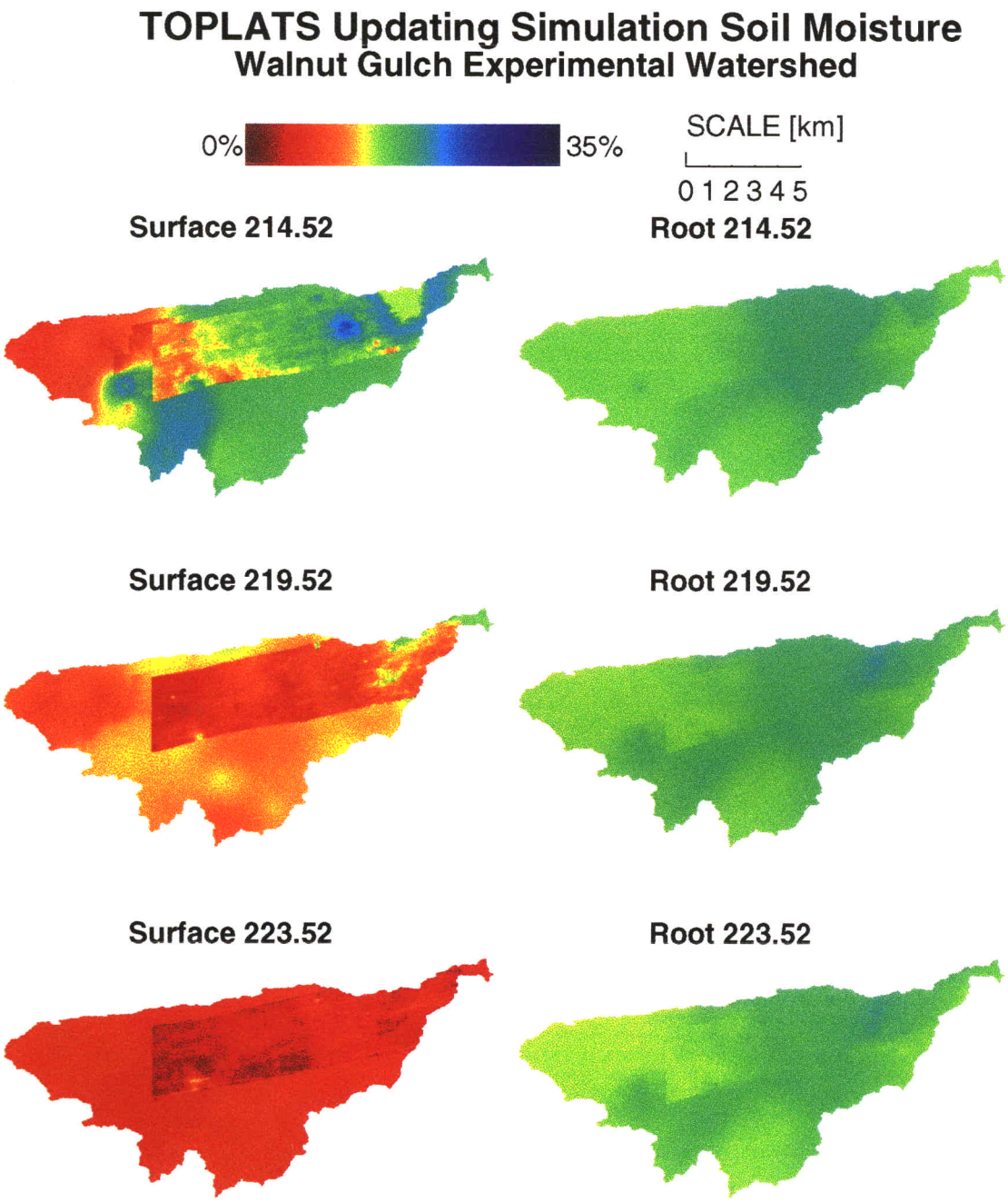

Figure 6.5: TOPLATS direct insertion assimilation simulation spatial soil moisture.

6.4 Statistical correction

In this technique, which this author termed 'statistical correction', simply adjusted the mean and standard deviation of the surface soil moisture states in the model to match the mean and standard deviation of the observations. The method assumes that the statistics of the observations are perfect, which is arguably more reasonable than assuming that each observation is in itself perfect which is the assumption implicit in direct insertion. It also assumes that the patterns predicted by the model are correct, but that the predicted surface soil moisture statistics are incorrect or contain a bias. As with updating, advection of information into deeper soil zones is accomplished solely through the model physics.

Time series plots of the model-predicted watershed average surface fluxes, temperature, soil moisture, and assimilation correction are given in Figures 6.6 and 6.7 for the statistical correction assimilation technique. In terms of the temporal response the statistical corrections technique matched observations closely in the surface zone and has a larger effects in deeper soil moisture zones and on surface fluxes than does direct insertion. It is also important to note that the overall magnitude of the surface soil moisture correction is larger with assimilation via statistical correction, although larger individual corrections were made by the direct insertion method. It is possible that the direct insertion method made unnecessarily large corrections in anomalous or erroneous observation areas.

Spatial predictions of surface and root zone soil moisture are shown in Figure 6.8. The spatial characteristics of the statistical interpolation technique is much better than with direct insertion. The spatial patterns are continuous and reflect the model's predictive capacity. The only displeasing feature is the absence of any of the observed detail in the soil moisture patterns, and the fact that there is no decrease in assimilation correction as a function of distance from the observation area.

The water-balance information for the statistical corrections assimilation technique is given in Table 6.3. Over the whole catchment, statistical corrections assimilation subtracted more than twice the catchment water subtracted by updating assimilation.

Table 6.3: Water-balance information for the TOPLATS statistical correction simulation.

Variable (mm)	Metflux Site: 1	2	3	4	5	6	7	8	*Watershed Average*
Precip	99.33	82.66	118.87	114.32	107.12	116.49	92.25	90.56	93.44
Capillary Rise	0.00	0.00	0.00	0.00	0.00	0.00	0.00	0.00	0.00
ET	39.27	36.81	36.21	36.19	39.87	35.89	35.09	39.61	36.76
Runoff	14.56	0.00	10.70	16.19	5.60	12.69	0.00	1.93	5.15
Recharge	0.00	0.00	0.00	0.00	0.00	0.00	0.00	0.00	0.00
Surface ΔS	4.41	2.96	5.67	6.38	3.86	5.87	3.73	4.49	5.69
Root ΔS	26.79	27.86	46.23	37.34	41.00	41.97	33.84	30.41	29.85
Trans ΔS	4.50	4.95	8.56	7.22	7.10	8.94	7.29	5.05	5.09
Leaf ΔS	0.01	0.01	0.01	0.01	0.06	0.01	0.08	0.01	0.03
in-out	45.49	45.85	71.96	61.94	61.65	67.90	57.16	49.02	51.53
Total ΔS	35.70	35.78	60.47	50.95	52.01	56.78	44.94	39.96	40.66
Error	9.79	10.07	11.49	10.99	9.64	11.12	12.22	9.06	10.87

Generally, the statistical corrections assimilation technique is only applicable to areas that have large numbers of remotely-sensed observations which are believed to effectively sample the statistics of the assimilation state. The method is however very computationally efficient, taking only slightly more computational time than the control simulation. It performs similarly to updating temporally, but it is able to spread observation information horizontally and does not preserve the local observation errors in the model fields. Its drawbacks are that it preserves none of the pattern in the observations and that it does not advect information vertically.

6.5 Assimilation information sensitivity

The sensitivity of model predictions to a single set of observations was explored using the statistical corrections assimilation method. To accomplish this, 14 different model simulations were performed, namely the control run (with no assimilation), the statistical corrections run (with all the observations), six statistical corrections runs without assimilation of one of its observations, and six statistical corrections run with just one of the six sets of observations assimilated.

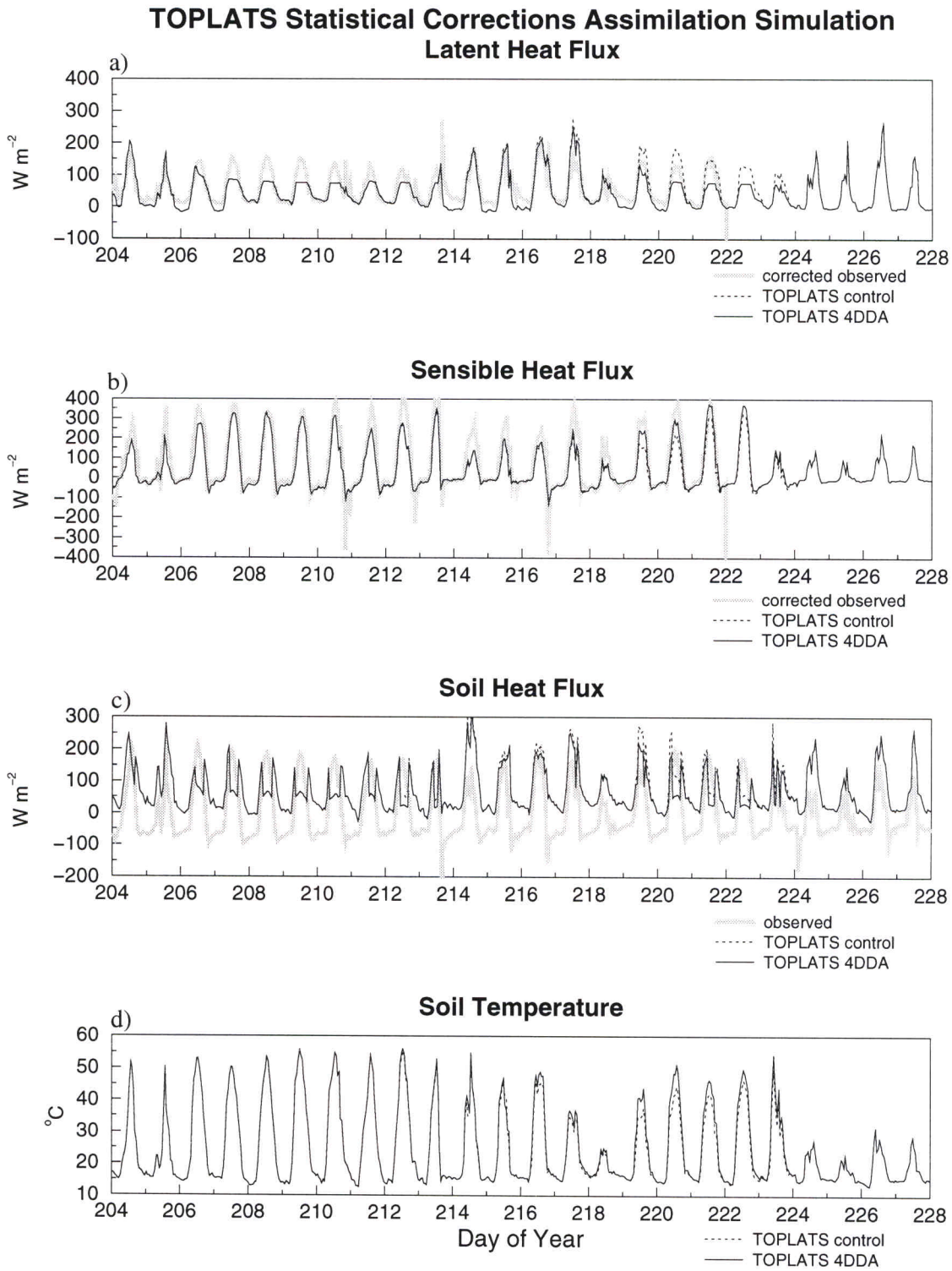

Figure 6.6: TOPLATS statistical corrections assimilation simulation watershed average surface fluxes and temperature.

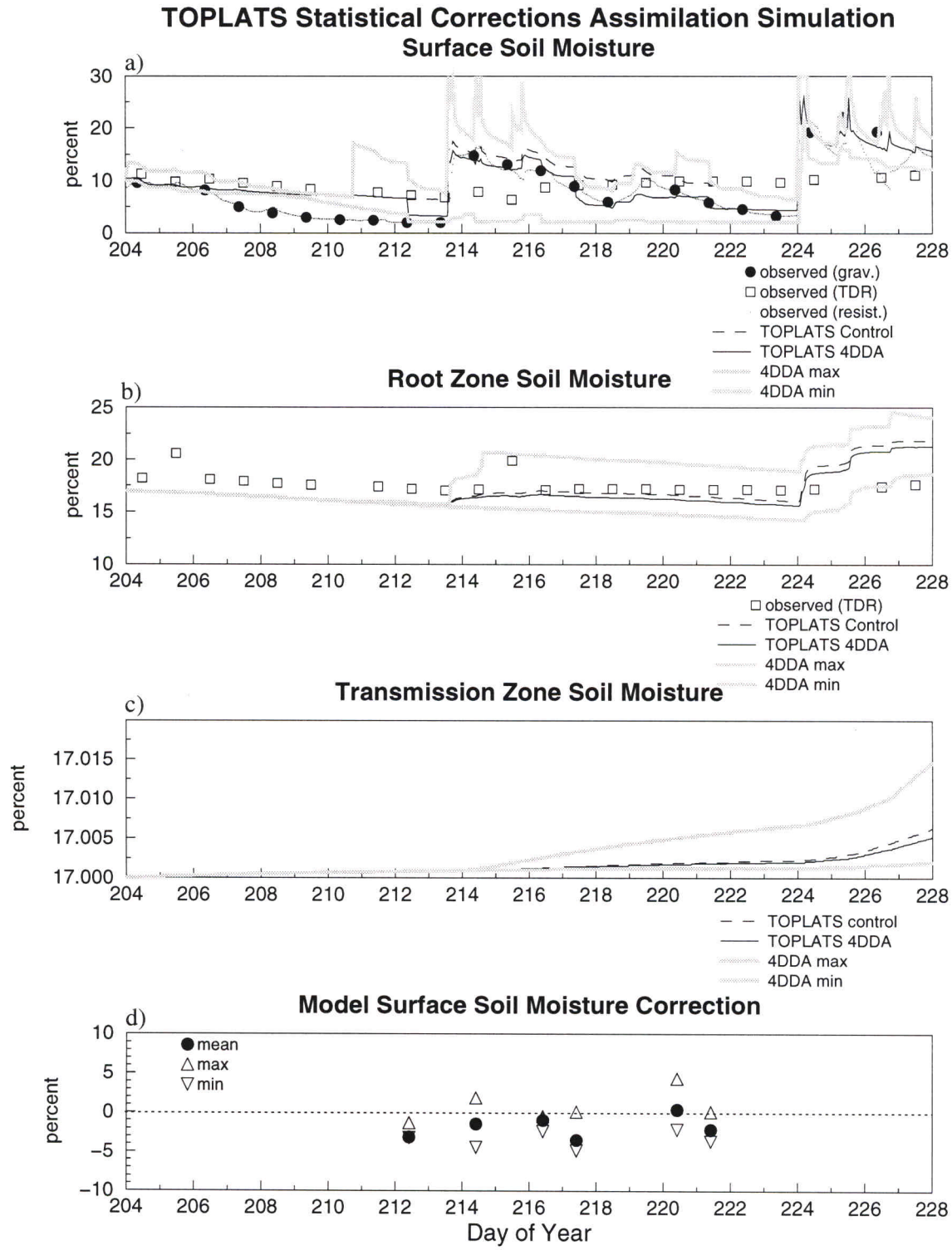

Figure 6.7: TOPLATS statistical corrections assimilation simulation watershed average soil moisture.

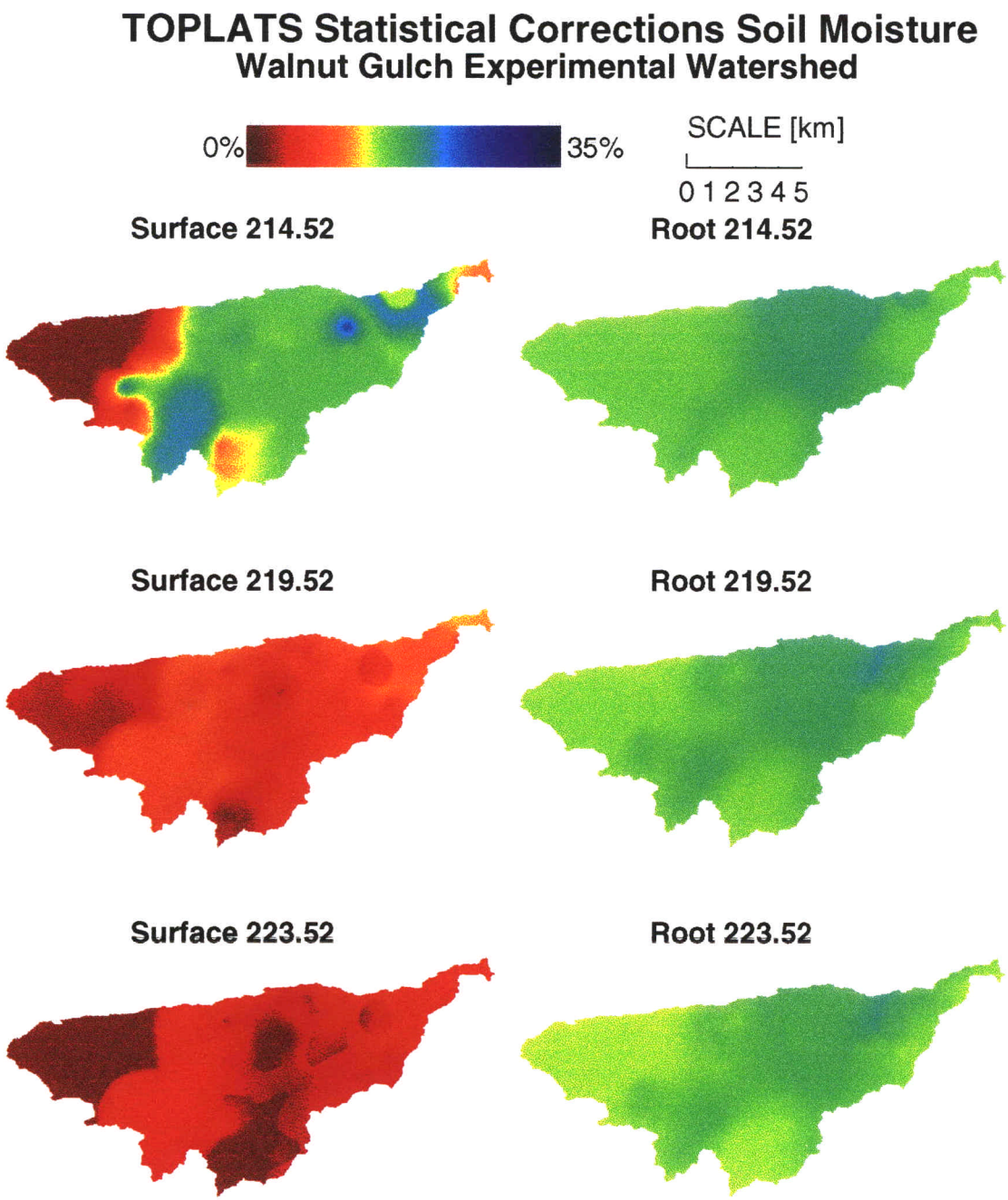

Figure 6.8: TOPLATS statistical corrections assimilation simulation spatial soil moisture.

The watershed average surface soil moisture time series for each of these simulations is shown in Figures 6.9 and 6.10 (Note: the simulations presented here use an early parameter set; hence they are not directly comparable to the runs described elsewhere in this chapter. They are comparable with each other, and the different calibration does not effect the conclusions). It is clear that the removal of any observation information negatively affects the model's predictive ability. The removal of some observation sets has less effect than the removal of other sets. For example, the removal of observations on days 216, 212, and 214 has very little consequence, while the removal of the observations on day 217 has a large affect. By only including one observation set in the assimilation, the optimal sampling interval after a storm can be assessed. In this case, observations two to three days after a storm have the most benefit for model prediction, with day 217 having the largest impact.

Spatial soil moisture patterns from these sensitivity runs are shown in Figures 6.11 and 6.12. These plots confirm that observations on day 217 have the most influence on the accurate spatial predictions of soil moisture on day 219. The removal of any observation degrades the quality of overall patterns predicted. Because the model is not able to simulate dry down events well the observations on day 217 (when the dry down from the day 213 storm completes) are of largest importance for model correction.

6.6 Statistical correction with updating

This method is simply a combination of the previous two methods. Here, a statistical correction is made followed by a direct insertion of observations where they exist. This has the effect of spreading the observation statistical information horizontally beyond the region of observation and of preserving the observed spatial patterns inside the area of observation.

The watershed average time series of surface fluxes and soil moisture for the statistical corrections-updating technique are shown in Figures 6.13 and 6.14. As expected, this assimilation technique performs very similarly to statistical corrections, but with the surface range of the soil moisture correction more typical of updating.

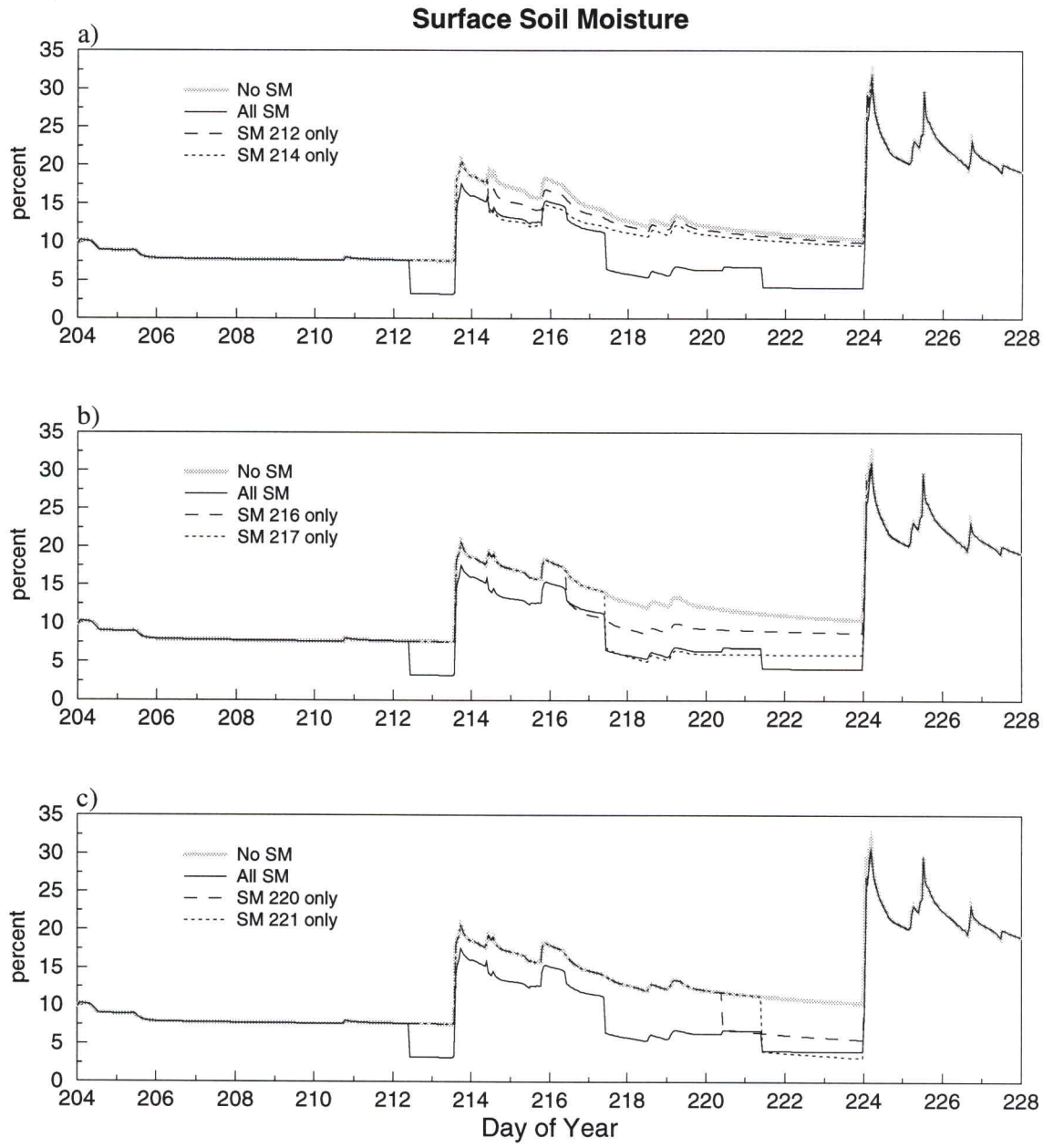

Figure 6.9: Sensitivity of assimilation information on watershed average surface soil moisture prediction using statistical corrections.

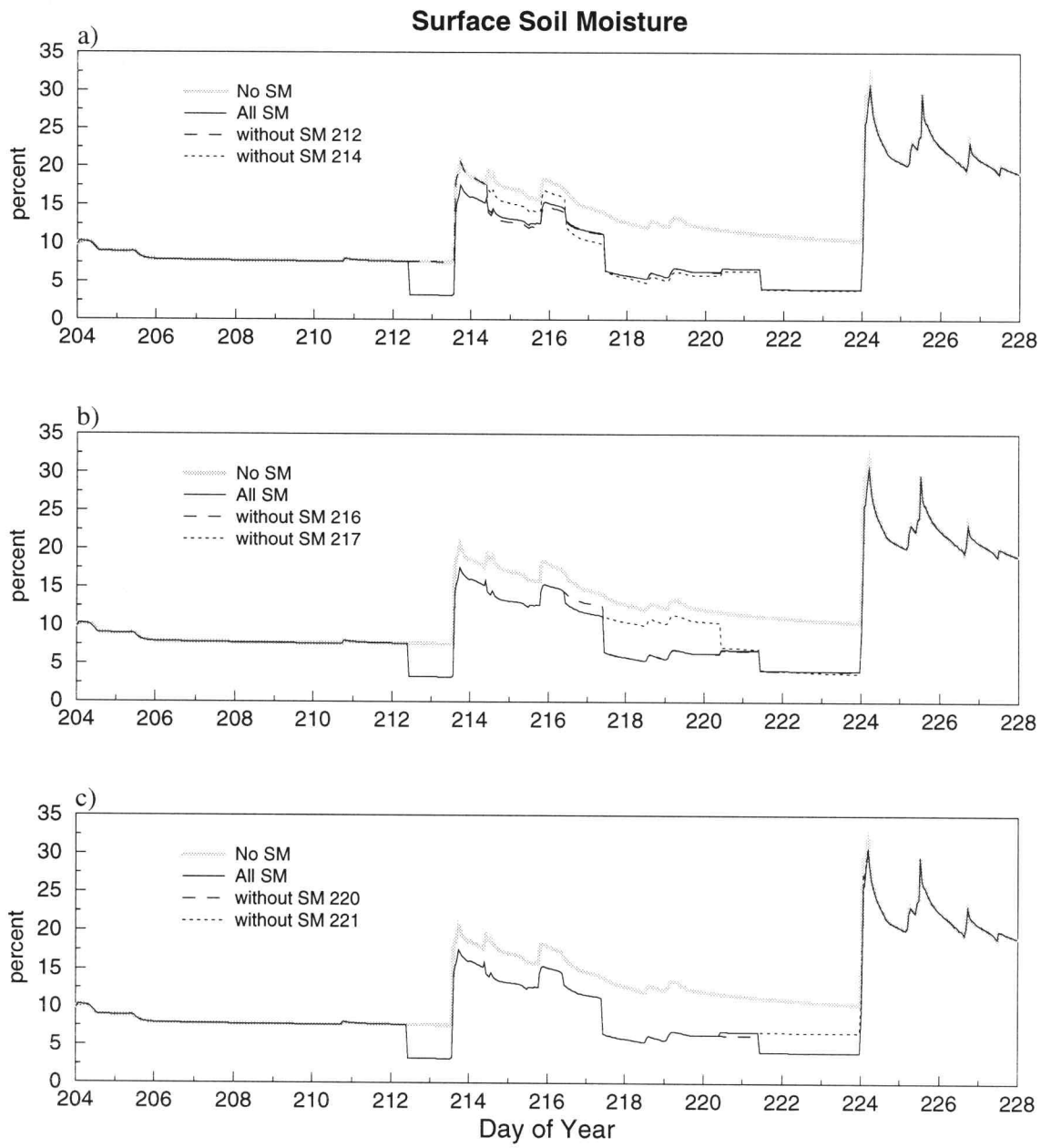

Figure 6.10: Sensitivity of assimilation information on watershed average surface soil moisture prediction using statistical corrections.

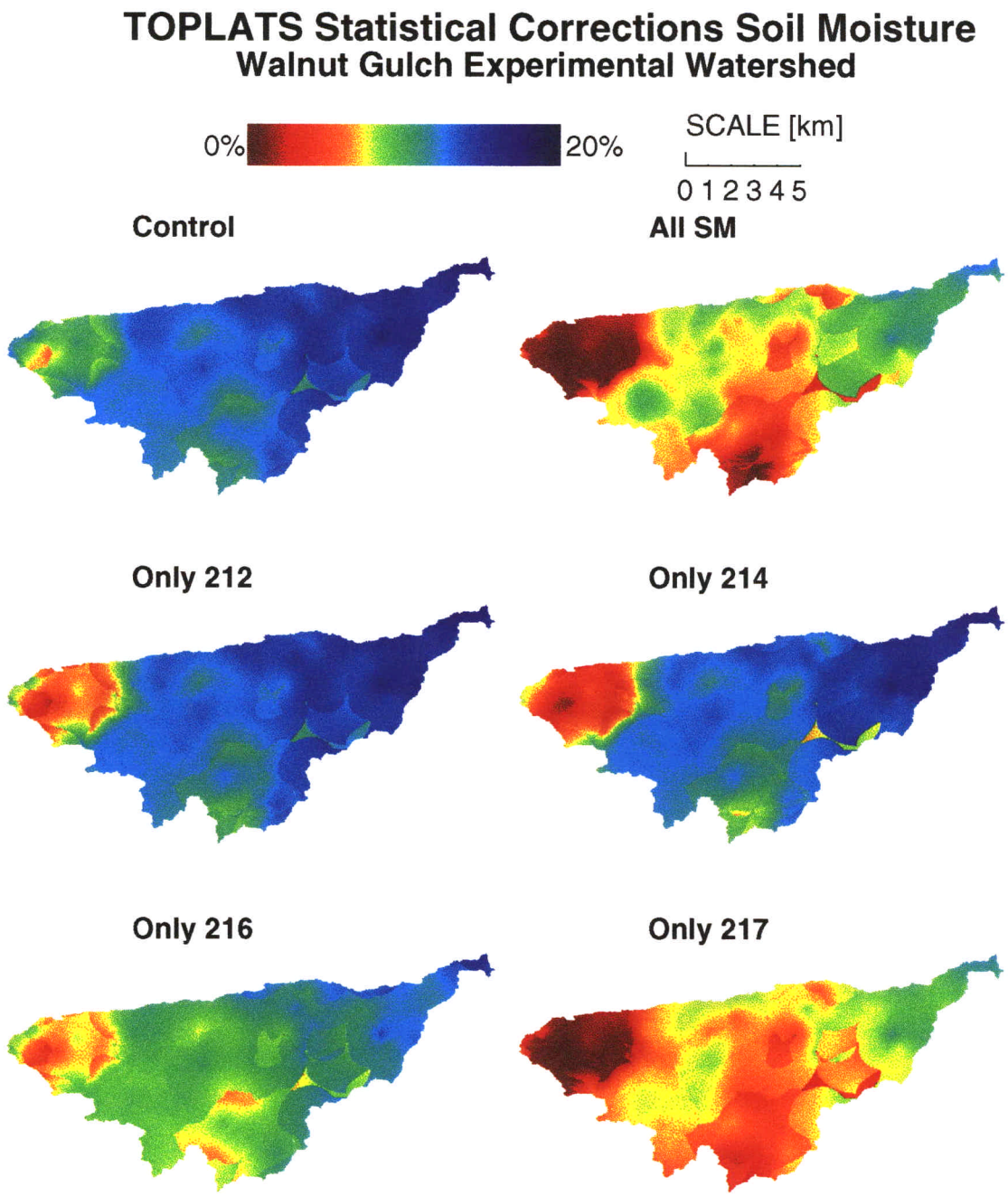

Figure 6.11: Sensitivity of assimilation information on spatial surface soil moisture prediction using statistical corrections.

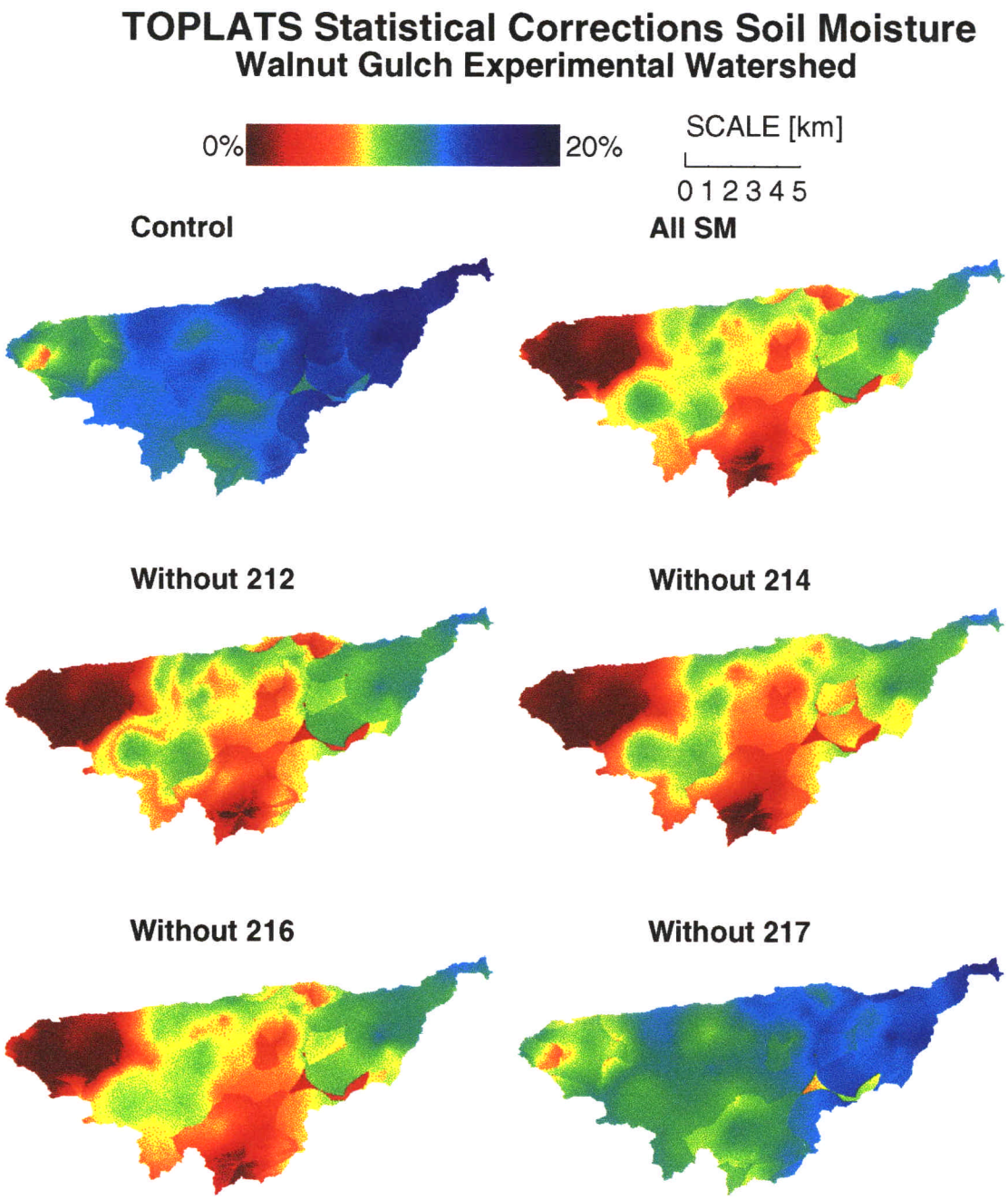

Figure 6.12: Sensitivity of assimilation information on spatial surface soil moisture prediction using statistical corrections.

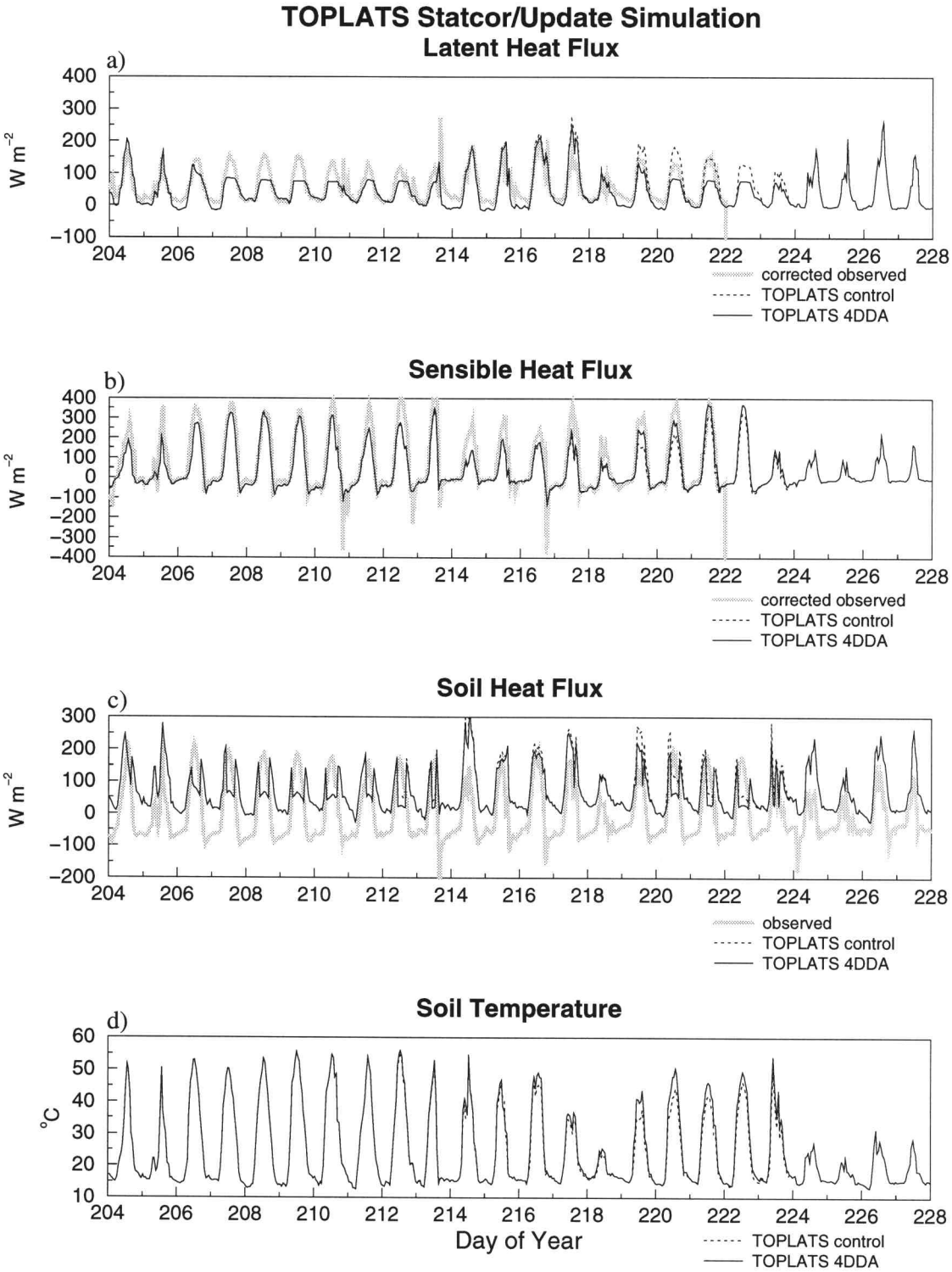

Figure 6.13: TOPLATS statistical corrections updating assimilation simulation watershed average surface fluxes and temperature.

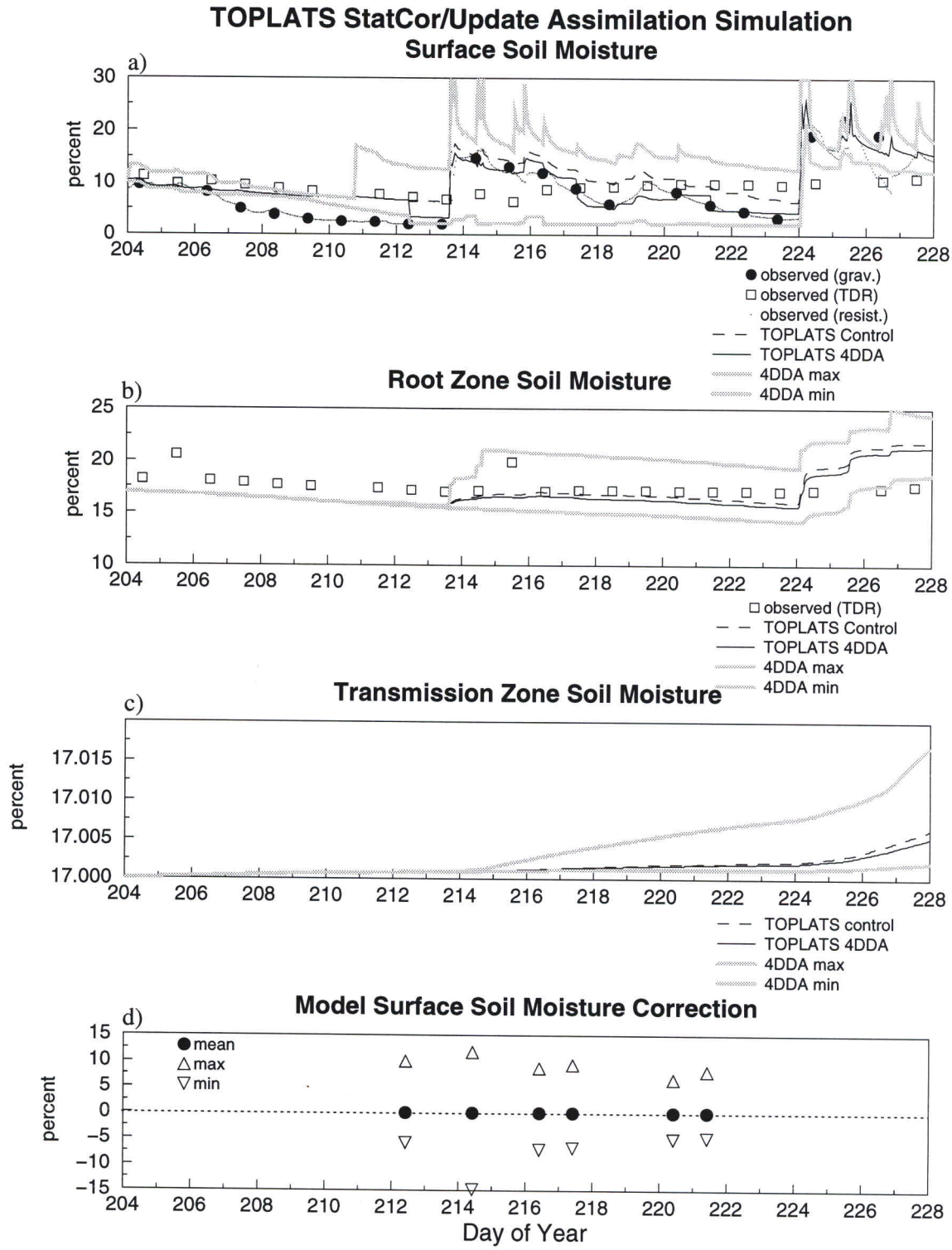

Figure 6.14: TOPLATS statistical corrections updating assimilation simulation watershed average soil moisture.

The spatial predictions of the statistical correction-updating assimilation technique are shown in Figure 6.15. These patterns are arguably preferable to either updating or statistical corrections separately, with the overall bias inside and outside the observation area better matched and preservation of the observation patterns where available However, this method again assumes that the observations are perfect; thus, the technique is not perfect because some of the observed patterns are probably erroneous.

6.7 Newtonian nudging

The Newtonian nudging data assimilation technique addresses several of the deficiencies apparent in the mode simple data assimilation methods and extends assimilation vertically into the root and transmission zones. In Newtonian nudging increments are added to the model's prognostic equation that 'pushes' the model towards an observation or set of observations in a predefined space-time window. The four-dimensional weighting function is determined using a set of three simple predefined (horizontal, vertical, and temporal) functions that assign a weight to an observation which decrease with the observation's temporal and spatial distance from the model point being corrected. The only assimilation parameters that need to be defined are the observation's vertical, horizontal, and temporal radii of influence.

Because precipitation has a large influence on soil moisture, it was decided that temporal nudging should not occur in time across precipitation events. For example, soil moisture states before a precipitation event should not be nudged towards an observation after the event because of the very different hydrologic processes which then operate.

Newtonian nudging most suitable for use with few observations, because it is very computationally demanding, and the horizontal assimilation weights tend to decrease as numbers of observations increase (i.e., the overall nudging weight is greater with 1 observation at a distance X, than with 1 observation at distance X and 100 observations at a distance 2X). This is counter intuitive since it makes more sense to have increasing weight with increasing information. The established Newtonian nudging methodology was therefore adapted for use with remote-sensing data (where there are many observations) by modifying the weighting

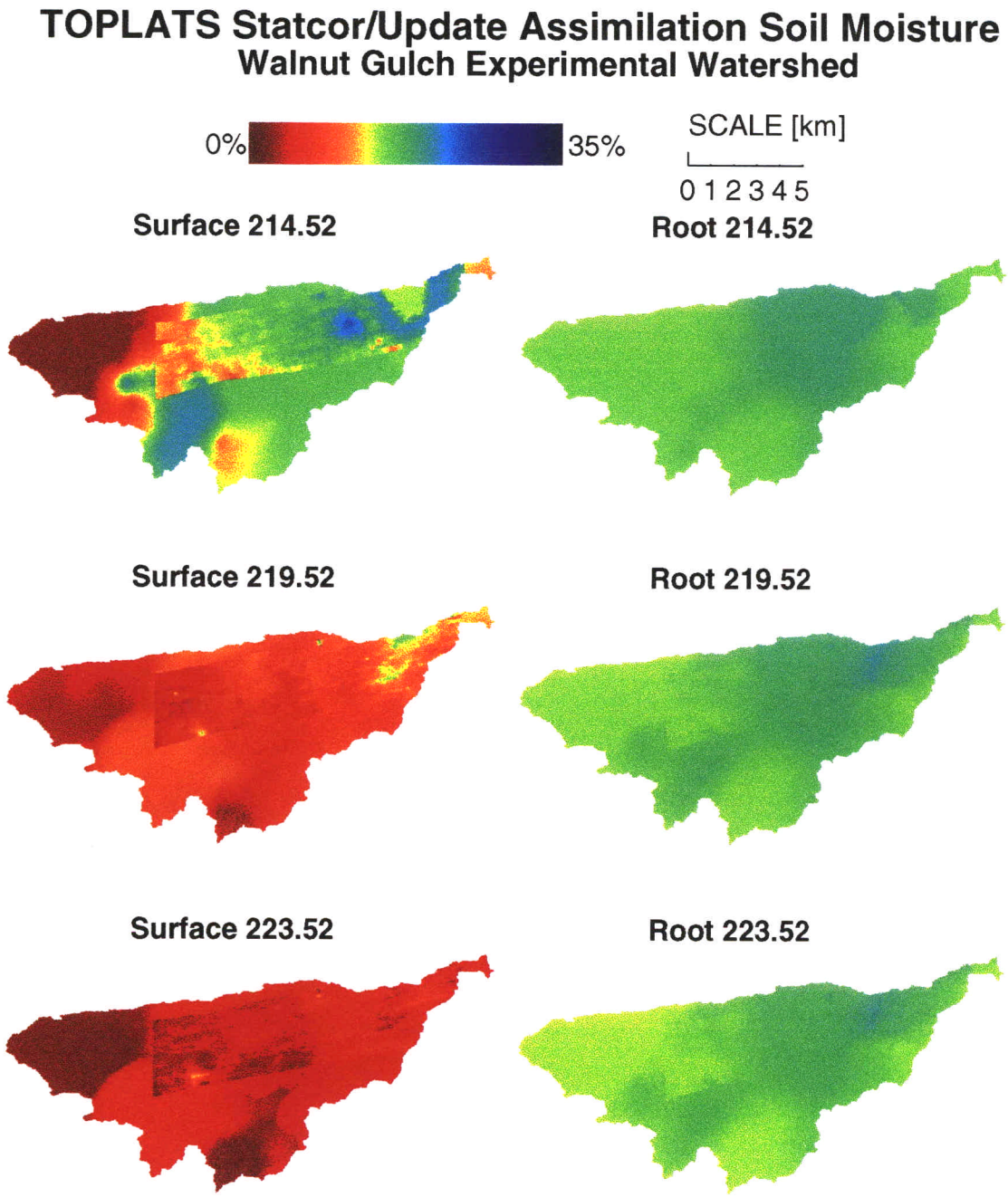

Figure 6.15: TOPLATS statistical corrections updating assimilation simulation spatial soil moisture.

structure -- so that is does not fall with increasing numbers of observations -- and by making the code very efficient.

At the outset of this research the validity of extrapolating information horizontally and vertically away from the observation area was questioned because the assimilation is in essence based on interpolation. To explore this concern, the Newtonian nudging methodology was modified to allow different extrapolation options. These options were Newtonian nudging-based weighting of the statistical corrections technique, nudging to individual observations, and making no data assimilation outside the area of observations. Inside the observation area, nudging to the observation 'analysis' or to sets of individual observations is allowed. Nudging to an analysis means that a single-grid model state is nudged towards a single observation located or interpreted to the model grid; this usually results in the preservation of local observation patterns. Nudging to individual observations means that a single-grid model state is nudged towards a weighted average of all the observations within the defined observation distance of influence. This second approach generally results in smoothing of small-scale observation patterns.

A number of parameters must be defined for the Newtonian nudging assimilation model because it operates on all three TOPLATS soil zones. Following Stauffer and Seaman (1990), most of these parameters (such as the analysis and observation quality factors) were set to unity so that they did not complicate the process. The spatial radii of influence parameters were set to values determined for use in the statistical interpolation technique (see section 6.9). The nudging factors are conventionally selected so that the time scale of the slowest physical adjustment process in the model and the nudging term are similar. Thus, the nudging factor is usually less than $1/\Delta t$: about 10% of this value seemed to work well in this study. The parameters specifying Newtonian nudging are shown in Table 6.4.

Different nudging options inside and outside the observation region were explored in a series of nudging simulations thus: (1) nudging to observations inside and nudging weighted statistical correction outside; (2) nudging to an analysis inside and nudging to observations outside; (3) nudging to an analysis inside and nudging to weighted statistical correction outside; and (4) nudging to observations both inside and outside the observation area.

Table 6.4: Newtonian nudging model parameters.

Parameter	Value	Source
Depth of observation	0.05 m	Schmugge *et al.*, 1994
Depth of surface zone	model assigned	
Depth of root zone	model assigned	
Depth of transmission zone	model assigned	
Temporal function (1=Lyne, 2=Stauffer)	1	
Temporal radius of influence	12 hours (not across precipitation events)	
Horizontal radius of influence	10,000 m	correlation analysis
Vertical radius of influence	0.5 m	correlation analysis
Surface zone nudging constant	0.2	subjective optimization
Root zone nudging constant	0.1	subjective optimization
Transmission zone nudging constant	0.0	subjective optimization
Surface zone grid analysis quality factor	1.0	Stauffer and Seaman, 1990
Root zone grid analysis quality factor	1.0	Stauffer and Seaman, 1990
Transmission zone grid analysis quality factor	1.0	Stauffer and Seaman, 1990
Surface zone observation quality control factor	1.0	Stauffer and Seaman, 1990
Root zone observation quality factor	1.0	Stauffer and Seaman, 1990
Transmission zone observation quality factor	1.0	Stauffer and Seaman, 1990

The spatial patterns produced by each of these options are shown in Figures 6.16 through 6.21. The first three methods have differing Newtonian nudging options inside and outside the observation area and, therefore, produce undesirable discontinuities at these boundaries. It is preferable that the same options are used in the entire model domain as in method 4. This last method also produces plausible spatial patterns that resemble model predictions. This last, clearly superior method that nudges to observations both inside and outside the observation area is the focus of the remainder of this section.

The assimilation feedbacks in the watershed average surface fluxes shown in Figure 6.20 are similar to those seen in other assimilation methods previously presented. The assimilation corrections and soil moisture time series shown in Figure 6.21 are of particular interest. Clearly, there are more time steps where corrections of smaller magnitudes are made, and the temporal weighting structure of nudging is very evident. Additionally, the time series of surface soil moisture have a much smoother look than previous methods. In updating, statistical corrections, and statistical interpolation (yet to be described), the entire model correction is made during one time step, producing an undesirable time series discontinuity. Newtonian nudging not only spreads this correction out to give a smoother time series, but also corrects the simulation based

on a future set of observations. This characteristic has disadvantages, in that it prohibits the application of this method in real-time.

The catchment water-balance shown in Table 6.5 shows a two fold increase in subtraction of water over the statistical corrections method and a five fold increase over updating.

Table 6.5: Water-balance information for the TOPLATS Newtonian nudging simulation.

	Metflux Site:								Watershed
Variable (mm)	*1*	*2*	*3*	*4*	*5*	*6*	*7*	*8*	**Average**
Precip	99.33	82.66	118.87	114.32	107.12	116.49	92.25	90.56	93.44
Capillary Rise	0.00	0.00	0.00	0.00	0.00	0.00	0.00	0.00	0.00
ET	39.44	38.36	38.16	39.85	43.99	37.30	34.88	38.41	37.32
Runoff	12.06	0.00	10.89	16.35	3.54	12.98	0.00	0.36	5.08
Recharge	0.00	0.00	0.00	0.00	0.00	0.00	0.00	0.00	0.00
Surface ΔS	4.41	2.96	5.67	6.38	3.86	5.87	3.73	4.49	5.69
Root ΔS	20.71	22.73	43.75	33.10	36.57	37.79	28.85	19.84	22.60
Trans ΔS	3.24	3.77	7.14	5.63	5.38	6.78	5.27	2.82	3.49
Leaf ΔS	0.01	0.01	0.01	0.01	0.06	0.01	0.08	0.01	0.03
in-out	47.83	44.30	69.82	58.13	59.59	66.21	57.37	51.79	51.03
Total ΔS	28.37	29.47	56.57	45.13	45.87	50.45	37.93	27.16	31.81
Error	19.46	14.83	13.26	13.00	13.72	15.76	19.45	24.63	19.22

Overall, the Newtonian nudging methodology results in spatial patterns that are very similar to those derived from statistical corrections, with the added benefit of vertical assimilation and more gradual temporal changes.

6.8 Statistical correction local nudging

This assimilation technique performs a statistical correction followed by local nudging towards the observed analysis in the observation area. This is very similar to the nudging to an analysis inside and nudging weighted statistical correction outside, as described in the previous section. The difference here is that assimilation is limited to the surface zone at the observation time step. The observation area analysis nudging simply adds some but not all local pattern information to the model field.

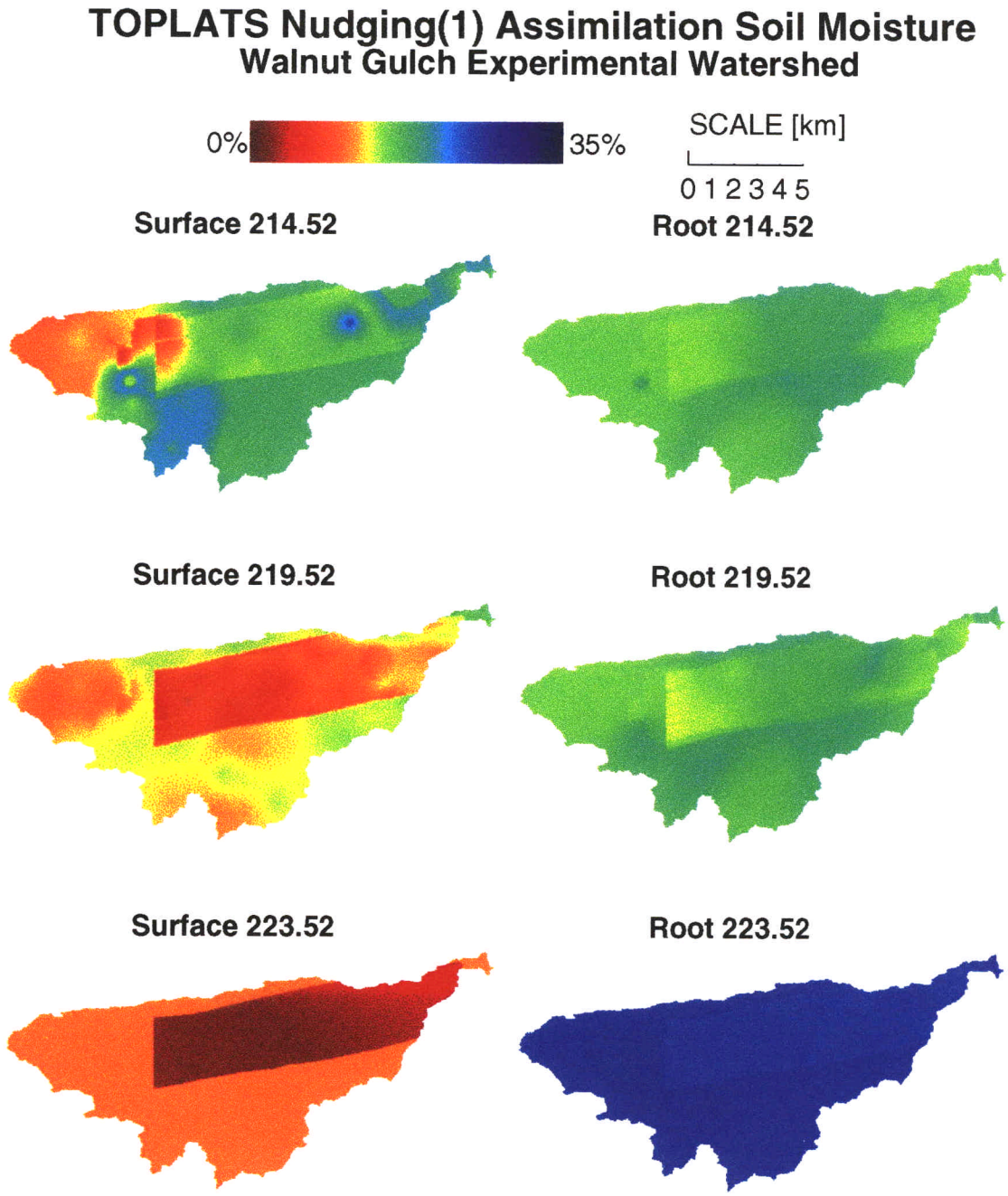

Figure 6.16: TOPLATS nudging(1) assimilation simulation spatial soil moisture.

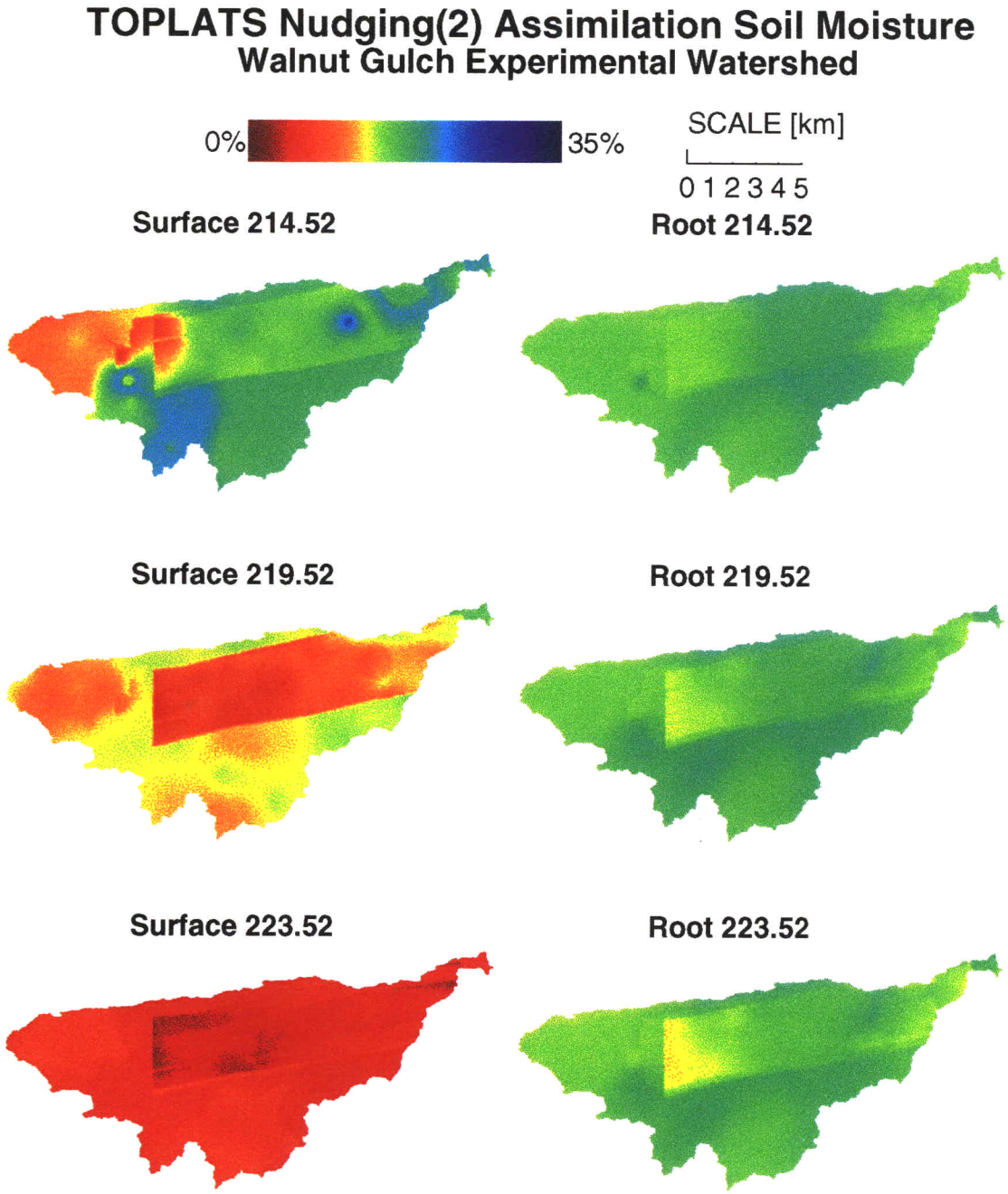

Figure 6.17: TOPLATS nudging(2) assimilation simulation spatial soil moisture.

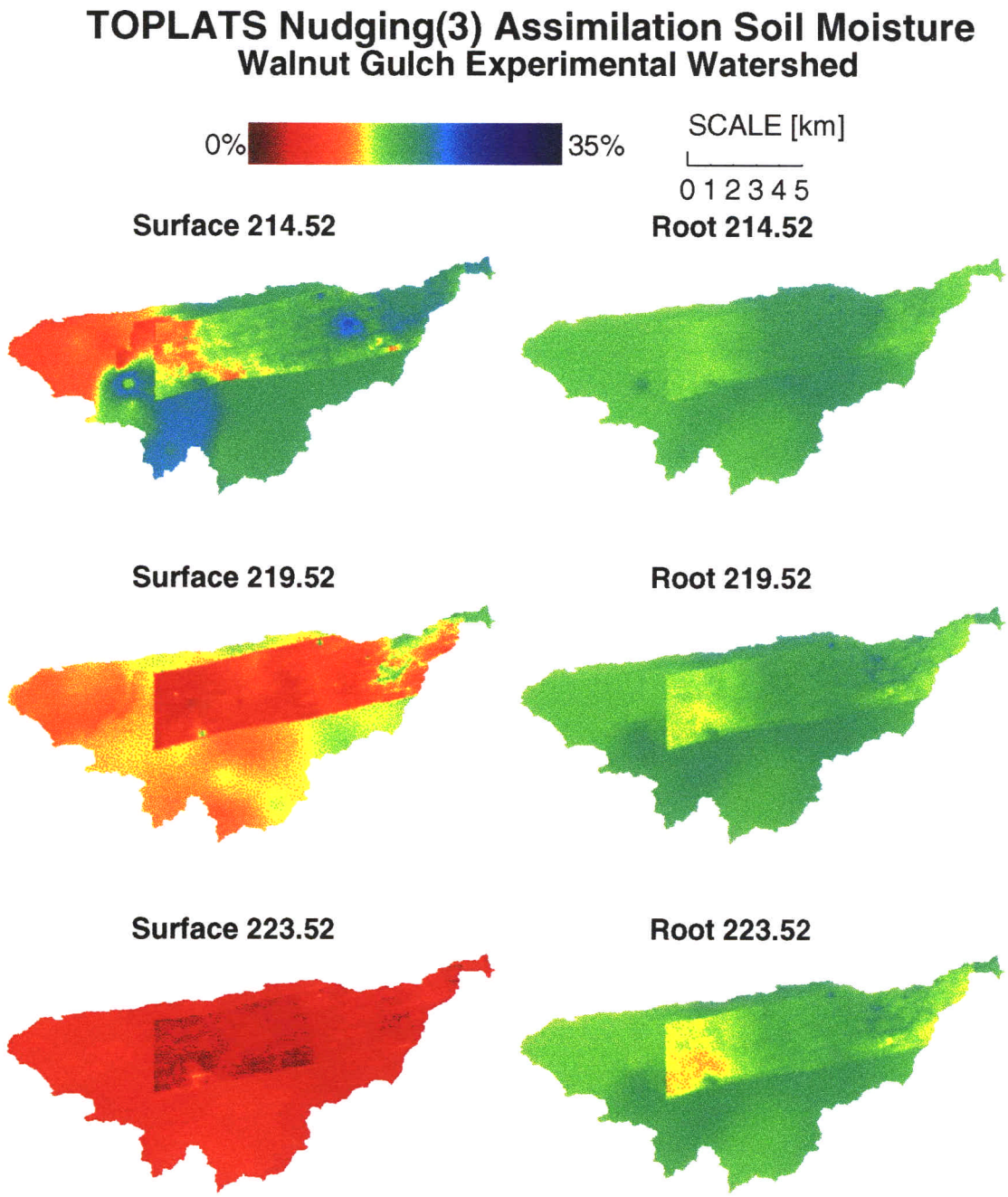

Figure 6.18: TOPLATS nudging(3) assimilation simulation spatial soil moisture.

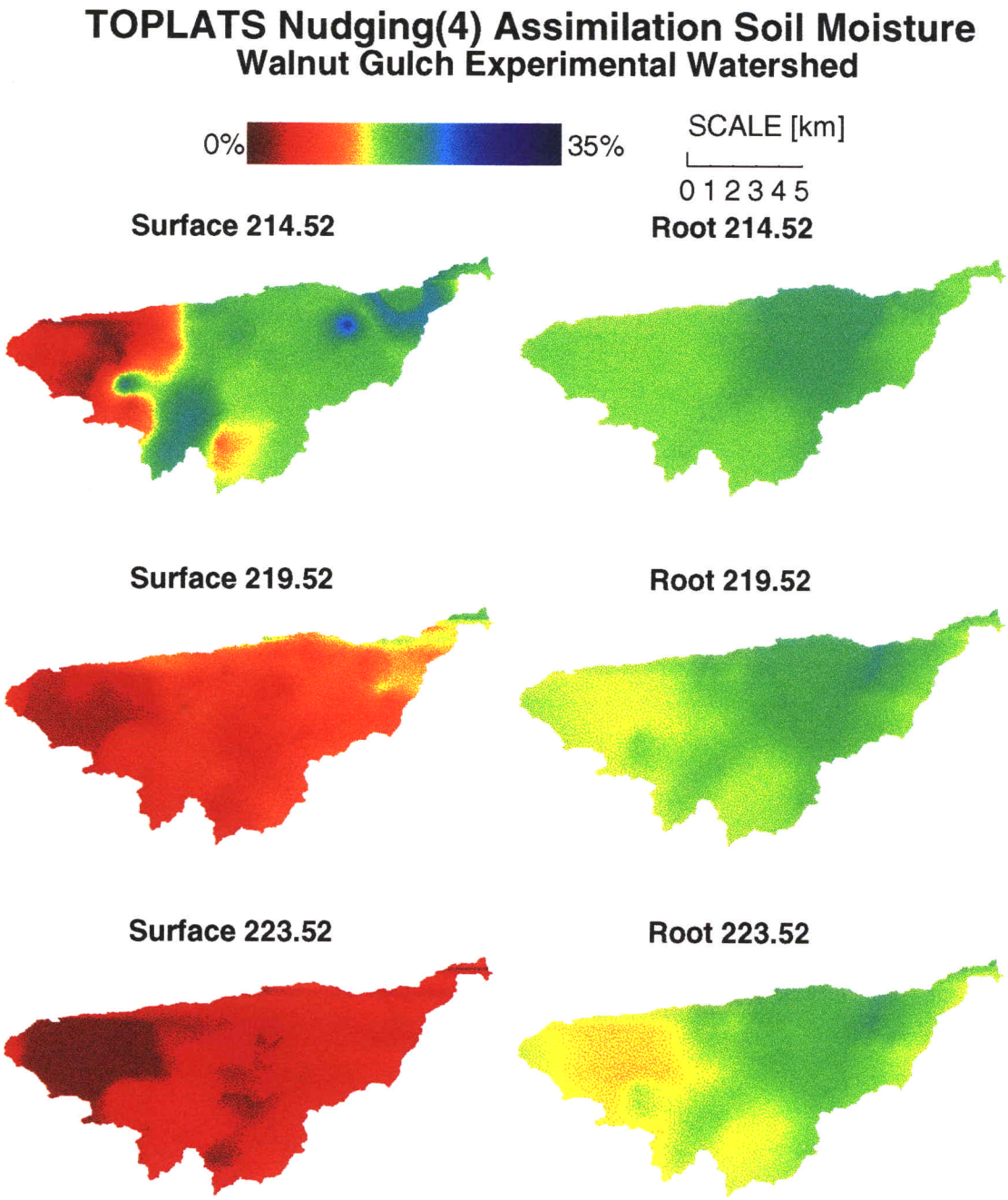

Figure 6.19: TOPLATS nudging(4) assimilation simulation spatial soil moisture.

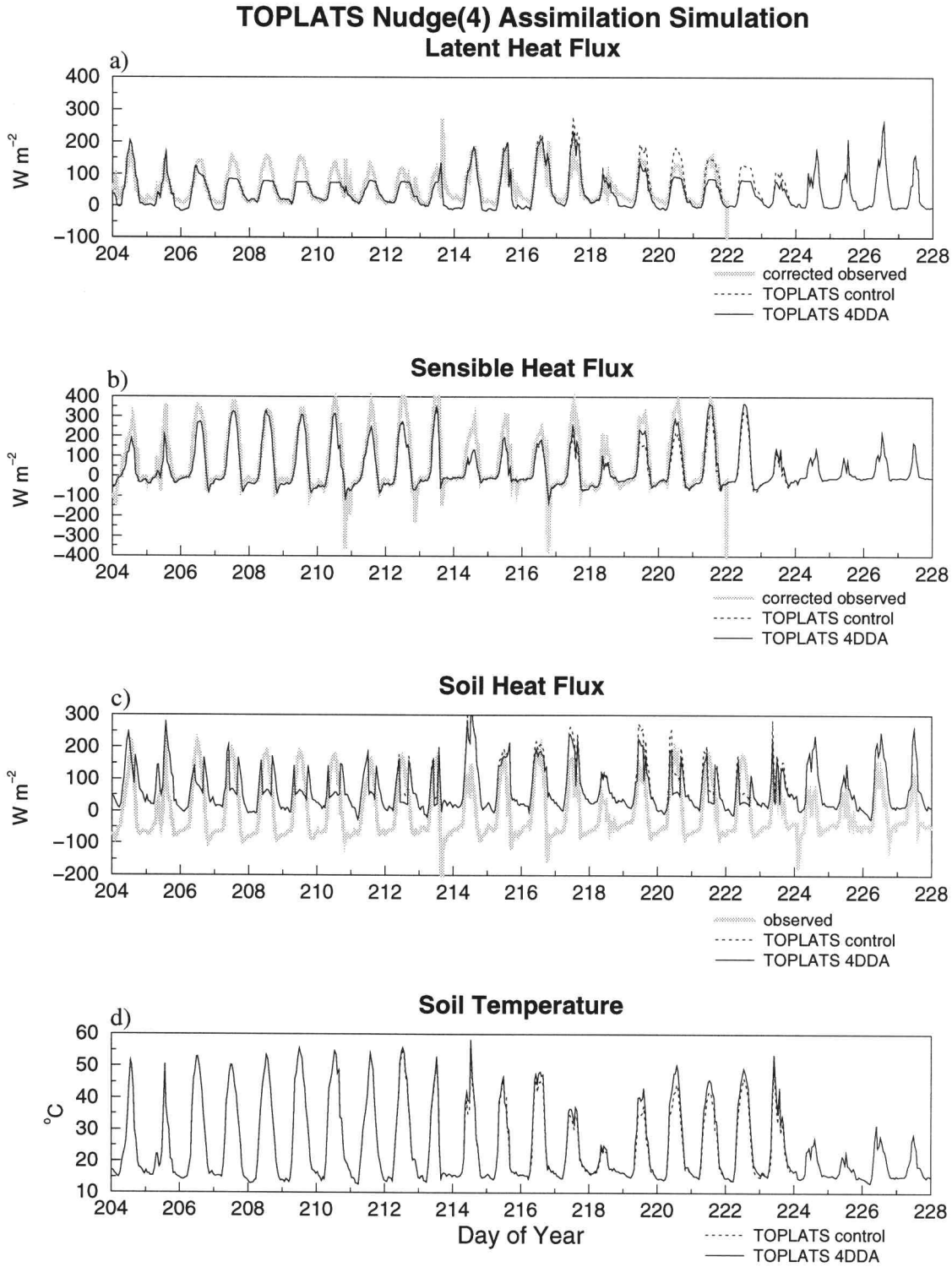

Figure 6.20: TOPLATS nudging(4) assimilation simulation watershed average surface fluxes and temperature.

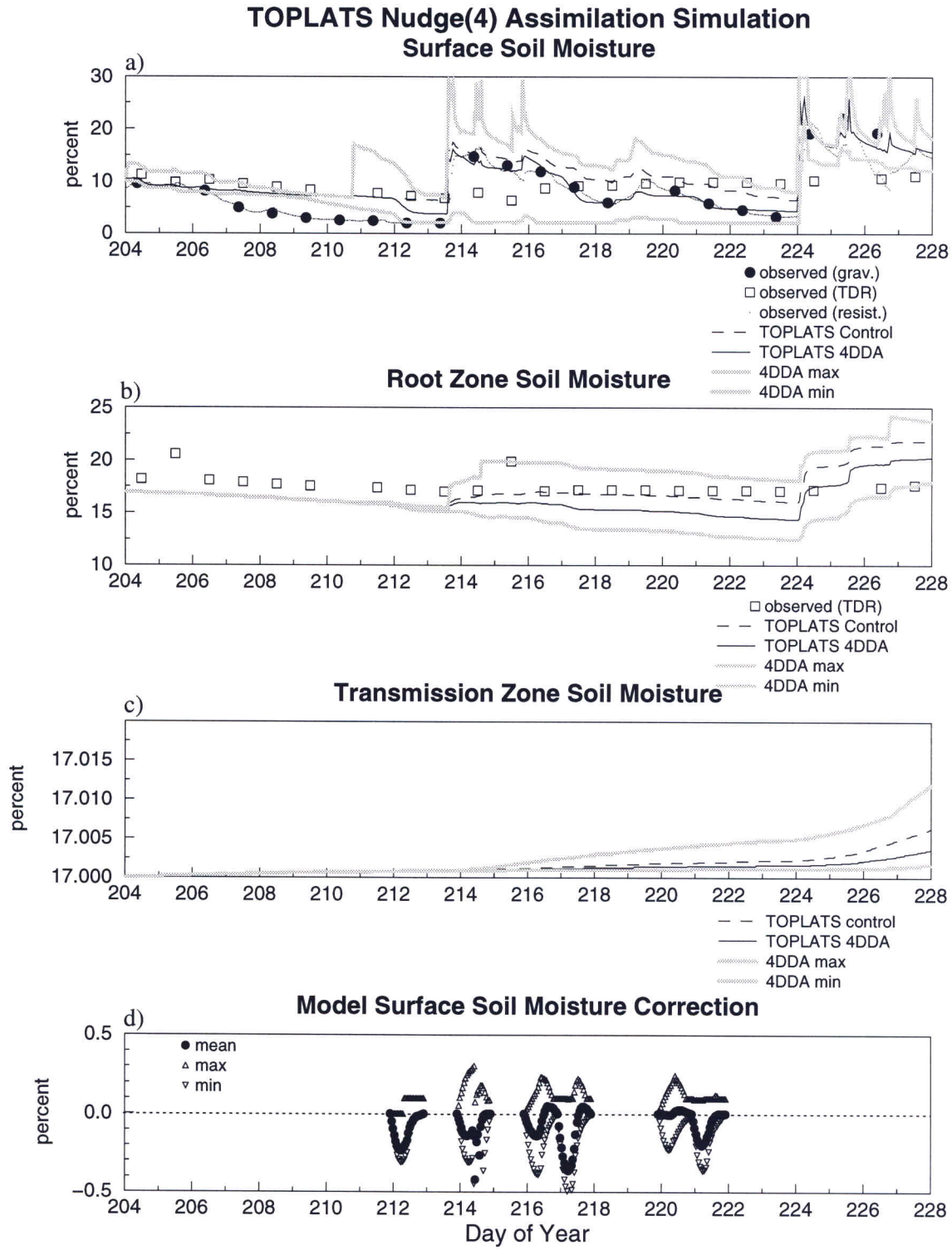

Figure 6.21: TOPLATS nudging(4) assimilation simulation watershed average soil moisture.

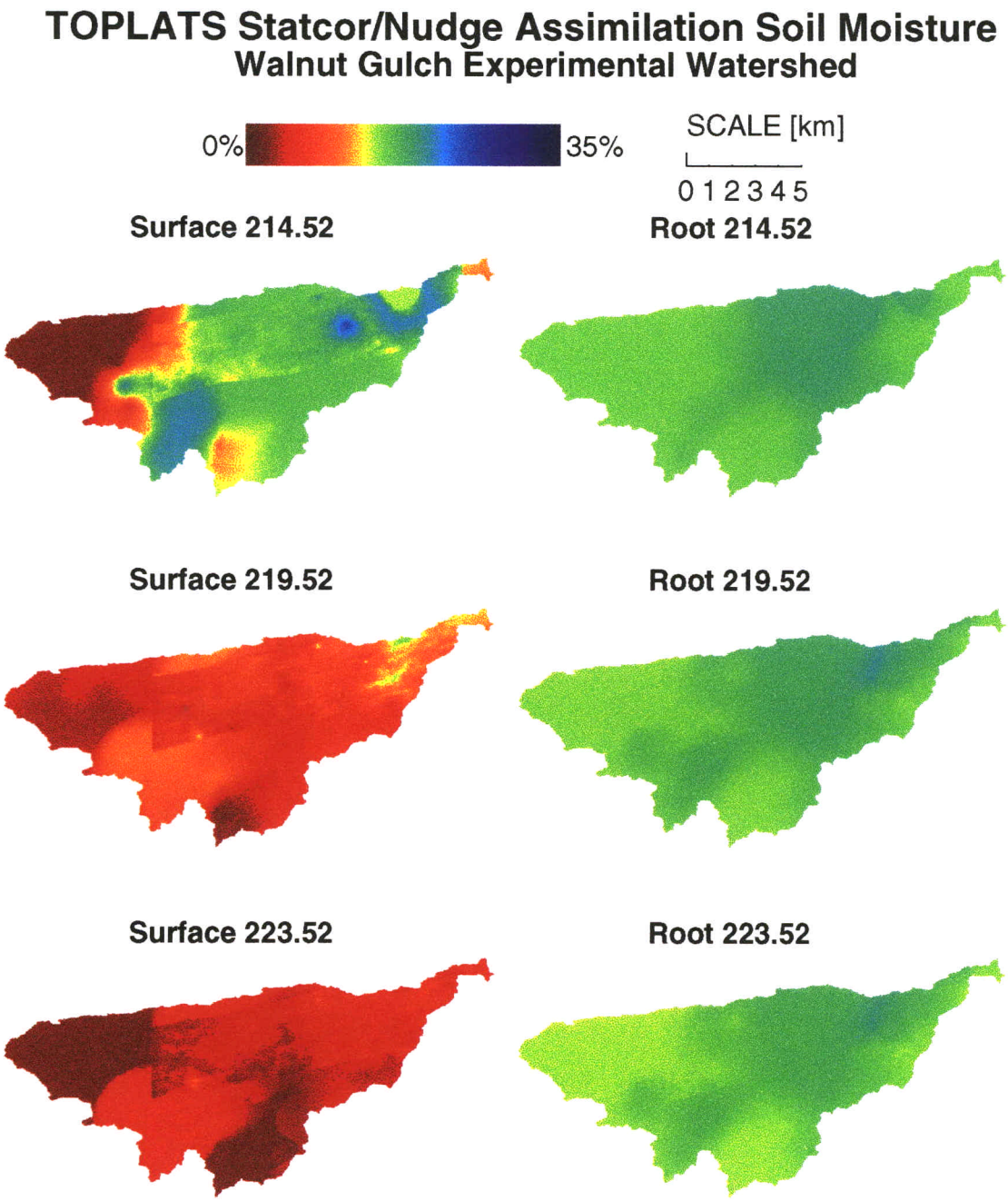

Figure 6.22: TOPLATS statistical corrections nudging assimilation simulation spatial soil moisture.

The temporal soil moisture patterns and corrections and assimilation surface flux feedbacks for this technique are very similar to statistical assimilation. The spatial soil moisture patterns (Figure 6.22) are superior to the updating, statistical corrections, or statistical corrections updating techniques because they show only very slight discontinuities at the edges of the observation area. Some observation pattern information is preserved in a nudging type merging with previous predictions.

The advantage of this method over Newtonian nudging is its computational efficiency, but its disadvantages include its inability to perform temporal or vertical assimilation which make it inferior to nudging.

6.9 Statistical interpolation

In order to implement optimal or statistical interpolation, the error characteristics of the model and observations must be assessed. Recall that statistical interpolation is implemented as follows:

$$f_A(r_i)=f_B(r_i)+\sum_{k=1}^{K} W_{ik}[f_O(r_k)-f_B(r_k)] \tag{6.1}$$

where K is the number of observation points, W_{ik} is the weight function, $f(r)$ is the analysis variable (soil moisture), r is the three-dimensional spatial coordinates, $f_A(r_i)$ is the analyzed value of f at the analysis gridpoint r_i, $f_B(r_i)$ is the background, or first-guess value of f at r_i, and $f_O(r_k)$ and $f_B(r_k)$ are the observed and background values, respectively, at the observation station r_k. The weights are determined by least squares minimization of the above and, with the assumptions of no correlation between background and observation error and isotropic, time invariant error correlation, the weights are found by solving K equations for K unknowns:

$$\sum_{l=1}^{K} W_{il}[\rho_B(r_l-r_k)+\epsilon_O^2\rho_O(r_l-r_k)]=\rho_B(r_i-r_k) \tag{6.2}$$

where ρ_O is the observation error correlation matrix, and ρ_B is the background error correlation matrix.

The observation error correlation (correlation of time series of correlated error observations minus uncorrelated error observations) is a measure of the correlation that the assimilation data

error contains. Usually, for observations taken with separate stationary instruments these observations can be assumed to be spatially uncorrelated (Daley, 1991). For remotely-sensed observations measured by the same instrument, observation error correlation is often present and cannot be ignored. To assess the error correlation in the PBMR soil moisture data, the time series of gravimetric observations which were assumed to have no error correlation were used. This correlation structure, along with the simulation correlation error structure, are plotted versus the distance separating the observation time series being compared (Figure 6.23). Because there is no identifiable pattern in these plots, it is assumed that there is no PBMR or TOPLATS soil moisture error correlation. This conclusion may need to be revisited in situations where more gravimetric information is available because it is based only on a short time series (six temporal points) at eight sites. Additionally, because the gravimetric data were used to calibrate the PBMR soil moisture inversion, independent gravimetric verification of these results is also desirable.

The background error correlation (time series correlations of observation minus prediction or background) is the primary tool that is used to advect observation information horizontally (and vertically) into data-sparse regions. To find this relationship, the correlation of time series of PBMR surface soil moisture minus TOPLATS surface soil moisture versus distance was plotted (Figure 6.24) for 5- and 6-period time series. Here, it is clear that the addition of 1 point has a lot of impact on the identifiability of the correlation structure, it is believed that a longer time series would produce a more identifiable structure. Because of the dense nature of remote-sensing observations, the total number of correlation points can exceed 600 million for the PBMR-TOPLATS data set. For this reason a 0.1% random subsample was used here which narrows the plotted points to a few hundred thousand.

Next, the background error correlation function (given in Chapter 2) was fit to the 6-period time step background error correlation data using a simplex technique that minimized the sum of the squared difference between the 0.1% random subsample of horizontal background error correlation points and the function fit. This fitted curve is shown in Figure 6.24, and its parameters are given in Table 6.6.

Table 6.6: Optimized background horizontal error correlation function parameter values.

	c parameter	*L* parameter
Original Value	1.5e-7	2415.1
100 random observation reanalysis	1.1e-7	3277.1
100 super-observation reanalysis	8.9e-8	12715.4

Statistical interpolation also allows for vertical assimilation, from a specification of a vertical background error correlation function. Unfortunately because PBMR observations are not available outside the surface soil zone, explicit definition of this function is not possible. A surrogate exists in other profile soil moisture measurements. In this study, the only soil moisture observation at depth are from TDR at two locations. Using these measurements, vertical background error correlations between the surface and root zone were found (TDR observations do not extend into the transmission zone). These values are given in Table 6.7.

Table 6.7: Vertical background error correlation.

Metflux Site	Original	100 Random Reanalysis	100 SuperObs Reanalysis
Lucky Hills (site 1)	*0.4*	*0.26*	*0.27*
Kendall (site 5)	*0.62*	*0.43*	*0.40*

To implement statistical interpolation, a set of K equations must be solved for K unknowns at each model grid point, where K is the number of observations. K may exceed 35,000 observations in the Monsoon '90 data, and there are over 90,000 model grid points, so clearly this is a major numerical problem. Compiler and computer memory limits meant the largest number of observations that could be used in this study was 8,000 (the full problem would require over 1.5 gigabytes of RAM and specialized compilers). Two methods were developed to reduce the number of observations to a more feasible number. The first was simply to pick a random subset of observations, while the second method takes the average of observation groups or regions to produce 'super-observations'. In both cases, the observation with the most information (the closest observation) was included in the random set, or else the super-observation was computed around it. Only 100 observations could be used at a time for

computational reasons (a 100 observation statistical interpolation simulation uses days of CPU time, while a 1000 observation simulation uses weeks).

Because the correlation error functions were calibrated for a control background (i.e., a simulation without data assimilation), their parameterization might change when assimilation is performed. For this reason the 100 random observation and the 100 super-observation statistical interpolation simulations were performed. Then, using this new background information, the horizontal and vertical correlation error functions were recalculated. These new correlation function parameters are given in Tables 6.6 and 6.7. The new soil moisture error correlation distance is shown in Figure 6.25, and the new background error correlation structures are shown in Figure 6.26. Finally, the random and super-observation statistical interpolation simulations were rerun with these new parameters.

The spatial patterns derived by the 100 random observation and super-observation statistical interpolation assimilation schemes are shown in Figures 6.27 and 6.28, respectively. It is clear that both approaches result in an undesirable linear streaking feature that extends outward from the observation area. This is also a feature that would be prominent in the fully posed problem (i.e., if we used all the observations). Of the two, it seems that the super-observation method where this streaking is much less pronounced is preferable. Further, in the observation area, the random observation method defaults to direct insertion and so fully retains the undesirable pattern structure of the observations. The random observation method was therefore dismissed as unacceptable, and only the characteristics of the super-observation method are assessed below.

The temporal surface flux assimilation feedbacks are shown in Figure 6.29 and are slightly more pronounced than in the other assimilation methods. The soil moisture time series shown in Figure 6.30 show a large root zone correction and an apparent over-correction in the surface zone. This may not be an over-correction because the simulation is a watershed spatial average while the observations are 8-site averages. The corrections provided by this method are temporally discontinuous because they are imposed during a single time step. Finally, the overall deviation of assimilation corrections is clearly larger for the PBMR observations after the day 213 rainstorm as would be expected for that storm.

The super-observation statistical interpolation scheme provides acceptable spatial patterns, albeit with an undesirable streaking pattern. The use of more, smaller-area average super-observations would tend to increase this streaking pattern, while less super-observations will diminish these patterns, but it would also reduce the assimilation of observed patterns.

The catchment water-balance is shown in Table 6.8. The statistical interpolation assimilation technique corrects the area average catchment water-balance by 44 mm, which exceeds the total evaporation over the simulation time period. This correction is primarily made by decreasing the root zone storage and a less dramatic reductions in evapotranspiration, runoff, and transmission zone storage.

Table 6.8: Water-balance information for the TOPLATS statistical interpolation simulation.

	Metflux Site:								Watershed
Variable (mm)	*1*	*2*	*3*	*4*	*5*	*6*	*7*	*8*	**Average**
Precip	99.33	82.66	118.87	114.32	107.12	116.49	92.25	90.56	93.44
Capillary Rise	0.00	0.00	0.00	0.00	0.00	0.00	0.00	0.00	0.00
ET	36.97	37.37	36.56	37.84	42.80	35.91	35.33	38.07	36.19
Runoff	12.40	0.00	11.16	16.52	3.38	12.68	0.00	0.89	5.11
Recharge	0.00	0.00	0.00	0.00	0.00	0.00	0.00	0.00	0.00
Surface ΔS	4.41	2.96	5.67	6.38	3.86	5.87	3.73	4.49	5.69
Root ΔS	-10.55	3.11	27.95	26.74	28.55	19.12	12.42	-6.66	0.40
Trans ΔS	1.08	1.58	3.20	3.96	3.57	2.70	2.32	1.10	1.91
Leaf ΔS	0.01	0.01	0.01	0.01	0.06	0.01	0.08	0.01	0.03
in-out	49.96	45.29	71.16	59.96	60.93	67.90	56.92	51.60	52.14
Total ΔS	-5.05	7.66	36.83	37.08	36.03	27.70	18.56	-1.07	8.03
Error	55.01	37.63	34.33	22.87	24.91	40.20	38.36	52.67	44.11

Overall, the statistical interpolation assimilation method works fairly well in this application. It has the advantage of using error correlation functions based on the characteristics of the observations and the model predictions. However, it has the disadvantage of being excessively demanding on computer resources when addressed as a fully posed problem with remote-sensing. Simplification using 'super-observations' is required. A further disadvantage of this method is its lack of temporal assimilation.

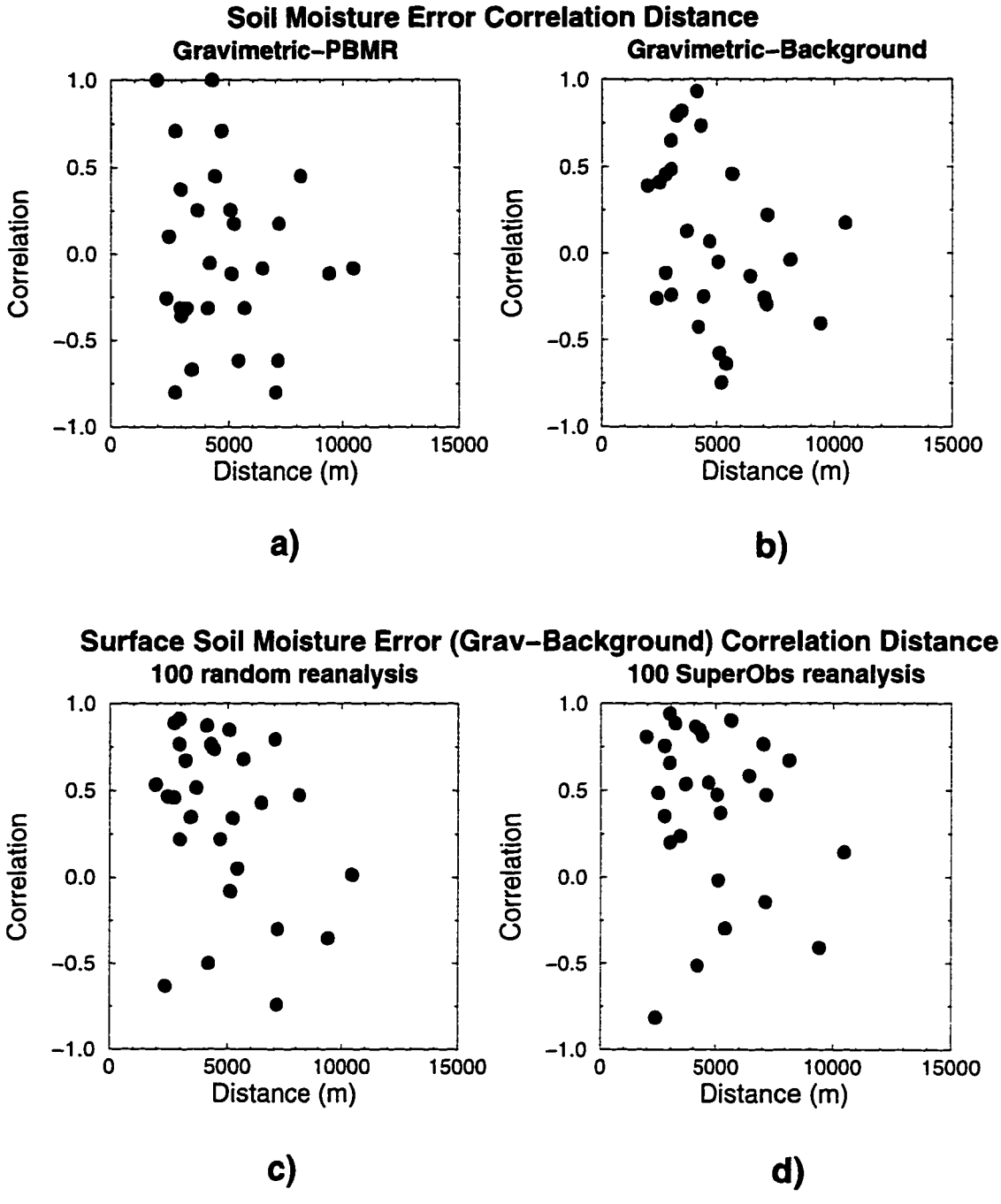

Figure 6.23: (a) PBMR and (b) TOPLATS soil moisture error correlation versus distance, and PBMR soil moisture error versus distance for (c) the 100 random observation reanalysis and (d) the 100 super-observation reanalysis.

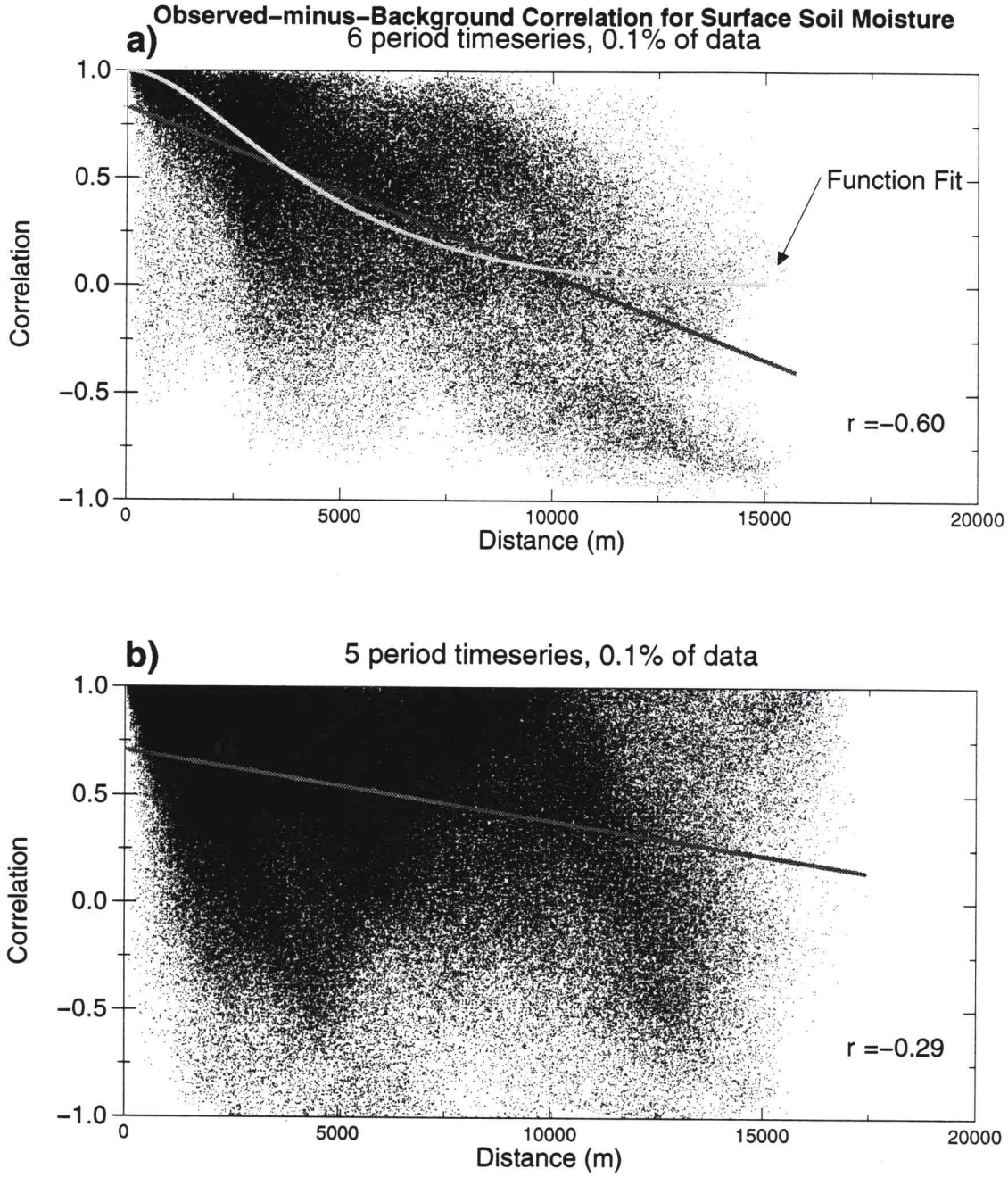

Figure 6.24: Surface soil moisture background error correlation versus distance for (a) 6-point time series, and (b) 5-point time series. Plots represent a 0.1% selection of total data.

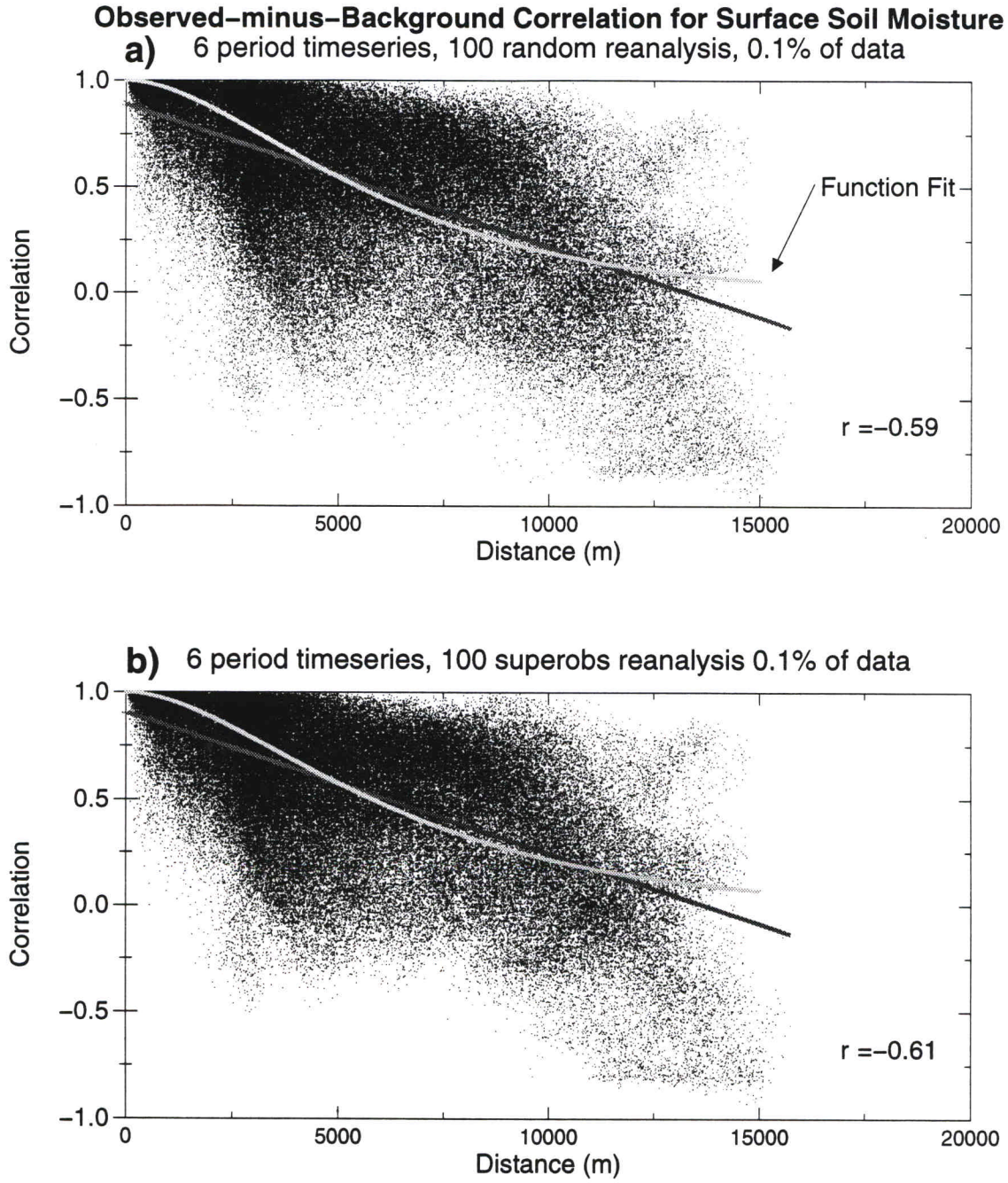

Figure 6.25: 6-point time series surface soil moisture background error correlation versus distance for (a) the 100 random observation reanalysis, and (b) the 100 super-observation reanalysis. Plots represent a 0.1% selection of total data.

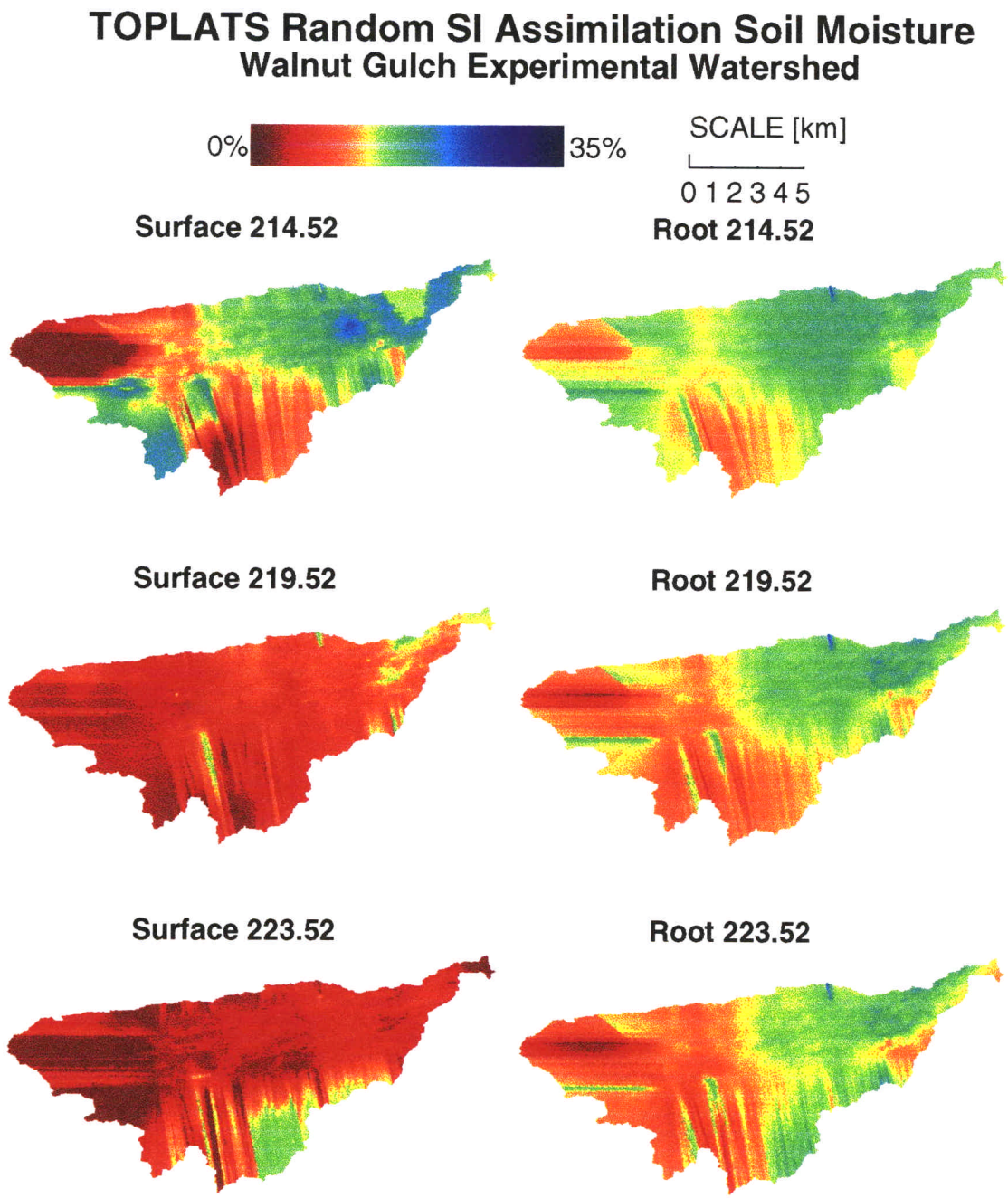

Figure 6.26: TOPLATS 100 random observation statistical interpolation assimilation simulation spatial soil moisture.

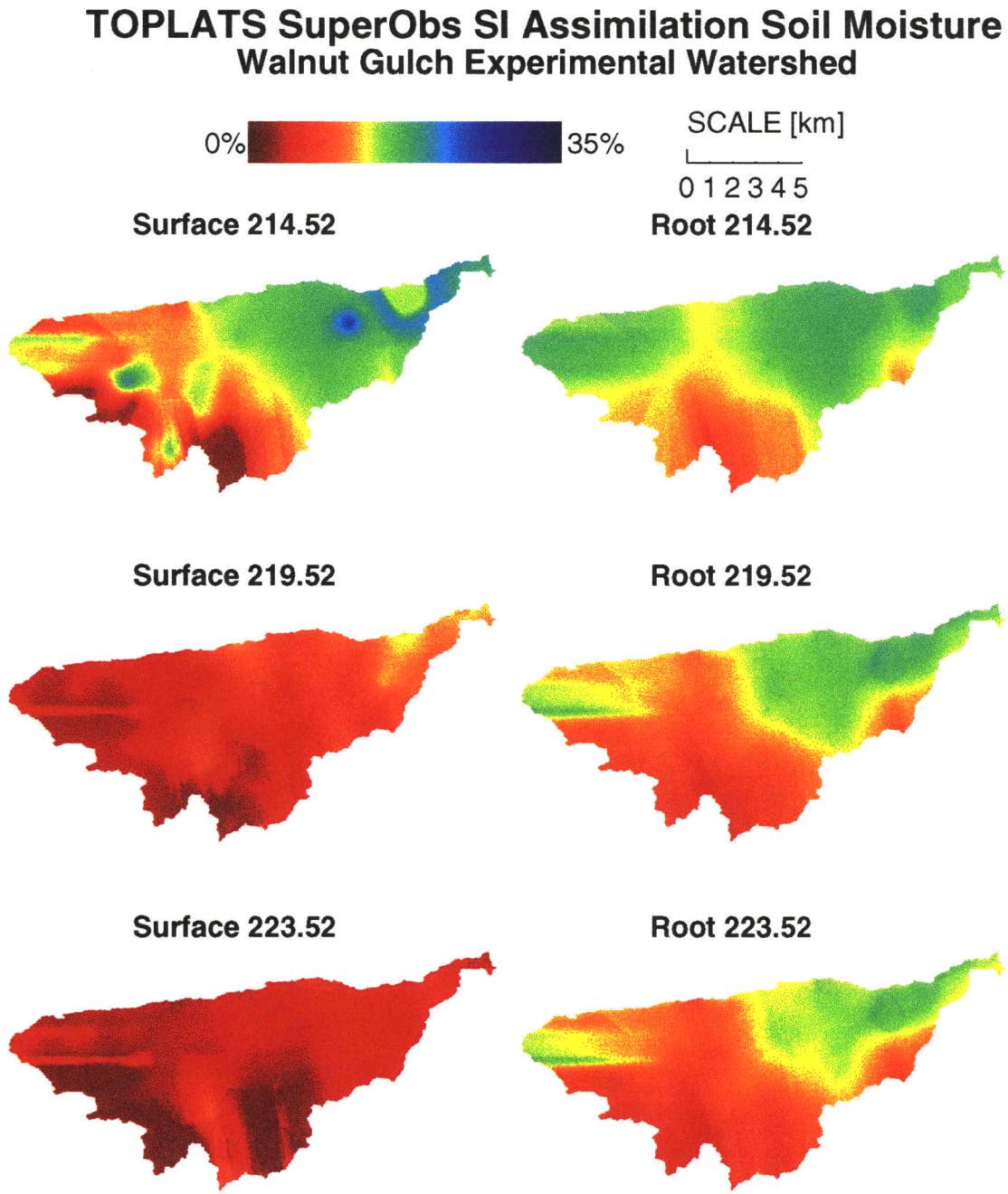

Figure 6.27: TOPLATS 100 super-observation statistical interpolation assimilation simulation spatial soil moisture.

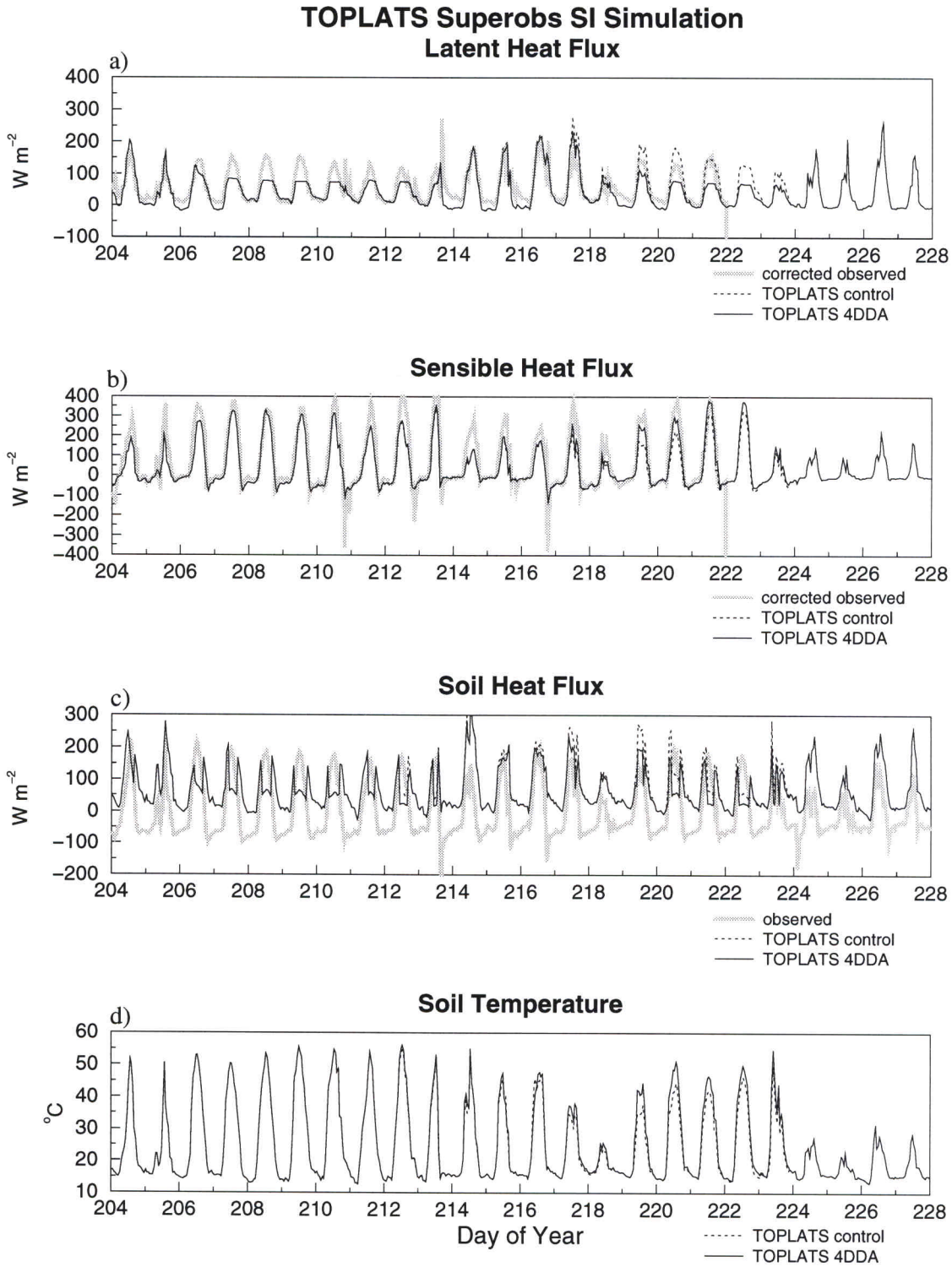

Figure 6.28: TOPLATS 100 super-observation statistical interpolation assimilation simulation watershed average surface fluxes and temperature.

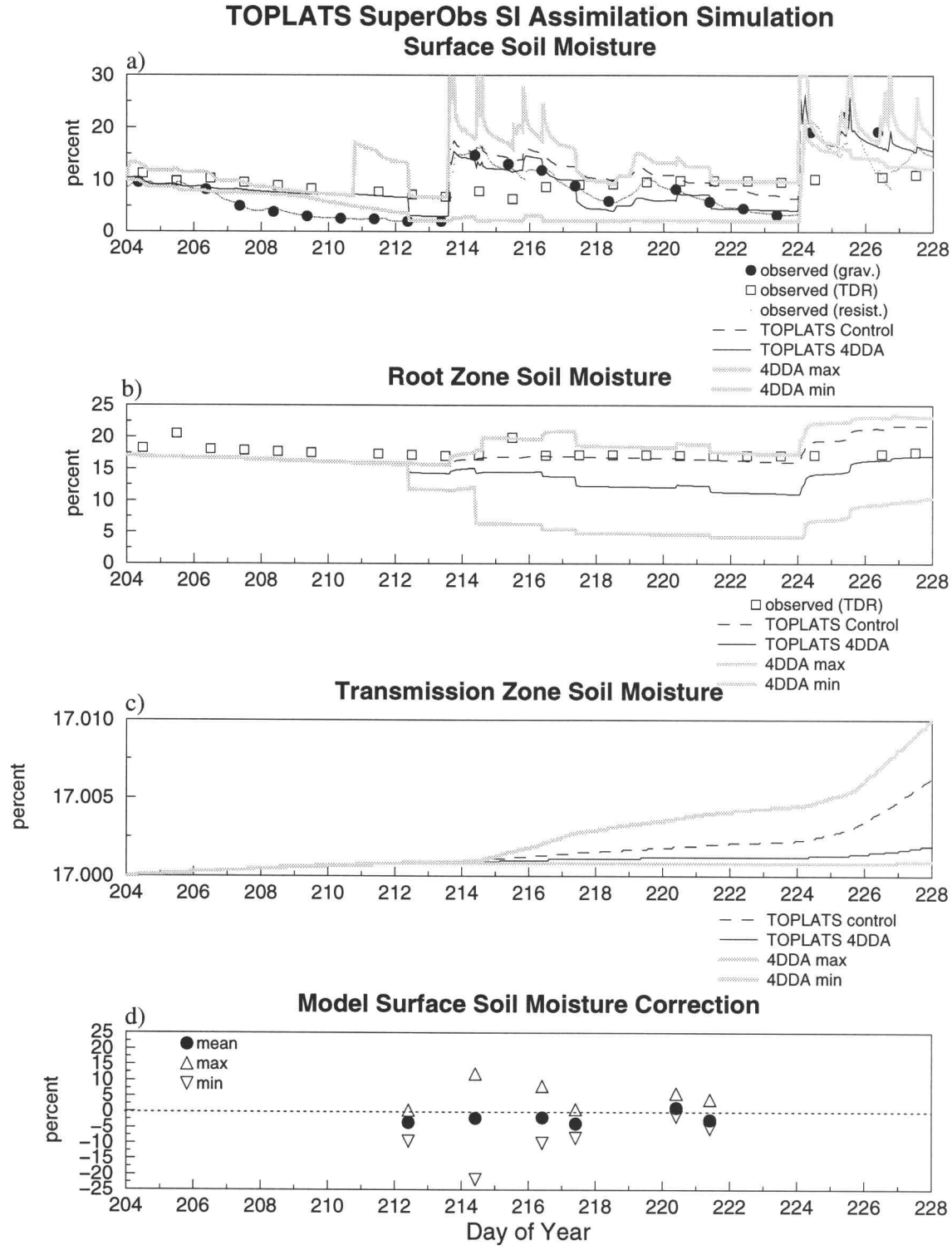

Figure 6.29: TOPLATS 100 super-observation statistical interpolation assimilation simulation watershed average soil moisture.

6.10 Comparison of assimilation methods

The relative differences in the spatial and temporal patterns produced by each assimilation technique described above are assessed here with the goal of identifying the best soil moisture assimilation method.

The day 219.5 model prediction of surface soil moisture for each assimilation method described above are shown in Figures 6.30 and 6.31. The calibrated control simulation significantly over-predicts the soil moisture for this time step, and the uncalibrated control run actually predicts different patterns of soil moisture using different watershed average parameters.

If the best spatial patterns are defined as being those without discontinuities at the edge of the observation area, and those that the model could reasonably predict given perfect forcing and parameters, this eliminates all the assimilation techniques except the statistical corrections, nudging using option set 4, and super-observation statistical interpolation which all perform similarly.

The temporal predictions of watershed average surface and root zone soil moisture for each assimilation method are shown in Figure 6.32. All methods perform similarly in the surface zone (with the exception of direct insertion, which is unable to impose an entire watershed correction and is therefore unable to adjust the model trajectory sufficiently). The nudging assimilation has the clear advantage of smoother temporal adjustments in comparison with all other methods. In the root zone, the time series plots fall into two distinct groups corresponding to those methods with and without the capacity for vertical assimilation. Of this second group, nudging assimilation performs a more conservative correction, while statistical interpolation performs a more aggressive correction. None of the methods produce time series that match the observations, which may be a trivial point because, with only two root zone observations, the root zone spatial variability is not adequately sampled.

Overall it might be concluded that the Newtonian nudging method has the most desirable soil moisture assimilation characteristics. It is the only true four-dimensional data assimilation method used in this study, and it produces relatively continuous soil moisture time series and reasonable spatial patterns.

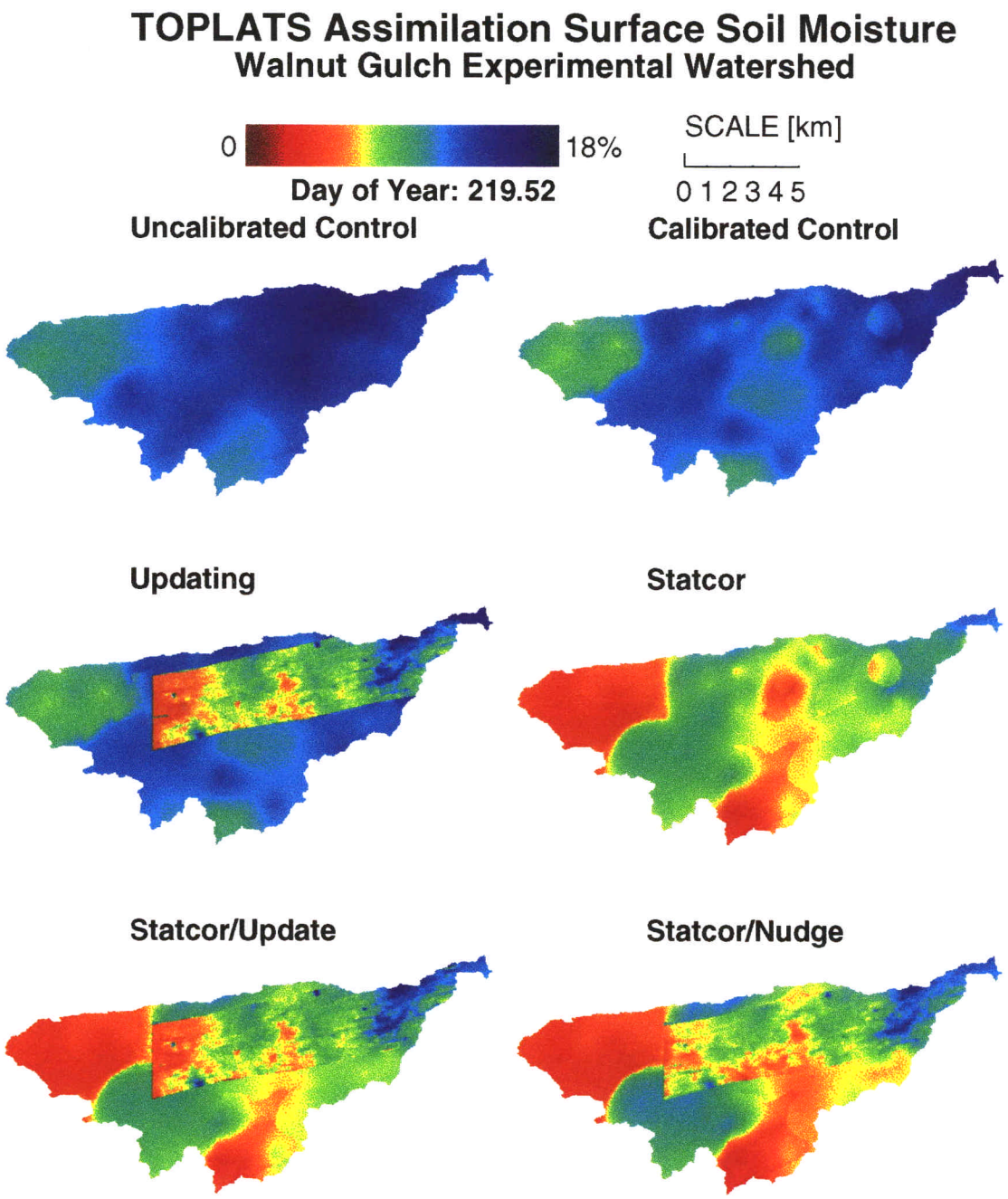

Figure 6.30: Comparison of TOPLATS spatial surface soil moisture on day 219 from various assimilation simulations.

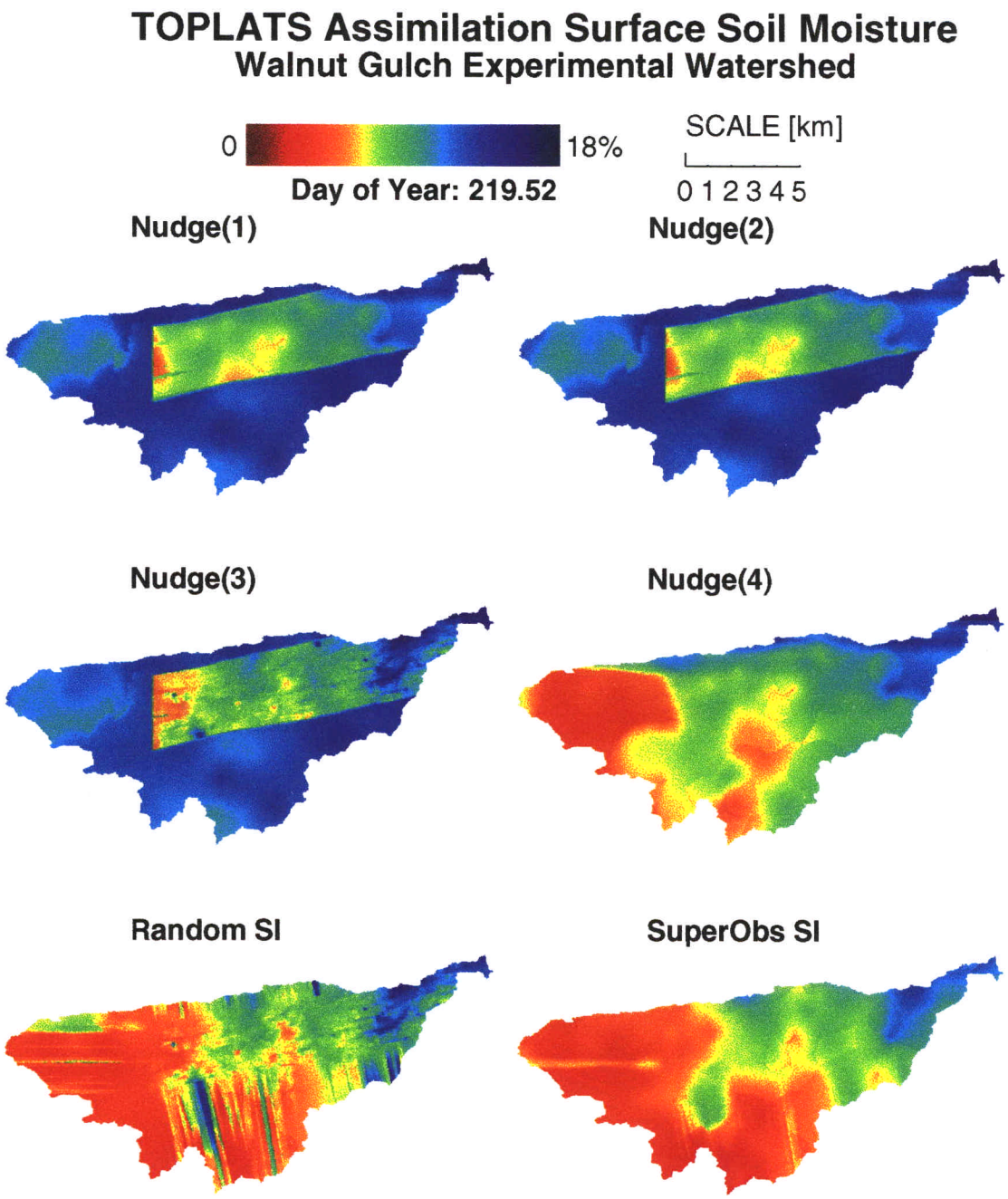

Figure 6.31: Comparison of TOPLATS spatial surface soil moisture on day 219 from various assimilation simulations.

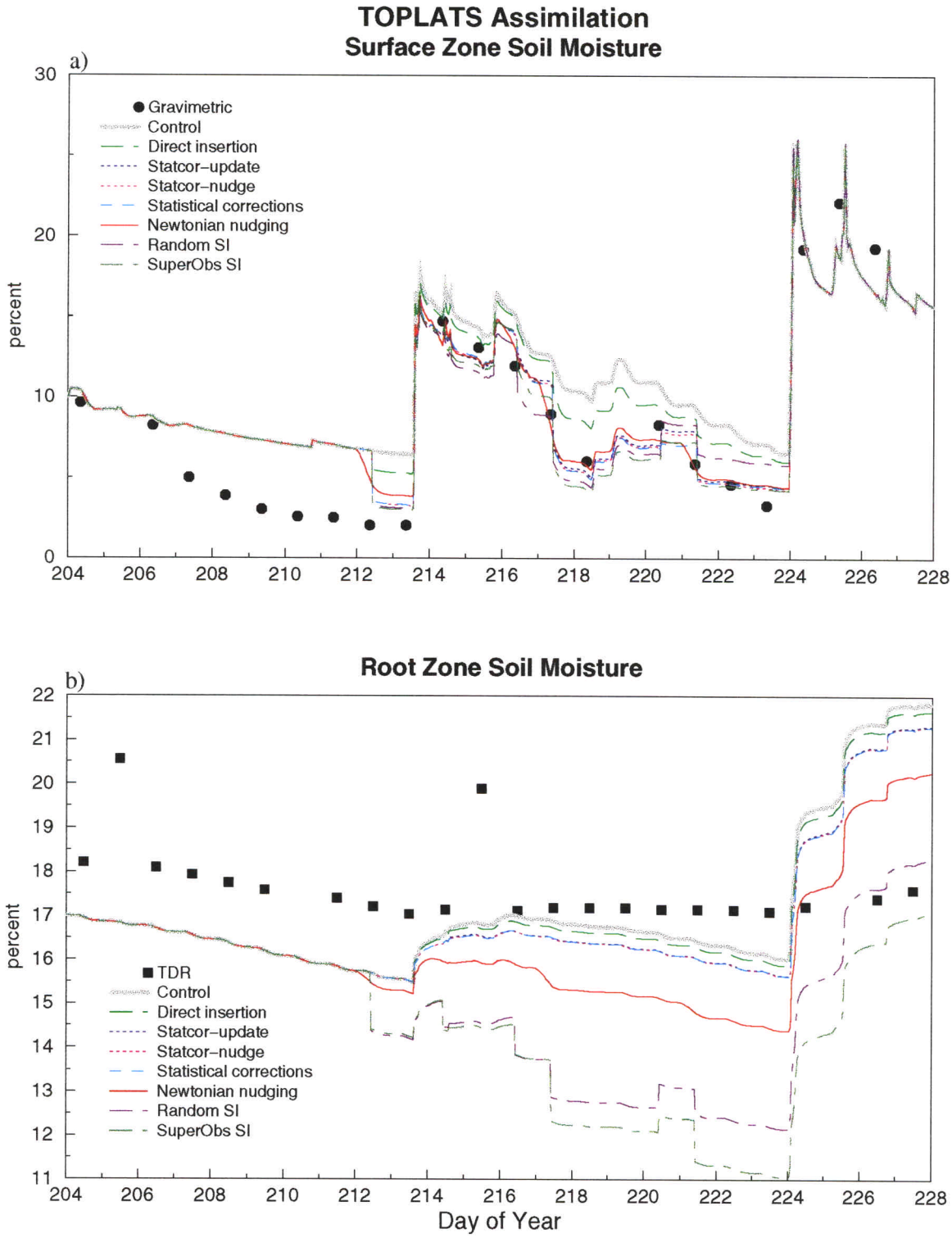

Figure 6.32: a) Comparison of TOPLATS watershed average surface zone soil moisture time series from various assimilation simulations. b) Comparison of TOPLATS watershed average root zone soil moisture time series from various assimilation simulations.

6.11 Conclusions

Many contributions concerning the application of data assimilation techniques to hydrologic modeling were described in this chapter. Four different data assimilation techniques were explored: (1) direct insertion or updating, (2) statistical corrections, (3) Newtonian nudging, and (4) statistical interpolation. Within each of these techniques, several options were explored. All assimilation methods resulted in an improvement in the model's overall trajectory, but the Newtonian nudging assimilation method was judged the best assimilation technique because it resulted in sensible spatial distributions of soil moisture and was able to advect information temporally, horizontally, and vertically. The statistical interpolation using super-observations and the statistical correction assimilation techniques also resulted in desirable soil moisture patterns.

A series of sensitivity runs showed that the removal of any assimilation information negatively affects the model's prediction trajectory, with the most critical information coming from observations made several days after a precipitation event at the conclusion of surface soil drying.

Other important aspects reported in this chapter include: (1) It is undesirable to assimilate temporally across precipitation events; (2) The suggestion that frequency of soil moisture observation should exceed frequency of rainfall; (3) The idea that it is valid and necessary to extrapolate soil moisture information away from the observation areas to preserve spatial continuity; (4) Demonstration that the error characteristics of the soil moisture observations and the model predictions can be assessed; and (5) The suggestion that the availability of longer time series of remotely-sensed soil moisture and more soil moisture profile observations will enable better definition of the error correlation functions.

7. CONCLUSIONS AND FUTURE DIRECTIONS

The spatial-temporal distribution of near-surface soil moisture is central to the regulation of land-atmosphere water, energy, and carbon interactions, but knowledge of the space-time dynamics of soil moisture and the processes which control it remains poor. The development of land hydrology parameterizations that emphasize soil moisture and innovative remote-sensing and surface-based techniques for measuring soil moisture together promise a mechanism for the synthesis of regional fields of this vital hydrologic variable. This study used data assimilation methods to calculate synthetic soil moisture fields by combining remotely-sensed soil moisture data with predictions made with a soil-vegetation-atmosphere transfer scheme.

7.1 Major conclusions and contributions

7.1.1 Precursory investigation

It was found that several data development procedures are a necessary precursor to hydrological data assimilation. They are summarized as follows:

(a) For successful assimilation studies, the modeled states need to be similar in definition to observations. In this study the soil layer used in the TOPLATS model was modified to include an additional surface layer to facilitate data assimilation of near-surface soil moisture derived from passive microwave radiometers which are only sensitive to moisture in the top 5-10 centimeters of soil.

(b) Data assimilation methodologies generally require high-quality, temporally continuous, spatially distributed model predictions. In this study the preparation of required model input data and parameter sets was laborious and time consuming for Walnut Gulch. Precipitation is the most important spatial forcing in semi-arid regions due to its highly variable convective nature, and much effort was devoted to deriving spatially distributed precipitation data sets. Additionally, spatially variable vegetation and soil parameters were derived from a detailed soil and vegetation survey and GIS coverages for Walnut Gulch (Breckenfeld, 1993), but their use proved to be problematic.

In general DEMs are required to find the topographic index. In this study an orthophoto-derived DEM was used which had the unique property that each value of elevation was

independent of those nearby. It therefore contained a substantial noise component, and it was necessary to remove this noise by developing and applying spatial averaging and hole-filling algorithms.

Finally, surface soil moisture assimilation data sets are required. In this study these were derived from NASA's Push Broom Microwave Radiometer brightness temperatures measured on six days during the Monsoon '90 field campaign (Schmugge *et al.*, 1994). An inverse distance weighting scheme was developed and applied between gravimetric-based calibrations made at several sites to convert each of the microwave brightness temperature images into soil moisture estimates.

7.1.2 SVATS calibration

Successful data assimilation requires model predictions with a low error component if information is to be advected into data-sparse temporal and spatial regions. Hence, unless there is continuous data coverage and frequent point samples, extensive model evaluation and calibration are required.

The hypothesis was that spatially-variable soil and vegetation information would improve local model predictions. The polygon nature of these data sets gave unrealistic simulations which were inconsistent with PBMR observations. A parameter sensitivity study revealed that spatial variations in vegetation parameters have little effect on model predictions, but that soil parameters have a large effect. This problem is probably not a simple mis-specification of parameter values, but rather an artifact of discretely assigning a single set of parameters to large areas (polygons) of soil; smoothing of these polygon features is likely to decrease these difficulties. Meanwhile, in this study soil and vegetation parameters were kept spatially constant, leaving only topographic index and precipitation as spatially varying entities.

The inability of TOPLATS to accurately simulate the latent and sensible heat fluxes observed at Monsoon '90 and their comparison with typical Sonoran Desert surface fluxes measured at other nearby sites led to doubt on the reliability of these Monsoon '90 flux measurements. In fact, the only area that had similar fluxes to those measured during Monsoon '90 was an irrigated agricultural field in Obregon, Mexico. A water-balance was performed for

the Monsoon '90 observation period, which showed that measured evapotranspiration exceeds precipitation by 40%, a result which is not physically realistic. To be consistent with the water-balance and for the purpose of TOPLATS model validation, measured values of *ET* were scaled down by 40% and (to preserve the energy-balance) sensible heat scaled up by 100%. This correction factor was verified using an accurate, sonic anemometer-based eddy correlation system deployed during the 1996 monsoon season.

The TOPLATS model has many parameters which must be specified for its implementation at Walnut Gulch. Several parameters were directly observable, and their values could be readily specified in the model, but others were non-physical and were derived by optimization. A series of automatic calibration procedures using Monte-Carlo, multi-objective, Pareto set techniques was developed for this SVATS and resulted in a substantial improvement in the model's performance at Walnut Gulch.

7.1.3 Data assimilation

7.1.3.1 Simple approaches

Several simple data assimilation approaches were developed to evaluate model and data error and for comparison with more sophisticated, computationally demanding methods. Direct insertion, the simplest form of data assimilation, was used as the first step towards the development of a soil moisture data assimilation system. Model state variables were simply replaced with observed data at the time of the observation in this updating scheme, and no spatial propagation of the observations was made. Updating improved model predictions in the areas where soil moisture was observed, but it created undesirable discontinuities in model predictions, preserved local observation error patterns, and was unable to extend information from the observation region to other areas.

A second simple assimilation technique, which this author termed 'statistical correction', was developed to address some of the weaknesses of updating. This technique involved adjusting the mean and standard deviation of the entire model domain to match the mean and standard deviation of the observation image. This technique is is only applicable to areas that have large numbers of observations (such as remotely-sensed data), but is also computationally

efficient. In the time domain, it performed similarly to updating, but also spread observation information horizontally and it did not preserve local observation errors within the model fields. Its drawback was that none of the patterns in the observations were preserved. The sensitivity of model predictions to omitting or including a set of observations was explored using the statistical corrections assimilation technique. It was found that the assimilation performance degrades with less observation information and that it degrades most profoundly when the nearest observation to the time of comparison was missing.

7.1.3.2 Newtonian nudging

Newtonian nudging was used to address the deficiencies in the above-described simple data assimilation methods and to extend information vertically into the root and transmission zones. Newtonian nudging is best used with few observations because it is computationally demanding and because, surprisingly, the weights tend to decrease with increasing numbers of observations. In fact, it makes more sense to have increasing weight with increasing information, the traditional Newtonian nudging method was adapted for use with remote-sensing data by modifying the weighting structure so that it does not fall with increasing numbers of observations. Overall, the Newtonian nudging methodology resulted in spatial patterns that are very similar to those derived from the statistical correction methodology, but it gave the added benefit of vertical assimilation and more gradual temporal change.

7.1.3.3 Statistical interpolation

The most critical aspect for the implementation of statistical interpolation is the specification of the background and observation error correlation structures. This study found no observation error correlation for the PBMR soil moisture observations. Thus, the only correlation structure to be defined was the background error correlation matrix. This correlation function was determined using 5 or 6 of the PBMR images, respectively. The addition of one more time step in the PBMR soil moisture time series results in a much better description of this correlation relationship. The hypothesis was made that an even longer time series would result in much better correlation relationships. A correlation function was then fitted to this correlation

relationship for use in the statistical interpolation algorithm using least squares, simplex minimization of its 2 parameters.

Statistical interpolation allows for vertical assimilation through specification of a vertical background error correlation function. Because PBMR observations are not available outside the surface soil zone of course, explicit definition of this function was not possible. A surrogate existed in the form of other profile soil moisture measurements. In this study, the only soil moisture observations at depth were from time domain reflectrometry at two locations. Using these measurements, the vertical background error correlations between the surface and root zone were found. The soil moisture correlation length scale was also explored and was found to exceed the observation area and to be unaffected by the soil moisture inversion algorithm.

As with Newtonian nudging, statistical interpolation works poorly with large numbers of observations. In statistical interpolation, solving for K (~35,000 per PBMR image) unknowns with K equations for each grid in the model domain (~90,000) poses an excessive computational demand. Therefore, the problem was scaled down using a random selection of observations including the closest observation, which contains the most information or by computing 'super-observations' which are simple averages of groups of observations. The random approach approximated the fully posed problem, giving undesirable banding patterns outside the observation area. The super-observation approach yielded smoother, more realistic spatial patterns. The random approach reverted to direct insertion where observations were available, which was undesirable.

7.2. Concluding summary

Important new contributions were made in this study. The most significant being the practical demonstration that it is feasible to assimilate soil moisture data into a spatially distributed hydrological model, and thereby enhancing its descriptive ability. Other contributions include the development of a remote-sensing sensitive SVATS, a detailed spatially variable Walnut Gulch data set, a methodology for the multi-objective automatic calibration of SVATS, and correction methods for Monsoon '90 surface fluxes. A new, simple and effective 'statistical correction' assimilation technique was introduced, and the Newtonian nudging

weighting structure and the statistical interpolation methodology was adapted for use with high-density remote-sensing observations. Overall, the Newtonian nudging assimilation technique provided superior model spatial and temporal prediction improvement.

7.3 Discussion

7.3.1 Walnut Gulch study area

This study either found or emphasized the importance of several hydrologic processes that are significant at the Walnut Gulch watershed. Precipitation is known to be the dominant force in determining the spatial structure of hydrologic response in semi-arid regions. This was confirmed through the ability of a relatively simple model to predict hydrologic spatial variability with precipitation as its only relevant spatially distributed input. But, the model's inability to accurately simulate observed runoff emphasized the importance of runoff redistribution processes at Walnut Gulch, and the need for a routing algorithm in the model. Observations that vegetation and soil moisture increase downslope that could not be simulated using TOPMODEL theory (assuming such increases are due to groundwater proximity), provided evidence for downslope runoff reinfiltration. The highly correlated time series of sensible, latent, and soil heat fluxes within Walnut Gulch, together with the close agreement between aggregate and area-averaged SVATS simulations support the conclusion that the land-surface-atmosphere interactions of areas at least the size of Walnut Gulch can be reliably represented with a single set of forcings, flux measurements, and model parameters. If a linear relationship were assumed for these correlation relationships it could be surmised that this concept holds for a radius of up to 60 km. Extensive studies of the correlation structures in soil moisture also reveal that these structures vary in time depending on the soil's state of drying but that their time series also have strong horizontal and vertical correlation structures.

Significant evaluation of measurements performed on Walnut Gulch yielded insights into their usefulness. The temperature variance and vertical propeller eddy correlation instruments used to measure Monsoon '90 surface fluxes were found to be suspect based on water balance studies and comparisons with more accurate measurements, so the use of such instruments in semi-arid locations should be avoided. Through extensive SVATS calibration studies, it was

found that traditional measurements of the partitioning of sand, silt, and clay lead to poor estimates of soil-water physical properties due to the removal of the coarse fraction before analysis. The inclusion of percent coarse fraction in this partitioning would alleviate these difficulties. Finally, because of the discrete polygonal nature of spatial soil and vegetation surveys, their use in distributed simulation studies is curtailed. A more realistic, continuous map of these characteristics is required.

7.3.2 Implications for hydrologic modeling

Even using simplified models of surface-vegetation-atmosphere interactions, making fine-resolution predictions for small areas presents a large computational task. Therefore, implementation at larger scales will require further simplification through the simulation of area statistics, or simply sacrificing fine resolutions for larger areas. But a more troublesome problem is the definition of parameters for these models. Even in an area such as Walnut Gulch where observations are plentiful, finding parameters for a simple SVATS model is daunting. Further, calibration of such a model for optimal performance in a given area is a monumental task requiring a large number of observations for validation. Therefore, these models will need to use fewer parameters that are more easily determined (i.e. through remote sensing) for them to make valid predictions regionally and globally.

7.3.3 Practical aspects of hydrologic data assimilation

7.3.3.1 Tradeoff between data assimilation complexity and data representation

There is a clear tradeoff between using a complex data assimilation technique and the ability to represent all the assimilation data in that technique due to the large computational burdens of performing data assimilation at fine resolutions using dense data sets. In this study, it was found that as the complexity of the data assimilation model increases, the size of the assimilated data set had to decrease to maintain computational efficiency. Complex methods have the ability to extract more useful information from assimilated data, whereas simpler methods use more of the data to extract similar information; this tradeoff allowed simpler assimilation techniques to perform about as well as complex techniques. Therefore, for

optimum performance, this argument supports the use of assimilation methods that are of moderate complexity so as to use sound assimilation methodologies and as much data as possible.

This tradeoff emphasizes the importance of the efficient representation of data in the more desirable complex methods. If the information in the data can be efficiently compressed or filtered before its use in data assimilation it may be more reasonable to use larger data sets in complex data assimilation strategies. This approach is further supported by the finding in this study that spatial patterns are less important than mean values in correcting gross model bias.

7.3.3.2 Resolution versus large area implementation

Since hydrologic data assimilation requires hydrologic modeling predictions, it is limited by a similar tradeoff between fine resolution and large area implementation. A statistically based assimilation implementation may be a viable approach for use in large areas. But ultimately, the tradeoff between resolution and area will need to be determined based on the needs of the application.

7.3.4 Operational implication for soil moisture remote sensing

7.3.4.1 Required soil moisture observation qualities

This research has several implications for the definition of the temporal and spatial observational requirements of an operational remotely-sensed soil moisture data assimilation system. First, based on the success of the statistical interpolation technique using super-observations, it is clear that the remotely-sensed observations need not be at the same high resolution of the model. In fact, a remotely-sensed spatial resolution of several kilometers may be adequate for the bias correction of a model at a resolution of tens of meters. This same relationship will probably not hold at larger resolutions because of limits in the correlation structure of soil moisture. For example, model and observation resolutions over 60 km may prohibit horizontal information advection into adjacent model grids due to a lack of spatial correlation. Second, this study showed the importance of obtaining observations of soil moisture near the conclusion of drying events (or several days after a precipitation event). Unfortunately,

the timing of precipitation events is not regular, so a best guess at an optimal sampling interval must be taken. Based on the timing of the Monsoon '90 precipitation, weekly soil moisture observations would be minimally acceptable. But, more frequent observations will, of course improve assimilation performance.

7.3.3.2 Required data

Several classes of data are essential for the operational implementation of soil moisture data assimilation. The most important is meteorological forcing data. As previously discussed, forcing averaged over large areas may be adequate, while precipitation forcing distributed to the desired prediction resolution is essential. It is likely this information can be reliably provided through numerical forecasting models, observation mesonets, and radar precipitation estimates. Next, operational soil moisture observations as described above are required. These must be supplemented by short-term *in-situ* gravimetric surface and root zone observations across the operational domain for error correlation specification, parameter calibration, and assimilation model validation. Observations of soil and vegetation characteristics are also critical for optimal model performance. Finally, to validate simulation results, and for use in parameter calibration, observations of surface water and energy fluxes are valuable, but not essential.

7.4 Recommended future research directions

Future research directions fall into four broad categories namely, SVATS enhancements, further refinement of hydrologic assimilation technology, assimilation of other land-surface states such as surface temperature, and extension of this research to regional and global scales. Potential research questions in each of these research areas are described below.

7.4.1 Future SVATS enhancements

Several enhancements of the TOPLATS will be necessary for its application on large scales and in diverse regions. These include the inclusion of a runoff routing scheme, a snow model, and other programmatic enhancements.

7.4.1.1 Runoff routing

The TOPLATS model currently has no mechanism for routing runoff created at the grid-scale through the catchment drainages and to the catchment outlet. This routing mechanism is important for the prediction of runoff hydrographs and downslope soil moisture levels, where runoff from upslope areas can reinfiltrate. The need for this mechanism was illustrated by the inability to make reasonable comparisons between observed Walnut Gulch runoff and the point runoff predicted by the model in this study. Because TOPLATS is a model based on topography, most of the necessary flow direction information is already present. Therefore, the incorporation of a simple, yet physically realistic routing scheme is reasonable, but will increase computation requirements significantly.

7.4.1.2 Snow model

Snow melt has important influences on the magnitudes and distributions of soil moisture at the start of the growing season. Therefore, for a proper simulation of surface hydrology (which is critical for optimal data assimilation performance) in areas that receive snow requires the incorporation of a snow model in the SVATS structure. Lynch-Stieglitz (1994) developed a 3-layer snow sub-model for the GISS (Goddard Institute for Space Studies) GCM that physically models heat and mass (water) flow within the snow pack. Radiation conditions determine the surface energy fluxes, and heat flow within the pack is governed by linear diffusion. Meltwater generated in a layer will remain until it exceeds the water-holding capacity of the layer, at which point it flows to the next layer and either refreezes, remains as a liquid, or flows through. Densification of the snow pack is also modeled through mechanical compaction and through a melting-freezing mechanism. Comparison with the baseline model shows that addition of this snow model improved prediction of ground and surface radiation temperatures and enabled simulation of snowpack ripening that characterize pack growth and ablation.

7.4.1.3 Programmatic enhancements

Several programmatic enhancements are essential for the use of the current TOPLATS model structure in large areas. These include parallelization of the code for faster

implementation at larger scales, the choice of statistical or distributed model implementation using the same code and input files; and the incorporation of automatic calibration methodologies in the main code.

7.4.1.4 Additional suggested modifications

According to Peters-Lidard *et al.* (1996a), TOPLATS overestimated ground heat flux during wet periods and underestimated it during dry periods due to its thermal conductivity function (defined by McCumber and Pielke, 1981). This problem affects all components of the energy-balance, but primarily sensible heat flux and temperature in the daytime and net radiation at night. Peters-Lidard *et al.* (1996a) suggested that the replacement of this function with one derived by Johansen (1975) solves this problem by calculating the thermal conductivity of the soil as a function of its saturation and quartz content. Additional modifications in the representation of moisture diffusion, parameterization of soil resistance, the inclusion of environmental controls on transpiration, and the incorporation of stability correction factors to correct the model's tendency for calculating erroneously large transpiration rates at night were suggested by Peters-Lidard *et al.* (1996b). It is also possible for the model's surface zone to collapse to a depth of zero if the water table rises to the surface, which would make comparison with remote-sensing less consistent.

7.4.2 Additional assimilation techniques

The assimilation techniques presented in this work point towards the development of a four-dimensional Newtonian nudging technique that utilizes the realistic correlation structure derived for the statistical interpolation technique, rather than the empirical weighting functions it currently used. Additionally, the development and use of more complex variational and Kalman filtering approaches might be investigated in the future, although their feasibility is questioned with the use of dense remote-sensing data.

This research also highlights the importance of developing computationally-efficient assimilation algorithms for use with large remotely-sensed data sets. It is suggested that

assimilating information extracted from observations using a Fourier Transform or Principle Components analysis may be much more efficient than assimilating the observations themselves.

Eventually, assimilation techniques may be developed that not only correct the model spatial and temporal trajectory using observations, but also are able to learn from these corrections to make better future predictions. This learning process might take the form of an automatic parameter adjustment or the removal of model processes that have little or no benefit for model predictive ability.

7.4.3 Temperature assimilation

A logical extension of this research is the assimilation of surface temperature. This can be implemented relatively easily with the existing assimilation methods developed in this research for soil moisture. A distinct advantage of moving in this research direction is the relative abundance of surface temperature observations. However, the very short memory and the small topographically determined correlation distances of surface temperature may well be disadvantages.

7.4.4 Extension to larger regional and global scales

Because of the perceived need for improved soil moisture estimates at various scales (i.e., global scales for climate studies and regional/continental scales for agricultural application) and limited data availability as scale increases, implementation of soil moisture assimilation methodologies at larger scales will probably need to proceed in parallel at both the global and regional scales. This will proceed best in a comprehensive coupled atmosphere-ocean-land model which will enable the impacts and feedbacks of the soil moisture assimilation strategy to be fully explored.

A critical component of this research will be to acquire and process large-area satellite microwave radiances from the SSM/I, ERS-1, or Radarsat sensors into soil moisture estimates. This is not a trivial task, because roughness and vegetation introduce different noise components into each of these sensors, which must be corrected.

APPENDICES

APPENDIX A: ACRONYMS AND ABBREVIATIONS

4D:	Four-Dimensional
4DDA:	Four-Dimensional Data Assimilation
AIRS:	Atmospheric Infrared Sounder
AMI:	Active Microwave Instrument
AMSU:	Advanced Microwave Sounding Unit
API:	Antecedent Precipitation Index
ASTER:	Advanced Spaceborne Thermal Emission and Reflection Radiometer
AVHRR:	Advanced Very High Resolution Radiometer
BATS:	Biosphere-Atmosphere Transfer Scheme
CLASS:	Canadian Land-Surface Scheme
CNES:	French National Space Centre
CPU:	Central Processing Unit
CZCS:	Coastal Zone Colour Scanner
DAO:	Data Assimilation Office
DAS:	Data Assimilation System
DEM:	Digital Elevation Model
DMSP:	Defense Meteorological Satellite Program
DMN:	French Direction de la Météorologie Nationale
DOY:	Day of Year
ECMWF:	European Centre for Medium-Range Weather Forecasts
EOS:	NASA's Earth Observing System
ERS:	European Space Agency Remote-Sensing Satellite
ESMR:	Electronically Scanning Microwave Radiometer
ESTAR:	Electronically Steered Thinned Array L-band Radiometer
FIFE:	First ISLSCP Field Experiment
GCIP:	GEWEX Continental-scale International Project
GCM:	General Circulation Model
GEWEX:	Global Energy and Water Cycle Experiment
GEOS:	Goddard Earth Observation System
GIS:	Geographical Information System
GISS:	Goddard Institute for Space Studies
GOES:	Geostationary Operational Environmental Satellite
HCMM:	Heat Capacity Mapping Mission
HRV:	High Resolution Viable
IFOV:	Instantaneous Field of View
ISLSCP:	International Satellite Land-Surface Climatology Project
LAI:	Leaf Area Index
LERTS/UA:	Laboratoire d'Etudes et de Reserches en Teledetection Spatiale /University of Arizona
MESSR:	Multispectral Electronic Self-Scanning Radiometer

MIMR:	Multifrequency Imaging Microwave Radiometer
MODIS:	Moderate-Resolution Imaging Spectrometer
MOS:	Marine Observation Satellite
MSL:	Mean Sea Level
MSP:	Multiband Sensor Package
MSS:	Multispectral Scanner
NASA:	National Aeronautics and Space Administration
NDVI:	Normalized Difference Vegetation Index
NMC:	National Meteorological Center
NOAA:	National Oceanic and Atmospheric Administration
NRC:	National Research Council
NWF:	Numerical Weather Forecasting
NWP:	Numerical Weather Prediction
OI:	Optimal Interpolation
PBMR:	PushBroom Microwave Radiometer
PDF:	Probability Density Function
PERIDOT:	Prévision á Echéance Rapprochée Incluant des Données et Télédectées
PVI:	Perpendicular Vegetation Index
RAM:	Random Access Memory
REA:	Representative Elementary Area
TDR:	Time Domain Reflectrometry
TIROS:	Television Infrared Observation Satellite
TM:	Thematic Mapper
TOPLATS:	TOPMODEL-based Land Atmosphere Transfer Scheme
SAR:	Synthetic Aperture Radar
SCS:	Soil Conservation Service
SiB:	Simple Biosphere Model
SIR-C:	Shuttle Imaging Radar-C
SPOT:	Systeme Pour d'Observation de la Terre
SMMR:	Scanning Multichannel Microwave Radiometer
SSM/I:	Special Sensor Microwave/Imager
SVATS:	Surface-Vegetation-Atmosphere Transfer Scheme
SWRC:	Southwest Watershed Research Center
USDA-ARS:	United States Department of Agriculture, Agricultural Research Service
USSR:	Union of Soviet Socialist Republics
UTM:	Universal Transverse Mercator
WSR-88D:	Weather Service Radar 88-Doppler

APPENDIX B: REQUIRED TOPLATS DATA

(1) FORCING DATA:

precipitation
shortwave radiation
longwave radiation
pressure
humidity
air temperature
wind speed

(2) MODEL PARAMETERS:

(A) SOIL

saturated hydrologic conductivity
saturation moisture content
residual moisture content
pore size distribution index
air entry suction head
bare soil albedo
damping depth of surface temperature wave
bare-soil roughness length
root zone depth

(B) VEGETATION:

wet canopy albedo
dry canopy albedo
canopy roughness length
canopy zero plane displacement
minimum stomatal resistance
leaf area index
critical leaf water potential
root activity factor
root density
root resistance
areal fraction of vegetation

(3) ASSIMILATION DATA:

All soil moisture and soil moisture related data
-*in-situ* ground-based soil moisture data
-remotely-sensed soil moisture data (PBMR, ESTAR, Radarsat, ERS, SSM/I, NASA-EOS-AIRS/AMSU/ASTER/MIMR/MODIS).
Small area runoff data

APPENDIX C: WALNUT GULCH, MONSOON '90 METEOROLOGICAL DATA

Local meteorological, energy flux, radiation, and soil temperature and moisture conditions were monitored at eight sites at Walnut Gulch Experimental Watershed in July and August of 1990. Nearly complete records are available from DOY 202 (July 21) through DOY 226 (August 14) inclusive for all eight sites. The following data are available:

Mean Horizontal Wind Speed. Cup anemometer at 4 m. [m/s]
Resultant Wind Vector Magnitude. [m/s]
Resultant Wind Vector Direction. [° from true north]
Standard deviation of wind direction [°]
Ground Temperature at 2.5 cm. [°C]
Ground Temperature at 2.5 cm.
Ground Temperature at 2.5 cm.
Ground Temperature at 5.0 cm.
Ground Temperature at 5.0 cm.
Ground Temperature at 15 cm.
Soil Heat Flux towards the surface at 5.0 cm. [W/m^2]
Soil Heat Flux at 5.0 cm.
Soil Heat Flux at 5.0 cm.
Surface Temperature. [°C].
Temperature of the infra-red thermometer body. [°C].
Net Radiation. [W/m^2].
Downward Short Wave Radiation. [W/m^2]
Air Temperature at 4 m. [°C]
Standard Deviation of above. [°C]
Air Temperature at 9 m. [°C]
Standard Deviation of above. [°C]
Sensible Heat Flux. Obtained by eddy correlation at 9 m. [W/m^2]
Mean Vertical Wind Speed. Obtained with a Gill propeller anemometer. [m/s]
Standard Deviation of above. [m/s]
Air Temperature at 2 m. Obtained with a thermistor probe. [°C]
Relative Humidity at 2 m. Obtained with a capacitive sensor in a Gill shield. [%]
Downward Photosynthetically Active Radiation (PAR). [micromoles/m2 s]
Reflected PAR. Obtained as above. [micromoles/m^2 s]
Downward Short Wave Radiation. Obtained with an Eppley pyranometer. [W/m^2]

At two sites, the following data are available from DOY 228 of 1990 to DOY 218 of 1992.

Net Radiation. Obtained with an REBS Q*6 net radiometer. [Wm/^{2}].
Downward Short Wave Radiation. Obtained with an Li-Cor silicon pyranometer. [W/m^2]
Soil Heat Flux towards the surface at 5.0 cm. [W/m^2]
Soil Heat Flux at 5.0 cm.
Soil Heat Flux at 5.0 cm.

Air Temperature at 4 m. [°C]
Standard Deviation of above. [°C]
Air Temperature at 2 m. Obtained with a thermistor probe. [°C]
Relative Humidity at 2 m. Obtained with a capacitive sensor in a Gill shield. [%]
Mean Horizontal Wind Speed. Obtained with a cup anemometer at 4 m. [m/s]
Resultant Wind Vector Magnitude. [m/s]
Resultant Wind Vector Direction. [° from true north]
Standard deviation of wind direction [°]
Soil Moisture at -2.5 cm [% by volume] Obtained by electric resistance sensors.
Soil Moisture at -5.0 cm.
Soil Moisture at -15 cm.
Ground Temperature at 2.5 cm. [°C]
Ground Temperature at 5.0 cm.
Ground Temperature at 15 cm.
Air Temperature at 9 m. [°C]
Mean Vertical Wind Speed. Obtained with a Gill propeller anemometer. [m/s]
Standard Deviation of #29. [°C]
Standard Deviation of #30. [m/s]
Sensible Heat Flux. Obtained by eddy correlation at 9 m. [W/m^2]

APPENDIX D: USDA-ARS RAINFALL DATA FORMAT

RECORD	COLUMN	FORMAT	DESCRIPTION
1	1-3	I3	WATERSHED ID
			45 - SAFFORD,AZ.
			63 - TOMBSTONE, AZ.
			(Walnut Gulch Watershed)
	4-6	I3	GAGE NUMBER
			1 - 100 24-Hour Gage
			300-99 6-Hour Gage
			500-99 weekly Gage
	7-16	5 I2	YEAR-MONTH-DAY-HOUR-MINUTES
			(YYMMDDHHMM) 24-Hour Clock
	17	I1	BEGINNING TIME CODE
			0 - Not Estimated 1 - Estimated
	18-20	I3	EVENT NUMBER
	21-24	I4	EVENT DURATION (Minutes)
	25-29	F5.2	DEPTH OF RAINFALL (Inches)
	30 - 32	I3	NUMBER OF BREAKPOINTS
	33	I1	EVENT TYPE CODE
			(1 -Rain, 2 -Snow, 3 -Rain & Snow
			4 -Hail, and 5 -Rain & Hail)
	34	I1	SIGNIFICANCE CODE
			0 - Insignificant 1 - Significant
	35	I1	INTENSITY ESTIMATION CODE
			0 - Some intensity values missing
			1 - All intensifies present
	36	I1	MIDNIGHT CROSSING CODE
			0 - Event does not cross midnight
			1 - Event crosses midnight
	37	I1	MAXIMUM DEPTH TABLE CODE
			0 - Depth table not computed
			1 - Depth table computed
	38	"P"	END OF RECORD ONE DESIGNATOR
2		11 F7.3	MAXIMUM DEPTH TABLE IN INCHES
			AFTER THE ELAPSED TIME OF: 2,4,5,
			10, 20, 30, 40, 45, 60, & 120 minutes
3+		I4	ELAPSED TIME IN MINUTES
		I1	ESTIMATION CODE
			0 - Not estimated
			1 - Estimated
		F5.2	ACCUMULATED RAINFALL INCHES
		I1	RAINFALL ESTIMATION CODE
			0 - Not estimated
			1 - Estimated
		F8.4	RAINFALL INTENSITY (inches per hour)
		I1	INTENSITY ESTIMATION CODE
			0 - Not estimated
			1 - Estimated

APPENDIX E: USDA-ARS RAINFALL DATA SAMPLE

Sample of Gage 58, Walnut Gulch Watershed (63) from 900629-900708 (6-29-90 through 7-8-90).

```
63 5890062922400135 53 0.04 210100P
 0.000 0.000 0.000 0.000 0.000 0.000 0.000 0.000 0.000 0.000 0.000
  00 0.000 0.00000 530 0.040 0.04530
63 5890070314450155 349 0.47 2011101P
 0.029 0.057 0.071 0.125 0.160 0.190 0.223 0.230 0.230 0.230 0.250
  00 0.000 0.00000 60 0.020 0.20000 110 0.070 0.60000 140 0.110 0.80000
 230 0.150 0.26670 290 0.170 0.20000 370 0.190 0.15000 440 0.200 0.08570
2190 0.210 0.00340 2290 0.220 0.06000 2450 0.230 0.03750 2660 0.240 0.02860
3170 0.240 0.00000 3240 0.340 0.85710 3260 0.360 0.60000 3300 0.380 0.30000
3330 0.410 0.60000 3370 0.430 0.30000 3410 0.440 0.15000 3490 0.470 0.22500
63 5890070414150160 68 0.02 311100P
 0.000 0.000 0.000 0.000 0.000 0.000 0.000 0.000 0.000 0.000 0.000
  00 0.000 0.00000 130 0.010 0.04620 680 0.020 0.01090
63 5890070516170165 42 0.52 1111101P
 0.065 0.130 0.155 0.252 0.350 0.420 0.494 0.516 0.520 0.520 0.520
  00 0.000 0.00000 50 0.030 0.36000 90 0.070 0.60000 120 0.120 1.00000
 150 0.150 0.60000 170 0.200 1.50000 210 0.330 1.95000 260 0.420 1.08000
 280 0.480 1.80000 310 0.500 0.40000 420 0.520 0.10910
63 5890070519290170 66 0.23 911101P
 0.060 0.087 0.100 0.120 0.130 0.140 0.140 0.140 0.148 0.223 0.230
  00 0.000 0.00000 30 0.040 0.80000 50 0.100 1.80000 100 0.120 0.24000
 200 0.140 0.12000 440 0.140 0.00000 500 0.190 0.50000 570 0.220 0.25710
 660 0.230 0.06670
63 5890070618300180 30 0.17 611101P
 0.027 0.053 0.067 0.100 0.153 0.163 0.170 0.170 0.170 0.170 0.170
  00 0.000 0.00000 60 0.080 0.80000 100 0.100 0.30000 130 0.140 0.80000
 160 0.160 0.40000 300 0.170 0.04290
63 5890070814450190 22 0.08 411100P
 0.000 0.000 0.000 0.000 0.000 0.000 0.000 0.000 0.000 0.000 0.000
  00 0.000 0.00000 50 0.020 0.24000 80 0.070 1.00000 220 0.080 0.04290
63 5890070822510195 55 0.15 711101P
 0.015 0.030 0.035 0.060 0.082 0.090 0.107 0.113 0.123 0.150 0.150
  00 0.000 0.00000 40 0.030 0.45000 140 0.080 0.30000 320 0.110 0.10000
 380 0.110 0.00000 440 0.120 0.10000 550 0.150 0.16360
```

APPENDIX F: MONTE-CARLO CALIBRATION RESULTS

Table F.1: Results of Monte-Carlo calibration of TOPLATS and Monsoon '90 Metflux sites. Data were derived from the minimum objectives of 3,995,956 single-grid simulations.

Default Parameter Values:	*10,000*	*1.0*	*1.00E+09*	*0.280*	*-300*	*0.500*	*297.0*	*250.0*	
Parameter Calibration Range	*0-1e6*	*0-100*	*1e6-1e12*	*0.1-0.5*	*0-1000*	*0-2*	*275-315*	*0-500*	**Best Obj.**
SITE	**RTACT**	**RTDENS**	**RTRES**	**SMPET**	**PSICRI**	**DHEAT**	**TDEEP**	**RSMIN**	**Value**
			Eddy Correlation Sensible Heat Flux						
1	712161	92.2	1.68E+11	0.479	-861	0.101	294.1	276.4	1283.70
2									
3									
4									
5	931255	95.3	1.33E+11	0.194	-786	0.104	303.5	151.5	1306.38
6	858272	93.0	2.39E+11	0.135	-578	0.102	299.3	167.7	1506.28
7	858272	93.0	2.39E+11	0.135	-578	0.102	299.3	167.7	1298.20
8	780434	96.5	2.27E+10	0.487	-188	0.105	292.5	219.1	1416.65
1-8	702016	98.6	1.06E+09	0.422	-294	0.101	294.4	249.2	1472.34
% Diff from 1-8 avg	*171*	*51*	*100*	*19*	*50*	*48*	*1*	*28*	*25*
Average	*828079*	*94.0*	*1.60E+11*	*0.286*	*-598*	*0.103*	*297.7*	*196.5*	*1362.24*
% Diff from Overall Avg	*71*	*60*	*55*	*17*	*18*	*54*	*0*	*36*	*100*
Standard Deviation	*75067*	*1.6*	*8.02E+10*	*0.162*	*234*	*0.002*	*4.0*	*46.0*	*86.14*
			Temperature Variance Sensible Heat Flux						
1	755334	41.3	1.11E+11	0.118	-523	0.101	295.4	326.4	1253.08
2	879106	70.6	1.88E+11	0.105	-768	0.107	298.7	179.4	1136.91
3	820750	57.8	1.84E+11	0.120	-652	0.101	295.6	218.6	1155.30
4	832936	56.8	1.49E+11	0.105	-705	0.101	294.6	267.1	1247.06
5	906999	82.6	1.27E+11	0.149	-852	0.101	297.2	344.6	1560.15
6	760430	86.6	4.17E+11	0.100	-882	0.102	299.9	281.5	1248.49
7	794407	65.5	7.93E+09	0.114	-307	0.107	297.2	215.5	1342.68
8	569915	79.7	1.67E+11	0.177	-721	0.101	298.7	210.8	1039.61
1-8	569915	79.7	1.67E+11	0.177	-721	0.101	298.7	210.8	1075.54
% Diff from 1-8 avg	*120*	*22*	*61*	*50*	*24*	*48*	*1*	*39*	*9*
Average	*652485*	*67.6*	*1.69E+11*	*0.124*	*-676*	*0.103*	*297.1*	*255.5*	*1247.91*
% Diff from Overall Avg	*34*	*15*	*53*	*64*	*33*	*55*	*0*	*17*	*100*
Standard Deviation	*225738*	*14.4*	*1.08E+11*	*0.025*	*175*	*0.002*	*1.7*	*55.4*	*146.11*
			Sensible Heat Flux Summary:						
Average	*720021*	*77.8*	*1.66E+11*	*0.186*	*-646*	*0.103*	*297.4*	*232.8*	*1291.88*
% Diff from Overall Avg	*48*	*32*	*54*	*46*	*27*	*54*	*0*	*25*	*100*
Standard Deviation	*202049*	*17.1*	*9.84E+10*	*0.129*	*203*	*0.002*	*2.8*	*59.4*	*138.15*
			Corrected Eddy Correlation Sensible Heat Flux						
1	721171	18.7	3.95E+11	0.111	-576	0.428	309.9	677.8	1836.64
2									
3									
4									
5	200435	1.9	6.61E+11	0.103	-567	0.285	308.3	679.7	1937.50
6	886598	32.4	5.53E+11	0.122	-11	0.527	301.9	699.1	3503.03
7	945615	21.5	9.26E+11	0.102	-8	0.362	304.1	674.6	2095.24
8	783288	2.1	7.96E+11	0.360	-29	0.163	292.0	654.9	2001.90
1-8	575842	15.1	5.53E+11	0.146	-20	0.216	298.3	694.5	1863.63
% Diff from 1-8 avg	*122*	*77*	*29*	*59*	*97*	*10*	*0*	*100*	*58*
Average	*707421*	*15.3*	*6.66E+11*	*0.160*	*-238*	*0.353*	*303.2*	*677.2*	*2274.86*
% Diff from Overall Avg	*46*	*74*	*86*	*54*	*53*	*56*	*2*	*119*	*100*
Standard Deviation	*265262*	*11.8*	*1.85E+11*	*0.100*	*272*	*0.124*	*6.3*	*14.1*	*619.84*

Corrected Temperature Variance Sensible Heat Flux

1	149601	55.6	6.44E+11	0.178	-222	0.646	309.2	684.7	3168.46
2	779310	41.3	3.69E+11	0.100	-289	0.475	302.8	688.0	2600.35
3	316461	48.6	7.44E+11	0.106	-7	0.251	285.4	696.8	2589.14
4	972709	7.4	7.52E+11	0.103	-6	0.264	293.4	611.4	2650.14
5	147383	2.4	7.32E+11	0.112	-433	0.671	306.0	676.5	5221.21
6	282331	81.5	5.01E+10	0.477	-367	0.115	286.5	2.9	96013522.61
7	194098	2.8	7.91E+11	0.106	-92	0.481	295.2	697.4	2858.53
8	612170	37.0	2.82E+11	0.309	-122	0.691	302.1	680.5	3058.10
1-8	511082	22.0	9.45E+11	0.101	-526	0.412	305.1	683.3	2239.95
% Diff from 1-8 avg	35	69	48	77	11	249	1	237	11953
Average	494258	34.6	5.45E+11	0.186	-192	0.449	297.6	592.3	12004458.57
% Diff from Overall Avg	2	41	53	46	62	99	0	92	1208
Standard Deviation	316625	26.6	2.58E+11	0.129	151	0.204	8.3	224.3	31752441.63

Corrected Sensible Heat Flux Summary

Average	576244	27.2	5.92E+11	0.176	-210	0.412	299.8	625.0	7388234.07
% Diff from Overall Avg	19	54	66	49	59	83	1	102	705
Standard Deviation	315453	24.0	2.40E+11	0.119	207	0.184	8.1	180.9	25583917.11

Overall Sensible Heat Flux Summary

Average	650128	54.2	3.65E+11	0.190	-423	0.252	298.4	422.2	3557974.43
% Diff from Overall Avg	34	8	2	45	17	12	0	37	288
Standard Deviation	269534	33.3	2.85E+11	0.130	295	0.200	6.1	235.9	18132024.80

Eddy Correlation Latent Heat Flux

1	467250	90.5	7.73E+10	0.285	-263	0.133	292.9	120.5	1491.86
2									
3									
4									
5	509378	81.8	1.59E+11	0.309	-752	0.508	304.3	108.0	4028.72
6	248387	75.9	1.34E+11	0.490	-926	0.642	291.7	104.3	2199.00
7	548650	46.4	1.17E+11	0.459	-691	0.578	295.5	109.8	1606.76
8	348683	78.3	1.76E+11	0.216	-806	0.355	296.9	72.6	2214.17
1-8	128126	50.0	7.81E+10	0.293	-760	0.212	295.1	113.6	1779.60
% Diff from 1-8 avg	66	29	88	33	60	79	5	44	9476
Average	424470	74.6	1.33E+11	0.352	-687	0.443	296.3	103.0	2308.10
% Diff from Overall Avg	13	27	63	2	35	96	0	67	100
Standard Deviation	110643	14.9	3.43E+10	0.105	226	0.182	4.4	16.2	909.88

Latent Heat Flux by Temperature Variance

1	140001	23.8	6.56E+10	0.429	-932	0.120	292.1	166.2	1744.72
2	269463	83.5	7.25E+09	0.379	-961	0.362	291.4	107.9	1950.40
3	246431	94.4	4.38E+11	0.500	-844	0.154	295.7	161.9	1728.47
4	312335	43.0	1.99E+10	0.451	-594	0.107	293.7	84.0	1985.05
5	40166	90.3	1.01E+11	0.495	-725	0.289	295.9	129.0	4411.34
6	907590	57.1	1.20E+11	0.414	-987	0.197	292.5	145.3	1892.02
7	378241	90.2	1.09E+10	0.460	-947	0.455	295.3	123.5	1840.69
8	497647	58.3	2.89E+09	0.349	-209	0.455	297.4	97.2	1954.27
1-8	395637	69.7	8.85E+10	0.478	-887	0.246	294.0	133.3	1732.08
% Diff from 1-8 avg	4	1	86	10	87	108	5	34	9220
Average	348984	67.6	9.56E+10	0.434	-775	0.267	294.2	126.9	2188.37
% Diff from Overall Avg	28	15	73	26	53	18	1	59	100
Standard Deviation	248049	24.3	1.36E+11	0.050	248	0.135	2.0	27.9	844.94

Latent Heat Flux Summary

Average	378017	70.3	1.10E+11	0.403	-741	0.335	295.0	117.7	2234.42
% Diff from Overall Avg	22	19	69	17	46	48	1	62	100
Standard Deviation	209572	21.5	1.10E+11	0.086	244	0.177	3.3	26.7	872.44

Timestep Corrected Eddy Correlation Latent Heat Flux

1	567195	63.5	6.34E+11	0.475	-427	0.152	293.5	171.1	2175.87
2									
3									
4									
5	759588	46.9	5.87E+11	0.485	-515	0.381	299.8	337.7	3961.85
6	996209	29.9	2.93E+11	0.485	-435	0.109	293.6	689.2	2833.51
7	338948	19.9	1.72E+11	0.410	-348	0.187	295.1	582.2	1622.93
8	206603	77.9	1.72E+11	0.350	-240	0.351	297.3	227.0	1923.93
1-8	609983	39.1	6.83E+11	0.430	-720	0.189	294.4	629.6	1900.90
% Diff from 1-8 avg	*61*	*44*	*7*	*1*	*51*	*60*	*5*	*210*	*10128*
Average	*593709*	*47.6*	*3.72E+11*	*0.441*	*-393*	*0.236*	*295.9*	*401.4*	*2503.62*
% Diff from Overall Avg	*358*	*44*	*764*	*207*	*2*	*81*	*1*	*1768*	*142*
Standard Deviation	*286244*	*21.2*	*2.00E+11*	*0.053*	*93*	*0.110*	*2.4*	*201.5*	*831.18*

Timestep Corrected Temperature Variance Latent Heat Flux

1	928463	75.5	4.68E+11	0.496	-287	0.116	293.1	169.3	4215.57
2	331499	17.5	1.54E+11	0.491	-613	0.119	289.7	115.6	3162.13
3	337409	59.4	7.93E+11	0.480	-465	0.102	294.9	211.8	3754.59
4	366523	92.5	7.12E+11	0.457	-583	0.103	294.4	222.4	3731.02
5	358673	85.6	9.03E+11	0.482	-374	0.109	289.2	254.8	242366.42
6	37742	41.6	6.58E+11	0.486	-483	0.101	291.5	563.6	2972.29
7	376154	40.0	5.40E+11	0.390	-650	0.157	295.2	517.0	3057.23
8	915925	73.2	8.38E+11	0.491	-768	0.318	297.8	187.8	3708.74
1-8	654741	95.9	9.20E+11	0.479	-488	0.102	294.2	523.8	2793.75
% Diff from 1-8 avg	*72*	*37*	*44*	*10*	*3*	*14*	*5*	*158*	*14932*
Average	*706549*	*60.7*	*6.33E+11*	*0.472*	*-528*	*0.141*	*293.2*	*280.3*	*33371.00*
% Diff from Overall Avg	*445*	*29*	*1373*	*228*	*37*	*8*	*0*	*1204*	*3126*
Standard Deviation	*302287*	*24.2*	*2.27E+11*	*0.033*	*146*	*0.069*	*2.8*	*155.3*	*78993.84*

Timestep Corrected Latent Heat Flux Summary

Average	*663149*	*55.7*	*5.33E+11*	*0.460*	*-476*	*0.177*	*294.2*	*326.9*	*21498.93*
% Diff from Overall Avg	*411*	*34*	*1139*	*220*	*23*	*36*	*0*	*1421*	*1978*
Standard Deviation	*301263*	*23.9*	*2.52E+11*	*0.045*	*144*	*0.099*	*2.9*	*184.2*	*63763.59*

Period Corrected Eddy Correlation Latent Heat Flux

1	418644	18.1	7.87E+10	0.483	-595	0.144	291.0	453.6	616.68
2									
3									
4									
5	254159	48.1	3.16E+11	0.323	-858	0.134	292.8	478.4	1825.56
6	572102	63.8	8.94E+10	0.386	-500	0.161	289.5	429.1	992.96
7	561216	71.2	5.29E+10	0.460	-691	0.279	289.5	451.2	688.38
8	46954	28.7	1.06E+09	0.305	-11	0.122	290.2	315.9	866.90
1-8	785991	67.6	1.79E+11	0.334	-864	0.110	290.2	440.0	907.74
% Diff from 1-8 avg	*107*	*4*	*72*	*23*	*82*	*7*	*6*	*117*	*4784*
Average	*370615*	*45.9*	*1.08E+11*	*0.391*	*-531*	*0.168*	*290.6*	*425.6*	*998.09*
% Diff from Overall Avg	*24*	*22*	*70*	*14*	*5*	*26*	*2*	*38*	*100*
Standard Deviation	*198772*	*20.2*	*1.09E+11*	*0.071*	*286*	*0.057*	*1.2*	*57.0*	*434.36*

Period Corrected Temperature Variance Latent Heat Flux

1	275277	22.0	3.17E+10	0.489	-719	0.109	290.5	516.4	760.62
2	134087	69.3	1.75E+09	0.500	-375	0.108	288.4	278.4	786.58
3	154469	48.9	3.02E+11	0.444	-667	0.107	291.7	476.4	846.16
4	342029	24.8	2.10E+10	0.450	-900	0.101	290.2	314.4	929.77
5	966375	53.9	3.37E+11	0.481	-925	0.106	289.7	418.0	1899.97
6	323170	42.2	2.31E+11	0.419	-847	0.114	290.2	492.7	934.77
7	929364	79.4	9.34E+09	0.484	-744	0.250	289.9	421.8	871.26
8	730565	99.1	4.68E+10	0.460	-471	0.107	290.4	289.8	920.68
1-8	70166	86.0	1.48E+11	0.430	-848	0.106	290.2	424.4	854.60
% Diff from 1-8 avg	*82*	*23*	*77*	*1*	*78*	*10*	*6*	*109*	*4498*
Average	*544417*	*55.0*	*1.23E+11*	*0.466*	*-706*	*0.125*	*290.1*	*401.0*	*993.73*
% Diff from Overall Avg	*12*	*7*	*66*	*35*	*39*	*45*	*2*	*30*	*100*
Standard Deviation	*330230*	*24.9*	*1.33E+11*	*0.026*	*185*	*0.047*	*0.9*	*88.8*	*347.89*

Period Corrected Latent Heat Flux Summary

Average	*477570*	*51.5*	*1.17E+11*	*0.437*	*-639*	*0.142*	*290.3*	*410.5*	*995.41*
% Diff from Overall Avg	*2*	*12*	*67*	*27*	*26*	*37*	*2*	*33*	*100*
Standard Deviation	*299090*	*23.6*	*1.24E+11*	*0.061*	*244*	*0.055*	*1.0*	*79.0*	*383.47*

Overall Corrected Latent Heat Flux Summary

Average	*496792*	*58.9*	*2.49E+11*	*0.430*	*-622*	*0.218*	*293.2*	*280.7*	*8081.34*
% Diff from Overall Avg	*2*	*0*	*30*	*25*	*23*	*3*	*1*	*9*	*99*
Standard Deviation	*299901*	*24.1*	*2.62E+11*	*0.072*	*240*	*0.146*	*3.3*	*169.7*	*37531.47*

Soil Heat Flux

1	129695	84.9	4.30E+10	0.144	-386	0.130	294.3	21.5	1310.02
2	565740	72.1	3.14E+10	0.152	-727	0.171	294.2	19.6	1025.45
3	129695	84.9	4.30E+10	0.144	-386	0.130	294.3	21.5	1025.51
4	129695	84.9	4.30E+10	0.144	-386	0.130	294.3	21.5	1891.13
5	428239	41.3	2.69E+11	0.130	-828	0.155	295.3	22.9	1091.79
6	565740	72.1	3.14E+10	0.152	-727	0.171	294.2	19.6	773.53
7	222181	63.0	3.09E+10	0.197	-955	0.238	293.3	17.3	1191.82
8	129695	84.9	4.30E+10	0.144	-386	0.130	294.3	21.5	1358.98
1-8	129695	84.9	4.30E+10	0.144	-386	0.130	294.3	21.5	1034.46
% Diff from 1-8 avg	*66*	*21*	*93*	*67*	*19*	*10*	*5*	*89*	*5466*
Average	*287585*	*73.5*	*6.69E+10*	*0.151*	*-597*	*0.157*	*294.3*	*20.7*	*1208.53*
% Diff from Overall Avg	*41*	*25*	*81*	*56*	*18*	*30*	*1*	*93*	*100*
Standard Deviation	*186587*	*14.5*	*7.67E+10*	*0.019*	*222*	*0.035*	*0.5*	*1.6*	*310.05*

Gravimetric Soil Moisture

1	944	75.8	9.47E+11	0.490	-291	0.101	309.9	61.3	10.69
2	389530	41.3	3.74E+11	0.392	-298	0.192	310.0	669.7	13.04
3	393298	11.5	1.78E+10	0.454	-228	0.128	310.0	260.3	17.96
4	155828	84.2	1.48E+09	0.457	-167	0.460	310.0	311.9	8.80
5	338449	57.3	1.85E+10	0.451	-83	0.184	309.9	406.8	20.02
6	427603	76.2	1.83E+11	0.266	-661	0.115	310.0	218.7	13.80
7	944	75.8	9.47E+11	0.490	-291	0.101	309.9	61.3	19.06
8	87058	15.1	1.63E+11	0.498	-230	0.103	307.9	562.1	20.59
1-8	164136	6.4	2.08E+10	0.475	-533	0.157	307.2	683.0	10.17
% Diff from 1-8 avg	*57*	*91*	*97*	*9*	*12*	*33*	*1*	*236*	*45*
Average	*411707*	*54.7*	*3.31E+11*	*0.437*	*-281*	*0.173*	*309.7*	*319.0*	*15.50*
% Diff from Overall Avg	*15*	*7*	*7*	*27*	*45*	*23*	*4*	*3*	*100*
Standard Deviation	*379297*	*27.0*	*3.73E+11*	*0.072*	*159*	*0.114*	*0.7*	*205.0*	*4.21*

Daily Difference Gravimetric Soil Moisture

1	239203	51.3	2.74E+11	0.172	-961	0.253	292.8	470.6	2.19
2	127811	71.7	6.20E+11	0.484	-530	0.601	285.0	587.0	4.40
3	561148	85.3	4.00E+10	0.495	-43	0.438	292.2	516.0	2.27
4	795017	27.3	4.39E+11	0.421	-983	0.199	292.1	473.3	7.98
5	587737	88.0	2.47E+10	0.274	-357	0.427	287.9	512.2	6.60
6	460119	39.9	9.62E+11	0.331	-838	0.225	292.7	636.3	15.21
7	482677	68.3	2.69E+11	0.490	-149	0.323	291.3	414.8	6.06
8	323075	23.0	7.26E+11	0.488	-729	0.104	285.0	377.6	22.94
1-8	247702	88.7	6.97E+11	0.443	-900	0.643	285.0	198.7	2.92
% Diff from 1-8 avg	35	26	9	2	89	444	8	2	84
Average	522098	56.9	4.19E+11	0.394	-574	0.321	289.9	498.5	8.46
% Diff from Overall Avg	8	3	17	15	13	42	3	61	100
Standard Deviation	233163	23.6	3.11E+11	0.114	339	0.150	3.2	79.3	6.70

Time period Difference Gravimetric Soil Moisture

1	944	75.8	9.47E+11	0.490	-291	0.101	309.9	61.3	2.14
2	944	75.8	9.47E+11	0.490	-291	0.101	309.9	61.3	4.41
3	944	75.8	9.47E+11	0.490	-291	0.101	309.9	61.3	0.47
4	220034	38.6	6.41E+11	0.343	-583	0.574	288.4	553.8	0.10
5	117678	72.1	1.24E+11	0.288	-74	0.611	285.0	160.6	7.56
6	384304	46.0	7.03E+11	0.498	-210	0.101	309.6	641.8	0.10
7	944	75.8	9.47E+11	0.490	-291	0.101	309.9	61.3	11.03
8	319012	4.5	8.86E+11	0.100	-613	0.660	285.0	222.8	2.98
1-8	944	75.8	9.47E+11	0.490	-291	0.101	309.9	61.3	0.32
% Diff from 1-8 avg	100	8	48	13	39	14	0	70	98
Average	193100	58.1	7.68E+11	0.399	-330	0.294	301.0	228.0	3.60
% Diff from Overall Avg	60	1	115	16	35	30	1	26	100
Standard Deviation	284545	24.6	2.68E+11	0.136	170	0.250	11.5	221.7	3.68

Resistance Soil Moisture

1	944	75.8	9.47E+11	0.490	-291	0.101	309.9	61.3	20.12
2	905651	49.4	8.63E+10	0.395	-785	0.126	308.8	372.8	21.42
3	944	75.8	9.47E+11	0.490	-291	0.101	309.9	61.3	24.68
4	647484	90.0	2.39E+11	0.329	-714	0.205	310.0	235.5	11.07
5	807987	48.1	8.40E+11	0.498	-283	0.101	308.9	532.1	19.89
6	331268	88.5	6.92E+11	0.293	-480	0.105	310.0	175.2	16.25
7	944	75.8	9.47E+11	0.490	-291	0.101	309.9	61.3	22.73
8	341274	57.6	4.29E+11	0.499	-668	0.105	308.8	124.7	12.54
1-8	708096	97.0	9.71E+11	0.496	-514	0.102	305.0	149.5	16.67
% Diff from 1-8 avg	87	38	52	14	8	13	1	26	10
Average	379562	70.1	6.41E+11	0.436	-475	0.118	309.5	203.0	18.58
% Diff from Overall Avg	22	19	79	27	6	48	4	34	100
Standard Deviation	347483	15.4	3.23E+11	0.079	203	0.034	0.5	160.2	4.54

Soil Moisture Summary

Average	376617	59.9	5.40E+11	0.416	-415	0.227	302.5	312.1	11.53
% Diff from Overall Avg	22	2	51	21	18	0	2	1	100
Standard Deviation	337648	23.9	3.65E+11	0.106	257	0.178	10.1	210.3	7.66

Metflux Sites 1-8 Overall Summary

Average	416938	65.1	4.29E+11	0.356	-583	0.195	297.1	347.8	1178.98
% Diff from Overall Avg	14	11	20	3	15	14	0	13	100
Standard Deviation	258947	30.0	3.80E+11	0.140	252	0.145	6.7	238.0	863.16

Overall Summary

Average	485214	58.8	3.57E+11	0.344	-508	0.226	297.4	308.8	918050.94
Standard Deviation	319834	26.5	3.27E+11	0.152	278	0.169	7.8	219.7	9324907.65

Table F.2: Results of Monte-Carlo calibration of TOPLATS and Monsoon '90 Metflux sites excluding night data. Data were derived from the minimum objectives of 2,120,922 single-grid simulations.

Default Parameter Values:	*10,000*	*1.0*	*1.00E+09*	*0.280*	*-300*	*0.500*	*297.0*	*250.0*	
Parameter Calibration Range	0-1e6	0-100	1e6-1e12	0.1-0.5	0-1000	0-2	275-315	0-500	**Best Obj. Value**
SITE	**RTACT**	**RTDENS**	**RTRES**	**SMPET**	**PSICRI**	**DHEAT**	**TDEEP**	**RSMIN**	
Eddy Correlation Sensible Heat Flux									
1	579183	76.8	1.81E+11	0.302	-749	0.101	293.2	251.5	1661.36
2									
3									
4									
5	159596	84.3	2.72E+11	0.166	-953	0.101	299.1	174.4	1905.61
6	580396	75.4	1.58E+11	0.101	-843	0.102	294.4	207.2	2108.93
7	330344	67.9	2.62E+10	0.311	-151	0.102	291.6	325.6	1672.30
8	31506	51.9	2.62E+10	0.424	-484	0.107	291.9	181.8	1793.08
1-8	289395	75.4	9.93E+10	0.347	-977	0.101	294.0	197.0	1711.28
% Diff from 1-8 avg	*30*	*26*	*72*	*4*	*64*	*38*	*1*	*43*	*1*
Average	*376205*	*71.2*	*1.33E+11*	*0.261*	*-636*	*0.103*	*294.0*	*228.1*	*1828.25*
% Diff from Overall Avg	*30*	*30*	*56*	*28*	*6*	*53*	*1*	*29*	*100*
Standard Deviation	*265393*	*11.0*	*9.50E+10*	*0.114*	*288*	*0.002*	*2.7*	*55.7*	*166.24*
Temperature Variance Sensible Heat Flux									
1	590108	51.3	5.48E+10	0.225	-839	0.101	293.0	309.4	1802.15
2	438969	90.7	5.14E+10	0.125	-707	0.106	300.3	147.3	1643.14
3	653392	100.0	3.76E+11	0.159	-854	0.100	288.3	355.3	1549.26
4	156813	79.8	6.04E+10	0.126	-607	0.102	289.5	333.6	1865.73
5	573854	71.9	2.66E+11	0.129	-757	0.101	297.8	372.9	2439.78
6	358456	83.3	1.65E+10	0.120	-887	0.101	290.8	606.6	1917.96
7	178575	76.6	1.75E+11	0.166	-692	0.100	292.8	285.4	1923.15
8	351220	82.6	5.23E+10	0.109	-846	0.111	301.7	157.2	1462.79
1-8	379428	73.5	3.37E+10	0.109	-514	0.122	295.1	230.0	1596.87
% Diff from 1-8 avg	*70*	*23*	*90*	*70*	*14*	*25*	*1*	*33*	*6*
Average	*550173*	*79.5*	*1.32E+11*	*0.145*	*-774*	*0.103*	*294.3*	*321.0*	*1825.50*
% Diff from Overall Avg	*2*	*45*	*56*	*60*	*29*	*53*	*1*	*0*	*100*
Standard Deviation	*254558*	*13.4*	*1.21E+11*	*0.035*	*92*	*0.004*	*4.7*	*134.2*	*282.56*
Sensible Heat Flux Summary									
Average	*483263*	*76.3*	*1.32E+11*	*0.190*	*-721*	*0.103*	*294.2*	*285.3*	*1826.56*
% Diff from Overall Avg	*11*	*39*	*56*	*48*	*20*	*53*	*1*	*11*	*100*
Standard Deviation	*272268*	*13.1*	*1.12E+11*	*0.095*	*204*	*0.003*	*4.1*	*119.6*	*244.46*
Corrected Eddy Correlation Sensible Heat Flux									
1	333842	20.2	7.43E+11	0.124	-953	0.698	307.5	673.8	2994.46
2									
3									
4									
5	651749	32.5	5.79E+11	0.314	-59	0.219	304.7	677.6	3236.56
6	951161	1.3	7.58E+11	0.108	-479	0.694	297.7	677.5	6053.32
7	268135	83.1	8.97E+11	0.128	-5	0.625	293.0	697.2	3523.98
8	476847	65.3	5.45E+11	0.440	-185	0.201	293.6	594.5	3261.55
1-8	582216	38.1	6.72E+11	0.117	-73	0.337	298.1	694.4	2783.26
% Diff from 1-8 avg	*206*	*36*	*91*	*68*	*88*	*106*	*0*	*101*	*65*
Average	*636347*	*40.5*	*7.04E+11*	*0.223*	*-336*	*0.487*	*299.3*	*664.1*	*3813.97*
% Diff from Overall Avg	*18*	*26*	*136*	*38*	*44*	*122*	*1*	*107*	*100*
Standard Deviation	*244692*	*29.8*	*1.29E+11*	*0.132*	*349*	*0.228*	*5.8*	*35.7*	*1132.16*

Corrected Temperature Variance Sensible Heat Flux

1	443167	19.6	7.57E+11	0.468	-594	0.412	306.3	699.8	3690.99
2	363882	48.3	4.41E+11	0.322	-571	0.681	309.5	680.9	3752.58
3	73503	18.6	8.38E+11	0.109	-185	0.301	285.5	694.9	3754.65
4	334194	1.6	1.66E+11	0.102	-132	0.176	299.0	699.6	4177.68
5	971783	2.7	7.04E+11	0.408	-78	0.679	309.4	691.6	7536.34
6	233133	89.8	5.87E+10	0.433	-738	0.166	285.2	3.8	93131379.27
7	380639	39.2	3.93E+11	0.233	-193	0.469	308.3	690.3	4348.33
8	945290	9.3	6.10E+11	0.498	-570	0.697	300.2	658.3	4578.88
1-8	22334	48.9	5.52E+11	0.191	-269	0.214	309.3	681.3	3635.43
% Diff from 1-8 avg	*96*	*25*	*30*	*59*	*63*	*48*	*0*	*116*	*19431*
Average	*530699*	*28.6*	*4.96E+11*	*0.322*	*-383*	*0.448*	*300.4*	*602.4*	*11645402.34*
% Diff from Overall Avg	*2*	*48*	*66*	*11*	*36*	*104*	*1*	*87*	*1210*
Standard Deviation	*319009*	*27.8*	*2.63E+11*	*0.147*	*243*	*0.208*	*9.5*	*226.6*	*30798804.35*

Corrected Sensible Heat Flux Summary

Average	*571333*	*33.2*	*5.76E+11*	*0.284*	*-365*	*0.463*	*300.0*	*626.1*	*7167868.35*
% Diff from Overall Avg	*6*	*39*	*93*	*22*	*39*	*111*	*1*	*95*	*706*
Standard Deviation	*297146*	*29.2*	*2.44E+11*	*0.150*	*289*	*0.217*	*8.3*	*181.6*	*24815528.11*

Overall Sensible Heat Flux Summary

Average	*518486*	*55.5*	*3.45E+11*	*0.241*	*-559*	*0.276*	*297.0*	*446.1*	*3452138.71*
% Diff from Overall Avg	*4*	*1*	*15*	*33*	*7*	*26*	*0*	*39*	*288*
Standard Deviation	*286515*	*30.9*	*2.90E+11*	*0.133*	*312*	*0.235*	*7.0*	*230.5*	*17587546.12*

Eddy Correlation Latent Heat Flux

1	289391	68.1	4.97E+10	0.279	-215	0.146	292.6	122.4	2340.90
2									
3									
4									
5	536099	62.5	4.29E+10	0.386	-935	0.648	302.6	106.9	6876.07
6	499417	57.2	5.93E+10	0.488	-773	0.281	293.3	87.3	3379.80
7	237423	92.0	5.39E+10	0.451	-529	0.360	296.0	101.6	2178.98
8	189934	24.4	6.96E+10	0.389	-957	0.660	296.5	59.5	3464.03
1-8	472057	87.6	4.96E+10	0.444	-621	0.245	295.3	103.9	2445.00
% Diff from 1-8 avg	*19*	*34*	*88*	*5*	*15*	*69*	*5*	*67*	*13036*
Average	*330453*	*60.8*	*5.51E+10*	*0.399*	*-682*	*0.419*	*296.2*	*95.5*	*3647.95*
% Diff from Overall Avg	*39*	*11*	*82*	*10*	*14*	*91*	*0*	*70*	*100*
Standard Deviation	*166751*	*21.8*	*9.03E+09*	*0.071*	*279*	*0.204*	*3.5*	*21.2*	*1696.63*

Latent Heat Flux by Temperature Variance

1	798889	65.4	5.73E+09	0.470	-33	0.165	290.9	153.0	2235.11
2	957250	21.4	1.54E+10	0.464	-476	0.226	296.2	90.1	2854.07
3	702169	89.5	1.37E+11	0.484	-382	0.124	294.9	173.0	2589.83
4	559862	24.1	2.41E+10	0.478	-810	0.115	294.7	83.5	2894.00
5	445671	26.0	1.72E+10	0.436	-960	0.237	293.1	146.3	6966.77
6	275644	96.1	2.30E+11	0.465	-711	0.179	294.2	135.6	3020.13
7	565124	67.7	3.14E+10	0.316	-636	0.162	295.0	112.3	2667.48
8	583867	65.5	1.83E+11	0.494	-817	0.444	298.6	85.3	2949.42
1-8	642358	33.7	8.76E+10	0.492	-915	0.115	294.6	107.0	2626.78
% Diff from 1-8 avg	*11*	*49*	*79*	*5*	*25*	*20*	*5*	*66*	*14012*
Average	*611059*	*57.0*	*8.04E+10*	*0.451*	*-603*	*0.207*	*294.7*	*122.4*	*3272.10*
% Diff from Overall Avg	*13*	*4*	*73*	*25*	*1*	*6*	*1*	*62*	*100*
Standard Deviation	*196455*	*27.7*	*8.32E+10*	*0.053*	*278*	*0.098*	*2.1*	*32.2*	*1416.08*

Latent Heat Flux Summary

Average	*503134*	*58.5*	*7.07E+10*	*0.431*	*-633*	*0.288*	*295.3*	*112.1*	*3416.66*
% Diff from Overall Avg	*7*	*7*	*76*	*19*	*6*	*31*	*1*	*65*	*100*
Standard Deviation	*230395*	*25.7*	*6.67E+10*	*0.066*	*281*	*0.181*	*2.8*	*31.3*	*1540.97*

Timestep Corrected Eddy Correlation Latent Heat Flux

1	989488	43.1	6.89E+11	0.417	-634	0.145	293.7	345.1	3341.05
2									
3									
4									
5	843390	56.3	9.02E+11	0.348	-614	0.276	300.1	614.6	6425.61
6	642270	35.4	3.69E+11	0.390	-457	0.110	293.2	637.3	4781.40
7	946536	87.9	2.97E+10	0.495	-14	0.225	294.7	449.6	2561.77
8	277696	61.4	2.23E+11	0.466	-375	0.498	296.6	193.3	3122.56
1-8	565407	53.5	5.84E+11	0.473	-547	0.159	295.1	590.5	2852.22
% Diff from 1-8 avg	*3*	*18*	*38*	*1*	*25*	*10*	*5*	*87*	*15223*
Average	*739876*	*56.8*	*4.43E+11*	*0.423*	*-419*	*0.251*	*295.7*	*448.0*	*4046.48*
% Diff from Overall Avg	*14*	*307*	*1103*	*148*	*54*	*32*	*0*	*376*	*272*
Standard Deviation	*260333*	*18.1*	*3.15E+11*	*0.053*	*224*	*0.137*	*2.5*	*166.8*	*1396.85*

Timestep Corrected Temperature Variance Latent Heat Flux

1	719882	17.0	5.62E+11	0.458	-871	0.101	293.4	450.4	4468.16
2	403645	68.0	1.16E+11	0.497	-874	0.126	294.2	664.4	3993.32
3	955508	21.7	5.61E+11	0.484	-864	0.102	292.3	691.0	4807.27
4	776594	96.8	2.48E+11	0.494	-191	0.104	294.9	408.8	5515.18
5	94975	6.9	4.09E+11	0.448	-388	0.112	293.5	604.5	15031.14
6	941869	29.5	5.39E+11	0.454	-432	0.103	291.0	660.3	4526.05
7	680022	22.5	1.38E+11	0.308	-319	0.120	295.0	692.8	4183.37
8	781054	21.2	2.36E+10	0.463	-750	0.212	297.5	678.0	5097.32
1-8	871179	79.1	8.90E+11	0.469	-456	0.110	294.9	675.8	4096.76
% Diff from 1-8 avg	*36*	*21*	*110*	*0*	*38*	*24*	*5*	*114*	*21910*
Average	*669194*	*35.4*	*3.25E+11*	*0.451*	*-586*	*0.123*	*294.0*	*606.3*	*5952.73*
% Diff from Overall Avg	*22*	*154*	*782*	*165*	*36*	*35*	*0*	*544*	*447*
Standard Deviation	*270024*	*28.7*	*2.06E+11*	*0.057*	*264*	*0.035*	*1.8*	*105.7*	*3461.61*

Timestep Corrected Latent Heat Flux Summary

Average	*696379*	*43.7*	*3.70E+11*	*0.440*	*-522*	*0.172*	*294.6*	*545.4*	*5219.56*
% Diff from Overall Avg	*19*	*213*	*905*	*158*	*43*	*9*	*0*	*479*	*379*
Standard Deviation	*268549*	*27.2*	*2.60E+11*	*0.057*	*263*	*0.109*	*2.3*	*153.3*	*2997.42*

Period Corrected Eddy Correlation Latent Heat Flux

1	513969	44.0	8.37E+10	0.473	-303	0.114	291.2	424.0	923.82
2									
3									
4									
5	526256	21.2	1.58E+11	0.412	-959	0.131	294.1	401.8	2945.13
6	269233	87.0	9.34E+10	0.463	-530	0.129	292.0	350.7	1540.98
7	248888	91.1	6.29E+11	0.463	-929	0.196	292.5	394.8	922.61
8	534422	83.8	1.74E+10	0.354	-49	0.111	291.0	275.7	1266.26
1-8	753064	92.6	3.13E+11	0.457	-692	0.126	290.9	383.0	1217.48
% Diff from 1-8 avg	*30*	*41*	*26*	*2*	*5*	*13*	*6*	*21*	*6441*
Average	*458554*	*65.4*	*1.96E+11*	*0.433*	*-554*	*0.136*	*292.1*	*369.4*	*1519.76*
% Diff from Overall Avg	*15*	*19*	*34*	*20*	*8*	*38*	*2*	*15*	*100*
Standard Deviation	*166034*	*27.8*	*2.21E+11*	*0.045*	*353*	*0.031*	*1.1*	*52.6*	*749.42*

Period Corrected Temperature Variance Latent Heat Flux

1	237098	66.4	1.95E+11	0.482	-607	0.123	290.3	519.8	978.69
2	577442	72.6	2.76E+10	0.447	-811	0.104	288.1	328.7	1153.99
3	591896	85.5	9.56E+10	0.500	-690	0.105	293.3	509.3	1156.57
4	54687	53.4	2.67E+11	0.466	-925	0.109	292.3	296.5	1367.36
5	470376	61.8	8.84E+10	0.494	-276	0.111	288.8	379.1	2821.69
6	470376	61.8	8.84E+10	0.494	-276	0.111	288.8	379.1	1469.17
7	537200	89.1	6.85E+10	0.419	-505	0.104	289.8	396.3	1257.29
8	327240	70.3	1.03E+11	0.474	-294	0.140	291.3	292.6	1374.20
1-8	470376	61.8	8.84E+10	0.494	-276	0.111	288.8	379.1	1279.01
% Diff from 1-8 avg	*19*	*6*	*79*	*6*	*62*	*23*	*7*	*20*	*6771*
Average	*420789*	*70.1*	*1.17E+11*	*0.472*	*-548*	*0.113*	*290.3*	*387.7*	*1447.37*
% Diff from Overall Avg	*22*	*28*	*61*	*31*	*9*	*48*	*2*	*21*	*100*

Standard Deviation	*191387*	*11.4*	*7.19E+10*	*0.026*	*237*	*0.012*	*1.7*	*81.6*	*539.38*
Period Corrected Latent Heat Flux Summary									
Average	*435314*	*68.3*	*1.47E+11*	*0.457*	*-550*	*0.122*	*291.0*	*380.7*	*1475.21*
% Diff from Overall Avg	*19*	*25*	*51*	*26*	*8*	*44*	*2*	*18*	*100*
Standard Deviation	*182979*	*19.6*	*1.53E+11*	*0.039*	*287*	*0.024*	*1.8*	*72.4*	*629.51*
Overall Corrected Latent Heat Flux Summary									
Average	*543120*	*57.6*	*1.92E+11*	*0.443*	*-570*	*0.195*	*293.7*	*340.0*	*3347.34*
% Diff from Overall Avg	*0*	*5*	*36*	*22*	*5*	*11*	*1*	*6*	*100*
Standard Deviation	*252247*	*26.5*	*2.17E+11*	*0.056*	*278*	*0.139*	*3.0*	*205.4*	*2474.00*
Soil Heat Flux									
1	392064	28.6	2.09E+10	0.173	-962	0.166	294.7	25.4	1344.00
2	436191	83.9	6.84E+10	0.146	-934	0.169	293.9	8.7	1044.11
3	392064	28.6	2.09E+10	0.173	-962	0.166	294.7	25.4	1041.67
4	392064	28.6	2.09E+10	0.173	-962	0.166	294.7	25.4	1933.26
5	336931	97.5	4.52E+11	0.104	-432	0.144	297.5	61.0	1100.64
6	436191	83.9	6.84E+10	0.146	-934	0.169	293.9	8.7	784.07
7	436191	83.9	6.84E+10	0.146	-934	0.169	293.9	8.7	1192.54
8	88510	65.3	4.67E+10	0.221	-419	0.188	293.2	10.1	1349.42
1-8	362041	13.9	3.68E+10	0.170	-914	0.189	294.7	94.2	1088.67
% Diff from 1-8 avg	*48*	*79*	*91*	*64*	*25*	*31*	*5*	*70*	*5749*
Average	*551276*	*62.5*	*9.58E+10*	*0.160*	*-817*	*0.167*	*294.5*	*21.7*	*1223.71*
% Diff from Overall Avg	*2*	*14*	*68*	*56*	*36*	*24*	*1*	*93*	*100*
Standard Deviation	*284657*	*27.5*	*1.36E+11*	*0.032*	*227*	*0.011*	*1.2*	*16.7*	*317.91*
Gravimetric Soil Moisture									
1	587827	64.8	1.56E+11	0.478	-929	0.101	310.0	11.4	10.77
2	215170	45.7	2.84E+11	0.467	-271	0.249	310.0	151.9	13.04
3	544178	4.2	4.56E+11	0.465	-223	0.130	310.0	17.2	17.96
4	114393	46.2	9.06E+11	0.396	-266	0.374	310.0	8.3	8.80
5	458189	7.1	6.18E+11	0.494	-610	0.208	309.8	313.7	20.02
6	393326	70.4	5.75E+11	0.452	-494	0.252	310.0	614.2	13.80
7	587827	64.8	1.56E+11	0.478	-929	0.101	310.0	11.4	19.11
8	494648	24.8	2.50E+11	0.491	-753	0.104	307.9	188.0	20.60
1-8	313209	86.1	7.29E+11	0.443	-125	0.141	307.2	211.5	10.17
% Diff from 1-8 avg	*40*	*31*	*72*	*5*	*83*	*2*	*1*	*33*	*45*
Average	*486945*	*41.0*	*4.25E+11*	*0.465*	*-559*	*0.190*	*309.7*	*164.5*	*15.51*
% Diff from Overall Avg	*10*	*25*	*43*	*29*	*7*	*14*	*4*	*49*	*100*
Standard Deviation	*224254*	*24.5*	*2.47E+11*	*0.029*	*274*	*0.093*	*0.7*	*199.4*	*4.21*
Daily Difference Gravimetric Soil Moisture									
1	391022	81.7	2.12E+10	0.244	-964	0.420	292.8	330.1	2.19
2	385940	26.9	2.67E+11	0.273	-360	0.259	285.0	247.4	4.40
3	21394	58.8	8.08E+11	0.248	-133	0.154	292.2	285.6	2.27
4	544428	12.0	3.91E+11	0.325	-656	0.133	292.1	677.7	7.98
5	107256	15.3	4.49E+11	0.317	-819	0.528	287.9	151.7	6.60
6	750578	36.8	1.80E+11	0.409	-453	0.306	292.7	592.0	15.21
7	318062	40.8	9.51E+11	0.467	-491	0.305	291.3	275.2	6.06
8	432322	42.2	2.00E+11	0.481	-593	0.104	285.1	494.8	22.97
1-8	312935	73.9	9.05E+11	0.257	-734	0.283	285.0	175.6	2.92
% Diff from 1-8 avg	*46*	*13*	*114*	*45*	*0*	*96*	*8*	*44*	*84*
Average	*493875*	*39.3*	*4.08E+11*	*0.345*	*-559*	*0.276*	*289.9*	*381.8*	*8.46*
% Diff from Overall Avg	*9*	*28*	*37*	*4*	*7*	*26*	*2*	*19*	*100*
Standard Deviation	*299881*	*21.4*	*3.00E+11*	*0.089*	*245*	*0.138*	*3.2*	*172.8*	*6.70*

Time period Difference Gravimetric Soil Moisture

1	587827	64.8	1.56E+11	0.478	-929	0.101	310.0	11.4	2.28
2	587827	64.8	1.56E+11	0.478	-929	0.101	310.0	11.4	4.46
3	587827	64.8	1.56E+11	0.478	-929	0.101	310.0	11.4	0.51
4	581275	5.9	7.55E+11	0.258	-349	0.126	289.4	322.4	0.10
5	566515	28.8	7.42E+11	0.278	-299	0.579	285.0	363.8	7.56
6	524941	62.6	7.13E+11	0.491	-538	0.110	309.9	275.4	0.11
7	587827	64.8	1.56E+11	0.478	-929	0.101	310.0	11.4	11.11
8	382957	88.7	8.17E+11	0.101	-445	0.684	285.0	320.9	2.98
1-8	587827	64.8	1.56E+11	0.478	-929	0.101	310.0	11.4	0.35
% Diff from 1-8 avg	*1*	*1*	*63*	*2*	*27*	*31*	*0*	*96*	*98*
Average	*613375*	*55.6*	*4.57E+11*	*0.380*	*-668*	*0.238*	*301.2*	*166.0*	*3.64*
% Diff from Overall Avg	*13*	*2*	*53*	*5*	*11*	*8*	*1*	*48*	*100*
Standard Deviation	*103882*	*24.1*	*3.01E+11*	*0.139*	*268*	*0.229*	*11.4*	*156.2*	*3.69*

Resistance Soil Moisture

1	587827	64.8	1.56E+11	0.478	-929	0.101	310.0	11.4	20.23
2	758173	79.6	2.42E+11	0.485	-722	0.174	308.9	443.9	21.42
3	587827	64.8	1.56E+11	0.478	-929	0.101	310.0	11.4	24.68
4	203720	73.7	8.14E+11	0.434	-88	0.314	310.0	501.7	11.07
5	386348	63.7	6.21E+11	0.496	-735	0.101	309.3	539.4	19.88
6	258262	64.9	8.12E+11	0.402	-799	0.165	310.0	442.6	16.25
7	587827	64.8	1.56E+11	0.478	-929	0.101	310.0	11.4	22.84
8	776669	48.5	4.33E+11	0.494	-723	0.102	308.9	561.8	12.53
1-8	287665	15.4	9.20E+10	0.495	-903	0.100	305.1	648.9	16.68
% Diff from 1-8 avg	*50*	*77*	*78*	*6*	*23*	*31*	*1*	*106*	*10*
Average	*580832*	*65.6*	*4.24E+11*	*0.468*	*-731*	*0.145*	*309.6*	*315.5*	*18.61*
% Diff from Overall Avg	*7*	*20*	*42*	*29*	*22*	*34*	*4*	*2*	*100*
Standard Deviation	*226261*	*8.4*	*2.71E+11*	*0.031*	*259*	*0.070*	*0.5*	*238.6*	*4.56*

Soil Moisture Summary

Average	*543756*	*50.4*	*4.29E+11*	*0.415*	*-629*	*0.212*	*302.6*	*256.9*	*11.56*
% Diff from Overall Avg	*1*	*8*	*44*	*15*	*5*	*3*	*2*	*20*	*100*
Standard Deviation	*231377*	*23.4*	*2.81E+11*	*0.100*	*272*	*0.154*	*10.1*	*216.1*	*7.66*

Metflux Sites 1-8 Overall Summary

Average	*500766*	*59.9*	*3.53E+11*	*0.362*	*-596*	*0.164*	*297.2*	*345.6*	*1690.86*
% Diff from Overall Avg	*7*	*9*	*18*	*0*	*1*	*25*	*0*	*8*	*100*
Standard Deviation	*222719*	*24.4*	*3.20E+11*	*0.144*	*296*	*0.072*	*7.2*	*240.9*	*1307.84*

Overall Summary

Average	*540694*	*54.8*	*2.98E+11*	*0.362*	*-600*	*0.219*	*297.3*	*321.3*	*889025.2*
Standard Deviation	*259484*	*27.1*	*2.78E+11*	*0.138*	*290*	*0.173*	*7.8*	*235.9*	*9045107.3*

APPENDIX G: TOPLATS SPATIALLY DISTRIBUTED CALIBRATED CONTROL RUN DIAGNOSTICS

Table G.1: Water-balance information for the TOPLATS-calibrated control simulation.

	Metflux Site:								*Watershed Average*
Variable (mm)	*1*	*2*	*3*	*4*	*5*	*6*	*7*	*8*	
Precip	99.33	82.66	118.87	114.32	107.12	116.49	92.25	90.56	93.44
Capillary Rise	0.00	0.00	0.00	0.00	0.00	0.00	0.00	0.00	0.00
ET	43.41	42.14	41.65	42.13	44.99	42.13	40.06	44.37	41.86
Runoff	14.70	0.00	13.92	19.38	5.15	15.84	0.00	1.92	6.21
Recharge	0.00	0.00	0.00	0.00	0.00	0.00	0.00	0.00	0.00
Surface ΔS	4.41	2.95	5.67	6.38	3.86	5.87	3.74	4.49	5.69
Root ΔS	30.96	31.41	48.19	38.70	44.19	43.13	38.75	33.59	33.51
Trans ΔS	5.85	6.15	9.43	7.72	8.87	9.51	9.62	6.18	6.14
Leaf ΔS	0.01	0.01	0.01	0.01	0.06	0.01	0.08	0.01	0.03
in-out	41.23	40.52	63.30	52.81	56.98	58.52	52.19	44.26	45.37
Total ΔS	41.23	40.52	63.30	52.81	56.98	58.52	52.19	44.26	45.37
Error	0.00	0.00	0.00	0.00	0.00	0.00	0.00	0.00	0.00

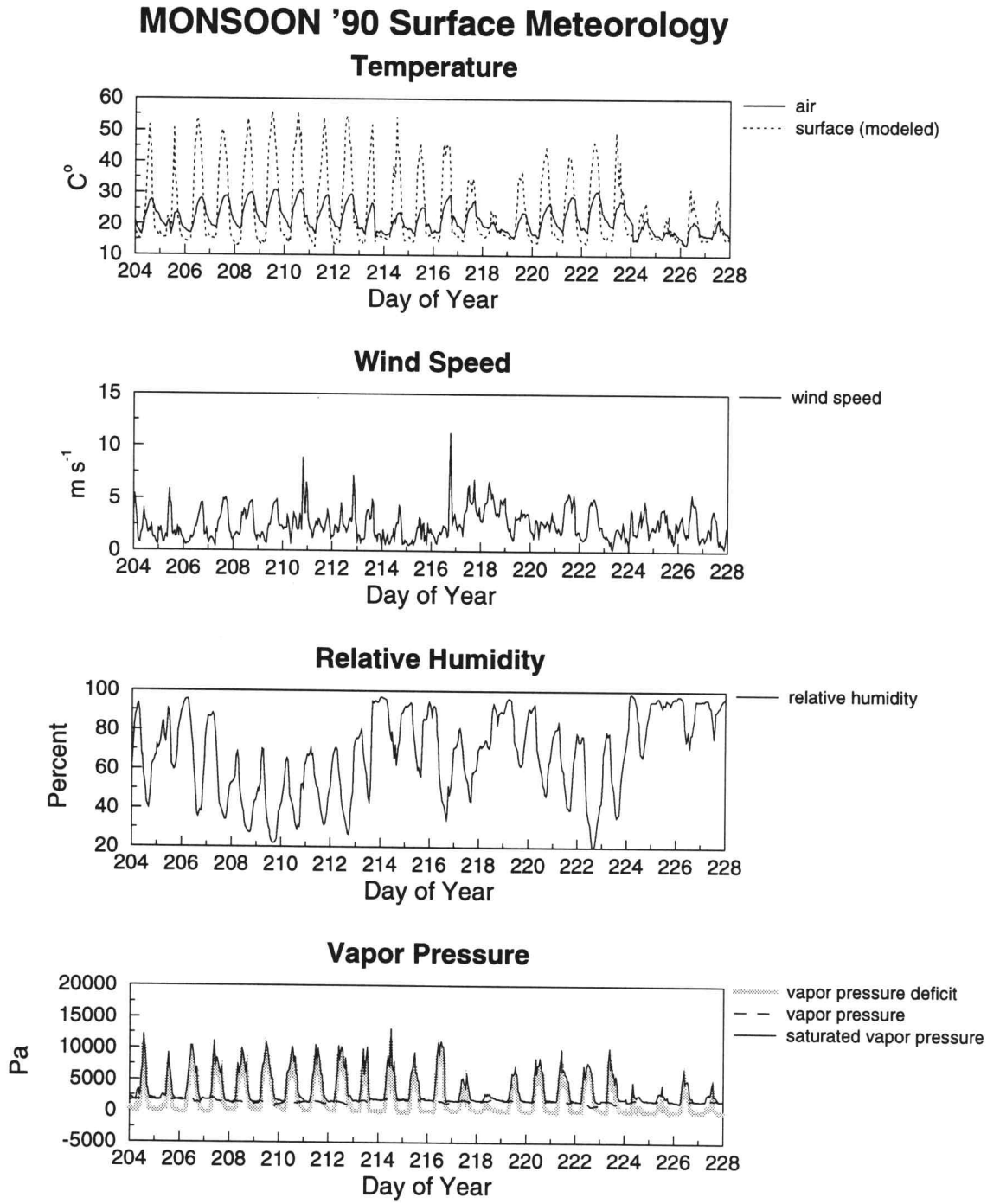

Figure G.1: TOPLATS calibrated control run watershed average surface meteorology.

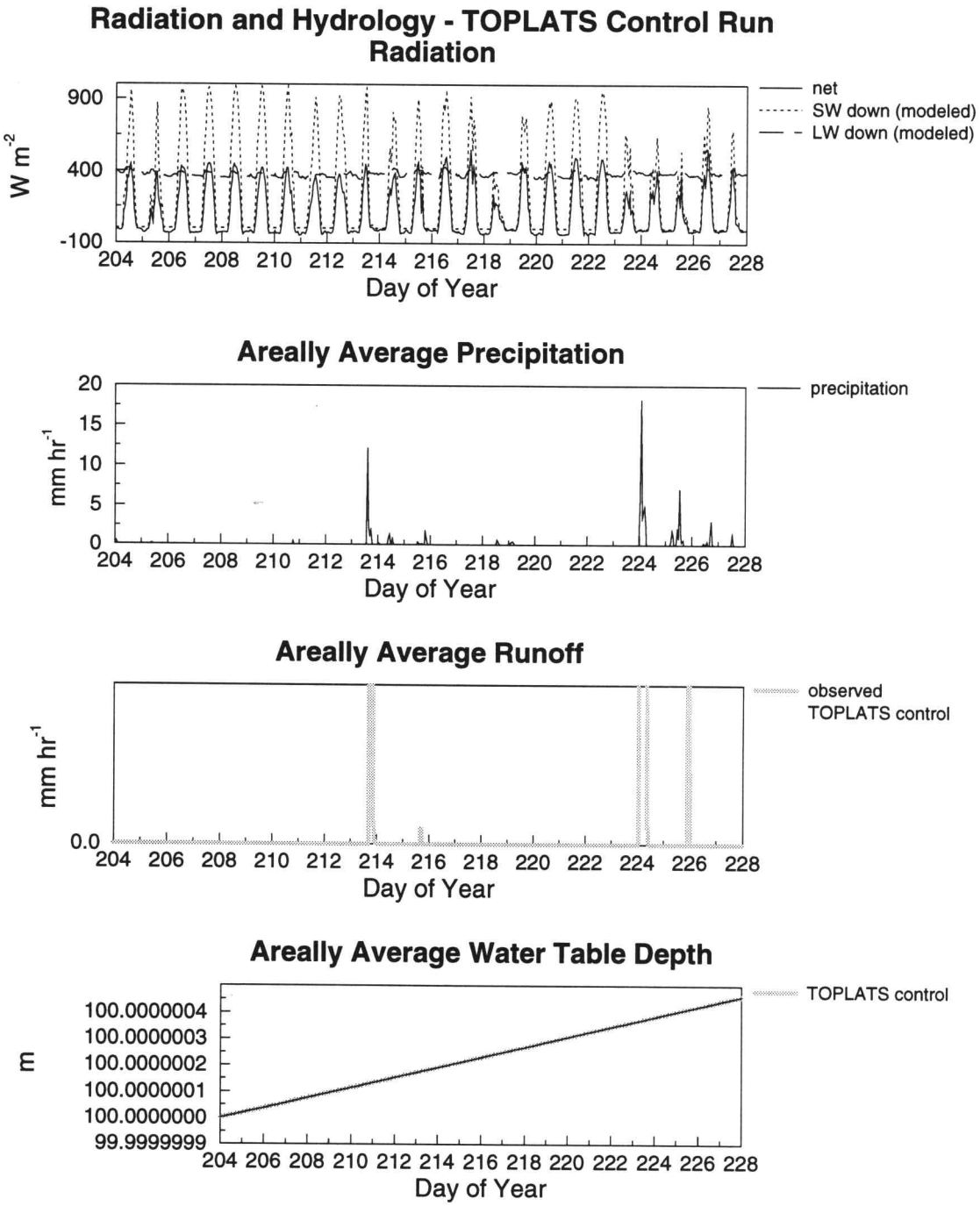

Figure G.2: TOPLATS calibrated control run watershed average radiation and hydrology.

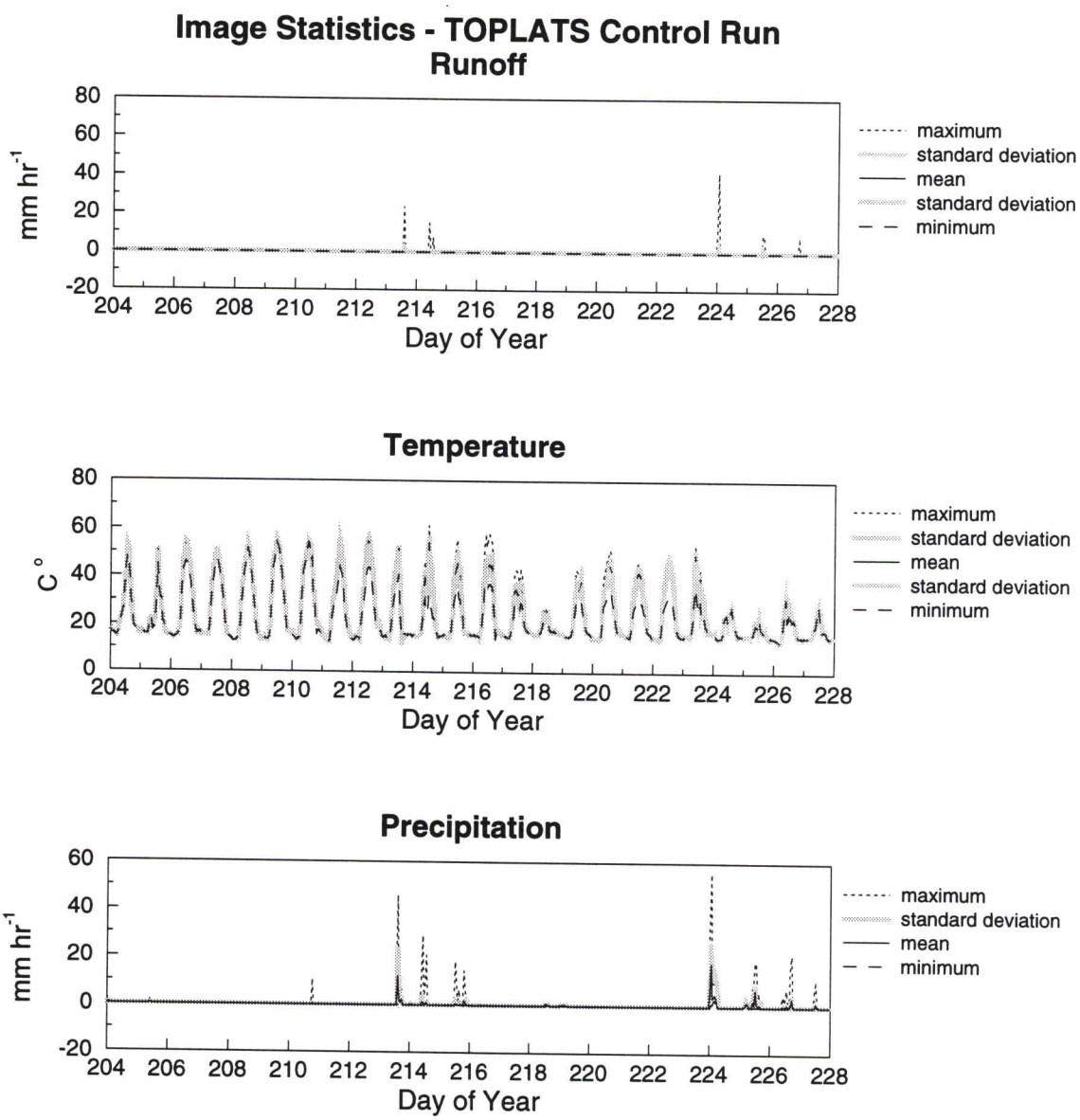

Figure G.3: TOPLATS calibrated control run temperature, runoff, and precipitation watershed statistics.

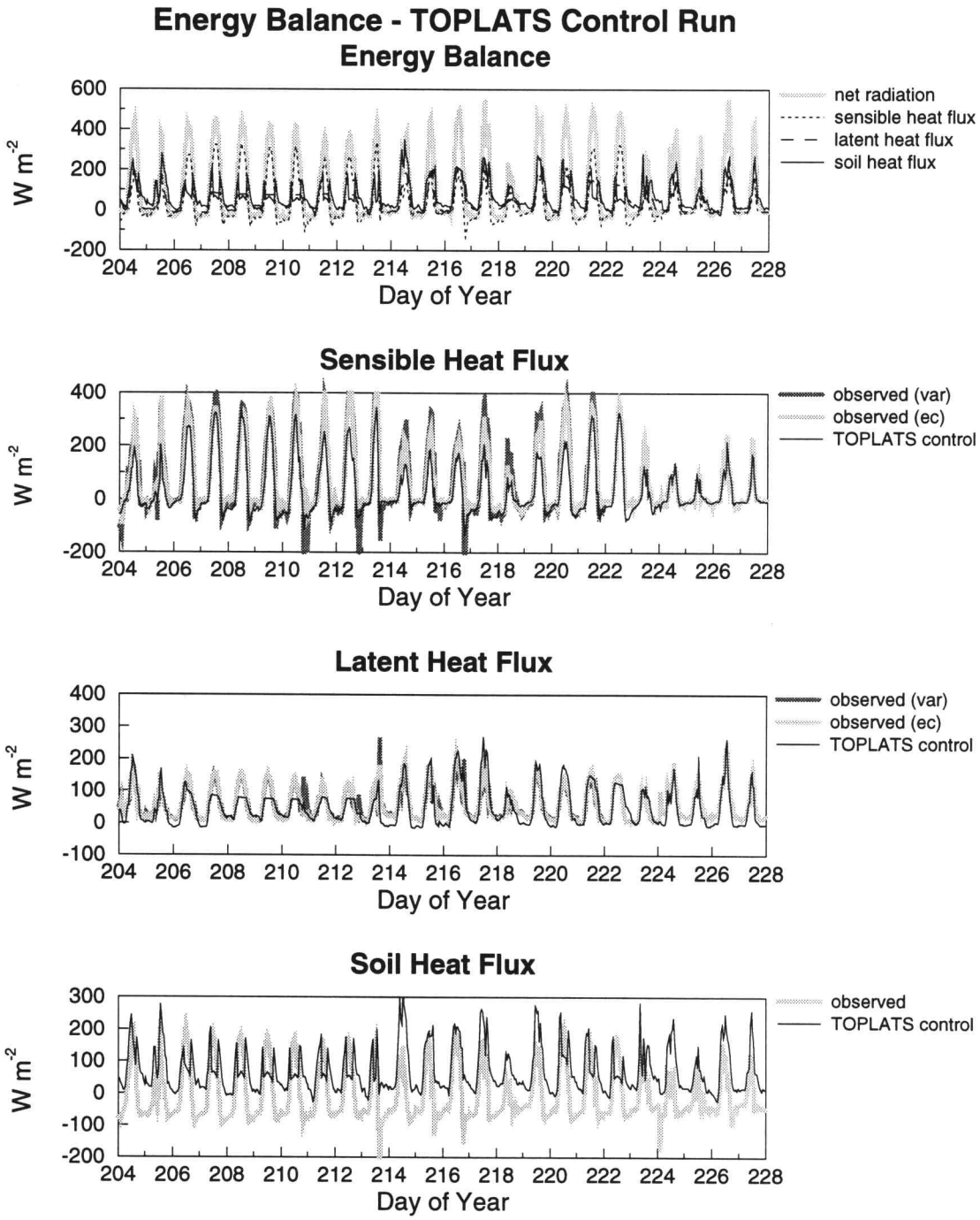

Figure G.4: TOPLATS calibrated control run watershed average energy balance.

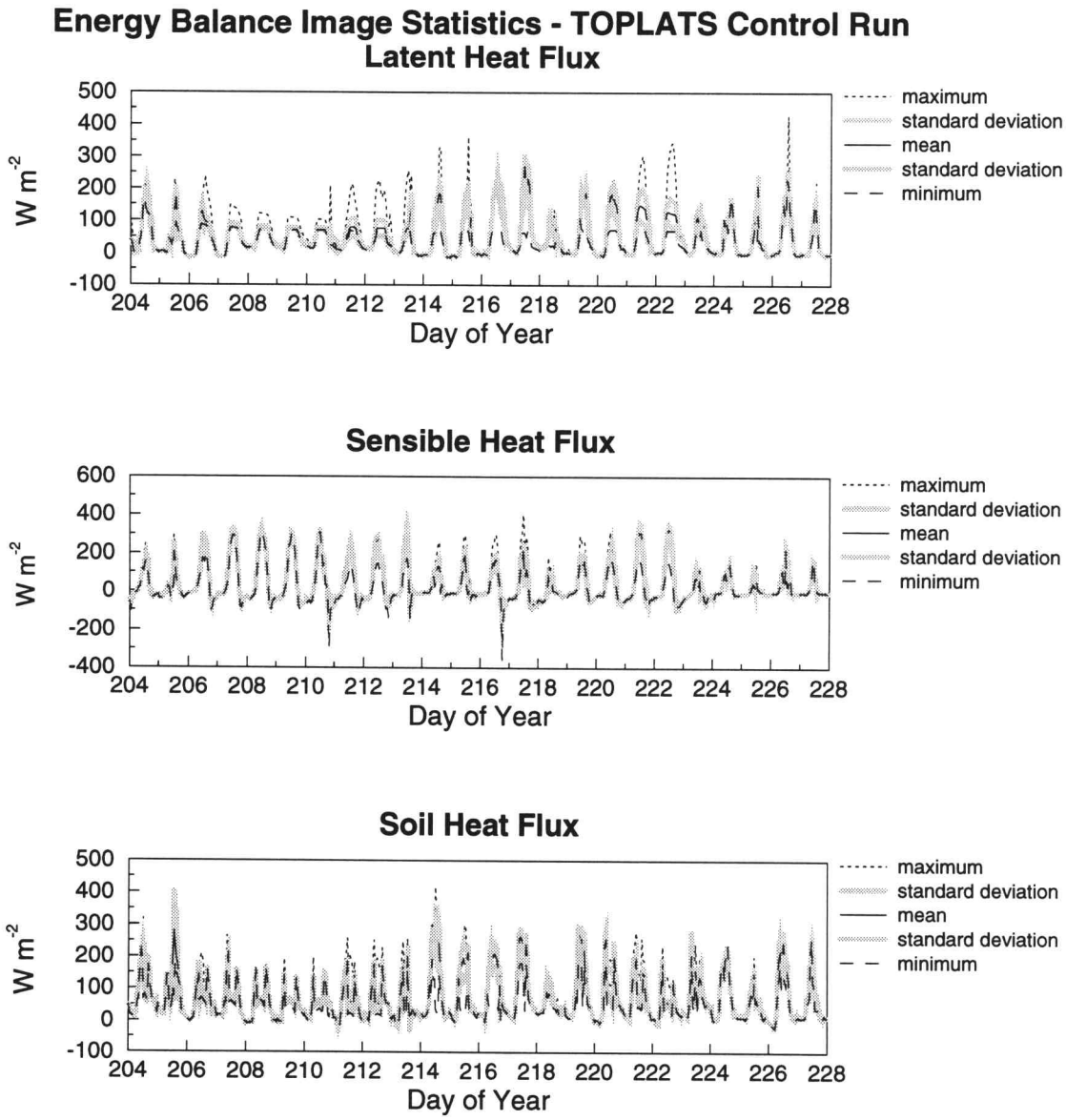

Figure G.5: TOPLATS calibrated control run energy balance watershed statistics.

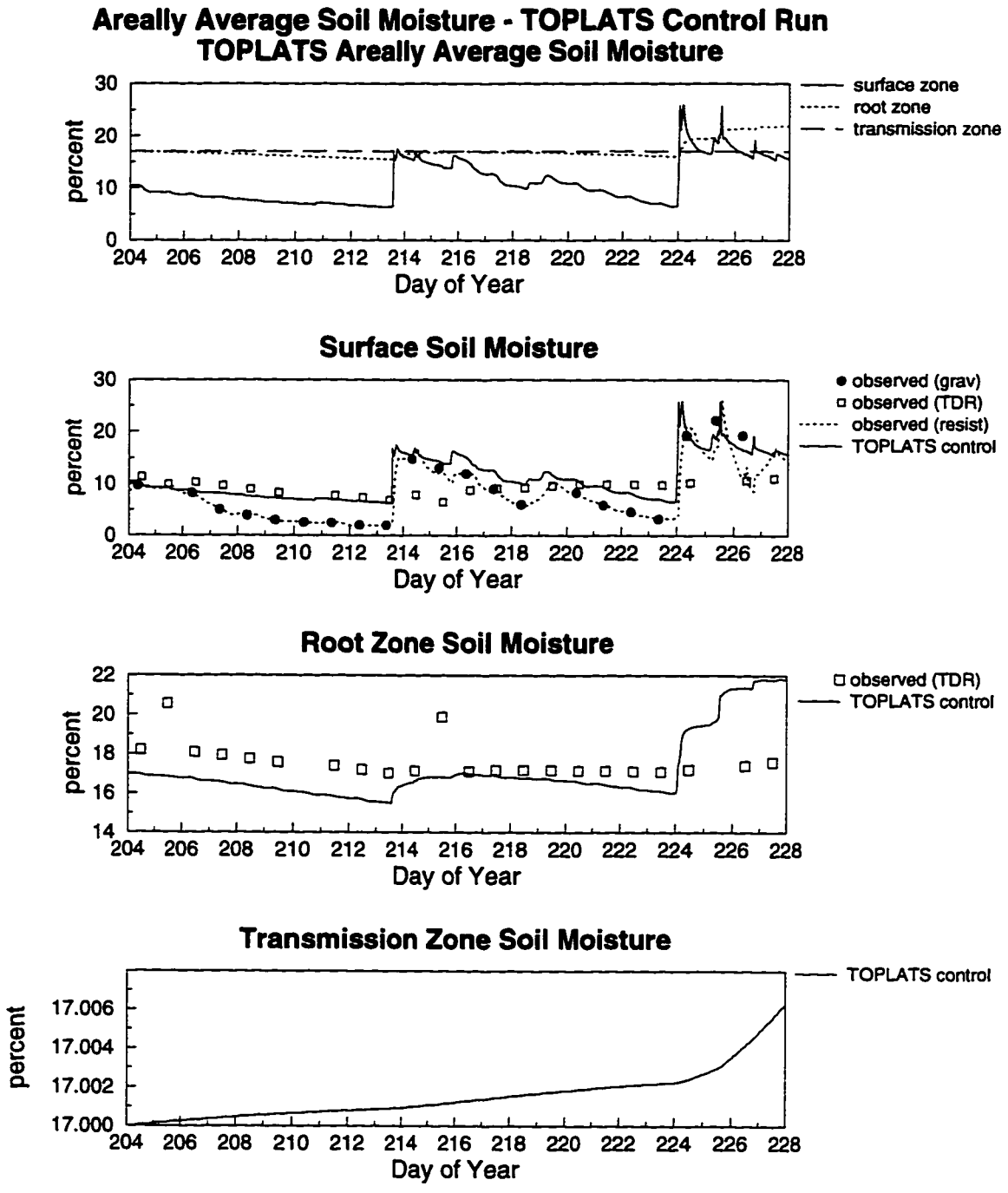

Figure G.6: TOPLATS calibrated control run watershed average soil moisture.

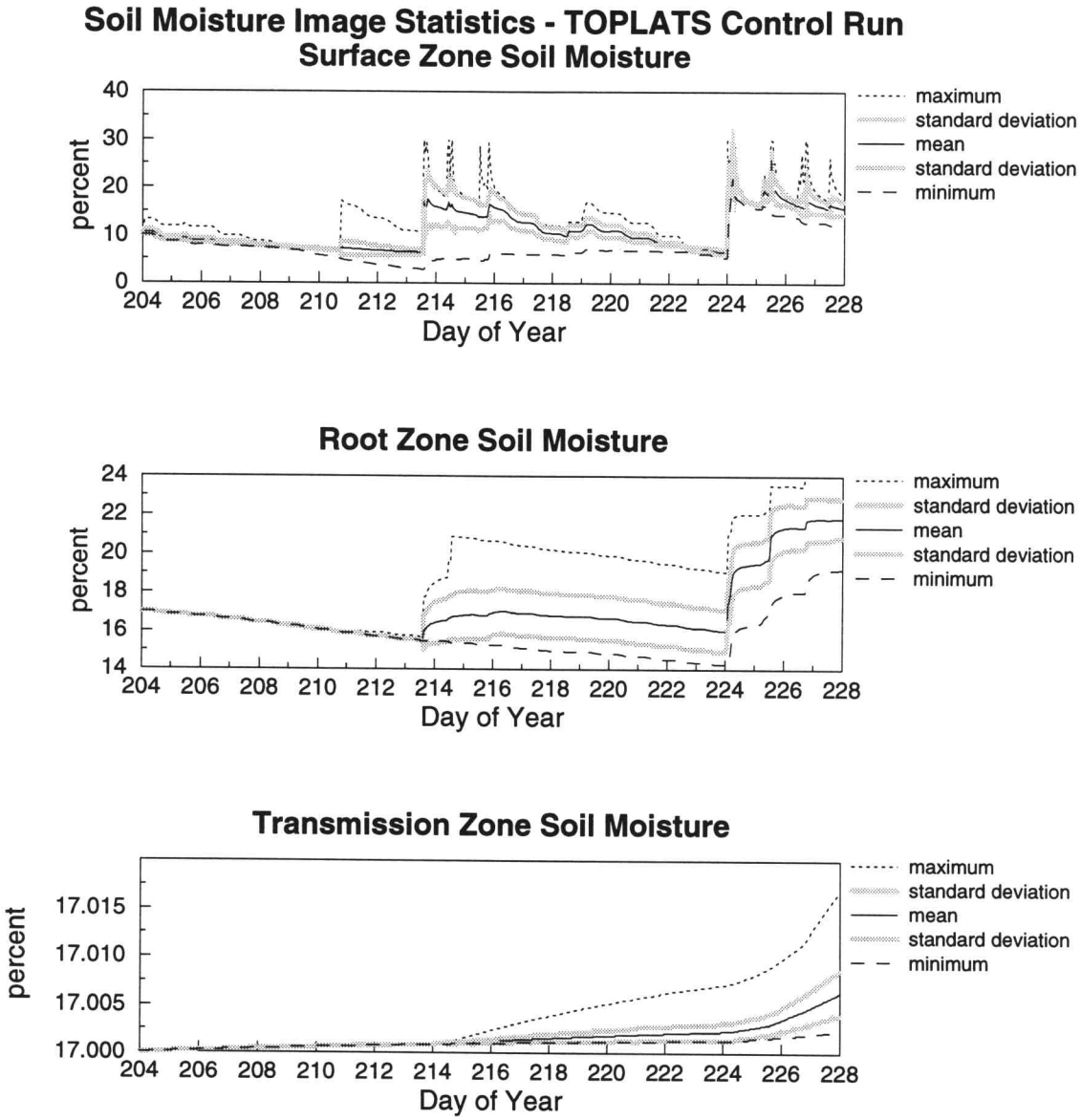

Figure G.7: TOPLATS calibrated control run soil moisture watershed statistics.

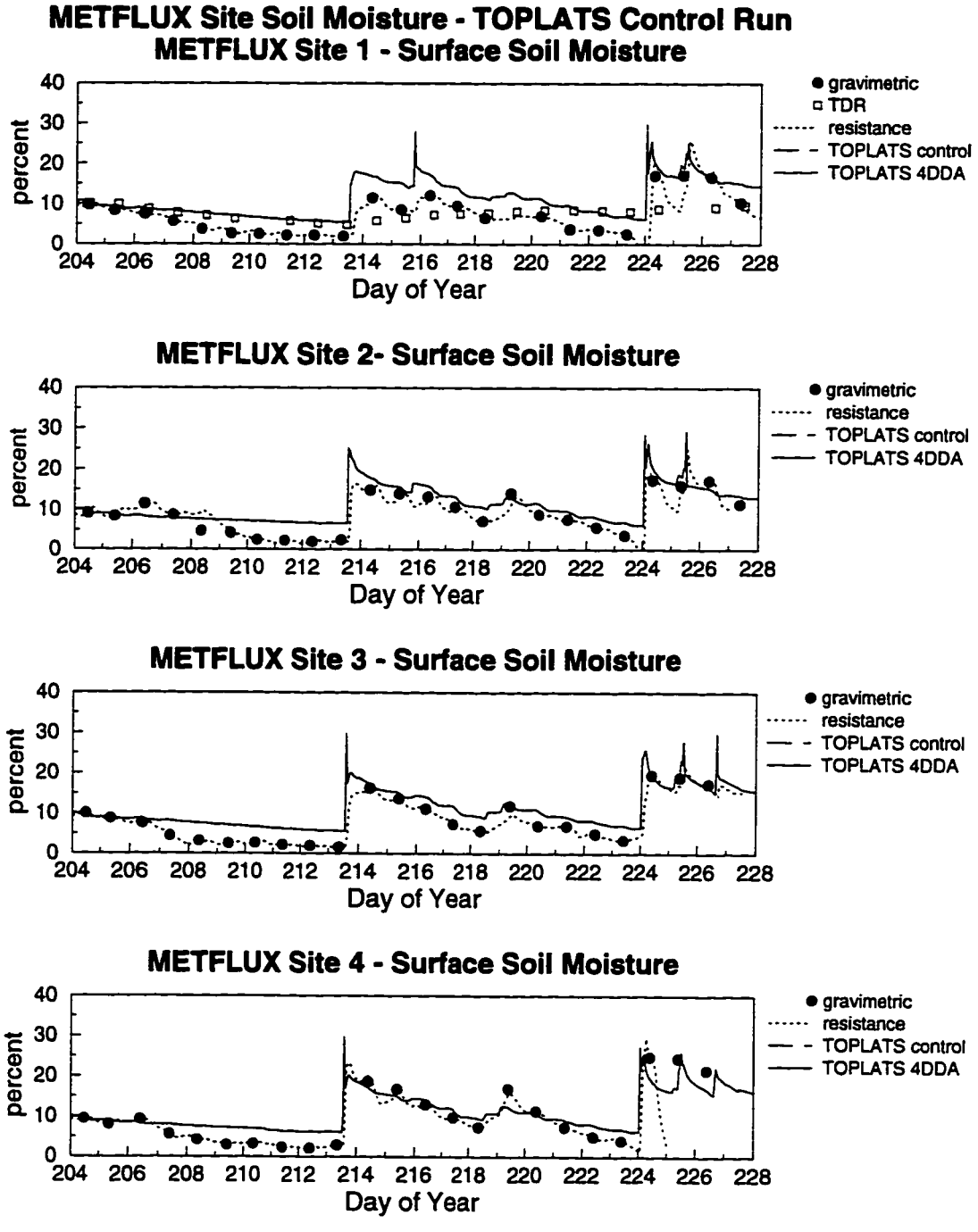

Figure G.8: TOPLATS calibrated control run Metflux sites 1-4 surface soil moisture.

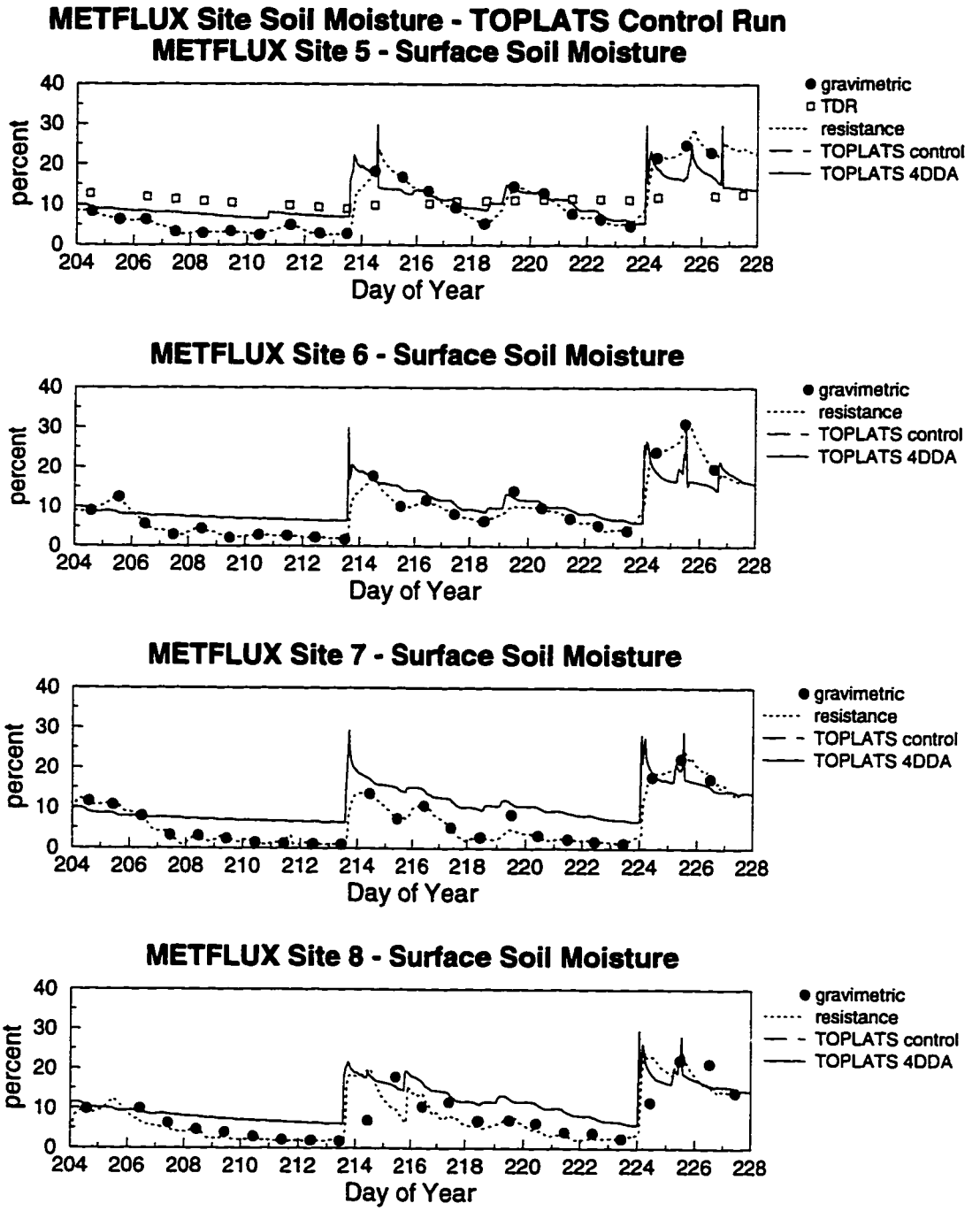

Figure G.9: TOPLATS calibrated control run Metflux sites 5-8 surface soil moisture.

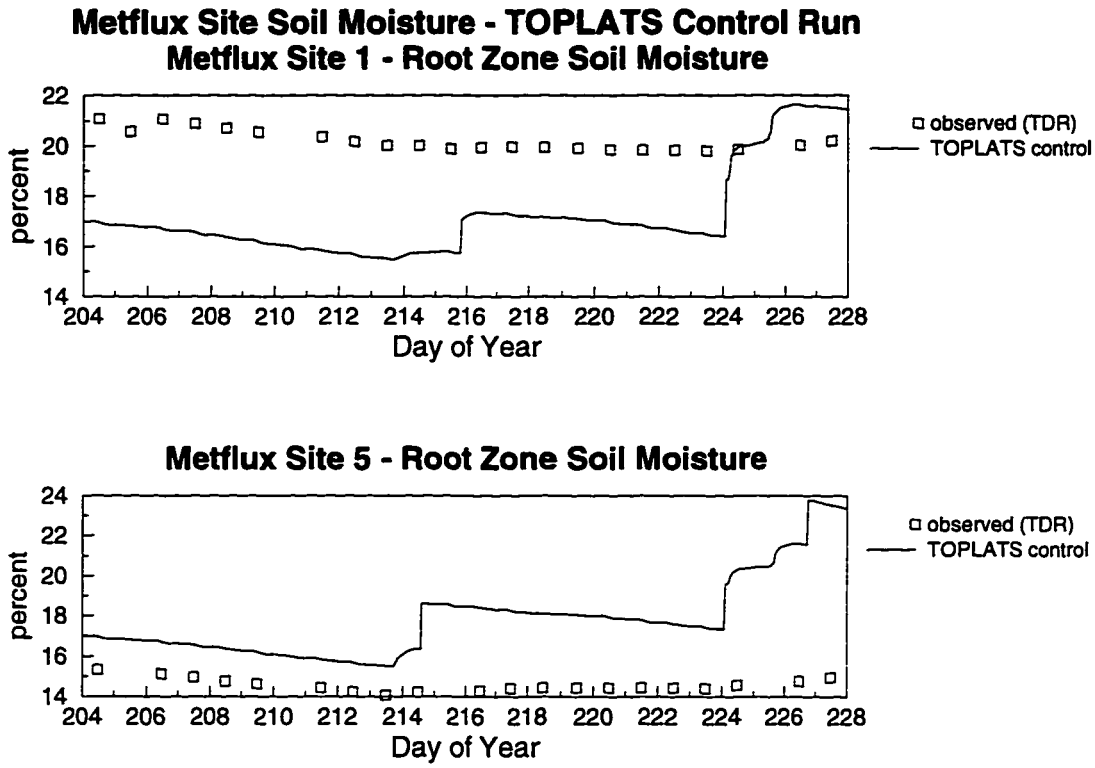

Figure G.10: TOPLATS calibrated control run Metflux sites 1 and 5 root zone soil moisture.

APPENDIX H: PERMISSIONS

Permission for all copyrighted illustrations is included below. Most permissions were granted via electronic mail, and are therefore reprinted here with headers for authenticity.

To: Paul Houser <houser@hwr.arizona.edu>
From: tmlilles@facstaff.wisc.edu (Thomas M. Lillesand)
Subject: Re: Permission

Mr. Houser:

Reprinting the figure in the context of your dissertation is fine. It would be appeciated if the figure legend would state the source and the fact that you obtained the authors' permission to reprint the figure.

Good luck on your work.

Tom Lillesand

Date: 13 Jul 1996 09:54:36 -0500
From: "Rick Lawford" <lawford@ogp.noaa.gov>
Subject: Re: Permission
To: "Paul Houser" <houser@hwr.arizona.edu>

Reply to: RE>Permission

Paul:

Permission granted - I assume you will reference it appropriately. Good luck in completing your thesis.

Rick Lawford

To: Paul "R." Houser <houser@hwr.arizona.edu>
From: Thomas Jackson <tjackson@hydrolab.arsusda.gov>
Subject: Re: Permission
Date: Fri, 12 Jul 96 11:08:08 EDT

Paul,

Yes you may use the figure. If you need an actual signature, send me a draft letter and I'll sign it.

Tom

Thomas J. Jackson

Date: Fri, 12 Jul 1996 16:21:44 -0500
From: jfamiglt@maestro.geo.utexas.edu (Jay Famiglietti)
Apparently-To: houser@hwr.arizona.edu

sure,
but it probably needs to be on u.t. letterhead (which i don't have here) so i'll do it when i get back. i'm sure you'll need to remind me, so just drop me another request around a week from Monday.
jay
ps i see that judith has been busy making movies

Date: Sun, 14 Jul 1996 23:13:01 -0700 (MST)
From: David Goodrich <goodrich@tucson.ars.ag.gov>
To: "Paul R. Houser" <houser@hwr.arizona.edu>
Subject: Re: Permission

Paul,

It is no problem to use them if they are adequately referenced.

I.E. after the figure caption reference as follows:

Figure 1.1. ... caption ... (from Kustas and Goodrich, 1994).

This is the way it is normally done but you may also want to check the fine print of WRR but I believe they allow copying with acknowledgment.

Cheers, Dave

Date: Fri, 19 Jul 1996 09:33:52 -0700 (MST)
From: Cary White <cary@hwr.arizona.edu>
To: houser@hwr.arizona.edu
Subject: Re: Permission

Paul Houser
Dept. of Hydorology and Water Resources
The University of Arizona
Tucson, AZ

Dear Paul,

You are more than welcome to excerpt portions of my Thesis for use in your dissertation. This includes data description text and figures and/or other material you feel is applicable.

Cary White

Date: Mon, 22 Jul 1996 09:29:53 -0400 (EDT)
From: Tom Schmugge <schmugge@hydrolab.arsusda.gov>
To: "Paul R. Houser" <houser@hwr.arizona.edu>
Subject: Re: Permission

Paul,

Yes you have my permission to use the figures you listed and any others from my publications that you may need with proper acknowledgement

Best wishes and if you need another reviewer for your thesis I would be happy to serve as one.

Tom Schmugge

PS I've been away for two weeks and thus the delay in reponding. Give my best to Jim

---

Date: Fri, 02 Aug 96 16:43:12 PST
From: "Paul W. Adams" <adamsp@ccmail.orst.edu>
To: houser@hwr.arizona.edu
Subject: Use of Publication Figure

Paul,

As far as the authors are concerned, you're most welcome to use the figure in your dissertation as long as the source is identified. I'm not positive, but Elsevier Publishers in Amsterdam may actually hold the copyright, so they might be the only ones who can officially grant permission for use. On the other hand, the research was federally funded & the two co-authors were federal employees, and in these circumstances I believe the publisher cannot restrict the use of the material. Also, as I understand it, unless someone profits from the duplication of the dissertation, material like this can be used under the "fair use" law. Perhaps you can get some advice from your Graduate School about this.

Best wishes for a successful Ph.D. defense!

Paul Adams, Ph.D.
Professor & Extension Specialist
Oregon State University
Forest Engineering Dept.
Peavy Hall 213
Corvallis, OR 97331
Ph. 541-737-2946
Fax 541-737-4316
e-mail: adamsp@ccmail.orst.edu

Date: Tue, 6 Aug 1996 11:43:42 +0100
To: houser@hwr.arizona.edu
From: haefner@geo.unizh.ch (Harold Haefner)

Dear Mr. Houser,

In reply to your e-mail of 23rd July, I can give you permission to use several figures from the thesis of Dr. Roger Meier provided that full reference/credit is given to him.

Nevertheless, I must remind you that these research activities have been carried out long ago with - for todays standards very limited / antiquated technical and methodological tools.

Yours sincerely, Prof. Dr. Haefner

Date: Tue, 06 Aug 1996 07:46:30 -0400
To: houser@hwr.arizona.edu (Paul R. Houser)
From: wang@sensor.gsfc.nasa.gov (James R. Wang)
Subject: Use of Figures

Dear Mr. Houser:
Sure you can use the fiugres in the paper published in the Remote Sensing of Environment, as long as you give the proper references.
Sincerely,
J. Wang

Date: Tue, 06 Aug 1996 07:50:30 -0400
To: houser@hwr.arizona.edu (Paul Houser)
From: wang@sensor.gsfc.nasa.gov (James R. Wang)
Subject: Use of figures

Dear Mr. Houser:
Of course you can use the figures published in the remote sensing of environment, as long as proper reference is given in your writeup. Good luck.
Sincerely,
J. Wang

Date: Thu, 26 Sep 96 07:51:56 CDT
From: gunst@galton.stat.smu.edu (Richard F. Gunst)
To: houser@hwr.arizona.edu
Subject: Figure 1

Paul,

I received your e-mail message about Figure 1. I have no objections to your using the figure. If you want to reprint the figure, you need to get permission from The Journal of Climate since they hold the copyright on the paper.

Dick Gunst

Subject: Re: Permission (fwd)
To: houser@hwr.arizona.edu (Paul R. Houser)
Date: Thu, 26 Sep 1996 09:12:03 -0400 (EDT)

Yes, thanks for asking.

>
> Dr. Milly,
>
> I would like to ask permission to use a figure (with proper references) in
> my dissertation literature review from your paper:
>
> Milly, P. C. D., 1986. Integrated remote sensing modeling of soil
> moisture: sampling frequency, response time, and accuracy of estimates.
> Integrated Design of Hydrological Networks (Proceedings of the Budapest
> Symposium, July 1986). IHAS Publ. no. 158, p. 201-211.
>
> Is this acceptable?
>
> Thanks, Paul Houser

Date: Thu, 26 Sep 96 16:19 EDT
From: "Jay Charney" <JJC11@PSUVM.PSU.EDU>
Subject: Re: permission
To: houser@HWR.ARIZONA.EDU

Paul,

>I am in the process of writing my dissertation literature review, and
>would like to ask permission to use a figure (400 mb zonal wind field at
>49 N) from your paper: "Use of incomplete historical data to infer the
>present state of the atmosphere:, 1969.

I am sorry to disappoint you, but I am not that Dr. Charney. I believe the paper you are referring to was authored by Jule Charney who died in 1984. In any event, you should be able to use the figure and reference the paper without having any problems from his estate or the publisher of the paper.

Good luck,
--Jay Charney
Penn State Meteorology

Date: Fri, 27 Sep 1996 11:09:09 -0400
From: bloom@dystopia.gsfc.nasa.gov (Stephen C. Bloom)
To: houser@hwr.arizona.edu
Subject: Re: Permission

Although Wayman Baker was the lead author on that paper, I really don't see his having any problems with your use of that figure. I am mildly curious, however, as to what use you indend for that figure.

Stephen Bloom

Stephen C. Bloom | Data Assimilation Office
Wk (301) 286-7349 | Code 910.3
Fx (301) 286-1757 | NASA/Goddard Space Flight Center
bloom@dystopia.gsfc.nasa.gov | Greenbelt, MD 20771

Date: Sat, 28 Sep 1996 00:15:25 -0600
To: "Paul R. Houser" <houser@hwr.arizona.edu>
From: Tom Schlatter <schlatter@fsl.noaa.gov>
Subject: Re: permission

Paul, I certainly have no problem with your using a few figures in your dissertation. I think the AMS has no problem with this, either, since it is research related. Good luck in your work. Tom

---

From: seaman@a01.meteo.psu.edu
Date: Tue, 1 Oct 1996 18:20:33 GMT
To: houser@hwr.arizona.edu
Subject: Re: permission

Dear Paul:

Feel free to help yourself!

Nelson Seaman

Date: Wed, 2 Oct 1996 12:35:26 -0700
From: daley@nrlmry.navy.mil (Dr. Roger Daley)
To: houser@hwr.arizona.edu
Subject: permission

Dear Mr. Houser

You certainly have my permission to use the figures from my book. However, please be advised that the copyright is held by Cambridge, and that you should contact them.

Best wishes

Roger daley

The following is a reprint of a FAX that was received on 8/8/1996 from Dr. Sabins:

Floyd F. Sabins
UCLA
3806 Geology
Box 951567
Los Angeles, CA 90095-1567

Dr. Sabins,

I am in the process of writing my dissertation, and would like to gain permission to use Figure 1.3 from your book "Remote Sensing, Principles and Interpretation" Second Edition, 1986. Please contact me at any of the above (Mail, Email, FAX), and let me know if I can use this figure with the appropriate reference.

Permission granted - good luck with your project
F F Sabins
8/8/96

Sincerely,

Paul R. Houser

REFERENCES

Abrahams, A. D., and A. J. Parsons, 1991. Relation between infiltration and stone cover on a semiarid hillslope, southern Arizona. *Journal of Hydrology*, **122**(1-4):49-59.

Adams, P. W., A. L. Flint, and R. L. Fredriksen, 1991. Long-term Patterns in Soil Moisture and Revegetation after a Clearcut of a Douglas-fir Forest in Oregon. *Forest Ecology and Management*, **41**:249-264.

Amer, S. A., T. O. Keefer, M. A. Weltz, D. C. Goodrich, and L. B. Bach., 1994. Soil Moisture Sensors for Continuous Monitoring. *Water Resources Bulletin*. **30**(1):69-83.

Andre, J., J. Goutorbe, and A. Perrier, 1986. HAPEX-MOBILHY: A Hydrologic Atmospheric Experiment for the Study of Water Budget and Evaporation Flux at the Climatic Scale. *Bulletin of the American Meteorological Society*, **67**(2):138-144.

Anthes, R. A., 1974. Data Assimilation and initialization of hurricane prediction models. *Journal of Atmospheric Science*, **31**:702-719.

Asrar, G. and D. J. Dokken, editors, 1993. EOS Reference Handbook. Earth Science Support Office; Document Resource Facility.

Baker, W. E., S. C. Bloom, J. S. Woollen, M. S. Nestler, E. Brin, T. W. Schlatter, and G. W. Branstator, 1987. Experiments with a Three-Dimensional Statistical Objective Analysis Scheme Using FGGE Data. *Monthly Weather Review*, **115**:272-296.

Basharinov, A. E., and A. M. Shutko, 1975. Simulation studies of the SHF radiation characteristic of soils under moist conditions. NASA Tech. Transl. TT F-16.

Basharinov, A. Y., and H. M. Shutko, 1978. Determination of the moisture content of the earth's cover by superhigh frequency (microwave) radiometric methods: A review. *Radiotek. Electron.*, **23**: 1778-1791 (Radio Engineering and Electronic Physics; English Translation, **23**:1-12)

Bell, K. R., B. J. Blanchard, T. J. Schmugge, and M. W. Witczak, 1980. Analysis of Surface Moisture Variations Within Large-Field Sites. *Water Resources Research*, **16**(4):796-810.

Bengtsson, L., 1975. 4-Dimensional Assimilation of Meteorological Observations. Global Atmospheric Research Programme (GARP), WMO-ICSU Joint Organizing Committee, GARP Publications Series, **15**.

Bengtsson, L., 1985. Four-Dimensional Data Assimilation. International Conference on the Results of the Global Weather Experiment and Their Implications for the World Weather Watch, Geneva, Switzerland, 27-31 May 1985, GARP Publications Series, **26**: 187-216.

Bengtsson, L., 1986. Four-Dimensional Data Assimilation. International Conference on the Results of the Global Weather Experiment and their Implications for the World Weather Watch, GARP Publications Series No. 26.

Benjamin, S. G., and N. L. Seaman, 1985. A simple scheme for objective analysis in curved flow. *Monthly Weather Review*, **113**:1184-1198.

Berglund, J., 1995. Development and Use of a Geographic Information System (GIS) for the Walnut Gulch Experimental Watershed. Unpublished report.

Bergthorsson, P., and B. R. Doos, 1955. Numerical weather map analysis. *Tellus*, **7**:329-340.

Betts, A. K., J. H. Ball, A. C. M. Beljaars, M. J. Miller, and P. Viterbo, 1994. Coupling between land-surface boundary-layer parameterizations and rainfall on local and regional scales: Lessons from the wet summer of 1993. 74th Annual Meeting, Fifth Symposium on Global Change Studies, Nashville, TN, American Meteorological Society, 174-181.

Beven, K., 1986. Runoff production and flood frequency in catchments of order n: an alternative approach. In V. K. Gupta, I. Rodriguez-Iturbe, and E. F. Wood (Eds.), Scale Problems in Hydrology, Reidel, Dordrecht, 107-131.

Beven, K., 1991. Spatially Distributed Modeling: Conceptual Approach to Runoff Prediction. In D. S. Bowles and P. E. O'Connell (eds.) Recent Advances in the Modeling of Hydrologic Systems, 373-387, Kluwer Academic.

Beven, K., 1995. The TOPMODEL Demonstration Programs. Centre for Research on Environmental Systems and Statistics, Institute of Environmental Systems and Biological Sciences, Lancaster University.

Beven, K., and E. F. Wood, 1983. Catchment Geomorphology and the Dynamics of Runoff Contribution Areas. *Journal of Hydrology*, **65**:139-158.

Beven, K., and M. J. Kirby, 1979. A physically based, variable contributing area model of basin hydrology. *Hydrological Sciences Bulletin*, **24**(1):43-69.

Beven, K.,A. Calver, and E. M. Morris, 1987. The Institute of Hydrology distributed model. Report 98, Institute of Hydrology, Wallingford, Oxon., United Kingdom.

Bhargava, M., and M. Danard, 1994. Application of Optimum Interpolation to the Analysis of Precipitation in Complex Terrain. *Journal of Applied Meteorology*, **33**:508-518.

Birkenheuer, D., 1996. Applying Satellite Gradient Moisture Information to Local-Scale Water Vapor Analysis Using Variational Methods. *Journal of Applied Meteorology*, **25**:24-35.

Blaikie, P., and H. Brookfield, 1987. Land Degredation and Society. Methuen, London.

Blanchard, B. J., M. J. Macfarland, T. J. Schmugge, and E. Rhodes, 1981. Estimation of Soil Moisture with API Algorithms and Microwave Emission. *Water Resources Bulletin*, **17**(5): 767-774.

Blanford, J. H., and L. W. Gay, 1992. Tests of a robust eddy correlation system for sensible heat flux. *Theoretical and Applied Climatology*, **46**(1), 53-60.

Bloom, S. C., L. L. Takacs, A. M. da Silva, and D. Ledevina, 1995. Data assimilation using incremental analysis updates. *Monthly Weather Review*, in press.

Bouttier, F., J. F. Mahfouf, and J. Noilhan, 1993 a. Sequential Assimilation of soil moisture from atmospheric low-level parameters, Part I: Sensitivity and calibration studies. *Journal of Applied Meteorology*, **32**(8):1335-1351.

Bouttier, F., J. F. Mahfouf, and J. Noilhan, 1993 b. Sequential Assimilation of soil moisture from atmospheric low-level parameters, Part II: Implementation in a mesoscale model. *Journal of Applied Meteorology*, **32**(8):1352-1364.

Brakensiek, D.L., and W. J. Rawls., 1994. Soil containing rock fragments: effects on infiltration. *Catena*, **23**:99-110.

Breckenfeld, D. J., 1993. Soil Survey of Walnut Gulch Experimental Watershed, Arizona. Soil Conservation Service unpublished document.

Brooks, R. H., and T. T. Corey, 1964. Hydraulic Properties of Porous Media. Hydrology Paper 3, Colorado State University.

Brutsaert, W. H., 1982. Evaporation into the atmosphere. D. Reidal, Boston, 299 pp.

Budgell, W. P., 1986. Nonlinear Data Assimilation for Shallow Water Equations in Branched Channels. *Journal of Geophysical Research*, **91**(C9):10633-10644.

Budyko, M. I., 1955. On the determination of evaporation from the land surface (in Russian), *Meteorol. Gidrol.*, **1**:52-58.

Buell, C., 1972. Correlation functions for wind and geopotential on isobaric surfaces. *Journal of Applied Meteorology*, **11**:51-59.

Burke, H. K., and W. J. Burke, 1979. Requirements of Space-Borne Microwave Radiometers for Detecting Soil Moisture Contents. *Satellite Hydrology*, American Water Resources Association, p. 377-383.

Bussieres, N. and W. Hogg, 1989. The Objective Analysis of Daily Rainfall by Distance Weighting Schemes on a Mesoscale Grid. *Atmosphere-Ocean*, Canadian Meteorological and Oceanographic Society, **27**(3):521-541.

Camillo, P. and T. J. Schmugge, 1983. Estimating soil moisture storage in the root zone from surface measurements. *Soil Science*, **135**(4):245-264.

Canuti, P., G. D'Auria, P. Pampaloni, and D. Solimini., 1992. MAC 91 on Montespertoli: An Experiment for Agro-Hydrology. International Geoscience and Remote Sensing Symposium 1992, The Institute of Electrical and Electronics Engineers, Inc., p. 1744-1746.

Carlson, T. N., E. M. Perry, and T. J. Schmugge, 1990. Remote Estimation of Soil Moisture Availability and Fractional Vegetation Cover for Agricultural Fields. *Agricultural and Forest Meteorology*, **52**: 45-69.

Carrol, T. R., 1981. Airborne Soil Moisture Measurement Using Natural Terrestrial Gamma Radiation. *Soil Science*, **132**(5):358-365.

Cavalieri, D. J., and K. M. St. Germain, 1995. Arctic Sea Ice Research With Satellite Passive Microwave Radiometers. *IEEE Geoscience and Remote Sensing Society Newsletter*, **97**:6-12.

Charney, J. G., M. Halem, and R. Jastrow, 1969. Use of incomplete historical data to infer the present state of the atmosphere. *Journal of Atmospheric Science*, **26**:1160-1163.

Chehbouni, A., J. P. Lhomme, E. G. Njoku, D. Nichols, D. Stannard, S. M. Moran, Y. H. Kerr, and B. Monteny, 1994. Estimation of Sensible Heat Flux Using Two and Three Components Model during Monsoon '90 Experiment. *IEEE. IGARSS '94*, 181-183.

Choudhury, B. J., T. J. Schmugge, A. Chang, and R. W. Newton, 1979. Effect of Surface Roughness on the Microwave Emission From Soils. *Journal of Geophysical Research*, **84**(C9): 5699-5706.

Chow, V. T., D. R. Maidment, and L. W. Mays, 1988. Applied Hydrology. McGraw-Hill Publishing Company.

Cognard, A., C. Loumagne, M. Normand, P. Olivier, C. Ottle, D. Vidal-Madjar, S. Louahala, and A. Vidal, 1995. Evaluation of the ERS/1 synthetic aperture radar capacity to estimate surface soil moisture: Two-year results over the Naizin watershed. *Water Resources Research*, **31**(4):975-982.

Cohn, S., 1982. Methods of Sequential Estimation for Determining Initial Data in Numerical Weather Prediction. Ph.D. thesis, Courant Institute of Mathematical Sciences, New York University, New York, NY, 183 p.

Courtier, P., and O. Talagrand, 1987. Variational assimilation of meteorological observations with the adjoint vorticity equation. II: Numerical results. *Q. J. R. Meterol. Soc.*, **113**:1329-1347.

Courtier, P., and O. Talagrand, 1990. Variational assimilation of meteorological observations with the direct and adjoint shallow-water equations. *Tellus*, **42A**:531-549.

Cressman, G. P., 1959. An Operational Objective Analysis System. *Monthly Weather Review*, **87**(10):367-374.

Daley, R., 1990 a. Applications of Kalman Theory to Atmospheric Data Assimilation. Mesoscale Data Assimilation, 1990 Summer Colloquium. National Center for Atmospheric Research, Boulder, Colorado, 6 June-3 July.

Daley, R., 1990 b. Basic Theory of Data Assimilation Part II: Continuous Data Assimilation Through Direct Insertion Methods. Mesoscale Data Assimilation, 1990 Summer Colloquium. National Center for Atmospheric Research, Boulder, Colorado, 6 June-3 July.

Daley, R., 1990 c. The Method of Successive Corrections. Mesoscale Data Assimilation, 1990 Summer Colloquium. National Center for Atmospheric Research, Boulder, Colorado, 6 June-3 July.

Daley, R., 1991. Atmospheric Data Analysis. Cambridge University Press.

Daughtry, C. S. T., M. A. Weltz, E. M. Perry, and W. P. Dulaney, 1991. Direct and Indirect Estimates of Leaf Area Index. Tenth Conference on Biometeorology and Aerobiology; Special Session on Hydrometeorology.

Deardorff, J. W., 1978. Efficient Prediction of Ground Surface Temperature and Moisture With Inclusion of a Layer of Vegetation. *Journal of Geophysical Research*, **83**(C4):1889-1903.

Deblonde, G., L. Garand, P. Gauthier, and C. Grassotti, 1995. Assimilation of SSM/I and GOES Humidity Retrievals with a One-dimensional Variational Analysis Scheme. *Journal of Applied Meteorology*, **34**:1536-1550.

Dick, T. M., 1992. Opening Remarks, Soil Moisture Modeling. Proceedings of the NHRC Workshop held March 9-10, 1992, NHRI Symposium No. 9 Proceedings.

Dickinson, R. E., 1984. Modeling evapotranspiration for three-dimensional global climate models. In *Climate Processes and Climate Sensitivity*, J. E. Hansen and T. Takahashi, editors, American Geophysical Union, Washington D.C., p. 58-72.

Dickinson, R. E., A. Henderson-Sellers, and P. J. Kennedy, 1993. Biosphere-Atmosphere Transfer Scheme (BATS) Version 1e as Coupled to the NCAR Community Climate Model. NCAR/TN-387+STR.

Dickinson, R. E., A. Henderson-Sellers, P. J. Kennedy, and M. F. Wilson, 1986. Biosphere-Atmosphere Transfer Scheme (BATS) for the NCAR Community Climate Model. NCAR Technical Note, NCAR/TN-275 + STR.

Dimet, F. L., and O. Talagrand, 1986. Variational algorithms for analysis and assimilation of meteorological observations: theoretical aspects. Tellus, **38A**:97-110.

Diskin, M. H., and L. J. Lane, 1972. A basinwide stochastic model for ephemeral stream runoff in south-eastern Arizona. *Int. Assoc. Hydrol. Sci.--Assoc. Int. Sci. Hydrol., Bull.* **17**(1):61-76.

Dobson, M. C., and F. T. Ulaby, 1986. Active Microwave Soil Moisture Research. *IEEE Transactions on Geoscience and Remote Sensing*, **GE-24**(1):23-36.

Dubois, P. C., J. J. van Zyl, and A. G. Guerra, 1992. Monsoon '90: Preliminary SAR Results. International Geoscience and Remote Sensing Symposium 1992, The Institute of Electrical and Electronics Engineers, Inc., p. 71-73.

Dunne, T., and L. B. Leopold, 1978. Water in Environmental Planning. W. H. Freeman and Company.

Eagleson, P. S., 1978. Climate, Soil, and Vegetation 3. A Simplified Model of Soil Moisture Movement in the Liquid Phase. *Water Resources Research*, **14**(5): 722-730.

Eley, J., 1992. Summary of Workshop, Soil Moisture Modeling. Proceedings of the NHRC Workshop held March 9-10, 1992, NHRI Symposium No. 9 Proceedings.

Eliassen, A., 1954. Provisional report on calculation of spatial covariance and autocorrelation of the pressure field. Report No. 5 (Oslo: Videnskaps-Akademiet Institut for Vaer og Klimaforskning).

Engman, E. T., 1991a. Applications of Microwave Remote Sensing of Soil Moisture for Water Resources and Agriculture. *Remote Sensing of Environment*, **35**:213-226.

Engman, E. T., 1991b. MACHYDRO-90: The Microwave Aircraft Experiment for Hydrology. International Geoscience and Remote Sensing Symposium 1991, The Institute of Electrical and Electronics Engineers, Inc., p. 749-751.

Engman, E. T., 1992a. Hydrologic Applications of SAR Derived Soil Moisture. International Geoscience and Remote Sensing Symposium 1992, The Institute of Electrical and Electronics Engineers, Inc., p. 1741-1743.

Engman, E. T., 1992b. Soil Moisture Needs in Earth Sciences. International Geoscience and Remote Sensing Symposium 1992, The Institute of Electrical and Electronics Engineers, Inc., p. 477-479.

Engman, E. T., 1995. Microwave Remote Sensing of Soil Moisture, Progress, Potential, and Problems. *IEEE IGARSS '95*, 489-491.

Enmark, H., 1993. ASTER Instrument Overview. ASTER Science Project internal presentation, 13 Aug. 1993.

Entekhabi, D., H. N., and E. G. Njoku, 1994. Solving the inverse problem for soil moisture and temperature profiles by sequential assimilation of multifrequency remotely sensed observations. *IEEE Transactions on Geoscience and Remote Sensing*, **32**(2):438-448.

Famiglietti, J. S., 1992. Aggregation and Scaling of Spatially-Variable Hydrological Processes: Local, Catchment-Scale and Macroscale Models of Water and Energy Balance. Dissertation, Dept. Of Civil Engineering and Operations Research, Princeton University.

Famiglietti, J. S., and E. F. Wood, 1991a. Evaporation and Runoff from Large Land Areas: Land Surface Hydrology for Atmospheric General Circulation Models. *Surveys in Geophysics*, **12**:179-204.

Famiglietti, J. S., and E. F. Wood, 1991b. Comparison of Passive Microwave and Model Derived Estimates for Soil Moisture Fields. *Proceedings of the 5th International Colloquium on Physical Measurements and Signatures in Remote Sensing*, Courcheval, France, European Space Agency, Noordwijk, The Netherlands.

Famiglietti, J. S., and E. F. Wood, 1994a. Application of multiscale water and energy balance models on a tallgrass prairie. *Water Resources Research*, **30**(11): 3061-3078.

Famiglietti, J. S., and E. F. Wood, 1994b. Multiscale modeling of spatially variable water and energy balance processes. *Water Resources Research*, **30**(11):3079-3093.

Famiglietti, J. S., E. F. Wood, M. Sivapalan, and D. J. Thongs, 1992. A catchment scale water balance model for FIFE. *Journal of Geophysical Research*, **97**(D17):18997-19007.

Famiglietti, J. S., P. R. Houser, and W. J. Shuttleworth, 1997. A Spatially-Distributed Hydrological Model (TOPLATS) for Soil Moisture Remote Sensing Applications. To be submitted to *Water Resources Research*.

Faurès, J-M, D. C. Goodrich, D. A. Woolhiser, and S. Sorooshian, 1995. Impact of small-scale spatial rainfall variability on runoff modeling. *Journal of Hydrology*, **173**:309-326.

Fennessey, N. M., P. S. Eagleson, W. Qinliang, and I. Rodriguez-iturbe, 1986. Spatial Characteristics of Observed Precipitation Fields: A Catalog of Summer Storms in Arizona. Volume 1 and 2. Report No: NASA-CR-176824 NASA-CR-176823

Feyen, J., C. Belmans, and D. Hillel, 1980. Comparison bwtween measured and simulated plant water potential during soil water extraction by potted ryegrass. *Soil Science*, **129**:180-185.

French, M. N., H. Andrieu, and W. Krajewski, 1994. A model for real-time quantative rainfall forecasting using remote sensing, 2, Case Studies. *Water Resources Research*, **30**(4):1085-1098.

Gandin, L. S., 1963. Objective Analysis of Meteorological Fields. Israel Program for Scientific Translations.

Gardner, W. R., 1958. Some steady-state solutions of the unsaturated moisture flow equation with application to evaporation from a water table. *Soil Science*, **85**:228-239.

Geleyn, J., 1990. Status Report on the French Mesoscale Operational Numerical Weather Prediction System. Summer Colloquium. National Center for Atmospheric Research, Boulder, Colorado, 6 June-3 July.

Georgakakos, K. P., and O. W. Baumer, 1994. Measurement and Analysis of On-site Soil Moisture Data. Soil Moisture Workshop, NASA, 25-28 January 1994.

Ghil, M., and P. Malanotte-Rizzoli, 1991. Data Assimilation in Meteorology and Oceanography. *Advances in Geophysics*, **33**:141-266.

Ghil, M., S. Cohn, J. Tavantzis, K. Bube, and E. Isaacson, 1981. Application of estimation theory to numerical weather prediction. Dynamic Meteorology: Data Assimilation Methods. Springer-Verlag, New York, NY, 139-224.

Gilbert, C. B., 1996. Personal Communication. Tombstone city clerk.

Goitom, T. G., and D. E. Woodward, 1988. Comparison of peak discharges of hydrologic models. *Hydraulic Engineering: Proceedings of the 1988 National Conference on Hydraulic Engineering*, Colorado Springs, CO, USA 1988 Aug 8-12. Publ by ASCE, Hydraulics Div, New York, NY, USA. p. 437-442.

Golding, B., 1990. The U. K. Meteorological Office Mesoscale Numerical Model Weather Prediction System (January 1990). Summer Colloquium. National Center for Atmospheric Research, Boulder, Colorado, 6 June-3 July.

Goodrich, D. C., 1993. Personal Communication.

Goodrich, D. C., 1996. Personal Communication. USDA-ARS Southwest Watershed Research Center, Tucson, Arizona.

Goodrich, D. C., D. A. Woolhiser, and T. O. Keefer, 1991. Kinematic routing using finite elements on a triangular irregular network. *Water Resources Research*, **27**(6):995-1004.

Goodrich, D. C., J-M Faurès, D. A. Woolhiser, L. J. Lane, and S. Sorooshian, 1995. Measurement and analysis of small-scale convective storm rainfall variability. *Journal of Hydrology*, **173**:283-308.

Goodrich, D. C., L. J. Lane, R. A. Shillito, S. N. Miller, K. H. Syed, D. A. Woolhiser, 1996. Linearity of Basin Response as a Function of Scale in a Semi-Arid Watershed, submitted to *Water Resources Research.*

Goodrich, D. C., T. J. Schmugge, T. J. Jackson, C. L. Unkrich, T. O. Keefer, R. Parry, L. B. Bach, and S. A. Amer, 1994. Runoff simulation sensitivity to remotely sensed initial soil water content. *Water Resources Research*, **30**(5):1393-1405.

Gunst, R. F., 1995. Estimating Spatial Correlations from Spatial-Temporal Meteorological Data. *Journal of Climate*, **8**:2454-2470.

Gupta, H. V., P. O. Yapo, and S. Sorooshian, 1996. Towards a New Paradigm for the calibration of Hydrologic Models. To be submitted for publication in *Water Resources Research.*

Gustafsson, N., 1990. An Overview of the HIRLAM Project and the Swedish PROMIS System. Summer Colloquium. National Center for Atmospheric Research, Boulder, Colorado, 6 June-3 July.

Haider, K. S., 1994. Spatial storm characteristics and basin response. M.S. Thesis, The University of Arizona, 261 pp.

Hartmann, H. C., 1995. Exploratory Geostatistical Analysis of Surface Soil Properties and Moisture Response for the Walnut Gulch Experimental Watershed, Arizona. Unpublished Report.

Hatfield, J. L., and M. Fuchs, 1990. Evapotranspiration Models. Management of Farm Irrigation Systems, American Society of Agricultural Engineers, p. 33-59.

Hawkins, R.H., F. .J. Wobber, and E. P. Springer., 1987. Remote Sensing-Arid Lands Workshop in Page, AZ, June 10-12, 1986. DOE/ER-0321.

Heilman, J. L., and D. G. Moore, 1979. Soil Moisture Applications of the Heat Capacity Mapping Mission. *Satellite Hydrology*, American Water Resources Association, p. 371-376.

Heilman, J. L., and D. G. Moore, 1981. HCMM Detection of High Soil Moisture Areas. *Remote Sensing of Environment*, **11**:73-76.

Hill, M. C., 1992. A computer program (MODFLOWP) for estimating parameters of a transient, three-dimensional ground-water flow model using nonlinear regression. U.S. Geological Survey Open-File Report, 91-484.

Hipps, L. E., E. Swiatek, and W. P. Kustas., 1994. Interactions between regional surface fluxes and the atmospheric boundary layer over a heterogeneous watershed. *Water Resources Research*, **30**(5):1387-1392.

Hoeksema, R. J., and P. K. Kitanidis, 1984. An application of the statistical approach to the inverse problem in two-dimensional groundwater modeling. *Water Resources Research*, **20**(7):1003-1020.

Hoke, J. E., and R. A. Anthes, 1976. The initialization of Numerical Models by Dynamic-Initialization Technique. *Monthly Weather Review*, **104**:1551-1556.

Horwitz, H., R. F. Nalepka, P. D. Hyde, and J. P. Morgenstern, 1977. Estimating the Proportions of Objects within a Single Resolution Element of a Multispectral Scanner. Proceedings Seventh International Symposium on Remote Sensing of Environment, Ann Arbor, Mich., **2**:1307-1320.

Hostetler, S. W., and F. Giorgi, 1993. Use of output from high-resolution atmospheric models in landscape-scale hydrologic models: An assessment. *Water Resources Research*, **29**(6):1685-1695.

Hou, Y. H., Y. R. Guo, and E. Westwater, 1993. Assimilation of precipitable water measurements into a mesoscale numerical model. *Monthly Weather Review*, **121**:1215-1238.

Houser, P. R., J. S. Famiglietti, W. J. Shuttleworth, and J. Berglund, 1996. Remote Sensing Soil Moisture using Four Dimensional Data Assimilation. American Geophysical Union, Spring 1996 conference.

Humes, K. S., W. P. Kustas and M. S. Moran, 1994a. Use of remote sensing and reference site measurements to estimate instantaneous surface energy balance components over a semi-arid rangeland watershed, *Water Resources Research*, **30**(5):1363.

Humes, K. S., W. P. Kustas, M. S. Moran, W. D. Nichols, and M. A. Weltz, 1994b. Variability of emissivity and surface temperature over a sparsely vegetated surface. *Water Resources Research*, **30**(5):1363-1373.

Ikawa, M., 1984. An Alternative Method of Solving Weak Constraint Problem and a Unified Expression of Weak and Strong Constraints in Variational Objective Analysis. *Papers in Meteorology and Geophysics*, **35**(3):71-79.

Jackson, T. J., 1980. Profile soil moisture from surface measurements. *Journal of the Irrigation and Drainage Division*, **106**:81-92.

Jackson, T. J., 1988. Research Toward an Operational Passive Microwave Remote Sensing System for Soil Moisture. *Journal of Hydrology*, **102**:95-112.

Jackson, T. J., 1996. The SGP97 Workshop. Personal communication.

Jackson, T. J., and T. J. Schumgge, 1991. Correction for the Effects of Vegetation on the Microwave Emission of Soils. International Geoscience and Remote Sensing Symposium 1991, The Institute of Electrical and Electronics Engineers, Inc., p. 753-756.

Jackson, T. J., D. M. Le Vine, A. Griffis, D. C. Goodrich, T. J. Schmugge, C. T. Swift, P. E. O'Neill, R. R. Roberts, and R. Parry, 1992. Soil Moisture Verification Study of the ESTAR Microwave Radiometer: Walnut Gulch, AZ 1991. International Geoscience and Remote Sensing Symposium 1992, The Institute of Electrical and Electronics Engineers, Inc., p. 486-488.

Jackson, T. J., M. E. Hawley, and P. E. O'Neill, P.E., 1987. Predicting soil moisture using passive microwave sensors. *Water Resources Bulletin*, **23**(1):11-19.

Jackson, T. J., T. J. Schmugge, and J. R. Wang, 1991. Passive Microwave Remote Sensing of Soil Moisture Under Vegetation Canopies. *Water Resources Research*, **18**:1137-1142.

Jacquemin, B., and J. Noilhan, 1990. Sensitivity study and validation of a land surface parameterization using Hapex-Mobilhy data set. *Boundary Layer Meteorology*, **52**:93-134.

Ji, J., 1988. A Simulating Test for Soil Moisture Sensing. International Geoscience and Remote Sensing Symposium 1988, The Institute of Electrical and Electronics Engineers, Inc., p. 1555-1556.

Jinno, L., A. Kawamura, R. Berndtsson, M. Larson, and J. Niemczynowicz, 1993. Real-time rainfall prediction at small space-time scales using a two-dimensional stochastic advection-diffusion model. *Water Resources Research*, **29**(5):1489-1504.

Johansen, O., 1975. Thermal conductivity of soils. Ph.D. thesis, Trondheim, Norway. (CRREL Draft Translation 637, 1977) ADA 044002.

Joiner, J., R. Atlas, S. Bloom, G. Brin, S. Cohn, A. Hou, D. Lamich, D. Ledvina, R. Ménard, L. Riishφjgarrd, R. Rood, A. da Silva, M. Sienkiewicz, J. Stobie, and R. Yang, 1996. New Data Types Working Document. DAO Office Note 96-13.

Jones, C., 1996. Global Weather Services From the U. K. World Wide Web Page: http://www.meto.govt.uk/sec5/NWP.

Jones, H. G., 1983. Plants and Microclimate: A Quantitative Approach to Environmental Plant Physiology. Cambridge University Press.

Julian, P., and H. J., Thiebaux, 1975. On some properties of correlation functions used in optimum interpolation schemes. *Monthly Weather Review*, **103**:605-616.

Kincaid, D. R., H. B. Osborn, and J. L. Gardner, 1966. Use of Unit-Source Watersheds for Hydrologic Investigations in the Semiarid Southwest. *Water Resources Research*, **2**(3):381-392.

Klute, A., Editor, 1986. Methods of Soil Analysis, Part 1 Physical and Mineralogical Methods, Second Edition. American Society of Agronomy, Inc.

Kolmogorov, A., 1941. Interpolated and extrapolated stationary random sequences. *Izvestia an SSSR, seriya mathematicheskaya*, **5**(2):85-95.

Kondratyev, K. Y. A., V. V. Malentyev, Y. U. I. Rabinovich, and E. M. Shulgina, 1977. Passive microwave remote sensing of soil moisture. 11th Symposium on Remote Sensing of the Environment. Eviron. Res. Inst. Mich., Ann Arbor, Mich., p. 1641-1661.

Koster, R. D., and M. J. Suarez, 1992. Modeling the land surface boundary in climate models as a composite of independent vegetation stands. *Journal of Geophysical Research*, **97**:2697-2715.

Kostov, K. G.,M. A. Michalev, N. M. Nedeltchev, A. Y. Spasov, B. I. Vichev, 1991. Bulgarian Effort Toward the Operational Use of Passive Microwave Remote Sensing of Soil Moisture. International Geoscience and Remote Sensing Symposium 1991, The Institute of Electrical and Electronics Engineers, Inc., p. 761-764.

Kuo, Y. H., and Y. R. Guo, 1989. Dynamic Initialization Using Observations from a Hypothetical Network of Profilers. *Monthly Weather Review*, **117**:1975-1998.

Kustas, W. P., M.S. Moran, R. D. Jackson, L. W. Gay, L. F. W. Duell, K. E. Kunkel, A. D. Matthias., 1990. Instantaneous and Daily Values of the Surface Energy Balance over Agricultural Fields Using Remote Sensing and a Reference Field in an Arid Environment. *Remote Sensing of Environment*, **32**:125-141.

Kustas, W. P., D. C. Goodrich, M. S. Moran, A. A. Amer, L. B. Bach, J. H. Blanford, A. Chehbouni, H. Claassen, W. E. Clements, P. C. Doraiswamy, P. Dubois, T. R. Clarke, C. S. Daughtry, D. I. Gellman, T. A. Grant, L. E. Hipps, A. R. Huete, K. S. Humes, T. J. Jackson, T. O. Keefer, W. D. Nichols, R. Parry, E. M. Perry, R. T Pinker, P. J. Pinter Jr., J. Qi, A. C. Riggs, T. J. Schmugge, A. M. Shutko, D. I Stannard, E. Swiatek, J. D. van Leeuwen, J. van Zyl, A. Vidal, J. Washburne, and M. A. Weltz, 1992. An interdisciplinary field study of the energy and water fluxes in the atmosphere-biosphere system over semiarid rangelands: Description and some preliminary results. *Bull. Am. Met. Soc.*, **72**(11):1682-1705.

Kustas, W. P. and D. C. Goodrich, 1994. Preface to the Special Section on MONSOON 90. *Water Resources Research*, **30**(5):1211-1225.

Kustas, W. P, J. H. Blanford, D. I. Stannard, C. S. J. Daughtry, W. D. Nichols, W. D., and M. A. Weltz, 1994a. Local energy flux estimates for unstable conditions using variance data in semiarid rangelands. *Water Resources Research*, **30**(5): 1351-1361.

Kustas, W. P., M. S. Moran, K. S. Humes, D. I. Stannard, P. J. Pinter, L. E. Hipps, E. Swiatek, E., and D. C. Goodrich, 1994b. Surface energy balance estimates at local and regional scales using optical remote sensing from an aircraft platform and atmospheric data collected over semi-arid rangelands. *Water Resources Research*, **30**(5): 1241-1260.

Kustas, W. P., T. J. Schmugge, K. S. Humes, T. J. Jackson, R. Parry, M. A. Weltz, and S. Moran, 1994c. Relationships between evaporative fraction and remotely sensed vegetation index and microwave brightness temperature for semiarid rangelands. *J. Appl. Meteorol.*, **32**(12): 1781-1790.

Kustas, W. P., E. M. Perry, P. C. Doraiswamy, and M. S. Moran, 1994d. Using Satellite Remote Sensing to Extrapolate Evapotranspiration Estimates in Time and Space over a Semiarid Rangeland Basin. *Remote sensing of environment*, **49**(3):275.

Kustas, W. P., L. E. Hipps, and K. S. Humes, 1995. Calculation of Basin-Scale Surface Fluxes by Combining Remotely Sensed Data and Atmospheric Properties in a Semiarid Landscape. *Boundary Layer Meteorology*, **73**(1-2):105.

Ladson, A. R., and I. D. Moore, 1992. Soil Water Prediction on the Konza Prairie by Microwave Remote Sensing and Topographic Attributes. *Journal of Hydrology*, **138**: 385-407.

Lange, A. A., 1989. Results of the WMO/CAS NWP Data Study and Intercomparison Project for forecasts for the northern hemisphere in 1988. World Weather Watch Technical Report No. 7, WMO/TD No. 317. World Meteorological Organization, Geneva.

Lawford, R. G., 1992. An Overview of Soil Moisture and its Role in the Climate System. Soil Moisture Modeling and Monitoring for Regional Planning, Proceedings of the NHRC workshop held March 9-10, 1992.

Le Vine, D. M., A. Griffis, C. T. Swift, and T. J. Jackson, 1992. ESTAR: A Synthetic Aperture Microwave Radiometer for Measuring Soil Moisture. International Geoscience and Remote Sensing Symposium 1992, The Institute of Electrical and Electronics Engineers, Inc., p. 483-485.

Lee, K. K., F. W. Deng, and J. H. Cushman, 1993. Multiscale adaptive estimation of the conductivity field from head and tracer data. *Stochastic Hydrology and Hydraulics*, **7**(1):66-82.

Lewis, J. M., 1990. Introduction to the Adjoint Method of Data Assimilation: Parts I and II. Mesoscale Data Assimilation, 1990 Summer Colloquium. National Center for Atmospheric Research, Boulder, Colorado, 6 June-3 July, p. 297-319.

Lewis, J. M., and J. C. Derber, 1985. The use of adjoint equations to solve a variational adjustment problem with advective constraints. *Tellus*, **37A**:309-322.

Li, Y., and J. Lewis, 1990. Assimilation Research at the Center for Analysis and Prediction of Storms: Application of an Elastic Mesoscale Model and its Adjoint for Data Assimilation. Mesoscale Data Assimilation, 1990 Summer Colloquium. National Center for Atmospheric Research, Boulder, Colorado, 6 June-3 July.

Lillesand, T. M., and R. W. Keifer, 1987. Remote Sensing and Image Interpretation, Second Edition. John Wiley and Sons.

Lin, D. S., E. F. Wood, J. S. Famiglietti, and M. Mancini, 1994. Impact of Microwave Derived Soil Moisture on Hydrologic Simulations Using a Spatially-Distributed Water Balance Model. *Proceedings of the 6th International Symposium on Physical Measurements and Signals in Remote Sensing*, European Space Agency, Val d'Isere, France.

Linsley, R. K., and M. R. Kohler, 1951. Predicting the runoff from storm rainfall. *U. S. Society of Engineers, Journal of the Hydraulics Division*, **91**(HY3):295-310.

Lönnberg, P., and A. Hollingsworth., 1986. The statistical structure of short-range forecast errors as determined from radiosonde data. Part II: The covariance of height and wind errors. *Tellus*, **38A**:137-161.

Loague, K., 1992. Soil water content at R-5. Part 1. Spatial and temporal variability. *Journal of Hydrology*, **139**:233-251.

Lorenc, A. C., 1981. A Global Three-Dimensional Multivariate Statistical Interpolation Scheme. *Monthly Weather Review*, **109**:701-721.

Lorenc, A. C., 1990a. Data Assimilation Methods: A Synthesis. Part I. Mesoscale Data Assimilation, 1990 Summer Colloquium. National Center for Atmospheric Research, Boulder, Colorado, 6 June-3 July.

Lorenc, A. C., 1990b. Data Assimilation Methods: A Synthesis. Part II. Mesoscale Data Assimilation, 1990 Summer Colloquium. National Center for Atmospheric Research, Boulder, Colorado, 6 June-3 July.

Lorenc, A. C., 1995a. Atmospheric Data Assimilation. Meteorological Office Forecasting Research Division Scientific Paper No. 34.

Lorenc, A. C., 1995b. Development of an Operational Variational Assimilation Scheme. *Journal of the Meteorological Society of Japan*, in review.

Lynch-Stieglitz, M., 1994. The Development and Validation of a Simple Snow Model for the GISS GCM. *Journal of Climate*, **7**:1842-1855.

Lyne, W. H., R., Swinbank, and N. T. Birch, 1982. A data assimilation experiment and the global circulation during the FGGE special observing periods. *Quarterly Journal of the Royal Meteorological Society*, **108**:575-594.

Maidment, D. R. editor, 1993. Handbook of Hydrology. McGraw-Hill, Inc.

Manabe, S., 1969. The atmospheric circulation and the hydrology of the earth's surface. *Monthly Weather Review*, **97**:739-774.

Mather, P. M., 1987. Computer Processing of Remotely Sensed Images: An Introduction, John Wiley and Sons.

Matthews, N., 1992. Interpolating Large-Scale Contour Information from Digital Terrain Data. U.S. Bureau of Land Management internal report.

Mayeux, B. C., 1995. The Relative Importance of Rainfall Intensity versus Saturated Hydraulic Conductivity for Runoff Modeling of a Semi-arid Watershed. Master's thesis, The University of Arizona, Department of Hydrology and Water Resources.

McCumber, M. C., and R. A. Pielke, 1981. Simulation of the effects of surface fluxes on heat and moisture in a mesoscale numerical model. *Journal of Geophysical Research*, **97**(11):739-774.

McFarland, M. J., 1992. An Overview of Soil Moisture Monitoring with Passive Microwave. Soil Moisture Modeling, Proceedings of the NHRC workshop held March 9-10.

McLaughlin, D., 1995. Recent developments in hydrologic data assimilation. *Reviews of Geophysics*, Supplement: U.S. National Report to International Union of Geodesy and Geophysics 1991-1994, p. 977-984.

McLaughlin, D. Entekhabi, S. Islam, M. French, and R. Bras, 1990. A distributed filtering approach to rainfall prediction. Proceedings on the Eight Conference on Hydrometeorology.

McPherson, R. D., K. H. Bergman, R. E. Kistler, G. E. Rasch, and D. S. Gordon, 1979. The NMC Operational Global Data Assimilation System. *Monthly Weather Review*, **107**: 1445-1461.

Medina, A., J. Carrera, and G. Galarza, 1990. Inverse modeling of coupled flow and solute transport problems. Proceedings of ModelCARE 90 Conference on Calibration and Reliability in Groundwater Modeling, K. Kovar (ed.), IAHS Publication 195.

Meier, R., 1981. Soil Moisture Detection with Microwave- and Thermal Infrared- Sensors in the Catchment Area Rietholzbach (Switzerland). Department of Geography, Remote Sensing Section, University of Zurich.

Menenti, M. and J. C. Ritchie, 1994. Estimation of effective aerodynamic roughness of Walnut Gulch Watershed with laser altimeter measurements. *Water Resources Research*, **30**(5):1329-1337.

Milly, P. C. D., 1986a. Integrated remote sensing modeling of soil moisture: sampling frequency, response time, and accuracy of estimates. Integrated Design of Hydrological Networks (Proceedings of the Budapest Symposium, July 1986). IHAS Publ. no. 158, p. 201-211.

Milly, P. C. D., 1986b. An event-based simulation model of moisture and energy fluxes at a bare soil surface. *Water Resources Research*, **22**:1680-1692.

Milly, P. C. D., 1991. A refinement of the combination equations for evaporation. *Survey of Geophysics*, **12**:145-154.

Mitchell, K., J. Schaake, and H. L. Pan, 1994. Land Surface Modeling and Assimilation Initiatives for GCIP NMC Mesoscale ETA Model. Global Energy and Water Cycle Experiment News, **4**(1):5-9.

Mkrtchjan, F. A., E. A. Teutov, A. M. Shutko, K. G. Kostov, M. A. Michalev, M. N. Nedeltchev, A. Y. Spasov, and B. I. Vichev, 1988. Microcomputer-based radiometer data acquisition and processing system for large area mapping of soil moisture content in the top one meter layer. Proceedings of the IGARSS '88 Symposium, Edinburgh, Scotland, 13-16 Sept. 1988, p. 1563-1564.

Mo, T., T. J. Schmugge, and B. J. Chodhury, 1980. Calculations of the spectral nature of the microwave emission from soils. NASA Technical Memo 82002, Greenbelt, MD.

Molod, A., H. M. Helfand, and L. L. Takacs, 1996. The Climatology of Parameterized Physical Processes in the GEOS-1 GCM and Their Impact on the GEOS-1 Data Assimilation System. *Journal of Climate*, **9**:764-785.

Moran, M.S., W. P. Kustas, A. Vidal, D. I. Stannard and J. Blanford, 1991. Use of ground-based remotely sensed data for surface energy balance calculations during Monsoon '90. *Proc. IGARSS 91 IEEE Geosci. and Rem. Sens. Symp.*, 3-6 June, Espoo, Finland, p. 33-37.

Moran, M. S., T. R. Clarke, W. P. Kustas, M. Weltz, and S. A. Amer, 1994a. Evaluation of hydrologic parameters in a semi-arid rangeland using remotely sensed spectral data. *Water Resources Research*, **30**(5):1287-1297.

Moran, M. S., W. P. Kustas, A. Vidal, D. I. Stannard, J. H. Blanford, and W. D. Nichols, 1994b. Use of ground-based remotely sensed data for surface energy balance evaluation of a semiarid rangeland. *Water Resources Research*, **30**(5):1339-1349.

Moran, M. S., D. C. Goodrich, and W. P. Kustas, 1994c. Integration of remote sensing and hydrologic modeling through multi-disciplinary semiarid field campaigns: MONSOON'90, Walnut Gulch '92, and SALSA-MEX. Sixth ISPRS International Sym. on Physical Measurements and Signatures in Remote Sensing, Val d'Isere, France, p. 981-991.

Munoz-Pardo, J., P. Rulle, and M. Vauclin, 1990. Spatial Variability of an Agricultural Field: Soil Texture, Soil Moisture and Yield Components of Two Rainfed Crops. *Catena*, **17**:369-381.

NASA, 1994. Space Shuttle Mission, STS-68: Space Radar Laboratory-2. NASA Press Kit, August 1994.

National Research Council (U.S.). Panel on Model-assimilated Data Sets for Atmospheric and Oceanic Research, 1991. Four-Dimensional Model Assimilation of Data: A Strategy for the Earth System Sciences. National Academy Press, Washington, D.C.

Newton, R. W., 1979. Characteristics of Microwave Emission of Significance to Satellite Remote Sensing of Soil Water. *Satellite Hydrology*, American Water Resources Association, p. 353-361.

Nichols, M. H, L. J. Lane, H. M. Arias,, and C. Watts, 1994. Comparative modeling of large watershed responses between Walnut Gulch, Arizona, USA, and Sonora, Mexico *IAHS-AISH publication*, **224**:351.

Nichols, M. H., L. J. Lane, and C. Manetsch, 1993. Analysis of spatial and temporal precipitation data over a densely gaged experimental watershed. *Management of Irrigation and Drainage Systems : Integrated Perspectives 1993*, Publ by ASCE, New York, NY, USA. p. 440-447.

Noilhan, J., and S. Planton, 1989. A simple parameterization of land surface process for meteorological models. *Monthly Weather Review*, **117**:536-549.

O'Neill, P., N. Chauhan, T. Jackson, and S. Saatchi, 1992. Synergistic Use of Active and Passive Microwave in Soil Moisture Estimation. International Geoscience and Remote Sensing Symposium 1992, The Institute of Electrical and Electronics Engineers, Inc., p. 492-494.

Ono, A., F. Sakuma, K. Arai, Y. Yamaguchi, H. Fujisada, P. Slater, K. Thome, F. Palluconi, and H. Kieffer, 1996. Preflight and in-flight Calibration Plan for Aster. *Journal of Atmospheric and Oceanic Technology*. **13**(2):321-335.

Osborn, H. B., and E. M. Larsen, 1973. Thunderstorm runoff in southeastern Arizona. *J. Hydraul. Div.*, ASCE, **99**(HY7):1129-1145.

Osborn, H. B., and L. Lane, 1969. Precipitation-Runoff Relations for Very Small Semiarid Rangeland Watersheds. *Water Resources Research*, **5**(2):419-425.

Osborn, H. B., and R. B. Hickok, 1968. Variability of Rainfall Affecting Runoff from a Semiarid Rangeland Watershed. *Water Resources Research*, **4**(1):199-203.

Osborn, H. B., K. G. Renard, and J. R. Simanton, 1979. Dense networks to measure convective rainfall in the southwestern United States. *Water Resources Research*, **15**(6):1701-1711.

Osborn, H. B., L. J. Lane, 1984. Climatic Change and Streamflow in the Southwest CONF-840744-2 American Society of Civil Engineers Irrigation and Drainage Div. specialty conference, Flagstaff, AZ, USA, 24 Jul 1984.

Palmer, W. C., 1965. Meteorological Drought. U.S. Department of Commerce, Weather Bureau research paper no. 45.

Paloscia, S., 1990. Multifrequency Microwave Radiometric Measurements of Soil Moisture. International Geoscience and Remote Sensing Symposium 1990, The Institute of Electrical and Electronics Engineers, Inc., p 1837-1840.

Pauwels, R. N., E. F. Wood, and T. J. Jackson, 1996. A combination of remote sensing and hydrological modeling to estimate soil moisture at the basin scale. In review, *Water Resources Research.*

Peebles, R., W., R. E. Smith, and S. J. Yakowitz, 1981. A leaky reservoir model for ephemeral flow recession. *Water Resources Research,* **17**(3):628-636.

Peters-Lidard, C. D., E. Blackburn, X. Liang, and E. F. Wood, 1996a. The effect of Ground Heat Flux Parameterization on Surface Energy Fluxes and Temperatures. Submitted to the *Journal of the Atmospheric Sciences, Special Issue on FIFE III.*

Peters-Lidard, C. D., M. S. Zion, and E. F. Wood, 1996b. A Soil-Vegetation-Atmosphere Transfer Scheme for Modeling Spatially Variable Water and Energy Balance Processes. Submitted to *Journal of Geophysical Research.*

Press, W. H., S. A. Teukolsky, W. T. Vetterling, and B. P. Flannery, 1986. Numerical Recipes in FORTRAN: The Art of Scientific Computing, Second Edition. Cambridge University Press.

Promes, P.M., T. J. Jackson, and P. E. O'Neill, 1988. Significance of agricultural row structure on the microwave emissivity of soils. *IEEE Trans. Geosci. Remote Sens.* **26**(5):580-589.

Quinn, P., and K. J. Beven, 1993. Spatial and Temporal Predictions of Soil Moisture Dynamics, Runoff, Variable Resource Areas, and Evapotranspiration for Plynlimon, Mid-Wales. *Hydrological Processes* **7**:425-448.

Quinn, P., K. Beven, P. Chevallier, and O. Planchon, 1991. The Prediction of Hillslope Flow Paths for Distributed Hydrological Modeling using Digital Terrain Models. *Hydrological Processes,* **5**:59-79.

Ragab, R., 1992. Assessment of the Relationship Between Remotely Sensed Topsoil Moisture Content and Profile Moisture Content. Soil Moisture Modeling and Monitoring for Regional Planning, Proceedings of the NHRC workshop held March 9-10.

Ragab, R., 1995. Towards a continuous operational system to estimate the root-zone soil moisture from intermittent remotely sensed surface moisture. *Journal of Hydrology,* **73**:1-25.

Rao, K. S., A. Sowmya, B. K. Mohan, P. Venkatachalam, N. Ahmed, R. L. Karale, and K. K. Narula, 1986. Computer-Aided Brightness Temperature Map of Indian Subcontinent - Inference on Soil Moisture Variations. *Remote Sensing of Environment,* **20**:195-207.

Rawls, W. J., L. R. Ahuja, D. L. Brakensiek, and A. Shirmohammadi, 1993. Infiltration and Soil Water Movement. In: Handbook of Hydrology; edited by D. R. Maidment, McGraw-Hill, Inc.

Renard, K. G., 1969. Evaporation from an ephemeral streambed - discussion (of paper 6368 by M. L. Sorey and W. G. Matlock, 1969). *Journal of the Hydraulics Division,* **95**(hy6):2200-2204.

Renard, K. G., L. J. Lane, J. R. Simanton, W. B. Emmerich, J. J. Stone, M. A. Weltz, D. C. Goodrich, and D. S. Yakowitz, 1993. Agricultural impacts in an arid environment: Walnut Gulch studies. *Hydrological Science and Technology,* **9**(1-4):145-190.

Reutov, E. A., and A. M. Shutko, 1986. Prior-knowledge based soil-moisture determination by microwave radiometry. *Soviet Journal of Remote Sensing*, **5**(1):100-125.

Reynolds, R. W., and T. M. Smith, 1994. Improved Global Sea Surface Temperature Analysis Using Optimum Interpolation. *Journal of Climate*, **7**:929-948.

Richards, L. A., 1931. Capillary Conduction of Liquids in Porous Mediums. *Physics* **1**:318-333.

Rood, R. B., S. E. Cohn, and L. Coy, 1994. Data Assimilation for EOS: The Value of Assimilated Data, Part 1. *The Earth Observer*, **6**(1):23-25.

Sabins, F. F. Jr., 1986. Remote Sensing Principles and Application. W. H. Freeman and Company.

Salvato, P. Jr., 1973. Iterative Techniques to Estimate Signature Vectors for Mixture Processing of Multispectral Data. Proc. Symposium on Machine Processing of Remotely Sensed Data. IEEE 73CH0834-2GE, **3B**:48-62.

Samper, J., J. Carrera, G. Galarza, and A. Medina, 1990. Application of an automatic calibration technique to modeling an alluvial aquifer. Proceedings of ModelCARE 90 Conference on Calibration and Reliability in Groundwater Modeling, K. Kovar (ed.), IAHS Publication 195.

Sasaki, Y., 1958. An objective analysis based on the variational method. *J. Meteor. Soc. Japan*, **36**:77-88.

Sasaki, Y., 1970. Some basic formalisms in numerical variational analysis. *Monthly Weather Review*, **98**:875-883.

Saxton, K.E., and A. T. Lentz, 1967. Antecedent retention indexes predict soil moisture. Journal of the Hydraulic Division, Proceedings of the American Society of Civil Engineers, p. 233-241.

Schlatter, T., 1975. Some Experiments with a Multivariate Statistical Objective Analysis Scheme. *Monthly Weather Review*, **103**:246-257.

Schmugge, T., 1985. Remote Sensing of Soil Moisture. *Hydrological Forecasting*, John Wiley and Sons.

Schmugge, T., 1995. Personal Communication.

Schmugge, T., A. Rango, and R. Neff, 1975. Satellite Microwave Observations of Soil Moisture Variations. NASA TN: No. X-71036.

Schmugge, T., and J. C. André, editors, 1991. Land Surface Evaporation; Measurement and Parameterization. Springer-Verlag.

Schmugge, T., and T. J. Jackson, 1991. A Dielectric Model of the Vegetation Effects on the Microwave Emission from Soils. International Geoscience and Remote Sensing Symposium 1991, The Institute of Electrical and Electronics Engineers, Inc., p. 757-759.

Schmugge, T., and T. J. Jackson, 1992. PBMR Observations of Surface Soil Moisture in Monsoon 90. International Geoscience and Remote Sensing Symposium 1992, The Institute of Electrical and Electronics Engineers, Inc., p. 480-482.

Schmugge, T., P. E. O'Neill, and J. R. Wang, 1986. Passive Microwave Soil Moisture Research. *IEEE Transactions on Geoscience and Remote Sensing*, **GE-24**(1):12-22.

Schmugge, T., T. J. Jackson, and H. L. McKim, 1980. Survey of Methods for Soil Moisture Determination. *Water Resources Research*, **16**(6):961-979.

Schmugge, T., T. J. Jackson, and H. L. McKim, 1979. Survey of In-Situ and Remote Sensing Methods for Soil Moisture Determination. *Satellite Hydrology*, American Water Resources Association.

Schmugge, T., T. J. Jackson, W. P. Kustas, and J. R. Wang, 1992. Passive Microwave Remote Sensing of Soil Moisture: results from HAPEX, FIFE and MONSOON 90. *ISPRS Journal of Photogrammetry and Remote Sensing*, **47**:127-143.

Schmugge, T., T. J. Jackson, W. P. Kustas, R. Roberts, R. Parry, D. C. Goodrich, S. A. Amer, and M. A. Weltz, 1994. Push broom microwave radiometer observations of surface soil moisture in Monsoon '90. *Water Resources Research*, **30**(5):1321-1328.

Schowengerdt, R. A., 1983. Techniques for Image Processing and Classification in Remote Sensing, Academic Press, Inc.

Schreiber, H. A., and D. R. Kincaid, 1967. Regression Models for Predicting On-Site Runoff from Short-Duration Convective Storms. *Water Resources Research*, **3**(2):389-395.

Seaman, N. L., 1990. Newtonian Nudging: A Four-Dimensional Approach to Data Assimilation. Mesoscale Data Assimilation, 1990 Summer Colloquium. National Center for Atmospheric Research, Boulder, Colorado, 6 June-3 July.

Sellers, P. J., Y. Mintz, and A. Dalcher, 1986. A simple biosphere model (SiB) for use within general circulation models. *Journal of Atmospheric Science*, **43**:505-531.

Shaw, R. H., and A. R. Pereira, 1982. Aerodynamic Roughness of a Plant Canopy: A Numerical Experiment. *Agricultural Meteorology*, **26**:51-65.

Shi, J., J. J. van Xyl, J. V. Soares, and E. T. Engman, 1992. Development of Soil Moisture Retrieval Algorithm for L-Band SAR Measurements. International Geoscience and Remote Sensing Symposium 1992, The Institute of Electrical and Electronics Engineers, Inc., p. 495-497.

Shi, J., J. V. Soares, L. Hess, E. T. Engman, and J. J. van Zyl, 1991. SAR-Derived Soil Moisture Measurements for Bare Fields. International Geoscience and Remote Sensing Symposium 1991, The Institute of Electrical and Electronics Engineers, Inc., p. 393-396.

Shuttleworth, W. J., 1993. Evaporation. In: Handbook of Hydrology; edited by D. R. Maidment, McGraw-Hill, Inc.

Shuttleworth, W. J., 1995. Personal Communication.

Shuttleworth, W. J., 1996. Personal Communication.

Shuttleworth, W. J., and R. J. Gurney, 1992. The theoretical relationship between foliage temperature and canopy resistance in sparse crops. *Q. J. R. Meteorol. Soc.* **116**:497-519.

Simanton, J. R., E. Rawitz, and E. D. Shirley, 1984. The effect of rock fragments on erosion of semiarid rangeland soils, Ch 7. In: Erosion and Productivity of Soils Containing Rock Fragments, SSSA Special Pub. 13:65-72.

Sivapalan, M., K. Beven, and E. F. Wood, 1987. On hydrologic similarity, 2, A scaled model of storm runoff production. *Water Resources Research*, **23**:2266-2278.

Smith, J. A., 1993. Precipitation. In: Handbook of Hydrology; edited by D. R. Maidment, McGraw-Hill, Inc.

Smith, R. E., D. C. Goodrich, D. A. Woolhiser, and C. L. Unkrich, 1995. KINEROS - A Kinematic Runoff and Erosion Model. Chapter 20 of Computer Models of Watershed Hydrology, Water Resources Pub., Highlands Ranch, CO., p. 697-732.

Soares, J. V., Bernard, R., O. Taconet, D. Vidal-Madjar, and A. Weill, 1988. Estimation of bare soil evaporation from airborne measurements. *Journal of Climate and Applied Meteorology*, **99**: 281-296.

Sorooshian, S., Huete, A., Woolhiser, D., Jackson, R., Slater, P., Smith, J., Warrick, A., and Wilkening, L., 1988. Utilization of EOS Data in Quantifying the Processes Controlling the Hydrologic Cycle in Arid/Semi-arid Regions. Research proposal to NASA, Earth Observing System (EOS), A.O. No. OSSA 1/88.

Sorooshian, S., Q. Duan, and V. K. Gupta, 1993. Calibration of Rainfall-Runoff Models: Application of Global Optimization to the Sacramento Soil Moisture Accounting Model. *Water Resources Research*, **29**(4):1185-1194.

Spangler, D. P., 1969. A Geophysical Study of the Hydrogeology of the Walnut Gulch Experimental Watershed, Tombstone, Arizona. Dissertation, The University of Arizona, Department of Geology.

Stannard, D. I., J. H. Blanford, W. P. Kustas, W. D. Nichols, S. A. Amer, T. J. Schmugge, and M. A. Weltz, 1994. Interpretation of surface flux measurements in heterogeneous terrain during Monsoon `90. *Water Resources Research*, **30**(5):1227-1239.

Stauffer, D. R., and N. L. Seaman, 1990. Use of Four-Dimensional Data Assimilation in a Limited-Area Mesoscale Model. Part I: Experiments with Synoptic-Scale Data. *Monthly Weather Review*, **118**:1250-1277.

Swain, P. H., and S. M. Davis, 1978. Remote Sensing: The Quantitative Approach, McGraw-Hill.

Talagrand, O., 1990. Variational Assimilation with the Adjoint Method Part II: Practice. Mesoscale Data Assimilation, 1990 Summer Colloquium. National Center for Atmospheric Research, Boulder, Colorado, 6 June-3 July.

Talagrand, O., and P. Courtier, 1987a. Variational assimilation of meteorological observations with the adjoint vorticity equation. I: Theory. *Quarterly Journal of the Royal Meteorological Society*, **113**:1311-1328.

Talagrand, O., and P. Courtier, 1987b. Variational assimilation of meteorological observations with the adjoint vorticity equation. II: Theory. *Quarterly Journal of the Royal Meteorological Society*, **113**:1329-1347.

Theis, S. W., B. J. Blanchard, and A. J. Blanchard, 1986. Utilization of active microwave roughness measurements to improve passive microwave soil moisture estimates over bare soils. *IEEE Trans. Geosci. Temote Sens.* **GE-24**(3):334-339.

Theis, S. W., B. J. Blanchard, and R. W. Newton, 1984. Utilization of vegetation indices to improve microwave soil moisture estimates over agricultural lands. *IEEE Trans. Geosci. Remote Sensing*, **GE-22**(6):490-496.

Thiebaux, H. J., 1976. Anisotropic correlation functions for objective analysis. *Monthly Weather Review*, **104**:994-1002.

Tromble, J. M., K. G. Renard, and A. P. Thatcher, 1974. Infiltration on three rangeland soil-vegetation complexes. *J. Range Manage.*, **27**:318-321.

Ulaby, F. T., G. A. Bradely, and M. C. Dobson, 1979. Potential Application of Satellite Radar to Monitor Soil Moisture. *Satellite Hydrology*, American Water Resources Association, p. 363-370.

Unland, H. E., P. R. Houser, W. J. Shuttleworth, and Z. L. Yang, 1996. Surface flux measurements and modeling at a semi-arid Sonoran desert site. *J. Agricultural and Forest Meteorology*, in press.

Van Den Berg, J. A., 1989. Towards the Regionalization of Hydraulic and Plant-Soil Parameters for Modeling Soil Moisture Conditions of a Catchment. *Earth Surface Processes and Landforms*, **14**: 615-629.

Van Geer, F. C., C. B. M. Te Stroet, and Z. Yangxian, 1991. Using Kalman filtering to improve and quantify the uncertainty of numerical groundwater simulations, 1. The role of system noise and its calibration. *Water Resources Research*, **27**(8):1987-1994.

Verseghy, D. L., 1991. CLASS - A Canadian Land Surface Scheme for GCMs. I. Soil Model. *International Journal of Climatology*, **11**: 111-133.

Wahba, G., and J. Wendelberger, 1980. Some New Mathematical Methods for Variational Objective Analysis Using Splines and Cross Validation. *Monthly Weather Review*, **108**:1122-1143.

Wang, J. R., and T. J. Schmugge, 1980. An empirical model for the complex dielectric permittivity of soils as a function of water content. *IEEE Trans. on Geoscience and Remote Sensing*, **GE-18**, 288-295.

Wang, J. R., T. J. Schmugge, J. C. Shiue, and E. T. Engman, 1989. Mapping Surface Soil Moisture with L-Band Radiometric Measurements. *Remote Sensing of Environment*, **27**:305-312.

Wang, W., and T. T. Warner, 1988. Use of four-dimensional data assimilation by Newtonian relaxation and latent heat forcing to improve a mesoscale-model precipitation forecast: A case study. *Monthly Weather Review*, **116**:2593-2613.

Washburne, J. C., 1994. A Distributed Surface Temperature and Energy Balance Model of a Semi-Arid Watershed. Dissertation, The University of Arizona, Department of Hydrology and Water Resources.

Wei, M. Y., 1995. Soil Moisture: Report of a Workshop Held in Tiburon, California 25-27 January 1994. NASA Conference Publication 3319.

Weiner, N., 1949. Extrapolation, interpolation and smoothing of stationary time series. John Wiley.

Weltz, M. A., J. C. Ritchie, and H. D. Fox, 1994. Comparison of laser and field measurements of vegetation height and canopy cover. *Water Resources Research*, **30**(5): 1311-1319.

Wetzel, P. J., and R. H. Woodward, 1987. Soil Moisture Estimation Using GOES-VISSR Infrared Data: A Case Study with a Simple Statistical Method. *Journal of Climate and Applied Meteorology*, **26**:107-117.

Whitaker, M. P. L., 1993. Small-Scale Spatial Variability of Soil Moisture and Hydraulic Conductivity in a Semi-Arid Rangeland Soil in Arizona. M.S. thesis, The University of Arizona, Tucson.

White, C. B,, 1996. Soil Moisture Variability in Land Surface-Atmosphere Interactions. M. S. thesis, Department of Hydrology and Water Resources, The University of Arizona.

White, C. B., P. R. Houser, A. M. Arain, Z.-L. Yang, K. Syed, and W. J. Shuttleworth, 1996. The aggregate description of semi-arid vegetation with precipitation-generated soil moisture heterogeneity. Submitted to *Hydrology and Earth System Sciences*.

Wilcox, B. P., M. K. Wood, and J. M. Tromble, 1988. Factors influencing infiltrability of semiarid mountain slopes. Journal of Range Management, 41(3):197-206.

Williams, D. G., 1996. Private Communication. RNR, The University of Arizona, Tucson, Arizona.

Williams, M. D., 1996. Evapotranspiration in southeastern Arizona semi-arid watersheds: Walnut Gulch and Cienega Creek. M.S. Thesis, The University of Arizona, 178 pp.

Wood, E., D. P. Lettenmaier, and V. G. Zatarian, 1992. A Land-Surface Hydrology Parameterization With Subgrid Variability for General Circulation Models. *Journal of Geophysical Research*, **97**(D3):2717-2728.

Wood, E., M. Sivapalan, K. Beven, and L. Band, 1988. Effects of spatial variability and scale with implications to hydrological modeling. *Journal of Hydrology*, **102**:29-47.

Yangxiao, Z., C. B. M. Te Stroet, and F. C. Van Geer, 1991. Using Kalman filtering to improve and quantify the uncertainty of numerical groundwater simulations, 2. Application to monitoring network design. *Water Resources Research*, **27**(8):1995-2006.

Zotova, E. N., and A. G. Geller, 1985. Soil moisture content estimation by radar survey data during the sowing campaign. *International Journal of Remote Sensing*, **6**(2):353-364.